ACS SYMPOSIUM SERIES 1084

Synthetic Liquids Production and Refining

EDITED BY

Arno de Klerk and David L. King

Synthetic Liquids Production and Refining

Downloaded by 89.163.35.42 on June 6, 2012 | http://pubs.acs.org
Publication Date (Web): November 29, 2011 | doi: 10.1021/bk-2011-1084.fw001

In Synthetic Liquids Production and Refining; de Klerk, A., et al.;
ACS Symposium Series; American Chemical Society: Washington, DC, 2011.

Downloaded by 89.163.35.42 on June 6, 2012 | http://pubs.acs.org
Publication Date (Web): November 29, 2011 | doi: 10.1021/bk-2011-1084.fw001

Downloaded by 89.163.35.42 on June 6, 2012 | http://pubs.acs.org
Publication Date (Web): November 29, 2011 | doi: 10.1021/bk-2011-1084.fw001

ACS SYMPOSIUM SERIES **1084**

Synthetic Liquids Production and Refining

Arno de Klerk, Editor
University of Alberta
Edmonton, Alberta, Canada

David L. King, Editor
Pacific Northwest National Laboratory
Richland, Washington, U.S.A.

Sponsored by the
ACS Division of Fuel Chemistry

American Chemical Society, Washington, DC

Distributed in print by Oxford University Press, Inc.

Downloaded by 89.163.35.42 on June 6, 2012 | http://pubs.acs.org
Publication Date (Web): November 29, 2011 | doi: 10.1021/bk-2011-1084.fw001

Library of Congress Cataloging-in-Publication Data

Synthetic liquids production and refining / Arno de Klerk, David L. King, editor[s] ; sponsored by the ACS Division of Fuel Chemistry.
p. cm. -- (ACS symposium series ; 1084)
Includes bibliographical references and index.
ISBN 978-0-8412-2681-4
1. Synthetic fuels. 2. Gases--Liquefaction. 3. Coal--Liquefaction. 4. Synthetic fuels--Refining. I. Klerk, Arno de. II. King, David L. III. American Chemical Society. Division of Fuel Chemistry.
TP360.S975 2011
662.6′6--dc23
2011043254

The paper used in this publication meets the minimum requirements of American National Standard for Information Sciences—Permanence of Paper for Printed Library Materials, ANSI Z39.48n1984.

Copyright © 2011 American Chemical Society

Distributed in print by Oxford University Press, Inc.

All Rights Reserved. Reprographic copying beyond that permitted by Sections 107 or 108 of the U.S. Copyright Act is allowed for internal use only, provided that a per-chapter fee of $40.25 plus $0.75 per page is paid to the Copyright Clearance Center, Inc., 222 Rosewood Drive, Danvers, MA 01923, USA. Republication or reproduction for sale of pages in this book is permitted only under license from ACS. Direct these and other permission requests to ACS Copyright Office, Publications Division, 1155 16th Street, N.W., Washington, DC 20036.

The citation of trade names and/or names of manufacturers in this publication is not to be construed as an endorsement or as approval by ACS of the commercial products or services referenced herein; nor should the mere reference herein to any drawing, specification, chemical process, or other data be regarded as a license or as a conveyance of any right or permission to the holder, reader, or any other person or corporation, to manufacture, reproduce, use, or sell any patented invention or copyrighted work that may in any way be related thereto. Registered names, trademarks, etc., used in this publication, even without specific indication thereof, are not to be considered unprotected by law.

PRINTED IN THE UNITED STATES OF AMERICA

Foreword

The ACS Symposium Series was first published in 1974 to provide a mechanism for publishing symposia quickly in book form. The purpose of the series is to publish timely, comprehensive books developed from the ACS sponsored symposia based on current scientific research. Occasionally, books are developed from symposia sponsored by other organizations when the topic is of keen interest to the chemistry audience.

Before agreeing to publish a book, the proposed table of contents is reviewed for appropriate and comprehensive coverage and for interest to the audience. Some papers may be excluded to better focus the book; others may be added to provide comprehensiveness. When appropriate, overview or introductory chapters are added. Drafts of chapters are peer-reviewed prior to final acceptance or rejection, and manuscripts are prepared in camera-ready format.

As a rule, only original research papers and original review papers are included in the volumes. Verbatim reproductions of previous published papers are not accepted.

ACS Books Department

Downloaded by 89.163.35.42 on June 6, 2012 | http://pubs.acs.org
Publication Date (Web): November 29, 2011 | doi: 10.1021/bk-2011-1084.fw001

Downloaded by 89.163.35.42 on June 6, 2012 | http://pubs.acs.org
Publication Date (Web): November 29, 2011 | doi: 10.1021/bk-2011-1084.pr001

Preface

Availability of affordable energy is a key factor in providing economic growth and an improved standard of living. For transportation, almost all of the liquid fuels are produced from crude oil. Alternative carbon sources are being used for transportation fuels only on a limited scale, and research efforts focusing on the conversion of coal, natural gas, biomass and waste to liquid products (XTL conversion) ebb and flow with the price of crude oil. Crude oil is still considered the cheapest and most convenient source of liquid fuels, despite continually voiced concerns regarding energy security. However, the cost-effective availability of crude oil could change, possibly dramatically, in a short period of time.

Against the backdrop of concern about CO_2-induced climate change, we are confronted with the "inconvenient reality" that over the medium term most of our energy requirements will be met by the conversion of fossil fuels. This is true both for transportation fuel production and for electric power generation. There was hope that in future nuclear power could significantly diminish the contribution of coal-based power generation (and CO_2 emissions), but this seems increasingly unlikely. The public perception of safety associated with nuclear power is moulded by the media and it was drastically undermined by the damage to the Fukushima nuclear power plant during the earthquake that struck Japan in March 2011.

There is also the looming spectre of "peak oil", the point in time when global crude oil production reaches a maximum. This is coupled by increasing demand for crude oil from the developing world. So, what do we do when there is a demand for liquid transportation fuels and petrochemicals, but crude oil is in short supply? The technological answer is to supplement conventional crude oil production with synthetic crude oil production. It is clear that society is not yet ready to forego carbon-based energy. Therefore, although it is not clear when a strong synthetic crude oil industry will emerge, but when it does emerge, it is essential that the best technology and technical understanding be available for application.

A symposium on "Coal-, Gas-, Biomass- and Waste-to-Liquids Conversion" was held at the 240th American Chemical Society National Meeting in Boston in August 2010. It provided the opportunity to gauge current activity and progress in this field. This work follows and builds upon previous symposia devoted to the study of biomass, coal and waste conversion.

The chapters cover carbon-based feed conversion, synthetic crude production and refining of the synthetic crude. It is our hope that this volume successfully captures some of the flavor and current thinking in carbon-based conversions.

In Synthetic Liquids Production and Refining; de Klerk, A., et al.;
ACS Symposium Series; American Chemical Society: Washington, DC, 2011.

Arno de Klerk
University of Alberta
Edmonton, Alberta, Canada

David L. King
Pacific Northwest National Laboratory
Richland, Washington, U.S.A.

Downloaded by 89.163.35.42 on June 6, 2012 | http://pubs.acs.org
Publication Date (Web): November 29, 2011 | doi: 10.1021/bk-2011-1084.pr001

In Synthetic Liquids Production and Refining; de Klerk, A., et al.;
ACS Symposium Series; American Chemical Society: Washington, DC, 2011.

Chapter 1

Overview of Feed-to-Liquid (XTL) Conversion

David L. King[*,a] **and Arno de Klerk**[**,b]

[a]Hydrocarbon Processing, Pacific Northwest National Laboratory,
P.O. Box 999, Richland, WA 99352, USA
[b]Department of Chemical and Materials Engineering,
University of Alberta, Edmonton, Alberta T6G 2V4, Canada
[*]Tel: +1 509-375-3908. E-mail: david.king@pnl.gov.
[**]Tel: +1 780-248-1903. E-mail: deklerk@ualberta.ca.

Downloaded by 89.163.35.42 on June 6, 2012 | http://pubs.acs.org
Publication Date (Web): November 29, 2011 | doi: 10.1021/bk-2011-1084.ch001

The overview addresses some important questions related to the future relevance of XTL technology, sustainability, non-carbon based carriers and carbon (CO_2) footprint. The difference between XTL conversion technologies are explained, which covers topics such as direct liquefaction, pyrolysis and indirect liquefaction (methanol and Fischer–Tropsch). The present status of XTL technology is discussed.

Introduction

The sustainability of conventional crude oil as the raw material for almost all production of liquid transportation fuels and petrochemicals is increasingly being questioned. Conventional crude oil is a finite natural resource and at some point in time the global crude oil supply will no longer be able to meet the global crude oil demand. This point of maximum crude oil production is popularly known as "peak oil". The concept gained considerable publicity in 1970 when the Hubbert-model succesfully predicted peak oil production in the United States (*1*). Since then about half of the crude oil producing countries have passed their peak oil production (*2*).

In Synthetic Liquids Production and Refining; de Klerk, A., et al.;
ACS Symposium Series; American Chemical Society: Washington, DC, 2011.

The challenge that is considered here is how this eventual shortfall in conventional crude oil supply can be addressed through the conversion of alternative carbon sources. Technologies for the production of synthetic crude oil from carbon based materials are often referred to biomass-to-liquids (BTL), coal-to-liquids (CTL), gas-to-liquids (GTL) and waste-to-liquids (WTL) processes, in each instance identifying the raw material that is being converted. These technologies, which include all the steps to produce liquid products, are collectively referred to as feed-to-liquids (XTL) conversion processes. Typical technologies found in an XTL process include among other catalytic liquefaction, gas reforming, gasification, water gas shift conversion, syngas cleaning, methanol synthesis, Fischer–Tropsch synthesis and syncrude refining.

Historically, the use of some of the alternative carbon sources predated the use of crude oil (*3*). The change from wood to coal to crude oil was a matter of availability and efficiency. Plainly speaking, conventional crude oil is readily available and a more efficient raw material for the production of fuels and chemicals than the alternatives. There is consequently little incentive to return to these alternative raw materials, unless availability of crude oil becomes a problem. This creates a dilemma for the development of XTL technology. Technology development takes time and unless it is proactively developed, it will not be ready by the time it becomes necessary to supplement a shortfall in crude oil derived products. The conundrum is not new and some well reasoned discussions can be found in the literature (*4*, *5*).

Although some XTL technologies have been commercialized, a study by the American Engineering Societies Commission on Energy (Table I) (*6*) indicated that the investment cost for implementation is quite high. The industrially applied processes, such as syngas-to-methanol and Fischer–Tropsch synthesis have low efficiencies and liquid yields compared to direct liquefaction technologies, but direct liquefaction technology has not been commercialized to the same extent.

There are still many technical challenges to overcome, particularly in the development of economic smaller-scale facilities and in the refining of the synthetic crude oil (syncrude) produced by XTL technology. One of the reasons why direct liquefaction technology has not been commercialized to the same extent as indirect liquefaction technology, is because the syncrude is more specific to the feed properties. The syncrude from direct liquefaction of coal is very different compared to the syncrude from direct liquefaction of biomass. The catalysis required to efficiently refine coal liquids presents many challenges (*7*), as does the refining of oxygenate-rich syncrudes (*8*). There are also challenges in the design of such refineries, which become quite inefficient if a conventional crude oil refining approach is followed (*9*). In fact, much of the gain in liquid yield and efficiency that was reported for direct liquefaction (Table I) is lost when conventional crude oil refining technology is employed to convert the syncrude into transportation fuels and petrochemicals.

The aim of this chapter is to provide an overview of the current state of technology development for XTL conversion and review some of the concerns associated with XTL conversion.

Downloaded by 89.163.35.42 on June 6, 2012 | http://pubs.acs.org
Publication Date (Web): November 29, 2011 | doi: 10.1021/bk-2011-1084.ch001

Downloaded by 89.163.35.42 on June 6, 2012 | http://pubs.acs.org
Publication Date (Web): November 29, 2011 | doi: 10.1021/bk-2011-1084.ch001

Table I. Coal-to-liquids process comparison based 25 000 t/day dry coal[a]

Coal-to-liquids process	*Liquid products from XTL*		*Capital cost [b] (US $billion, 2011)*
	Efficiency (%) [c]	*Syncrude (bbl/day) [d]*	
Fischer–Tropsch synthesis	32	43 300	1.7
Syngas-to-methanol synthesis	44	53 500	1.9
H-Coal (syncrude mode)	56	61 100	1.7
H-Coal (fuel oil mode)	66	66 800	1.4
Exxon Donor Solvent	65	75 400	1.9
Solvent Refined Coal I	70 [e]	77 400	1.8
Solvent Refined Coal II	77	72 300	1.9

[a] Based on dry Illinois no.6 coal, which contains about 15% ash on a dry basis; elemental analysis: 78% C, 5% H, 1% N, 2% S and 14% O. [b] Original data for 1978, US Gulf Coast location, 90% on stream factor and no associated refinery, except in syngas-to-methanol (HF alkylation) and EDS (flexicoker). [c] Efficiency was defined as the energy content of the liquid products divided by the energy content of coal and power required. [d] In some instances it includes a significant volume of LPG in total volume of syncrude. [e] Includes upgraded solid fuel in calculation.

Does XTL Have a Future?

Three criticisms are often lobbied against XTL technology. The first is that XTL technology is not sustainable. Industrial applications of XTL conversion are mainly based on coal and natural gas, which are non-renewable resources and have the same longterm prognosis as crude oil. The second criticism is that XTL technology is carbon based. It can therefore not be considered a “clean” alternative when compared to technologies that employ carbon-free carriers, such as electricity and hydrogen. The third criticism is that XTL technology is generally associated with a large CO_2 footprint and that the ultimate use of the products, being carbon-based, also have an associated CO_2 footprint. Let us examine each in turn.

Sustainability

Sustainability is unfortunately too often erroneously equated with the use of renewable resources. “Renewable” does not imply “sustainable”. Sustainability requires responsible use and a self-imposed maximum production rate must be placed on the resource.

History provides us with many examples of the strategic importance of energy to society and the need to provide energy in a sustainable fashion. The following two examples illustrate the role of sustainability in energy use:

Downloaded by 89.163.35.42 on June 6, 2012 | http://pubs.acs.org
Publication Date (Web): November 29, 2011 | doi: 10.1021/bk-2011-1084.ch001

(i) The use of wood as renewable energy source formed the basis of the bronze industry in Crete. Crete became a major producer and exporter of bronze weaponry, but deforestation killed the industry and ultimately contributed to the decline of the civilization. The British iron industry was faced with a similar fate. Deforestation for the production of wood-derived charcoal was turned around in time by the use of coal, which is also a non-renewable resource (*10*).

(ii) In another ironic twist of fate, whales were saved from extinction by coal and crude oil, which are a non-renewable resources. Whales can in principle be considered a renewable resource and whales were the main source of lamp oil in the mid-nineteenth century. Increasing demand for lamp oil resulted in relentless whaling, with whale-derived lamp oil becoming an increasingly scarce and costly commodity. Coal pyrolysis showed promise in providing an alternative source of lamp oil and started making inroads in the market, but was soon after replaced by crude oil as primary source for the production of lamp oil (*11*).

Neither wood nor whales were sustainably used, even though both were renewable resources. Just like coal and crude oil in the past bought society time to restore some of the depleted natural resources, XTL technology can buy society some time to find alternatives for our energy needs. XTL technology is just a bridging measure, but nonetheless an important bridging measure. Without a smooth transition from crude oil, there will be an energy shortfall. History teaches us that when there is a lack of energy, societies will go into decline, or make war in order to forcefully satisfy their energy requirements. The need for XTL is therefore clear, despite the fact that XTL in itself is not in the long run a sustainable solution.

The problem is that society grows and with that growth comes the increasing need for energy. In an editorial by Rudy Baum (*12*), the essence of the dilemma is captured: “The problem with … growth is that we live on a finite planet. No matter what growth’s apologists claim about finding more resources or harnessing new technology, … growth, by definition, must at some point collide with reality.” A sustainable solution for society’s energy needs requires societal change and it is not something that can be supplied by technology alone.

Non-Carbon Based Carriers

The present infrastructure for transportation relies heavily on carbon based energy carriers in the form of motor-gasoline, jet fuel, diesel fuel and fuel oil. It is, of course, possible to change this dependence on carbon, but the technology and social impetus to make such a transition is not in place yet.

There are not that many energy sources that are not based on carbon. The main alternatives are nuclear, solar, hydro-electric, geothermal, wind and tidal. With the exception of nuclear energy, the other possibilities are all location dependent and transient in nature. For example, until we devise a way to collect and transmit solar energy from outer space, there are significant constraints. Only half of the planet is exposed to solar radiation at any given time and the efficiency of solar energy collection can be hampered by natural phenomena like a cloudy sky. Nuclear energy is not without its own life cycle issues, such as radioactive waste disposal. The use of transient sources appears increasingly to require new developments or inventions in energy storage.

XTL provides the opportunity to convert nonrenewable and renewable carbon sources into carbon-based materials that can be used with existing infrastructure. As such, XTL technology has a role to play while ways are devised to harness energy sources that are not based on carbon, and while the infrastructure is changed to make use of such energy.

The preceding discussion on non-carbon based carrier focused on energy only, but there is another aspect to consider. Carbon is also used for petrochemicals. The volumes being consumed are less (Table II) (*13*), but petrochemicals do not present the same replacement alternatives as energy. In many applications carbon based petrochemicals have no foreseeable replacement, e.g. pharmaceuticals. There is consequently a long term role for XTL technology in petrochemical production. A virtue of XTL technology is that it can recycle carbon, thereby converting waste petrochemicals back into useful petrochemicals.

Table II. Global energy consumption in 2007

Description	*Energy equivalent (EJ)* [a]
Total energy consumption	465
Fossil fuel energy consumption	298
fuels/energy applications	271
petrochemicals	27

[a] 1 EJ = 10^{18} J.

CO_2 Footprint

All carbon that is used for energy applications will ultimately be turned into CO_2. Measuring CO_2 emissions from a process is therefore not a good metric of the CO_2 footprint. There are four aspects to consider in the evaluation of the CO_2 footprint of XTL technology (Figure 1):

(i) Source of energy. Energy is required to drive the process of XTL conversion, since the conversion of one carbon-carrier into another carbon-carrier requires work. At present XTL technologies employ the carbon feed source as source of energy too. This implies that the heat that is rejected to perform the work has an associated CO_2 footprint. One way that has been suggested to reduce the CO_2 footprint of XTL conversion is to decouple the energy supply from the carbon based feed that is being converted. For example, in steam reforming of methane the heat to drive the reforming process is provided externally. If a non-carbon based energy source is employed (e.g. nuclear power), it would eliminate

Downloaded by 89.163.35.42 on June 6, 2012 | http://pubs.acs.org
Publication Date (Web): November 29, 2011 | doi: 10.1021/bk-2011-1084.ch001

the CO_2 footprint associated with reforming for synthesis gas or H_2 production.

(ii) Thermodynamics. The Second Law of thermodynamics makes it clear that there is a big difference between energy as *heat*, and energy as *work*. In order to perform work, we have to reject heat. It is impossible to perform useful work without expending the energy associated with the work and the energy lost as heat to satisfy the laws of nature. It is consequently impossible to perform the work associated with XTL conversion without rejecting heat. The least amount of heat that can be rejected can be determined from the Second Law of thermodynamics. A process that is 100 % thermodynamically efficient, still rejects heat. If the energy source is carbon-based there is always a finite CO_2 footprint, which is not related to XTL technology, but that is associated with the transformation (work) being performed.

(iii) Stoichiometry of the chemistry. The nature of the carbon-carrier that is desired, in relation to the nature of the raw material, affects the potential carbon-footprint. The overall XTL conversion is subject to the stoichiometry of the reaction chemistry that is employed. This can be viewed as the carbon equivalent of thermodynamic efficiency, since it determines the amount of carbon from the feed that can be converted into products at 100 % reaction selectivity. Usually the carbon efficiency of the chemistry is related to the difference in the H:C ratio of the feed compared to that of the product. Most carbon based raw materials have a $H:C < 2$, natural gas being the exception, whereas many carbon based products (fuels and petrochemicals) have a H:C ratio that is closer to two. When the H:C of the product is more than that of the feed, one of two things must happen: hydrogen must be added, or carbon must be rejected. Hydrogen is normally supplied by carbon rejection through the water gas shift reaction (Eq. 1). One way that has been suggested to reduce the CO_2 footprint of XTL conversion is to decouple the hydrogen supply from the carbon based feed, e.g. nuclear powered water electrolysis (Eq. 2).

$$\text{Water gas shift: } H_2O + CO \rightleftharpoons H_2 + CO_2 + \text{energy} \qquad \textbf{(1)}$$

$$\text{Water electrolysis: } H_2O + \text{energy} \rightleftharpoons H_2 + \tfrac{1}{2}\,O_2 \qquad \textbf{(2)}$$

(iv) Process engineering. The thermodynamic efficiency, in combination with the carbon efficiency of the chemistry, determines the best possible performance of a process. These are theoretical values and in practice it is the process engineering that determines how close we can get to these ideal values that are governed by the laws of nature. The selectivity of carbon conversion and the recovery efficiency of the carbon-based products are determined by the engineering design of the process. It is also the process engineering that determines how effectively the energy

Downloaded by 89.163.35.42 on June 6, 2012 | http://pubs.acs.org
Publication Date (Web): November 29, 2011 | doi: 10.1021/bk-2011-1084.ch001

supply and the hydrogen supply can be decoupled from the carbon-based feed.

In conclusion it can be said that XTL technology does not inherently have a large CO_2 footprint. The large CO_2 footprint of current industrial XTL technologies is mainly related to the use of carbon-based feed to generate energy and hydrogen. To a lesser extent inefficiencies in process engineering contributes to lower carbon conversion selectivity and poorer product recovery.

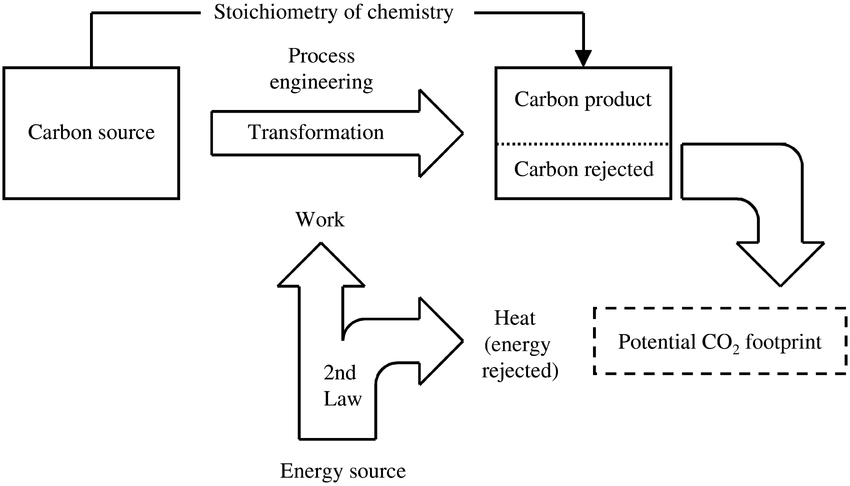

Figure 1. Origin of the CO_2 footprint associated with XTL technology.

XTL Technology Classification

The purpose of XTL technology is to convert carbon-based raw materials into different and more useful liquid products. The liquid products must have an advantage over the feed to make the transformation desirable and necessary. In petrochemical applications the carbon-based products have a very specific chemical identity. In fuel applications, the carbon-based products are usually mixtures with specific physical and combustion properties that are required by the energy application (e.g. engine technology).

The term “feed-to-liquids” captures another objective of XTL technology, namely transportability. As an energy-carrier, liquid carbon-based materials are the most convenient for distributed end-user applications. In the past many such applications were served by solid energy-carriers, but solids handing is more cumbersome. Although gases and liquids are both easier to handle than solids, liquids have much higher volumetric densities than gases, making liquids more efficient to store and transport. Mobile energy requirements are therefore more conveniently met by carbon-based liquid transportation fuels than any other energy carrier.

Downloaded by 89.163.35.42 on June 6, 2012 | http://pubs.acs.org
Publication Date (Web): November 29, 2011 | doi: 10.1021/bk-2011-1084.ch001

XTL technologies can be classified into two broad categories based on the conversion approach: *direct liquefaction* and *indirect liquefaction*. During direct liquefaction the identity of the feed is partly retained in the product. The feed is liquefied by physical and/or chemical changes. Some of the small molecules can be extracted without change, but the majority of the material is broken down into smaller molecules, thereby losing some of its chemical identity. During indirect liquefaction the identity of the feed is completely lost and the product takes on a new identity that is determined by the conversion technology. The feed is first converted into synthesis gas (H_2+CO) and then liquefied through synthesis. A comparison of characteristics (Table III) shows that direct liquefaction has more in common with conventional crude oil refining than indirect liquefaction.

Based on the comparison in Table III, it is anticipated that XTL conversion by direct liquefaction to produce a synthetic crude oil (syncrude) will be more efficient that indirect liquefaction. In fact, this is what has been found in practice (Table I).

However, the syncrude from indirect liquefaction is sulfur and nitrogen free. Subsequent refining of syncrude from indirect liquefaction is potentially easier than refining of the syncrude from either direct liquefaction, or conventional crude oil (*14*). The decoupling of feed properties from syncrude properties by indirect liquefaction is also potentially useful. The syngas-to-syncrude conversion technology can be selected to produce a syncrude with properties to best match the application, a luxury that is not available to the same extent in direct liquefaction processes.

Downloaded by 89.163.35.42 on June 6, 2012 | http://pubs.acs.org
Publication Date (Web): November 29, 2011 | doi: 10.1021/bk-2011-1084.ch001

Table III. Comparison of direct liquefaction, indirect liquefaction and conventional crude oil conversion

Description	*XTL conversion*		*Crude oil*
	Direct	*Indirect*	
Conversion process			
feed properties affect XTL technology	Yes	No [a]	-
feed properties affect product properties	Yes	No	Yes
feed C-C bonding retained to some extent	Yes	No	Yes
product phase from primary feed conversion	Liquid	Gas	Liquid [b]
Liquid product properties			
contains sulfur	Yes	No	Yes
contains nitrogen	Yes	No	Yes
contains oxygen	Yes	Yes	Yes

[a] Some technology selection is affected by the nature of the feed, e.g. gasifier-type. [b] Primary feed conversion entails desalting and separation by distillation.

Direct Liquefaction

Direct liquefaction usually involves some degradation of the molecular structure in order to liquefy the material. Degradation of the molecular structure lead to the production of lower molecular weight products, including gas. Gas can be liquefied under pressure and in the present description direct liquefaction is considered in its broadest sense, namely the direct production of liquids by whatever means, which includes pyrolysis and methods that do not involve reactions, such as dissolution and condensation under pressure. The reader must be aware that this broad definition is not employed in all literature.

Historical Overview

Downloaded by 89.163.35.42 on June 6, 2012 | http://pubs.acs.org
Publication Date (Web): November 29, 2011 | doi: 10.1021/bk-2011-1084.ch001

The oldest form of direct liquefaction is *pyrolysis*. When solid carbon-based feed materials are heated under inert conditions, thermal decomposition (thermal cracking) takes place. The lighter products become hydrogen enriched compared to the feed, whereas the heavier products become more carbonaceous compared to the feed.

The yield of liquid and gaseous products from pyrolysis is limited. Nevertheless, this process formed the basis for the production of "town gas" in the nineteenth century, with many of the larger European cities installing a gas distribution network to provide lighting (*15*). The main feed material was coal and the associated coal pyrolysis liquids (coal tar) became an important feedstock for the chemical industry in the late nineteenth century and early twentieth industry.

Although pyrolysis processes are an important group of direct liquefaction processes, historically the main aim of pyrolysis was gas production, not the production of liquids. The first "true" liquefaction, where the production of a liquid product was the main aim, involved the treatment of coal with hydriodic acid.

Berthelot demonstrated in 1869 that coal could be almost completely digested by hydriodic acid over a period of 24 hours at 270 °C (*16*). Similar experiments were performed by Fischer and Tropsch (later to become the inventors of the Fischer–Tropsch synthesis), who extended the work to include the use of phosphorus, as well as sodium formate.

Bergius is credited with invention of direct liquefaction by hydrogenation. His initial work in 1912-1914 focused on non-catalytic hydrogenation and it employed biomass and coal as feed materials. This later evolved into catalytic hydrogenation by the addition of an iron ore based catalyst (*3*, *16*). The principle that was demonstrated by Bergius formed the basis for most of the *catalytic direct liquefaction* technology that was subsequently developed.

The single stage catalytic direct coal liquefaction (DCL) process developed by Bergius produced a low quality motor-gasoline. This problem was overcome by Pier, who devised a two-step process (*3*). The first step was less severe catalytic DCL to produce a heavier syncrude, containing 70-80% distillate and heavier oil. The second step was a refining step, where the syncrude was hydrocracked over a supported tungsten sulfide catalyst. Since this catalyst was in current terms not an "ideal" hydrocracking catalyst, the large amount of motor-gasoline produced

In Synthetic Liquids Production and Refining; de Klerk, A., et al.;
ACS Symposium Series; American Chemical Society: Washington, DC, 2011.

Downloaded by 89.163.35.42 on June 6, 2012 | http://pubs.acs.org
Publication Date (Web): November 29, 2011 | doi: 10.1021/bk-2011-1084.ch001

was rich in aromatics and had good motor-gasoline properties for that time. The combination of syncrude production *and* refining was required to produce a commercially useful product. This became one of the key processes for the production of transportation fuels in Germany just before and during the Second World War, the other being Fischer–Tropsch synthesis (see section on "Indirect liquefaction"). In total the German coal-to-liquids industry produced about 100 000 bbl/day of transportation fuels, about one third of its needs at that time (*17*). Developments in other parts of the world were smaller, the only other commercial scale facility was the DCL facility at Billingham in the UK (*18*).

In a parallel development in the late 1920's, the concept of non-catalytic coal hydrogenation by use of a hydrogen-donor solvent was explored by Pott and Broche. Commercialization failed due to coal liquid filtration problems (*19*), but the Pott-Broche process nevertheless formed the basis for subsequent developments in *non-catalytic direct liquefaction* (also referred to as *solvent extraction*).

Interest in direct liquefaction waned after the Second World War, but work on coal liquefaction did not stop. Crude oil was cheap at around US $2/bbl and was readily available. A significant resurgence in interest came only after the 1973 "Oil Crisis", when the price of crude oil rapidly increased. Considerable effort in field of coal-to-liquids conversion, mainly in Germany and the USA, led to the development of a number of DCL processes (Table IV) (*6*, *20–23*). Later on, work in Japan led to the development of the NEDOL catalytic liquefaction process (*24*). In both the USA and in China the H-Coal process formed the basis for further developments, which included the development of the Shenhua direct coal liquefaction process.

Although some of the earlier work on direct liquefaction employed biomass and waste products (*25*, *26*), it was never the main focus in direct liquefaction, which was directed at coal. This skews the picture somewhat and as will be shown, direct liquefaction is not at all restricted to coal conversion.

Table IV. Some of the notable direct coal-liquefaction processes that were developed during the 1960-1980's

Process	*Country*	*Technology*
COED (Char-Oil-Energy Dev.)	USA	Multi-step coal pyrolysis
EDS (Exxon Donor Solvent)	USA	Solvent extraction
H-Coal	USA	Catalytic liquefaction (ebullated bed)
Kohleöl	Germany	Catalytic liquefaction (slurry bed)
Lurgi-Ruhrgas retort	Germany	Pyrolysis (fast)
SRC (Solvent Refined Coal)	USA	Solvent extraction with H_2 co-feed

Downloaded by 89.163.35.42 on June 6, 2012 | http://pubs.acs.org
Publication Date (Web): November 29, 2011 | doi: 10.1021/bk-2011-1084.ch001

Biomass-to-Liquids (BTL)

Plants and animals contain carbon matter that can be harvested directly for use as chemicals and fuels. The fraction of the plant and animal matter that is useful for direct recovery is usually very little. The type and severity of the processes employed for direct liquefaction affects the carbon recovery that is possible.

As with other carbon based feed materials, carbon recovery is important, but there are two additional considerations that are applicable to biomass. The first consideration relates to the energy density of the raw material. Biomass has a low energy density and a low density of production (i.e. distributed production), which causes the transportation of biomass to a BTL facility to become a significant cost factor in any BTL process (*27*). The second consideration relates to land use, and the food versus fuel debate. Dedicating land for cultivating crops or use by animals reduces the natural habitat of many other species. Even when the land is not considered arable, it still contains some bio-diversity. The production of biomass for fuel rather than biomass for food is also a contentious issue. The debate is often emotive. BTL conversion is therefore under a moral obligation to make the most efficient possible use of the biomass.

Direct liquefaction approaches in BTL can be clasified based on the type of conversion that is applied:

(a) Mechanical extraction. This is the oldest form of BTL and was mostly applied to recover oils and fats. Some plant species, algae and animals have high oil and fat contents. For example, the historic use of whales for the production of lamp oil. It is only a small fraction of the biomass that can be recovered in this way. The yield from mechanical extraction is often improved through the action of temperature and/or a solvent, but even so, mechanical extraction has a low inherent yield that is dependent on the type of biomass.

(b) Hydrolysis. Starches, hemi-cellulose and cellulose are all polymers of different sugars with the basic formula: $[C_x(H_2O)_{x-1}]_n$. The ether linkages between the sugar monomers can be hydrolyzed to produce the sugars. Direct liquefaction by hydrolysis is a depolymerization process that makes use of the simple chemistry that is common to all of these materials. Lignin, which is also an abundant constituent of plant material, can also be hydrolyzed to produce a more diverse range of aromatic products. Hyrolysis is often combined with some form of biomass pretreatment to liberate the bio-polymers for subsequent hydrolysis.

(c) Pyrolysis. The application of heat to biomass causes two classes of non-catalysed reactions to take place. The first is dehydration, which severs ether linkages between carbon structures and increases the degree of unsaturation of the carbon structures. The second is thermal cracking, which leads to the free radical decomposition of the material. The net result of these transformations is the production of an aqueous product, pyrolysis oil and “coke”. The aqueous product contains most of the more polar oxygenates in an aqueous solution, wereas the pyrolysis oil contains the less polar organic matter. The “coke” is the carbon rejection product. Further upgrading can be performed on the individual or combined product phases.

(d) Catalytic liquefaction. The direct catalytic conversion of biomass includes strategies akin to catalytic direct coal liquefaction that process the complete biomass feed and processes that target a subset of biomass derived feed, such as aqueous-phase reforming (*28*). In aqueous-phase reforming hydrogen is produced by sacrificing some of the carbon as CO_2. Hydrogen co-production solves two downstream refining problems related to the direct liquefaction product: the O:C ratio is decreased and the effective H:C ratio is increased.

Downloaded by 89.163.35.42 on June 6, 2012 | http://pubs.acs.org
Publication Date (Web): November 29, 2011 | doi: 10.1021/bk-2011-1084.ch001

Coal-to-Liquids (CTL)

Much of the historical development of direct liquefaction technology revolved around CTL conversion. The discussion will not be repeated here. A salient point that needs to be highlighted is the role of hydrogen.

Coal has a low H:C ratio ($H:C < 1$), with high rank coals being less hydrogen rich and less ameanable to direct liquefaction. Although the aim of CTL is to convert the coal into a liquid product, the fragments from molecular degradation must be stabilized. The H:C ratio is already so low that it is not possible to achieve a good yield if the fragments from molecular degradation must be stabilized by carbon rejection. The key aspect that differentiates direct coal liquefaction methodologies is the way in which hydrogen is supplied to the coal liquid from CTL conversion (Figure 2).

The following direct liquefaction approaches are found in CTL:

(a) Solvent dissolution. Solvent dissolution is a purely physical process whereby the coal is dissolved in a suitable solvent. The coal remains a liquid product only in combination with the solvent. The physical structure of the coal is altered, but no chemical degradation of the coal molecules take place. This restricts the temperature of dissolution to less than 150 °C (*29*). No hydrogen is transferred and once the solvent is removed, an ash free coal is precipitated from the solution. Dissolution at higher temperatures (>150 °C) causes extractive disintegration and can be considered solvent extraction, or non-catalytic liquefaction.

(b) Non-catalytic liquefaction (solvent extraction). This is the Pott-Broche approach. The solvent physically dissolves the coal, but due to the high temperature, the coal molecules are thermally decomposed. The free radicals produced by the decomposed coal molecules are stabilized by transferring hydrogen from the solvent molecules to the coal molecules. The solvent must be re-hydrogenated, but that can take place either *in situ* or *ex situ* from the liquefaction reactor. The solvent is often referred to as a hydrogen-donor solvent and the textbook example of such a solvent is tetralin. In industrial practice the hydrogen-donor solvent is usually prepared by hydrogenating a fraction of the coal liquids.

In Synthetic Liquids Production and Refining; de Klerk, A., et al.;
ACS Symposium Series; American Chemical Society: Washington, DC, 2011.

Downloaded by 89.163.35.42 on June 6, 2012 | http://pubs.acs.org
Publication Date (Web): November 29, 2011 | doi: 10.1021/bk-2011-1084.ch001

(c) Catalytic liquefaction. This is the Bergius approach. In its purest form, a catalyst is added to the coal and all hydrogen is transferred as molecular hydrogen (H_2) by hydrogenation catalysis to the coal. In practice the liquefied coal acts as a solvent and direct catalytic coal hydrogenation takes place in parallel with solvent extraction. Hydrogenation of the coal liquid, which acts as a hydrogen-donor solvent, takes place *in situ* and by the same hydrogenation catalysis as the direct hydrogenation of the coal molecules. Both catalytic and free radical reactions take place during catalytic liquefaction.

(d) Pyrolysis. The pyrolysis of coal in coke-ovens or by retorting causes the thermal decomposition of coal. In the absence of another hydrogen source, the coal itself must supply the hydrogen for stabilization. This is achieved by a disporportion of hydrogen to produce lighter more hydrogen rich pyrolysis oils and heavier more carbon rich coke, i.e. a classic carbon rejection strategy.

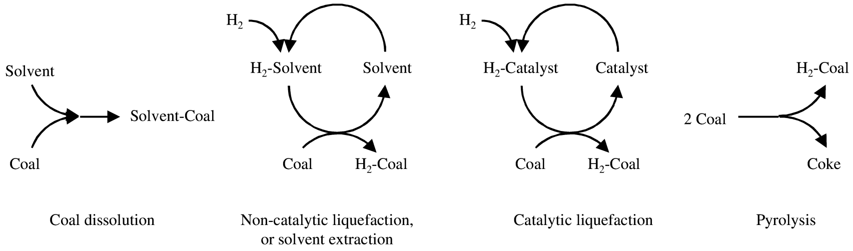

Coal dissolution

Non-catalytic liquefaction, or solvent extraction

Catalytic liquefaction

Pyrolysis

Figure 2. Different approaches of hydrogen transfer in direct coal liquefaction.

Gas-to-Liquids (GTL)

Natural gas is normally distributed as a gas, but it may also be directly supplied as a liquid product. In fact, direct liquefaction to produce liquefied natural gas (LNG) is an important competitor of gas-to-liquid conversion by indirect liquefaction and methanol synthesis in specific. Distance to market is a deciding factor, because of the specialised nature of LNG transportation. LNG production and transportation by sea is more economical for distances of 10 000 km or less, but shipping costs erode the advantage of LNG over methanol synthesis when longer distances are involved (*30*).

The production of LNG is a physical process whereby the gas is directly liquefied. Once liquefied, the LNG must be cryogenically stored (-160 °C at near atmospheric pressure) in well-insulated storage tanks to limit vaporisation losses. Vaporisation rates during storage in properly insulated tanks is around 0.1 % per day of the tank content (*30*). Storage is therefore usually supplied with reliquefaction capability.

Downloaded by 89.163.35.42 on June 6, 2012 | http://pubs.acs.org
Publication Date (Web): November 29, 2011 | doi: 10.1021/bk-2011-1084.ch001

Waste-to-Liquids (WTL)

A large fraction of the materials that are classified as solid organic wastes, can also be classified as biomass. These include products such as agricultural crop residues, manure, forestry residues and sludges from municipal wastewater treatment. The main waste products that cannot necessarily be classified as biomass too, are municipal refuse, scrap tires and industrial wastewater sludges.

Strictly speaking, solid organic waste materials should be ameanable to the different direct liquefaction options listed for coal-to-liquid conversion. Yet, historically many developments in the field of direct conversion of WTL focused on thermal conversion (*25*). The nature of the waste has a tremendous impact on the most efficient way for direct liquefaction and two main types of thermal conversion are differentiated:

(a) Depolymerization. Materials that are hydrogen-rich and not extensively cross-linked with sulfur, can be depolymerized by mild thermal cracking (*31*, *32*), or by catalytic cracking (*33*, *34*). Many forms of waste plastic can be readily converted into high quality syncrudes in this way. Depolymerization is essentially a mild form of pyrolysis.

(b) Pyrolysis. More severe thermal treatment leads to the production of typical pyrolysis products, with the accompanying production of coke.

Current Status

Large industrial scale application of direct liquefaction was for a long time limited to the production of liquefied natural gas.

Commercial activity and interest in biomass conversion is focused mainly on the mechanical recovery and hydrolysis of oils, fats, sugars and starches. The mechanical recovery of triacylglycerols in the form of oils and fats spawned a whole BTL industry based on the the production of fatty acid methyl esters (FAME). The FAME is obtained by transesterification (hydrolysis with methanol) of the triacylglycerols. FAME can be employed directly as a high cetane number diesel fuel blending component. In an analogous conversion, sugars and starches are mechanically recovered from biomass. The sugars and starches are then hydrolysed and fermented to produce ethanol. Ethanol can be employed directly as high octane number motor-gasoline blending component. Despite research activity in biomass pyrolysis and catalytic liquefaction, there are no industrial applications yet.

The resurgence of interest in direct coal liquefaction in the USA after the “Oil Crisis” came to naught, as low crude oil prices and high crude oil availability made CTL unattractive. Taking a longer term view China started investigating DCL technology in the 1990’s (*35*). This led to the development and construction of the first commercial direct coal liquefaction facility since the Second World War. The Shenhua DCL facility in the Ordos desert was successfully commissioned on December 30, 2008 (*36*).

The following data has been reported (*37*): The Shenhua DCL facility has a size of 24,000 barrels per day crude oil equivalent and it produces mainly distillate. The H-Coal process was the predecessor technology and the direct liquefaction process employed in the Shenhua facility is a combination of new developments and already existing technology (Figure 3). The capital cost was US $1.5 billion. This is equivalent to a cost of US $62 500 per daily barrel of capacity. The coal conversion rate exceeded 90 % with a syncrude yield around 57 % on a daf coal basis. The CO_2 footprint is 0.88 t CO_2/t daf coal, or 0.48 t CO_2/bbl syncrude. The calculated break even cost was US $35-40/bbl (cost per barrel of crude oil).

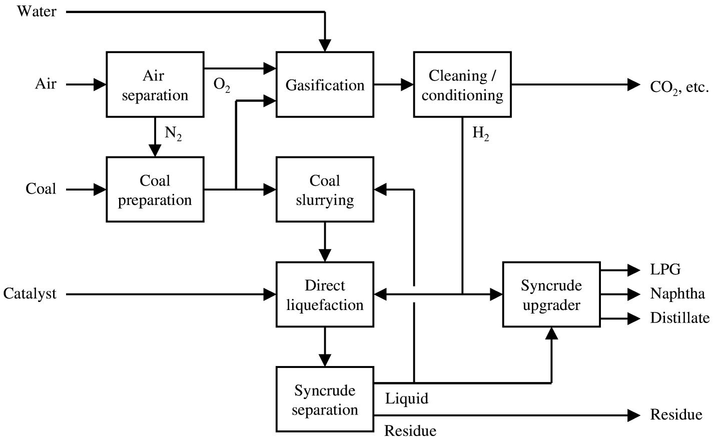
Water
Air
Air separation
O_2
N_2
Gasification
Cleaning / conditioning
CO_2, etc.
H_2
Coal
Coal preparation
Coal slurrying
Catalyst
Direct liquefaction
Syncrude upgrader
LPG
Naphtha
Distillate
Syncrude separation
Liquid
Residue
Residue

Figure 3. Simplified process flow diagram of the Shenhua DCL facility.

The reported syncrude yield of 57 % is in good agreement with the H-Coal yield of 56 % in Table I. Using the capital cost data in Table I and the 6/10th exponential method scaling rule (*38*), the estimated capital cost of a similar sized facility is US $1 billion (excluding location factor), which is less than the actual constructed cost of US $1.5 billion.

Aspects that are highlighted:

(a) Industrial scale direct liquefaction is clearly a very capital intensive proposition, even though the break even cost suggests that it can be a very profitable investment.

(b) Although the main conversion unit employs direct liquefaction, the process requires H_2. The H_2 is supplied by gasification. The CO_2 footprint is associated with H_2 production and the gasifier is the main source of CO_2.

(c) The products are not on-specification transporation fuels, but upgraded syncrude fractions. The naphtha and distillate must still be refined.

Downloaded by 89.163.35.42 on June 6, 2012 | http://pubs.acs.org
Publication Date (Web): November 29, 2011 | doi: 10.1021/bk-2011-1084.ch001

Indirect Liquefaction

Indirect liquefaction as first step involves the complete degradation of the raw material by gasification or gas reforming to produce synthesis gas (H_2+CO). Oxygen from an air separation unit is often employed as oxidant instead of air. Air can be used, albeit with the accompanying inefficiency of nitrogen dilution in all subsequent steps of the process. After synthesis gas generation, the synthesis gas is cleaned and conditioned for the indirect liquefaction technology. During synthesis gas cleaning and conditioning all heteroatom contaminants are removed and the pure synthesis gas contains only the elements hydrogen, carbon and oxygen. The indirect liquefaction technology converts the synthesis gas into liquid products, which can then be recovered and refined. Irrespective of the specific technology selection, generically, the steps during indirect liquefaction are similar (Figure 4).

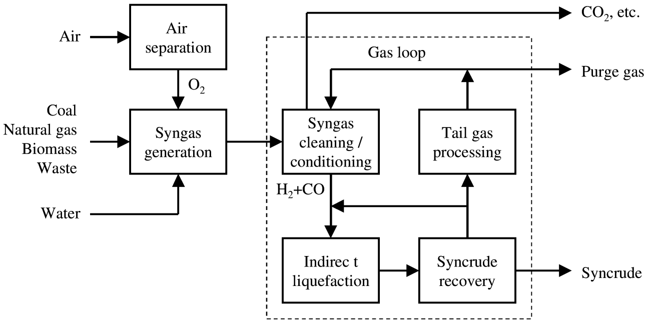

Figure 4. Generic process flow diagram for indirect liquefaction.

The use of synthesis gas as intermediate, has an important consequence for the quality of the syncrude produced by indirect liquefaction. Since the pure synthesis contains only the elements hydrogen, carbon and oxygen, the products also contain only those three elements. The syncrude from indirect liquefaction is much easier to refine to final consumer products, than the syncrude from direct liquefaction, which contains the elements that were present in the raw material feed.

Historical Overview

In contrast to direct liquefaction, two very different technologies had to be developed in order to make indirect liquefaction possible. The first was a process to break down the carbon-based raw material into single carbon fragments. The second was a process to take these single carbon fragments and stick them together again to produce a liquid product.

Indirect liquefaction is not possible without *gasification*, the process that converts the raw material into synthesis gas. The development coal-to-gas conversion (coal gasification) took place in the early nineteenth century (*39*). Two types of gas were produced, producer gas and blue gas. Producer gas is a typical synthesis gas and blue gas is the hydrogen-rich product from steam gasification. Over time many improvements were made and many different

Downloaded by 89.163.35.42 on June 6, 2012 | http://pubs.acs.org
Publication Date (Web): November 29, 2011 | doi: 10.1021/bk-2011-1084.ch001

gasification processes were developed (*40*). The production of synthesis gas was an established technology at the beginning of the twentieth century and the stage was set for the development of synthesis gas conversion technology.

The first syngas-to-liquids conversion process was patented in 1913 for the production of methanol (*41*). This led to the first commercial application of *methanol synthesis* in 1923 at the Badische Analin und Soda Fabrik (BASF), which employed a mixed zinc oxide and chromium oxide ($ZnO-Cr_2O_3$) catalyst (*42*).

In the same year Fischer and Tropsch demonstrated that a mixture of oxygenates can be prepared over an alkali-containing iron catalyst. This oxygenate-rich mixture was called synthol. It was this invention that led to the commercial scale development of hydrocarbon synthesis by Roelen using a $Co-ThO_2$-based catalyst and that is known as *Fischer–Tropsch synthesis*. The first commercial Fischer–Tropsch facility was commissioned in 1935 in Germany and was soon followed by an number of facilities constructed under license inside and outside of Germany (*18*). Fischer–Tropsch synthesis made an important but smaller contribution than direct liquefaction technologies to the synthetic liquids production in Germany during the Second World War.

After the Second World War a commercial Fischer–Tropsch facility was constructed and operated from 1951-1957 in the USA. This facility employed natural gas as source for synthesis gas production and used an Fe-based Fischer–Tropsch catalyst. In 1955 yet another commercial facility started production in South Africa. This facility employed a combination of German and United States technology for Fischer–Tropsch synthesis and also made used of Fe-based Fischer–Tropsch catalysts.

In the late 1960's a new Cu-Zn-based catalyst was introduced for methanol synthesis, which allowed the process to be conducted at much milder conditions (*42*). This new lower temperature and lower pressure process displaced the older $ZnO-Cr_2O_3$-based process completely (*43*).

In contrast to methanol synthesis, there was a proliferation of technologies and catalysts for Fischer–Tropsch synthesis.

Downloaded by 89.163.35.42 on June 6, 2012 | http://pubs.acs.org
Publication Date (Web): November 29, 2011 | doi: 10.1021/bk-2011-1084.ch001

Synthesis Gas Generation

The technologies that are employed for the generation of synthesis gas from the feed material can be roughly classified into *gasification* and *gas reforming* technologies.

Gasification technologies are mainly employed for the conversion of solid feed materials, but can be used to liquid and gaseous feed materials too. The conversion is thermal and relies on the free radical decomposition of the feed in the presence of an oxidant and steam. The partial combustion of the feed provides the energy for the endothermic decomposition reactions. Although most gasification technologies rely mainly on thermal conversion, the mineral matter in the feed and the deliberate addition of a disposable catalyst, can modify the process so that both thermal and catalytic conversion takes place in parallel. Three main categories of gasification technology are found and the classification can take place based on the gas exit temperature (the actual gasification temperature in the reactor is >800 °C in all of the technologies), or the reactor type (*40*):

(a) Low temperature (<650 °C) gasification; moving bed gasifier.
(b) Medium temperature (~1000 °C) gasification; fluidized bed gasifier.
(c) High temperature (>1400 °C) gasification; entrained flow gasifier.

Gas reforming technologies are employed only for feed materials that are gaseous or can be vaporized. The conversion is catalytic (usually a nickel-based catalyst), which lowers the temperature required for synthesis gas generation. The energy can be supplied directly by partial combusion of the feed, or indirectly by a furnace. Reforming technologies can be classified along these lines (*44*):

(a) Adiabatic oxidative reforming (partial combustion of feed).
(b) Steam reforming (indirect heating).

Downloaded by 89.163.35.42 on June 6, 2012 | http://pubs.acs.org
Publication Date (Web): November 29, 2011 | doi: 10.1021/bk-2011-1084.ch001

Methanol Synthesis

Present day methanol synthesis facilities employ the low-pressure process using Cu-Zn-based catalysts (*43*). The reaction is very exothermic. Reaction engineering is mainly concerned with heat management, catalyst stability and the ability to achieve high selectivity to methanol.

The synthesis gas for methanol synthesis typically contains H_2 and CO in a 2:1 molar ratio, as well as around 5% CO_2. The process requires some CO_2 in the synthesis gas for methanol synthesis to take place (*42*). In order to reduce side product formation and improve heat management, the per pass conversion of CO is limited to <35%. The unconverted synthesis gas is recycled in the gas loop (Figure 4).

One of the main advantages of methanol synthesis over other indirect liquefaction technologies, is the homogeneity of the product. Although some by-products are formed, methanol is produced with >90% selectivity. Methanol is a liquid product that is easily recovered from the unconverted synthesis gas by product cooling and distillation. It requires no further on site refining beyond recovery and separation.

Methanol can be directly employed as a fuel (*45*), or it can be converted to other fuel products such as dimethyl ether (DME), methoxy fuel ethers and hydrocarbons. The methanol to gasoline (MTG) process based on H-ZSM-5 conversion of methanol (*46*), has been around for many decades. Methanol is also a commodity chemical and almost half the global consumption is employed for the production of formaldehyde and acetic acid (*47*). More recently the direct conversion of methanol to propylene (MTP) (*48*), further adds to the chemical potential of methanol.

Fischer–Tropsch Synthesis

Unlike methanol synthesis, which aims to produce a single compound product, Fischer–Tropsch syncrude is truly a synthetic crude oil. The syncrude is a mixture of various hydrocarbons and oxygenates with a wide boiling point distribution. The composition of the syncrude depends on the Fischer–Tropsch technology employed and can be selected to best match the product refining requirements (*49*).

The carbon number distribution is expressed in terms of an α-value, which is the chain growth probability during synthesis. High temperature Fischer–Tropsch (HTFT) processes have an α-value of ~0.65, whereas low temperature Fischer–Tropsch (LTFT) processes have an α-value of ~0.90. As a consequence the product from HTFT synthesis contains very little >360 °C boiling material, whereas about half the product from LTFT synthesis is wax.

Fischer–Tropsch synthesis is very exothermic. The per pass CO conversion during Fischer–Tropsch synthesis is higher than during methanol synthesis and heat management is one of the key features of the reactor design. Depending on the technology, the per pass CO conversion is limited in order to reduce the heat load and decrease the catalyst deactivation rate (*50*). Some of the unconverted synthesis gas can be recycled in the gas loop (Figure 4) and the extent of recycle is determined by the gas loop and syncrude recovery design.

Syncrude recovery after Fischer–Tropsch synthesis is more complex than for methanol synthesis. Depending on the technology the syncrude may be distributed between gaseous, oil, aqueous and solid phases at standard conditions (*49*). Some form of downstream refining is therefore necessary to convert the different Fischer–Tropsch syncrude phases into a more useful and transportable product.

Current Status

Methanol synthesis and Fischer–Tropsch synthesis are the only two indirect liquefaction technologies that have been commercialized.

There was a major change in the methanol business in the last two decades, with the appearance of mega-methanol facilities. These mega-methanol facilities have capacities around 1-2 million tons per year (22 000 to 44 000 bbl/day oil equivalent final product). Three quarters of the methanol production is from gas-to-liquid facilities. Countries with large natural gas reserves and limited domestic markets for natural gas, encouraged the construction of such large scale methanol facilities to convert the natural gas into a transportable liquid product that can be sold on the international market. The installed methanol capacity increased from 43 to 64 million tons per year from 2004 to 2008. As a consequence, the total installed methanol capacity by far exceeds global methanol consumption, which is 42 million tons per year (*47*). However, methanol is not a high value chemical and its price is marginally higher than the spot price for crude oil (*47*, *51*).

The commercial scale Fischer–Tropsch-based facilities that are still in operation or are presently under construction, are listed in Table V (*49*). Like methanol synthesis, most installed Fischer–Tropsch capacity employs natural gas as feed material. Only the Sasol facilities in South Africa were designed for coal-to-liquids conversion and in 2004 the Sasol 1 facility was converted from coal-to-liquids into a gas-to-liquids facility (*49*).

Downloaded by 89.163.35.42 on June 6, 2012 | http://pubs.acs.org
Publication Date (Web): November 29, 2011 | doi: 10.1021/bk-2011-1084.ch001

In some of the Fischer–Tropsch-based facilities there has been a change in emphasis from fuels production to petrochemical production to increase profitability. There has also been a trend away from the production of on-specification transportation fuels (e.g. PetroSA facility in South Africa) to the production of only intermediates and blending components (e.g. Oryx GTL facility in Qatar) (*9*).

Table V. Commercial Fischer-Tropsch facilities that are still in operation or are under construction

Year of start-up	*Name*	*Location*	*Nameplate FT capacity (bbl/day)* [a]	*FT technology*
1955	Sasol 1	Sasolburg, South Africa	6 750	Fe-LTFT
1980	Sasol Synfuels (Sasol 2 and 3)	Secunda, South Africa	120 000	Fe-HTFT
1993	PetroSA (Mossgas)	Mossel Bay, South Africa	22 500	Fe-HTFT
1993	SMDS	Bintulu, Malaysia	12 500	Co-LTFT
2007	Oryx GTL	Ras Laffan, Qatar	34 000	Co-LTFT
2011	Pearl GTL	Ras Laffan, Qatar	140 000	Co-LTFT
2012 ?	Escravos GTL	Escravos, Nigeria	34 000	Co-LTFT

[a] The original nameplate Fischer–Tropsch capacity and it excludes later modifications, associated natural gas liquid capacity and it does not reflect operational difficulties that prevents production at nameplate capacity, e.g. Oryx GTL.

The main detractor from investment in Fischer–Tropsch based indirect liquefaction is cost. A significant escalation of capital cost has been seen in recent GTL projects. It was reported that the estimated cost of the Escravos GTL project increased to US $6 billion (*52*). This is equivalent to a cost of US $180 000 per daily barrel of capacity – roughly three times the cost of the Shenhua direct coal liquefaction facility. Sasol also announced a doubling of the capacity at the Sasol 1 site at a cost of US $1.1 billion (*53*). This is equivalent to a cost of around US $200 000 per daily barrel of capacity. Although the Shell Pearl GTL project also had to contend with an increase in capital cost (*54*), the cost per daily barrel is closer to that of the Shenhua direct coal liquefaction project. A direct comparison is more difficult, because Pearl GTL co-processes natural gas liquids, thereby increasing the total capacity of the facility to 260 000 bbl/day (*55*). Considering the size of the investment required for GTL facilities, it is not surprising to find that few of the Fischer–Tropsch based GTL projects that were planned less than a decade ago, actually proceeded. Yet, despite the high capital cost, even for Fischer–Tropsch based CTL that is more expensive than GTL, production becomes economical at US $50-70 per daily barrel of crude oil (*56*).

Downloaded by 89.163.35.42 on June 6, 2012 | http://pubs.acs.org
Publication Date (Web): November 29, 2011 | doi: 10.1021/bk-2011-1084.ch001

Downloaded by 89.163.35.42 on June 6, 2012 | http://pubs.acs.org
Publication Date (Web): November 29, 2011 | doi: 10.1021/bk-2011-1084.ch001

Aspects that are highlighted:

(a) Industrial scale indirect liquefaction, like direct liquefaction, is very capital intensive, but the break even cost suggests that it can be a very profitable investment.
(b) The main economic driving force for investment in indirect liquefaction is the price difference between the raw material (e.g. cheap natural gas) and conventional crude oil.
(c) Methanol synthesis is a less complex indirect liquefaction technology for the production of synthetic liquids than Fischer–Tropsch synthesis.
(d) Fischer–Tropsch synthesis is potentially more versatile than methanol synthesis and it has been applied for the production of on-specification transportation fuels, intermediates, blending components and petrochemicals. The value of Fischer–Tropsch synthesis depends on how the syncrude is refined.

Conclusions

There is a need for XTL technology to enable the production of transportation fuels and petrochemicals from alternative carbon sources than conventional crude oil. The alternative carbon sources employed as feed can be renewable products, such as biomass, waste products, or natural resources such as coal and natural gas. The three main criticisms levelled against the relevance and need for XTL conversion were addressed:

(a) Sustainability. The use of renewable resources and sustainability must not be confused. Even though XTL technology can convert renewable resources into useful products, it does not enable or undermine sustainability. Sustainability requires balance between consumption and production, which in a finite environment implies a steady state (not perpetual growth).
(b) Non-carbon based carriers. Non-carbon based energy sources have their application, but are not without shortcomings. XTL technology has a role to play, not only to provide carbon-based energy carriers, but XTL technology enables carbon recycling and it is capable of generating non-energy carbon-carriers like petrochemicals.
(c) Carbon (CO_2) footprint. Much of the CO_2 footprint associated with XTL technology is not inherent to XTL conversion, but it is associated with source of energy that is employed to drive the XTL conversion. If this energy is derived from a non-carbon source, the remaining CO_2 footprint is much smaller. The other significant source of CO_2 is due to H_2 production. Any H_2 that is produced by the water gas shift reaction produces an equimolar amount of CO_2 in addition to the CO_2 that is produced to provide energy for the conversion. In this respect direct liquefaction has an advantage over indirect liquefaction, since it avoids oxygen addition to all of the carbon in the feed, which decreases the H_2

In Synthetic Liquids Production and Refining; de Klerk, A., et al.;
ACS Symposium Series; American Chemical Society: Washington, DC, 2011.

demand of the XTL process. Furthermore, part of the direct liquefaction feed can be rejected as hydrogen depleted coke, which sequesters the carbon as carbon and not as CO_2.

In addition, some general observations were made with respect to XTL conversion:

(d) Direct liquefaction technologies in general have higher carbon yields and require less energy, but the liquid products are more difficult to refine to useful final products than the syncrude produced by indirect liquefaction.
(e) The main detractor from XTL technology is the high capital cost of XTL facilities. With pressure to reap the benefit of "economy of scale" there is resistance to invest in smaller facilities. The barrier to entry for new technology is therefore high and this stifles progress.
(f) Over the past two decades most new large-scale industrial XTL facilities were constructed for gas-to-liquids conversion by indirect liquefaction (methanol synthesis and Fischer–Tropsch synthesis).
(g) Even though XTL can be profitable at current oil and gas prices, crude oil is still too cheap and too readily available to stimulate significant interest in XTL conversion.

Downloaded by 89.163.35.42 on June 6, 2012 | http://pubs.acs.org
Publication Date (Web): November 29, 2011 | doi: 10.1021/bk-2011-1084.ch001

References

1. Cavallo, A. J. *Oil Gas J.* **2005**, *103* (21), 22–26.
2. Duncan, R. C. *Oil Gas J.* **2004**, *102* (27), 18–21.
3. Stranges, A. N. *ACS Symp. Ser.* **1983**, *228*, 21–42.
4. Hoffman, E. J. *Synfuels. The Problems and the Promise*; Energon; Laramie, 1982.
5. Harlan, J. K. *Starting with Synfuels: Benefits, Costs, and Program Design Assessment*; Ballinger: Cambridge, MA, 1982.
6. Nowacki, P. *Coal Liquefaction Processes*; Noyes Data Corp.: Park Ridge, NJ, 1979.
7. Cusumano, J. A.; Dalla Betta, R. A.; Levy, R. B. *Catalysis in Coal Conversion*; Academic Press: New York, 1978.
8. De Klerk, A.; Furimsky, E. *Catalysis in the Refining of Fischer–Tropsch Syncrude*; Royal Society of Chemistry: Cambridge, U.K., 2010.
9. De Klerk, A. In *Advances in Fischer-Tropsch Synthesis, Catalysts, And Catalysis*; Davis, B. H., Occelli, M. L. Eds.; Taylor & Francis (CRC Press): Boca Raton, 2009, pp 331−364.
10. Anderson, L. L.; Tillman, D. A. *Synthetic Fuels from Coal. Overview and Assessment*; Wiley: New York, 1979.
11. Tugendhat, C.; Hamilton, A. *Oil. The Biggest Business*; Eyre Methuen: London, 1975.
12. Baum, R. *Chem. Eng. News* **2010**, *88* (26), 3.

13. Davis, S. *Petrochemical Industry Overview*; SRI Chemical Economics Handbook, Marketing Research Report, Section 350; Stanford Research Institute: Menlo Park, CA, 2008.
14. De Klerk, A. *Green Chem.* **2007**, *9*, 560–565.
15. Probstein, R. F.; Hicks, R. E. *Synthetic Fuels*; McGraw-Hill: New York, 1982.
16. Storch, H. H. In *Chemistry of Coal Utilization*, Vol. 2; Lowry, H. H., Ed.; Wiley: New York, 1945, pp 1750−1796.
17. Batchelder, H. R.; Nelson, H. W. *Prepr. Pap.-Am. Chem. Soc., Div. Fuel Chem.* **1974**, *19* (3), 162–177.
18. Stranges, A. N. *Stud. Surf. Sci. Catal.* **2007**, *163*, 1–27.
19. Lee, E. S. In *Coal Conversion Technology*, Wen, C. Y., Lee, E. S., Eds.; Addison-Wesley: Reading, MA, 1979, pp 428−545.
20. Howard-Smith, I.; Werner, G. J. *Coal Conversion Technology*; Noyes Data Corp.: Park Ridge, NJ, 1976.
21. Mangold, E. C.; Muradaz, M. A.; Ouellette, R. P.; Rarah, O. G.; Cheremisinoff, P. N. *Coal Liquefaction and Gasification Technologies*; Ann Arbor Science Publishers: Ann Arbor, 1982.
22. *Handbook of Synfuels Technology*; Meyers, R. A., Ed.; McGraw-Hill: New York, 1984.
23. Romey, I. In *Synthetic Fuels*; Beghi, G., Ed.; Riedel: Dordrecht, 1985, pp 93−111.
24. Hirano, K. *Fuel Process. Technol.* **2000**, *62*, 109–118.
25. Jones, J. L. *ACS Symp. Ser.* **1978**, *76*, 3–20.
26. *Fuels from Biomass and Wastes*; Klass, D. L., Emert, G. H., Eds.; Ann Arbor Science Publishers: Ann Arbor, 1981.
27. Zwart, R. W. R.; Boerrigter, H.; Van der Drift, A. *Energy Fuels* **2006**, *20*, 2192–2197.
28. Huber, G. W.; Dumesic, J. A. *Catal. Today* **2006**, *111*, 119–132.
29. Berkowitz, N. *An Introduction to Coal Technology*, 2nd ed; Academic Press: San Diego, 1994, pp 181−183.
30. Lom, W. L. *Liquefied Natural Gas*; Wiley: New York, 1974.
31. Westerhout, R. W. J.; Waanders, J.; Kuipers, J. A. M.; Van Swaaij, W. P. M. *Ind. Eng. Chem. Res.* **1997**, *36*, 1955–1964.
32. Costa, P. A.; Pinto, F. J.; Ramos, A. M.; Gulyurtlu, I. K.; Cabrita, I. A.; Bernardo, M. S. *Energy Fuels* **2007**, *21*, 2489–2498.
33. Ohkita, H.; Nishiyama, R.; Tochihara, Y.; Mizushima, T.; Kakuta, N.; Morioka, Y.; Ueno, A.; Namiki, Y.; Tanifuji, S.; Katoh, H.; Sunazuka, H.; Nakayama, R.; Kuroyanagi, T. *Ind. Eng. Chem. Res.* **1993**, *32*, 3112–3116.
34. You, Y. S.; Shim, J-S.; Kim, J-H.; Seo, G. *Catal. Lett.* **1999**, *59*, 221–227.
35. Comolli, A. G.; Lee, T. L. K.; Popper, G. A.; Stalzer, R. H.; Zhou, P. *Prepr. Pap.-Am. Chem. Soc., Div. Fuel Chem.* **1998**, *43* (3), 441–446.
36. Si, T. Shenhua Shows the Way To Make Gas from Coal. *China Daily*, January 22, 2009.
37. Sun, Q. CTL Development in China. Congressional Noontime Briefing, Washington DC, April 24, 2008.

Downloaded by 89.163.35.42 on June 6, 2012 | http://pubs.acs.org
Publication Date (Web): November 29, 2011 | doi: 10.1021/bk-2011-1084.ch001

38. Ulrich, G. D.; Vasudevan, P. T. *Chemical Engineering Process Design and Economics. A Practical Guide*, 2nd ed; Process Publishing: Durham, NH, 2004, pp 331−335.
39. Massey, L. G. In *Coal Conversion Technology*, Wen, C. Y., Lee, E. S., Eds.; Addison-Wesley: Reading, MA, 1979, pp 313−427.
40. Higman, C.; Van der Burgt, M. *Gasification*, 2nd ed; Elsevier: Amsterdam, 2008.
41. Hirst, L. L. In *Chemistry of Coal Utilization*, Vol. 2; Lowry, H. H., Ed.; Wiley: New York, 1945, pp 1846−1868.
42. Marschner, F.; Moeller, F. W. In *Applied Industrial Catalysis*, Vol. 2; Leach, B. E., Ed.; Academic Press: New York, 1983, pp 215−243.
43. Tijm, P. J. A.; Waller, F. J.; Brown, D. M. *Appl. Catal., A* **2001**, *221*, 275–282.
44. Aasberg-Petersen, K.; Christensen, T. S.; Dybkjær, I.; Sehested, J.; Østberg, M.; Coertzen, R. M.; Keyser, M. J.; Steynberg, A. P. *Stud. Surf. Sci. Catal.* **2004**, *152*, 258–405.
45. Olah, G. A.; Goeppert, A.; Prakash, G. K. S. *Beyond Oil and Gas: The Methanol Economy*; Wiley-VCH: Weinheim, 2006.
46. Chang, C. D. *Catal. Rev.-Sci. Eng.* **1983**, *25*, 1–118.
47. Saade, G. A. *Methanol. Chemical Economics Handbook Marketing Research Report*; Stanford Research Institute: Menlo Park, CA, 2009.
48. Koempel, H.; Liebner, W. *Stud. Surf. Sci. Catal.* **2007**, *167*, 261–267.
49. De Klerk, A. *Fischer–Tropsch Refining*; Wiley-VCH: Weinheim, 2011.
50. Dry, M. E. In *Catalysis Science and Technology*, Vol. 1; Anderson, J. R., Boudart, M., Eds.; Springer: Berlin, 1981, pp 159−255.
51. Davis, S. *Petroleum liquid Feedstocks – Naphtha and Gas Oil. Chemical Economics Handbook Marketing Research Report*; Stanford Research Institute: Menlo Park, CA, 2010.
52. *Pet. Econ.* **2008**, *75* (10), 30.
53. *Chem. Eng. News* **2009**, *87* (49), 23.
54. Forbes, A. *Pet. Econ.* **2007**, *74* (7), 30.
55. Overtoom, R.; Fabricius, N.; Leenhouts, W. In *Proceedings of the 1st Annual Gas Processing Symposium*; Alfadala, H. E., Reklaitis, G. V. R., El-Halwagi, M. M., Eds.; Elsevier: Amsterdam, 2009, pp 378−386.
56. Williams, R. H.; Larson, E. D.; Liu, G.; Kreutz, T. G. *Energy Procedia* **2009**, *1*, 4379–4386.

Downloaded by 89.163.35.42 on June 6, 2012 | http://pubs.acs.org
Publication Date (Web): November 29, 2011 | doi: 10.1021/bk-2011-1084.ch001

Downloaded by PENNSYLVANIA STATE UNIV on June 6, 2012 | http://pubs.acs.org
Publication Date (Web): November 29, 2011 | doi: 10.1021/bk-2011-1084.ch002

Chapter 2

Experimental and Kinetic Investigation of CO_2 and H_2O/N_2 Gasification of Biomass Fuels

Heidi C. Butterman*[*] and Marco J. Castaldi

**Columbia University Environmental Engineering, HKSM, 500 W. 120th St.,
918 S.W. Mudd Building, New York, New York 10027**
[*]E-mail: hcb11@dewbrook.com

Characterization of the thermal decomposition of various woods, grasses and the biomass structural components, lignin and cellulose, was performed using a TGA with online GC analysis in both CO_2 and H_2O/N_2 gasification environments. CO_2 was observed to be a more efficient gasification environment that resulted in improved bio-char conversion during gasification. Introduction of CO_2 as co-feed into the gasification environment resulted in enhanced CO and depressed H_2 and CH_4 concentrations enabling greater control in the syngas ratio produced by adjustment of the level of CO_2 introduced.

Mass decomposition and H_2, CO, CO_2 and CH_4 gas evolution studies were performed for the various feedstocks at heating rates of from 1–100°C min^{-1} in both gasification media. When comparing the residual mass fractions of lignin and cellulose gasified in CO_2 subjected to slow (1°C min^{-1}) and fast (100°C min^{-1}) heating rates, greater differential processing of the two components was possible with 65%, rather than 42%, of the lignin remaining following cellulose decomposition at the slow heating rate. Selective isolation of the thermally resistant lignin, retaining a greater residual fraction of this structural component, was observed during CO_2 gasification at the lowest heating rates. While cellulose thermal decomposition was observed to occur over a narrow temperature window, ~275–425°C, thermal degradation of lignin occurs over a much wider range beginning about 175°C and finishing after

700°C with more than a 35% mass loss after 700°C in a CO_2 gasification environment.

A least squares best fit analysis for the global kinetic parameters gave an average pyrolysis activation energy for lignin and cellulose in CO_2 as 43 and 211 kJ mol^{-1}, while that for lignin and cellulose in H_2O/N_2 was 53 and 203 kJ mol^{-1}, respectively. The analysis showed a pyrolysis best fit reaction order of three for lignin and one for cellulose. The various biomass feedstocks showed activation energies between 28–72 kJ mol^{-1} and reaction orders of one or two, with samples high in cellulose content showing correspondingly higher energies and lower reaction order.

Downloaded by PENNSYLVANIA STATE UNIV on June 6, 2012 | http://pubs.acs.org
Publication Date (Web): November 29, 2011 | doi: 10.1021/bk-2011-1084.ch002

Introduction

Global emissions standards have become more stringent and public environmental consciousness has grown while demand for energy and fuels continues to rise. The carbon neutral status of biomass feedstocks enable them to address the issues of energy supply and security in a more sustainable manner. The dual polysaccharide and cross-linked aromatic chemical structure of ligno-cellulosic biomass offers the opportunity to create a wide variety of chemicals many of whom are identical to their petroleum derived counterparts. Tremendous potential exists in the thermochemical processing of ligno-cellulosics that can be realized once greater control in separation of the structural components can be achieved.

The processing of biomass feedstocks in a TGA is significantly different from that which occurs in an actual full scale reactor. Nevertheless, carefully controlled experiments can yield useful kinetic parameters and mechanism insight regarding thermochemical decomposition of ligno-cellulosics. In the development of a kinetic model for thermal decomposition, the true kinetic model will have kinetic parameters that are heating rate independent. Heat transfer limitations due to high heating rates or large sample sizes, with a resultant "thermal lag" in which the inside of the sample has not yet reached the TGA temperature, can result in the calculation of kinetic parameters that do not describe the actual kinetics and can only result in a global heating rate dependent correlation model.

Kinetic parameters offer insight into the relative ease of thermal conversion. They can indicate transition between regimes in which different mechanisms are operating to control the thermochemical decomposition. A broad collection of feedstock-specific values can help in operations modeling and design of process equipment. To optimize the use of biomass feedstocks, a better understanding of their chemical and kinetic behavior during thermal degradation is essential. More accurate and extensive kinetic parameters can enable the formulation of more realistic models used in the design of thermal treatment operations and processes.

Due to thermal lag between the temperature recorded in the gasification medium near the sample surface and the actual temperature within the sample volume, kinetic parameters determined from TGA measurements often tend to underestimate the intrinsic values with lower estimates of both activation energy and pre-exponential factor as transport limiting conditions become more significant. Varhegyi et al. (*1*) accounted for the heating rate dependent kinetics during cellulose pyrolysis by using the slow heating rate value of the activation energy and adjusting the pre-exponential factor to account for thermal inertia effects. Additionally, the global apparent activation energy determined from a single step decomposition model representing a multi-step process can add to this underestimate since it tends to be lower (*1*) than any of the E_{act} values for the individual steps. Employing a least squares kinetic analysis based on TGA measurements, they chose first order global kinetics for both cellulose and lignin. First order kinetics adequately described the cellulose decomposition mechanism involving several reactions with alternative pathways to char, condensable volatiles and gas products. The explanation for the good fit from the first order model, for the cellulosic component, was that a single high activation energy rate determining step controlled the cellulose decomposition.

The thermal degradation of ligno-cellulosic materials involves both the low temperature pyrolysis decomposition of the polysaccharide structures of cellulose and hemicellulose and the pyrolytic-gasification decomposition behavior of the more thermally resistant lignin structure whose processing occurs over a much wider temperature range and whose degradation is much more difficult to model. By studying various biomass feedstocks along with surrogate models for their chemical structures, polycrystalline cellulose powder and Organosolv lignin, a better characterization of their gas evolution and mass decomposition during thermal treatment can be formulated.

The conditions under which TGA mass loss data is governed by intrinsic gasification activity and not significantly influenced by transient chemisorption dynamics was studied by Feng and Bhatia (*2*). They identified criteria and conditions under which intrinsic kinetic carbon gasification parameters could be extracted from TGA data under CO_2 and O_2 environments. A TGA study of the pyrolysis of sawdust and its three structural components under syngas and H_2 atmospheres was investigated by Wang et al. (*3*). The maximum mass loss rate was shifted to higher temperatures at higher heating rates, an observation confirmed in the current study. Though lignin and hemicellulose were not found to significantly effect each other's pyrolysis behavior, when mixed with cellulose, they were observed to synergistically effect the pyrolysis characteristics of cellulose, indicating a coupling effect of the degradation mechanisms seen in the actual biomass sample.

Caballero et al. (*4*) investigated the pyrolysis of almond shells and attempted to characterize the volatiles yield and thermal degradation kinetics. The yield in hydrocarbons above 800°C from the gasification of almond shells was significantly greater than what would have been predicted based on a summative yield from both the lignin and holocellulose fractions. Treating the behavior of the biomass, either mass decomposition or gas evolution, as a weighted average of the structural components of the raw material was unable to characterize the behavior of the intact ligno-cellulosic feedstock since it did not take into account the importance of the component interactions, both the strong influence of the coupled mechanisms and physical association of the biomass structural components.

Downloaded by PENNSYLVANIA STATE UNIV on June 6, 2012 | http://pubs.acs.org
Publication Date (Web): November 29, 2011 | doi: 10.1021/bk-2011-1084.ch002

Downloaded by PENNSYLVANIA STATE UNIV on June 6, 2012 | http://pubs.acs.org
Publication Date (Web): November 29, 2011 | doi: 10.1021/bk-2011-1084.ch002

Describing a cluster of coupled independent parallel first order reactions by a single global first order expression can also result in a global activation energy that is much lower than that of any of the individual reactions in the set. At very high heating rates or very high mineral concentrations individual DTG peaks for a given component can merge, as discussed by Antal and Varhegyi (*5*), masking the true component kinetics.

A TGA study of the thermal decomposition of sugarcane bagasse and waste wood assuming a 3-parallel-reaction model combining the independent thermal decomposition of the three pseudocomponents was performed by Manya et al. (*6*). They used a nonlinear least squares regression algorithm to find the set of kinetic parameters that gave a best fit to their data set assuming three kinetic equations and taking initial values from the study of Gronli et al. (*7*). The kinetic parameters derived from the Manya et al. summative model found that a first order reaction equation for Avicel cellulose and a third order equation for Kraft alkali lignin gave the best fit.

The TGA results of Varhegyi et al. (*8*) justified the validity in assuming the significance of the role of parallel reactions in the pyrolytic decomposition of cellulose. A single one of two parallel high temperature (370°C) reactions, that was an irreversible first order decomposition with apparent activation energy of 238 kJ mol^{-1}, correlated well with their experimental observations of cellulose pyrolysis at 10°C min^{-1} in an inert medium (Ar or He).

The round-robin study of Avicel cellulose compiled by Gronli et al. (*9*) and performed at eight different European laboratories using 5 different TGAs observed good agreement between results from the different labs at the slow 5°C min^{-1} heating rate but considerable scatter at the faster 40°C min^{-1} rate. Their kinetic parameters derived using the eight data sets was based on an irreversible single step first order rate equation for cellulose pyrolysis and a least squares regression analysis.

Wang et al. (*3*) studied the hydro-pyrolysis of biomass and tried to distinguish between the degradation rates of the three structural components and assess their influence on each other. They observed that while lignin and hemicellulose could alter the pyrolysis of cellulose by shifting the maximum mass loss rate, the temperature at which it occurs and the final mass loss value, lignin and hemicellulose (xylan) could not be observed to affect each other's pyrolytic degradation. Their observation of the influence on cellulose pyrolysis has important implications for those attempting to model biomass thermal degradation. Three independent parallel reactions that are neither coupled to each other nor influenced by the mineral impurities present in the actual biomass samples will not capture the behavior of real feedstocks and will yield kinetic parameters that do not accurately represent the complex processes occurring during ligno-cellulosic thermal treatment.

Sonobe and Worasuwannarak (*10*) used a distributed activation energy model to determine kinetic parameters from biomass samples pyrolyzed at 10°C min^{-1} in He. They observed strong interaction between the cellulose and lignin fractions that resulted in a decrease in tar yield but an increase in char yield and found that the catalytic effect of the alkali and alkaline earth minerals were responsible for much of the variability between biomass feedstocks that became apparent in the activation energy distribution curve.

Using a least squares optimization with a single first order reaction kinetic model for Avicel cellulose, Varhegyi et al. (*11*) experimentally determined the activation energy for the thermal decomposition, at the slower heating rate of 10°C min^{-1}, to be 234 kJ mol^{-1} with a pre-exponential factor of 3.98×10^{17} sec^{-1} and a reaction order of 1.2. These values compare favorably with the current study in which the average CO_2 and H_2O/N_2 cellulose pyrolysis activation energy at 10°C min^{-1} were determined as 230 and 212 kJ mol^{-1} with pre-exponential factors of 2.38×10^{19} and 2.56×10^{20} sec^{-1} $K^{-½}$, respectively. The activation energy calculated at the faster heating rate of 80°C min^{-1} was 205 kJ mol^{-1} with a pre-exponential factor of 1.3×10^{15} sec^{-1} and the same reaction order. It is interesting to note that their kinetic models built on either the assumption of independent parallel reactions or a series of successive reactions resulted in mass loss fraction profiles and kinetic parameters that fit the experimental data as well as the single global decomposition reaction model for cellulose. The capability of a model to suitably fit experimental observations cannot be taken as a validation of its ability to accurately describe the thermal degradation process. Further chemical information is necessary before any kinetic model could be selected as actually describing the thermochemical degradation process.

A TGA, GC/MS and GC/FID study was performed by Muller-Hagedorn et al. (*12*) studying both the kinetics and gas evolution of hornbeam, walnut and pine woods. A five parallel reaction model was employed with a power law dependence on the mass fraction of volatiles. Mean kinetic parameters were reported for heating rates of 2, 5 and 10°C min^{-1} as a result of the thermal degradation in a helium environment following drying and water and acid washing of the wood samples. The cellulose reaction orders were found to be 0.8 or 0.9 while that of the lignin component was either 1.3 or 1.4. The activation energies determined for the lignin fraction were 99, 95, 93 and for the two cellulose reactions 93/181, 99/183, 93/181 kJ mol^{-1} for the hornbeam, walnut and Scots pine, respectively. As a result of the lower inorganic salt content of coniferous woods, they tend to produce less ash residue and their lignins tend to be more thermochemically stable than those of deciduous woods. The mineral content was found by Muller-Hagedorn et al. to not only result in earlier pyrolytic decomposition but also significantly different volatile profiles dominating at low and high pyrolytic temperatures. This led them to believe that a set of several parallel reactions were actually necessary to characterize lignin thermal decomposition resulting in an overall reaction order for lignin greater than one.

Using TGA and DSC at a heating rate of 40°C min^{-1} in a N_2 atmosphere, Stenseng et al. (*13*) examined the pyrolytic (<600°C) decomposition of wheat straw and cellulose to determine the influence of sample size on thermal lag between the actual sample and measured thermocouple temperatures. Only for materials having a relatively high heat of reaction such as cellulose having a value that they determined by DSC to be between 630 – 710 kJ kg^{-1} (102 – 115 kJ mol^{-1}) did Stenseng et al. stress the importance of using very small TGA samples <1mg and low heating rates <40°C min^{-1}.

Downloaded by PENNSYLVANIA STATE UNIV on June 6, 2012 | http://pubs.acs.org
Publication Date (Web): November 29, 2011 | doi: 10.1021/bk-2011-1084.ch002

Downloaded by PENNSYLVANIA STATE UNIV on June 6, 2012 | http://pubs.acs.org
Publication Date (Web): November 29, 2011 | doi: 10.1021/bk-2011-1084.ch002

A similar study to characterize the thermochemical decomposition of cellulose in N_2 at heating rates of 0.1 – 60°C min^{-1} and to determine the heat of reaction during pyrolysis using TGA and DSC was performed by Milosavljevic et al. (*14*). They estimated the main cellulose pyrolytic degradation pathway to be endothermic with an enthalpy change of 538 kJ kg^{-1} (87 kJ mol^{-1}) for tar forming conversion to condensable volatiles while the char forming combustion processes they measured as exothermic with an enthalpy change of approximately –2000 kJ kg^{-1} (–324 kJ mol^{-1}).

The kinetic study of sawdust and rice husk by Park et al. (*15*) was a TGA investigation of pyrolysis (200-400°C) in a N_2 atmosphere at 15°C min^{-1} and steam gasification (600-900°C) in a 0.5 atm H_2O/1.0 atm N_2 environment at 30°C min^{-1}. Their pyrolysis data best fit a first order global decomposition while the gasification data best fit a 2/3 order of reaction. The global activation energies during pyrolysis for sawdust and rice husk were found to be 83.5 and 82.9 kJ mol^{-1}, respectively.

Introduction of steam as a reactant influent results in enhanced H_2 production during gasification of a wide variety of hydrocarbon fuels that include woods, grasses, agricultural residues and coal. Introduction of CO_2 during high temperature steam gasification results in enhanced CO production and depressed CH_4 and H_2 levels (*16*, *17*). While both H_2O and CO_2 have been shown (*18–23*) to increase char reactivity by modifying surface activity and pore structure of the char, CO_2 creates a more porous char structure with a more extensive channel network that can result in a unique set of pyrolysates as compared to steam processing. Through a prudent selection of the gasification medium, greater control of the volatile evolution products is possible. As a result of biomass gasification, a synthesis gas is produced whose main components are CO, H_2 and CH_4. Other volatile components released during pyrolytic thermal decomposition include H_2O, CO_2, acetic acid, formaldehyde, phenol, acetaldehyde, formic acid and acetone. The detection of those species was not reliable since the experiments were performed under high levels of N_2 and CO_2 dilution. A brief discussion of several of the reactions referred to in the present study, including the water gas shift reaction, methanation reactions, steam reforming and Boudouard reaction appears in Supporting Information.

The current investigation presents an experimental kinetic analysis to more completely characterize the nature of and contrast the differences in thermal decomposition of biomass feedstocks in CO_2 and H_2O/N_2 environments. TGA mass decomposition profiles in both CO_2 and H_2O/N_2 media at varying heating rates for a variety of woods, grasses and residues as well as the structural components, lignin and cellulose, are presented along with micro-GC gas evolution profiles for H_2, CO and CH_4 evolution from lignin and cellulose in both CO_2-enriched and H_2O/N_2 environments. Using a least squares analysis on the mass loss fraction rate, kinetic parameters as well as the equations used to derive them are presented for the reaction order, activation energy, temperature dependence exponent and pre-exponential factor of the various biomass feedstocks. The present study involves a more comprehensive comparison than currently exists quantifying the kinetic behavior of a variety of biomass feedstocks undergoing thermal degradation in both CO_2 and H_2O/N_2 reactive environments.

These global kinetic parameters derived from the mass decomposition curves can aid in modeling thermal treatment processes involving ligno-cellulosics.

Experimental Setup

Gasification System

Figure 1 shows a schematic diagram of the gasification test facility in the Combustion Lab at Columbia University SEAS Henry Krumb School of Mines. It consists of a Temperature Programmer Interface/Thermal Analyzer (Instrument Specialists) that regulates the temperature and heating rate of the quartz furnace in the Thermogravimetric Analyzer (Dupont 951). The carrier flow consists of N_2 (UHP) and CO_2 (Bone Dry) whose flow rates are regulated by means of calibrated rotameters (Gilmont GF 1060). A syringe pump (kd-Scientific 780-100) introduced liquid distilled water into a stainless steel in-house made vaporizer that produces slightly superheated steam (~110—120°C). The vaporizer temperature was continuously monitored by external surface thermocouples (Omega E-type) coupled to a digital readout (Omega DP460-T) prior to entering the furnace. The total inlet flow (steam + N_2 + CO_2) was maintained at a rate of ~80 mL min^{-1} during the H_2O/N_2 runs and ~75 mL min^{-1} during the 100% CO_2 gasification runs. The level of water introduced was maintained at room temperature saturation values while the volumetric % CO_2 fed into the line varied from 0-60%. Gaseous steam was introduced into the furnace by means of a side arm through which flowed the steam and a portion of the N_2 remaining after a fraction was diverted for purge flow to prevent deposition onto the TGA electronics. The gasification process was run with excess H_2O and CO_2 to ensure that the hydrocarbon feedstock was the limiting agent in the gasification reactions.

The sample is suspended from a quartz rod and sits inside an inert platinum pan. Gas evolution data is recorded as a function of temperature with the mass decay as a function of temperature displayed graphically in real time using the Instrument Specialists programmer interface software. The influent and products of gasification exit the furnace and enter an ice-water condensation column that removes any moisture and condensable volatiles from the gas evolution products prior to entering the Agilent 3000A micro-gas chromatograph.

Methodology of Gasification Testing

Wood samples were prepared by controlled core drilling within planks of untreated wood to produce dry, unheated sawdust while the herbaceous feedstocks were air-dried, ground by mortar and pestle and then ball-milled. Chemical degradation was minimized by limiting the amount of mechanical processing done on the feedstock. Distinctly different gas evolution profiles exhibited by the green pine needles as compared to the dried pine needles was taken as evidence of this observable degradation. To maintain the original mineral content of the herbaceous samples, the grasses and needles were not water washed, but used as received. Only the beachgrass sample needed careful inspection and pretreatment cleaning to mechanically remove all sand grains prior to processing.

Downloaded by PENNSYLVANIA STATE UNIV on June 6, 2012 | http://pubs.acs.org
Publication Date (Web): November 29, 2011 | doi: 10.1021/bk-2011-1084.ch002

Downloaded by PENNSYLVANIA STATE UNIV on June 6, 2012 | http://pubs.acs.org
Publication Date (Web): November 29, 2011 | doi: 10.1021/bk-2011-1084.ch002

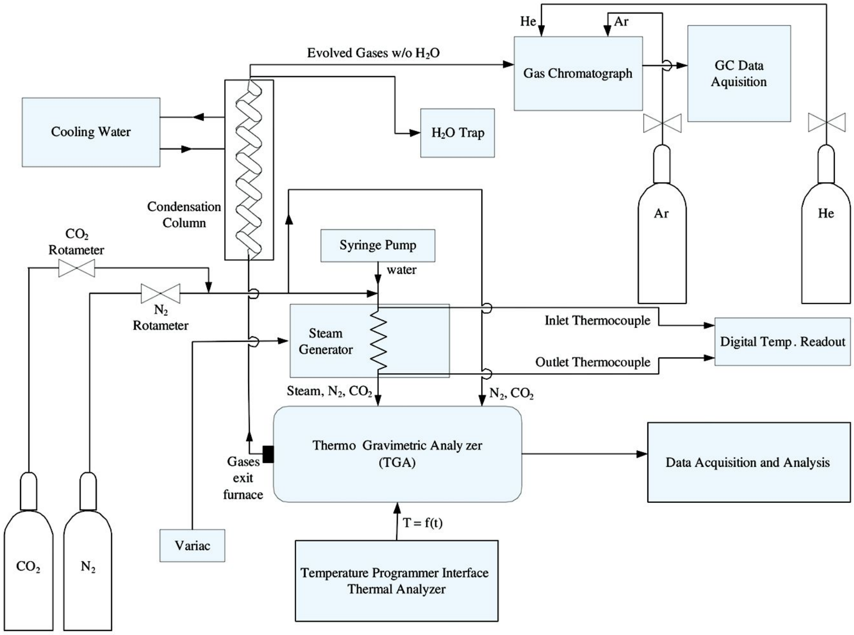
He
Ar
Evolved Gases w/o H_2O
Gas Chromatograph
GC Data Aquisition
Cooling Water
H_2O Trap
Condensation Column
Ar
He
CO_2 Rotameter
Syringe Pump
water
N_2 Rotameter
Steam Generator
Inlet Thermocouple
Digital Temp. Readout
Outlet Thermocouple
Steam, N_2, CO_2
N_2, CO_2
Thermo Gravimetric Analy zer (TGA)
Data Acquisition and Analysis
Gases exit furnace
CO_2
N_2
Variac
T = f(t)
Temperature Programmer Interface Thermal Analyzer

Figure 1. Schematic of the experimental apparatus.

The feedstocks included spruce, white pine, Douglas fir, poplar, sugar maple, red oak, alfalfa, American beachgrass, pine needles, maple bark, blue noble fir needles, Sigma Aldrich Organosolv lignin and powdered micro-crystalline cellulose. The typical size of the samples ranged from 21-25 mg. Both a small sample size (<25 mg) and a slow heating rate (~1-2 °C min^{-1}) were employed to ensure minimal heat and mass transport limitations, also known as thermal lag effects, enabling us to extract reliable kinetic parameters. The sample weights were measured in real time by the TPI/TA software with independent verification of initial mass by means of a Mettler scale accurate to +/- 0.1mg.

The relatively small sample in the TGA pan and the relatively high flow rate of the feed result in significant dilution of the gas evolution products detected by the micro-GC. During thermal processing, mass decomposition profiles are displayed in real time and the sample mass is recorded as a function of both temperature and time enabling creation of mass loss and derivative mass loss fraction data.

To characterize the mass decomposition as a function of temperature, a single step global n^{th} order rate equation was used to characterize the mass loss fraction profile with global kinetic parameters to be determined. These included the reaction order, apparent activation energy and pre-exponential factor. The temperature dependence factor (T^w) was also tested to determine that value of the exponent w that could give the best overall fit from the choice of 0, ½, or 1. A least squares minimization of the rate of mass loss fraction ($d\alpha/dT$) was employed to determine a best fit for the reaction order when testing n = 1, 2, or 3. Lignin, cellulose and various biomass feedstocks were gasified in CO_2 and H_2O/N_2 environments at varying heating rates of 1, 2, 5, 10, 20, 50 and 100°C min^{-1} to determine the kinetic parameters that could best describe the mass decomposition profiles. Organosolv lignin and microcrystalline cellulose were chosen as the representative structural components since their isolation involved the most benign chemical processing available.

Results and Discussion

To ensure that the global kinetic parameters that are determined accurately describe the thermal decomposition process, a sufficiently slow heating rate, small sample size and thermocouple that can adequately characterize the temperature within the sample is necessary. Decreased residence time as a result of rapid heating rate, or increased mass transfer resistance due to larger sample size (smaller surface to volume ratio) can lead to a shift in the maximum mass loss rate temperature T_{max} to higher values with a corresponding shift in the apparent kinetic parameters. The tests performed showed a distinct shift in T_{max} for lignin and cellulose in CO_2 from 342 to 436°C and 324 to 440°C, respectively. T_{max} identifies the inflection point in the pyrolysis mass loss curve where the degradation rate is a maximum. This maximum degradation rate during pyrolysis, $(d\alpha/dT)_{max}$, that also corresponds to the maximum value of the derivative that occurs over the gasification interval 110-980°C, is used as the normalization parameter for the %Fit error term.

In general the activation energy for the global pyrolytic lignin decomposition tended to increase and the order of reaction monotonically decreased with increasing heating rate. The true global kinetics derived from dynamic TGA data should be heating rate independent and so we placed more confidence in the reaction order derived for the ligno-cellulosic components from the slowest heating rate runs: order three for lignin in CO_2 and H_2O/N_2, and order one for cellulose in CO_2 and H_2O/N_2 during pyrolysis.

Curves for the lignin, cellulose, woods and grasses/residues mass loss fraction, α, and its derivative, $d\alpha/dT$, appear in Figures 2-11. The derivative graphs for lignin, woods, and grasses/residues showed both pyrolytic and gasification peaks only during CO_2 thermal treatment where a more complete conversion of the char to ash residue and volatiles resulted during high temperature CO_2 gasification. The 10°C min^{-1} pyrolytic decomposition of the highly cellulosic woods in CO_2 showed behavior more characteristic of cellulose while that of the highly lignitic bark and needle residues in CO_2 showed curves more typical of lignin with earlier decays possibly due to a catalytic effect conferred by the high mineral content of the residue feedstocks.

Downloaded by PENNSYLVANIA STATE UNIV on June 6, 2012 | http://pubs.acs.org
Publication Date (Web): November 29, 2011 | doi: 10.1021/bk-2011-1084.ch002

Downloaded by PENNSYLVANIA STATE UNIV on June 6, 2012 | http://pubs.acs.org
Publication Date (Web): November 29, 2011 | doi: 10.1021/bk-2011-1084.ch002

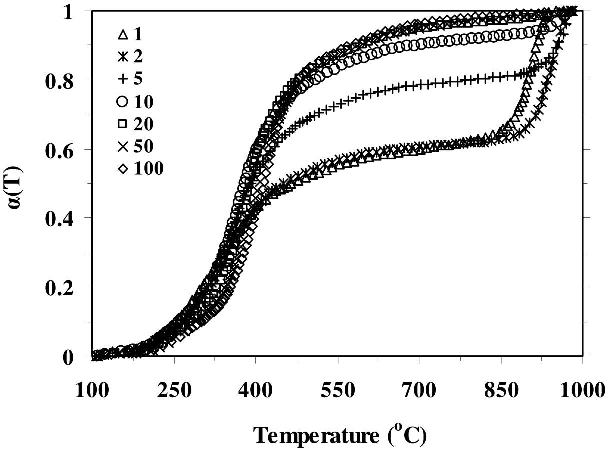

Figure 2. Lignin mass loss fraction α during CO_2 processing 110-980°C for heating rates of 1-100°C min^{-1}.

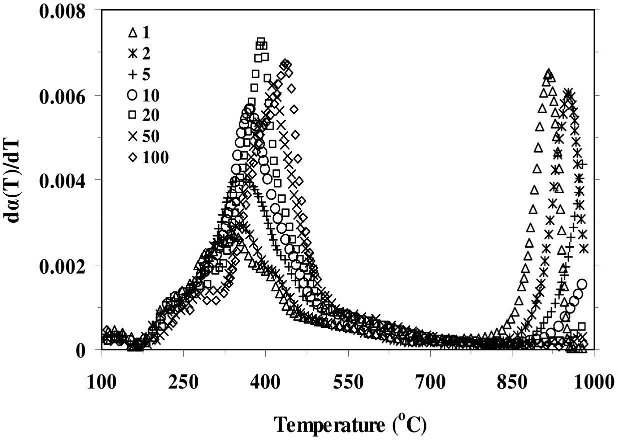

Figure 3. Lignin derivative mass loss fraction dα/dT during CO_2 processing 110-980°C for heating rates of 1-100°C min^{-1}.

Organosolv lignin was selected as the structural surrogate that, as a result of the relatively benign chemical isolation with less extensive cleavage of side chains and destruction of cross-linkages, could most closely approximate the characteristic thermochemical and, consequently, kinetic behavior of the native lignin. Since lignin decomposes over a broad range in temperatures, the global reaction order for lignin decomposition is expected to be relatively high. This is in contrast to the rapid decomposition, with a strong pyrolytic derivative spike for cellulose with a significantly lower reaction order n ~ 1. Since the derivative curve is more sensitive to changes than the mass loss curve, a non-linear least squares minimization was performed on the differences in derivative mass loss fraction as calculated and determined experimentally.

The migration of the inflection point in the mass loss α(T) curve both during pyrolysis (T_{max}) and during high temperature gasification of lignin in CO_2, corresponds to the shift in the derivative peaks to higher temperatures at higher heating rates. Both the transition to higher temperatures (longer residence times) observed in the mass loss curves (Figures 2, 4, and 6) as well as a transition to steeper slopes (greater thermal gradients existing across the lignin sample surface) appears as a general rise in pyrolytic peak of the mass loss rate profiles (Figures 3, 5 and 7).

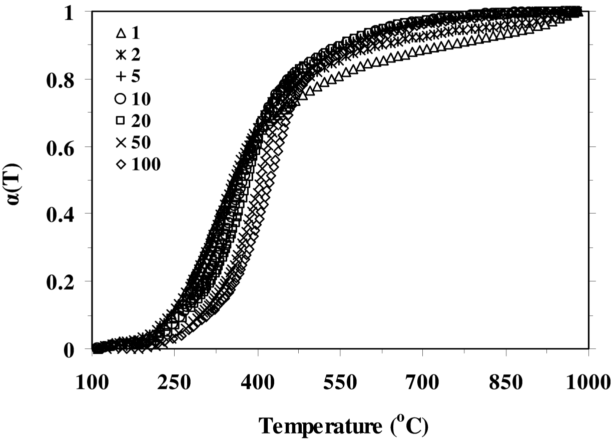

Figure 4. Lignin mass loss fraction α during H_2O processing 110-980°C for heating rates of 1-100°C min^{-1}.

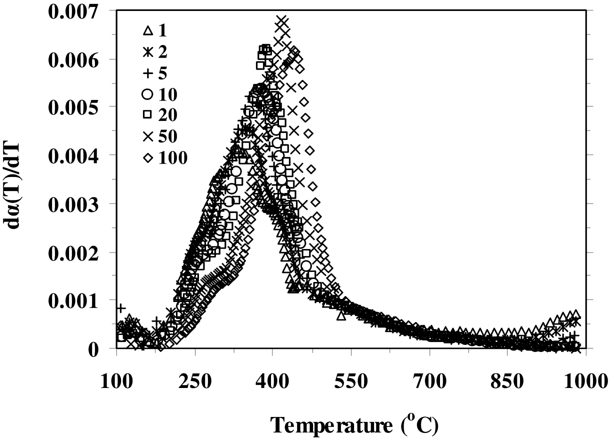

Figure 5. Lignin derivative mass loss fraction dα/dT during H_2O processing 110-980°C for heating rates of 1-100°C min^{-1}.

In Synthetic Liquids Production and Refining; de Klerk, A., et al.;
ACS Symposium Series; American Chemical Society: Washington, DC, 2011.

Downloaded by PENNSYLVANIA STATE UNIV on June 6, 2012 | http://pubs.acs.org
Publication Date (Web): November 29, 2011 | doi: 10.1021/bk-2011-1084.ch002

Downloaded by PENNSYLVANIA STATE UNIV on June 6, 2012 | http://pubs.acs.org
Publication Date (Web): November 29, 2011 | doi: 10.1021/bk-2011-1084.ch002

Figures 2, 4, 6, 8, and 10 represent mass loss fraction curves for the various feedstocks. Unlike the mass decomposition curve that is normalized by the initial mass, the mass loss fraction curve has a contour determined by both the initial and final mass values. While thermal treatment of lignin in a H_2O/N_2 medium results in no significant mass loss during high temperature gasification, a significant reduction in char residue can result during CO_2 processing if the heating rate is sufficiently slow (~1-2°C min^{-1}). At slower heating rates (1-5°C min^{-1}) three distinct decay regions for pyrolysis, gasification and high temperature burnout can be seen in Figure 2. These correspond to the high temperature peaks in the derivative graphs of Figure 3. In contrast, at the higher heating rates (20-100°C) pyrolysis and gasification regions without the high temperature burnout of the lignin char can be seen in Figure 2 in which the mass loss curves rise rapidly to completion, representing greater levels of residual char at higher heating rates. This corresponds to the absence of a second peak in the high heating rate derivative curves.

The current experimental study involves slow heating rate gasification (1-100°C min^{-1}) in both H_2O/N_2 and CO_2 environments, at atmospheric pressure and heated from ambient to 1000°C, with the production of low levels of char and high conversion to volatiles. Fast pyrolysis, that is characterized by extremely high heating rates (~500-2000°C min^{-1}) and rapid quenching of the liquid and condensable volatile products, results in high levels of liquid (tar) and low yields of gaseous species. It attempts to terminate any subsequent reactions that could result in conversion to gaseous products or additional solid when the highly reactive char reacts with the gaseous pyrolysates to undergo secondary reactions. In general, conversion to gaseous products is favored by high gasification temperatures and slow heating rates, conversion to solid char is favored by slow heating rates and low pyrolysis temperatures, and conversion to liquid products is most likely under extremely high heating rates at low temperatures while under a purge flow to remove gaseous products or a quench for condensable volatiles.

Flash pyrolysis of biomass has gained much attention recently as a means of producing liquid fuels from the bio-oil produced. To maximize the liquid production, higher heating rates to minimize carbonization are employed as are lower pyrolysis temperatures and shorter residence times to minimize secondary thermal cracking that would promote conversion to volatiles and thus lower liquid yields. The operating conditions that optimize thermochemical conversion of ligno-cellulosics to liquids rather than volatiles or char involve pyrolysis rates greater than 100°C sec^{-1} under temperatures of ~350-550°C for residence times of less than one second with the volatiles produced being rapidly quenched to condense the bio-oil. The composition is low in alkanes though high in oxygenated compounds such as aldehydes, ketones and methoxyphenol species.

Slow pyrolysis of biomass feedstocks is conducive to production of large volumes of a high energy density solid char while fast pyrolysis favors the formation of a liquid bio-oil fuel. High temperatures (~1000°C) produce a syngas that can be cleaned and used as a gaseous fuel or that can undergo subsequent processing as a feedstock for green fuel or chemical production. Operational parameters and design criteria for pyrolytic reactors and gasification units rely on a knowledge of the temperature dependent gas evolution behavior, a

In Synthetic Liquids Production and Refining; de Klerk, A., et al.;
ACS Symposium Series; American Chemical Society: Washington, DC, 2011.

characterization of the char reactivity and some information regarding the slagging and corrosion potential of the high mineral content in the ligno-cellulosics. Through small differences in operational parameters significant improvements in process efficiency and greater control of feedstock conversion can be achieved. The purpose of the current study was to investigate the thermal decomposition of a variety of biomass feedstocks with the aim of extracting meaningful kinetic, structural, and thermochemical information essential for the design of biomass reactor systems.

The first structural component to begin degradation is hemi-cellulose at about 175°C, followed by lignin at 200°C and finally cellulose at 275°C. Though the polysaccharides have completed their decay within about a 150°C interval, lignin continues decomposition in an inert environment for another 450°C. It was observed that using a CO_2 gasification medium rather than N_2, along with a slow (1-2°C min^{-1}) heating rate, resulted in continued thermal decomposition until the 32-37% lignin residual was converted to about 2% ash by 1000°C. The Boudouard reaction between the carbon lattice skeleton and the CO_2 gasification environment resulted in enhanced conversion during thermal treatment at high gasification temperatures. While high heating rates and short residence times for the vapor phase products favor high pyrolytic liquids, slow heating rates and long residence times under elevated pressures are conditions that are conducive to maximum char yields. Preventing conditions under which secondary reactions between the volatile phase products and the reactive char can occur is important in enabling the determination of primary reaction kinetics. Through the determination of global apparent kinetic parameters for the ligno-cellulosic structural components and a knowledge of their relative fractional contribution in a given biomass feedstock as well as an adequate characterization of the mineral impurities in the sample, a thermal decomposition rate can be estimated to aid in the design of biomass gasifiers.

Since the cellulose decomposition occurs over a very narrow temperature range, ~275-450°C, a much sharper peak in the derivative graph occurs and the global decomposition reaction can be modeled as first order. Since the lignin decomposition is spread over a wide temperature range spanning both pyrolysis and gasification temperatures, ~200-700°C, a broad diffuse peak in the derivative graph occurs and the global decomposition of lignin needs to be modeled by a higher order reaction. Lignin pyrolysis was determined, through a least squares minimization, to most closely fit a global third order decomposition. For moderate to high heating rates of lignin, at high temperature during gasification in either a H_2O/N_2 or CO_2 gasification medium, a first order reaction could best describe the global decomposition based on a least squares minimization of the derivative mass loss fraction. This is indicative of a process experiencing a transition in kinetic mechanism where a single reaction order may not adequately describe the thermal decomposition over a very wide temperature range.

Lignin begins thermal degradation at a much lower temperature than cellulose and this is represented in the considerably lower activation energies calculated for lignin as compared to cellulose. Biomass feedstocks, particularly the grasses, begin thermal decomposition earlier than either of these two structural

Downloaded by PENNSYLVANIA STATE UNIV on June 6, 2012 | http://pubs.acs.org
Publication Date (Web): November 29, 2011 | doi: 10.1021/bk-2011-1084.ch002

Downloaded by PENNSYLVANIA STATE UNIV on June 6, 2012 | http://pubs.acs.org
Publication Date (Web): November 29, 2011 | doi: 10.1021/bk-2011-1084.ch002

components, exhibiting a catalytic effect conferred by the high mineral content that is most significant in the herbaceous and residue samples.

Biomass gasification involves the thermochemical degradation of the oxygenated hydrocarbon feedstock. During progressive heating in the TGA, the sample undergoes dehydration, pyrolysis, gasification and combustion reactions as the material experiences mass decomposition that involves cleavage, depolymerization, condensation and oxidation reactions between molecular and radical species. Reaction with the gasification environment as well as the catalytic effect due to the mineral impurities present in the biomass sample can significantly alter the products resulting from thermal treatment. A large measure of control exists permitting the desired outcome products through suitable adjustment of the gasification parameters. By performing thermal processing at low temperature, with a high heating rate and permitting a short gas residence time, the production of liquid fuels and chemicals can be maximized. A slow heating rate with high pressure and a low purge gas flow at low temperature with long residence time for the primary volatiles to undergo secondary reactions is conducive to maximum solid char yield.

Figure 4 shows the results of lignin gasification using only steam as the reactive medium. One evident difference between Figures 2 and 4 is the existence of a significant high temperature mass decomposition present during CO_2 but not H_2O/N_2 processing. This gasification mass decay in CO_2 is seen as a second peak in the derivative graph (Figure 3) that is absent during lignin processing in H_2O/N_2 (Figure 5). If the goal is optimization of gaseous products then a slow heating rate, high temperature, long gas residence time and a reactive gasification medium such as CO_2 would facilitate the conversion to volatiles. CO_2 was more capable of accessing the porous microstructure of the highly reactive char. The CO_2 molecule could more easily diffuse into the porous network than the N_2 or H_2O molecule resulting in a more complete chemical conversion at the high gasification temperatures.

Whereas nearly all of the cellulose decomposition during CO_2 thermal treatment occurs during pyrolysis, as seen by a single derivative mass loss peak in Figure 7, lignin decomposition during CO_2 processing results in significant mass loss both during pyrolysis and gasification, as seen by two peaks in the derivative mass loss curve in Figure 3.

The results of the present study concerning the pyrolytic decomposition of cellulose agree well with the experimental and modeling results of Varhegyi et al. (*8*). Two parallel high temperature (370°C) reactions, one being an irreversible first order decomposition with an apparent activation energy of 238 kJ mol^{-1}, correlated well with their experimental observations.

This is in good agreement with the current results of cellulose pyrolysis between 110-450°C at 10°C min^{-1} in a CO_2 environment in which the decomposition best fit a first order reaction with a global activation energy of 230 kJ mol^{-1}. The rapid pyrolytic decomposition of cellulose, that was found to be similar in either a CO_2 or a H_2O/N_2 medium, occurs over a significantly narrower window between ~275-450°C as seen in Figure 6. The transition of the mass decomposition curves and their inflection points to higher temperatures is seen in Figure 7.

Higher heating rates correspond to shorter residence times that significantly impact the heat transport into the cellulose and the volatiles evolution out of the cellulose that is more significant during endothermic cellulose pyrolysis. This results in more shallow mass loss curves as seen in Figure 6, and a monotonic decrease in the derivative peaks with increasing heating rate as seen in Figure 7.

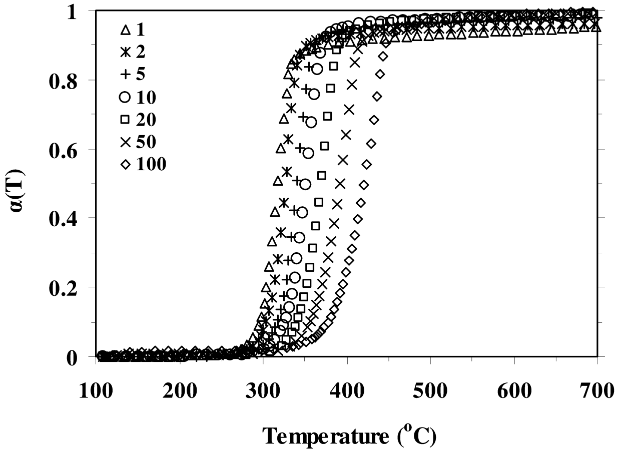

Figure 6. Cellulose mass loss fraction α during CO_2 processing 110-980°C for heating rates of 1-100°C min^{-1}.

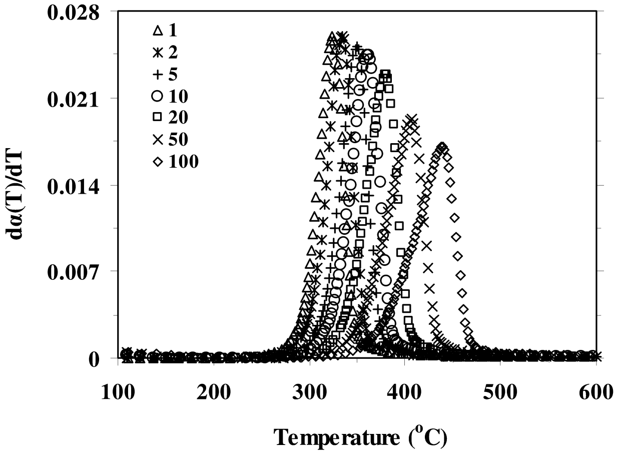

Figure 7. Cellulose derivative mass loss fraction dα/dT, CO_2 processing 110-980°C for heating rates of 1-100°C min^{-1}.

In Synthetic Liquids Production and Refining; de Klerk, A., et al.;
ACS Symposium Series; American Chemical Society: Washington, DC, 2011.

Downloaded by PENNSYLVANIA STATE UNIV on June 6, 2012 | http://pubs.acs.org
Publication Date (Web): November 29, 2011 | doi: 10.1021/bk-2011-1084.ch002

We observed samples of 30mg or more to result in the development of a hard non-porous balloon structure in the lignin pan that often burst as the volatile pyrolysates attempted to leave the encased volume. Larger size samples resulted in significantly different proportions in the pyrolysates, derived from either inner volume or surface reactions, since much greater char fractions (25-37% rather than 13-26%) remained in the pan and correspondingly lower conversions to volatiles resulted. Large samples can impede the evolution of volatiles, particularly when surface reactions result in a thermally resistant or non-porous coating. This we observed as a protective ash coating on the grasses, bark and needles and as an impervious hard glassy coating covering the large lignin samples.

Figures 8 and 9 show the results of thermal decomposition for various wood samples and Figures 10 and 11 for various grasses and residues in CO_2 at 10°C min^{-1}. All wood samples exhibit a 3 stage degradation behavior more indicative of lignin than cellulose. Interestingly, a 10°C min^{-1} heating rate for pure lignin resulted in a second peak in the derivative mass loss curve (only a portion of which can be seen in Figure 3) occurring at higher temperatures above 1000°C, whereas for the wood samples they occurred at lower gasification temperatures relative to lignin. The shift in the second derivative peak for lignin to higher temperatures (Figure 3) at subsequently higher heating rates is due to thermal lag while the shift in the second peak to lower gasification temperatures for the actual biomass feedstocks is likely the result of a catalytic effect due to the mineral impurities contained in the woods, grasses and residues. The net effect of these inorganic impurities is to result in a decrease in the apparent activation energy with a resultant earlier decomposition.

Downloaded by PENNSYLVANIA STATE UNIV on June 6, 2012 | http://pubs.acs.org
Publication Date (Web): November 29, 2011 | doi: 10.1021/bk-2011-1084.ch002

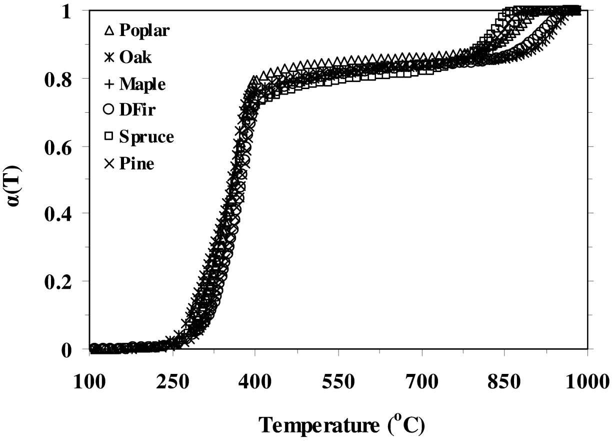

Figure 8. Woods mass loss fraction α during CO_2 processing 110-980°C at 10°C min^{-1}.

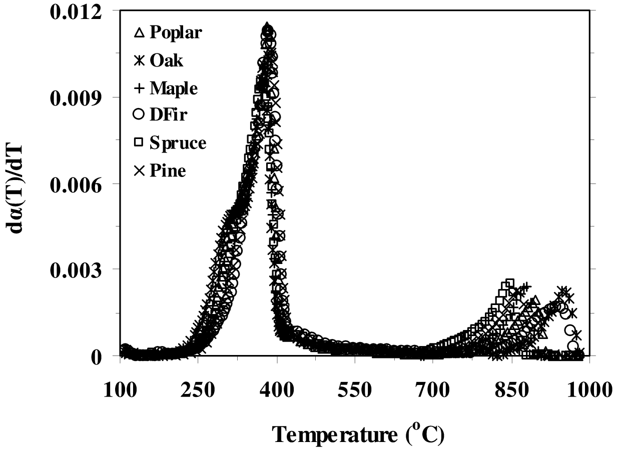

Figure 9. Woods derivative mass loss fraction dα/dT, CO_2 processing 110-980°C at 10°C min^{-1}.

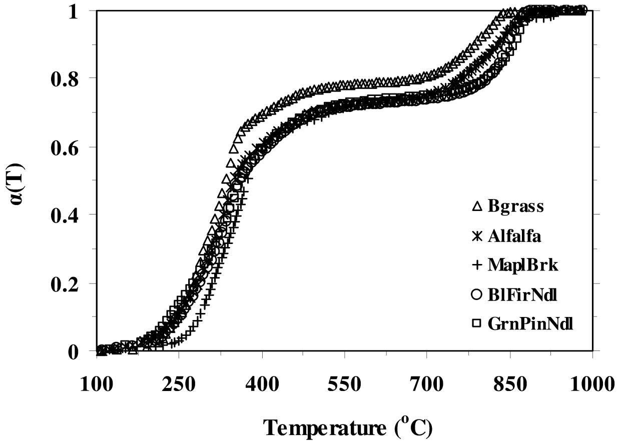

Figure 10. Grasses and Residues mass loss fraction α during CO_2 processing 110-980°C at 10°C min^{-1}.

The influence of water washing on the derivative peaks were examined in the experimental and kinetic model study of Gomez et al. (*24*, *25*). Removal of the mineral content from the herbaceous feedstocks by water washing or removal of the extractives was observed (*25*) to shift the DTG peaks to higher temperatures. The biomass feedstocks in the current study were not pre-processed and the significantly higher mineral content of the grasses was held accountable for the presence of the derivative peaks at lower temperatures, seen in Figure 11, as compared to those of the pure structural components observed in Figures 3 and 7.

Downloaded by PENNSYLVANIA STATE UNIV on June 6, 2012 | http://pubs.acs.org
Publication Date (Web): November 29, 2011 | doi: 10.1021/bk-2011-1084.ch002

Downloaded by PENNSYLVANIA STATE UNIV on June 6, 2012 | http://pubs.acs.org
Publication Date (Web): November 29, 2011 | doi: 10.1021/bk-2011-1084.ch002

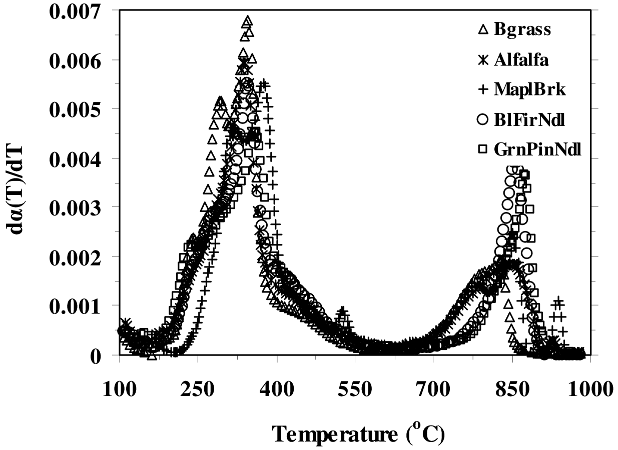

Figure 11. Grasses and Residues derivative mass loss fraction dα/dT, CO_2 processing 110-980°C at 10°C min^{-1}.

The initial mass of the dried sample was defined as the mass at 110°C, a temperature sufficiently high so as to ensure dehydration but low enough to commence a mass decay prior to the onset of pyrolytic decomposition. The final mass for the biomass thermal conversion was defined as that measured at 980°C that either represented ash or mineral-char residue depending on the gasification medium and heating rate. To characterize thermal degradation during pyrolysis and gasification and enable comparison of results from the present study with previous investigations, reference mass values at 110°C and 980°C were selected that are consistent with values appearing in previous studies (*6*, *24*). TGA processing occurred at a uniform heating rate from ambient (~22-23°C) to approximately 1000°C with no pre-treatment or moisture removal prior to a thermal decomposition run. Selection of the initial and final mass endpoint values was necessary to define the mass loss fraction α and its derivatives, from which kinetic parameters were subsequently derived.

At 1°C min^{-1} and in a CO_2 gasification medium all of the biomass feedstocks were converted to ash residuals by 980°C. Pyrolysis kinetic parameters were calculated between 110-450°C and gasification parameters were calculated between 110-980°C. Systematic errors in zeroing the pan mass and calibrating the sample thermocouple as well as the definition of initial and final masses, can result in large differences in mass and temperature profiles between different studies, leading to the wide variation in kinetic parameters reported for similar substances, undergoing thermal treatment at the same heating rate in comparable gasification environments. The similarity in mass decomposition profiles and kinetic parameters observed in the current study and by other investigators using a wide variety of purge flows during pyrolysis that include N_2, Ar, He, H_2O, CO and CO_2 indicate that during low temperature thermal treatment, the gasification medium often plays a less significant role than the source from which and the actual processing method by which the feedstock was derived. The gasification environment is much more critical during high temperature processing in CO_2

Downloaded by PENNSYLVANIA STATE UNIV on June 6, 2012 | http://pubs.acs.org
Publication Date (Web): November 29, 2011 | doi: 10.1021/bk-2011-1084.ch002

than in other media since the CO_2 results in a significantly more complete processing of the biomass feedstocks at high gasification temperatures where the Boudouard reaction enables CO_2 to access the char and more completely process the fuel. This assignment of what constitutes the "final mass" defines the mass loss fraction α though it more significantly influences the kinetic parameters for gasification in CO_2 where an additional 35% mass loss in lignin can occur during high temperature processing. Inconsistency in determination of the initial mass and the final mass (residual char) can lead to variability in the calculated parameters from different studies. For this reason many investigators have included them as unknowns to be determined in the least squares parameter set (*3*, *5*, *7*, *8*, *26*).

Extraction of kinetic parameters from a least squares analysis of the rate of mass loss fraction, dα/dT, was determined from the smoothed TGA data. The mass loss fraction α is defined as

$$\alpha \equiv \frac{M_i - M(t)}{M_i - M_f}$$

where

$$1-\alpha = \frac{M(t) - M_f}{M_i - M_f}$$

with the rate equation defined in terms of the global decomposition order of reaction n

$$\frac{d\alpha}{d\tau} = \kappa(1-\alpha)^n$$

The rate constant κ is expressed in terms of the pre-exponential factor A, the activation energy E and the temperature dependence coefficient w.

$$\kappa = AT^w \exp(\frac{-E}{RT})$$

The TGA heating rate β was varied with runs performed at 1, 2, 5, 10, 20, 50, and 100°C min^{-1} with each run determining a unique set of parameters for the given feedstock processed in either a CO_2 or a H_2O/N_2 thermal treatment environment.

$$\beta = \frac{dT}{d\tau}$$

From the first derivative

$$\frac{d\alpha}{dT} = \frac{A}{\beta} T^w \exp(\frac{-E}{RT})(1-\alpha)^n$$

we can solve for A

$$A = \frac{\beta \frac{d\alpha}{dT}}{T^{w}(1-\alpha)^{n}} \exp(\frac{E}{RT})$$

and from the second derivative

$$\frac{d^2\alpha}{dT^2} = \frac{d\alpha}{dT}\left[\frac{w}{T} + \frac{E}{RT^2} - \left(\frac{n}{1-\alpha}\right)\frac{d\alpha}{dT}\right]$$

we can solve for E

$$E = RT^2\left[\frac{\left(\frac{d^2\alpha}{dT^2}\right)}{\left(\frac{d\alpha}{dT}\right)} + \left(\frac{n}{1-\alpha}\right)\frac{d\alpha}{dT} - \frac{w}{T}\right]$$

An average value for E and A were determined for each run at a specific heating rate β for various values of reaction order n (1, 2, 3) and temperature exponent w (0, 1/2, 1)

$$\overline{E}(\beta, n, w) = \frac{1}{\alpha_f - \alpha_i}\sum_{j=i}^{f} E_j(\alpha_{j+1} - \alpha_j)$$

$$\overline{A}(\beta, n, w) = \frac{1}{\alpha_f - \alpha_i}\sum_{j=i}^{f} A_j(\alpha_{j+1} - \alpha_j)$$

The quality of fit between the numerically calculated value for the rate of mass loss as compared to the experimentally determined smoothed derivative TGA values was determined using the normalized first derivative expression for the % Fit. Best fits were selected for pyrolysis and gasification based on a minimization of squared deviations of the rate of mass loss rather than the mass loss fraction since the derivative was more sensitive than the function itself with normalization of the expression by the rate of mass loss maxima representing the inflection point of the pyrolysis curve. The summations were taken over the intervals 110-450°C for pyrolysis and 110-980°C for gasification calculations.

Downloaded by PENNSYLVANIA STATE UNIV on June 6, 2012 | http://pubs.acs.org
Publication Date (Web): November 29, 2011 | doi: 10.1021/bk-2011-1084.ch002

$$\%Fit = 100\frac{\sqrt{\frac{\sum_{j=1}^{N}\left[\left(\frac{d\alpha}{dT}\right)_{calc}-\left(\frac{d\alpha}{dT}\right)_{aveTGA}\right]^2}{N}}}{\left(\frac{d\alpha}{dT}\right)_{max}}$$

Hu et al. (*27*) compared a least squares analysis for modeling slow biomass pyrolysis with three models: one having a single step and two each having three pseudocomponents. They identified the best fit simulation to give reaction orders of 3.52 for the component modeling lignin, 1.69 for that modeling hemicellulose and 1.27 for the third pseudocomponent corresponding to cellulose at a heating rate of 10°C min^{-1}. This agrees with the current study at the slowest heating rates, during which heat and mass transport limitations play the least significant role, where lignin showed the best fit for order 3 and cellulose showed the best fit for order 1 during pyrolysis while the biomass samples ranged between 1 and 2.

In the Avicel cellulose study compiled by Gronli et al. (*9*), a first order cellulose decomposition with an apparent activation energy of 244 ± 10 kJ mol^{-1} at 5°C min^{-1} and 222 ± 8 kJ mol^{-1} at the 40°C min^{-1} heating rate was calculated based on an average of the results compiled from all eight labs using five different instruments and a wide range of inert purge flow rates. The cellulose pyrolysis activation energies found in the present study are in good agreement with these values ranging from ~188-230 kJ mol^{-1}.

The kinetic study of sawdust and rice husk by Park et al. (*15*) was a TGA investigation of pyrolysis (200-400°C) in a N_2 atmosphere at 15°C min^{-1} and steam gasification (600-900°C) in a 0.5 atm H_2O/1.0 atm N_2 environment at 30°C min^{-1}. Their pyrolysis data best fit a first order global decomposition while the gasification data best fit a 2/3 order of reaction. The global activation energies during pyrolysis for sawdust and rice husk were found to be 83.5 and 82.9 kJ mol^{-1}, respectively. These values are comparable with the pyrolytic activation energies observed in the present study for the woods that ranged from 54.3-71.8 kJ mol^{-1}.

The kinetic model of Caballero et al. (*4*), for the thermal degradation of the holocellulose and lignin fractions in almond shells, determined activation energies using a two parallel independent decomposition reaction scheme. These activation energies were much lower for the lignin reactions (89 – 82, 28 – 31 kJ mol^{-1}) than for the holocellulose reactions (178, 249 kJ mol^{-1}). The parameters of the model were optimized using a least squares fit on the mass loss derivative, analogous to the method in the current study, and their calculations resulted in reaction orders for lignin between 1.4 – 1.9. One of their earlier studies, Font et al. (*28*), determined an activation energy of 256.8 kJ mol^{-1} with a reaction order of n = 1 for cellulose pyrolysis during almond shell decomposition. In the present investigation, the analogous best fit reaction orders determined were of one for cellulose, two for several of the high-lignin component feedstocks and three for the Organosolv lignin. Similarly, the best fit values for the lignin pyrolytic activation energies were 39 and 48 kJ mol^{-1} and cellulose activation energies were 205 and 206 kJ

Downloaded by PENNSYLVANIA STATE UNIV on June 6, 2012 | http://pubs.acs.org
Publication Date (Web): November 29, 2011 | doi: 10.1021/bk-2011-1084.ch002

mol^{-1} in CO_2 and H_2O/N_2, respectively. These values from the current study are intermediate between those from each parallel reaction set of Caballero et al. (*4*).

A TGA study comparing experimental and numerical results for the kinetic analysis of corn straw pyrolysis was performed by Li et al. (*29*). The cellulose pseudocomponent gave a best fit for reaction order one and a global activation energy of 175 – 202 kJ mol^{-1}. They correlated the lignin pseudocomponent, to a range of reaction orders between 1.3 – 3.7 from the different corn straw samples, and a range of activation energies of between 30 – 52 kJ mol^{-1}. These values are in good agreement with those of the present study.

In the TGA study of waste wood by Reina et al. (*26*, *30*), they found that even with a sample size as large as 25mg, if the sample thickness was constrained to less than 1mm and the thermocouple was placed in direct contact with the sample, heat and mass transport limitations within the sample could be avoided. By sieving the samples to select a distribution between 0.3-0.7 mm they were able to avoid intra-particle effects that could effect the kinetic parameters. In the low temperature regime that they studied between 250-275°C, an apparent reaction order between 2.55-2.93 was observed while at their high temperature regime between 700-900°C and under conditions of flash pyrolysis (700°C min^{-1}), the apparent reaction order was one. The shift to lower reaction order ($3 \rightarrow 2 \rightarrow 1$) at higher heating rates for lignin in both CO_2 and H_2O/N_2 as well as the best fit of reaction order one observed for all biomass feedstocks during high temperature gasification in the current study agrees with their first order rate. Their results are in good agreement with the least squares best fit pyrolysis reaction order of 2 for forestry residues and 3 for lignin observed in the current study. At a heating rate of 2°C min^{-1} the low temperature activation energy of three types of waste woods were 127.61, 129.36 and 136.18 kJ mol^{-1} for pallets, furniture and forest wood, respectively. These global activation energies in N_2 are between those found in the current study for CO_2 pyrolysis between 110-450°C of the hardwood and softwood feedstocks (62 kJ mol^{-1}) and microcrystalline cellulose (207 kJ mol^{-1}).

The kinetic parameters determined by Antal and Varhegyi (*5*) for cellulose pyrolysis were in good agreement with those of the present study. The values for cellulose from non-pretreated sugar cane bagasse at 10°C min^{-1} were 215 and 15.4, for non-pretreated cellulose from wheat straw at 20°C min^{-1} were 232 and 16.8, and for the 21 non-pretreated Avicel cellulose experiments at heating rates of 2–80°C min^{-1} the values were 238±10 kJ mol^{-1} and 18.0±0.9 log(sec^{-1}) for the activation energy and log of the pre-exponential factor, respectively. Comparison of their five identical Avicel experiments with no pretreatment at a heating rate of 10°C min^{-1} using an Ar purge gas and sample sizes between 0.5–2.5mg in a 6mm pan gave good agreement with our results for 20μm microcrystalline cellulose in a CO_2 purge flow at 10°C min^{-1} with a sample size of ~22mg in a 10mm pan. Their values for E and log A were 234±4 and 17.7±0.2 in Ar while values found in the current study were 230 kJ mol^{-1} and 19.4 log(sec^{-1}K$^{-½}$) in CO_2. The mass decomposition of cellulose was similar in both Ar and N_2. We observed very similar mass decay profiles for both cellulose (high E_{ave}) and lignin (low E_{ave}) in CO_2 and H_2O/N_2 during pyrolysis at the same heating rate, explaining the similar activation energies in different gasification media during low temperature thermal processing.

Downloaded by PENNSYLVANIA STATE UNIV on June 6, 2012 | http://pubs.acs.org
Publication Date (Web): November 29, 2011 | doi: 10.1021/bk-2011-1084.ch002

The activation energies calculated for the lignin pseudocomponent in the temperature range 225-675°C were 53.6, 57.5, 58.2 and 60.9 kJ mol^{-1} for untreated bagasse and waste wood and water-washed bagasse and waste wood, respectively. The corresponding values for log A (pre-exponential factor) were 1.9, 2.1, 2.3 and 2.3, respectively. The cellulose activation energies were 243.3, 245.7, 249.6 and 250.8 kJ mol^{-1}, respectively. The corresponding cellulose pre-exponential factor A for all of the four biomass samples was 1.0 x 10^{18} sec^{-1}. The activation energies for the two structural components agree with those of the present study for pyrolysis at a 1-5°C min^{-1} heating rate where for lignin in CO_2, lignin in H_2O/N_2, cellulose in CO_2, and cellulose in H_2O/N_2, the E_{ave} values were 49.3, 47.8, 207 and 206 kJ mol^{-1}, respectively. Their rate equations had a pre-exponential factor that included the temperature dependence within it while our rate equation possessed a $T^{1/2}$ factor and their reported best fit kinetic parameters were for thermal decomposition spanning pyrolysis and low temperature gasification. Their observations of the significantly lower activation energies of lignin as compared to cellulose, the shift to higher decomposition temperatures with increased heating rate and a measurable catalytic effect resulting in lower activation energies and higher mass decay rates for the biomass TGA data and summative model curves are in good agreement with the trends that were observed in the current study for the lignin, cellulose, grasses, woods and residues at various heating rates.

General cautions for extraction of accurate kinetic parameters from TGA data suggest the use of small (<25mg) samples in pans whose diameter is greater than 5mm to minimize mass transport effects leading to diffusion resistance and increased vapor phase residence time for the char promoting secondary reactions. The suitability of determining activation energies at high heating rates greater than 40°C min^{-1} is questionable (*5*) since the actual temperature of the sample will deviate from the thermocouple reading and heat transfer effects between the sample and the surrounding gas medium may lead to the statistical determination of best fit parameters possessing a high degree of dispersion. Evidence for the existence of thermal lag can be seen in the transition of lignin global reaction order from 3 to 2 to 1 as the heating rate increases from 1°C min^{-1} to 100°C min^{-1}. Further evidence can be seen in the migration of the pyrolytic inflection point T_{max} to higher temperatures at progressively faster heating rates. For lignin in CO_2 the values were 342, 351, 353, 372, 393, 414, and 436°C; for lignin in H_2O/N_2 the values were 329, 349, 355, 378, 387, 417, and 443°C; and for cellulose in CO_2 the values were 324, 334, 350, 362, 381, 407, and 440°C. The situation can become even more acute at elevated temperatures for decomposition reactions that are highly endothermic where the high reaction rates and energy demands may not be met resulting in higher activation energies determined during dynamic TGA analysis than might otherwise have been extracted from static TGA data. This observed shift in the apparent activation energy of cellulose, during CO_2 pyrolysis when heated at 1°C/min and 100°C/min, was from 188 to 227 kJ/mole, respectively. The corresponding shift in activation energies determined at higher heating rates for lignin in CO_2 and lignin in H_2O/N_2 were from 22 to 63 and 48 to 61 kJ/mole, respectively. Also, systematic errors that cannot be removed or compensated for through more extensive data sets or statistical smoothing of

Downloaded by PENNSYLVANIA STATE UNIV on June 6, 2012 | http://pubs.acs.org
Publication Date (Web): November 29, 2011 | doi: 10.1021/bk-2011-1084.ch002

variability can confound the estimation of parameter values. Determination of lignin kinetic parameters involves slower more variable rates with a reaction that transitions in order, is less easily described by a single global decay rate, and spans a wide temperature range while being coupled to the hemicellulose and cellulose decomposition mechanisms. This leads to much greater dispersion in the kinetic parameters as observed in the present study with higher values for the error term of the lignin least-squares minimization (~0.55) when compared to that of the cellulose (~0.25). The least-squares error value was determined for each feedstock at every given heating rate by testing various values for the order of reaction n = 1, 2 and 3 with values for the temperature exponent w = 1/2 and 1.

When performing dynamic TGA analysis to extract kinetic parameters a very slow heating rate <20°C min^{-1} needs to be employed. This upper rate can be significantly lower and may be feedstock dependent based on the exothermic or endothermic nature of the thermal decomposition reactions. At a high heating rate, short residence times and high temperature gradients can result in explosive release of volatiles or a liquid surface that can coat the material and then subsequently cool to a glassy low porosity skin. Rapid release of volatile jets can remove material that might otherwise enter into repolymerization reactions with the char or they can permit continued gas phase thermal cracking without secondary reactions that would enhance char formation. The creation of a liquid outer layer on thermally resistant material would be conducive to production of a smoother spherule-type surface geometry. This was observed when the Organosolv lignin was heated at 100°C min^{-1}. Consequently, the activation energy calculated for gasification of lignin in either CO_2 or H_2O/N_2 showed a thermal lag shift in E_{act} due to (a) large thermal gradients that existed within the lignin sample at high heating rates with delayed thermal decomposition as evidenced by the T_{max} shift, and (b) rapid conversion during gasification at higher temperatures under larger temperature gradients than those that existed at slower gasification rates. These two competing factors along with the residence time available and the distribution of chemical reactions occurring were what was held accountable for the rise and then fall in calculated activation energies for bagasse and lignin that were observed by Fushimi et al. (*31*). The shift for bagasse was from 77.4 to 87.0 to 33.2 kJ mol^{-1} and for lignin from 52.8 to 55.7 to 22.9 kJ mol^{-1} when heated from ambient to 700°C at 1, 10 and 100°C sec^{-1}. This agrees with the trends in gasification E_{act} observed in the present study for lignin in both CO_2 (50.7, 131, 76.6, 69.5, 49.0, 40.3, 41.0) and H_2O/N_2 (51.1, 45.8, 68.1, 26.4, 28.1, 32.6, 36.5) at 1, 2, 5, 10, 20, 50 and 100°C min^{-1}. Competing chemical and physical processes that limit the ability of the gasification medium to react with the outer surface or to access the inner network of channels, as well as induced inter- and intra-particle temperature gradients result in transport limitations that limit the ability to calculate meaningful kinetic parameters. In the present study, TGA sample sizes greater than 25mg and heating rates greater than 10°C min^{-1} produced least squares best fit parameters that were significantly lower during lignin gasification in CO_2 shifting from an average E_{act} of 91 kJ mol^{-1} at 1-2°C min^{-1} to an average 41 kJ mol^{-1} at 50-^{1}00°C min^{-1}.

Downloaded by PENNSYLVANIA STATE UNIV on June 6, 2012 | http://pubs.acs.org
Publication Date (Web): November 29, 2011 | doi: 10.1021/bk-2011-1084.ch002

From Tables I-IV, the average least squares best fit global activation energy values for lignin and cellulose during CO_2 pyrolysis are 39 and 205 kJ mol^{-1}, during H_2O/N_2 pyrolysis are 48 and 206 kJ mol^{-1}, during CO_2 gasification are 51 and 208 kJ mol^{-1}, and during H_2O/N_2 gasification 48 and 203 kJ mol^{-1}, respectively. While the best fit analysis resulted in a third order global pyrolytic decomposition for lignin and first order for cellulose in either medium, the woods pyrolyzed in CO_2 at 10°C min^{-1} were first order though the grasses and residues pyrolyzed at 10°C min^{-1} were all second order with significantly lower activation energies (27.6-46.2 kJ mol^{-1}) as compared to those of the woods (54.3-71.8 kJ mol^{-1}). The significantly lower activation energies and earlier onset of pyrolytic decomposition of grasses and residues can be attributed to a catalytic effect conferred by the high mineral content of the herbaceous and woody residue feedstocks. The global decomposition gasification reaction order was found to be one for all feedstocks evaluated in both CO_2 and H_2O/N_2.

The exponent, w, of the temperature factor in the rate equation for $d\alpha/dT$ that gave the most consistently good fit for the lignin runs at $n = 3$ and the cellulose runs at $n = 1$ had the value $w = 1/2$. The T^w factor allows some measure of flexibility in compensating for the high heating rate thermal lag that becomes more pronounced at elevated furnace temperatures. This effect tends to lead to a shift in the pre-exponential factor to higher values in order to accurately describe the shifted mass loss data at high heating rates. This transition in pre-exponential factor, A_{ave}, was observed during CO_2 cellulose pyrolysis from $6.7x10^{16}$ to $1.4x10^{18}$ to $3.9x10^{20}$ (1 sec^{-1} $K^{-½}$).

Table V provides a summary of kinetic parameters determined in this investigation while Table VI contains a summary of kinetic data determined in other studies for various ligno-cellulosic feedstocks over a wide range in processing temperatures, heating rates, and gasification media. Pre-treatment, that included washing or drying, can significantly alter the sample and some of the wide variability in the subsequently extracted parameters can be attributed to the feedstock pre-processing. In the current study, a uniformly best fit value for the reaction order across all feedstocks and all heating rates during the entire range in gasification temperatures was $n = 1$. While cellulose pyrolysis was determined to be a best fit first order decomposition, the slow heating rate (1-2°C min^{-1}) best fit value for lignin was a third order pyrolysis reaction. This shift to lower reaction orders in the gasification range was also observed by Park et al. (*15*) for saw dust and rice husk (1 to 2/3) in H_2O/N_2, Kalita et al. (*40*) for saw dust (5.1 to 0.61), rice husk (5.19 to 0.48) and bamboo dust (3.55 to 0.28) in air, and Guo et al. (*43*) for palm shells (1 to 2/3) in N_2.

Downloaded by PENNSYLVANIA STATE UNIV on June 6, 2012 | http://pubs.acs.org
Publication Date (Web): November 29, 2011 | doi: 10.1021/bk-2011-1084.ch002

Downloaded by PENNSYLVANIA STATE UNIV on June 6, 2012 | http://pubs.acs.org
Publication Date (Web): November 29, 2011 | doi: 10.1021/bk-2011-1084.ch002

Table I. Summary of CO_2 pyrolysis kinetic parameters (110-450°C) from the present investigation

Biomass	***β*** ***(°C min^{-1})***	***T_{max}*** ***(°C)***	***A*** ***(sec^{-1} K$^{-1/2}$)***	***E*** ***(kJ mol^{-1})***	***n***
Lignin	1	342	1.82	22.3	3
Lignin	2	351	3.72E-01	28.4	3
Lignin	5	353	2.11E+01	49.3	3
Lignin	10	372	2.10E+03	50.6	2
Lignin	20	393	1.56E+05	40.9	1
Lignin	50	414	2.47E+02	46.4	1
Lignin	100	436	1.16E+03	63.3	1
Cellulose	1	324	6.71E+16	188	1
Cellulose	2	334	9.03E+17	207	1
Cellulose	5	350	1.40E+18	219	1
Cellulose	10	362	2.38E+19	230	1
Cellulose	20	381	3.69E+21	225	1
Cellulose	50	407	1.42E+20	202	1
Cellulose	100	440	3.89E+20	227	1
Poplar	10	383	1.92E+09	71.8	1
Maple	10	376	6.28E+05	58.0	1
Oak	10	374	4.15E+12	54.5	1
Douglas fir	10	385	3.82E+10	69.9	1
Pine	10	387	6.65E+05	65.1	1
Spruce	10	373	2.89E+10	54.3	1
Blue fir needles	10	345	1.83E+03	31.6	2
Green pine needles	10	359	4.72E+01	27.6	2
Maple bark	10	376	1.41E+03	42.9	2
Alfalfa	10	339	1.18E+03	33.1	2
Beachgrass	10	346	1.88E+08	46.2	2

In Synthetic Liquids Production and Refining; de Klerk, A., et al.;
ACS Symposium Series; American Chemical Society: Washington, DC, 2011.

Table II. Summary of H_2O pyrolysis kinetic parameters (110-450°C)

Biomass	*β (°C min^{-1})*	*T_{max} (°C)*	*A (sec^{-1} K$^{-1/2}$)*	*E (kJ mol^{-1})*	*n*
Lignin	1	329	3.17E+02	47.8	3
Lignin	2	349	6.35E+01	58.3	3
Lignin	5	355	7.68E+09	56.6	2
Lignin	10	378	1.09E+02	57.1	2
Lignin	20	387	6.56E+01	36.3	1
Lignin	50	417	3.54E+19	50.3	1
Lignin	100	443	8.03E+17	60.9	1
Cellulose	1	316	4.55E+20	206	1
Cellulose	5	341	1.81E+19	192	1
Cellulose	10	355	2.56E+20	212	1

Table III. Summary of CO_2 gasification kinetic parameters (110-980°C)

Biomass	*β (°C min^{-1})*	*T_{max} (°C)*	*A (sec^{-1} K$^{-1/2}$)*	*E (kJ mol^{-1})*	*n*
Lignin	1	342	8.08E+26	50.7	1
Lignin	2	351	1.64E+28	131	1
Lignin	5	353	1.89E+26	76.6	1
Lignin	10	372	9.01E+28	69.5	1
Lignin	20	393	4.83E+26	49.0	1
Lignin	50	414	7.74E+26	40.3	1
Lignin	100	436	4.34E+26	41.0	1
Cellulose	1	324	3.63E+18	190	1
Cellulose	2	334	1.13E+18	211	1
Cellulose	5	350	4.19E+18	223	1
Cellulose	10	362	2.35E+19	231	1
Cellulose	20	381	2.03E+23	228	1
Cellulose	50	407	1.32E+25	193	1
Cellulose	100	440	5.45E+23	195	1
Poplar	10	383	1.73E+28	145	1
Maple	10	376	8.47E+28	143	1
Oak	10	374	1.07E+27	147	1

Continued on next page.

Downloaded by PENNSYLVANIA STATE UNIV on June 6, 2012 | http://pubs.acs.org
Publication Date (Web): November 29, 2011 | doi: 10.1021/bk-2011-1084.ch002

Table III. (Continued). Summary of CO_2 gasification kinetic parameters (110-980°C)

Biomass	*β* (*°C min^{-1}*)	*T_{max}* (*°C*)	*A* (*sec^{-1} $K^{-1/2}$*)	*E* (*kJ mol^{-1}*)	*n*
Douglas fir	10	385	1.07E+27	145	1
Pine	10	387	4.18E+28	141	1
Spruce	10	373	2.60E+28	141	1
Blue fir needles	10	345	2.32E+27	148	1
Green pine needles	10	359	1.03E+28	126	1
Maple bark	10	376	5.16E+26	115	1
Alfalfa	10	339	6.22E+25	72.6	1
Beachgrass	10	346	2.91E+26	75.0	1

Table IV. Summary of H_2O gasification kinetic parameters (110-980°C)

Biomass	*β* (*°C min^{-1}*)	*T_{max}* (*°C*)	*A* (*sec^{-1} $K^{-1/2}$*)	*E(kJ mol^{-1})*	*n*
Lignin	1	329	8.35E+28	51.1	1
Lignin	2	349	3.64E+27	45.8	1
Lignin	5	355	3.59E+16	68.1	1
Lignin	10	378	4.13E+24	26.4	1
Lignin	20	387	5.17E+23	28.1	1
Lignin	50	417	7.56E+22	32.6	1
Lignin	100	443	5.18E+22	36.5	1
Cellulose	1	316	3.80E+20	208	1
Cellulose	5	341	1.84E+20	197	1
Cellulose	10	355	1.39E+20	207	1

Downloaded by PENNSYLVANIA STATE UNIV on June 6, 2012 | http://pubs.acs.org
Publication Date (Web): November 29, 2011 | doi: 10.1021/bk-2011-1084.ch002

Downloaded by PENNSYLVANIA STATE UNIV on June 6, 2012 | http://pubs.acs.org
Publication Date (Web): November 29, 2011 | doi: 10.1021/bk-2011-1084.ch002

Table V. Summary table of kinetic parameters found in the current investigation

Author (Ref.)	*Biomass Material*	*ΔT (°C)*	*β (°C min^{-1})*	*Gasification Medium*	*E (kJ mol^{-1})*	*A (sec^{-1} $K^{-1/2}$)*	*n*
Butterman and Castaldi (this study)	Organosolv lignin	110-450	5	CO_2	49.3	2.11E+01	3
		110-980	1		50.7	8.08E+26	1
		110-450	1	H_2O/N_2	47.8	3.17E+02	3
		110-980	1		51.1	8.35E+28	1
	Microcrystalline cellulose	110-450	2	CO_2	207	9.03E+17	1
		110-980	2		211	1.13E+18	1
		110-450	1	H_2O/N_2	206	4.55E+20	1
		110-980	1		208	3.80E+20	1
	Poplar	110-450	10	CO_2	71.8	1.92E+09	1
		110-980			145	1.73E+28	1
	Oak	110-450	10	CO_2	54.5	4.15E+12	1
		110-980			147	1.07E+27	1
	Maple	110-450	10	CO_2	58.0	6.28E+05	1
		110-980			143	8.47E+28	1
	Douglas Fir	110-450	10	CO_2	69.9	3.82E+10	1
		110-980			145	1.07E+27	1
	Spruce	110-450	10	CO_2	54.3	2.89E+10	1
		110-980			141	2.60E+28	1
	Pine	110-450	10	CO_2	65.1	6.65E+05	1
		110-980			141	4.18E+28	1

Continued on next page.

Downloaded by PENNSYLVANIA STATE UNIV on June 6, 2012 | http://pubs.acs.org
Publication Date (Web): November 29, 2011 | doi: 10.1021/bk-2011-1084.ch002

Table V. (Continued). Summary table of kinetic parameters found in the current investigation

Author (Ref.)	*Biomass Material*	*ΔT (°C)*	*β (°C min^{-1})*	*Gasification Medium*	*E (kJ mol^{-1})*	*A (sec^{-1} K$^{-1/2}$)*	*n*
	Beachgrass	110-450	10	CO_2	46.2	1.88E+08	2
		110-980			75.0	2.91E+26	1
	Alfalfa	110-450	10	CO_2	33.1	1.18E+03	2
		110-980			72.6	6.22E+25	1
	Maple Bark	110-450	10	CO_2	42.9	1.41E+03	2
		110-980			115	5.16E+26	1
	Blue Fir Needles	110-450	10	CO_2	31.6	1.83E+03	2
		110-980			148	2.32E+27	1
			10				
	Green Pine Needles	110-450	10	CO_2	27.6	4.72E+01	2
		110-980			126	1.03E+28	1
			10				

Downloaded by PENNSYLVANIA STATE UNIV on June 6, 2012 | http://pubs.acs.org
Publication Date (Web): November 29, 2011 | doi: 10.1021/bk-2011-1084.ch002

Table VI. Summary table of kinetic parameters obtained in previous studies

Author (Ref.)	*Biomass Material*	*ΔT (°C)*	*β (°C min^{-1})*	*Gasification Medium*	*E (kJ mol^{-1})*	*A (sec^{-1} $K^{-1/2}$)*	*n*
Ollero et al. (*32*)	Orujillo (oil-stone wood residue)	800-950	isothermal	$0.5CO_2/0.5N_2$	133.33	1.258E+02	
Tancredi et al. (*33*)	Eucalyptus sawdust char pre-treat @ 600°C char pre-treat @ 800°C	800-850 775-850	isothermal isothermal	CO_2 CO_2	242-261 230-257		
Marquez-Montesinos et al. (*23*)	Grapefruit skin char pre-treat @ 700°C pre-treat @ 700°C	725-800 725-800	isothermal isothermal	CO_2 $0.03H_2O/0.97N_2$	197-249 146-201	(4.5E+06 - 7.37E+08)	
De Groot et al. (*34*)	Cottonwood char pre-treat @ 1000°C	900	isothermal	$0.3CO_2/0.7N_2$	196.2	1.0E+20	1
	Douglas fir char pre-treat @ 1000°C	950	isothermal	$0.3CO_2/0.7N_2$	220.9	2.5E+21	1
Khalil et al. (*35*)	Birch char pre-dried 3 Partial Reactions Power Law Model	110-1000	10	CO_2	118 149 262	4.17E+04 1.0E+05 1.05E+09	1 1 0.44
	Pine char pre-dried	110-1000	10	CO_2	118 149 262	2.95E+04 6.61E+04 1.78E+09	1 1 0.75

Continued on next page.

Downloaded by PENNSYLVANIA STATE UNIV on June 6, 2012 | http://pubs.acs.org
Publication Date (Web): November 29, 2011 | doi: 10.1021/bk-2011-1084.ch002

Table VI. (Continued). Summary table of kinetic parameters obtained in previous studies

Author (Ref.)	*Biomass Material*	*ΔT (°C)*	*β (°C min^{-1})*	*Gasification Medium*	*E (kJ mol^{-1})*	*A (sec^{-1} K$^{-1/2}$)*	*n*
Plante et al. (*36*)	Poplar char pre-dried	850 950	isothermal	CO_2	80.3	5.249	2 1
Sun et al. (*37*)	Wood chip waste	700-850	isothermal	$0.5H_2O/0.5N_2$	171.4	3.594	1
Barrio et al. (*38*)	Norwegian birch char	750-950	isothermal	H_2O (1.0 Atm)	237	2.62E+08	
	Danish beech char	750-950	isothermal	H_2O (1.0 Atm)	211	1.71E+07	
Wang et al. (*3*)	Sawdust (pre-dried)	30-600	5	H_2	166.4	9.5E+09	1
	Lignin (pre-dried)	30-600	5	H_2 (@ 80% conversion)	157.7	2.5E+07	1
Jauhiainen et al. (*39*)	Pomace (solid olive residue)	110-775	5	$0.2O_2/0.8He$			
	-holocellulose				153.7	9.319E+11	1.57
	-lignin				66.4	1.371E+04	2.94
	Pomace	110-775	5	He			
	-holocellulose				181.8	1.402E+14	0.96
	-lignin				69.4	1.236E+04	3.79
Kalita et al. (*40*)	Sawdust	200-350	10	Air	134.87	2.35E+10	5.10
		350-590			23.79	4.15E-02	0.61
	Rice husk	225-365			126.19	1.49E+09	5.19
		365-590			28.13	6.68E-02	0.48
	Bamboo dust	190-365			98.22	3.6E+06	3.55
		365-930			2.89	1.7E-04	0.28

Downloaded by PENNSYLVANIA STATE UNIV on June 6, 2012 | http://pubs.acs.org
Publication Date (Web): November 29, 2011 | doi: 10.1021/bk-2011-1084.ch002

Author (Ref.)	*Biomass Material*	*ΔT (°C)*	*β (°C min^{-1})*	*Gasification Medium*	*E (kJ mol^{-1})*	*A (sec^{-1} K$^{-1/2}$)*	*n*
Shen et al. (*41*)	Pine	40-370	10	Air	118.7		1
		370-800			145.3		1
	Aspen	40-370	10	Air	113.7		1
		370-800			204.7		1
	Birch	40-370	10	Air	116.0		1
		370-800			211.1		1
	Oak	40-370	10	Air	117.2		1
		370-800			150.4		1
Gronli et al. (*9*)	Avicel cellulose	270-400	5	N_2	243.95	1.064E+19	1
Manya et al. (*6*)	Kraft alkali lignin	110-900	5	N_2	65.4	4.077E+02	3
	Sugarcane bagasse	110-900	5	N_2			
	-cellulose						
	-lignin				243.3	7.94E+17	1
	Waste wood				53.6	1.0E+02	3
	-cellulose	110-900	5	N_2			
	-lignin				245.7	1.0E+18	1
					57.5	2.0E+02	3

Continued on next page.

Downloaded by PENNSYLVANIA STATE UNIV on June 6, 2012 | http://pubs.acs.org
Publication Date (Web): November 29, 2011 | doi: 10.1021/bk-2011-1084.ch002

Table VI. (Continued). Summary table of kinetic parameters obtained in previous studies

Author (Ref.)	*Biomass Material*	*ΔT (°C)*	*β (°C min^{-1})*	*Gasification Medium*	*E (kJ mol^{-1})*	*A (sec^{-1} $K^{-1/2}$)*	*n*
Gomez et al. (*25*)	Avicel cellulose	150-500	5	N_2	242.6	1.0E+19	1
	Pine	200-900	20	N_2			
	-cellulose				243.79	1.02E+18	1
	-lignin				93.66	4.68E+05	3
	Beech	200-900	20	N_2			
	-cellulose				243.69	1.02E+18	1
	-lignin				90.03	3.02E+05	3
	Thistle	200-900	20	N_2			
	-cellulose				239.68	1.02E+19	1
	-lignin				57.84	1.74E+03	3
Orfao et al. (*42*)	Pine wood						
	-lignin	20-900	5	N_2	18.1	1.57E-02	1
	Eucalyptus						
	-lignin	20-900	5	N_2	20.2	2.43E-02	1
	Pine bark						
	-lignin	20-900	5	N_2	20.4	1.23E-02	1
Li et al. (*29*)	Corn straw stalks	40-900	20	N_2			
	-cellulose				202	8.0E+14	1.1
	-lignin				48	6.5E+01	3.7
	Leaves	40-900	20	N_2			
	-cellulose				179	6.4E+12	1.3
	-lignin				44	9.0E+00	2.6
Font et al. (*28*)	Almond shells	100-700	10	N_2			
	-Cellulose				256.8	1.46E+20	1
	-Lignin				109.9	7.27E+06	1

Downloaded by PENNSYLVANIA STATE UNIV on June 6, 2012 | http://pubs.acs.org
Publication Date (Web): November 29, 2011 | doi: 10.1021/bk-2011-1084.ch002

Author (Ref.)	*Biomass Material*	*ΔT (°C)*	*β (°C min^{-1})*	*Gasification Medium*	*E (kJ mol^{-1})*	*A (sec^{-1} K$^{-1/2}$)*	*n*
Gronli et al. (*7*)	Beech	150-450	5	N_2			
	-cellulose				236	3.80E+17	1
	-lignin				46	3.98	1
	Birch	150-450	5	N_2			
	-cellulose				236	3.31E+17	1
	-lignin				46	3.98	1
	Spruce	150-450	5	N_2	236		
	-cellulose				46	2.69E+17	1
	-lignin					3.80	1
Hu et al. (*27*)	Cotton straw	400-900	5	N_2			
	-cellulose				173	3.8E+12	1.3
	-lignin				65	2.1E+03	3.5
	Cherry bay branch	400-900	5	N_2			
	-cellulose				223	5.8E+16	1.1
	-lignin				47	1.4E+01	1.8
	Rice husk	400-900	5	N_2			
	-cellulose				263	8.8E+20	1.2
	-lignin				76	2.5E+04	3.8
	Camphor branch	400-900	5	N_2			
	-cellulose				202	5.8E+14	1.0
	-lignin				71	8.4E+03	3.0
Varhegyi et al. (*1*)	Avicel cellulose	255-360	2	He	240	3.16E+18	1
		255-390	10		240	3.16E+18	1
		255-415	50		240	1.26E+18	1
Antal et al. (*5*)	Avicel cellulose	250-350	2	He	238	1.0E+18	1

Continued on next page.

Table VI. (Continued). Summary table of kinetic parameters obtained in previous studies

Author (Ref.)	*Biomass Material*	*ΔT* *(°C)*	*β* *(°C min^{-1})*	*Gasification Medium*	*E* *(kJ mol^{-1})*	*A* *(sec^{-1} $K^{-1/2}$)*	*n*
Muller-Hagedorn et al. (*12*)	Scots pine		5	He			
	-cellulose	280-390			181	5.27E+12	0.9
	-lignin	100-400			93	2.10E+05	1.4
Varhegyi et al. (*11*)	Avicel cellulose	200-400	10	Ar	234	3.98E+17	1.2

Downloaded by PENNSYLVANIA STATE UNIV on June 6, 2012 | http://pubs.acs.org
Publication Date (Web): November 29, 2011 | doi: 10.1021/bk-2011-1084.ch002

Downloaded by PENNSYLVANIA STATE UNIV on June 6, 2012 | http://pubs.acs.org
Publication Date (Web): November 29, 2011 | doi: 10.1021/bk-2011-1084.ch002

In general the reaction order was found to be higher and the activation energy lower for lignin than cellulose. Comparing the lignin vs. cellulose reaction orders, Jauhiainen et al. (*39*) found for olive residue in O_2-He 2.94/1.57 and in He 3.79/0.96; Manya et al. (*6*) for sugarcane bagasse and waste wood in N_2 3/1; Gomez et al. (*24*) for pine, beech and thistle in N_2 3/1; Li et al. (*29*) for corn straw stalks in N_2 3.7/1.1 and corn leaves in N_2 2.6/1.3; Hu et al. (*27*) for cotton straw in N_2 3.5/1.3, cherry bay branch in N_2 1.8/1.1, rice husk in N_2 3.8/1.2, and camphor branch in N_2 3.0/1.0; and Muller-Hagedorn et al. (*12*) for hornbeam in He 1.3/0.9, walnut in He 1.4/0.8 and Scots pine in He 1.4/0.9, respectively. Comparing the lignin vs. cellulose activation energies, Khalil et al. (*35*) examined pre-dried birch char and pine char gasified in CO_2 and their model determined lignin and cellulose components having activation energies of 118/262 kJ mol^{-1}; Manya et al. (*6*) found for sugarcane bagasse in N_2 53.6/243.3 kJ mol^{-1}; Gomez et al. (*24*) for pine in N_2 93.66/243.79, beech in N_2 90.03/243.69, and thistle in N_2 57.84/239.68 kJ mol^{-1}; Li et al. (*29*) for corn straw stalks in N_2 48/202 kJ mol^{-1}; Font et al. (*28*) for almond shells in N_2 109.9/256.8 kJ mol^{-1}; Gronli et. al. (*7*) for alder, beech, birch and spruce in N_2 46/236 kJ mol^{-1}; Hu et al. (*27*) for cotton straw in N_2 65/173, cherry bay branch in N_2 47/223, for rice husk in N_2 76/263, and camphor branch in N_2 71/202 kJ mol^{-1}; and Muller-Hagedorn et al. (*12*) for hornbeam in He 99/181, walnut in He 95/183, and Scots pine in He 93/181 kJ mol^{-1}, respectively. The great variability in kinetic parameters for similar feedstocks can be attributed to the wide range in pre-processing techniques, temperature interval over which thermal treatment occurs, reactor geometry and gasification medium, heating rate and sample size, level of moisture and type of mineral impurities, definition of what constitutes the initial and final weight loss fractions, as well as the selection of which parameters are left to be freely determined or chosen from a pre-selected set of values as a result of the kinetic analysis. Comparison of high temperature gasification parameters associated with pre-processed chars is difficult if not impossible without a detailed knowledge of the chemical and thermal history of the pyrolyzed char. For similar feedstocks undergoing slow TGA pyrolysis greater variability exists as a result of pre-treatment rather than gasification medium. Though similar mass decomposition curves may occur in various studies, several different sets of global kinetic parameters can adequately describe the thermal decomposition, which can account for some of the wide variability in kinetic parameters reported in the literature.

During pyrolysis significant gas evolution, particularly in CO and CO_2, occurs at about 400°C due to a cluster of ligno-cellulosic decomposition reactions that signals the transition between thermal regimes. Steam introduced for gasification at pyrolysis temperatures combines through the water gas shift reaction (WGS)

$$H_2O + CO \rightarrow CO_2 + H_2 \qquad \Delta H = -41.2\ \text{kJ mol}^{-1} \qquad (1)$$

with any CO available in the reactor to produce H_2 that can, through direct hydrogenation methanation reactions,

$$2CO + 2H_2 \rightarrow CH_4 + CO_2 \qquad \Delta H = -246.9\ \text{kJ mol}^{-1} \qquad (2)$$

$$CO + 3H_2 \rightarrow CH_4 + H_2O \qquad \Delta H = -205.7\ kJ\ mol^{-1} \qquad (3)$$

$$C + 2H_2 \rightarrow CH_4 \qquad \Delta H = -74.4\ kJ\ mol^{-1} \qquad (4)$$

result in a continuous production of low concentrations of CH_4 throughout the thermal decomposition process.

The distribution of volatile evolution products during gasification can be adjusted through the selection of gasification medium. Steam injection during high temperature thermal processing, has been shown to result in elevated levels of H_2 and CO, through the steam reforming reaction,

$$C + H_2O \rightarrow CO + H_2 \qquad \Delta H = +131.3\ kJ\ mol^{-1} \qquad (5)$$

for a variety of hydrocarbon fuels that include woods, grasses, agricultural residues and coal (*21*). CO_2 injection during gasification can result in increased levels of CO through the reverse water gas shift reaction (rWGS) that is thermodynamically favored at higher temperatures

$$H_2 + CO_2 \rightarrow CO + H_2O \qquad \Delta H = +41.2\ kJ\ mol^{-1} \qquad (6)$$

and most importantly by the Boudouard reaction

$$CO_2 + C \rightarrow 2CO \qquad \Delta H = +172.5\ kJ\ mol^{-1} \qquad (7)$$

that is responsible for the high temperature processing of the char in a CO_2 environment. Cleavage and condensation reactions that reduce the ligno-cellulosic feedstocks into a graphitic char structure result in common features in the gas evolution behavior during gasification of the wide variety of biomass feedstocks examined in the present study.

To compare differences in thermal decomposition products during CO_2 enhanced steam gasification of ligno-cellulosic feedstocks, GC profiles for the evolution of both major and minor species including the C_1-C_3 hydrocarbons were taken for lignin and cellulose in various $CO_2/H_2O/N_2$ environments. Figures 12, 13 and 14 compare concentrations for H_2, CO and CH_4, respectively, in $0.04H_2O/0.96N_2$ (=0%CO_2) and $0.6CO_2/0.04H_2O/0.36N_2$ (=60%CO_2) environments. As we observed in previous studies for various biomass feedstocks (*16*, *17*, *44*), addition of CO_2 can be seen to decrease the levels of H_2 and CH_4 and increase the level of CO produced during high temperature gasification of both lignin and cellulose. Comparing gas concentration profiles (Figures 12-14) for Organosolv lignin and microcrystalline cellulose on a mass basis, lignin tends to produce higher concentrations of H_2 and CH_4 (attributable to methyl and methoxy cleavage) while cellulose tends to produce higher concentrations of CO (attributable to carbonyl cleavage). These differences were also observed by Fushimi et al. (*45*) in their study of the steam gasification of lignin and cellulose at 1°C sec^{-1}. They observed the enhanced H_2 production from lignin

Downloaded by PENNSYLVANIA STATE UNIV on June 6, 2012 | http://pubs.acs.org
Publication Date (Web): November 29, 2011 | doi: 10.1021/bk-2011-1084.ch002

Downloaded by PENNSYLVANIA STATE UNIV on June 6, 2012 | http://pubs.acs.org
Publication Date (Web): November 29, 2011 | doi: 10.1021/bk-2011-1084.ch002

that commenced at about 500°C and the greater volume of CO evolution from cellulose with a peak centered at about 425°C. A sharp rise in CO evolution from cellulose during steam gasification occurring at about 450°C can be seen in Figure 13 while the rise in H_2 evolution from lignin is seen in Figure 12 to commence at about 675°C in the present study. Yang et al. (*46*) also observed these higher yields of H_2 and CH_4 from lignin with a strong CH_4 peak at 500°C in their FTIR spectrum. Yang et al. observed a rise in CO production by cellulose at about 400°C and a rise in H_2 production by lignin after 450°C that they attributed to the cleavage of the aromatic hydrogen during rearrangement and condensation of the lignin structure. Cracking and reforming of carboxyl functional groups were found to correspond with CO_2 evolution, cracking of hydroxyl groups correlated with H_2O evolution, cracking of carbonyl groups corresponded to CO evolution and cracking of methoxy groups resulted in CH_4 evolution. A similar rise in CH_4 evolution for lignin beginning at about 500°C, as well as the relatively higher levels of H_2 and CH_4 for the lignin component (Figures 12 and 14) were also observed in the current study. Jakab et al. (*47*) observed a bimodal distribution for CH_4 from their ball milled lignin having peaks at 440°C and 600°C. A lignin CH_4 local maxima in the vicinity of 550-600°C was also observed in the present study (Figure 14, Lignin 0%). Low temperature CH_4 evolution correlated well with the aromatic methoxy group content of the lignin whereas high temperature CH_4 evolution was found to correlate with the total carbon content. This would indicate that the CH_4 maximum observed during gasification results during condensation of the carbon char skeleton as CO is desorbing from the char surface and residual CH_3 and H radicals are cleaved off to form a graphitic char structure.

CH_4 peaks between 475-650°C were observed by Liu et al. (*48*) for both fir and birch lignin that correlate well with the CH_4 maxima between 475-700°C observed in the present study for Organosolv lignin. While the low temperature pyrolysis evolution of CH_4 can be attributed to the methoxy cleavage, the high temperature evolution of CH_4 can be attributed to the methyl and methylene groups that are more strongly held to the lignitic structure, all of whose presence account for the much higher CH_4 evolution observed from lignin as compared to that released from cellulose. A jump in the CH_4 production by lignin corresponding to this temperature interval can be seen in the neighborhood of 525°C in Figure 14. The presence of these species accounts for the much higher CH_4 evolution observed from lignin as compared to that released from cellulose. Jakab et al. observed a bimodal distribution for CO from lignin centered about 400°C in contrast to the broad CO distribution observed in the current study centered around 650°C. The cellulose CO evolution could be described as rising at about 450°C and then increasing abruptly again at gasification temperatures above 850°C, particularly in a CO_2 enhanced gasification environment as seen in Figure 13 (Cellulose 60%). Maximum CO_2 evolution was found to correlate well with the carboxyl group content as measured by the signal in the FTIR spectra supporting their assumption that CO_2 evolution is primarily a result of decarboxylation reactions. They observed a bimodal distribution centered about 400°C for both CO_2 and CO with a sharp rise in CO above 400°C, similar to observations of CO evolution commencing during gasification seen in Figure 13 (Lignin 0%, Cellulose 0%). Liu et al. studied the gas evolution from birch and fir lignin and their FTIR CO peaks between 525-650°C correlate well with the rise in CO concentration in this interval for Organosolv lignin that can be seen in Figure 13. The onset of H_2 depression begins at about 675°C for both feedstocks whereas the onset of CO enhancement does not begin until about 775°C for cellulose and 850°C for lignin.

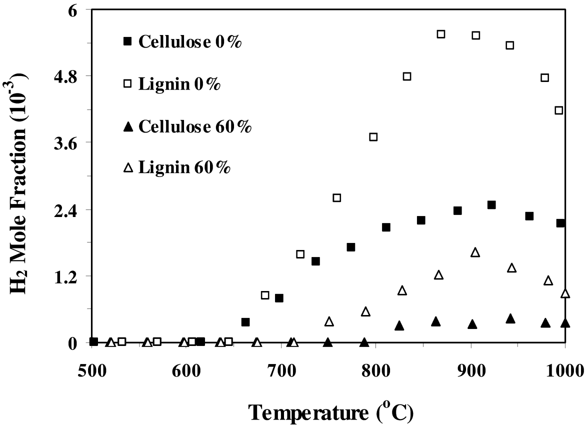

Figure 12. Comparison of H_2 gas evolution for 0%CO_2 (0.04H_2O/0.96N_2) and 60%CO_2 (0.6CO_2/0.04H_2O/0.36N_2), at 10°C min^{-1}.

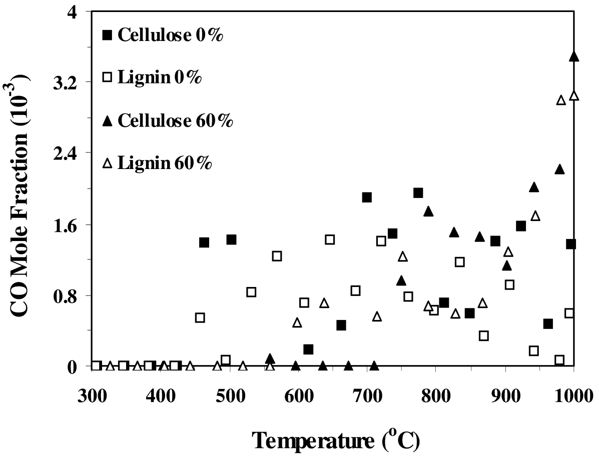

Figure 13. Comparison of CO gas evolution for 0%CO_2 (0.04H_2O/0.96N_2) and 60%CO_2 (0.6CO_2/0.04H_2O/0.36N_2), at 10°C min^{-1}.

Downloaded by PENNSYLVANIA STATE UNIV on June 6, 2012 | http://pubs.acs.org
Publication Date (Web): November 29, 2011 | doi: 10.1021/bk-2011-1084.ch002

Downloaded by PENNSYLVANIA STATE UNIV on June 6, 2012 | http://pubs.acs.org
Publication Date (Web): November 29, 2011 | doi: 10.1021/bk-2011-1084.ch002

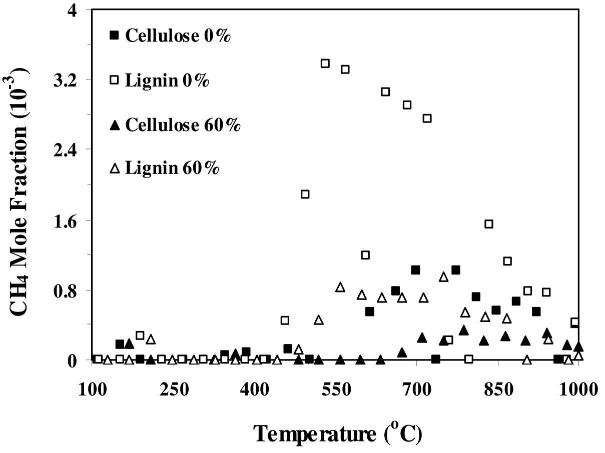

Figure 14. Comparison of CH_4 gas evolution for 0%CO_2 ($0.04H_2O/0.96N_2$) and 60%CO_2 ($0.6CO_2/0.04H_2O/0.36N_2$), at 10°C min^{-1}.

Though the thermal decomposition and hence the kinetic behavior of a biomass feedstock can only be approximated by averaging that of the isolated fractions of which it is composed, the process of extraction results in structural changes while removing the possibility of interactions. The more benign the isolation of the structural fraction, the more closely it can represent the gas evolution and mass degradation contribution in the actual feedstock. Though the kinetic parameters derived from the isolated structural components may vary depending on the method of extraction, with a weighted average incapable of replicating the actual biomass parameters, the trends appear to be similar with better correlation in the mass decomposition rates than in the actual concentrations of the volatiles measured during thermal degradation. Comparison of gas evolution and mass decomposition profiles from various wood and grass feedstocks (*17*) with those of lignin and cellulose in the present study along with a knowledge of the relative fractions of the ligno-cellulosic structural components indicates better correlation in the mass decomposition rather than the gas evolution profiles when attempting to model the biomass based on a weighted average of the lignin and cellulosic fractions. Caballero et al. (*4*) observed differences between the gas evolution from the structural components in almond shells and the evolution of oxygenated hydrocarbons from the surrogate molecules based on an independent decomposition weighted model.

Injection of CO_2 at gasification temperatures, through the Boudouard eq (7) and rWGS eq (6) reactions, results in CO production that drives the reverse steam reforming reaction eq (5) resulting in lower levels of H_2 produced above 700°C during CO_2 enhanced thermal treatment. Decreased concentrations of H_2 available to enter into the methanation reactions, eq (2) and eq (3), above 700°C can be correlated with the rapid drop in CH_4 production from the steam gasification of lignin evident in Figure 14. A non-phenolic α-ether cleavage pathway in lignin degradation identified by Kawamoto et al. (*49*, *50*) along with the methyl and methoxy radicals available above 400°C, can account for the elevated levels of

Downloaded by PENNSYLVANIA STATE UNIV on June 6, 2012 | http://pubs.acs.org
Publication Date (Web): November 29, 2011 | doi: 10.1021/bk-2011-1084.ch002

CH_4 from lignin at about 450°C. In contrast to the phenolic reactions that occur earlier in lignin decomposition (~250°C), these non-phenolic cleavages do not produce OH radicals that tend to combine with available CO to produce CO_2. Instead, the non-phenolic pathway enables CO in the reactor to enter into the methanation reactions at ~450°C, that can help to account for the rapid rise in CH_4 production observed near this temperature as seen in Figure 14.

Those thermal decomposition reactions that are exothermic and less constrained by heat transport to the sample site, whether as an internal or surface reaction, are less hampered by thermal transport restrictions. These processes are more conducive to char formation though strongly mediated by the catalytic effect of mineral impurities that can enhance both the rate and amount of char produced. The global kinetics of lignin decomposition is exothermic and correspondingly a high lignin content is associated with high levels of char formation. In comparison to the exothermic decomposition of the thermally resistant, aromatic and highly cross-linked chemical structure of lignin, is the endothermic decomposition of the polysaccharide cellulose structure that degrades at a much lower temperature and results in significantly less char. These differences were observed in the current study when comparing the pyrolysis products resulting from decomposition of wood and herbaceous feedstocks. The woods and forestry residues high in lignin content resulted in large volumes of black pyrolytic char. The grasses higher in cellulose and mineral content resulted in slightly smaller volumes of pyrolytic char that were coated with a light colored mineral residue.

Since determination of best fit kinetic parameters E and A from a least squares analysis of either the TGA or the smoothed DTG curves has been shown (*51–53*) to give very similar results, this indicates that no significant distortion occurs as a result of the smoothing procedure. Therefore, the parameter chosen for the present least squares kinetic analysis was the derivative (DTG) mass loss fraction. However, since TGA data is most significantly influenced by inherent systematic errors, a least squares analysis of the data is not amenable to standard statistical measures. Least squares parameters, nevertheless, are very useful in enabling the formulation of kinetic models that offer good correlation with experimental data and can aid in process design and feedstock selection.

Conclusions

Thermal treatment at a slow heating rate (1°C min^{-1}) and using CO_2 as the gasification medium enabled processing of the cellulose components at a low pyrolysis temperature leaving a much larger fraction of the thermally resilient lignin isolated for subsequent thermal and/or chemical conversion. At high temperatures the use of a CO_2 gasification medium enabled a more complete processing of lignin to volatiles since the CO_2 created a more reactive char structure and was more capable of accessing the existing porous structure of the biomass char. The polysaccharide cellulosic components complete their decomposition at much lower temperatures and over a narrower interval resulting in a first order global decomposition rate while the aromatic and highly cross-linked structure of lignin results in a more thermally resistant component

Downloaded by PENNSYLVANIA STATE UNIV on June 6, 2012 | http://pubs.acs.org
Publication Date (Web): November 29, 2011 | doi: 10.1021/bk-2011-1084.ch002

whose decomposition occurs over a much wider temperature range resulting in a higher order decomposition rate whose best fit value was determined to be n = 3. Thermal degradation of biomass feedstocks represents the net effect of a set of coupled mechanisms for the various structural components complicated further by the extractives that they contain and the catalytic effect resulting from their mineral impurities. To convey the detailed complexity and accurately model the temperature and time dependent nature of the gasification process requires an understanding of the physical and chemical phenomena that govern the thermal decomposition. The gasification medium and the heating rate influence the chemical decomposition products and the physical pore structure development as observed in the distinctly different gas evolution and mass decomposition profiles.

The ability to more accurately characterize the thermochemical degradation of biomass fuels by a quantitative description of the mass decomposition during the various thermal regimes enables the development of analytical process design models that can more realistically predict and potentially offer greater control of reactor performance. Both chemical kinetic and heat and mass transport phenomena influence the thermochemical decomposition of biomass feedstocks. Characterization of biomass thermal degradation is further complicated by the existence of coupled decomposition mechanisms, the presence of extractives and inorganic impurities that confer a catalytic effect. While the aromatic and highly cross-linked structure of lignin results in a more thermally resistant component, the polysaccharide cellulosic components complete their decomposition at much lower temperatures and over a narrower interval. Thermal treatment at a slow heating rate (1°C min^{-1}) and using CO_2 as the gasification medium enabled processing of the cellulose components at a low pyrolysis temperature leaving a much larger fraction of the thermally resilient lignin isolated for subsequent thermal and/or chemical conversion. At high temperatures the use of a CO_2 gasification medium enabled a more complete processing of lignin to volatiles since the CO_2 created a more reactive char structure and was more capable of accessing the existing porous structure of the biomass char. The gasification medium and the heating rate influence the chemical decomposition products and the physical pore structure development. Larger data sets and additional parameters are insufficient to adequately address the non-statistical nature of systematic experimental errors that occur while attempting to determine kinetic parameters from thermogravimetric analyses. These non-statistical errors preclude a straightforward multiple non-linear least squares regression to optimize the experimental parameters from a set of TGA experiments. As a result, several very different sets of parameters can adequately model the thermal treatment of any one of the biomass structural components once the heating rate and gasification medium are specified. A global mass loss rate equation with an apparent activation energy and pre-exponential factor resulting from a least squares best fit analysis on the order of reaction and the temperature dependence exponent in the rate equation can serve as an initial design tool to enable the modeling of processes occurring in a biomass gasifier.

Larger data sets and additional parameters are insufficient to adequately address the non-statistical nature of systematic experimental errors that occur while attempting to determine kinetic parameters from thermogravimetric analyses. These non-statistical errors preclude a straightforward multiple non-linear least squares regression to optimize the experimental parameters from a set of TGA experiments. As a result, several very different sets of parameters can adequately model the thermal treatment of any one of the biomass structural components once the heating rate and gasification medium are specified. A global mass loss rate equation with an apparent activation energy and pre-exponential factor resulting from a least squares best fit analysis on the order of reaction and the temperature dependence exponent in the rate equation can serve as an initial design tool to enable the modeling of processes occurring in a biomass gasifier.

Introduction of steam as a reactant influent results in enhanced H_2 production during gasification of a wide variety of hydrocarbon fuels that include woods, grasses, agricultural residues and coal. Introduction of CO_2 during high temperature steam gasification results (*16*, *17*) in enhanced CO production and depressed CH_4 and H_2 levels. Careful selection of the gasification medium offers greater control of the volatile evolution products. Injection of CO_2 to enhance the CO and depress the H_2 during gasification resulted in our ability to tune the syngas ratio (H_2/CO) by adjusting the %CO_2 introduced. This offers greater flexibility and control since it is then possible to achieve a more suitable ratio tailored to the particular application such as a Fischer Tropsch synthesis (0.8-2.4) or the production of specialty chemicals (0.4-0.9).

Using a least squares analysis on the rate of mass loss fraction ($d\alpha/dT$) for lignin and cellulose during both CO_2 and H_2O/N_2 processing enabled the extraction of global kinetic parameters. For slow heating rates ~1-2°C min^{-1} and small sample sizes ~20-25 mg, the lignin was found to best fit a third order reaction during CO_2 and H_2O pyrolysis while cellulose best fit first order kinetics.

The temperature factor exponent w in the rate equation that gave the most consistently good fit for the lignin runs with n = 3 and the cellulose runs with n = 1 was w = 1/2. The T^w term has been incorporated by previous investigators into the pre-exponential factor A and it was allowed to transition in their kinetic models to higher values in order to account for the shifted mass loss curves at high heating rates. This transition in pre-exponential factor was observed during CO_2 cellulose pyrolysis from $6.7x10^{16}$ to $1.4x10^{18}$ to $3.9x10^{20}$. Actual biomass samples in CO_2 showed first order kinetics for the woods and second order kinetics for the grasses and residues. As the heating rate was increased from 1-100°C min^{-1}, thermal lag effects could be seen as a shift in the apparent kinetic parameters (E_{act}, A, n), with a uniform migration of the pyrolytic inflection point T_{max} for lignin and cellulose in CO_2 from 342 to 436°C and 324 to 440°C, respectively.

The Organosolv lignin exhibited significantly lower activation energies than the cellulose powder. The lignin was also observed to evolve significantly higher levels of H_2 and CH_4 during H_2O/N_2 processing. The pyrolysis (110-450°C) activation energy in CO_2 for lignin was ~39 kJ mol^{-1} while that for cellulose was ~205 kJ mol^{-1}. The wood E_{act} values ranged from 54.3-71.8 kJ mol^{-1}. The grasses and residues had substantially lower values from 27.6-46.2 kJ mol^{-1} with an earlier onset of their mass decays, that can be partly attributable to their high mineral content and its catalytic effect on their thermal decomposition. The pyrolysis activation energy in H_2O/N_2 for lignin was ~48 kJ mol^{-1} while that for cellulose was ~206 kJ mol^{-1}. The H_2O/N_2 gasification E_{act} energies for lignin and

Downloaded by PENNSYLVANIA STATE UNIV on June 6, 2012 | http://pubs.acs.org
Publication Date (Web): November 29, 2011 | doi: 10.1021/bk-2011-1084.ch002

cellulose were ~48 and 203 kJ mol^{-1} while during CO_2 gasification they were ~51 and ~208 kJ mol^{-1}, respectively.

The reduction to best fit first order rate expressions for all biomass samples during the entire gasification run (110-980°C) can indicate the difficulty in modeling the entire thermal treatment into the bulk mass transport region, as the decomposition mechanism changes between regimes, by a single rate order expression. Pyrolytic CO_2 decomposition of the highly cellulosic woods showed thermal degradation behavior and kinetic parameters more characteristic of cellulose while that of the high lignin bark and needle residues exhibited thermal decay curves and kinetic parameters more typical of lignin- lower activation energy, higher reaction order and earlier decomposition onset. This behavior can be correlated with the presence of a high mineral content in the residue feedstocks offering a catalytic char conversion that was not observed when the sample was water-washed prior to thermal processing.

Downloaded by PENNSYLVANIA STATE UNIV on June 6, 2012 | http://pubs.acs.org
Publication Date (Web): November 29, 2011 | doi: 10.1021/bk-2011-1084.ch002

Databases Accessed

- Energy Research Centre of the Netherlands, Phyllis Database for Biomass and Waste. http://www.ecn.nl/phyllis (accessed July 2010).
- U.S. D.O.E. Energy Efficiency and Renewable Energy Biomass Program: Biomass Feedstock Composition and Property Database. http://www1.eere.energy.gov/biomass/feedstock_databases.html (accessed July 2010).

References

1. Varhegyi, G.; Antal, M. J.; Jakab, E.; Szabo, P. *J. Anal. Appl. Pyrolysis* **1997**, *42*, 73–87.
2. Feng, B.; Bhatia, S. K. *Chem. Eng. Sci.* **2002**, *57*, 2907–2920.
3. Wang, G.; Li, W.; Li, B.; Chen, H. *Fuel* **2008**, *87*, 552–558.
4. Caballero, J. A.; Font, R.; Marcilla, A. *Thermochim. Acta* **1996**, *276*, 57–77.
5. Antal, M. J.; Varhegyi, G. *Ind. Eng. Chem. Res.* **1995**, *34*, 703–717.
6. Manya, J. J.; Velo, E.; Puigjaner, L. *Ind. Eng. Chem. Res.* **2003**, *42*, 434–441.
7. Gronli, M. G.; Varhegyi, G.; Di Blasi, C. *Ind. Eng. Chem. Res.* **2002**, *41*, 4201–4208.
8. Varhegyi, G.; Jakab, E. *Energy Fuels* **1994**, *8*, 1345–1352.
9. Gronli, M.; Antal, M. J.; Varhegyi, G. *Ind. Eng. Chem. Res.* **1999**, *38*, 2238–2244.
10. Sonobe, T.; Worasuwannarak, N. *Fuel* **2008**, *87*, 414–421.
11. Varhegyi, G.; Antal, M. J. *Energy Fuels* **1989**, *3*, 329–335.
12. Muller-Hagedorn, M.; Bockhorn, H.; Krebs, L.; Muller, U. *J. Anal. Appl. Pyrolysis* **2003**, *68-69*, 231–249.
13. Stenseng, M.; Jensen, A.; Dam-Johansen, K. *J. Anal. Appl. Pyrolysis* **2001**, *58-59*, 765–780.

14. Milosavljevic, I.; Vahur, O.; Suuberg, E. M. *Ind. Eng. Chem. Res.* **1996**, *35*, 653–662.
15. Park, D. K.; Goo, J. H.; Kim, S. D.; Lee, S. H.; Lee, J. G. *Proc. Sixth Korea−China Workshop Clean Energy Technol.* **2006**, *1*, 321–331.
16. Butterman, H. C.; Castaldi, M. J. *Ind. Eng. Chem. Res.* **2007**, *46*, 8875–8886.
17. Butterman, H. C.; Castaldi, M. J. *Environ. Eng. Sci.* **2009**, *26*, 703–713.
18. Ochoa, J.; Casanello, M. C.; Bonelli, P. R.; Cukierman, A. L. *Fuel Process. Technol.* **2001**, *74*, 161–176.
19. Ye, D. P.; Agnew, J. B.; Zhang, D. K. *Fuel* **1998**, *77*, 1209–1219.
20. Messenbock, R. C.; Dugwell, D. R.; Kandiyoti, R. *Fuel* **1999**, *78*, 781–793.
21. Zhang, L.; Huang, J.; Fang, Y.; Wang, Y. *Energy Fuels* **2006**, *20*, 1201–1210.
22. Dutta, S.; Wen, C. Y. *Ind. Eng. Chem. Processes Des. Dev.* **1977**, *16*, 20–30.
23. Marquez-Montesinos, F.; Cordero, T.; Rodriguez-Mirasol, J.; Rodriguez, J. J. *Fuel* **2002**, *81*, 423–429.
24. Gomez, C. J.; Manya, J. J; Velo, E.; Puigjaner, L. *Ind. Eng. Chem. Res.* **2004**, *43*, 901–906.
25. Gomez, C. J.; Varhegyi, G.; Puigjaner, L. *Ind. Eng. Chem. Res.* **2005**, *44*, 6650–6660.
26. Reina, J.; Velo, E.; Puigjaner, L. *Thermochim. Acta* **1998**, *320*, 161–167.
27. Hu, S.; Jess, A.; Xu, M. *Fuel* **2007**, *86*, 2778–2788.
28. Font, R.; Marcilla, A.; Verdu, E.; Devesa, J. *J. Anal. Appl. Pyrolysis* **1991**, *21*, 249–264.
29. Li, Z.; Zhao, W.; Meng, B.; Liu, C.; Zhu, Q.; Zhao, G. *Bioresour. Technol.* **2008**, *99*, 7616–7622.
30. Reina, J.; Velo, E.; Puigjaner, L. *Ind. Eng. Chem. Res.* **1998**, *37*, 4290–4295.
31. Fushimi, C.; Araki, K.; Yamaguchi, Y.; Tsutsumi, A. *Ind. Eng. Chem. Res.* **2003**, *42*, 3922–3928.
32. Ollero, P.; Serrera, A.; Arjona, R.; Alcantarilla, S. *Biomass Bioenergy* **2003**, *24*, 151–161.
33. Tancredi, N.; Cordero, T.; Rodriguez-Mirasol, J.; Rodriguez, J. J. *Fuel* **1996**, *75*, 1505–1508.
34. De Groot, W. F.; Shafizadeh, F. *Fuel* **1984**, *63*, 210–216.
35. Khalil, R.; Varhegyi, G.; Jaschke, S.; Gronli, M. G.; Hustad, J. *Energy Fuels* **2009**, *23*, 94–100.
36. Plante, P.; Roy, C.; Chornet, E. *Can. J. Chem. Eng.* **1988**, *66*, 307–312.
37. Sun, H.; Song, B. H.; Jang, Y. W.; Kim, S. D.; Li, H.; Chang, J. *Korean J. Chem. Eng.* **2007**, *24*, 341–346.
38. Barrio, M.; Gobel, B.; Risnes, H.; Henriksen, U.; Hustad, J. E.; Sorensen, L. H. In *Progress in Thermochemical Biomass Conversion*; Bridgwater, A. V., Ed.; Blackwell Science Publishing: Oxford, U.K., 2001; Vol. 1, pp 32−46.
39. Jauhiainen, J.; Conesa, J. A.; Font, R.; Martin-Gullon, I. *J. Anal. App. Pyrolysis* **2004**, *72*, 9–15.
40. Kalita, P.; Mohan, G.; Kumar, G. P.; Mahanta, P. *J. Renewable Sustainable Energy* **2009**, *1*, 1–12.
41. Shen, D. K.; Gu, S.; Luo, K. H.; Bridgwater, A. V.; Fang, M. X. *Fuel* **2009**, *88*, 1024–1030.

Downloaded by PENNSYLVANIA STATE UNIV on June 6, 2012 | http://pubs.acs.org
Publication Date (Web): November 29, 2011 | doi: 10.1021/bk-2011-1084.ch002

42. Orfao, J. J. M.; Antunes, F. J. A.; Figueiredo, J. L. *Fuel* **1999**, *78*, 349–358.
43. Guo, J.; Lua, A. C. *Biomass Bioenergy* **2001**, *20*, 223–233.
44. Butterman, H. C.; Castaldi, M. J. *Environ. Sci. Technol.* **2009**, *43*, 9030–9037.
45. Fushimi, C.; Araki, K.; Yamaguchi, Y.; Tsutsumi, A. *Ind. Eng. Chem. Res.* **2003**, *42*, 3929–3936.
46. Yang, H.; Yan, R.; Chen, H.; Lee, D. H.; Zheng, C. *Fuel* **2007**, *86*, 1781–1788.
47. Jakab, E.; Faix, O.; Till, F.; Szekely, T. *J. Anal. Appl. Pyrolysis* **1995**, *35*, 167–179.
48. Liu, Q.; Wang, S.; Zheng, Y.; Luo, Z.; Cen, K. *J. Anal. Appl. Pyrolysis* **2008**, *82*, 170–177.
49. Kawamoto, H.; Horigoshi, S.; Saka, S. *J. Wood Sci.* **2007**, *53*, 268–271.
50. Kawamoto, H.; Nakamura, T.; Saka, S. *Holzforschung* **2008**, *62*, 50–56.
51. Varhegyi, G.; Szabo, P.; Jakab, E.; Till, F. *J. Anal. Appl. Pyrolysis* **2001**, *57*, 203–222.
52. Varhegyi, G.; Chen, H.; Godoy, S. *Energy Fuels* **2009**, *23*, 646–652.
53. Becidan, M.; Varhegyi, G.; Hustad, J. E.; Skreiberg, O. *Ind. Eng. Chem. Res.* **2007**, *46*, 2428–2437.

Downloaded by PENNSYLVANIA STATE UNIV on June 6, 2012 | http://pubs.acs.org
Publication Date (Web): November 29, 2011 | doi: 10.1021/bk-2011-1084.ch002

Downloaded by OHIO STATE UNIV LIBRARIES on June 6, 2012 | http://pubs.acs.org
Publication Date (Web): November 29, 2011 | doi: 10.1021/bk-2011-1084.ch003

Chapter 3

Evaluation of Trace Element Partitioning during the Initial Phase of Coal Combustion Using GFAAS

**Anna A. Raeva,[1] Evguenii I. Kozliak,*,[1] David T. Pierce,[1]
and Wayne S. Seames[2]**

**[1]Department of Chemistry, University of North Dakota,
Grand Forks, North Dakota 58202, U.S.A
[2]Department of Chemical Engineering, University of North Dakota,
Grand Forks, North Dakota 58202, U.S.A
*E-mail: jkozliak@chem.und.edu**

The partitioning of three toxic semi-volatile trace elements (TEs), arsenic, antimony, and selenium during coal combustion was evaluated using a novel *in situ*/direct method. The method involves the use of a graphite furnace atomic absorption spectrometer (GFAAS) as a simultaneous high temperature (up to 2800 °C) *in situ* pyrolysis simulator, sample collector, and analytical platform. Several methods for determining activation parameters were compared and a simple, yet accurate method was selected. The importance of performing accurate measurements, including the synchronization of absorbance and temperature, was shown.

Three forms of occurrence of TEs in coal were modeled. The partitioning of organically associated TEs was simulated by placing TEs within the GFAAS graphite furnace, which upon heating generates an environment that simulates the burning organic structure of coal. For excluded minerals, the effect of graphite was reduced by inserting a Ta-lining inside the furnace. The activation energy of Se atomization was not affected by the presence of a Ta lining whereas it increased for As. Mineral inclusions were modeled by introducing the target TE into the furnace as a homogeneous mixture with a specific inorganic matrix. $NaAlO_2$ did not affect activation

In Synthetic Liquids Production and Refining; de Klerk, A., et al.;
ACS Symposium Series; American Chemical Society: Washington, DC, 2011.

energies for any of TEs studied, perhaps due to the non-specific effects of this anionic matrix. By contrast, $Ca(OAc)_2$ caused a sizable increase in activation energy, presumably, due to the preferential adsorption of TE oxides on basic CaO surfaces. The comparison of numerical values provided insights into the mechanisms associated with TE vaporization and atomization.

Introduction

Modeling gas-solid phase trace element (TE) partitioning in coal fired furnaces is an important step in understanding the fate and speciation of TEs. The ability to accurately predict TE partitioning is essential for assessing the environmental impacts of coal combustion for traditional pulverized coal combustors (*1–16*). It is also important for emerging advanced power systems such as gasification and oxy-coal combustion where TE buildup can foul heat transfer surfaces and accelerate corrosion. However, determination of TE partitioning during coal combustion is not practically feasible because of the complexity of the micro-environment of burning coal particles; the region that has the greatest influence on TE partitioning and speciation.

Specifically, it is impossible to sample TEs from all areas within the combustion microenvironment with the time resolution and accuracy required to correctly model and predict TE partitioning and speciation. Collection of samples from the bulk gas environment that evolves from the combustion microenvironment does not generate data of sufficient resolution to allow adequate prediction based on original coal properties and global operating parameters.

TEs in the original biomass are integrated into the organic structure of coal during the coalification process and thus may be strongly bound to the coal (organically associated). The individual TEs are thus exposed to a very high temperature, reducing environment during combustion. TE can also be present within minerals that are included into the coal matrix during coalification (inclusions) or excluded minerals that get mixed into the coal after coalification but prior to combustion. The chemical microenvironment is so different in each of these three regimes surface (Figure 1) (*17*, *18*) that TE partitioning can be distinctly different for each. In mineral inclusions, carbon is still accessible but the TE chemical association occurs with inorganics rather than with coal. By contrast, in the excluded mineral fraction, coal is not readily accessible.

In our prior work, we developed a method to simulate the behavior of organically associated TEs (*19*), which simultaneously uses a graphite furnace atomic absorption spectrometer (GFAAS) as an extremely high temperature *in situ* pyrolysis simulator, sample collector and analysis platform. The method takes advantage of the similarity of graphite to the carbon of coal. The graphite furnace allows the simulation of TE partitioning under conditions similar to those experienced during coal particle pyrolysis (reducing environment, high in carbon). As was shown in our prior study (*19*), activation energies for TE atomization in the GFAAS were independent of the process' operational parameters which were

Downloaded by OHIO STATE UNIV LIBRARIES on June 6, 2012 | http://pubs.acs.org
Publication Date (Web): November 29, 2011 | doi: 10.1021/bk-2011-1084.ch003

varied over a wide range. However, activation energies were dependent on the TE studied.

Organically associated TEs were modeled in our prior study simply by introducing TE aqueous solutions into the furnace (*19*).In the present work, we have expanded the method to study TEs in the two mineral regimes. Mineral inclusions were mimicked by simultaneously introducing TE standard solutions and water-soluble inorganic matrices, as a homogeneous mixture, into the furnace. Two matrices, $NaAlO_2$ and $Ca(OAc)_2$ were selected as being representative of important major inorganic constituents in coal (*2*). A scenario characteristic of excluded minerals was created by introducing TEs into a Ta-lined furnace. The metal (tantalum) lining was used to separate the furnace graphite from TEs.

The graphite furnace in a GFAAS acts as a flow reactor, with only atoms detected. Thus TE vaporization is assessed indirectly, through the detection of atoms in the vapor phase; i.e., the activation energy is measured for the element's *atomization* and then it is assumed that this accurately represents its *vaporization*. Another inherent limitation of GFAAS is that a temperature ramp is inherent for this instrument, making any isothermal experiments impossible. Several methods have been developed for determination of TE *atomization* activation energies in GFAAS (*20–22*). However, since using a GFAAS for determination of element *partitioning* was not anticipated in any previous work, a separate essential task, selecting an accurate way of calculating the TE atomization/vaporization activation energies, was addressed in this study.

It is of note that the use of a GFAAS is representative only for early stages of coal combustion, with a near-anaerobic environment on a microscale, since it is not possible to introduce oxygen into the graphite furnace.

Downloaded by OHIO STATE UNIV LIBRARIES on June 6, 2012 | http://pubs.acs.org
Publication Date (Web): November 29, 2011 | doi: 10.1021/bk-2011-1084.ch003

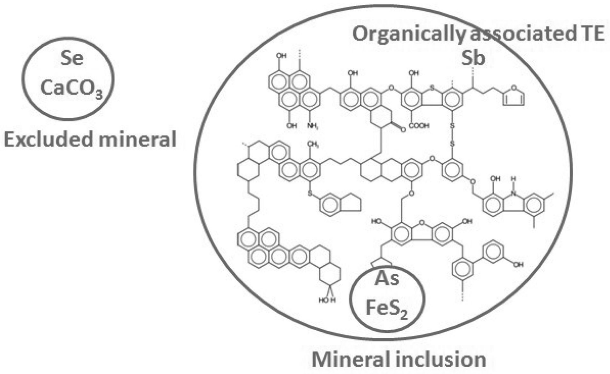

Figure 1. Forms of occurrence of TEs in coal.

Experimental Section

Materials and Reagents

Solutions of As(III), Sb(III), and Se(IV) were prepared by dilution of the corresponding 1,000 ppm stock solutions (RICCA, Arlington, TX, USA) with water deionized to 18 MOhm·cm resistivity (Millipore, Billerica, MA, USA; model Direct-Q® 3). The stock solutions contained acidic solutions of As_2O_3, $SbCl_3$, and SeO_2, respectively. Upon dilution, the analyte concentrations were in the range of 0 – 250 ppb. All solutions contained 2% of trace metal grade HNO_3 (Fisher Scientific, Pittsburgh, PA, USA) to assure reproducibility. The following detection limits were obtained for As, Sb and Se, respectively: 1, 2, and 2 ppb. Reproducibility of all measurements was within 5%.

Solutions containing TEs and matrices were prepared by spiking one of the standard TE solutions described above with one of two representative matrices: $NaAlO_2$ or $Ca(OAc)_2$.1 M $Ca(OAc)_2$ (Hampton Research, Aliso Viejo, CA) and $NaAlO_2$ (Pfaltz and Bauer, Waterbury, CT, USA) were diluted to obtain a concentration in the range of 0.01 – 0.1 M. Matrix concentrations were chosen so that the reference signal did not exceed 1.0. Higher reference signals may introduce an artifact in the absorbance signal.

Ta-lined furnaces were prepared by inserting Ta linings inside the furnaces according to the procedure described by L'vov *et al.* (*23*) Ta linings were cut from a 0.127 mm thick Ta foil (Alfa Aesar, Ward Hill, MA, USA) to a 14 mm length by 16 mm width size. The lining was folded into a cylindrical shape and inserted into the furnace. Then a hole was drilled into the lining aligned with the hole in the GFAAS graphite furnace.

Absorbance Measurements and Instrument Operation

Absorbances were measured using a Z-2000 Zeeman flame/furnace tandem atomic absorption spectrometer (Hitachi High Technologies, Japan). The graphite furnace used in this study was a longitudinally heated Pyro Tube HR cuvette (Hitachi, Tokyo, Japan). It had a cylindrical shape with a length of 29 mm and diameter of 5 mm. The absorbance values for selected dilutions did not exceed 0.6. The absorbance signal was measured every 20 ms with a time constant of 0.1 s to ensure accurate measurements. Absorbance vs. time profiles of atomization were recorded using the original GFAAS software. The temperature programs used for TE determinations are given in Table I.

The flow rate used in these experiments was 30 mL/min as recommended by the manufacturer, Hitachi (*24*). All experiments were conducted in triplicate. The TEs were deposited as aqueous samples on the center of the furnace using an autosampler. The injection volume was set to 20 µL. It was shown previously that operational parameters such as TE concentrations, flow rate, and ashing temperature do not have an effect on activation energies (*19*).

When the effect of a matrix on TE atomization was studied, TE solutions were prepared in the solution of the matrix. To make sure that the furnace was not overloaded with a matrix, a cleaning step was performed after each experiment. This cleaning step involved heating the furnace to 2800 °C for 15 s. Then a blank

Downloaded by OHIO STATE UNIV LIBRARIES on June 6, 2012 | http://pubs.acs.org
Publication Date (Web): November 29, 2011 | doi: 10.1021/bk-2011-1084.ch003

was analyzed to verify that the absorbance and reference signals had returned to their normal values.

Table I. Temperature programs used for As, Sb, and Se determinations

Stage	*Temperature, °C*		*Time, s*	
	Start	*End*	*Ramp*	*Hold*
Dry	80	140	40	
Ash	50, 650	50, 650	20	
Atomize	2700 (As, Se) 2300 (Sb)	2700 (As, Se) 2300 (Sb)		5
Clean	2800	2800		4

Temperature Measurements and Instrument Modifications

A Modline 5 infrared (IR) thermometer (Model 52-3024 with a 2B lens, IRCON, Niles, IL, USA) was positioned above the furnace to measure the temperature of the furnace wall. The thermometer provided a RS-485 digital output of factory-calibrated temperatures which was sent to a host computer. Factory calibration was traceable to NIST blackbody standards. Operated in this manner, the IR thermometer is capable of measuring accurate temperatures over a range of 750 – 3000 °C within a focal distance of 152 – 305 mm and with a response of 6.6 ms to 60 s.

Absorbance and temperature measurements were synchronized by recording and aligning (in time) optically-encoded signals embedded within the AA output and then recording absorbance along with the thermometer analog current output. The synchronization is described in detail elsewhere (*19*).

Calculation of Activation Energies

Three methods described in the literature, developed by Smets (*20*), Yan (*21*), and Chung (*22*) were used to calculate activation energies.

Smets' Method

The Smets' method is based on calculation of the rate constants of atom formation:

$$k_1 = \frac{n(t)}{\int_t^{\infty} n(t)dt} = \frac{A(t)}{\int_t^{\infty} A(t)dt} \qquad (1)$$

Downloaded by OHIO STATE UNIV LIBRARIES on June 6, 2012 | http://pubs.acs.org
Publication Date (Web): November 29, 2011 | doi: 10.1021/bk-2011-1084.ch003

Downloaded by OHIO STATE UNIV LIBRARIES on June 6, 2012 | http://pubs.acs.org
Publication Date (Web): November 29, 2011 | doi: 10.1021/bk-2011-1084.ch003

where k_1 is the first-order rate constant, *n(t)* is the number of analyte atoms at time *t*, and *A(t)* is the absorbance value at time t (*20*).

Absorbance *vs.* time profiles from the GFAAS software provided by the GFAAS manufacturer were used to find *A(t)*. An example of such a profile for Sb is shown in Figure 2.

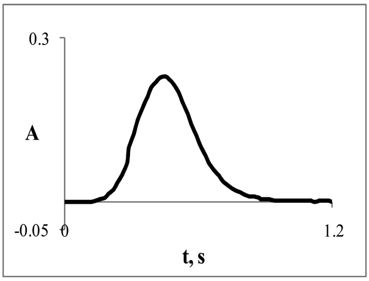

Figure 2. Absorbance profile for 100 ppb Sb.

The integrated absorbances, $\int_t^{\infty} A(t)dt$, were calculated using OriginPro8.1 and the following equation:

$$\int_t^{\infty} A(t)dt = A_{total} - \int_0^t A(t)dt \tag{2}$$

where A_{total} is the total area under the pertinent absorbance *vs.* time curve.

The rising part of the absorbance *vs.* time curve was used to construct an Arrhenius plot. The points taken were from 10×noise to $0.9 \times A_{max}$. For the experiments with $Ca(OAc)_2$, absorbance profiles for As (Figure 3) and Sb contained double peaks. In these cases, the multiple peak fit function in OriginPro 8.1 was used for peak deconvolution. The fit used was Gaussian.

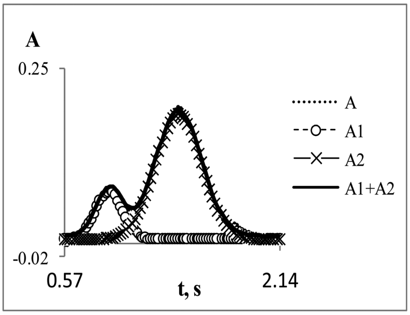

Figure 3. Deconvolution of two peaks observed with 100 ppb As and 0.01 M $Ca(OAc)_2$. The two peaks evolving at different temperatures are labeled A_1 and A_2, respectively.

Downloaded by OHIO STATE UNIV LIBRARIES on June 6, 2012 | http://pubs.acs.org
Publication Date (Web): November 29, 2011 | doi: 10.1021/bk-2011-1084.ch003

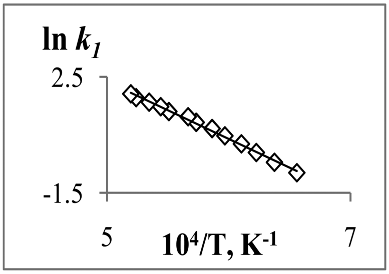

Figure 4. The lnk_1 vs. 10^4/T function for 100 ppb Sb constructed using Smets' method.

Activation energies were calculated from the slope and pre-exponentials were calculated from the intercept of Arrhenius plots of lnk_1 *vs.* 1/T. An example of such a plot for Sb is shown in Figure 4. In the case where multiple peaks were obtained, as in Figure 4, separate plots were used for each of the peaks. Temperature *vs.* time data were obtained using a Modline 5 IR thermometer.

Chung's Method

In Chung's method, the rate constant of atom formation is calculated using the following equation:

$$k_1 = k_2 \frac{A(t)}{A_{\max} - A(t)} \qquad (3)$$

where k_2 is the rate constant of atom dissipation and A_{max} is the maximum absorbance (*22*).

The value of k_2 was calculated from the slope of the plot of ln$A(t)$ *vs.* t with a starting time for this calculation of $t_o = t_{max}$ (the time at the absorbance maximum). Then, activation parameters were calculated from the slope and intercept of the Arrhenius plots of lnk_1 *vs.* 1/T.

Yan's Method

For Yan's method, the following equations were used to calculate activation parameters:

$$\ln Y = -\frac{E_a}{RT} + \frac{\ln(k_0 p^{x-1} R(1 - 2RT / E_a)}{\alpha E_a} \qquad (4)$$

where

$$\ln Y = \ln\left(\left\{\ln\left[k_2 \int_0^{\infty} Adt /(k_2 \int_t^{\infty} Adt - A)\right]\right\}/T^2\right) \qquad (5)$$

And k_0 is the pre-exponential factor; p is the proportionality constant between the number of gaseous analyte atoms and the measured absorbance; α is the heating rate, dT/dt; and x is the reaction order.

Activation energies were obtained from the slope and pre-exponential factors were calculated from the intercept of the plot of ln$Y$ *vs.* 1/T. This plot was a straight line for the appropriate reaction order, x (subject to arbitrary selection).

Results and Discussion

Application and Comparison of Various Methods To Calculate Activation Energies

The analytical platform in a GFAAS acts as a flow reactor with changing temperatures. Therefore, the activation parameters of TE vaporization can only be determined by indirect methods, such as the methods developed by Smets, Yan, and Chung (*20*, *22*, *25*).The formulas used in these methods are shown in the Experimental section. Here, we address the mathematical and physical significance of these formulas, starting with their derivation, in order to select the treatment which would be most suitable for the application targeted.

Smets' Method

The method developed by Smets is most widely used for the determination of activation energies. In this method, the expression for the atom formation rate constant, k_1, is obtained. Then, the activation energy is determined from the slope of an Arrhenius plot of lnk_1 *vs.* 1/T (*20*). An example of such a plot for Sb is shown in Figure 4.

The rate of change of the number of atoms in the optical pathway, dn/dt, can be expressed as the difference between the rate of atoms' formation, R_{form}, and the rate of their dissipation, R_{dis}:

$$\frac{dn}{dt} = R_{form} - R_{dis} \tag{6}$$

Using a steady-state approximation for n, the following relation may be obtained:

$$\int_0^\infty R_{form}\,dt = \int_0^\infty R_{dis}\,dt \tag{7}$$

Equalizing the integrals used in this method is a more accurate representation of steady state than just setting the term dn/dt to zero in equation (6) because this treatment provides values averaged over the entire peak. The differential form of this relation would only be accurate near the peak's maximum.

Equation (1) introduced earlier is used to calculate k_1. Equation (8) used by Smets is valid only when the number of atoms which have left the furnace prior to

Downloaded by OHIO STATE UNIV LIBRARIES on June 6, 2012 | http://pubs.acs.org
Publication Date (Web): November 29, 2011 | doi: 10.1021/bk-2011-1084.ch003

the time *t* when, $\int_0^t k_2 n(t)dt$, is larger than *n(t),* a measured quantity that accounts for the GFAAS signal at this particular time *t*.

$$N_0 - N = \int_0^t k_2 n dt \tag{8}$$

Thus, Smets' method is applicable only for the initial part of absorbance *vs.* time signal where *n(t)* can be considered negligible.

Downloaded by OHIO STATE UNIV LIBRARIES on June 6, 2012 | http://pubs.acs.org
Publication Date (Web): November 29, 2011 | doi: 10.1021/bk-2011-1084.ch003

Chung's Method

The Arrhenius plots of lnk_1 *vs.* 1/T obtained by the Smets' method often curve towards the abscissa at high temperatures. This is because this method does not account for a bias toward atom dissipation occurring toward the end of the temperature ramp. Instead, it uses the steady-state approximation, which is valid only for the initial part of absorbance *vs.* time signal. An attempt to improve the linearity of the Arrhenius plots was made by Chung (*22*). He used equation (6) described in the Smets' method to express the rate of metal vapor generation. Then, a steady-state approximation was applied to the number of atoms present in the gas phase, *n(t)*:

$$k_1 N = k_2 n(t) \tag{9}$$

where $k_1$is the rate constant of atom formation, k_2 is the rate constant of atom dissipation, and *N* is the number of unatomized analyte species. *N* is expressed as:

$$N = N_0 - n(t) \tag{10}$$

Equation (9) is only valid near the absorbance peak maximum. Note that Smets used a more general integral form of this approximation, equation (7). Equation (10) is valid only when the number of atoms that have left the furnace before time *t,* $\int_0^t k_2 n(t)dt$, is smaller than *n(t).* An advantage of Chung's method is that *n(t)* is a measured quantity that accounts for the GFAAS signal intensity whereas $\int_0^t k_2 n(t)dt$ is a quantity that cannot be measured directly.

Chung ultimately derived equation (3)where $k_2$is obtained from the slope of the plot of ln*A(t) vs. t,* starting with $t_o = t_{max}$ (*21*, *22*). An example of such a plot for Sb is shown in Figure 5.

Downloaded by OHIO STATE UNIV LIBRARIES on June 6, 2012 | http://pubs.acs.org
Publication Date (Web): November 29, 2011 | doi: 10.1021/bk-2011-1084.ch003

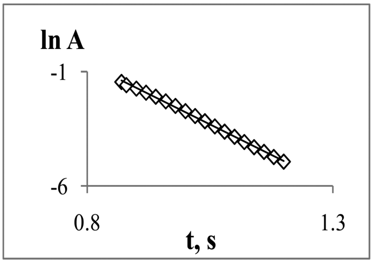

Figure 5. The ln A vs. t for 100 ppb Sb used to calculate k_2.

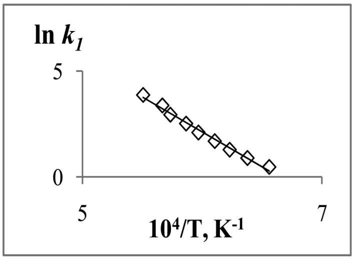

Figure 6. The $\ln k_1$ *vs.* $10^4/T$ *for 100 ppb Sb constructed using Chung's method.*

Based on the form of equation (10) and steady-state approximation (9) used by Chung, this method should be used for the part of absorbance *vs.* time signal that is closest to A_{max}. We expected that Chung's method would be more applicable to steeply rising peaks where the *n(t)* term is more important than the $\int_0^t k_2 n(t)dt$ term. To obtain the activation energy, $k_1$is substituted into the Arrhenius equation (11):

$$\ln k_1 = -\frac{E_a}{RT} + const \tag{11}$$

An example is shown in Figure 6.

Yan's Method

A successful attempt to reconcile and improve both Smets' and Chung's methods and to improve the linearity of Arrhenius plots was made by Yan *et al.* (*21*, *25*) They corrected equation (1) by eliminating several assumptions used when this equation was derived (*21*)(*25*).

First, equation (8) was modified to yield equation (12) (*21*).

$$N_0 - N = \int_0^t k_2 n(t)dt + n(t) \tag{12}$$

Downloaded by OHIO STATE UNIV LIBRARIES on June 6, 2012 | http://pubs.acs.org
Publication Date (Web): November 29, 2011 | doi: 10.1021/bk-2011-1084.ch003

where a new term, *n(t)*, is introduced so that the number of vaporized atoms (N_0 - N) is equal to the sum of the number of atoms which left the furnace before time *t* ($\int_0^t k_2 n dt$) plus the number of atoms present in the furnace at time *t*, *n(t)*.

Similar to Smets, Yan *et al.* used a more general integral form of the steady-state approximation (7).

The rest of the derivation, with our comments explaining details omitted in the original paper, is provided in the Appendix. The final equation of this method is equation (4) (*21*)where ln*Y* is described by equation (5). The activation energy value is obtained from the slope of the linear plot of ln*Y* *vs.* 1/T (*21*)such as the one shown in Figure 7 for Sb.

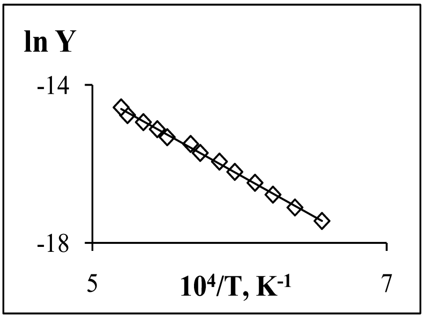

Figure 7. The ln Y vs. 10^4/T for 100 ppb Sb constructed using Yan's method

The second term in the right hand side of equation (4) contains the absolute temperature, *T*. As *T* is under the logarithm, this term is assumed to be nearly constant. It was reported that the linearity of the Arrhenius plot was significantly improved when equation (4) was used instead of the Arrhenius plot of lnk_1 *vs.* 1/T (*25*). The method developed by Yan *et al.* is the most inclusive of those available and would be applicable for all peak types (i.e., both gradually and steeply rising) and for a broader temperature range than the methods developed by Smets and Chung. In addition, Yan's method may be used even if the kinetics for analyte concentration are not first order.

While Yan's method is the most accurate method, it is also much more complicated and time consuming than the other two, simpler methods. It was thus desirable to determine whether one of the simpler methods would yield similar values for this specific application.

Synchronization

Accurate temperature measurements are essential if accurate kinetic activation parameters are to be determined. Temperatures reported in two ways, i.e., 1) programmed by a GFAAS and 2) measured by an IR thermometer, are shown in Figure 8.

Downloaded by OHIO STATE UNIV LIBRARIES on June 6, 2012 | http://pubs.acs.org
Publication Date (Web): November 29, 2011 | doi: 10.1021/bk-2011-1084.ch003

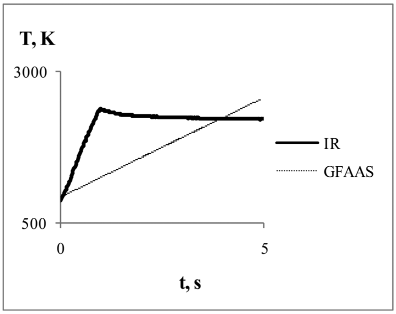

Figure 8. Temperature vs. time plots recorded using an IR thermometer and calculated from the GFAAS temperature program.

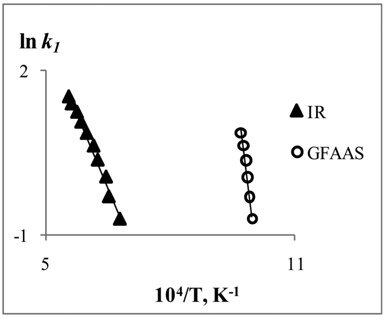

Figure 9. The lnk_1 vs. 10^4/T obtained using the temperatures recorded with an IR thermometer and calculated from the GFAAS temperature program.

Without an external device for temperature measurements, it is impossible to determine when the temperature reaches the plateau and, therefore, obtain the correct Arrhenius plot (Figure 9). This in turn results in a grossly inaccurate activation energy (112 *vs.* 36 kcal·mol^{-1}). In addition, since absorbance and temperature were measured independently by two instruments, they must be synchronized. Otherwise, incorrect values of activation parameters can be obtained. An adequate synchronization for a digitally controlled GFAAS is described in our previous publication (*19*).

Reducing **Environment (Graphite Furnace): Direct Comparison of Three Methods To Calculate Activation Parameters**

The methods described above were used to calculate the activation energies for As, Sb, and Se atomization in a GFAAS (Table II). The microenvironment occurring in the graphite furnace was similar to that organically associated TEs experience during early stages of coal combustion, i.e., reducing, high in carbon, and not influenced by inorganics.

Table II. Activation energies for TEs calculated using the methods developed by Smets (*20*), Chung (*22*), and Yan *et al.* (*25*)

TE	*Activation energy, kcal·mol⁻¹*		
	Smets	*Chung*	*Yan*
As	60 ± 7	101± 12	57 ± 7
Sb	37 ± 4	78 ± 4	34 ± 1
Se	69 ± 5	185 ± 16	71 ± 6

Downloaded by OHIO STATE UNIV LIBRARIES on June 6, 2012 | http://pubs.acs.org
Publication Date (Web): November 29, 2011 | doi: 10.1021/bk-2011-1084.ch003

Calculations using the Smets' and Yan' methods yielded statistically indistinguishable activation energy values. By contrast, the activation energies calculated using Chung's method were significantly and consistently higher (ca. 2-fold) than those calculated by the other methods. The physical and mathematical significance of this observed difference was discussed in the previous section. Namely, Chung's method uses the steady-state approximation in its differential form, which is only applicable to the data points near the absorbance maximum. Thus, it is most suitable for analytical measurements where the element's maximum absorbance signal is to be obtained, but it appears to be unsuitable for the current application.

Normally when activation energies are calculated, data points are taken from the initial parts of absorbance vs. time curves. In our application, unless the Arrhenius plot ends up having two different slopes at low and high temperatures, there is no reason for using the points near the peak's maximum and beyond. Other than the case of biphasic Arrhenius plots, which were never observed in this application, Yan's method would be preferred if the atomization kinetics varied substantially from first order. Since no such kinetic features were observed for any of the TEs studied under any of the conditions used (see below), the simpler Smets' method can be recommended for measuring the activation energies of TE vaporization as for any other applications where slowly rising peaks are obtained.

Neutral Environment Representing Excluded Mineral (Ta-Lined Furnaces)

Typical absorbance *vs.* time profiles as well as Arrhenius plots of lnk_1 *vs.* 10^4/T for As and Se atomization in a Ta-lined graphite furnace are shown in Figures 10, 11, 12, and 13, respectively).

For both elements, a small pre-peak appeared in the absorbance profile (Figures 10 and 11). The occurrence of two peaks may indicate the existence of two mechanisms for TE atomization. The pre-peak was not large enough to allow calculation of an activation energy. Thus, for both elements activation energies were calculated only from the second peak.

Downloaded by OHIO STATE UNIV LIBRARIES on June 6, 2012 | http://pubs.acs.org
Publication Date (Web): November 29, 2011 | doi: 10.1021/bk-2011-1084.ch003

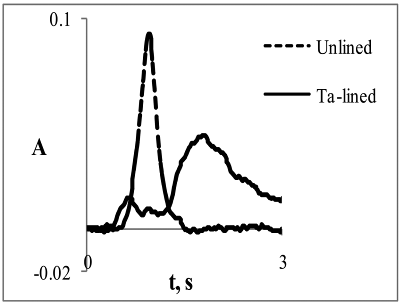

Figure 10. Absorbance profiles for 100 ppb As obtained in unlined and Ta-lined graphite furnace platforms.

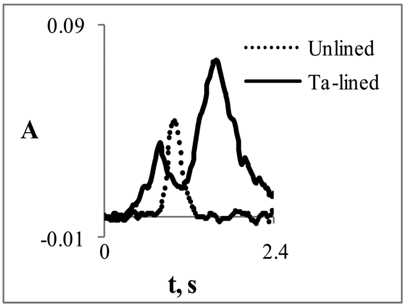

Figure 11. Absorbance profiles for 100 ppb Se obtained in unlined and Ta-lined graphite furnace platforms.

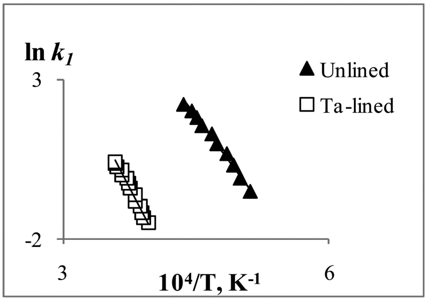

Figure 12. The lnk_1 vs. 10^4/T for 100 ppb As in unlined and Ta-lined graphite furnace platforms.

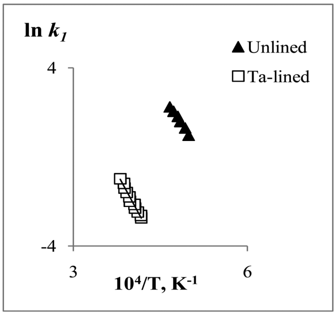

Figure 13. The lnk_1 *vs.* $10^4/T$ *for 100 ppb Se in unlined and Ta-lined graphite furnace platforms.*

Table III. Activation energies for As and Se obtained in a Ta-lined furnace and compared to unlined graphite furnace

TE	*Activation energy, kcal·mol^{-1}*	
	Unlined Graphite Furnace	*Ta-lined Graphite Furnace*
As	60 ± 7	89 ± 8
Se	69 ± 5	77 ± 8

For Se, the activation energy was not significantly affected by the presence of a Ta lining (Table III). This indicates that the partitioning of this TE from the organic fraction and excluded minerals may be similar despite the drastic difference in microenvironments for these two forms of occurrence; reducing for the carbon-rich organic fraction and near-neutral for excluded mineral. An apparent chemical reason for this observed effect is that the rate-limiting step for Se atomization does not involve carbon. This, in turn, indicates that Se occurs in the vapor phase predominantly in its molecular form, apparently as one of the oxides. Relatively high E_a values corroborate this hypothesis because they exceed the energy essential for evaporation or desorption of simple chemicals, which is ca. 20-30 kcal/mol (*26–29*).

An implication of this observation for coal combustion is that Se occurring as its acidic oxide, SeO_2, is expected to adsorb preferentially on basic surfaces, regardless of the presence of oxygen or time it spends in the hot or cold zones. This assumption was confirmed while studying the matrix effects, see below.

In contrast to Se, the activation energy for As determined in a Ta-lined furnace was significantly higher than that in the unlined graphite furnace (Table III). Apparently, graphite acts as a reducing agent and this step is rate-limiting for As atomization. This hypothesis is also supported by the fact that the As absorbance signal obtained in a Ta-lined furnace was lower than that in an unlined graphite furnace.

Downloaded by OHIO STATE UNIV LIBRARIES on June 6, 2012 | http://pubs.acs.org
Publication Date (Web): November 29, 2011 | doi: 10.1021/bk-2011-1084.ch003

Downloaded by OHIO STATE UNIV LIBRARIES on June 6, 2012 | http://pubs.acs.org
Publication Date (Web): November 29, 2011 | doi: 10.1021/bk-2011-1084.ch003

Thus carbon impacts As atomization and vaporization. Even ignoring other effects, such as matrix bonding and speciation of the original material, a lower fraction of the original As present in excluded minerals is expected to vaporize compared to As organically associated with the coal. Also, molecular species of arsenic are expected to evolve from excluded minerals whereas the organic fraction is expected to generate As in its elemental form. This difference may, in turn, affect where these vapors would preferentially adsorb. While As atoms may be near-randomly distributed across a wide range of surfaces, acidic arsenic oxides would sorb onto basic sites contained on fly ash surfaces, such as those associated with calcium, iron, and aluminum (if the latter occurs as a cation rather than aluminate anion).

The As absorbance peak is also shifted towards higher temperatures when the Ta-lining was used as compared to the plain graphite furnace (Figure 10). This feature illustrates the physical essence of the Smets' method [equation (1)] used in this work to calculate activation parameters, which becomes apparent while considering the linear Arrhenius plots (Figures12 and 13). If the y-intercepts of the Arrhenius plot, i.e., the pre-exponentials, are similar for two peaks, then the same slope, i.e., activation energy, would imply that both peaks' rise will start at similar temperatures.

However, as seen in Figures 10 and 11, in reality the peaks may have either similar or dissimilar positions. The derivation of the Smets method takes this observed feature into account. Even when the Arrhenius pre-exponentials are of similar magnitude while using plain and Ta-lined graphite furnaces (Table IV), the peak shapes are different (Figures 10 and 11). This affects the important integral term, $\int_0^t k_2 n(t)dt$, so the peaks do not have to start at the same temperature for the same E_a.

For example, for As the peak obtained in the unlined graphite furnace matches the pre-peak obtained with a Ta-lined furnace, as expected since they reflect the same process (Figure 10). However, the main peak is significantly shifted toward higher temperatures, also as expected based on the differences in activation energies. By contrast, the position of the Se peak obtained in the unlined graphite furnace is not significantly different from that obtained using the Ta-lined furnace (Figure 11). Yet, they yield statistically similar activation energies.

Since Sb appears to evaporate as a molecular species, no influence of carbon was expected and, so, no experiments using a Ta-lined graphite furnace were conducted with this TE.

The Effect of Inorganic Matrices Representing Mineral Inclusions

The effect of two representative inorganic matrices, $NaAlO_2$ and $Ca(OAc)_2$, on the activation energies for As, Sb, and Se atomization was determined (Table V).

Addition of 0.01 M $NaAlO_2$ did not cause any statistically significant effect on the activation energies for all three elements. Figures 14, 15, and 16 show that neither the peak shapes nor temperatures at which the peaks start rising depend on whether this matrix is present. This observation indicates that aluminates are not expected to influence the partitioning of these three TEs.

Table IV. Pre-exponential factors calculated for As, Sb, Se in various microenvironments

TE	*ln A (A, s^{-1})*				
	Unlined Graphite Furnace	*Graphite Furnace*			
		No matrix	*0.01 M $NaAlO_2$*	*0.01 – 0.1 M $Ca(OAc)_2$*	
				Peak 1	*Peak 2*
As	18.8 ± 0.5	17.3 ± 1.2	16.0 ± 0.3	14.7 ± 0.8	14.8 ± 2.2
Sb	Not Determined	12.7 ± 0.1	14.8 ± 0.4	12.7 ± 0.5	15.7 ± 1.3
Se	17.4 ± 2.3	20.3 ± 0.9	16.7 ± 0.2	27.5 ± 5.0	

Table V. The effect of two representative inorganic matrices on the atomization activation energies for As, Sb, and Se

TE	*Activation energy, $kcal \cdot mol^{-1}$*			
	No matrix	*0.01 M $NaAlO_2$*	*0.01 – 0.1 M $Ca(OAc)_2$**	
			Peak 1	*Peak 2*
As	60 ± 5	61 ± 2	51 ± 2	70 ± 8
Sb	37 ± 2	34 ± 3	41 ± 3	65 ± 5
Se	69 ± 5	57 ± 7	136 ± 9	

* $Ca(OAc)_2$ concentration was 0.01 M for As and Se and 0.1 M for Sb

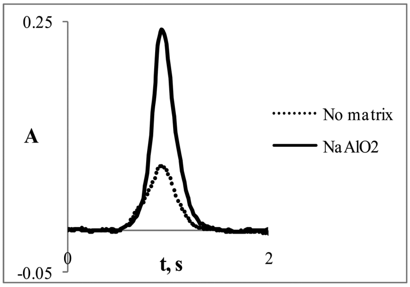

Figure 14. Absorbance profile for 100 ppb As with and without 0.01 M $NaAlO_2$.

Downloaded by OHIO STATE UNIV LIBRARIES on June 6, 2012 | http://pubs.acs.org
Publication Date (Web): November 29, 2011 | doi: 10.1021/bk-2011-1084.ch003

Downloaded by OHIO STATE UNIV LIBRARIES on June 6, 2012 | http://pubs.acs.org
Publication Date (Web): November 29, 2011 | doi: 10.1021/bk-2011-1084.ch003

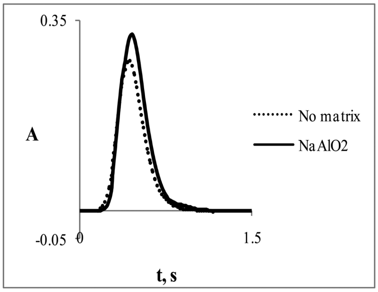

Figure 15. Absorbance profile for 100 ppb Sb with and without 0.01 M $NaAlO_2$.

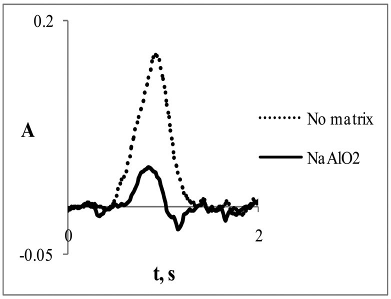

Figure 16. Absorbance profile for 100 ppb Se with and without 0.01 M $NaAlO_2$.

In contrast to aluminate, calcium showed a significant effect on the activation energies for As, Sb, and, particularly, Se. A higher activation energy indicates significant chemical interactions between the TE and this matrix, which is supported by the literature. Note that $Ca(OAc)_2$ readily decomposes upon heating to CaO. SeO_2 retention by CaO was reported by several authors (*2*)(*7*)(*30*)–(*32*). Thus, CaO is expected to retain Se in mineral exclusions unless high temperatures (around 2300 °C) are reached. Then, if this TE is released to the vapor phase, it will be in its elemental form rather than its oxide.

For As and Sb, two absorbance peaks instead of one were observed (*cf.* Figure 3). Activation energies were calculated separately for each peak upon their deconvolution, as described in the Experimental section. Their occurrence suggests the existence of two competing atomization mechanisms for each TE. The activation energy calculated using the data points of the first peak matched that obtained without a matrix, thus indicating that this peak is likely due to the interaction of TE vapors with carbon. By contrast, the activation energy calculated using the second peak's data points was significantly higher (listed in Table V), apparently reflecting the TE's interaction with the given inorganic matrix, i.e., calcium. This increase in E_a indicates a significant TE retention by CaO.

However, the retention for As and Sb was not as strong as in the case of Se. Perhaps, this effect is due to the difference in preferred forms of occurrence of TEs in the vapor phase. Since Se evaporates in the form of its acidic oxide, its retention by basic CaO is expected. By contrast, if other TEs, e.g., As, vaporize mostly as atoms, a less pronounced influence of CaO is expected. Indeed, even though two peaks were observed for As in the presence of calcium (*cf.* Figure 3), the activation energies calculated with and without this matrix were similar (Table V).

The slight influence of CaO on the evaporation of Sb, along with the occurrence of two peaks, indicates that this TE, in the presence of a cationic matrix and carbon, may still evaporate in both atomic and molecular forms, although the atomic form is dominant.

Work documenting the influence of various inorganic matrices on TE vaporization will be published separately. The current study provided some qualitative information on TE speciation in the vapor phase as well as quantitative information on the kinetics of their vaporization, i.e., the Arrhenius activation parameters. This information can be used in modeling TE behavior in coal-fired furnaces.

Downloaded by OHIO STATE UNIV LIBRARIES on June 6, 2012 | http://pubs.acs.org
Publication Date (Web): November 29, 2011 | doi: 10.1021/bk-2011-1084.ch003

Conclusions

Activation parameters for the atomization/partitioning of three semi-volatile trace elements, As, Sb, and Se, were estimated for three different forms of occurrence: organically associated TEs, TEs present in excluded minerals and mineral inclusions. Three methods for activation parameter calculation were compared. A relatively simple Smets' method was shown to be accurate and efficient for this application. Differences in atomization in a neutral environment (a Ta-lined graphite furnace) compared to a reducing environment (unlined graphite furnace) were only found for As, probably because it was the only element for which the rate-limiting step involved graphite. $NaAlO_2$, being an anionic matrix, did not affect the activation energies of any of the three TEs. By contrast, $Ca(OAc)_2$ caused an increase in activation energies in all three cases but the effect was most pronounced for Se. This increase was presumably due to the adsorption of acidic TE species on this cationic matrix.

Acknowledgments

Funding for this study was provided by the U.S. Department of Energy (Grant DE-FG02-6ER46292). Neither the United States Government nor the agency thereof, nor any of the employees, makes any warranty, express or implied, or assumes any legal liability or responsibility for the accuracy, completeness, or usefulness of any information disclosed. Reference herein does not necessarily constitute or imply its endorsement, recommendation, or favoring by the United States Government or the agency thereof or by the State of North Dakota. The authors also thank Oleg V. Klykov for conducting several experiments.

Downloaded by OHIO STATE UNIV LIBRARIES on June 6, 2012 | http://pubs.acs.org
Publication Date (Web): November 29, 2011 | doi: 10.1021/bk-2011-1084.ch003

Appendix

In the following full derivations, all of the equations are numbered consecutively with index A (Appendix). Some of them were also used in the main manuscript. These were assigned the same numbers as equation numbers here. The derivations follow the original papers (*22–24*) but several additional explanations essential for the current application are provided.

Smets' Method: Full Derivation

In the Smets method, the expression for the rate constant of atom formation, k_1, is obtained first. Then, the activation energy is determined from the slope of the Arrhenius plot of ln k_1 *vs.* 1/T (*20*).The rate of change of the number of atoms in the optical pathway, dn/dt, can be expressed as the difference between the rate of atoms' formation, R_{form}, and the rate of their dissipation, R_{dis}:

$$\frac{dn}{dt} = R_{form} - R_{dis} \qquad \text{(1A), (6)}$$

Using the steady-state approximation for n in its integral form, ie., averaging over the entire temperature range, relations may be obtained upon setting the rate of change of n to zero:

$$\int_0^\infty R_{form}\,dt = \int_0^\infty R_{dis}\,dt \qquad \text{(2A), (7)}$$

or

$$\int_0^\infty R_{form}\,dt = <k_2> p\int_0^\infty A\,dt \qquad \text{(3A)}$$

where dissipation is assumed to be a first order reaction with the rate constant k_2. Note that n, the number of atoms in the optical pathway, is proportional to A, the measured absorbance. $<k_2>$ is the mean value of the rate constant of atom dissipation taken over the entire signal duration:

$$<k_2> = \frac{\int_0^\infty k_2 n\,dt}{\int_0^\infty n\,dt} \qquad \text{(4A)}$$

Atom formation is also assumed to be a first order reaction:

$$R_{form} = k_1 N \qquad \text{(5A)}$$

where k_1 is the rate constant of atom formation and N is the number of analyte atoms left on the furnace surface. The initial number of atoms introduced into the furnace, N_0, is expressed as:

$$N_0 = \frac{1}{\beta}\int_0^{\infty} R_{form}\,dt \tag{6A}$$

where β is the atomization efficiency. The number of atoms (N_0 - N) vaporized during the time t is equal to:

$$N_0 - N = \frac{1}{\beta}\int_0^{t} R_{form}\,dt \tag{7A}$$

or

$$N_0 - N = \int_0^{t} k_2 n\,dt \qquad \text{(8A), (8)}$$

where β is assumed to be 1.This is a limitation of any GFAAS method. Based on (7A), (6A), (5A), (3A) and the fact that:

$$R_{dis} = k_2 n = k_2 pA \tag{9A}$$

an expression for the rate constant can be obtained (*20*):

$$k_1 = \frac{k_2 A}{< k_2 > \int_0^{\infty} A\,dt - > k_2 < \int_0^{t} A\,dt} \tag{10A}$$

or

$$k_1 = \frac{A}{\int_t^{\infty} A\,dt} \qquad \text{(11A), (1)}$$

where

$$> k_2 <= \frac{\int_0^{t} k_2 n\,dt}{\int_0^{t} n\,dt} \tag{12A}$$

In Smets' method, k_2, the rate constant of atom dissipation, is present in both the numerator and denominator of equation (10A) and, thus, it cancels out when k_2, $<k_2>$ (the mean value of the rate constant of atom dissipation taken over the entire signal duration) and $>k_2<$ (the mean value of the rate constant of atom dissipation taken over the *(0,t)* interval) are assumed to be equal. This is true when k_2 is temperature independent because it is not calculated over the same temperature range.

Downloaded by OHIO STATE UNIV LIBRARIES on June 6, 2012 | http://pubs.acs.org
Publication Date (Web): November 29, 2011 | doi: 10.1021/bk-2011-1084.ch003

Equation (8A) used by Smets is only valid when the number of atoms which left the furnace before time *t,* $\int_0^t k_2 n(t)dt$, is larger than *n(t),* a measured quantity that accounts for the AA signal.

Chung's Method: Full Derivation

Chung (*22*) used equation (1A) described in the derivation of Smets' method to express the rate of appearance of metal vapor.

Then, a steady-state approximation was applied to the number of atoms present in the gas phase, *n(t)*:

$$k_1 N = k_2 n(t) \qquad \text{(13A), (9)}$$

$$k_1 = k_2 \frac{n(t)}{N} \qquad \text{(14A)}$$

where k_1 is the rate constant of atom formation, k_2 is the rate constant of atom dissipation, and *N* is the number of unatomized analyte species. *N* is expressed as:

$$N = N_0 - n(t) \qquad \text{(15A), (10)}$$

Equation (15A) is valid only when the number of atoms which left the furnace before time *t,* $\int_0^t k_2 n(t)dt$, is smaller than *n(t). n(t)* is a measured quantity and it accounts for the AA signal whereas $\int_0^t k_2 n(t)dt$ is the amount that cannot be measured.

Based on the fact that:

$$n(t) = pA(t) \qquad \text{(16A)}$$

and

$$N_0 = pA_{\max} \qquad \text{(17A)}$$

Chung obtained the following equation (*22*):

$$k_1 = k_2 \frac{A(t)}{A_{\max} - A(t)} \qquad \text{(18A), (3)}$$

The value of k_1 is calculated from the experimental data using equation (18A) where k_2 is obtained from the slope of the plot of ln *A(t) vs. t,* where the starting time for this calculation is $t_o = t_{max}$ (*21*, *22*). Based on the form of equation (15A) used by Chung, this method should be used for the part of the absorbance *vs.* time

Downloaded by OHIO STATE UNIV LIBRARIES on June 6, 2012 | http://pubs.acs.org
Publication Date (Web): November 29, 2011 | doi: 10.1021/bk-2011-1084.ch003

signal closest to A_{max}. To obtain the value of activation energy, *k1* is substituted into the Arrhenius equation:

$$\ln k_1 = -\frac{E_a}{RT} + const \qquad (19A), (11)$$

Yan's Method: Full Derivation

Yan *et al.* corrected equation (11A) by eliminating several assumptions used when it was derived by the others (*21*, *25*).

First, they modified equation (8A) to the following equation (*21*):

$$N_0 - N = \int_0^t k_2 n(t)dt + n(t) \qquad (20A), (12)$$

where a new term, *n(t)* is taken into account so that the number of vaporized atoms, (N_0 - *N*), is equal to the number of atoms which left the furnace before time *t* ($\int_0^t k_2 ndt$) plus the number of atoms present in the furnace at time *t*, *n(t)*. Equation (8A) used by Smets is valid when *n(t)* is smaller than $\int_0^t k_2 ndt$.

Based on equation (6A) and the assumption that the atomization efficiency is equal to 1, N_0, the initial number of atoms, is equal to:

$$N_0 = \int_0^\infty R_{form} dt = \int_0^\infty k_2 ndt \qquad (21A)$$

where atom formation is assumed to be a first order reaction. Thus,

$$N = N_0 - \int_0^t k_2 n(t)dt - n(t) = \int_0^\infty k_2 n(t)dt - \int_0^t k_2 n(t)dt - n(t) = \int_t^\infty k_2 n(t)dt - n(t) =$$

$$= p(k_2 \int_t^\infty A(t)dt - A(t)) \qquad (22A)$$

or

$$N = p(k_2 \int_t^\infty A(t)dt - A(t)) \qquad (23A)$$

where *p,* the proportionality constant between the number of gaseous analyte atoms and the measured absorbance, is assumed to be independent of time and temperature (*21*). The change in the integration limits in this derivation (23A) is due to the subtraction of one integral from the other taking place on the step preceding this switch.

Downloaded by OHIO STATE UNIV LIBRARIES on June 6, 2012 | http://pubs.acs.org
Publication Date (Web): November 29, 2011 | doi: 10.1021/bk-2011-1084.ch003

Downloaded by OHIO STATE UNIV LIBRARIES on June 6, 2012 | http://pubs.acs.org
Publication Date (Web): November 29, 2011 | doi: 10.1021/bk-2011-1084.ch003

Assuming an Arrhenius-type temperature dependence of the reaction rate constant, the rate of atom formation (R_{form}) is given by (*21*):

$$R_{form} = -\frac{dN}{dt} = k_1 N = k_0 e^{-E_a/RT} N \tag{24A}$$

or

$$\frac{dN}{N} = k_0 e^{-E_a/RT} dt \tag{25A}$$

where k_0 is the frequency factor and E_a is the activation energy of atomization.

Using the expression for N obtained in (23A) and the expression for the heating rate, $\alpha = dT/dt$, to substitute dt with dT, the following equation is obtained:

$$-\frac{d(k_2 \int_t^\infty A dt - A)}{k_2 \int_t^\infty A dt - A} = k_0 \alpha^{-1} e^{-E_a/RT} dT \tag{26A}$$

The integration of (26A) results in (*21*):

$$-\int_0^t \frac{d(k_2 \int_t^\infty A dt - A)}{k_2 \int_t^\infty A dt - A} = k_0 \alpha^{-1} \int_0^T e^{-E_a/RT} dT \tag{27A}$$

To calculate the activation energy, both the right and left sides of equation (27A) need to be calculated. The right side of equation (27A) contains an integral which cannot be assessed analytically. It was calculated by Coats and Redfern:[33]

$$\int_0^T e^{-E_a/RT} dT = \frac{RT^2}{E_a}\left[1 - \frac{2RT}{E_a}\right] e^{-E_a/RT} \tag{28A}$$

by making the following substitution:

$$u = E_a / RT$$

$$du = -\frac{E_a}{RT^2} dT$$

$$\int_0^T e^{-E_a/RT} dT = -\int_\infty^u e^{-u} u^{-2} \left(\frac{-E_a}{R}\right) du = \frac{E_a}{R} \int_u^\infty e^{-u} u^{-2} du$$

and using the following approximation:[33]

$$\int_u^\infty e^{-u} u^{-2} du \approx u^{-1} e^{-u} \sum_{n=0}^{\infty} \frac{(-1)^n (2)_n}{u^{n+1}} \tag{29A}$$

Given this, the left side of equation (25A) is equal to:

$$-\int_0^t \frac{d(k_2 \int_t^\infty A dt - A)}{(k_2 \int_t^\infty A dt - A)^x} = -\ln \frac{k_2 \int_t^\infty A dt - A}{k_2 \int_0^\infty A dt} \qquad (30A)$$

The substitution of equation (28A) and equation (30A) into equation (27A) results in the final equation suggested by Yan *et al.* for the use in the calculation of activation parameters from experimental data (*21*):

$$\ln Y = -E_a / RT + \ln(k_0 p^{x-1} R(1 - 2RT / E_a) / \alpha E_a \qquad (31A), (4)$$

where

$$\ln Y = \ln\left(\left\{\ln\left[k_2 \int_0^\infty A dt / (k_2 \int_t^\infty A dt - A)\right]\right\} / T^2\right) \text{ for } x = 1 \qquad (32A), (5)$$

The activation energy is obtained from the slope of the plot of ln *Y vs.* 1/T (*21*). This plot is a straight line.

References

1. Seames, W. S.; Wendt, J. O. L. Partitioning of arsenic, selenium, and cadmium during the combustion of Pittsburgh and Illinois #6 coals in a self-sustained combustor. *Fuel Process. Technol.* **2000**, *63*, 179–196.
2. Bool, L. E.; Helble, J. J. A laboratory study of the partitioning of trace elements during pulverized coal combustion. *Energy Fuels* **1995**, *9*, 880–887.
3. Clarke, L. B. The fate of trace elements during coal combustion and gasification: An overview. *Fuel* **1993**, *72*, 731–736.
4. Esenlik, S.; Karayigit, A. I.; Bulut, Y.; Querol, X.; Alastuey, A.; Font, O. Element behaviour during combustion in coal-fired Orhaneli power plant, Bursa-Turkey. *Geol. Acta* **2006**, *4*, 439–449.
5. Frandsen, F.; Dam-Johansen, K.; Rasmussen, P. Trace elements from combustion and gasification of coal: An equilibrium approach. *Prog. Energy Combust. Sci.* **1994**, *20*, 115–138.
6. Furimsky, E. Characterization of trace element emissions from coal combustion by equilibrium calculations. *Fuel Process. Technol.* **2000**, *63*, 29–44.
7. Galbreath, K. C.; Toman, D. L.; Zygarlicke, C. J.; Pavlish, J. H. Trace element partitioning and transformations during combustion of bituminous and subbituminous U. S. coals in a 7-kW combustion system. *Energy Fuels* **2000**, *14*, 1265–1279.

Downloaded by OHIO STATE UNIV LIBRARIES on June 6, 2012 | http://pubs.acs.org
Publication Date (Web): November 29, 2011 | doi: 10.1021/bk-2011-1084.ch003

8. Guo, X.; Zheng, C. G.; Xu, M. H. Characterization of arsenic emissions from a coal-fired power plant. *Energy Fuels* **2004**, *18*, 1822–1826.
9. Helble, J. J. Model for the air emissions of trace metallic elements from coal combustors equipped with electrostatic precipitators. *Fuel Process. Technol.* **2000**, *63*, 125–147.
10. Linak, W. P.; Wendt, J. O. L. Trace metal transformation mechanisms during coal combustion. *Fuel Process. Technol.* **1994**, *39*, 173–198.
11. Lundholm, K.; Nordin, A.; Backman, R. Trace element speciation in combustion processes: Review and compilations of thermodynamic data. *Fuel Process. Technol.* **2007**, *88*, 1061–1070.
12. Seames, W. S.; Wendt, J. O. L. The partitioning of arsenic during pulverized coal combustion. *Proc. Combust. Inst.* **2000**, *28*, 2305–2312.
13. Seames, W. S.; Wendt, J. O. L. The partitioning of radionuclides during coal combustion. *Adv. Environ. Res.* **2000**, *4*, 43–55.
14. Senior, C. L.; Zeng, T.; Che, J.; Ames, M. R.; Sarofim, A. F.; Olmez, I.; Huggins, F. E.; Shah, N.; Huffman, G. P.; Kolker, A.; Mroczkowski, S.; Palmer, C.; Finkelman, R. Distribution of trace elements in selected pulverized coals as a function of particle size and density. *Fuel Process. Technol.* **2000**, *63*, 215–241.
15. Thompson, D.; Argent, B. B. Thermodynamic equilibrium study of trace element mobilisation under pulverised fuel combustion conditions. *Fuel* **2002**, *81*, 345–361.
16. Yan, R.; Gauthier, D.; Flamant, G. Partitioning of trace elements in the flue gas from coal combustion. *Combust. Flame* **2001**, *125*, 942–954.
17. Tomeczek, J.; Palugniok, H. Kinetics of mineral matter transformation during coal combustion. *Fuel* **2002**, *81*, 1251–1258.
18. Raask, E. The mode of occurrence and concentration of trace elements in coal. *Prog. Energy Combust. Sci.* **1985**, *11*, 97–118.
19. Raeva, A. A.; Pierce, D. T.; Seames, W. S.; Kozliak, E. I. A method for measuring the kinetics of organically associated inorganic element vaporization during coal combustion. *Fuel Process. Technol.* **2011**, *92*, 1333–1339.
20. Smets, B. Atom formation and dissipation in electrothermal atomization. *Spectrochim. Acta* **1980**, *35*, 33–41.
21. Yan, X.; Lin, T.; Liu, Z. Improvement of the Smets method in electrothermal atomic-absorption spectrometry. *Talanta* **1990**, *37*, 167–171.
22. Chung, C. H. Atomization mechanism with Arrhenius plots taking the dissipation function into account in graphite furnace atomic absorption spectrometry. *Anal. Chem.* **1984**, *56*, 2714–2720.
23. L'Vov, B. V.; Pelieva, L. A. The efficiency of lining a graphite furnace with tantalum foil in atomic absorption spectrometry. *Can. J. Spectrosc.* **1978**, *23*, 1–4.
24. *Analysis Guide for Z-2000 Series Polarized Zeeman Atomic Absorption Spectrometer (Graphite Furnace)*, 1st ed.; Hitachi High-Technologies Corporation: Tokyo, 2004.

Downloaded by OHIO STATE UNIV LIBRARIES on June 6, 2012 | http://pubs.acs.org
Publication Date (Web): November 29, 2011 | doi: 10.1021/bk-2011-1084.ch003

25. Yan, X. P.; Ni, Z. M. Kinetic studies on the mechanism of atomization in electrothermal atomic absorption spectrometry with and without chemical modifiers. *Fresenius' J. Anal. Chem.* **2001**, *370*, 1052–1060.
26. Cuypers, F.; De Dobbelaere, C.; Hardy, A.; Van Bael, M. K.; Helsen, L. Thermal behaviour of arsenic trioxide adsorbed on activated carbon. *J. Hazard. Mater.* **2009**, *166*, 1238–1243.
27. Zhang, N.; Lin, L. S.; Gang, D. Adsorptive selenite removal from water using iron-coated GAC adsorbents. *Water Res.* **2008**, *42*, 3809–3816.
28. Kaiser, N. Nucleation of antimony on amorphous carbon. *Phys. Status Solidi A* **1984**, *81*, 99–103.
29. Avgul, N. N.; Kiselev, A. V. Physical adsorption of gases and vapors on graphitized carbon blacks. *Chem. Phys. Carbon* **1970**, *6*, 1–124.
30. Seames, W. S.; Wendt, J. O. L. Regimes of association of arsenic and selenium during pulverized coal combustion. *Proc. Combust. Inst.* **2007**, *31*, 2839–2846.
31. Folgueras, M. B.; Diaz, R. M.; Xiberta, J.; Alonso, M. Effect of inorganic matter on trace element behavior during combustion of coal-sewage sludge blends. *Energy Fuels* **2007**, *21*, 744–755.
32. Sterling, R. O.; Helble, J. J. Reaction of arsenic vapor species with fly ash compounds: Kinetics and speciation of the reaction with calcium silicates. *Chemosphere* **2003**, *51*, 1111–1119.

Downloaded by OHIO STATE UNIV LIBRARIES on June 6, 2012 | http://pubs.acs.org
Publication Date (Web): November 29, 2011 | doi: 10.1021/bk-2011-1084.ch003

Downloaded by UNIV OF DELAWARE MORRIS LIB on June 6, 2012 | http://pubs.acs.org
Publication Date (Web): November 29, 2011 | doi: 10.1021/bk-2011-1084.ch004

Chapter 4

The Use of S-XANES To Track Thermal Transformations of Metal Sulfides in Argonne Premium Coals

Trudy B. Bolin[*]

Argonne National Laboratory, Argonne, IL 60439
[*]E-mail: bolitru@aps.anl.gov

Argonne Premium Coal Samples are used by researchers world-wide as standards in coal research. They consist of a suite of eight samples of varying rank from the United States. The Sulfur X-ray Near-Edge Absorption Spectroscopy (S-XANES) third-derivative analysis method utilizes a well-defined library of model compounds to curve fit each sample spectrum and enables sulfur speciation to within about 10% for materials such as coals and kerogens. This direct non-destructive characterization technique, used in conjunction with other techniques such as X-ray photoelectron spectroscopy (XPS), can provide valuable information about chemical and thermal sulfur transformations. The S-XANES third-derivative analysis method provides quantitative results for organic sulfur species in coal but has not been used to quantify pyritic sulfur until recently. In general, the direct determination of the pyrite content, a metal sulfide, has been problematic. It is known through wet chemical methods that several of the Argonne premium coal samples exceed 50 mole% pyrite but only show a weak pyrite feature in the S-XANES absorbance and third-derivative spectrum. It has been shown that particle size effects are responsible for attenuating the pyrite signal for high-pyrite-containing Argonne Premium coals. In this study, iron sulfide transformations at two stages of pyrolysis for an Illinois # 6 Argonne Premium coal and an isolated pyrite sample are quantified using S-XANES.

In Synthetic Liquids Production and Refining; de Klerk, A., et al.;
ACS Symposium Series; American Chemical Society: Washington, DC, 2011.

Downloaded by UNIV OF DELAWARE MORRIS LIB on June 6, 2012 | http://pubs.acs.org
Publication Date (Web): November 29, 2011 | doi: 10.1021/bk-2011-1084.ch004

Introduction

Organic sulfur forms in Argonne Premium Coals (*1*), kerogens (*2*), and petroleum asphaltenes (*3*) have been quantified previously by the S-XANES third-derivative analysis method. However, the amount of pyrite in Argonne Premium Coals was not reported using the S-XANES third-derivative analysis method even though pyrite was used to fit the spectra (*1*). Alternate methods had to be used to examine the pyrite content in the coals, and these alternate methods had their own inherent limitations. For example, it was found using iron K-edge absorption spectroscopy that there were ferrous and ferric forms of iron in addition to pyrite in the Argonne Coals (*4*). Another study used fits to the S-XANES absorption spectrum to quantify pyrite but found that a sensitivity correction factor had to be used for pyrite in order to make their values be consistent with those determined by wet chemical methods (*5*).

Pyrite in coals can have a wide variety of morphologies (*6*). Natural particle size ranges can be from microns to millimeters (*7*). The relatively dense iron sulfide poses problems and make it difficult to use S-XANES to quantify the amount of pyrite present in any given sample since its signal strength will depend on its particle size for large (>5 micron) particles. This signal attenuation, or particle size effect, can be overcome by finely grinding each sample (*8*). Fine grinding removes the need for a sensitivity factor since the signal depth response for organic sulfur and iron sulfide are almost identical.

Fine grinding the coal samples greatly enhanced the pyrite signal and gave pyrite values using the S-XANES third-derivative analysis method that were in close agreement with those determined by wet chemical methods. It was shown that particle size effects was the main reason for the pyrite signal attenuation observed prior to grinding. For example, Figure 1 shows the S-XANES absorbance and third-derivative absorbance edge spectra for a Pennsylvania Upper Freeport coal sample before and after reducing the particle size by fine grinding. With this knowledge it is now possible to reliably quantify not only pyrite, but other dense sulfides, such as pyrrhotite and troillite, in coal and other complex carbonaceous solids. It also enables studies of the thermal decomposition of pyrite and other metal sulfides in coal and sedimentary organic matter.

Experimental

A pyrite sample was obtained from the Spectrum Manufacturing Chemical Corporation, and Illinois #6 coal was obtained from the Argonne Premium Coal sample program. The samples were pyrolyzed at 400°C for 5 minutes and for 24 hours. This corresponds to a laboratory vitrinine reflectance (R_o) of 0.7 and 1.5, respectively, according to the “easy R_o” maturity scale (*9*). S-XANES was then used to track pyrite (FeS_2) decomposition into pyrrhotite, ($Fe_{(1-x)}S$). Sample grinding was performed using an agate mortar and pestle after the pyrolysis was complete in order to avoid altering the native pyrite particle size. Figure 2 shows the absorbance spectra and the third-derivative of absorbance spectra for pyrite and pyrrhotite model compounds used for the analysis of the third-derivative spectra. Figure 3 shows the absorbance spectra and the third-derivative of absorbance spectra for organic sulfur model compounds used in the analysis corresponding to aliphatic sulfide (dibenzyl sulfide), aromatic sulfide (diphenyl sulfide), and thiophenic (2,5-dimethylthiophene.)

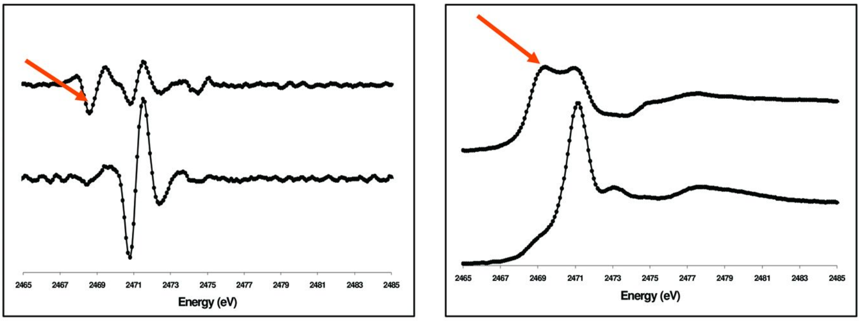

Figure 1. Pennsylvania Upper Freeport third- derivative spectrum (left) and absorption spectrum (right). In both plots, the spectra correspond to; (top) +250 mesh, ground; and (bottom) +250 mesh, unground. The arrows show the features due to pyrite.

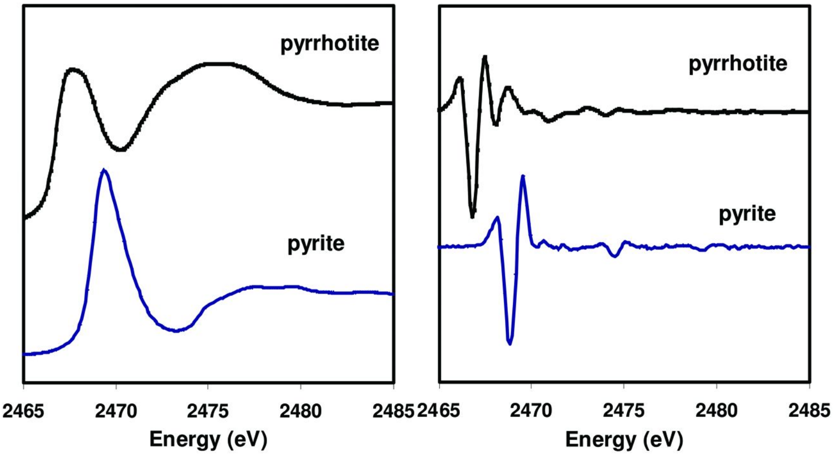

Figure 2. Absorbance spectra and the third-derivative of absorbance spectra for pyrite and pyrrhotite model compounds.

Downloaded by UNIV OF DELAWARE MORRIS LIB on June 6, 2012 | http://pubs.acs.org
Publication Date (Web): November 29, 2011 | doi: 10.1021/bk-2011-1084.ch004

Downloaded by UNIV OF DELAWARE MORRIS LIB on June 6, 2012 | http://pubs.acs.org
Publication Date (Web): November 29, 2011 | doi: 10.1021/bk-2011-1084.ch004

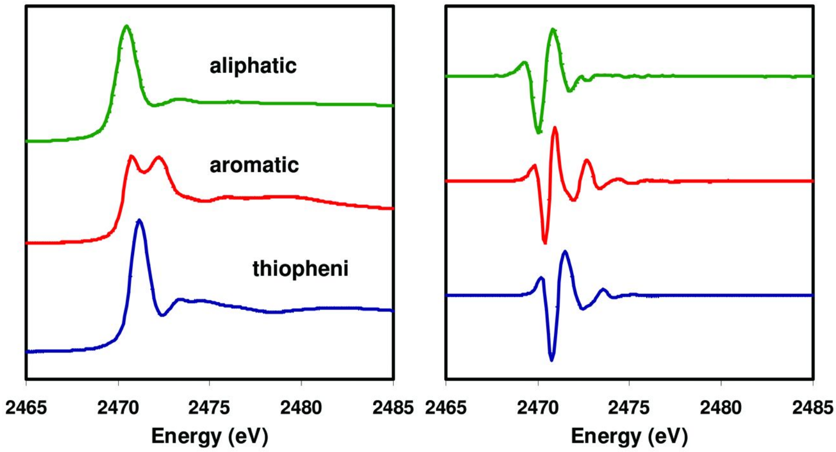

Figure 3. Absorbance spectra and the third-derivative of absorbance spectra for organic sulfur model compounds.

Results and Conclusions

Figure 4 shows the initial third-derivative spectra for Illinois #6 coal and pyrite and following pyrolysis to R_o=0.7 and 1.5. The spectra for pyrolyzed pyrite are almost identical to the initial sample. On the other hand, significant differences are found among the Illinois #6 samples both in the energy region for iron sulfide and organic sulfur. Table I shows the results of the fits to the third-derivative spectra expressed on a mole percent total sulfur basis. Upon pyrolysis to Ro=0.7, pyrite begins to convert into pyrrhotite and after R_o=1.5 more than half of the pyrite has transformed. In contrast for pyrite, no pyrrhotite is observed after pyrolysis up to R_o=1.5. Sulfate is found as a very small impurity in the initial pyrite sample. Table II shows the Illinois #6 results for organic sulfur expressed on a mole percent organic sulfur basis. The values for aliphatic sulfide, aromatic sulfide, and thiophenic sulfur are in close agreement with previous analyses (*1*). Most of the aliphatic sulfide is lost upon pyrolysis to R_o=0.7 and is entirely lost after pyrolysis to R_o=1.5. Most of the evolved organic matter from coal occurs during pyrolysis before R_o=1.5. It is widely known that pyrite can serve as a source of sulfur for generating H_2S during open system pyrolysis. Mobile hydrocarbons from the organic matter in coal serve as a source of hydrogen in the production of H_2S associated with the decomposition of pyrite. It is clear that isolated pure pyrite is stable under the pyrolysis conditions used in the present study. The current work demonstrates that the initial partial decomposition of pyrite in Illinois #6 coal occurs at extremely mild pyrolysis conditions and is driven by the availability hydrogen supplied by the organic matter in coal.

Future work will focus on the effects of pyrolysis on metal sulfide transformations for the entire suite of Argonne Premium Coal samples.

Downloaded by UNIV OF DELAWARE MORRIS LIB on June 6, 2012 | http://pubs.acs.org
Publication Date (Web): November 29, 2011 | doi: 10.1021/bk-2011-1084.ch004

Table I. Third-derivative fit results for the total sulfur content

	mole % total sulfur basis			
	Organic	*Pyrite*	*$Fe_{(1-x)}$ S*	*SO_4*
I#6 Initial	59	41	0	0
I#6 R_o=0.7	62	27	11	0
I#6 R_o=1.5	51	23	26	0
Pyrite Initial	0	99	0	1
Pyrite R_o=0.7	0	98	0	2
Pyrite R_o=1.5	0	100	0	0

Table II. Illinois #6 third-derivative fit results for organic sulfur content

	mole % organic sulfur basis		
	Aliphatic Sulfide	*Aromatic Sulfide*	*Thiophenic*
I#6 Initial	28	21	51
I#6 R_o=0.7	5	26	70
I#6 R_o=1.5	0	26	74

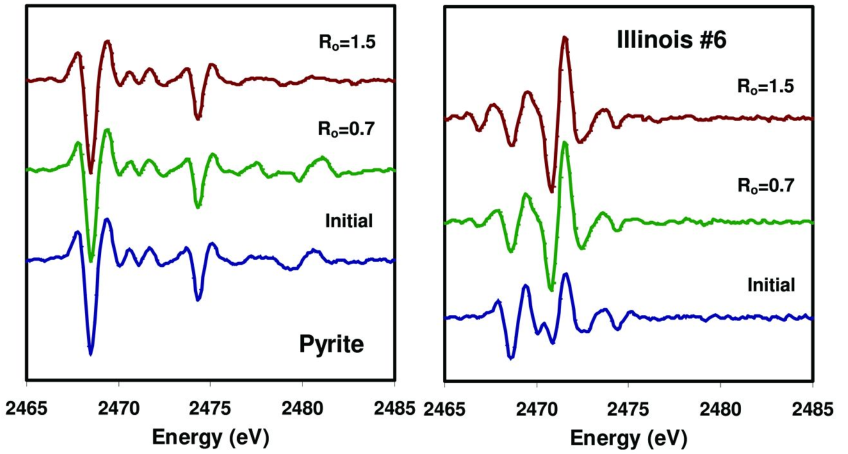

Figure 4. Initial third-derivative spectra for pyrite and Illinois #6 coal following pyrolysis to R_o=0.7 and 1.5.

Downloaded by UNIV OF DELAWARE MORRIS LIB on June 6, 2012 | http://pubs.acs.org
Publication Date (Web): November 29, 2011 | doi: 10.1021/bk-2011-1084.ch004

Acknowledgments

Use of the Advanced Photon Source was supported by the U.S. Department of Energy, Office of Basic Energy Sciences, under contract no. DE-AC02-06CH11357. The author thanks S. R. Kelemen and M. Sansone for many helpful discussions.

References

1. George, G. N.; Gorbaty, M. L.; Kelemen, S. R.; Sansone, M *Energy Fuels* **1991**, *5*, 93.
2. Kelemen, S. R.; Afeworki, M.; Gorbaty, M. L.; Sansone, M.; Kwiatek, P. J.; Walters, C. C.; Freund, H.; Siskin, M.; Bence, A. E.; Curry, D. J.; Solum, M.; Pugmire, R. J.; Vandenbroucke, M.; Leblond, M; Behar, F. *Energy Fuels* **2007**, *21*, 1548–1461.
3. George, G. N.; Gorbaty, M. L. *J. Am. Cem. Soc.* **1989**, *111*, 3182.
4. Wasserman, S. R.; Winans, R.; McBeth, R. *Energy Fuels* **1996**, *10*, 392–400.
5. Huffman, G. P.; Mitra, S.; Huggins, F. E.; Shah, N.; Vaidya, S.; Lu, F. *Energy Fuels* **1991**, *5* (4), 574–581.
6. Ryan, B.; Ledda, A. *Geological Fieldwork*; Paper 1998-1; British Columbia Geological Survey Branch, 1997.
7. Southam, G.; Donald, R.; Rostad, A.; Brock, C. *Geology* **2001**, *29* (1), 47–50.
8. Bolin, T. B. *Energy Fuels* **2010**, *24* (10), 5479–5482.
9. Sweeny, J. J.; Burnham, A. K. *AAPG Bull.* **1990**, *74*, 1559–1570.

Chapter 5

On the Preparation of Low Temperature Iron Fischer-Tropsch Catalysts: Strategies That Work and Those That Do Not

P. Julius Pretorius[*]

Saskatchewan Research Council, 125-15 Innovation Blvd.,
Saskatoon S7N 2X8, Saskatchewan, Canada
[*]Current address: Alberta Innovates Technology Futures,
250 Karl Clark Rd., Edmonton, Alberta T6N 1E4, Canada
E-mail: Julius.Pretorius@albertainnovates.ca

Downloaded by UNIV OF DELAWARE MORRIS LIB on June 6, 2012 | http://pubs.acs.org
Publication Date (Web): November 29, 2011 | doi: 10.1021/bk-2011-1084.ch005

Iron-based Fisher-Tropsch (FeFT) catalysts have a number of advantages over cobalt-based catalysts that make them attractive in the Biomass to Liquids (BTL) arena. This includes their ability to operate optimally with syngas of $H_2/CO \leq 1.5$. Historically, Low Temperature FeFT (LTFeFT) catalysts have been prepared by precipitating a copper-doped iron (hydr)oxide from a copper-containing iron nitrate solution. A major drawback of this preparation route is the resulting large quantity of nitrate-rich waste water. Recently, an approach utilizing carboxylic acids was proposed to overcome many of the environmental problems associated with the preparation of LTFeFT catalysts. Although promising, no FT performance data for catalysts prepared according to the organic acid method have been reported. We compared the performance of FT catalysts prepared according to the historical procedure and variants thereof with that of catalysts prepared according to the organic acid method. The catalysts prepared *via* the historical route exhibited superior surface area, pore volume and FT activity compared to those prepared *via* the carboxylic route. Fundamental principles of aqueous solution chemistry and precipitation theory provide an explanation for these differences.

In Synthetic Liquids Production and Refining; de Klerk, A., et al.;
ACS Symposium Series; American Chemical Society: Washington, DC, 2011.

Downloaded by UNIV OF DELAWARE MORRIS LIB on June 6, 2012 | http://pubs.acs.org
Publication Date (Web): November 29, 2011 | doi: 10.1021/bk-2011-1084.ch005

Introduction

A number of factors related to concerns about climate change, dwindling fossil fuel supplies and a general move towards renewable energy sources are fuelling interest in the utilisation of biomass as a feedstock for transportation fuels, fuel additives and chemicals.

The main contenders are Biomass to Ethanol (BTE) and Biomass to Liquids (BTL) utilizing the Fischer-Tropsch process. Both processes utilise synthesis gas (syngas, a mixture of hydrogen and carbon monoxide) and catalytic systems to produce the required products. While no commercial syngas to ethanol plants are operational anywhere in the world, a number of Fischer-Tropsch plants produce *ca.* 225 000 bbld of product worldwide. None of these plants, however, utilise biomass as feedstock. It is generally accepted that this is due to the challenging economic proposition of biomass-based plants.

In principle cellulosic biomass is available at a lower feed price than carbon sources like coal, but the low energy density and the dispersed nature of feedstock contribute to the economic challenges associated with BTL operations. In a market-driven environment, BTL must be economically competitive with crude oil. In contrast to Biomass to Ethanol plants, the Fischer-Tropsch process provides greater flexibility with regards to the product slate. Although this flexibility may be somewhat more onerous in the refining of the final product, it does have the major advantage that, unlike ethanol plants, plant profitability is not tied to a single product. This lowers investment risk substantially compared to that associated with an ethanol plant, since the final products can be selected to meet market demands.

Although a number of metals may be used as Fischer-Tropsch catalysts, iron- and cobalt-based catalysts find commercial application. Iron-based Fisher-Tropsch (FeFT) catalysts have a number of characteristics that make them attractive in the Biomass to Liquids (BTL) arena. Syngas obtained from biomass gasification typically have an H_2/CO ratio of 1 – 1.5. Co-based FT catalysts require an $H_2/CO \geq 2$ to prevent deactivation due to coke formation. Thus, a process based on a Co catalyst would require a separate WGS plant, thereby adding cost and diminishing the overall thermodynamic efficiency of the process (*1*). In contrast, Fe-based catalysts operate without problem with low H_2 syngas.

The original Ruhrchemie method for preparation of Low Temperature FeFT (LT FeFT) catalysts consists of precipitating a copper-doped iron (hydr)oxide from a copper-containing iron nitrate solution. The resulting precipitate is washed to remove unwanted ions followed by the addition of additional promoters (*2*). The preparation takes place in an aqueous environment and requires large quantities of water. Furthermore, a large quantity of process water containing highly soluble nitrate salts is produced (*3*). This complicates both the reuse and discharging into the environment of the process water.

A promising new approach that circumvents many of the environmental problems associated with the preparation of LTFeFT catalysts was recently proposed (*3*, *4*). Although the preparation methodology appears to be promising, the FT synthesis performance of catalysts needs to be investigated as this has not been reported previously.

In Synthetic Liquids Production and Refining; de Klerk, A., et al.;
ACS Symposium Series; American Chemical Society: Washington, DC, 2011.

In this chapter, the performance of FT catalysts prepared according to organic acid method is compared to catalysts prepared according to the traditional Ruhrchemie and related methods.

Experimental

Ruhrchemie Preparation

Catalyst precursors were prepared according to the method described by Dry (*2*, *5*). A heated Na_2CO_3 (Sigma-Aldrich) solution was titrated with a heated solution containing $Fe(NO_3)_3.9H_2O$ (Sigma-Aldrich) and $Cu(NO_3)_2.2.5H_2O$ (Sigma-Aldrich). The resulting precipitate was filtered and washed to remove residual Na^+ and NO_3^-. Potassium waterglass (Zaccil 30) was added to the washed filter cake. The final potassium level was adjusted to the required value by washing the filter cake with acidified deionized water. The filter cake was dried at 110°C for 18 hours followed by calcination at 400°C for 4 hours .

Modified Ruhrchemie Preparation

In this preparation, a solution containing $Fe(NO_3)_3.9H_2O$ (Sigma-Aldrich) and $Cu(NO_3)_2.2.5H_2O$ (Sigma-Aldrich) was titrated with a Na_2CO_3 (Sigma-Aldrich) solution. The effect of solution temperature was investigated at ambient and elevated temperature. The resulting precipitate was filtered and washed to remove residual Na^+ and NO_3^-. Potassium waterglass (Zaccil 30) was added to the washed filter cake. The final potassium level was adjusted to the required value by washing the filter cake with acidified deionized water. The filter cake was dried at 110°C for 18 hours followed by calcination at 400°C for 4 hours.

Goethite Method (*6*)

Catalyst precursors were prepared by the slow addition of an acidified solution consisting of $Fe(NO_3)_3.9H_2O$ (Sigma-Aldrich) and $Cu(NO_3)_2.2.5H_2O$ (Sigma-Aldrich) to a KOH solution. The mixture was sparged with air throughout the addition. The resulting yellow precipitate was aged for 36 hours at 70°C. After 36 hours, the precipitate was filtered and washed to remove residual Na^+ and NO_3^-. Potassium waterglass (Zaccil 30) was added to the washed filter cake. The potassium level was adjusted to the required level by washing the filter cake with acidified deionized water. The filter cake was dried at 110°C for 18 hours followed by calcination at 400°C for 4 hours.

Organic Acid Preparation

Catalyst precursors were prepared according to the methodology described Hu *et al.* (*4*) To a volume of deionized water in a three-necked flask, formic acid (Sigma-Aldrich) and metallic Fe powder (Höganäs Ancorsteel 1000C) were added to ensure an Fe/CHOOH molar ratio of 2. The mixture was continuously stirred at 600 rpm using an overhead stirrer. Air was continuously passed through the

Downloaded by UNIV OF DELAWARE MORRIS LIB on June 6, 2012 | http://pubs.acs.org
Publication Date (Web): November 29, 2011 | doi: 10.1021/bk-2011-1084.ch005

system to assist in the dissolution of metallic iron and oxidation of ferrous species. The three-necked flask was equipped with a condensor to prevent evaporation. After 24 hours, the resulting precipitate was filtered and washed. An appropriate amount of $Cu(NO_3)_2.2.5H_2O$ (Sigma-Aldrich) was dissolved in a minimal quantity of deionised water. The solution was added to the filter cake and mixed thoroughly. An aliquot of potassium waterglass was added to the copper-promoted slurry. The final potassium level was adjusted to the required value by washing the filter cake with an aliquot of acidified deionized water. The filter cake was dried at 110°C for 18 hours followed by calcination at 400°C for 4 hours.

Downloaded by UNIV OF DELAWARE MORRIS LIB on June 6, 2012 | http://pubs.acs.org
Publication Date (Web): November 29, 2011 | doi: 10.1021/bk-2011-1084.ch005

Fischer-Tropsch Synthesis

All synthesis reactions were conducted in a $1000dm^3$ Parr Continuously Stirred Tank Reactor (CSTR). H_2 and CO flow into the reactor was controlled by separate mass flow controllers (Brooks). Ar was used as an inert tracer. The reactor system was equipped with two knock-out pots operating at 180°C and 6°C respectively. Reactor tail gas was analyzed with gas chromatographs equipped with Thermal Conductivity and Flame Ionization detectors. TCD results were used to calculate CO conversion and CO_2 and CH_4 selectivities. Liquid hydrocarbon products drained from the cold pot were analyzed on the FID. Prior to synthesis, the catalyst was activated *in-situ* for 16 hours ($H_2/CO = 1.5$, GHSV = 7000 $cm^3{}_n g^{-1} h^{-1}$, P = 12 bar, T = 250°C) (*7*). For FT synthesis, the reactor was operated at $H_2/CO = 1$ to 1.8, P = 20 bar, T = 240°C and GHSV = 3000 to 5000 $cm^3{}_n g^{-1} h^{-1}$. Durasyn 164 (Ineos) was used as the initial slurry medium.

Results and Discussion

Table I shows the elemental composition, surface areas and pore volumes of calcined catalyst precursors. The catalyst composition aimed for was 5 g Cu/100 g Fe and 5 g K/ 100 g Fe, with tolerances of ±1 g/100 g Fe for each element.

It is apparent that preparation methodology influenced the nature of the catalyst precursor. The Ruhrchemie preparation produced high surface area and pore volume material, in agreement with those reported by Dry (*2*). The Modified Ruhrchemie preparations produced material with surface areas similar to the standard Ruhrchemie preparation. However, both ambient and elevated temperature preparations produced material of lower pore volume than the standard Ruhrchemie preparation. The Goethite and Formic acid preparations produced material with surface areas and pore volumes significantly lower than those observed for the Ruhrchemie preparations.

X-ray diffractograms for the various preparations are shown in Figure 1. The standard Ruhrchemie and Modified Ruhrchemie at ambient temperature methods produced 2-line ferrihydrite, while the Modified Ruhrchemie at elevated temperature produced 6-line ferrihydrite. After calcination, the material produced by the Goethite preparation transformed into hematite. The Formic acid preparation method produced a mixture of phases. Samples P20 and P23 consisted of mixtures of magnetite, maghemite, hematite and metallic iron. Metallic iron is indicative of incomplete dissollution of the starting material.

The Fischer-Tropsch performance of catalysts is shown in Figure 2. The catalysts exhibited distinct differences in activity. Catalysts P12, P14 and P25 (Standard Ruhrchemie) and P17 (Modified Ruhrchemie, ambient temperature) exhibited the highest FT activity, followed by P18 (Modified Ruhrchemie, elevated temperature). Catalysts P24 (Goethite method), P20 and P23 (Formic acid) exhibited the lowest activity of all the catalysts investigated.

In Figures 3 and 4, observed activities at 100 hours and at the end of run are plotted as functions of calcined precursor specific surface area and pore volume. It is apparent that catalyst activity is positively correlated with these parameters. Because textural properties and iron oxyhydroxide phase depend on preparation conditions, it is fair to expect a dependency of catalyst activity on oxyhydroxide precursor phase (*8*). In Figures 5 and 6, catalyst precursor phases are superimposed on activity and physical property data.

Table I. Calcined catalyst surface area, pore volume, phase- and elemental composition

Catalyst	*SA* m^2/g	*PV* cm^3/g	*Phase*	*K* g/100g Fe	*Cu* g/100g Fe
P12[a]	264.2	0.42	Ferrihydrite	4.5	4.9
P14[a]	275.8	0.47	Ferrihydrite	5.5	5.1
P25[a]	255.9	0.48	Ferrihydrite	1.7	5.0
P17[b]	268.7	0.29	Ferrihydrite	5.1	5.1
P18[c]	252	0.34	6L Ferrihydrite	4.4	5.2
P24[d]	54.9	0.15	Hematite	8.2	5.3
P20[e]	22.2	0.07	Hematite Maghemite Magnetite Iron	4.2	4.2
P23[e]	23.9	0.13	Hematite Maghemite Magnetite Iron	9.1	6.1

[a] Ruhrchemie. [b] Modified Ruhrchemie, ambient temp. [c] Modified Ruhrchemie, elevated temp. [d] Goethite. [e] Formic acid.

Downloaded by UNIV OF DELAWARE MORRIS LIB on June 6, 2012 | http://pubs.acs.org
Publication Date (Web): November 29, 2011 | doi: 10.1021/bk-2011-1084.ch005

Downloaded by UNIV OF DELAWARE MORRIS LIB on June 6, 2012 | http://pubs.acs.org
Publication Date (Web): November 29, 2011 | doi: 10.1021/bk-2011-1084.ch005

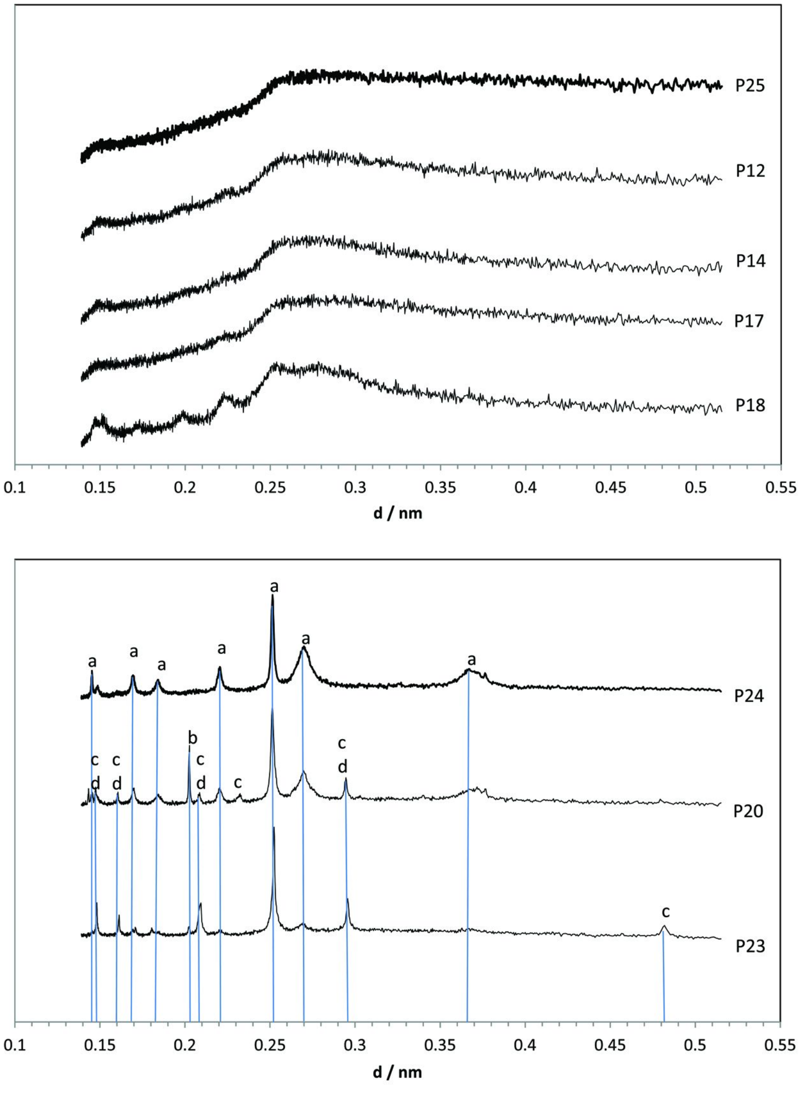

Figure 1. X-ray diffractograms obtained for calcined catalyst precursors prepared according to the the various preparation procedures. In the bottom figure, a = hematite, b = iron, c = magnetite, d = maghemite. The diffractograms in the top figure are typical of 2- and 6-line ferrihydrite with no other phases present (8). Diffractograms were collected using Co Kα radiation.

Downloaded by UNIV OF DELAWARE MORRIS LIB on June 6, 2012 | http://pubs.acs.org
Publication Date (Web): November 29, 2011 | doi: 10.1021/bk-2011-1084.ch005

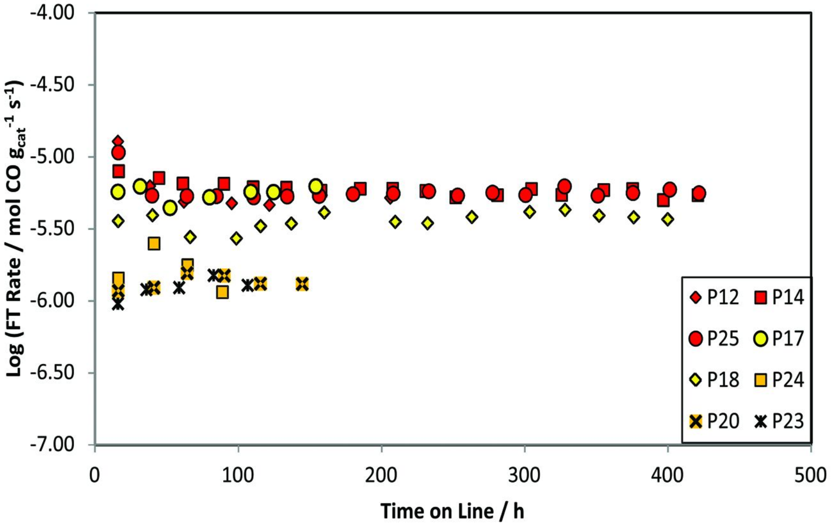

Figure 2. Fischer-Tropsch activities exhibited by catalysts investigated.

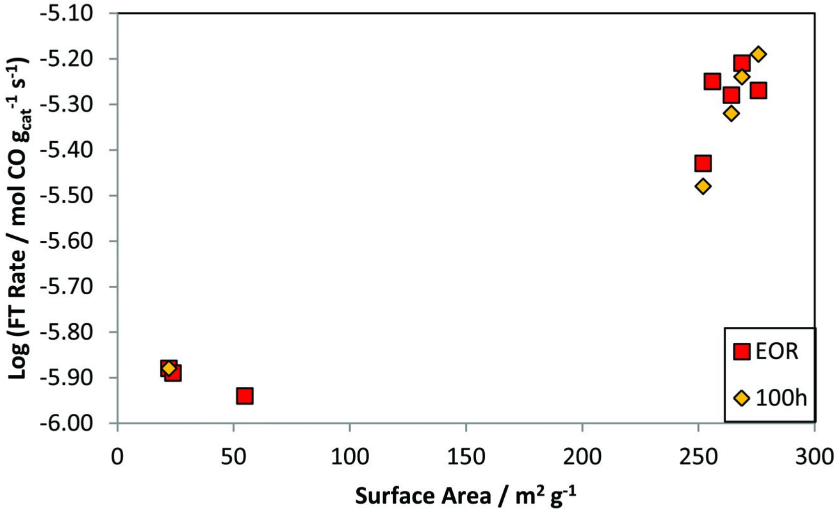

Figure 3. Observed Fischer-Tropsch activities as a function of calcined precursor surface area.

Downloaded by UNIV OF DELAWARE MORRIS LIB on June 6, 2012 | http://pubs.acs.org
Publication Date (Web): November 29, 2011 | doi: 10.1021/bk-2011-1084.ch005

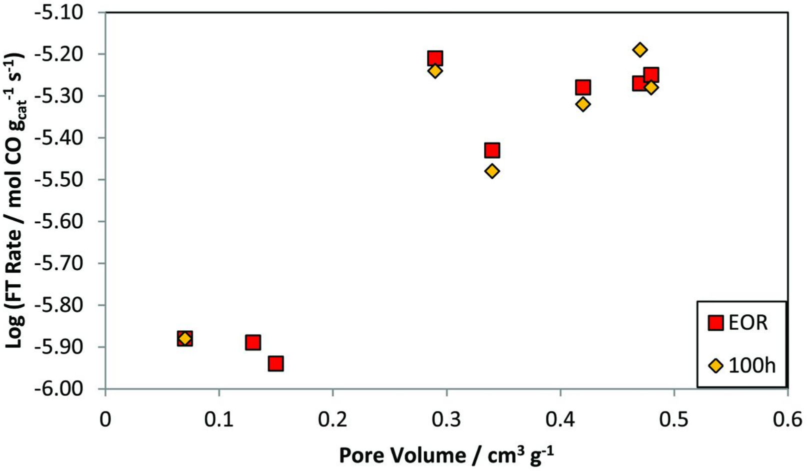

Figure 4. Observed Fischer-Tropsch activities as a function of calcined precursor pore volume.

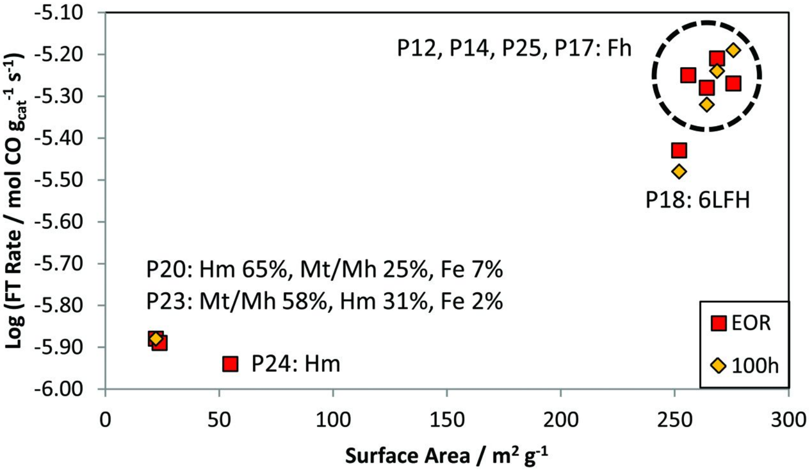

Figure 5. Relationship between Fischer-Tropsch activities, calcined precursor surface area and calcined precursor iron (hydr)oxide phase.

Downloaded by UNIV OF DELAWARE MORRIS LIB on June 6, 2012 | http://pubs.acs.org
Publication Date (Web): November 29, 2011 | doi: 10.1021/bk-2011-1084.ch005

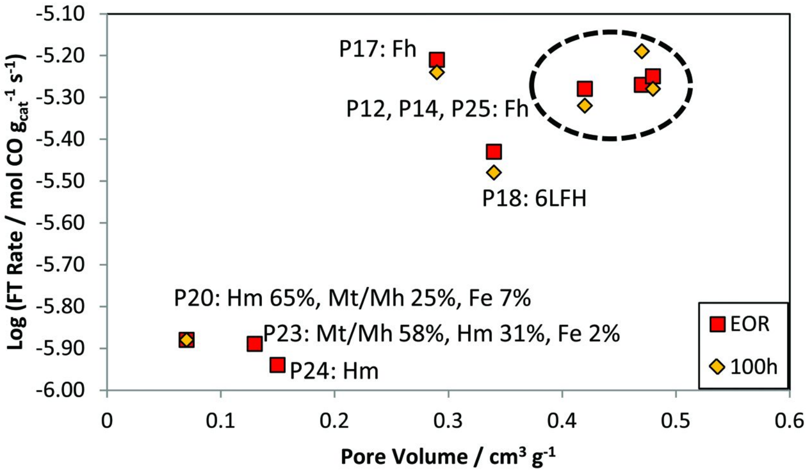

Figure 6. Relationship between Fischer-Tropsch activities, calcined precursor pore volume and calcined precursor iron (hydr)oxide phase.

It is evident that the best performing catalysts belong to the 2-line ferrihydrite family. Two-line Ferrihydrite is a poorly crystalline nanoparticle with dimensions ranging from 2 – 6 nm (*8–11*).

The positive relationship between catalyst activity, surface area and pore volume agrees with historical results (*2*, *5*, *12*). However, it appears that the importance of the 2-line ferrihydrite phase has not always been appreciated as Fischer-Tropsch literature mainly refers to hematite (α-Fe_2O_3) (*5*, *13–18*), maghemite (γ-Fe_2O_3) (*19*) or magnetite (Fe_3O_4) (*20*, *21*) as the catalyst precursor.

We conclude that high surface area, ferrihydrite precursors give rise to the most active catalysts. In the following sections, we will discuss the prerequisites for preparing high surface area 2-line ferrihydrite. The organic acid preparation will then be discussed in terms of these prerequisites.

Fundamentals of Precipitation

A requirement for the formation of small, amorphous precipitates is metastable, highly supersaturated solutions (*22–25*). The steps involved in the formation of a precipitate are nucleation, crystal growth and ripening. During nucleation, ions or molecules interact to form a critical nucleus which is the smallest entity required for the spontaneous formation of a second phase. The size and size distribution of crystallites are determined in the nucleation process. Nucleation is followed by crystal growth *via* the continuous deposition of substrate on the nuclei. The process of ripening consolidates small crystallites into larger crystals.

Thermodynamically, the process of nucleation consists of two components (*22*). The free energy of nucleation, ΔG_j, is the sum of the free energy of bond formation, ΔG_{bulk} and the free energy of generating the interface between the nuceus and the surrounding solvent, ΔG_{surf}:

Downloaded by UNIV OF DELAWARE MORRIS LIB on June 6, 2012 | http://pubs.acs.org
Publication Date (Web): November 29, 2011 | doi: 10.1021/bk-2011-1084.ch005

$$\Delta G_j = \Delta G_{bulk} + \Delta G_{surf} \tag{1}$$

ΔG_{bulk}, the free energy gain due to bond formation, may be expressed as

$$\Delta G_{bulk} = -jkT \ln \Lambda \tag{2}$$

with j = number of molecular units forming the nucleus, *k* = Boltzman's constant, T = temperature and Λ = saturation ratio, given by

$$\Lambda = (IAP/K_s)^{1/\eta} \tag{2a}$$

with IAP = ion activity product, K_s = solubility product and η = number of ions in the empirical formula of the precipitate. Equation 2 may also be expressed in terms of the volume of the spherical nucleus:

$$\Delta G_{bulk} = -(4\pi r^3/3V)kT \ln \Lambda \tag{3}$$

where r = nucleus radius and V = volume of the molecular units constituting the nucleus.

In the formation of the interface between the nucleus and the solvent, work is expended. The free energy of surface formation, ΔG_{surf} for a spherical nucleus is given by

$$\Delta G_{surf} = 4\pi r^2 \gamma \tag{4}$$

with γ = size-independent interfacial energy between the nucleus and the surrounding solvent.

Substituting (3) and (4) into (1), we obtain

$$\Delta G_j = -(4\pi r^3/3V)kT \ln \Lambda + 4\pi r^2 \gamma \tag{5}$$

From (5) it is apparent that as the nucleus grows, the first term becomes more negative while the second term becomes more positive. At a critical particle size, ΔG reaches a maximum and then decreases with increasing particle size. The point where $d\Delta G/dr = 0$ signifies the critical particle size, r*, where spontaneous crystallization commences. By differentiating (5) with respect to r, an expression for r* is obtained:

$$r^* = \frac{2V\gamma}{kT \ln \Lambda} \tag{6}$$

The nucleation activation energy ΔG^* corresponds to the value of $\Delta G(r^*)$. The importance of the degree of saturation is evident from (5) and (6).

A high degree of saturation is required for small critical nucleus size as well as low nucleation activation energy. Low nucleation activation energy is

Downloaded by UNIV OF DELAWARE MORRIS LIB on June 6, 2012 | http://pubs.acs.org
Publication Date (Web): November 29, 2011 | doi: 10.1021/bk-2011-1084.ch005

a prerequisite for fast nucleation to occur, as is evident from (7), the rate of nucleation:

$$J = Ae^{\frac{-\Delta G^*}{kT}} \ldots\ldots\ldots\ldots\ldots\ldots\ldots\ldots\ldots\ldots\ldots\ldots (7)$$

A is the pre-exponential factor, k is the Boltzman's constant and T is the temperature. With increasing degree of saturation, ΔG^* decreases and J increases exponentially.

Crystal growth is responsible for increasing particle size by continued deposition of substrate on the nuclei. Different rate laws for crystal growth have been proposed (*23*). An empirical law often used is given by $V = B(\Lambda - 1)^{\zeta}$, where B is a constant, Λ is the degree of saturation and ζ is an adjustable parameter. To minimize crystal growth requires that a large number of nuclei be formed fast (i.e. at high initial Λ), to effect a fast decrease of the solution's degree of saturation, Λ.

From this we can conclude that, in order to prevent the formation of crystalline solids, a high degree of initial saturation is required with the concomitant fast and extensive nucleation.

Ferrihydrite is the iron (hydr)oxide exhibiting the highest surface area (*8*, *26*). To prepare ferrihydrite, conditions conducive to the fast precipitation of the ferric (hydr)oxide are required. Hence, solution concentration, temperature and rate of reagent addition have to be optimized and carefully controlled.

The Chemistry of the Organic Acid Method

The organic acid method consists of (i) the dissolution of metallic iron to form ferrous iron, (ii) the oxidation of ferrous iron to ferric iron, (iii) the hydrolysis of ferric iron to form ferric hydroxyl compounds and (iv) the precipitation and crystallization of ferric (hydr)oxides. The following section explores the underlying chemistry in greater detail.

The general case for the dissolution of metallic iron in the presence of a non-oxidizing acid is given in (8).

$$Fe(s) + 2H^+ \Leftrightarrow Fe^{2+} + H_2(g) \ldots\ldots\ldots\ldots\ldots\ldots\ldots\ldots\ldots\ldots\ldots\ldots (8)$$

The aqueous Fe(II) species formed in the dissolution process has to be oxidized to form ferric iron, which, in turn, is required for the formation of ferric (hydr)oxides. The oxidation reaction is given by (9) (*27*)

$$Fe^{2+} + H^+ + \tfrac{1}{4}O_2 \Leftrightarrow Fe^{3+} + \tfrac{1}{2}H_2O \ldots\ldots\ldots\ldots\ldots\ldots\ldots\ldots\ldots\ldots\ldots (9)$$

The rate of the oxidation reaction is given by (10) (*28*)

$$-d[Fe^{2+}]/dt = k[Fe^{2+}]\,[OH^-]^2\,P_{O2} \ldots\ldots\ldots\ldots\ldots\ldots\ldots\ldots\ldots\ldots\ldots (10)$$

From (10) it is evident that conditions characterized by high $[Fe^{2+}]$, high pH and high oxygen partial pressure will favour the oxidation of Fe(II).

The hydrolysis behavior of ferric iron is complex (*8*, *27*, *29*). A general reaction scheme for the hydrolysis of Fe(III) may be written as:

$Fe^{3+} + H_2O \Leftrightarrow FeOH^{2+} + H^+$

$Fe^{3+} + 2H_2O \Leftrightarrow Fe(OH)_2^{\ +} + 2H^+$

$Fe^{3+} + 3H_2O \Leftrightarrow Fe(OH)_3 + 3H^+$

:

:

$nFe^{3+} + xH_2O \Leftrightarrow Fe_n(OH)_x^{(3n-x)} + xH^+$ ....(11)

The hydrolysis reaction is fast with first order rate constants estimated to be in the order of $10^4 – 10^6$ s^{-1} (*30*).

The formation of iron (hydr)oxide solids take place by using the neutral $Fe(OH)_3$ species as a “growth monomer” that attaches to the already formed polynuclear iron species (*31*).

$Fe_n(OH)_x^{(3n-x)} + Fe(OH)_3 \Leftrightarrow Fe_{(n+1)}(OH)_{(x+3)}$..............……………….(12)

The rate of (12) is given by (*31*, *32*)

$-d[Fe^{3+}]/dt = k[Fe(OH)_3]$……..……………………….(13)

In Figure 7 an example of a typical pH profile observed during the organic acid method is shown. The dissolution of metallic iron and the subsequent oxidation of Fe(II) to Fe(III) consumes protons, explaining the increase in pH over the first 7 hours of the experiment. During this time, the solution maintained a grey colour due to the suspended metallic iron particles. After 7 hours a gradual colour change to red-brown occurred, which signified the onset of hydrolysis and precipitate formation. The colour change and intensified between 7 and 8 hours.

The sharp increase in pH during this time is indicative of an increase of the rate of proton consuming processes, most likely the oxidation of Fe(II) according to reaction (9). The sharp drop in pH from a maximum at 6 after *ca.* 8.5 hours is most likely due to the dominance of the hydrolysis process, the loss of protons from the system according to reactions (8) and (9), and the buffering of solution pH by the amphoteric iron (hydr)oxide surface sites.

A second aspect to note from the data presented in Figure 7 is the slowness of the reaction. If the peak pH of 6 is taken as indicative of the completion of the reaction, it takes more than 8 hours for the reaction to complete. This is not surprising when we consider the chemistry of the system.

Downloaded by UNIV OF DELAWARE MORRIS LIB on June 6, 2012 | http://pubs.acs.org
Publication Date (Web): November 29, 2011 | doi: 10.1021/bk-2011-1084.ch005

Downloaded by UNIV OF DELAWARE MORRIS LIB on June 6, 2012 | http://pubs.acs.org
Publication Date (Web): November 29, 2011 | doi: 10.1021/bk-2011-1084.ch005

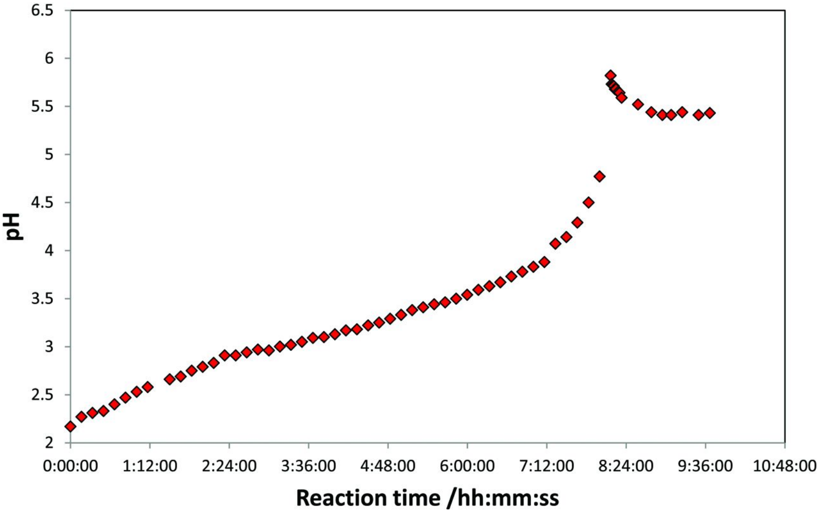

Figure 7. Progression of the organic acid prepration of iron (hydr)oxides as monitored by solution pH.

From experience it is known that the dissolution process (reaction 8) is by nature significantly slower than the subsequent reactions constituting the organic acid method. This is exacerbated further by causing the dissolution process to be proton limited by the utilization of a sub-stoichiometric (i.e. acid:Fe < 2) amount of acid to initiate dissolution.

Because the dissolution process is slow compared to the other reactions, we may anticipate that (a) the rate of Fe(II) oxidation to form Fe(III) will be determined by [Fe^{2+}] (*cf* equation 10), which will (b) lead to low Fe(III) concentrations so that Fe^{3+} will become a limiting reagent in the fast Fe(III) hydrolysis process, thus implying low concentrations for $Fe_n(OH)_x^{(3n-x)}$ species, and (c) because of the low concentration of $Fe_n(OH)_x^{(3n-x)}$ species, specifically $Fe(OH)_3$, the rate of precipitate formation will be slow (*cf* equation 13).

The limiting influence that the slow supply of Fe(II) has on the Fe(III) formation kinetics (and hence the eventual precipitation kinetics) is further exacerbated by the low pH throughout the process and the poor solubility of O_2 in water (*cf* equation 10). All of these factors suggest that a condition of low S is prevalent in the reaction vessel. Thus, slow precipitate formation resulting in crystalline material of low surface area and pore volume is to be expected.

Conclusions

The Fischer-Tropsch synthesis performance of LT FeFT catalysts prepared according to four different methods was investigated. It was found that preparation method influenced the physical properties of catalyst precursors. The traditional Ruhrchemie approach, and its modifications, yielded high surface area and pore volume catalysts. These catalysts belonged to the ferrihydrite family of iron (hydr)oxides. The Goethite and Organic Acid methods yielded low surface area, low pore volume crystalline iron (hydr)oxides.

Catalyst activity was found to be dependant on catalyst precursor surface area, pore volume and (hydr)oxide phase. Catalysts prepared from 2-line ferrihydrite precursors exhibited higher Fischer-Tropsch activity than those prepared from the more crystalline phases of 6-line ferrihydrite, hematite and hematite/maghemite/magnetite mixtures.

The results suggest that the Organic Acid preparation method proposed by Hu *et. al* (*4*) may not be appropriate for the production of LT FeFT catalysts. Investigation of the solution chemistry underlying this method shows that, due to low reaction rates and concomitant low saturation levels in the aqueous phase, it is inherently geared towards producing highly crystalline low surface area and pore volume catalyst precursors.

Downloaded by UNIV OF DELAWARE MORRIS LIB on June 6, 2012 | http://pubs.acs.org
Publication Date (Web): November 29, 2011 | doi: 10.1021/bk-2011-1084.ch005

References

1. Bartholomew, C. H.; Hecker, W. C. Brigham Young University, 2009.
2. Dry, M. E. In *Fischer-Tropsch Technology*; Steynberg, A., Dry, M. E., Eds.; Elsevier: Amsterdam, 2004.
3. Ritter, S. K. *Chem. Eng. News* **2003**, *81*, 30.
4. Hu, X. D.; O'Brien, R. J.; Tuell, R.; Conca, E.; Rubini, C.; Petrini, G. US 7,199,077 B2, 2007.
5. Dry, M. E. In *Catalysis Science and Technology*; Anderson, J. R., Boudart, M., Eds.; Springer-Verlag: 1981; Vol. 1, p 159.
6. Coughlin, B. R.; Stone, A. T. *Environ. Sci. Technol.* **1995**, *29*, 2445.
7. Huyser, J. J.; Janse Van Vuuren, M. J. WO 2009/022263, 2009.
8. Cornell, R. M.; Schwertmann, U. *The Iron Oxides. Structure, Properties, Reactions, Occurrences and Uses*, 2nd ed.; Wiley-VCH: Weinheim, Germany, 2003.
9. Michel, F. M.; Ehm, L.; Antao, S. M.; Lee, P. L.; Chupas, P. J.; Liu, G.; Strongin, D. R.; Schoonen, M. A. A.; Phillips, B. L.; Parise, J. B. *Science* **2007**, *316*, 1726.
10. Carta, D.; Casula, M. F.; Corrias, A.; Falqui, A.; Navarra, G.; Pinna, G. *Mater. Chem. Phys.* **2009**, *113*, 349.
11. Pinney, N.; Kubicki, J. D.; Middlemiss, D. S.; Grey, C. P.; Morgan, D. *Chem. Mater.* **2009**, *21*, 5727.
12. Dry, M. E. *Catal. Lett.* **1990**, *7*, 241.
13. Diffenbach, R. A.; Fauth, D. J. *J. Catal.* **1986**, *100*, 466.
14. Li, S.; Meitzner, G. D.; Iglesia, E. *J. Phys. Chem. B* **2001**, *105*, 5743.
15. Hofer, L. J. E.; Peebles, W. C.; Dieter, W. E. *J. Am. Chem. Soc.* **1946**, *68*, 1953.
16. Shroff, M. D.; Kalakkad, D. S.; Coulter, K. E.; Kohler, S. D.; Harrington, M. S.; Jackson, N. B.; Sault, A. G.; Datye, A. K. *J. Catal.* **1995**, *156*, 185.
17. Li, S.; Ding, W.; Meitzner, G. D.; Iglesia, E. *J. Phys. Chem. B* **2002**, *106*, 85.
18. de Smit, E.; Beale, A. M.; Nikitendo, S.; Weckhuysen, B. M. *J. Catal.* **2009**, *262*, 244.

19. Duvenhage, D. J.; Demirel, B. US 2009/0075814 A1, 2009.
20. Hofer, L. J. E.; Anderson, R. B.; Peebles, W. C.; Stein, K. C. *J. Phys. Chem.* **1951**, *55*, 1201.
21. Soled, S.; Iglesia, E.; Fiato, R. A. *Catal. Lett.* **1990**, *7*, 271.
22. Stumm, W. *Chemistry of the Solid-Water Interface*; Wiley-Interscience: New York, 1992.
23. Stumm, W.; Morgan, J. J. *Aquatic Chemistry*, 3rd ed.; John Wiley and Sons, Inc.: New York, 1996.
24. Morse, J. W.; Casey, W. H. *Am. J. Sci.* **1988**, *288*, 537.
25. Fritz, B.; Noguera, C. *Rev. Mineral. Geochem.* **2009**, *70*, 371.
26. Jambor, J. L.; Dutrizac, J. E. *Chem. Rev.* **1998**, *98*, 2549.
27. Cotton, F. A.; Wilkinson, G.; Murillo, C. A.; Bochmann, M. *Advanced Inorganic Chemistry*, 6th ed.; John Wiley and Sons, Inc.: New York, 1999.
28. Stumm, W.; Lee, F. G. *Ind. Eng. Chem.* **1961**, *53*, 143.
29. Baes, C. F.; Mesmer, R. F. *The Hydrolysis of Cations*; John Wiley and Sons, Inc.: New York, 1976.
30. Brandt, C.; van Eldik, R. *Chem. Rev.* **1995**, *95*, 119.
31. Grundl, T.; Delwiche, J. *J. Contam. Hydr.* **1993**, *14*, 71.
32. Lamb, A. B.; Jacques, A. G. *J. Am. Chem. Soc.* **1938**, *60*, 1215.

Downloaded by UNIV OF DELAWARE MORRIS LIB on June 6, 2012 | http://pubs.acs.org
Publication Date (Web): November 29, 2011 | doi: 10.1021/bk-2011-1084.ch005

Downloaded by DUKE UNIV on June 6, 2012 | http://pubs.acs.org
Publication Date (Web): November 29, 2011 | doi: 10.1021/bk-2011-1084.ch006

Chapter 6

Fischer-Tropsch Synthesis: Effect of Pt Promoter on Activity, Selectivities to Hydrocarbons and Oxygenates, and Kinetic Parameters over 15%Co/Al_2O_3

**Wenping Ma,[1] Gary Jacobs,[1] Robert Keogh,[1] Chia H. Yen,[2]
Jennifer L. S. Klettlinger,[2] and Burtron H. Davis*,[1]**

**[1]Center for Applied Energy Research, University of Kentucky,
2540 Research Park Drive, Lexington, Kentucky 40511, U.S.A.
[2]NASA Glenn Research Center, 21000 Brookpark Rd.,
Cleveland, Ohio 44135, U.S.A.
*E-mail: davis@caer.uky.edu. Phone: 859-257-0251.**

The effect of Pt promoter on the catalytic performance of 15%Co/Al_2O_3 catalyst was studied in a 1-L continuously stirred tank reactor (CSTR). Catalytic performance parameters investigated include catalyst activity, CH_4 and C_{5+} selectivities, olefin and paraffin contents, 1-olefin and 2-olefin selectivities, oxygenate selectivity, and kinetic behavior. The addition of 0.5% Pt increased the CO hydrogenation rate constant by 140%, consistent with the finding that the Pt promoter significantly increased Co reduction and thus the number of surface Co^0 sites. However, Pt did not alter Co site time yield (STY). Both the unpromoted and Pt promoted 15%Co/Al_2O_3 catalysts displayed the same Co STY value at 220°C, 5.5×10^{-3} s^{-1}. A comparison of selectivities of the unpromoted and Pt promoted 15%Co/Al_2O_3 was made at similar CO conversion levels. The Pt promoter increased light hydrocarbon (C_2-C_4) formation and simultaneously decreased heavier hydrocarbon formation, probably due to hydrogen dissociation on Pt metal and spillover onto Co metal, leading to an increase in the chain termination rate. Pt promoter did not apparently change the overall olefin and paraffin contents, but CO conversion was found to be a primary factor in influencing secondary reactions

In Synthetic Liquids Production and Refining; de Klerk, A., et al.;
ACS Symposium Series; American Chemical Society: Washington, DC, 2011.

of olefins on the 15%Co/Al_2O_3 catalyst. Furthermore, 0.3-1.0% water soluble oxygenates were found to be formed on the Co catalyst. At similar CO conversion levels, Pt slightly improved the oxygenates selectivity. Effects of CO conversion and H_2/CO ratio on hydrocarbon and oxygenate selectivities are also discussed in this paper. Finally, the kinetic behavior of both unpromoted and Pt promoted 15%Co/Al_2O_3 catalysts was studied using the CAER kinetic model, $-r_{CO} = kP_{CO}^{a}P_{H_2}^{b}/(1 + mP_{H_2O}/P_{H_2})$. Kinetic parameters for both catalysts were assessed and are reported in this study.

Keywords: Fischer-Tropsch synthesis; Pt-Co/Al_2O_3; Co metal; CoO; Pt; hydrocarbon selectivity; oxygenate selectivity; kinetics

Downloaded by DUKE UNIV on June 6, 2012 | http://pubs.acs.org
Publication Date (Web): November 29, 2011 | doi: 10.1021/bk-2011-1084.ch006

Introduction

It has been realized that unpromoted Co/Al_2O_3 Fischer-Tropsch synthesis (FTS) catalysts generally have low Co reduction degree after a standard hydrogen treatment (i.e., 350°C for 10 h) due to the strong interaction between Co and the Al_2O_3 support. To overcome this shortcoming, noble metals such as Pt, Ru, Pd, Re, and Rh have been employed as effective additives (*1–12*). A number of studies have demonstrated that the activities of the noble metal promoted Co/Al_2O_3 catalysts, on a per gram of catalyst basis, are two-three fold times higher than that of unpromoted Co/Al_2O_3 catalysts (*2*, *3*, *5*, *9*). This very positive promotional effect has been studied by many characterization techniques including TPR, TPR-XANES, TPR-EXAFS, and hydrogen chemisorption with pulse reoxidation (*1–6*). The results demonstrate that the noble metal promoter (e.g., Pt) not only significantly improves the reducibility of Co oxide species, perhaps via a H_2 dissociation and spillover pathway, but it may also increase Co dispersion to a lesser extent, since the additional species that are reduced are typically those that are smaller and more strongly interacting. Consequently, smaller average Co^0 particles and higher surface Co^0 site densities can be achieved when the catalysts contain noble metal promoters (*1*). Goodwin et al. (*13*) applied the SSITKA method to study how noble metals such as Ru influence the intrinsic activity of Co and claimed that Ru increased the CO conversion due to an increase in Co active sites, while the intrinsic activity of the Co catalysts remained constant. The influence of noble metals on the reactivity of CO hydrogenation was found to depend strongly on loading. For example, high Pt loading decreased catalyst activity by forming a Co-Pt phase (*14*). The promotional impact of noble metals (e.g., Pt) on Co reduction degree and Co dispersion was less prominent in a Co/SiO_2 catalyst, since even without Pt promotion the catalyst reduced more readily than Co/Al_2O_3 (*15–17*).

Although extensive characterization studies have been conducted to reveal the nature of the Pt promotional effect on catalyst behavior as addressed above, fewer studies have dealt with how Pt impacts the hydrocarbon and oxygenate formation

Downloaded by DUKE UNIV on June 6, 2012 | http://pubs.acs.org
Publication Date (Web): November 29, 2011 | doi: 10.1021/bk-2011-1084.ch006

rates. Vada et al. (*2*) conducted an investigation where they examined the effect of 1% of Pt or Re promoters on FTS for 8.7% Co/Al_2O_3 catalysts under 1 to 5 atm, 200-220°C and H_2/CO ratios of 2.0-7.3. Both promoters only increased CO conversion, but did not change hydrocarbon selectivity. A similar conclusion was drawn by Schanke et al. (*3*) who used Pt-Co catalysts with low Pt/Co ratios. Li et al. (*18*) studied the Pt promotional effect on the FTS reaction on Fe based catalyst. It was reported that Pt improved Fe reduction and it was also a good hydrogenation promoter to decrease olefin selectivity. Xu et al. (*19*) also studied the impact of the noble metal on hydrocarbon formation rates over Fe/SiO_2 catalysts. Pt suppressed CH_4 formation and increased the C_{2+} rate. However, it should be noted that the conclusions over the unpromoted and Pt promoted catalysts in these studies were made over large CO conversion ranges, e.g. 42-87%. Therefore, we can infer that the conclusions made included the CO conversion effect, and therefore did not reflect the actual effect of Pt. Furthermore, Li et al. (*18*) reported that Pt slightly increased the WGS rate on Fe based FTS catalyst. Panagiotopoulou et al. (*20*) reported that pure Pt is more active than either Ru or Pd for the WGS reaction. However, how Pt metal influences the WGS reaction over Co based FTS catalysts was not defined in these studies.

Promoters may also impact the oxygenate formation rate during FTS. Takeuchi et al. (*21*) reported that Ir, Ru, or Re supported Co catalysts increase oxygenate selectivities. Alkali (*22*), copper (*23*), and rhenium (*21*) were reported to increase the selectivity of C_2-oxygenates. However, it is not clear how Pt influences oxygenate formation in addition to increasing the extent of reduction of cobalt oxides. The kinetic effect of water over Co based catalysts has been studied previously (*24*, *25*). A kinetic model , $-r_{CO} = kP_{CO}{}^{a}P_{H_2}{}^{b}/(1 + mP_{H_2O}/P_{H_2})$, including a water effect term, m, was used to successfully describe the kinetic behavior for Co/Al_2O_3 and Co/SiO_2 catalysts. Previously it was found that kinetic parameter values were found to vary with both support type and Co cluster size; in this contribution, we conducted kinetic experiments using 15%Co/Al_2O_3 with and without Pt promoter to determine the influence of Pt on kinetic parameters.

In summary, the present study is to investigate three aspects of Pt promotional effects during FTS: 1) hydrocarbon (HC) selectivity, 2) oxygenate selectivity, and 3) kinetic parameters. The first two aspects were assessed at several similar CO conversion levels, so that the actual role of Pt during FTS is reflected. For the third aspect, kinetic experiments over 0.5%Pt-15%Co/Al_2O_3 and 15%Co/Al_2O_3 catalysts were conducted using the kinetic plan proposed previously (*24*).

Experimental

Catalyst Preparation

The 15%Co/Al_2O_3 catalysts with and without Pt were prepared using an aqueous slurry impregnation method (*26*). Cobalt nitrate was used as the cobalt precursor. The support was Catalox SBA 200 γ-Al_2O_3. Following cobalt addition, the catalyst was dried at 80°C and 100°C in a rotary evaporator. The batch of dried cobalt nitrate on alumina was split into two equivalent parts. One of them was used to load 0.5%Pt by incipient wetness impregnation and another part was used as an unpromoted reference sample. The Pt precursor was tetraammine Pt(II) nitrate. Finally, the catalysts were calcined in flowing air for 4 h at 350°C.

BET Measurement

BET measurements for the catalysts were conducted using a Micromeritics Tri-Star system to determine the loss of surface area with loading of the metal. Prior to the measurement, samples were slowly ramped to 160°C and evacuated for 24 h to approximately 50 mTorr.

Hydrogen Chemisorption with Pulse Reoxidation

Hydrogen chemisorption measurements were performed using a Zeton Altamira AMI-200 unit, which utilizes a thermal conductivity detector (TCD). The sample weight was always 0.220 g. The catalyst was activated at 350°C for 10 h using a flow of pure hydrogen and then cooled under flowing hydrogen to 100°C. The sample was then held at 100°C under flowing argon to prevent physisorption of weakly bound species prior to increasing the temperature slowly to the activation temperature. At that temperature, the catalyst was held under flowing argon to desorb the remaining chemisorbed hydrogen so that the TCD signal returned to the baseline. The TPD spectrum was integrated and the number of moles of desorbed hydrogen was determined by comparing to the areas of calibrated hydrogen pulses. Prior to experiments, the sample loop was calibrated with pulses of nitrogen in helium flow and compared against a calibration line produced from gas tight syringe injections of nitrogen under helium flow.

After TPD of hydrogen, the sample was reoxidized at the activation temperature by injecting pulses of pure oxygen in helium referenced to helium gas. After oxidation of the cobalt metal clusters, the number of moles of oxygen consumed was determined, and the percentage reduction calculated assuming that the Co^0 reoxidized to CO_3O_4. While the uncorrected dispersions (uc) are based on the assumption of complete reduction, the corrected dispersions (c), which are reported in this work, include the percentage of reduced cobalt as follows:

- $\%D_{uc}$ = (# of Co^0 atoms on surface × 100%)/(total # Co atoms in the sample)
- $\%D_c$ = (# of Co^0 atoms on surface × 100%)/[(total # Co atoms in the sample) (fraction reduced)]

Temperature Programmed Reduction (TPR)

TPR profiles of fresh catalyst samples were obtained using a Zeton Altamira AMI-200 unit. Calcined fresh samples were first heated and purged in flowing argon to remove traces of water. TPR was performed using 30 ml/min of a $10\%H_2/Ar$ mixture referenced to argon. The ramp rate was 5°C/min from 50°C to 1100°C, and the sample was held at 1100°C for 30 min.

Downloaded by DUKE UNIV on June 6, 2012 | http://pubs.acs.org
Publication Date (Web): November 29, 2011 | doi: 10.1021/bk-2011-1084.ch006

Downloaded by DUKE UNIV on June 6, 2012 | http://pubs.acs.org
Publication Date (Web): November 29, 2011 | doi: 10.1021/bk-2011-1084.ch006

Catalyst Pretreatment

The calcined Co/Al_2O_3 catalysts (~10g) were ground and sieved to 80-325 mesh before loading into a fixed-bed reactor for *ex-situ* reduction. The ex-situ reduction was conducted at 350°C and atmospheric pressure for 10 h using a gas mixture of H_2/He with the molar ratio of 1:3. The reduced catalyst was then transferred under the protection of N_2 inert gas to a 1-L continuously stirred tank reactor (CSTR), containing 315 g of melted Polywax 3000. The transferred catalyst was further reduced *in-situ* at 230 °C at atmospheric pressure using pure hydrogen for another 10 h before starting the FTS reaction.

Kinetic Experiment

The kinetic experiments were conducted using a 1-L CSTR with 15%Co/Al_2O_3 catalysts with and without Pt. The experiments were carried out following the kinetic experimental plan proposed previously (*24*). In brief, total reactor pressure was kept constant during the kinetic experiments. Constant partial pressure of CO or H_2 was achieved by adjusting the N_2 fraction in the syngas. In this study, a constant CO partial pressure of 0.51 MPa (P_{H_2} = 0.51 to 1.27 MPa), and a constant H_2 partial pressure of 0.81 MPa (P_{CO} = 0.32 to 0.81 MPa) and temperatures between 205 and 220°C were used. Throughout the test, total reaction pressure was maintained at 2.03 MPa. The fraction of N_2 in the feed was 12.5 to 50 vol%. In total, four ratios of H_2/CO (2.5, 2.0, 1.5, and 1.0) and four space velocities (13, 8, 4.8 and 3.0 NL/g-cat/h for 15%Co/Al_2O_3; 20, 10, 7 and 5 NL/g-cat/h for 0.5%Pt-15%Co/Al_2O_3) were used during the experiment. Space velocity was usually changed in a decreasing order for each ratio of H_2/CO. After testing at the four different space velocities for each ratio of H_2/CO was completed, the reaction conditions were returned to a set of reference conditions - 220 °C, 2.03 MPa, H_2/CO = 2.5, 8 or 10 Nl/g-cat/h, and N_2% =12.5 - in order to measure the extent of deactivation of the catalyst. In general, the reaction period for each space velocity was 6-24 h. Total mass closure during the kinetics experiment is 100 ± 3%.

Product Analysis

Inlet and outlet gases were analyzed on-line by a Micro GC equipped with four packed columns. The liquid organic and aqueous products were analyzed using a HP 5890 GC with capillary column DB-5 and a HP 5790 GC with Porapak Q packed column, respectively. The reactor wax withdrawn periodically was analyzed by a high temperature HP5890 GC employing an alumina clad column.

Downloaded by DUKE UNIV on June 6, 2012 | http://pubs.acs.org
Publication Date (Web): November 29, 2011 | doi: 10.1021/bk-2011-1084.ch006

Results and Discussion

Catalyst Characterization

Table 1 lists the BET results of the support and catalysts. The surface area of γ-Al_2O_3 used in this study is 200 m ^{2}/g. Addition of 15% cobalt led to a decrease in the surface area to 158 m^2/g (21% decrease). This is close to the value (200×0.8=160 m^2/g) one would expect for an equivalent amount of CO_3O_4 being present in the catalyst (20%) if γ-Al_2O_3 is the main contributor to the surface area. The pore diameter before and after loading of 15%Co (7.6 to 8.0 nm) did not change significantly, suggesting blocking of pores by Co was not significant. After adding 0.5% Pt to the catalyst, the surface area and pore volume were essentially unchanged.

Table 1. Results of BET surface area, porosity, and hydrogen chemisorption with pulse reoxidation

	BET			Chemisorption		
Support & Catalyst	BET Area m^2/g	Pore volume cm^3/g	Average pore diameter, nm	Reduction$^{(a)}$ degree, %	Cobalt disp., %	Cobalt cluster size, nm
Catalox SBA-200	200.0	0.49	7.6			
15%Co/Al_2O_3	157.6	0.32	8.1	40.9	10.0	9.0
0.5%Pt-15%Co/Al_2O_3	155.3	0.32	8.1	64.1	12.7	8.1

TPR and hydrogen chemisorption/pulse reoxidation results of the Co/Al_2O_3 catalysts are also summarized in Table 1. The reduction degree of Co supported on the γ-Al_2O_3 was only 41%, reflecting the strong interaction between Co and γ-Al_2O_3, while Co dispersion was ~10%. This resulted in an average Co cluster size of 9.0 nm. The addition of 0.5%Pt significantly improved Co reduction (64%). Co dispersion was improved by Pt promoter as well, but only to a small extent (10.0→12.7%).

Activities and Selectivity of Co/Al_2O_3 Catalysts with and without Pt

The changes in CO conversion with time over 15%Co/Al_2O_3 and 0.5%Pt-15%Co/Al_2O_3 catalysts at reference conditions (i.e., 220 °C, 2.03 MPa, H_2/CO = 2.5, N_2% =12.5 and 8-10 Nl/gcat/h) are shown in Figure 1. Both Co/Al_2O_3 catalysts are quite stable during 170 h of testing. However, the 0.5%Pt promoted 15%Co/Al_2O_3 catalyst is more active than the unpromoted one. Even at a higher space velocity, CO conversion of the Pt promoted Co catalyst is 54% higher than that of the unpromoted one (37% at 10 Nl/gcat/h versus 24% at 8 Nl/gcat/h). The significant increase in activity by Pt promoter has been explained by the Pt promoter remarkably increasing the extent of reduction of cobalt oxides to the metal, as confirmed in Table 1.

Downloaded by DUKE UNIV on June 6, 2012 | http://pubs.acs.org
Publication Date (Web): November 29, 2011 | doi: 10.1021/bk-2011-1084.ch006

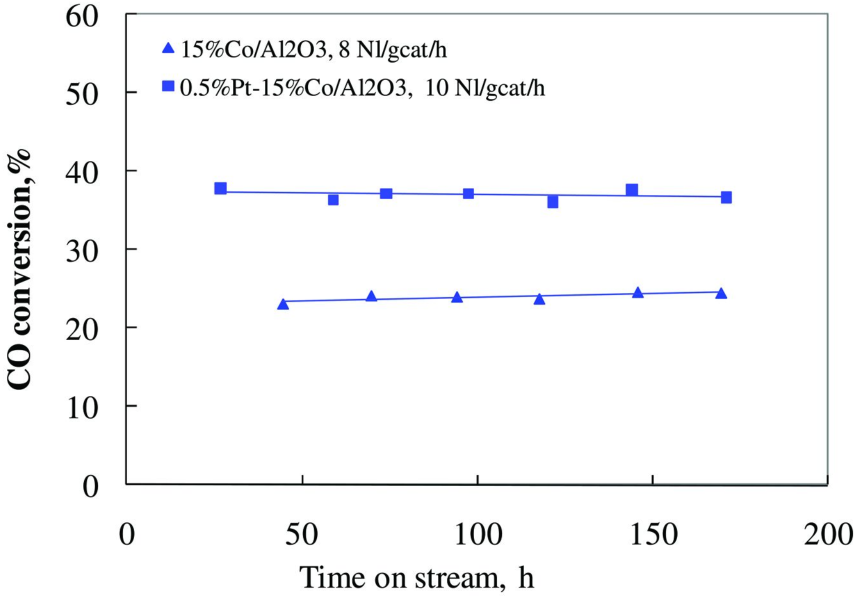

Figure 1. Change of CO conversion with time over 15%Co/ Al_2O_3 catalysts with and without Pt at baseline conditions (220°C, $H_2/CO=2.5$, 2.0MPa, and $N_2=12.5\%$).

To further illustrate the stable behavior of the Co catalysts, the hydrocarbon selectivities of the unpromoted and Pt promoted 15%Co/Al_2O_3, including 1-olefins, 2-olefins and olefin/paraffin ratios of different carbon numbers at different times, are given in Figures 2-3, respectively. The results clearly show that the variations in selectivities towards 1-olefin, 2-olefin and paraffins with time at the reaction conditions over the two 15%Co/Al_2O_3 catalysts are insignificant. Figures 2-3 show hydrocarbon selectivities depend on carbon numbers. 1-olefin selectivity decreased, and 2-olefin selectivity increased with increasing carbon number, and the olefin/paraffin ratios of both catalysts peak at C_3. These observations are consistent with the open literature, and they have been ascribed to diffusion enhanced 1-olefin readsorption (*27*), greater adsorptivity of higher molecular weight olefins (*28*), and/or increased solubility with increased molecular weight resulting in longer residence times in a slurry reactor (*29*).

The Co site-time-yields (STY) obtained at 220°C in this work are comparable with literature values. Our previous study using 25%Co/Al_2O_3 catalysts (medium and wide pore) showed that Co STYs at 220°C were in the range of $55.0\text{-}77.0\times10^{-3}$ s^{-1} (*25*). Borg et al. (*30*) reported that Co STYs were $31\text{-}63\times10^{-3}$ s^{-1} at 210 °C (equivalent to $46.8\text{-}90\times10^{-3}$ s^{-1} at 220 °C). In this paper, the Co STY obtained on the two 15%Co/Al_2O_3 catalysts are the same, 55×10^{-3} s^{-1}, which is consistent with our previous study and literature values.

Downloaded by DUKE UNIV on June 6, 2012 | http://pubs.acs.org
Publication Date (Web): November 29, 2011 | doi: 10.1021/bk-2011-1084.ch006

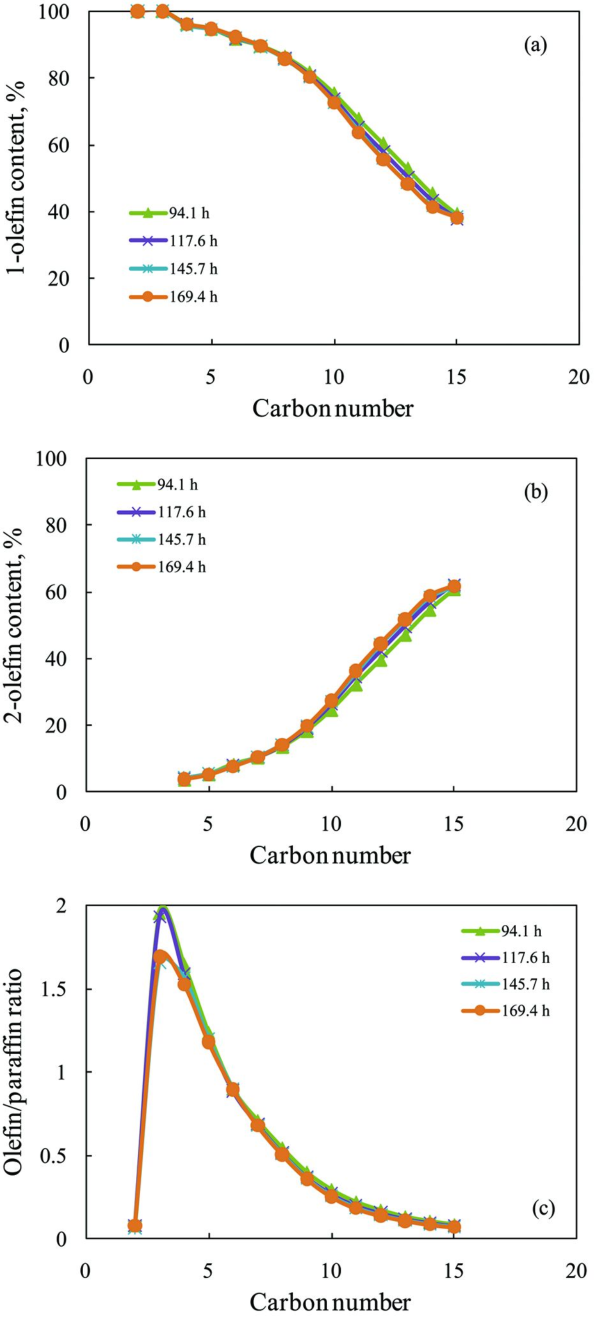

Figure 2. Selectivities to 1-olefin (a), 2-olefin(b) and olefin/paraffin ratio (c) as function of carbon number and time over 15%Co/Al_2O_3 catalyst (220°C, H_2/CO=2.5, 2.0MPa, and N_2=12.5%).

Downloaded by DUKE UNIV on June 6, 2012 | http://pubs.acs.org
Publication Date (Web): November 29, 2011 | doi: 10.1021/bk-2011-1084.ch006

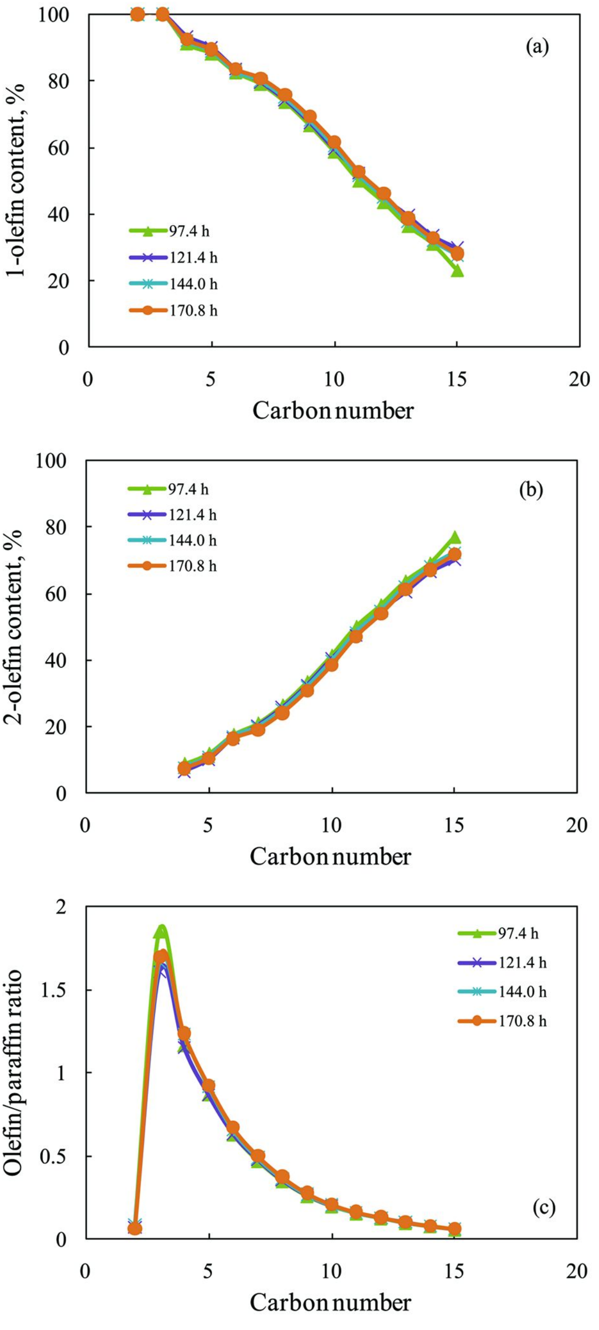

Figure 3. Selectivities to 1-olefin (a), 2-olefin(b) and olefin/paraffin ratio (c) as function of carbon number and time over 15%Co0.5%Pt/Al_2O_3 catalyst (220°C, H_2/CO=2.5, 2.0MPa, and N_2=12.5%).

Downloaded by DUKE UNIV on June 6, 2012 | http://pubs.acs.org
Publication Date (Web): November 29, 2011 | doi: 10.1021/bk-2011-1084.ch006

Effect of H_2/CO Ratio on HC Selectivities on Co/Al_2O_3 Catalysts

A number of studies were conducted to define the effects of H_2/CO ratio and promoters on catalyst selectivities [2-6, 18-22]. However, the conclusions were made without considering the conversion effect, as mentioned earlier. In fact, CO conversion may greatly impact catalyst selectivities by changing the secondary reaction of primary olefins. Therefore, the effect of H_2/CO or promoter must be investigated at similar or the same CO conversion levels. Table 2 summarizes the effect of H_2/CO ratio on overall HC selectivity and CO_2 selectivity at three CO conversion levels, 21%, 37% and 47% over the two Co/Al_2O_3 catalysts. As expected, the selectivities to CH_4 and light HCs over the two catalysts show higher values at higher H_2/CO ratio (2.5), which is assumed to be due to a higher partial pressure of H_2 in the reactor enhancing the secondary hydrogenation of primary olefins. This assumption is evident by changes in the 1-olefin and 2-olefin selectivities and the olefin-paraffin ratios in the carbon range of C_2-C_{15} over the two catalysts with the variation of H_2/CO ratio as shown in Figures 4 and 5. For C_2-C_{15}, the higher H_2/CO ratio (2.5) resulted in lower 1-olefin selectivity but higher 2-olefin selectivity, and lower olefin to paraffin (OTP) ratios. Apparently, higher H_2/CO ratios led to lower CO_2 selectivity on the 15%Co/Al_2O_3 catalysts (Table 2). This should be due to a low WGS reaction rate resulting from relatively low CO pressure in the reactor and/or high P_{H_2} promoting the reverse WGS reaction.

Table 2. Effects of H_2/CO ratio and CO conversion on HC selectivities over 15%Co/Al_2O_3 and 15%Co0.5%Pt/ Al_2O_3 catalysts at 220°C and 2.0MPa

Catalyst	Time h	H_2/CO	CO conversion %	HC selectivity (C base), % C_1	C_2-C_4	C_{5+}	CO_2 selectivity %
15%Co/Al_2O_3	213.4	2.5	21.0-24.6	11.4	12.0	76.6	0.2
	284.3	2.0		8.9	7.4	83.8	0.3
15%Co-0.5%Pt/Al_2O_3	226.2	2.5	36.9	10.3	11.8	77.9	1.1
	362.0	2.0		8.2	10.5	81.3	1.6
	265.3	2.5	46.6-48.3	10.2	11.8	78.0	1.8
	366.2	2.0		7.9	10.3	81.8	2.5

In Synthetic Liquids Production and Refining; de Klerk, A., et al.;
ACS Symposium Series; American Chemical Society: Washington, DC, 2011.

Downloaded by DUKE UNIV on June 6, 2012 | http://pubs.acs.org
Publication Date (Web): November 29, 2011 | doi: 10.1021/bk-2011-1084.ch006

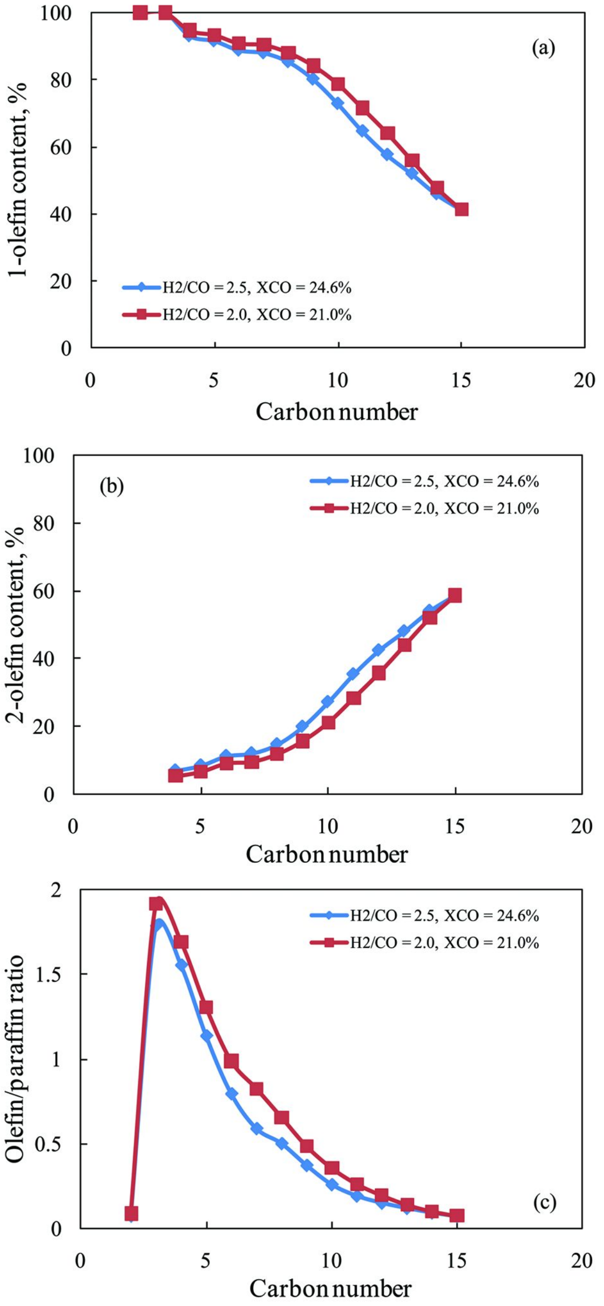

Figure 4. Effects of H_2/CO ratio and carbon number on selectivities to 1-olefin (a) and 2-olefin (b), and olefin/paraffin ratio (c) over 15%Co/Al_2O_3 catalyst (220°C and 2.0MPa).

Downloaded by DUKE UNIV on June 6, 2012 | http://pubs.acs.org
Publication Date (Web): November 29, 2011 | doi: 10.1021/bk-2011-1084.ch006

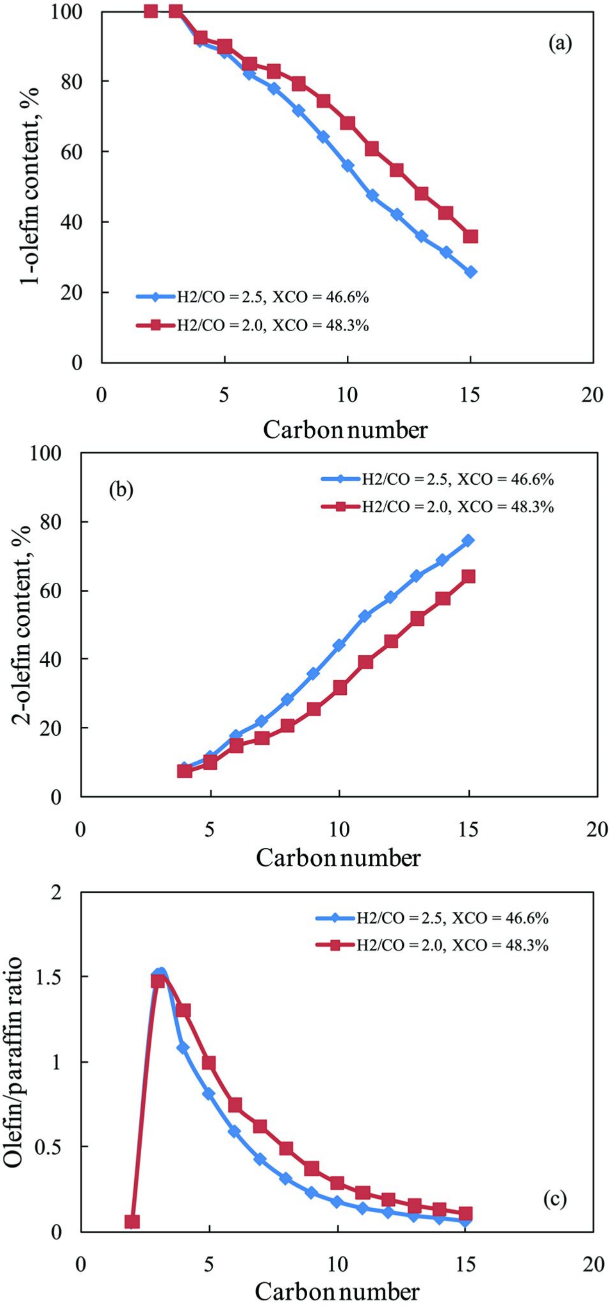

Figure 5. Effects of H_2/CO ratio and carbon number on selectivities to 1-olefin (a) and 2-olefin (b), and olefin/paraffin ratio (c) over 15%Co-0.5%Pt/Al_2O_3 catalyst (220°C and 2.0MPa).

Downloaded by DUKE UNIV on June 6, 2012 | http://pubs.acs.org
Publication Date (Web): November 29, 2011 | doi: 10.1021/bk-2011-1084.ch006

Effect of CO Conversion on Olefin and Paraffin Selectivities on Co/Al_2O_3 Catalysts

As indicated in Table 3, increasing CO conversion results in a slight lowering of the CH_4 selectivity, has little effect on the C_{5+} selectivity and slightly increases the CO_2 selectivity. Two reasons have been used to explain the CO conversion effect. One hypothesis is that the variation of water partial pressure with CO conversion impacts the secondary hydrogenation of olefins, or that water increases the transport rates of heavier hydrocarbons (*27*, *30*). These results suggest that CO conversion may be an important factor that affects selectivity. Thus, in order to investigate the influence of promoters on selectivity, the CO conversion effect should first be eliminated. To further illustrate the effect of CO conversion on the formation of 1- and 2-olefins, as well as olefin/paraffin ratios, results for the unpromoted and Pt promoted 15%Co/Al_2O_3 catalysts are provided in Figures 6 and 7, respectively. For both catalysts, olefin/paraffin ratios and 1-olefin content in the carbon range of C_2-C_{15} decreased with increasing CO conversion (Figure 6a and Figure 7a), and these were accompanied by increases in 2-olefin selectivities (Figure 6b and Figure 7b). Again, the results indicate CO conversion effects on the secondary reactions of primary olefins.

Table 3. Effect of Pt on hydrocarbon selectivities on 15%Co/Al_2O_3 catalysts at different CO conversion levels at 220°C and 2.0MPa

Catalyst	Time	H_2/CO	CO conversion	HC selectivity (C base), %			CO_2 selectivity
	h		%	C_1	C_2-C_4	C_{5+}	%
15%Co/Al_2O_3	235.3	2.5	37.0-40.8	10.4	8.6	81.1	0.5
15%Co-0.5%Pt/Al_2O_3	226.2			10.3	11.8	77.9	1.1
15%Co/Al_2O_3	238.7		65.4-67.0	9.9	9.7	80.4	0.8
15%Co-0.5%Pt/Al_2O_3	242.9			10.0	11.7	78.3	3.3
15%Co/Al_2O_3	267.8	2.0	12.0-13.3	10.4	8.6	81.0	0.1
15%Co-0.5%Pt/Al_2O_3	313.3			9.9	12.5	77.6	0.5
15%Co/Al_2O_3	305.3		32.3-36.0	8.9	7.7	83.5	0.5
15%Co-0.5%Pt/Al_2O_3	362.0			8.2	10.5	81.3	1.6
15%Co/Al_2O_3	309.2		48.0-50.0	7.8	7.7	84.5	0.8
15%Co-0.5%Pt/Al_2O_3	366.2			7.9	10.3	81.8	2.5

Downloaded by DUKE UNIV on June 6, 2012 | http://pubs.acs.org
Publication Date (Web): November 29, 2011 | doi: 10.1021/bk-2011-1084.ch006

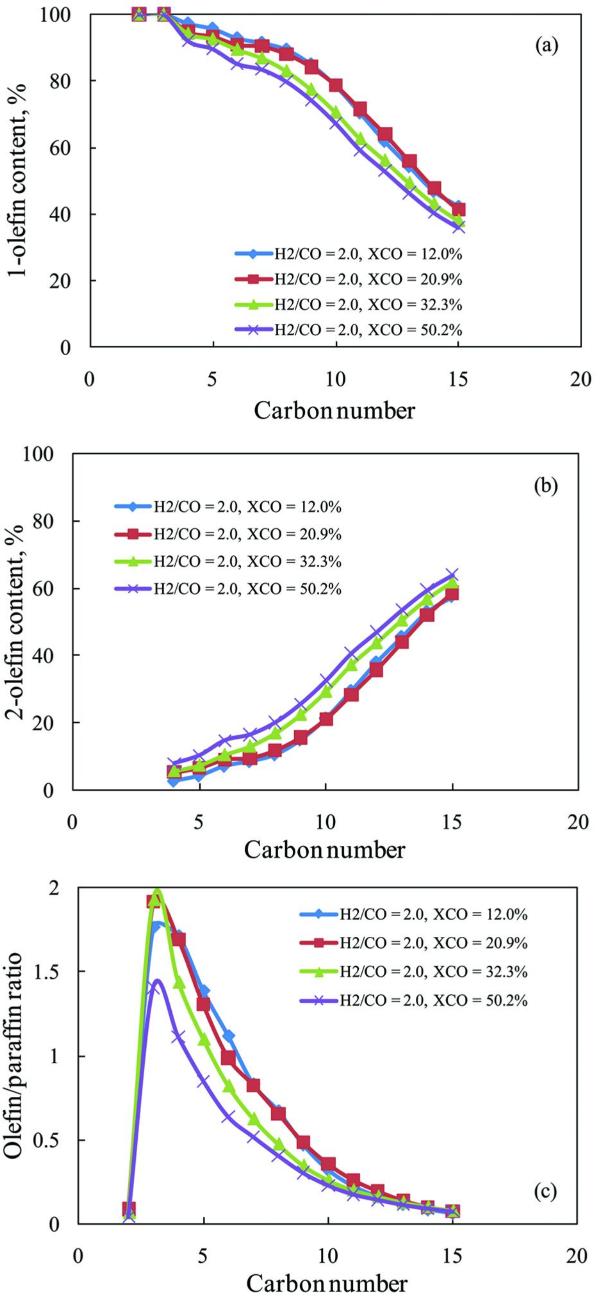

Figure 6. Effects of CO conversion and carbon number on selectivities to 1-olefin (a) and 2-olefin (b), and olefin/paraffin ratio (c) over 15%Co/Al_2O_3 catalyst (220°C and 2.0MPa).

Downloaded by DUKE UNIV on June 6, 2012 | http://pubs.acs.org
Publication Date (Web): November 29, 2011 | doi: 10.1021/bk-2011-1084.ch006

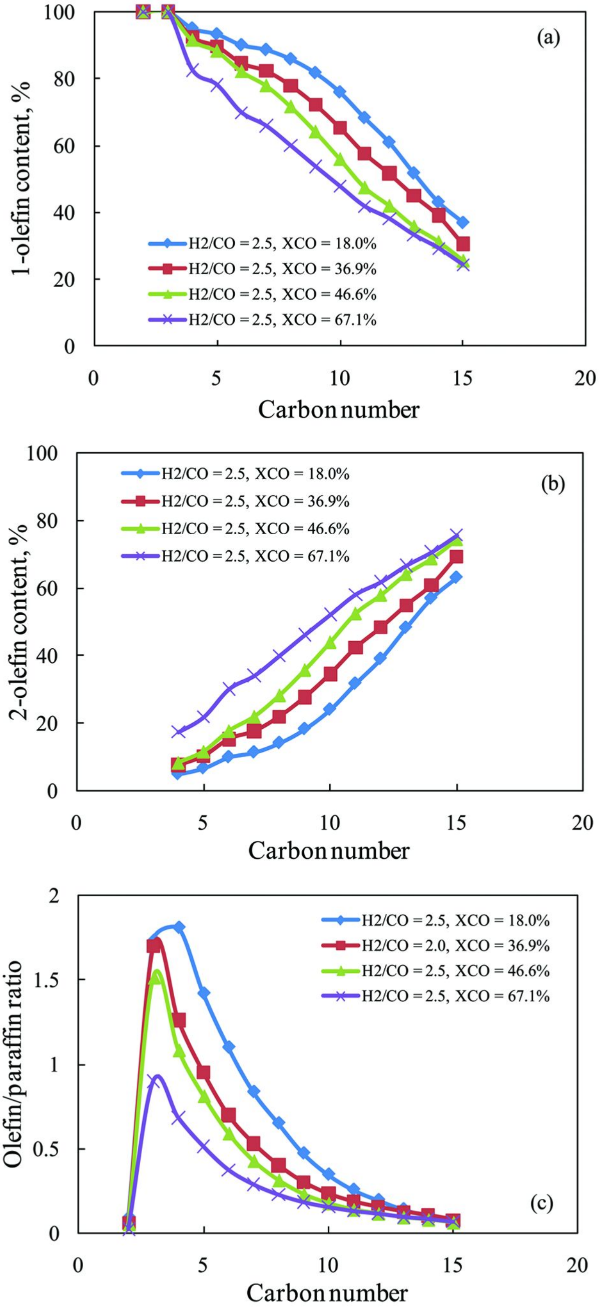

Figure 7. Effects of CO conversion and carbon number on selectivities to 1-olefin (a) and 2-olefin (b), and olefin/paraffin ratio (c) over 15%Co-0.5%Pt/Al_2O_3 catalyst (220°C and 2.0MPa).

Downloaded by DUKE UNIV on June 6, 2012 | http://pubs.acs.org
Publication Date (Web): November 29, 2011 | doi: 10.1021/bk-2011-1084.ch006

Effect of Pt Promoter on HC Selectivities on Co/Al_2O_3 Catalysts

Comparisons of hydrocarbon selectivity and CO_2 selectivity over the unpromoted and Pt promoted 15%Co/Al_2O_3 catalysts at five different CO conversion levels (i.e., 12, 32, 37, 48, and 65%), at H_2/CO ratios of 2.5 and 2.0 are summarized in Table 3. Interestingly, while CH_4 selectivity was nearly unchanged after using Pt promoter at all five CO conversion levels, other light hydrocarbon (C_2-C_4) selectivities in the case of the Pt promoted catalyst in all cases were higher than those of the unpromoted Co/Al_2O_3 catalyst (10.3-12.6% versus 7.7-9.7%). This was accompanied by lower C_{5+} selectivities on the 0.5%Pt-15%Co/Al_2O_3 catalyst (77.6 - 81.8% versus 80.4-83.5%). It is known that the WGS reaction is responsible for the formation of CO_2 under typical FTS reaction conditions. From the data in Table 3, Pt promoted WGS, as indicated by the higher CO_2 selectivity for the 0.5%Pt-15%Co/Al_2O_3 (0.5-3.3% CO_2 selectivities in the CO conversion range of 12-67%) relative to the unpromoted catalyst (0.1-0.8%). This result is consistent with the results reported in an early WGS study over Pt/CeO_2 catalyst, which claimed that higher Pt loading resulted in higher WGS rates (*31*).

The 1-olefin selectivity, 2-olefin selectivity, and total olefin/paraffin ratios of the 15%Co/Al_2O_3 and 0.5%Pt-15%Co/Al_2O_3 catalysts obtained at a H_2/CO ratio of 2.0 were used to study the effect of Pt on olefin and paraffin selectivities (see Figures 8, 9, and 10). For all carbon numbers, total olefin/paraffin ratios, 1-olefin content, and 2-olefin content over the carbon range examined for the two catalysts were essentially the same if we took into account experimental error (within ±3.7% for 1-olefin selectivities; within ±7.8% for 2-olefin selectivities and within ±10.8 % for olefin/paraffin ratios). This indicates that the presence of the Pt promoter does not measurably change the characteristics of secondary reactions occurring on the Co/Al_2O_3 catalyst. Compared to the CO conversion and H_2/CO ratio effects, as discussed above, CO conversion and H_2/CO ratio are two main factors that influence the rates of secondary reactions of olefins.

Several studies with Pt-Co catalysts have suggested that Pt only significantly increased the CO hydrogenation rate of Co catalysts by increasing Co reduction and dispersion, without changing HC selectivities (*2*, *3*). Vada et al. (*2*) conducted FTS over 8.7%Co/Al_2O_3 and 1%Pt promoted 8.7%Co/Al_2O_3 (conditions: 200°C, 5 bar, and H_2/CO of 2.0) using a fixed-bed reactor. They found that CH_4 selectivity was unchanged over the two catalysts, consistent with the results obtained in the current study. However, they did not report the selectivities to other light hydrocarbons or C_{5+} hydrocarbons. Thus, their conclusion that hydrocarbon selectivity was unaffected by the presence of Pt or Re seems to have been made on the basis of CH_4 selectivity alone. Schanke et al. (*3*) studied Pt promoted Co catalyst for the hydrogenation reaction using a fixed-bed reactor at a CO conversion range of 10-20% under methanation conditions (210°C, 1atm, H_2/CO of 7.3). For the C_1-C_4 hydrocarbons produced on the 9%Co/Al_2O_3 and 8.9%Co/SiO_2 catalysts, they observed similar CH_4 and C_2-C_4 selectivities over the unpromoted and Pt promoted Co/Al_2O_3 catalysts, but relatively larger differences in selectivities over the Co/SiO_2 catalysts. Based on these results, they also concluded that Pt does not influence hydrocarbon selectivity. However, it should be noted that a 10% CO conversion difference is large enough to bring about a

Downloaded by DUKE UNIV on June 6, 2012 | http://pubs.acs.org
Publication Date (Web): November 29, 2011 | doi: 10.1021/bk-2011-1084.ch006

conversion effect on selectivity when comparing hydrocarbon selectivity, and the reaction conditions used by the authors were not representative of typical FTS conditions. Recently, Yu et al. (*18*) studied the role of Pt in Fe based catalysts. It was reported that Pt increased FTS activity, but suppressed the selectivity to light HCs and olefins. However, it must be noted that the comparison of the HC selectivities was made over a wide CO conversion range 42-82% even though the reaction conditions (250°C, H_2/CO =0.67, 1.5MPa) used were typical of FTS conditions. Therefore, the CO conversion effect on HC selectivity was not decoupled from the promoter effect. In the current study, the conclusion that the Pt promoter increases the C_2 – C_4 light hydrocarbon formation rates and decreases the heavier hydrocarbon rates was made only after the CO conversion impact was removed (i.e., by comparing at comparable CO conversion rates), and thus the results reflect the actual effect of Pt during FTS.

The influence of Pt on increasing light HC selectivity is likely due to changes in the H_2 adsorption characteristics of the Co/Al_2O_3 catalyst with Pt addition. It is known that H_2 is able to adsorb and dissociate on Pt metal (*2*, *31*). During reduction of Co catalysts, the dissociated H_2 on Pt (Pt-H) is suggested to spill over to nucleate reduced cobalt sites in cobalt oxides, thus significantly shifting the two reduction steps (i.e., Co_3O_4 to CoO and CoO to Co^0) to lower temperatures, leading to significant improvements in the degree of Co^0 reduction during activation, and in turn, much higher Co^0 active site densities (*1*). During FTS, a fraction of Pt metal may still be present on the catalyst surface and may continue to facilitate the dissociation of molecular H_2, and furthermore, to continue to provide dissociated H to Co^0, which increases the hydrocarbon chain termination rate. This role of Pt appears to explain the experimentally observed higher light hydrocarbon selectivities and lower C_{5+} selectivities for the 0.5%Pt-15%Co/Al_2O_3 catalyst relative to the unpromoted one.

However, invoking this role of Pt to understand CH_4 selectivity is unsatisfactory. As addressed previously, CH_4 selectivity was largely unchanged by Pt promoter addition in the case of the 15%Co/Al_2O_3 catalyst, consistent with the results reported by Vada et al. (*2*). The discrepancy between the impacts that Pt has on influencing CH_4 selectivity with that of the other lighter hydrocarbons (i.e., C_2 – C_4) may be due to differences in the mechanisms of CH_4 formation from those of higher hydrocarbons. It has been reported that CH_4 formation during FTS reactions follows two different reaction paths on Co catalysts (*32*, *33*). One is the methanation pathway, in which hydrogen reacts with active carbon or methylene; another is the normal FTS polymerization pathway, which may take place through a carbide mechanism. It was recently reported that the methanation pathway accounts for 60-85% of the CH_4 formed during FTS on Co, and thus is the predominant way to form CH_4 product on cobalt catalysts (*33*). Therefore, even if Pt promoter enhanced H_2 dissociation over Co based catalyst, and it increased the chain termination rate to methane, the dominant CH_4 formation pathway by methanation may not be affected by Pt promoter. This could potentially explain why CH_4 selectivity was not significantly affected by Pt, while the other hydrocarbons were.

Downloaded by DUKE UNIV on June 6, 2012 | http://pubs.acs.org
Publication Date (Web): November 29, 2011 | doi: 10.1021/bk-2011-1084.ch006

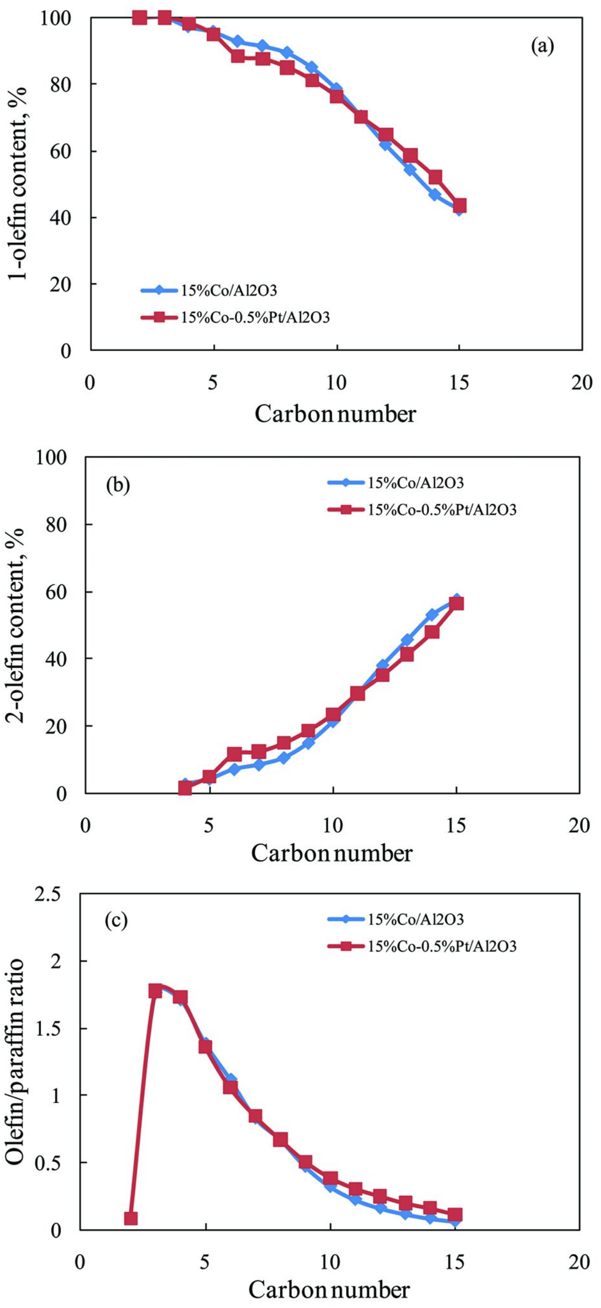

Figure 8. Effects of Pt promoter and carbon number on selectivities to 1-olefin (a) and 2-olefin (b), and olefin/paraffin ratio over 15%Co/Al_2O_3 catalyst (220°C, H_2/CO=2.0, 2.0MPa and X_{CO} = 12.0-13.3%).

Downloaded by DUKE UNIV on June 6, 2012 | http://pubs.acs.org
Publication Date (Web): November 29, 2011 | doi: 10.1021/bk-2011-1084.ch006

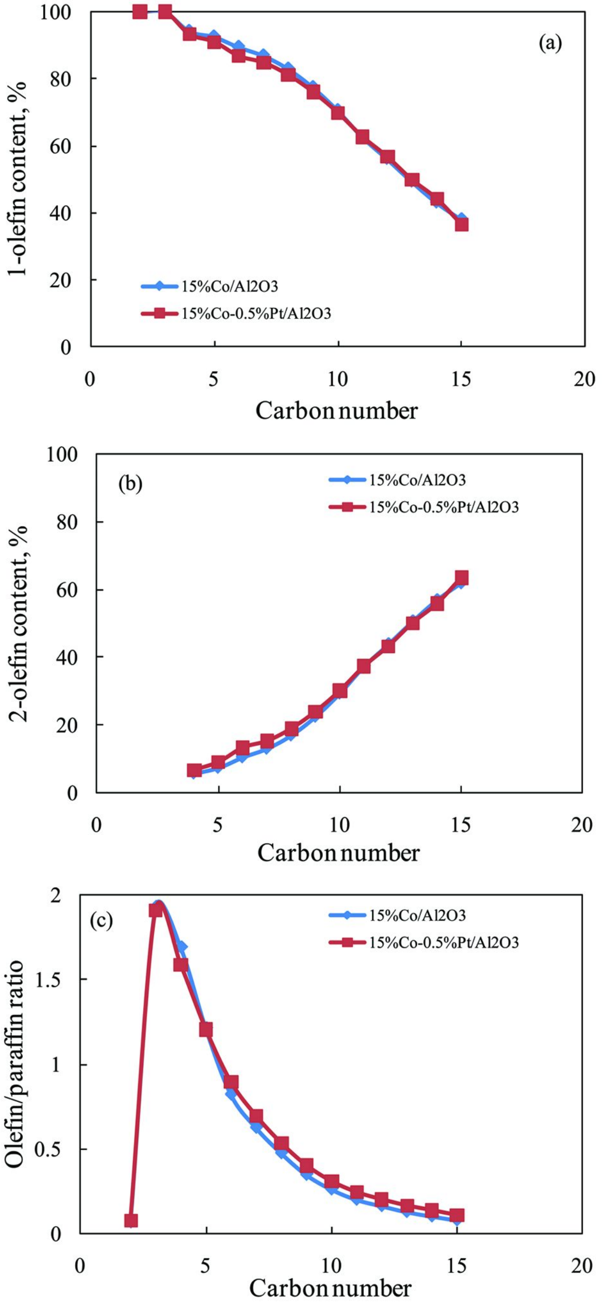

Figure 9. Effects of Pt promoter and carbon number on selectivities to 1-olefin (a) and 2-olefin (b), and olefin/paraffin ratio over 15%Co/Al_2O_3 catalyst (220°C, $H_2/CO=2.0$, 2.0MPa and X_{CO} = 32.3-36.8%).

Downloaded by DUKE UNIV on June 6, 2012 | http://pubs.acs.org
Publication Date (Web): November 29, 2011 | doi: 10.1021/bk-2011-1084.ch006

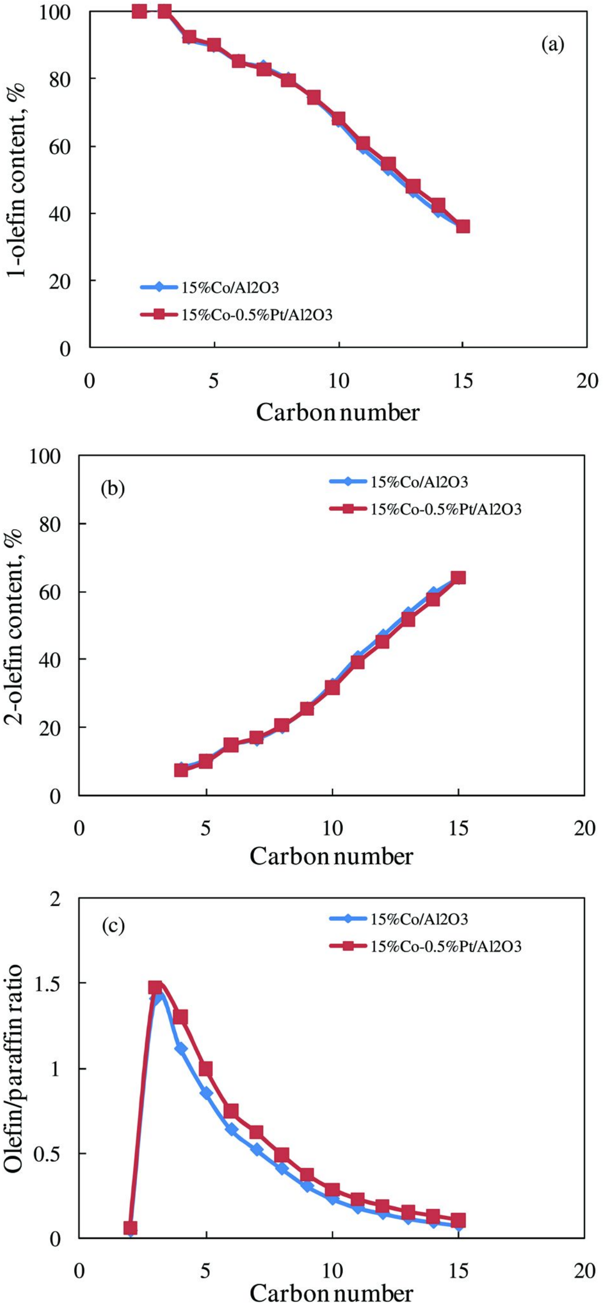

Figure 10. Effects of Pt promoter and carbon number on selectivities to 1-olefin (a) and 2-olefin (b), and olefin/paraffin ratio over 15%Co/Al_2O_3 catalyst (220°C, H_2/CO=2.0, 2.0MPa and X_{CO} = 48.3-50.2%).

Downloaded by DUKE UNIV on June 6, 2012 | http://pubs.acs.org
Publication Date (Web): November 29, 2011 | doi: 10.1021/bk-2011-1084.ch006

The addition of Pt promoter in Co/Al_2O_3 may slightly decrease the average Co cluster size and increase the active Co^0 site density. Again, this is due at least in part to the promoting effect that Pt has in facilitating cobalt reduction. For the case of catalysts activated at the same conditions (e.g., 10 hours in hydrogen at 350°C), relative to Co/Al_2O_3 alone, the Pt promoted catalyst will facilitate the reduction of an additional fraction of cobalt and, typically, this tends to be the smaller cobalt oxide species in stronger interaction with the alumina support. The net result may thus be a slightly smaller cobalt cluster size. With catalyst aging, however, this may change. Nevertheless, differences in cobalt cluster size probably do not explain the differences in $C_{2\text{-}4}$ and C_{5+} hydrocarbon selectivities observed on the unpromoted and Pt promoted Co catalysts in this study. The unpromoted Co catalyst has an average Co cluster diameter of 9.0 nm, and adding Pt only decreased the average diameter to 8.1 nm, which is suggested in one investigation to be the optimal Co size for achieving the highest C_{5+} selectivity (*30*). We conclude then that the observed higher light gas selectivity and lower C_{5+} selectivity is due to a direct role of Pt, and not to the indirect impact of Pt on the resulting average Co cluster size.

Effect of H_2/CO Ratios, CO Conversion, and Pt Promoter on Oxygenate Selectivities

The water soluble oxygenates produced on the $15\%Co/Al_2O_3$ catalyst account for only 0.3-1.0% of the total combined hydrocarbon/oxygenate products, which is less than that of Fe-K catalysts (i.e., 1.5-2% and 3.0%) reported by Davis et al. (*34*), and Ma et al. (*35*), respectively. Furthermore, the water soluble oxygenates identified in this study mainly consist of methanol and ethanol. Thus, it is narrower than that (e.g., C_1-C_5) observed over precipitated and supported Fe catalysts (*34*, *35*).

Even though the amount of oxygenates produced on cobalt based catalysts during FTS reactions is small, it is of interest to find out how the conditions, CO conversions and promoters (e.g., Pt) impact their formation, since the variation in oxygenates with the parameters may imply different reaction paths. Table 4 shows the oxygenate selectivities obtained at different CO conversion levels at the H_2/CO ratios of 2.5 and 2.0 over $15\%Co/Al_2O_3$ and $0.5\%Pt\text{-}15\%Co/Al_2O_3$ catalysts. At a H_2/CO feed ratio of 2.5, the oxygenate selectivity over unpromoted $15\%Co/Al_2O_3$ decreased slightly (0.9 to 0.5%) with increasing CO conversion (15 to 65%). When the H_2/CO feed ratio was decreased to 2.0, this oxygenate selectivity trend (0.7→0.3%) versus CO conversion (12→50%) was retained. However, when comparing oxygenate selectivities at 12-15% and 32-41% CO conversion levels for the two catalysts, it is observed that the oxygenate selectivities at the high H_2/CO ratio of 2.5 are slightly greater than those at the low H_2/CO ratio of 2.0 (0.9 vs 0.7% and 0.7 vs 0.4%). The same changing pattern of oxygenate selectivity with CO conversion is also observed on the $0.5\%Pt\text{-}15\%Co/Al_2O_3$ catalyst at H_2/CO ratio of 2.0 – i.e., the oxygenate selectivity decreased from 0.9 to 0.4% as CO conversion increased from 26 to 48%. The oxygenate selectivity data of the Pt-Co catalyst at 67% CO conversion (H_2/CO ratio of 2.5) was obtained (0.62%), which allows us to compare the oxygenate selectivities of the un-promoted and

Pt promoted 15%Co/Al_2O_3 catalysts at both H_2/CO ratios of 2.5 and 2.0. At the CO conversion levels of 32-37% (H_2/CO of 2.0) and 65-67% (H_2/CO of 2.5), the 0.5%Pt promoted 15%Co/Al_2O_3 catalyst exhibited slightly higher oxygenate selectivity than the unpromoted 15%Co/Al_2O_3 catalyst. Note that even though the absolute increases in the oxygenate selectivity values by the Pt promoter are small (0.5 versus 0.6% and 0.4 versus 0.5%), the percentage change caused by adding the Pt promoter is not small (20%). Therefore, by summarizing the results above, it is concluded that the selectivity to water soluble oxygenate produced on Co/Al_2O_3 catalysts is in the range of 0.3-1.0%, and the Pt promoter slightly increased the oxygenate formation rates. Furthermore, oxygenate formation decreased with increasing CO conversion; and larger H_2/CO ratios slightly promoted the oxygenate formation rate.

Downloaded by DUKE UNIV on June 6, 2012 | http://pubs.acs.org
Publication Date (Web): November 29, 2011 | doi: 10.1021/bk-2011-1084.ch006

Table 4. Change of oxygenates with H_2/CO ratios and CO conversions over 15%Co/ Al_2O_3 and 15%Co0.5%Pt/ Al_2O_3 catalysts at 220°C and 2.0MPa

H_2/CO [(a)]	15%Co/Al_2O_3			15%Co-0.5%Pt/Al_2O_3		
	TOS, h	X_{CO}, %	Soxy, %	TOS, h	X_{CO}, %	Soxy, %
2.5	188-195	15.2	0.87			
	213-235	40.8	0.66			
	235 -239	65.4	0.51	226-243	67.1	0.62
2.0	265-268	12.0	0.73	313-339	26.3	0.89
	284-305	32.3	0.42	339-362	36.8	0.51
	305-309	50.2	0.33	362-366	48.3	0.40

The observed trend of lower oxygenate selectivity at higher CO conversion over Co/Al_2O_3 in this study is consistent with the results over precipitated Fe catalysts reported previously by Davis et al. (*34*) and Satterfield et al. (*36*). It was claimed that the secondary reaction of oxygenate dehydration is thermodynamically favored and the reaction takes place on catalysts possessing acid sites (*36*). Therefore, it could be that dehydration of alcohols to olefins is enhanced at higher CO conversions over Co/Al_2O_3 catalysts, resulted in diminishing oxygenates at high conversion since the Al_2O_3 support has both acid and base properties (*37*).Another explanation is that CO concentration decreased significantly at higher CO conversions, which could lower the oxygenate formation rates (*36*). However, to understand the oxygenate trend observed, it is necessary to consider the reaction conditions used. In our case, CO conversion was increased by decreasing the space velocity (SV), thereby increasing the probabilities of CO dissociation and CO insertion (*38*). Oxygenate formation and hydrocarbon production are generally assumed to be formed through CO insertion and carbide mechanisms, respectively [28]. Thus, it is speculated that as the contact times of reactants increased - resulting in higher CO conversion rates - the probability that reactions of undissociated CO insertion took place decreased, causing decreases in oxygenate selectivity. This assumption is consistent with the claims in a FTS study over mono- and bimetallic Co and Fe catalysts (*39*). Furthermore, the improved WGS reaction at high CO conversion (to be discussed) might be a reason according to the assumption addressed above since the CO fraction used to synthesize hydrocarbons/oxygenates decreased as the WGS reaction was enhanced.

The experimental results of this study indicate slightly higher oxygenate selectivities at a higher H_2/CO ratio (2.5) at two different CO conversion levels on the unpromoted 15%Co/Al_2O_3 catalyst (Table 4). This cannot be fully explained by a popular FTS mechanism, that of hydrogen-assisted CO dissociation over Fe and Co FTS catalysts proposed recently (*40–42*), since more H_2 in the syngas should improve CO dissociation and benefit hydrocarbon formation according to the mechanism. However, Baetzold et al. (*43*) proposed a CO insertion mechanism to explain oxygenate formation rates in a kinetic study, with several steps being described as: $H + CO \rightarrow HCO \rightarrow H_2CO \rightarrow H_3CO \rightarrow CH_3OH$. In terms of this group of pathways, the additional hydrogen in higher H_2/CO ratio syngas could promote these elemental reactions and thereby increase oxygenate rates. However, additional studies are needed to verify this hypothesis.

Ir, Ru, Re (*3*, *21*), alkali (*22*), and Cu (*23*) were reported to increase oxygenate formation rates. A slight improvement in oxygenate selectivity by Pt promoter addition to Co/Al_2O_3 was observed in this study. This experimental result appears to be consistent with some characterization and theoretical studies associated with CO adsorption on the Pt/Al_2O_3 catalyst. An experimental study using the FTIR technique reported that CO was linearly adsorbed on 2.9% Pt/Al_2O_3 catalyst at up to 740 K and 10 Pa (*44*). A study using density functional theory (DFT) indicated the adsorption of CO onto the surfaces of both the thin Pt layers and the 3-atom nanoparticles supported on alumina substrates (*45*). Therefore, if this is the case, small amounts of adsorbed CO on Pt may spill over to the surface of Co and participate in chain growth according to the CO insertion model, resulting in the formation of oxygenates. However, other paths may not be ruled out. In a recent study regarding oxygenate formation on Co-CeO_2 catalyst, it was suggested that oxygenates were formed at the interface of Co-CeO_2, perhaps through the spillover of an alkylidene species to the CeO_2 support, where a hydroxyl group may be formed (*46*). If oxygenates are formed in a similar manner over Co-Al_2O_3, the rate could conceivably be enhanced by Pt, since Pt addition tends to facilitate the reduction of smaller, more strongly interacting cobalt oxide species. That is to say, Pt addition may result in a relative increase in the Co-Al_2O_3 interface (i.e., responsible for oxygenate production) relative to the on-top area of cobalt, which is suggested to catalyze normal FT synthesis of hydrocarbons.

Downloaded by DUKE UNIV on June 6, 2012 | http://pubs.acs.org
Publication Date (Web): November 29, 2011 | doi: 10.1021/bk-2011-1084.ch006

Downloaded by DUKE UNIV on June 6, 2012 | http://pubs.acs.org
Publication Date (Web): November 29, 2011 | doi: 10.1021/bk-2011-1084.ch006

Effect of Pt Promoter on the Kinetic Behavior of 15%Co/Al_2O_3

A kinetic assessment of the effect of water on Co/SiO_2 and Co/Al_2O_3 catalysts was reported previously. The kinetic model used by CAER researchers is a power law model, mathematically described as $-r_{CO} = kP_{CO}^{a}P_{H_2}^{b}/(1 + mP_{H_2O}/P_{H_2})$ (*24*, *25*), where $k = k_0\ exp\ (-E_a/RT)$ is the apparent kinetic rate constant, *a* and *b* are the apparent reaction orders for CO and H_2, respectively, and *m* is defined to be a water effect parameter. In an ongoing effort to evaluate the kinetic parameters of conventional Co based catalysts, kinetic experiments were conducted over the unpromoted and 0.5%Pt promoted 15%Co/Al_2O_3 catalysts. The kinetic parameters of the two catalysts are listed in Table 5.

Table 5. Kinetic parameter values over 15%Co/ Al_2O_3 and 15%Co0.5%Pt/ Al_2O_3 catalysts at 220°C

Catalyst	a	b	m	k	E_a	k_0
				mol/gcat/h/MPa$^{(a+b)}$	kJ/mol	mol/gcat/h/MPa$^{(a+b)}$
15%Co/Al_2O_3	-0.34	0.53	0.097	0.0162	114.3	2.05E+10
0.5%Pt-15%Co/Al_2O_3	-0.19	0.5	0.13	0.0338	98.6	1.02E+09

The reaction orders of *a* and *b* in the model were calculated to be –0.19 and 0.5, respectively, for the 0.5%Pt-15% Co/Al_2O_3 catalyst, and -0.34 and 0.53 for the unpromoted 15%Co/Al_2O_3 catalyst, which are consistent with many of the values reported in the literature (*24*, *25*, *47*). However, comparing the ratio of b/a shows a more negative ratio for the Pt promoted Co/Al_2O_3 catalyst relative to the un-promoted catalyst (-2.6 versus -1.56). This appears to indicate that the Pt promoter facilitates H_2 adsorption to a greater extent relative to CO adsorption. This deduction is consistent with the assumption in the previous part that was used to explain higher light hydrocarbons obtained on the Pt catalysts. The *k* value of the 0.5%Pt-15% Co/Al_2O_3 catalyst is 140% greater than that of the unpromoted one (0.0338 versus 0.0162 mol/g-cat/h/MPa$^{(a+b)}$), which is consistent with the characterization results that Pt significantly increases the Co^0 site density. In terms of the positive *m* values (0.13 and 0.1) obtained for both catalysts, a small negative water effect on the FTS rate over the two catalysts was obtained. It appears that the Pt promoted catalyst is slightly more sensitive to water than the unpromoted one, perhaps due to the slightly smaller average Co^0 cluster size.

Activation energies, E_a, and pre-exponential factors, k_0, of the two Co/Al_2O_3 catalysts were also obtained. Comparing the values shown in Table 5, the unpromoted Co/Al_2O_3 catalyst displayed greater E_a and k_0 values than the Pt promoted catalyst. Greater E_a would decrease reaction rate constant, *k*, while a larger k_0 has a positive impact on *k* based on the Arrhenius equation. The apparent reaction rate constant for the Pt promoted Co/Al_2O_3 catalyst is greater than that of the unpromoted one and, therefore, the increase in the activity of the 0.5%Pt-15%

Co/Al_2O_3 catalyst is mainly due to the effect that Pt has on decreasing activation energy, E_a, from a kinetic point of view. The Pt promoted $15\%Co/Al_2O_3$ catalyst showed a smaller k_0.

Conclusions

The effect of Pt promoter on the FTS activity and selectivities to hydrocarbons and oxygenates over $15\%Co/Al_2O_3$ catalyst was investigated using a 1L CSTR. The Pt promoter significantly increased the active site density of Co^0, mainly by enhancing the degree of reduction of Co, and, to a less extent, the average cobalt cluster size, since Pt facilitated the reduction of smaller, more strongly interacting cobalt oxides with the support. Consequently, the Pt promoted $15\%Co/Al_2O_3$ catalyst displayed an apparent reaction rate constant that was about 1.4 times higher than the unpromoted catalyst due to the higher Co site density of the Pt promoted $15\%Co/Al_2O_3$ catalyst, also evidenced by the same Co site time yield obtained for the two Co/Al_2O_3 catalysts (5.5×10^{-3} s^{-1} at 220°C). The Pt promoter decreased the activation energy, E_a. This is probably due to Pt reducing the Co particle size. However, this tentative conclusion requires more study.

The effects of Pt on hydrocarbon and oxygenates selectivities were studied at several similar CO conversion levels. Pt increased light HC formation but suppressed heavier hydrocarbon formation. Pt increased the chain termination probability, probably by increasing H_2 dissociation and assisting in the spillover of dissociated H to Co metal. Small amounts of oxygenate (0.3-1.0%) were found in the aqueous phase over the Co/Al_2O_3 catalysts, and the addition of Pt to the catalyst increased oxygenate formation. Pt metal slightly enhanced CO adsorption and/or Pt increases Co-Pt interface by decreasing Co size; these could be reasons for the observed higher oxygenates on the $0.5\%Pt\text{-}15\%Co/Al_2O_3$ catalyst.

CO conversion and the H_2/CO ratio in the syngas feed affect HC selectivity and oxygenate selectivity. Increases in CO conversion or decreases in the H_2/CO ratio resulted in lower CH_4 and olefins. The secondary reaction of primary olefins are significantly enhanced at higher CO conversions or higher H_2/CO ratio, suggesting CO conversion and the H_2/CO feed ratio are two main factors that influence the secondary reaction of 1-olefins for the Co/Al_2O_3 catalysts.

Values of the kinetic parameters of the unpromoted and Pt promoted $15\%Co/Al_2O_3$ catalysts were calculated based on the kinetic model, $-r_{CO} = kP_{CO}{}^{a}P_{H_2}{}^{b}/(1 + mP_{H_2O}/P_{H_2})$. Both unpromoted and Pt promoted $15\%Co/Al_2O_3$ display a negative water effect, consistent with previous results of several Co/Al_2O_3 catalysts having different structures.

Acknowledgments

This work was supported by NASA contract, #NNX07AB93A and the Commonwealth of Kentucky.

Downloaded by DUKE UNIV on June 6, 2012 | http://pubs.acs.org
Publication Date (Web): November 29, 2011 | doi: 10.1021/bk-2011-1084.ch006

References

1. Jacobs, G.; Chaney, J. A.; Patterson, P. M.; Das, T. K.; Davis, B. H. *Appl. Catal.* **2004**, *264*, 203–212.
2. Vada, S.; Hoff, A.; Adnanes, E.; Schanke, D.; Holmen, A. *Top. Catal.* **1995**, *2*, 155–162.
3. Schanke, D.; Vada, S.; Blekkan, E. A.; Hilmen, A. M.; Hoff, A.; Holmen, A. *J. Catal.* **1995**, *156*, 85–95.
4. Yu, L. H.; Zhang, S. M.; Guo, X. Z.; Wang, D.; Wang, S. R.; Wu, S. H. *Cent. Eur. J. Chem.* **2007**, *5*, 144–155.
5. Xu, D. Y.; Li, W. Z; Duan, H. M.; Ge, Q. J.; Xu, H. Y. *Catal. Lett.* **2005**, *102*, 229–235.
6. Hosseini, S. A.; Taeb, A.; Feyzi, F. *Catal. Commun.* **2005**, *6*, 233–240.
7. Li, Y.; Wang, T.; Wu, C.; Qin, X.; Tsubaki, N. *Catal. Commun.* **2009**, *10*, 1868–1874.
8. Panpranot, J., Jr.; Goodwin, J. G.; Sayari, A. J. *J. Catal.* **2002**, *211*, 530–539.
9. Iglesia, E.; Soled, S. L.; Fiato, R. A. *J. Catal.* **1992**, *137*, 212–224.
10. Jongsomjit, B.; Panpranot, J.; Goodwin, J. G., Jr. *J. Catal.* **2001**, *204*, 98–109.
11. Martens, J. H. A.; Blik, V. H. F. J.; Prins, R. *J. Catal.* **1986**, *97*, 200–209.
12. Bae, J. W.; Kim, S. M.; Park, S. J.; Lee, Y. J.; Ha, K. S.; Jun, K. W. *Catal. Commun.* **2010**, *11*, 834–838.
13. Jongsomjit, B.; Panpranot, J.; Goodwin, J. G., Jr.; Sayari, A. *J. Catal.* **2002**, *211*, 530.
14. Guczi, L.; Hoffer, T.; Zsoldos, Z.; Zyade, S.; Maire, G.; Garin, F. *J. Phys. Chem.* **1991**, *95*, 802.
15. Jacobs, G.; Ma, W. P.; Davis, B. H.; Cronauer, D. C.; Kropf, A. J.; Marshall, C. L. *Catal. Lett.* **2010**, *140*, 106–115.
16. Khodakov, A. Y.; Chu, W.; Fongarland, P. *Chem. Rev.* **2007**, *107*, 1692–1744.
17. Storsæter, J. S.; Tøtdal, B.; Walmsley, J. C.; Tanem, B. S.; Holmen, A. *J. Catal.* **2005**, *236*, 139–152.
18. Yu, W.; Wu, B. S.; Xu, J.; Tao, Z. C.; X, H. W.; Li, Y. W. *Catal. Lett.* **2008**, *125*, 116–122.
19. Xu, J.; Bartholomew, C. H.; Sudweeks, J.; Eggett, G. H. *Top. Catal.* **2003**, *26*, 55.
20. Panagiotopoulou, P.; Kondarides, D. I. *J. Catal.* **2009**, *267*, 57–66.
21. Takeuchi, K.; Matsuzaki, T.; Arakawa, H.; Sugi, Y. *Appl. Catal.* **1985**, *18*, 325.
22. Marsuzzaki, T.; Hanaoka, T.; Takeuchi, K.; Sugi, Y. *Catal. Lett.* **1991**, *10*, 109.
23. Coutry, P.; Durant, D.; Freund, E.; Sugier, A. *J. Mol. Catal.* **1981**, *17*, 241.
24. Das, T. K.; Conner, W. A.; Li, J. L.; Jacobs, G.; Dry, M. E.; Davis, B. H. *Energy Fuels* **2005**, *19*, 1430.
25. Ma, W.; Jacobs, G.; Sparks, D. E.; Gnanamani, M. K.; Pendyala, V. R. R.; Yen, C. H.; Klettlinger, J. L. S.; Tomsik, T. M.; Davis, B. H. *Fuel* **2011**, *90*, 756–765.

Downloaded by DUKE UNIV on June 6, 2012 | http://pubs.acs.org
Publication Date (Web): November 29, 2011 | doi: 10.1021/bk-2011-1084.ch006

In Synthetic Liquids Production and Refining; de Klerk, A., et al.;
ACS Symposium Series; American Chemical Society: Washington, DC, 2011.

26. Espinoza, R. L.; Visagie, J. L.; van Berge, P. J.; Bolder, F. H. U.S. Patent 5733839, 1998.
27. Iglesia, E.; Reyes, S. C.; Madon, R. J.; Soled, S. L. *J. Catal.* **1991**, *129*, 238.
28. Anderson, R. B. In *Catalysis*; Emmett, P. H., Ed.; Van Nostrand-Reinhold: New York, 1956; Vol. 4, Chapters 2, 3.
29. Zimmerman, W. H.; Bukur, D. B. *Can. J. Chem. Eng.* **1990**, *68*, 292.
30. Borg, Ø.; Dietzel, P. D. C.; Spjelkavik, A. I.; Tvetenc, E. Z.; Walmsleyd, J. C.; Diplasb, S.; Eri, S.; Holmen, A.; Rytter, E. *J. Catal.* **2008**, *259*, 164.
31. Jacobs, G.; Graham, U. M.; Chenu, E.; Patterson, P. M.; Dozier, A.; Davis, B. H. *J. Catal.* **2005**, *229*, 499–512.
32. Lee, W. H.; Bartholomew, C. H. *J. Catal.* **1989**, *120*, 256.
33. Ma, W.; Jacobs, G.; Das, T. K.; Davis, B. H., submitted.
34. Davis, B. H. DOE Quarterly Report; Contract No. DE-AC22-91PC94055; March 1996.
35. Ma, W. P.; Kugler, E. L.; Dadyburjor, D. B. *Energy Fuels* **2007**, *21*, 1832.
36. Stenger, H. G., Jr.; Satterfield, C. N. *Ind. Eng. Chem. Process Des. Dev.* **1985**, *24*, 411–415.
37. Kul'ko, E. V.; Ivanova, A. S.; Budneva, A. A.; Paukshtis, E. A. *Kinet. Catal.* **2005**, *46* (1), 132–137. Translated from *Kinetika i Kataliz* **2005**, *46* (1), 141–146.
38. Dai, X.; Yu, C. *J. Nat. Gas Chem.* **2008**, *17*, 365–368.
39. de la Peña O'Shea, V. A.; Álvarez-Galván, M. C.; Campos-Martín, J. M.; Fierro, J. L. G. *Appl. Catal.*, *326* (227), 65–73.
40. Bhatelia, T.; Ma, W.; Jacobs, G.; Davis, B. H.; Bukur, D. B. *Chem. Eng. Trans.* **2011** *25*, PRES'11 Proceedings.
41. Huo, C.-F.; Li, Y.-W.; Wang, J.; Jiao, H. *J. Am. Chem. Soc.* **2009**, *131*, 14713–14721 9.
42. Chang, J.; Bai, L.; Teng, B-T.; Zhang, R-L.; Yang, J.; Xu, Y. Y.; Xiang, H. W.; Li, Y. W. *Chem. Eng. Sci.* **2007**, *62*, 4983–4991.
43. Baetzold, R. C.; Monnier, J. R. *J. Phys., Chem.* **1986**, *90*, 2944–2949.
44. Dulaurent, O.; Bianchi, D. *Appl. Catal.* **2000**, *196*, 271–280.
45. Yourdshahyan, Y.; Cooper, V. R.; Kolpak, A. M.; Rappe, A. M. *Proc. SPIE, Intern. Soc. Opt. Eng.* **2003**, *5223*, 223–231.
46. Gnanamani, M. K.; Ribeiro, M. C.; Ma, W.; Shafer, W. D.; Jacobs, G.; Graham, U. M.; Davis, B. H. *Appl. Catal.* **2011**, *393*, 17–23.
47. Das, T. K.; Zhan, X. D.; Li, J. L.; Jacobs, G.; Dry, M. E.; Davis, B. H. *Stud. Surf. Sci. Catal.* **2007**, *163*, 1430.

Downloaded by DUKE UNIV on June 6, 2012 | http://pubs.acs.org
Publication Date (Web): November 29, 2011 | doi: 10.1021/bk-2011-1084.ch006

Chapter 7

Evaluation of Promoted Mo Carbide Catalysts for Fischer-Tropsch Synthesis: Synthesis, Characterisation, and Time-on-Stream Behaviour

Dai-Viet N. Vo and Adesoji A. Adesina[*]

Reactor Engineering & Technology Group, School of Chemical Engineering,
The University of New South Wales, Sydney, Australia 2052
[*]Tel.: +61 2 9385 5268. Fax: +61 2 9385 5966.
E-mail: a.adesina@unsw.edu.au.

Downloaded by STANFORD UNIV GREEN LIBR on June 6, 2012 | http://pubs.acs.org
Publication Date (Web): November 29, 2011 | doi: 10.1021/bk-2011-1084.ch007

This chapter is a synopsis of recent investigations on the performance of promoted Mo carbide catalysts for Fischer-Tropsch reaction. The catalyst precursor, supported MoO_3 was carburized using optimal carburization conditions (H_2:C_3H_8=5:1 at 973 K). The transformation of the Mo oxide precursor was identified as a 2-step process involving the formation of oxycarbide intermediate phase. XRD measurements showed that promoted and unpromoted Mo carbide catalysts contained both α- and β-MoC_{1-x} phases. Weak and strong basic as well as acid sites were detected on the catalyst surface while strong basic site concentration increased with dopant addition. Although both CO and H_2 chemisorbed on Mo carbide catalysts, CO seemed to adsorb more strongly than H_2 as reflected by the higher CO uptake and heat of desorption. Promoter addition improved CO uptake on catalyst surface in the order; K>Na>Ce>unpromoted catalysts which also paralleled the trend for strong basic site concentration and CO consumption rate. Mo carbide catalysts displayed remarkably stable activity with time-on-stream after the initial drop within the first 10 hours unlike traditional FT catalysts. This behaviour was observed over a wide range of feed compositions and different temperatures. However, the addition of K, Na and Ce as promoters revealed that the K-promoted catalyst was the most superior in terms of CO consumption and olefin formation rates although total olefin-to-paraffin ratio was highest for unpromoted catalyst. Optimal CO consumption rate was observed at H_2 mole fraction of 0.67. Promoter improved chain growth probability by up to 37% and it increased with decreasing H_2 mole fraction. A new reaction-deactivation model was developed and used to describe the time-on-stream reaction data. The analysis showed that the Ce-promoted catalyst exhibited the least resistance to deactivation albeit at a relatively low activity level.

Downloaded by STANFORD UNIV GREEN LIBR on June 6, 2012 | http://pubs.acs.org
Publication Date (Web): November 29, 2011 | doi: 10.1021/bk-2011-1084.ch007

Introduction

Hydrocarbon synthesis via Fischer-Tropsch reaction is regarded as an economically viable alternative to clean fuels production in various gas-to-liquid (GTL) fuels processes. The depletion of petroleum resources and increasing price of crude oil have renewed interest in the Fischer-Tropsch synthesis (FTS). Although Fe- and Co-based catalysts have been used commercially for several decades, their activity and stability can be compromised by different confounding factors during Fischer-Tropsch reaction (*1*). Specifically, conventional FT catalysts (such as Co and Fe) may be deactivated with time-on-stream due to carbon deposition (*2*, *3*). Whilst noble metals (e.g. Pt and Rh) are resistant to deposited carbon, the high price and low availability make them inappropriate for industrial scale (*4*). Hence there is a need for an alternative catalyst system exhibiting high stability and FT activity. Following the discovery of Pt-like characteristics in the carbides of early transistion metals (*5*, *6*) Mo carbide has become an attractive catalyst for different catalytic reactions including NH_3 synthesis (*7*), hydrotreating reaction (*8*), alcohol production (*9*), CH_4 dry reforming (*10*) and particularly Fischer-Tropsch synthesis (*11–13*). Chen and Adesina found that FTS over Co-Mo oxide catalyst exhibited high olefin selectivity, carbon resistance as well as sulphur resilience (*14*) due to the formation of an oxycarbide phase during its activation with an H_2/CO gas mixtures. This suggests that the Mo carbide catalyst may be an alternative catalyst with favourable activity and stability for hydrocarbon production since sulphur compounds are common impurities in most of gas fields and coke formation is one of the primary causes of catalyst deactivation.

MoC_{1-x} ($0 \leq x < 1$) catalyst may be synthesized by several methods, namely; solution-derived precursor method (*15*, *16*), sonochemical synthesis (*17*), gas-phase reaction of volatile metal compounds and pyrolysis of metal precursors (*18*). Nonetheless, the most common method for producing Mo carbide catalyst with high surface area for catalytic reactions is the temperature-programmed reaction technique developed by Boudart and co-workers (*5*, *19*, *20*). In general, temperature-programmed carburization between MoO_3 precursor with gaseous agents, e.g. pure CO (*12*) or a mixture of CO/CO_2 (*18*), H_2/CO (*21*), and H_2/CH_4 (*22*) is preferred than solid carbon since utilization of pure carbon requires higher carburization temperature resulting in low catalyst surface area (*23*).

Downloaded by STANFORD UNIV GREEN LIBR on June 6, 2012 | http://pubs.acs.org
Publication Date (Web): November 29, 2011 | doi: 10.1021/bk-2011-1084.ch007

Carburization conditions and carburizing gases influenced the physicochemical properties, structure and catalytic performance of MoC_{1-x} catalyst.

A mixture of H_2/CH_4= 4:1 is commonly used to synthesize Mo carbide in many previous studies (*24*). However, methane is more difficult to activate than higher alkanes and requires higher reaction temperature. Different mixtures of H_2/hydrocarbon, viz; H_2/C_2H_2 (*25*), H_2/C_2H_6 (*26*, *27*) and H_2/C_4H_{10} (*27*) have been utilized to carburize Mo oxide to Mo carbide phase. The results showed that the mixture of H_2/higher hydrocarbons used as carbon source reduced carburization temperature and improved BET surface area of the resulting solid.

In our laboratory, a mixture of H_2/C_3H_8 has been used as carbon source for producing Mo carbide catalyst. In fact, Al_2O_3-supported Mo carbide catalyst with high surface area of 92-204 m^2 g_{cat}^{-1} was first synthesized from a metal sulphide precursor carburized with H_2/C_3H_8 (*28*). Partial pressure of carburizing gas affected the degree of carburization and amount of carbonaceous deposit on MoC_{1-x} catalyst surface while H_2 is responsible for removing free carbon (*29*). Indeed, H_2/C_3H_8=5 was reported as the optimal feed composition for maximum carburization rate (*29*). Therefore, it has been used as carburizing agent for Mo carbide synthesis in this study.

In Fischer-Tropsch synthesis, promoter addition played an important role in catalytic activity and selectivity as well as stability (*4*). Alkali oxides (K, Na, Li, etc) were often used as dopant for conventional FT catalysts since it facilitated CO chemisorption and enhanced chain growth probability as well as reaction rate (*30*, *31*). CeO_2-promoter improved metal dispersion and hence increased amount of active site for CO hydrogenation (*32*). Promotion with alkali and rare-earth oxides may also have beneficial effects on Mo carbide catalyst system. Additionally, until now, CO hydrogenation has not been investigated on promoted Mo carbide catalyst carburized with H_2/higher hydrocarbon. Thus, the objective of this study was to determine the influence of promoter type (K, Na and Ce) on the long-term attributes of the MoC_{1-x}/Al_2O_3 catalyst for Fischer-Tropsch synthesis as well as the physicochemical properties.

Experimental Details

Catalyst Preparation

Promoted Mo carbide catalysts were prepared by co-impregnation followed by temperature-programmed carburization method which was described in detail in previous studies (*28*, *29*). Calculated amounts of aqueous $(NH_4)_6Mo_7O_{24}.4H_2O$ solution and promoter precursors, namely K_2CO_3, Na_2CO_3, $Ce(NO_3)_3$ were co-impregnated with γ-alumina pretreated at 973 K (using a heating rate of 5 K min^{-1} from ambient temperature) for 6 h in air to ensure thermal stability. The resulting slurry was dried in an oven for 16 h at 403 K (and referenced as solid sample, D-CAT) and subsequently calcined at 773 K for 5 h in air. The calcined solid was then carburized in a computer-controlled fixed-bed reactor (6.25 mm OD stainless steel tube placed axially in an electrical furnace monitored by a Eurotherm temperature controller) with a mixture of $5H_2{:}1C_3H_8$ (accurately regulated at 50 ml min^{-1} by Brooks electronic mass flow controllers) as carbon source at 973 K for 2 h to produce 2%M-10%MoC_{1-x}/Al_2O_3 (M= K, Na or Ce). At the end of carburization process, the fixed-bed reactor was flushed with N_2 flow to cool down to FT reaction temperature before switching to syngas mixture for CO hydrogenation reaction.

The Fischer-Tropsch activity evaluation was carried out in the same fixed-bed reactor with H_2:CO = 2:1 at 453-503 K and atmospheric pressure for 120 h. Since CO_2, H_2, CO and H_2O could not be measured on the FID-GC (Shimadzu model GC 17A), the conversion, X, was computed as;

$$X = \frac{\text{total carbon in the formation rates of all hydrocarbon products measured}}{\text{total rate of CO fed}} \times 100\% \quad (1)$$

Fibre glass insulation was wrapped around the ends of the reactor to minimize heat loss and thus prevent product condensation. Additionally, the reactor exit line was maintained at 473 K by a heating tape to ensure that hydrocarbon products were kept in gas phase for online GC composition analysis. Gas hourly space velocity (GHSV) through the reactor was kept constant at 10 L g_{cat}^{-1} h^{-1} (typically 0.15 g catalyst bed with average particle size, d_p = 100 μm) for all runs to minimize transport intrusions. Reproducibility check performed for selected runs indicated an experimental error in the rate measurement of 1.8 to 4.7% depending on the hydrocarbon chain length.

Catalyst Characterisation

BET surface area, average pore volume, and pore diameter were measured at 77 K in a Quantachrome Autosorb-1 unit using N_2 physisorption. NH_3 temperature-programmed desorption (NH_3-TPD) and CO_2-TPD were conducted on a Micromeritics 2910 AutoChem unit with different ramping rates (5-30 K min^{-1}) up to 973 K to quantify acid-basic site concentration (NH_3 and CO_2 uptake respectively) and strength (heat of desorption). About 0.15 g of the MoC_{1-x} catalyst was employed with 10%NH_3 or 10%CO_2 diluted in inert gas as the adsorbing gas. The properties of active sites for CO and H_2 chemisorption on MoC_{1-x} catalyst surface were also determined from CO-TPD and H_2-TPD respectively using 10%CO and 10%H_2 in N_2. X-ray diffraction measurements for synthesized Mo carbide catalysts were performed on a Philips X'pert Pro MPD system with Ni-filtered Cu Kα (λ= 1.542 Å) at 45 kV and 40 mA.

Thermogravimetric analysis runs (temperature-programmed calcination and temperature-programmed carburization) were performed in a ThermoCahn TGA 2121 unit. For the temperature-programmed calcination of both promoted and unpromoted MoO_3/Al_2O_3 precursor, about 65 mg of the D-CAT solid sample was placed in a quartz boat was initially heated up to 393 K in argon and held at this temperature for 30 min to remove moisture and volatile compounds followed by ramping up to 973 K at 10 K min^{-1} in high purity air (50 ml min^{-1} at room temperature). The sample was kept isothermally at this temperature for 60 min before cooling down to 303 K.

Temperature-programmed carburization runs were conducted with a mixture of $5H_2/1C_3H_8$ (50 ml min^{-1}) from 303 to 973 K with different heating rates (5-20 K min^{-1}) to study the solid-state MoC_{1-x} formation kinetics.

Downloaded by STANFORD UNIV GREEN LIBR on June 6, 2012 | http://pubs.acs.org
Publication Date (Web): November 29, 2011 | doi: 10.1021/bk-2011-1084.ch007

Downloaded by STANFORD UNIV GREEN LIBR on June 6, 2012 | http://pubs.acs.org
Publication Date (Web): November 29, 2011 | doi: 10.1021/bk-2011-1084.ch007

Results and Discussion

Thermogravimetric Studies

Figure 1a shows that the temperature-programmed carburization of the unpromoted and promoted catalysts is characterized by the appearance of two major peaks (P1 and P2). Indeed, Figure 1b confirms that this behaviour is independent of the heating rate employed. The low temperature peak (P1) may be ascribed to the formation of oxycarbide phase while the second peak P2 located at high temperature belonged to carbide phase (*29*). Interestingly, carbide formation rate estimated from the derivative weight value seemed to improve with promoter addition in the order, Na > K > Ce > unpromoted catalyst as seen in Figure 1c. However, carbide formation temperature increased with K and Na promoter while Ce promoter exhibited a negligible effect on carburization temperature (cf. Figure 1a).

As seen in Figure 1b, the peak temperature shifted to higher temperature location with increasing heating rate. Since there was a linear relationship between carburization temperature and ramping rate as shown in Figure 1d, activation energy, E_a and pre-exponential factor, A, for the formation of oxycarbide and carbide phases may be estimated using the Kissinger equation (*33*, *34*) (cf. Figure 2) given as;

$$\ln\left(\frac{\beta}{T_P^2}\right) = \ln\left(\frac{AR}{E_a}\right) - \frac{E_a}{RT_P} \qquad (2)$$

where β is ramping rate (K min^{-1}) whilst T_p (K) and R are peak temperature and universal gas constant respectively.

As seen in Figure 3, activation energy for production of carbide phase was generally higher than that of oxycarbide phase for all catalysts. This would suggest similarity in the solid-state reaction mechanism irrespective of the presence and type of promoter. In fact, the 2-step transformation process implicates a topotactic reaction mechanism in which oxygen atoms in the MoO_3 lattice were substituted by carbon atoms (from the C_3H_8 molecule) with negligible structural disruption (*23*, *29*). The relatively low activation energy for the oxycarbide phase compared to the carbide phase suggests that the initial O → C atom exchange is more facile than the final replacement in the oxycarbide to the carbide phase.

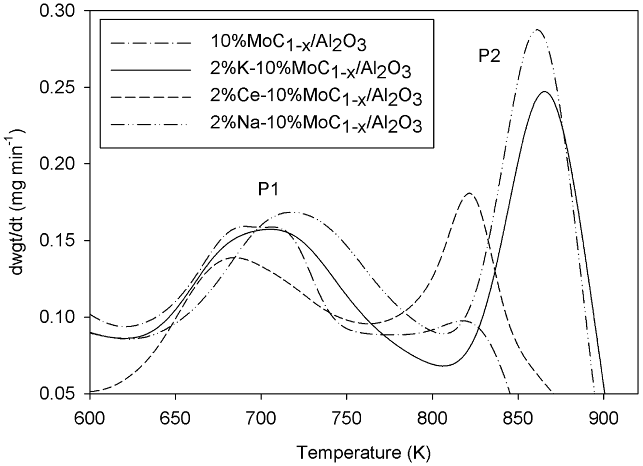

a) Influence of promoter on carburization temperature at 20 K min^{-1}

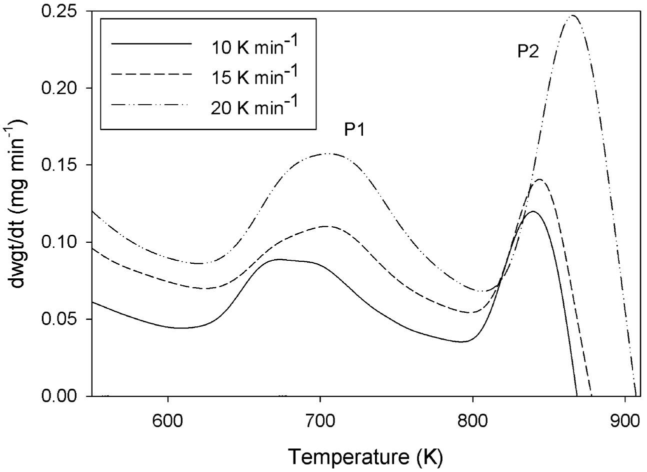

b) Temperature-programmed carburization of 2%K-10%MoC_{1-x}/Al_2O_3 catalyst

Downloaded by STANFORD UNIV GREEN LIBR on June 6, 2012 | http://pubs.acs.org
Publication Date (Web): November 29, 2011 | doi: 10.1021/bk-2011-1084.ch007

Downloaded by STANFORD UNIV GREEN LIBR on June 6, 2012 | http://pubs.acs.org
Publication Date (Web): November 29, 2011 | doi: 10.1021/bk-2011-1084.ch007

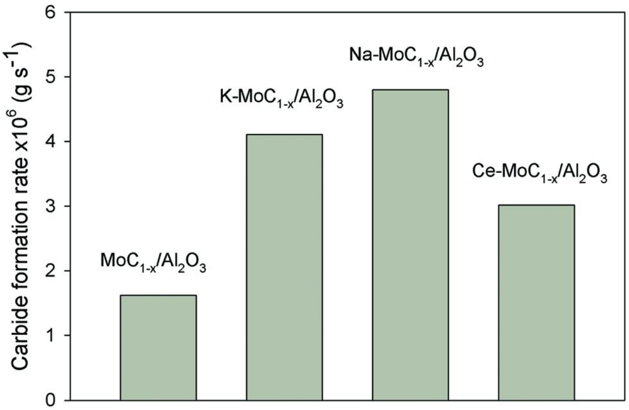

c) Effect of promoter addition on carbide formation rate using a heating rate of 20 K min^{-1}

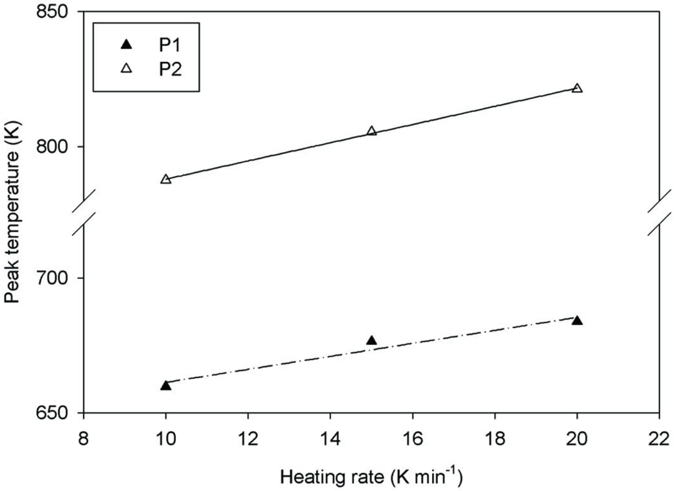

d) Effect of heating rate on peak temperature for 2%Ce-10%MoC_{1-x}/Al_2O_3 catalyst.

Figure 1. Temperature-programmed carburization of promoted and unpromoted Mo carbide catalysts.

Downloaded by STANFORD UNIV GREEN LIBR on June 6, 2012 | http://pubs.acs.org
Publication Date (Web): November 29, 2011 | doi: 10.1021/bk-2011-1084.ch007

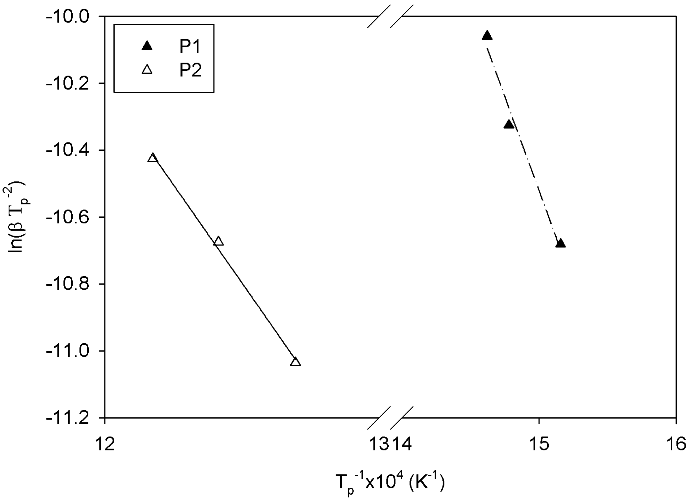

Figure 2. Estimation of activation energy for the production of oxycarbide and carbide phases for 2%Ce-10%MoC_{1-x}/Al_2O_3 catalyst.

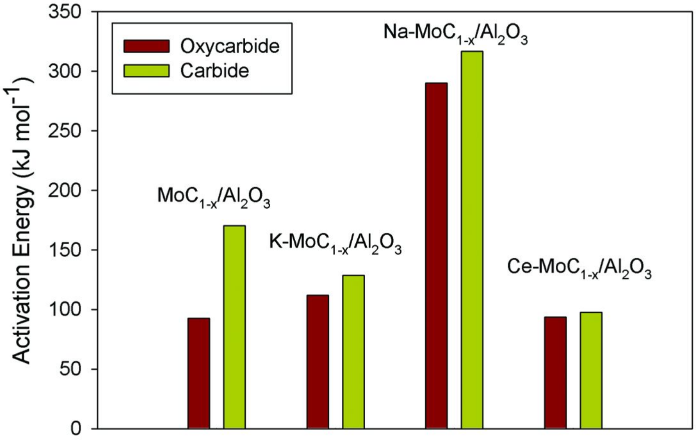

Figure 3. Activation energy for the formation of oxycarbide and carbide phases.

Physicochemical Properties of Mo Carbide Catalysts

X-ray diffraction measurements of both promoted and unpromoted Mo carbide catalysts are shown in Figure 4. XRD patterns were interpreted using the Joint Committee on Powder Diffraction Standards (JCPDS) database (*35*). The high intensity peaks located at $2\theta = 45.7^0$ and 66.7^0 belonged to γ-Al_2O_3 support as seen in all X-ray diffractograms. Both face-centered cubic (FCC) α-MoC_{1-x} and hexagonal closed packed (HCP) β-MoC_{1-x} were formed on unpromoted and promoted Mo carbide catalysts. The peaks located at $2\theta = 36.6^0$ and 61.3^0 corresponded to [111] and [220] α-MoC_{1-x}, respectively whilst β-MoC_{1-x} phase possessed typical peaks at *2θ*= 34.0^0 and 39.5^0. Since the peaks for MoO_3 (*2θ* = 23.4^0, 25.5^0 and 26.8^0) were not detected in any of the XRD patterns, MoO_3 precursor was most likely completely converted to α-MoC_{1-x} and β-MoC_{1-x} phases during carburization.

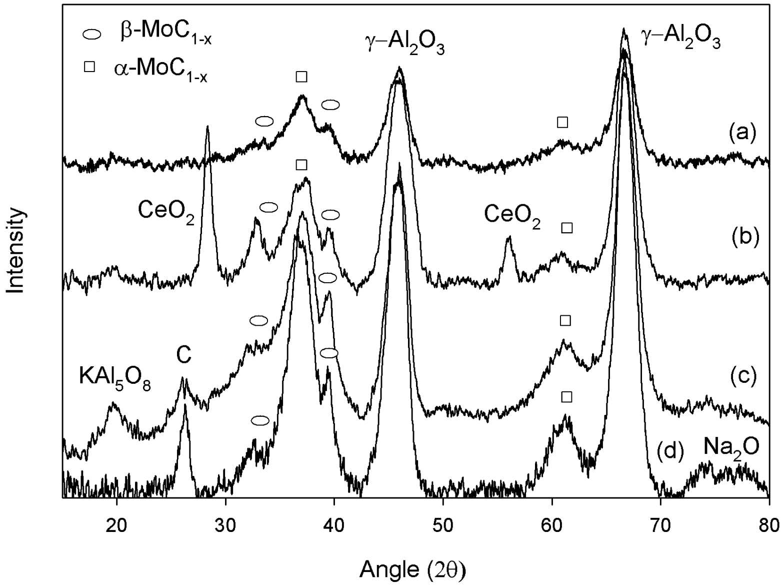

Figure 4. XRD patterns for both promoted and unpromoted Mo carbide catalysts. (a) 10%MoC_{1-x}/Al_2O_3, (b) 2%Ce-10%MoC_{1-x}/Al_2O_3, (c) 2%K-10%MoC_{1-x}/Al_2O_3, and (d) 2%Na-10%MoC_{1-x}/Al_2O_3.

As seen in XRD pattern of 2%Ce-10%MoC_{1-x}/Al_2O_3 catalyst (Figure 4b), the peaks found at 28.53^0 and 56.40^0 were ascribed to the corresponding [111] and [311] CeO_2 phases formed during calcination at 773 K in air;

$$4Ce(NO_3)_3 + O_2 \rightarrow 4CeO_2 + 6N_2O_5 \uparrow \quad (3)$$

whilst the KAl_5O_8 phase (*2θ*= 19.6^0) formed in K-doped catalyst (Figure 4c) may have arisen from;

$$K_2CO_3 \rightarrow K_2O + CO_2 \uparrow \quad (4)$$

and

$$K_2O + 5Al_2O_3 \rightarrow 2KAl_5O_8 \quad (5)$$

As seen in XRD pattern (d), the formation of Na_2O phase for 2%Na-10%MoC_{1-x}/Al_2O_3 may be due to the thermal decomposition of Na_2CO_3;

$$Na_2CO_3 \rightarrow Na_2O + CO_2 \uparrow \quad (6)$$

Downloaded by STANFORD UNIV GREEN LIBR on June 6, 2012 | http://pubs.acs.org
Publication Date (Web): November 29, 2011 | doi: 10.1021/bk-2011-1084.ch007

In Synthetic Liquids Production and Refining; de Klerk, A., et al.;
ACS Symposium Series; American Chemical Society: Washington, DC, 2011.

The average crystallite size for both promoted and unpromoted Mo carbide catalysts was estimated from Scherrer equation (*36*);

$$d_p = \frac{0.9\lambda}{B\cos\theta} \qquad (7)$$

where d_p being crystallite dimension whilst λ, B, and θ are wavelength, peak width and Bragg angle respectively. As seen in Table I, MoC_{1-x} particles possessed small average crystallite size of less than 10 nm in all cases suggesting that Mo carbide particles were well dispersed on support surface. Indeed, BET surface area of Mo carbide catalyst was higher than that of the corresponding Mo oxide and comparable to or better than the pure γ-Al_2O_3 support that has been similarly thermally treated. This observation further confirmed the fine dispersion of MoC_{1-x} particles on alumina support.

Table I. Physical properties of promoted MoC_{1-x}/Al_2O_3 catalysts

Catalysts	*Particle diameter (nm) from equation (7)*	*Average BET surface area (m^2 g^{-1})*	*Average pore volume (cm^3 g^{-1})*	*Average pore diameter (nm)*
Pure γ-Al_2O_3 support	–	179.3	0.68	15.2
10%MoO_3/Al_2O_3	–	182.4	0.55	12.0
2%K-10%MoO_3/Al_2O_3	–	167.7	0.63	15.3
2%Na-10%MoO_3/Al_2O_3	–	163.9	0.53	12.9
2%Ce-10%MoO_3/Al_2O_3	–	190.7	0.66	13.9
10%MoC_{1-x}/Al_2O_3	9.8	194.0	0.73	15.0
2%K-10%MoC_{1-x}/Al_2O_3	5.8	184.3	0.64	13.8
2%Na-10%MoC_{1-x}/Al_2O_3	7.4	177.4	0.60	13.5
2%Ce-10%MoC_{1-x}/Al_2O_3	6.7	210.4	0.76	10.5

The decomposition of promoter precursor to form metal oxides detected in X-ray diffractograms was also in agreement with results from temperature-programmed calcination as seen in Figure 5. The low temperature peak formed between 408 to 425 K for all spectra was assigned to the formation of Mo oxide;

$$(NH_4)_6Mo_7O_{24} \rightarrow 6NH_3\uparrow + 7MoO_3 + 3H_2O \qquad (8)$$

while the second peak located at 498 K (Ce-promoted), 469 K (K-doped), and 514 K (Na-doped catalyst) implicated the production of the corresponding CeO_2, K_2O, and Na_2O (cf. equations (3), (4), and (6)). As seen in Figure 5, the peak located at high calcination temperature of 643 K for K-doped catalyst may be due to the formation of KAl_5O_8 (cf. equation (5)).

In Synthetic Liquids Production and Refining; de Klerk, A., et al.;
ACS Symposium Series; American Chemical Society: Washington, DC, 2011.

Downloaded by STANFORD UNIV GREEN LIBR on June 6, 2012 | http://pubs.acs.org
Publication Date (Web): November 29, 2011 | doi: 10.1021/bk-2011-1084.ch007

Downloaded by STANFORD UNIV GREEN LIBR on June 6, 2012 | http://pubs.acs.org
Publication Date (Web): November 29, 2011 | doi: 10.1021/bk-2011-1084.ch007

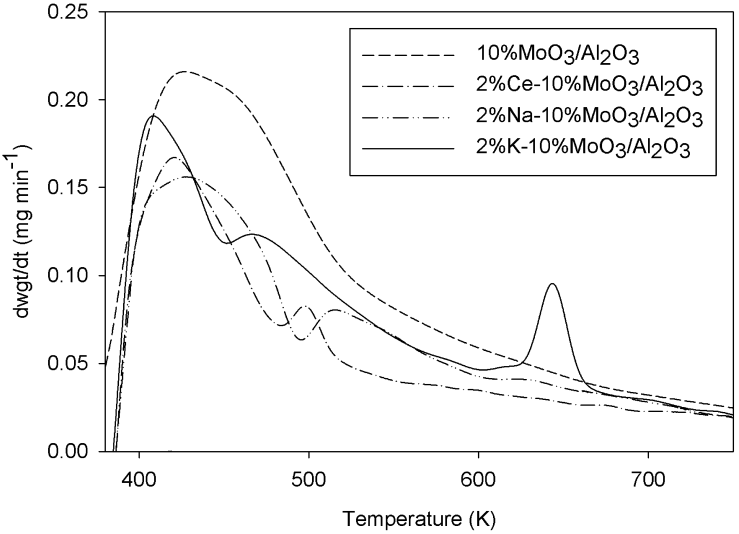

Figure 5. Temperature-programmed calcination for both promoted and unpromoted MoO_3/Al_2O_3.

NH_3 temperature-programmed desorption of Mo carbide catalyst is illustrated in Figure 6. It is apparent that two types of acid sites were present on all catalysts. The low temperature peak, P1, (located at 535-570 K) and the high temperature peak P2 (667-737 K) were ascribed to the formation of weak and strong acid centres. Interestingly, the weak acid site was also detected on calcined pure Al_2O_3 support (cf. Figure 7) suggesting that the second peak P2 (strong acid site) was probably formed by the production of the MoC_{1-x} phase. The strong acid centre may be due to an electron deficiency arising from co-ordinative unsaturated site in the MoC_{1-x} (surface vacant site). CO_2-TPD spectra (cf. Figure 8) show that supported Mo carbide catalysts possess both weak (P1) and strong (P2) basic centres although these sites were also present in the alumina support as seen in Figure 9.

The physicochemical properties of alumina-supported MoC_{1-x} catalysts are summarized in Table II. As may be expected, heat of desorption for strong acid and basic sites were higher than that of corresponding weak centres. However, the site concentration (NH_3 and CO_2 uptake) for strong acid or basic centres were not always greater than those of weak sites. Acid site concentration (NH_3-uptake) and NH_3 heat of desorption for strong acid site decreased with metal oxide addition in the order; unpromoted > Ce > Na > K while the trend for the basic site is K > Na > Ce > unpromoted. The error bands associated with individual parameter estimates are also given in the table.

In Synthetic Liquids Production and Refining; de Klerk, A., et al.;
ACS Symposium Series; American Chemical Society: Washington, DC, 2011.

Downloaded by STANFORD UNIV GREEN LIBR on June 6, 2012 | http://pubs.acs.org
Publication Date (Web): November 29, 2011 | doi: 10.1021/bk-2011-1084.ch007

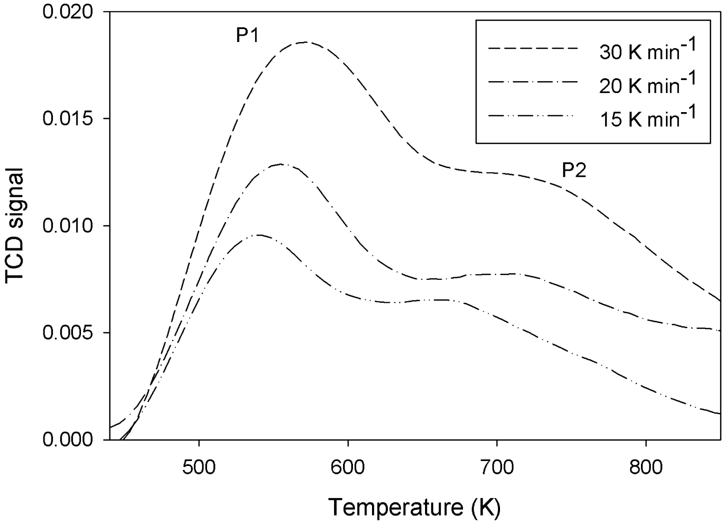

Figure 6. NH_3-TPD spectra for 2%Na-10%MoC_{1-x}/Al_2O_3 catalyst.

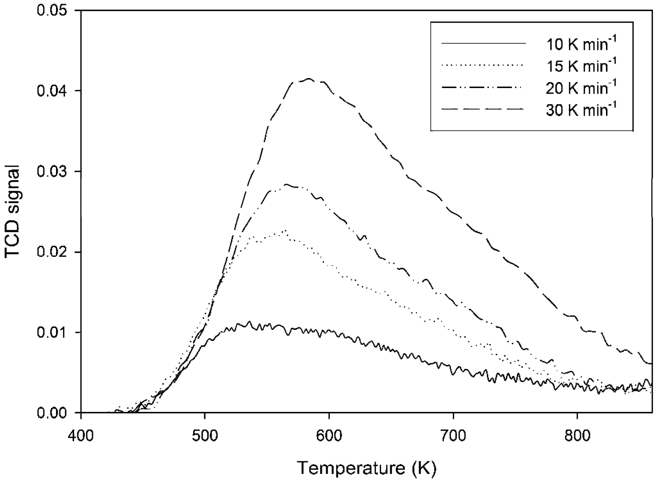

Figure 7. NH_3-TPD spectra for calcined pure Al_2O_3 support.

Downloaded by STANFORD UNIV GREEN LIBR on June 6, 2012 | http://pubs.acs.org
Publication Date (Web): November 29, 2011 | doi: 10.1021/bk-2011-1084.ch007

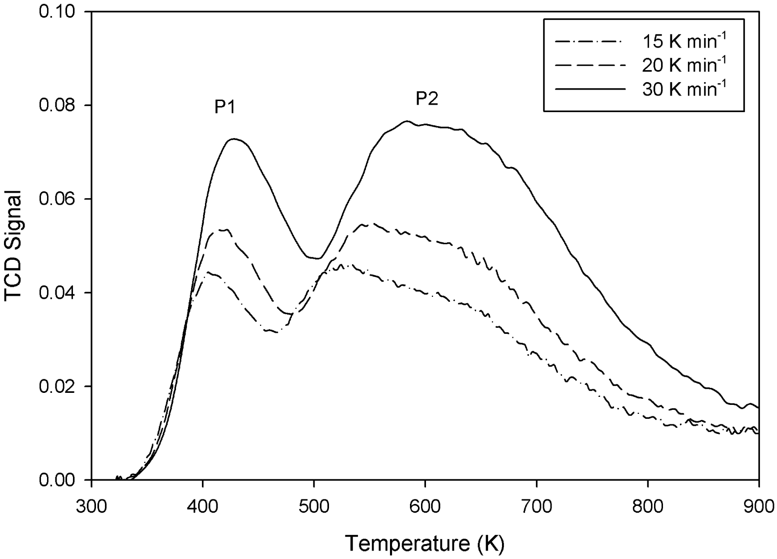

Figure 8. CO_2-TPD profiles for 2%Na-10%MoC_{1-x}/Al_2O_3 catalyst.

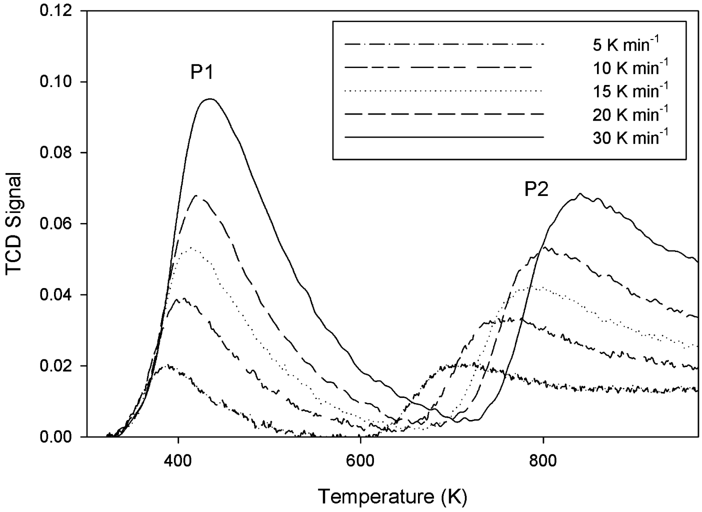

Figure 9. CO_2-TPD profiles for calcined pure Al_2O_3 support.

Downloaded by STANFORD UNIV GREEN LIBR on June 6, 2012 | http://pubs.acs.org
Publication Date (Web): November 29, 2011 | doi: 10.1021/bk-2011-1084.ch007

Table II. Physicochemical properties of Mo carbide catalysts

Catalyst	*Adsorbed CO_2, A_{CO_2} (mol CO_2 g_{cat}^{-1} × 10^5)*		*CO_2 heat of desorption (kJ mol^{-1})*		*Adsorbed NH_3, A_{NH_3} (mol NH_3 g_{cat}^{-1} × 10^5)*		*NH_3 heat of desorption (kJ mol^{-1})*		*Acidic:Basic site ratio*	
	Peak 1	*Peak 2*	*Peak 1*	*Peak 2*	*Peak 1*	*Peak 2*	*Peak 1*	*Peak 2*	*Peak 1*	*Peak 2*
MoC_{1-x}	2.72±0.018	0.62±0.004	34.91±0.228	137.07±0.894	12.90±0.084	22.20±0.145	37.91±0.247	320.12±2.088	4.74	35.81
K-MoC_{1-x}	0.43±0.007	4.27±0.067	56.96±0.890	150.24±2.347	7.56±0.118	6.39±0.100	39.92±0.624	60.04±0.938	17.58	1.50
Na-MoC_{1-x}	1.20±0.028	4.19±0.098	42.18±0.982	66.34±1.544	4.96±0.115	6.58±0.153	58.66±1.365	97.04±2.258	4.13	1.57
Ce-MoC_{1-x}	0.19±0.002	3.98±0.038	44.04±0.420	92.62±0.884	9.82±0.094	9.59±0.092	37.47±0.358	118.69±1.133	51.68	2.41
Calcined Al_2O_3	2.64±0.012	1.63±0.007	50.00±0.226	57.42±0.259	18.80±0.085	–	50.00±0.226	–	7.12	–

Downloaded by STANFORD UNIV GREEN LIBR on June 6, 2012 | http://pubs.acs.org
Publication Date (Web): November 29, 2011 | doi: 10.1021/bk-2011-1084.ch007

Although strong basic site was also observed on pure calcined Al_2O_3 support, the improvement of associated heat of desorption for this site on both promoted and unpromoted catalysts was probably due to the formation of MoC_{1-x} phase (*37*, *38*). Even so, as seen in Table II, the ratio of acid to basic site concentration for both weak (peak 1) and strong (peak 2) sites is higher than unity for all catalysts suggesting that Mo carbide catalyst surface was primarily acidic.

CO-TPD and H_2-TPD for the Na-promoted MoC_{1-x} catalyst are shown in Figures 10 and 11. It is evident that both H_2 and CO chemisorbed on Mo carbide catalyst surface. However, CO chemisorption seemed to be stronger than H_2 adsorption on carbide catalysts since the latter possesses lower heat of desorption and uptake (about 50% of these attributes for CO) as seen in Figures 12 and 13.

CO uptake decreased in the order, K > Na > Ce > unpromoted catalysts parallel to the trend for strong basic site concentration. The increase in CO chemisorption in the doped catalysts was ascribed to higher electron density arising from donation by the alkali promoter (*39*, *40*). Nevertheless, promoter addition also led to a reduction in H_2 uptake and heat of desorption (cf. Figures 12 and 13).

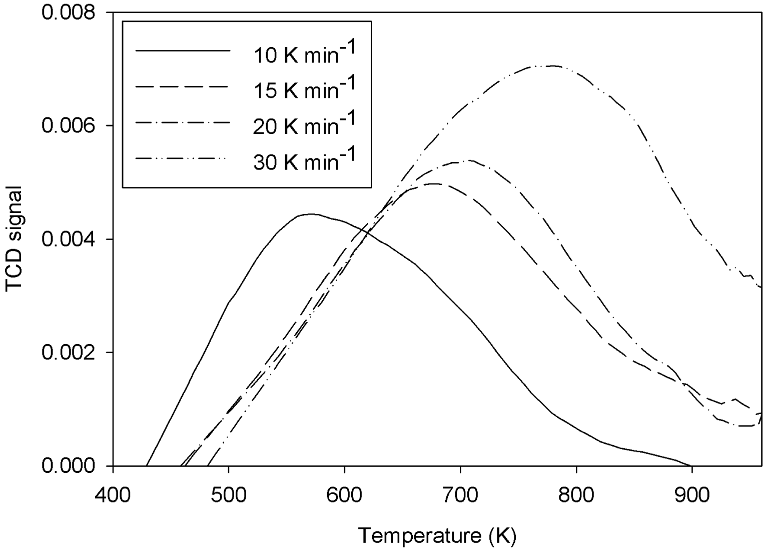

Figure 10. H_2-TPD spectrum of 2%Na-10%MoC_{1-x}/Al_2O_3 catalyst.

Downloaded by STANFORD UNIV GREEN LIBR on June 6, 2012 | http://pubs.acs.org
Publication Date (Web): November 29, 2011 | doi: 10.1021/bk-2011-1084.ch007

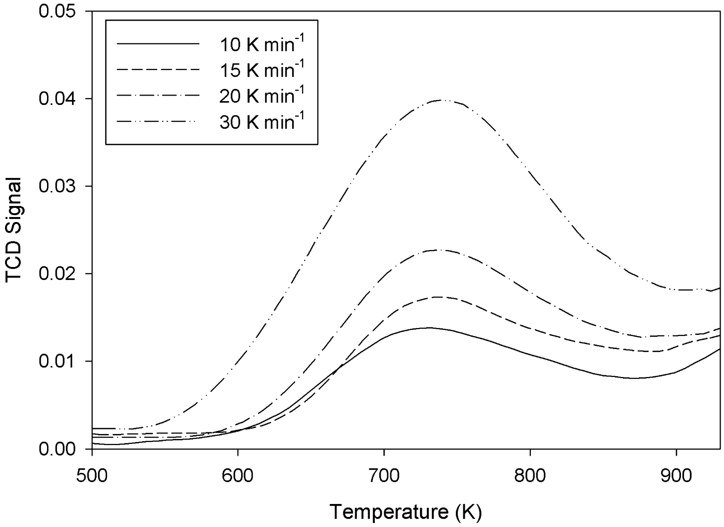

Figure 11. CO-TPD spectrum of 2%Na-10%MoC_{1-x}/Al_2O_3 catalyst.

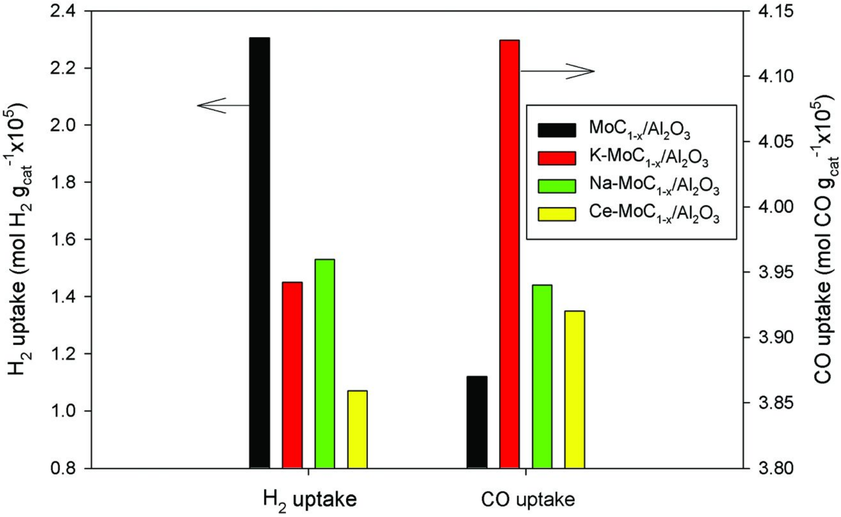

Figure 12. Influence of promoter on H_2 and CO chemisorption for Mo carbide catalysts.

Downloaded by STANFORD UNIV GREEN LIBR on June 6, 2012 | http://pubs.acs.org
Publication Date (Web): November 29, 2011 | doi: 10.1021/bk-2011-1084.ch007

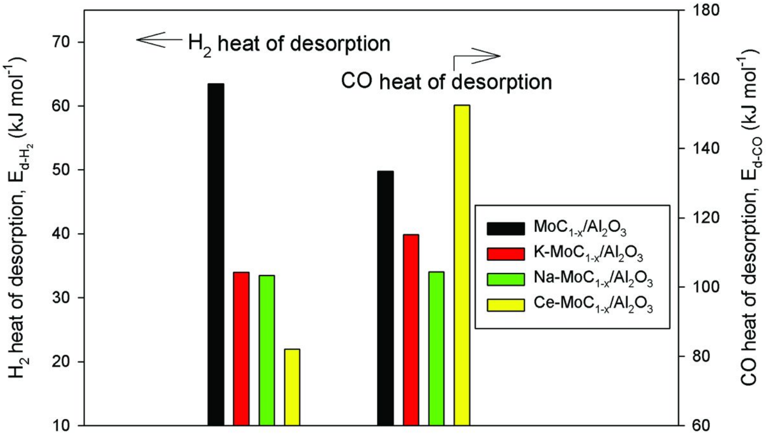

Figure 13. Effect of promoter on H_2 and CO heat of desorption for Mo carbide catalysts.

Fischer-Tropsch Evaluation

The CO consumption rate (measured in terms of the total carbon in the formation rate of all hydrocarbon products) with time-on-stream for the Mo carbide catalysts is depicted in Figure 14. The CO consumption rate, r_{CO} initially dropped with time before levelling off on all catalysts. Apart from the Na-doped catalyst, rate was essentially constant after about 10 hours on-stream. In particular, the Ce- and Na-promoted catalysts approached the same level of FT activity as the unpromoted sample after 2 days whilst r_{CO} on the K-promoted Mo catalyst was significantly higher (over twice) than other catalysts. Interestingly, CO consumption rate decreased in the order; K> Na > Ce> unpromoted catalyst identical to the trend seen for CO uptake suggesting that CO adsorption site may be the active site for Fischer-Tropsch synthesis over Mo carbide catalysts.

Since K-promoted Mo carbide catalyst exhibited optimal CO consumption rate, FTS runs with different H_2 mole fraction, y_{H_2} of 0.50-0.83 (i.e. H_2:CO ratio of 1:1 to 5:1) were further carried out over this catalyst. As seen in Figure 15, CO consumption rate increased with y_{H_2} and reached an optimum at 0.67. The optimal H_2 mole fraction for CO hydrogenation rate over Mo carbide catalysts appeared to be lower than that of Co and Fe catalysts where a maximum at $0.8 \leq y_{H_2} \leq 0.9$ has been previously reported (*4*, *41*). Mo carbide catalysts seemed to be more tolerant of higher CO partial pressure since the active site of MoC_{1-x} has an oxycarbide structure due to CO molecular adsorption (*42*, *43*). In fact, Furimsky (*8*) reported that since MoC_{1-x} catalysts possess both face-centred cubic and hexagonal closed packed structures, the carbon deficiency in these phases may accommodate the oxygen end of the adsorbed yielding an oxycarbide phase.

Downloaded by STANFORD UNIV GREEN LIBR on June 6, 2012 | http://pubs.acs.org
Publication Date (Web): November 29, 2011 | doi: 10.1021/bk-2011-1084.ch007

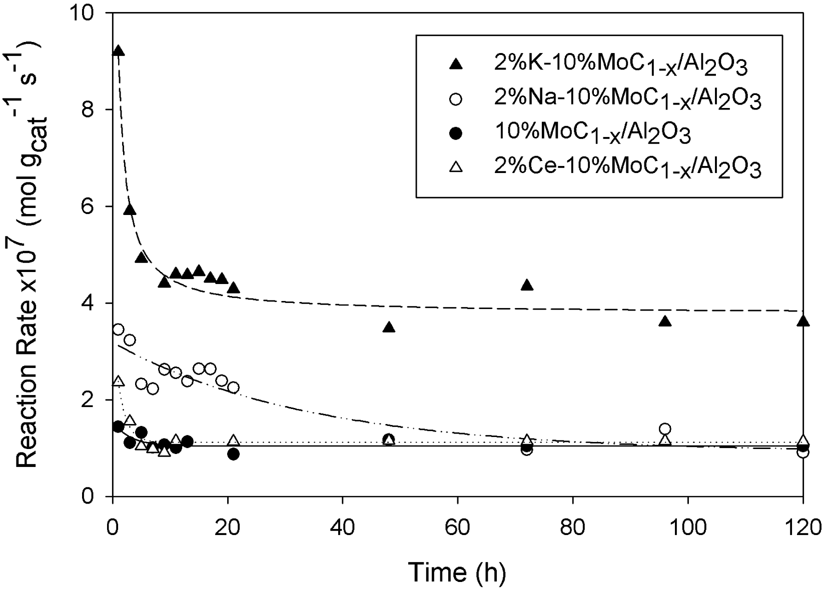

Figure 14. CO consumption rate with time-on-stream over Mo carbide catalysts at 473 K and H_2:CO=2:1.

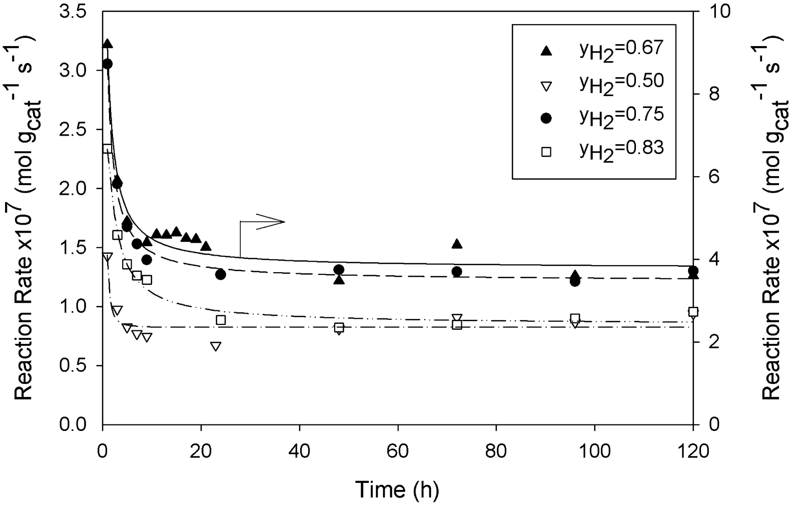

Figure 15. Effect of H_2 mole fraction on CO consumption rate with time-on-stream over K-promoted Mo carbide catalyst at 473 K.

Downloaded by STANFORD UNIV GREEN LIBR on June 6, 2012 | http://pubs.acs.org
Publication Date (Web): November 29, 2011 | doi: 10.1021/bk-2011-1084.ch007

Figure 16 shows the influence of reaction temperature on CO consumption rate for K-doped catalyst. Generally, FT activity was stable with time-on-stream at reaction temperature between 453-493 K. The CO reaction rate profiles conformed with the expected Arrhenius-dependency on temperature. Estimated activation energy, *E*, and pre-exponential factor, *A* for CO hydrogenation reaction over Mo carbide catalysts at steady-state are summarized in Table III. Activation energy varied from 52 to 68 kJ mol^{-1} for the promoted catalysts and was lower than that for the undoped catalyst.

Olefin formation rate, r_{olefin} for Mo carbide catalysts at 473 K with H_2:CO ratio of 2 is depicted in Figure 17. Olefin production profile exhibited a similar trend to CO reaction rate with time-on-stream. Although Na- and Ce-doped catalysts initially displayed higher olefin formation rate than unpromoted catalyst, the activities dropped to somewhat lower steady-state values than that for the unpromoted catalyst.

Furthermore, the unpromoted catalyst appeared to exhibit the highest level of total olefin-to-paraffin ratio (*TOPR*) as seen in Figure 18 while the Na-promoted catalyst gave the worst olefin selectivity. This would indicate that the promoters added either reduced the olefin termination rate or enhanced the paraffin termination rate. Since the latter involves higher concentration of surface hydrogen, it is more likely that promoter addition only encouraged stronger adsorption of olefin precursors but poorer desorption rates.

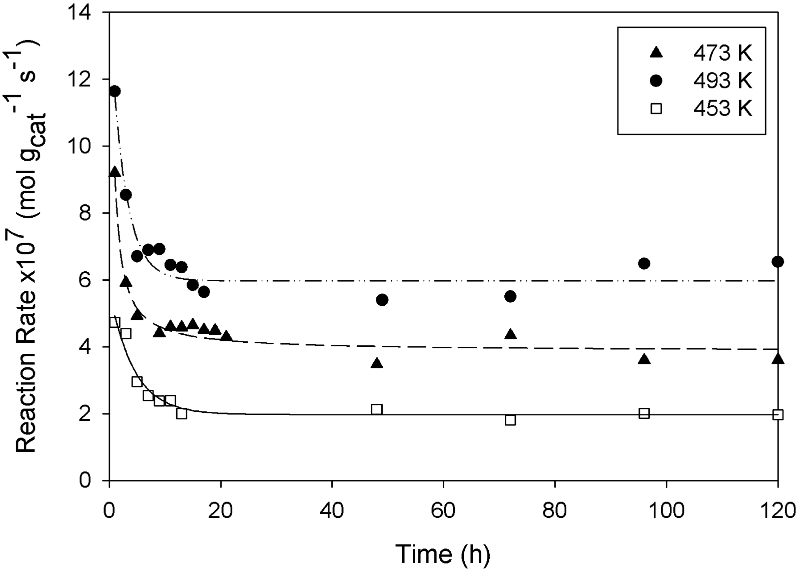

Figure 16. Effect of reaction temperature on CO consumption rate over 2%K-10%MoC_{1-x}/Al_2O_3 catalyst at H_2:CO=2:1.

Downloaded by STANFORD UNIV GREEN LIBR on June 6, 2012 | http://pubs.acs.org
Publication Date (Web): November 29, 2011 | doi: 10.1021/bk-2011-1084.ch007

Table III. Associated Arrhenius parameters for FTS over Mo carbide catalysts

Catalyst	*10%MoC$_{1-x}$/ Al$_2$O$_3$*	*K-MoC$_{1-x}$/ Al$_2$O$_3$*	*Na-MoC$_{1-x}$/ Al$_2$O$_3$*	*Ce-MoC$_{1-x}$/ Al$_2$O$_3$*
Activation energy, *E* (kJ mol^{-1})	68.0±0.44	52.2±0.82	60.5±1.41	57.1±0.55
Pre-exponential factor, *A* (s^{-1})	3.73±0.02	2.08±0.03×10^{-1}	4.75±0.11×10^{-1}	4.72±0.05×10^{-1}

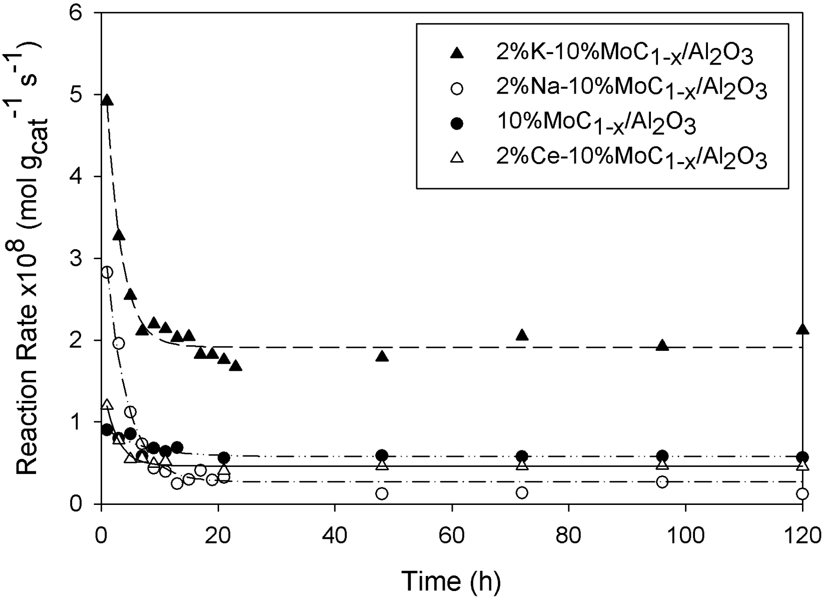

Figure 17. Olefin formation rate over Mo carbide catalysts with time-on-stream at 473 K and H$_2$:CO=2:1.

As seen in Figure 19, total olefin-to-paraffin ratio reached the steady state after 10 h following an initial drop for each reaction temperature. The increase in *TOPR* with temperature is in agreement with other studies (*44*, *45*). At a specified feed composition, the *TOPR* dependency on temperature is;

$$TOPR = \frac{r_{Olefin}}{r_{Paraffin}} = \frac{A_{Olefin}e^{\frac{-E_{olefin}}{RT}}}{A_{Paraffin}e^{\frac{-E_{Paraffin}}{RT}}} = \frac{A_{Olefin}}{A_{Paraffin}}e^{\frac{-\Delta E}{RT}} \qquad (9)$$

where $\Delta E = E_{Olefin} - E_{Paraffin}$, thus for $E_{Olefin} > E_{Paraffin}$, *TOPR* will increase with temperature. As may be seen from Table IV, ΔE varied between 57 to 142 (kJ

In Synthetic Liquids Production and Refining; de Klerk, A., et al.;
ACS Symposium Series; American Chemical Society: Washington, DC, 2011.

mol^{-1}) for the Mo carbide catalysts. The activation energy difference between olefin and paraffin, ΔE, was highest for Na but lowest for K promoter.

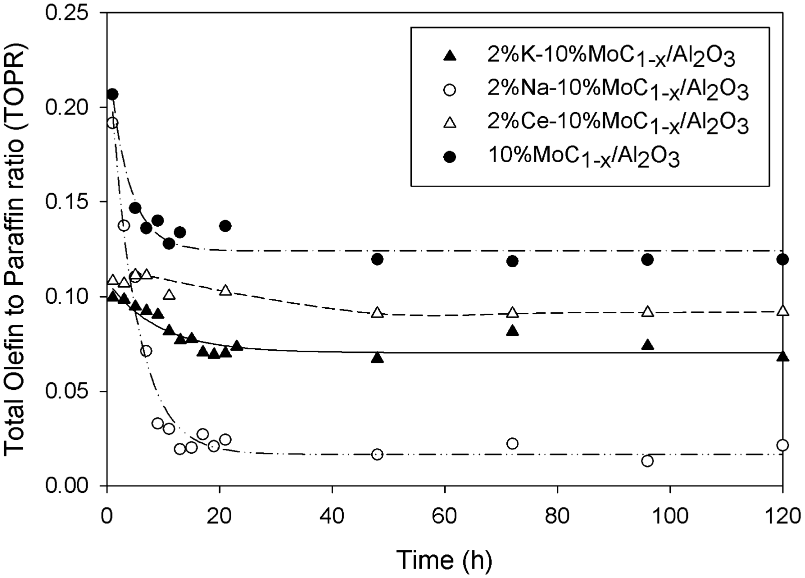

Figure 18. Time-on-stream behaviour of total olefin-to-paraffin ratio (TOPR) over Mo carbide catalyst system at 473 K and H_2:CO=2:1.

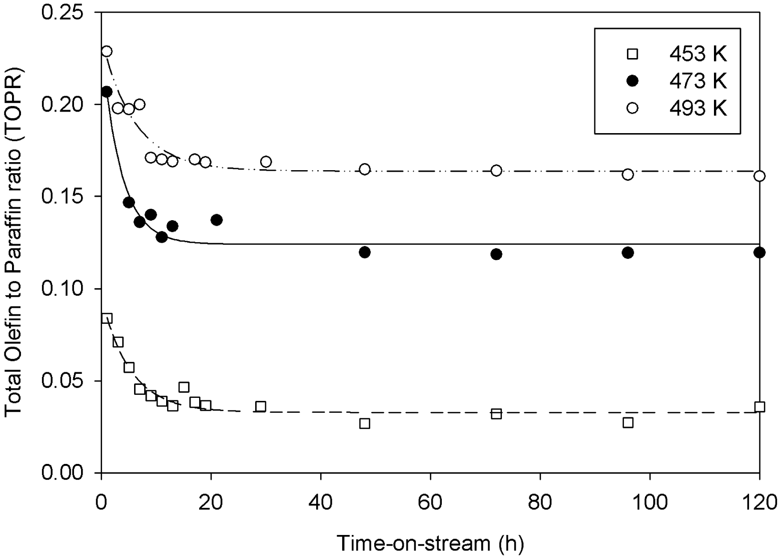

Figure 19. Effect of reaction temperature on total olefin-to-paraffin ratio (TOPR) with respect to time-on-stream over 10%MoC_{1-x}/Al_2O_3 catalyst at H_2:CO=2:1.

Downloaded by STANFORD UNIV GREEN LIBR on June 6, 2012 | http://pubs.acs.org
Publication Date (Web): November 29, 2011 | doi: 10.1021/bk-2011-1084.ch007

Table IV. Estimated activation energy difference for olefin and paraffin formation during FTS over Mo carbide catalysts

Catalyst	$10\%MoC_{1-x}/Al_2O_3$	$2\%K\text{-}10\%MoC_{1-x}/Al_2O_3$	$2\%Na\text{-}10\%MoC_{1-x}/Al_2O_3$	$2\%Ce\text{-}10\%MoC_{1-x}/Al_2O_3$
$\Delta E = E_{Olefin} - E_{Paraffin}$ (kJ mol^{-1})	65.9±0.43	57.5±0.90	142.0±3.30	76.2±0.73
$\frac{A_{Olefin}}{A_{Paraffin}}$	$1.41\pm0.01\times10^{6}$	$1.47\pm0.02\times10^{5}$	$7.83\pm0.18\times10^{13}$	$2.02\pm0.02\times10^{7}$

Downloaded by STANFORD UNIV GREEN LIBR on June 6, 2012 | http://pubs.acs.org
Publication Date (Web): November 29, 2011 | doi: 10.1021/bk-2011-1084.ch007

The effect of feed composition on total olefin-to-paraffin ratio over K-promoted MoC_{1-x}/Al_2O_3 catalyst is depicted in Figure 20. Interestingly, *TOPR* also initially dropped with time-on-stream and appeared to be stable after 10 h for different feed compositions. The optimal y_{H_2} for *TOPR* was observed at 0.67. However, the decrease in total olefin-to-paraffin ratio with increasing H_2 mole fraction beyond 0.67 was probably due to higher termination rate to paraffins than formation rate of olefins at high y_{H_2} values (*29*).

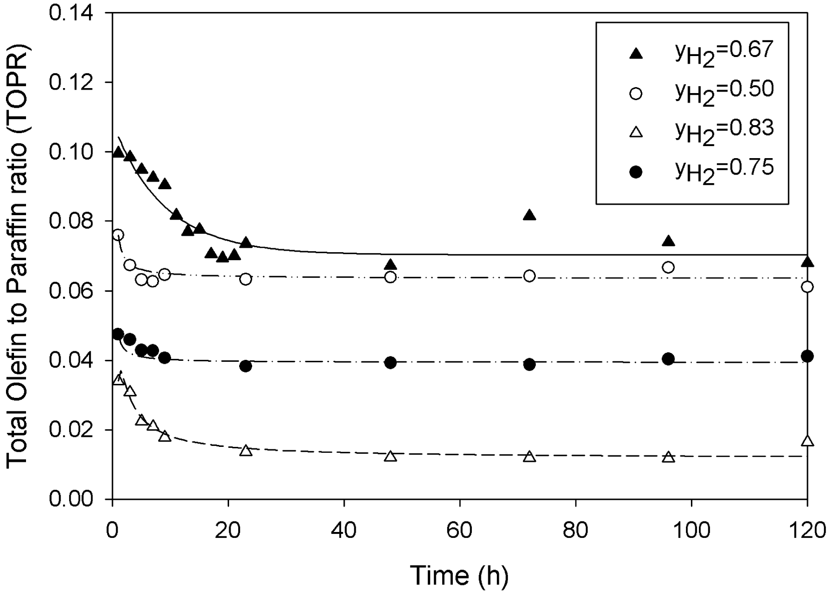

Figure 20. Influence of H_2 mole fraction on total olefin-to-paraffin ratio (TOPR)with time-on-stream over K-promoted Mo carbide catalyst at 473 K.

Product distribution in Fischer-Tropsch synthesis generally follows a polymerization scheme. Chain growth probability, α may be estimated from Anderson-Schulz-Flory model (*4*) given as;

$$r_n = k_{ASF}(1-\alpha)^2\alpha^{n-1} \tag{10}$$

where r_n is hydrocarbon formation rate with carbon number, n whilst k_{ASF} is Anderson-Schulz-Flory constant. As seen in Figure 21, chain growth factor for both promoted and unpromoted Mo carbide catalysts increased with time-on-stream but attained a maximum (at different times depending on catalyst type) followed by a gradual drop suggesting that long surface hydrocarbon precursors were now probably too big to participate in further chain growth as a result of slower propagation rate. Previous studies of FTS on Mo carbide catalyst synthesized using H_2/CH_4 have also reported relatively low α value (≤ 0.4) (*13*, *46*, *47*). It is apparent that promoter addition improved chain growth factor by up to 37% as seen in Figure 21.

Downloaded by STANFORD UNIV GREEN LIBR on June 6, 2012 | http://pubs.acs.org
Publication Date (Web): November 29, 2011 | doi: 10.1021/bk-2011-1084.ch007

Downloaded by STANFORD UNIV GREEN LIBR on June 6, 2012 | http://pubs.acs.org
Publication Date (Web): November 29, 2011 | doi: 10.1021/bk-2011-1084.ch007

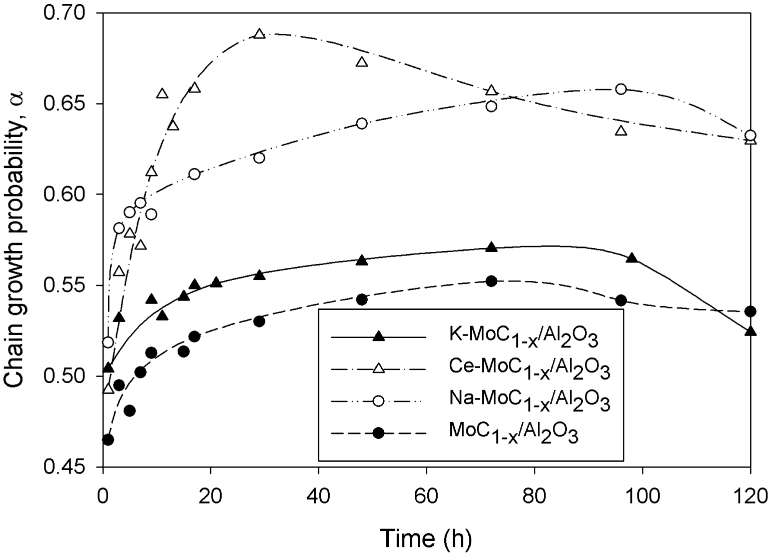

Figure 21. Influence of time-on-stream on chain growth probability over Mo carbide catalysts at 473 K and H_2:CO=2:1.

The influence of reaction temperature on chain growth factor over Mo carbide catalyst is shown in Figure 22. Chain growth probability increased with reaction temperature and exhibited a maximum at 493 K. However, the decrease in α value beyond 493 K was probably due to higher surface hydrocarbon cracking compared to propagation beyond this temperature.

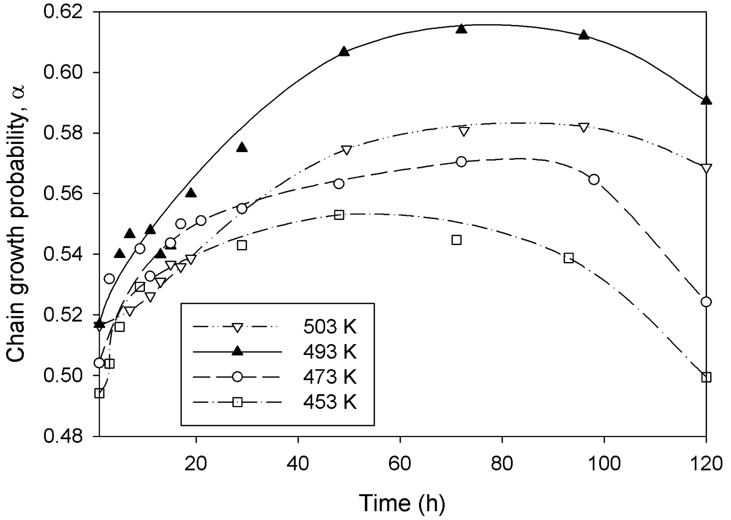

Figure 22. Effect of time-on-stream on chain growth factor over 2%K-10%MoC_{1-x}/Al_2O_3 catalyst at H_2:CO=2:1.

Downloaded by STANFORD UNIV GREEN LIBR on June 6, 2012 | http://pubs.acs.org
Publication Date (Web): November 29, 2011 | doi: 10.1021/bk-2011-1084.ch007

The influence of feed composition on chain growth probability over K-promoted Mo carbide catalyst at 473 K is illustrated in Figure 23. Chain growth factor also increased with time-on-stream for all feed compositions. The increase in chain growth probability with decreasing y_{H_2} is consistent with other studies on traditional FT catalysts (*44*, *45*, *48*).

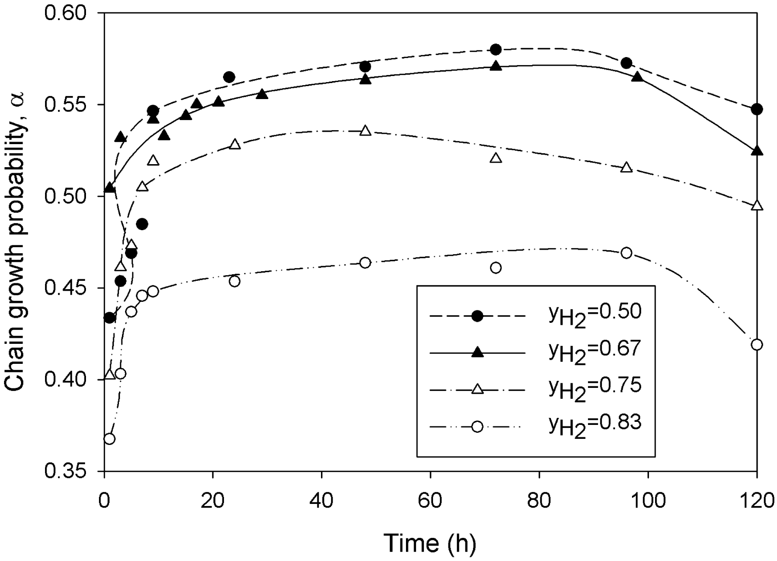

Figure 23. Effect of H_2 mole fraction on chain growth factor over 2%K-10%MoC$_{1-x}$/Al$_2$O$_3$ catalyst at 473 K.

Activity decay with time-on-stream during FT reaction may be due to different causes such as water, carbon and feed impurities (*49*, *50*). For the system where deactivation is most likely due to carbon-deposition, the decay behaviour may be described by;

$$-\frac{da}{dt} = k_d a^m \tag{11}$$

where *a* is the ratio of reaction rate at specified time, *t*, to that of the freshly-prepared catalyst under same reaction conditions. k_d is deactivation coefficient and m is an empirical parameter, indicative of the nature of the deactivation mechanism. Assuming a power-law kinetic model for the actual FT reaction, namely;

$$-r_{CO} = k'a(t)C_{CO}^{n} \tag{12}$$

with *n* as reaction order with respect to CO concentration and *k'*, is the pseudo-rate constant, then equations for reaction-deactivation model may be derived for different reactor types as detailed in Hardiman *et al.* (*51*). In this case, the experimental reactor functioned as a well-mixed flow system, thus, the relevant time-on-stream conversion, *X*, behaviour may be given as (*52*);

$$\frac{X}{(1-X)^n} = k'\boldsymbol{\tau}'C_{A_0}^{n-1}[1+(m-1)k_d t]^{\frac{1}{1-m}} \tag{13}$$

for $m \neq 1$ (the case for $m = 1$ i.e. exponential activity decay law has been given by Hardiman *et al.* (*51*)). Nonlinear regression analysis of the conversion history data for each catalyst yielded the parameter estimates for k', k_d, m and n as provided in Table V.

Table V. Parameter estimates of equation (4) at 473 K

Catalyst	k' ($mol^2\ g_{cat}^{-1}\ s^{-1}\ lit^{-1}$)	k_d (s^{-1})	*m*
$10\%MoC_{1-x}/Al_2O_3$	$3.24\pm0.02\times10^{-10}$	2.73±0.02	7.7±0.05
$2\%K\text{-}10\%MoC_{1-x}/Al_2O_3$	$3.22\pm0.05\times10^{-8}$	8.45±0.13	5.7±0.09
$2\%Na\text{-}10\%MoC_{1-x}/Al_2O_3$	$2.41\pm0.06\times10^{-9}$	3.82±0.09	6.7±0.16
$2\%Ce\text{-}10\%MoC_{1-x}/Al_2O_3$	$3.10\pm0.03\times10^{-5}$	2.66±0.03	3.4±0.03

*The reaction order, $n = -1$, in all cases.

It is apparent from these estimates that the deactivation mechanism was a function of the promoter type, as indicated by different *m*-values. Significantly, m decreased (from *m*=7.7 for the unpromoted catalyst) with promoter addition (*m*=3.4 for Ce-catalyst). Since small k_d value is desirable, it is evident that the ceria-promoted catalyst with the least k_d seems to be the most resistant to deactivation. The superior longevity and stability (albeit at relatively low activity level) of the Ce-promoted catalyst may be due to the higher water adsorption capacity of CeO_2 compared to other alkali promoters (*53*). Water is a co-product of the FTS. The comparatively lower hydrocarbon synthesis rate of the Ce-catalyst may, however, be attributed to its low H_2 chemisorptive properties (cf. Figures 12 and 13). This proposition implicates water as a possible deactivating agent during FTS.

Post-Reaction Characterisation

Figure 24 shows the effect of reaction temperature on BET surface area of post-reaction Mo carbide catalysts. Generally, surface area of Mo carbide catalysts after reaction was lower than that of fresh catalysts. Additionally, surface area of spent catalysts reduced exponentially with reaction temperature for both promoted and unpromoted MoC_{1-x} catalysts. This was probably due to the formation of deposited carbon blocking the catalyst pores. In fact, the average pore volume for K- (0.59 $cm^3\ g^{-1}$), Na- (0.51 $cm^3\ g^{-1}$), Ce-promoted (0.51 $cm^3\ g^{-1}$) and unpromoted (0.56 $cm^3\ g^{-1}$) catalysts after reaction was inferior to that of corresponding fresh Mo carbide as seen in Table I.

Downloaded by STANFORD UNIV GREEN LIBR on June 6, 2012 | http://pubs.acs.org
Publication Date (Web): November 29, 2011 | doi: 10.1021/bk-2011-1084.ch007

Downloaded by STANFORD UNIV GREEN LIBR on June 6, 2012 | http://pubs.acs.org
Publication Date (Web): November 29, 2011 | doi: 10.1021/bk-2011-1084.ch007

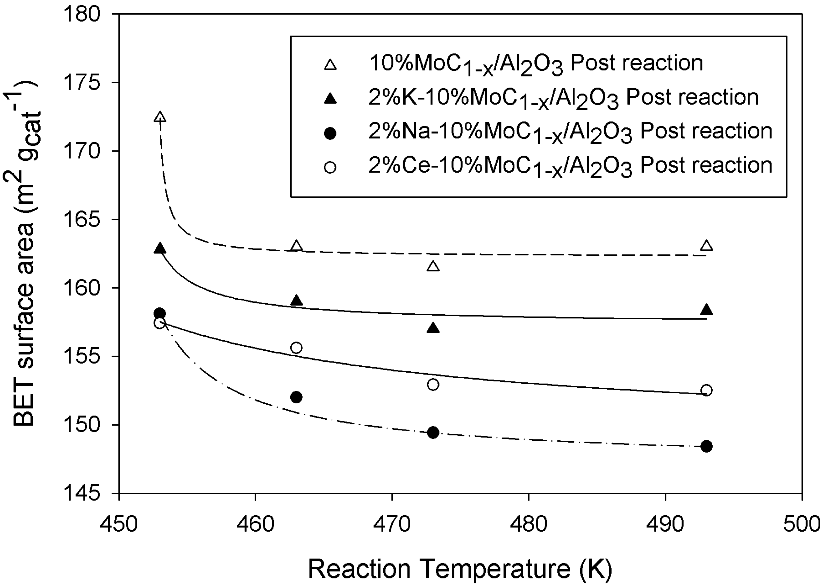

Figure 24. Influence of reaction temperature on BET surface area of both promoted and unpromoted Mo carbide catalysts after FT synthesis.

Conclusions

Temperature-programmed carburization between different promoted MoO_3/Al_2O_3 precursors with H_2/C_3H_8 has been carried out to produce both promoted and unpromoted Mo carbide catalysts possessing high surface area of 177 - 210 m^2 g_{cat}^{-1}. Both α and β-MoC_{1-x} particles were finely dispersed on Al_2O_3 support surface with small particle diameter of less than 10 nm. MoO_3/Al_2O_3 precursor was transformed completely to final carbide phase via the formation of an intermediate oxycarbide form during temperature-programmed carburization. Undoped and promoted Mo carbide catalysts have both acid and basic centres, nevertheless, the acid:basic site ratio on catalyst surface dropped rapidly from about 36 (in the unpromoted Mo carbide) to between 1.5 to 2.5 in the promoted system. Promoter addition improved strong basic site concentration in the order; K>Na>Ce>unpromoted catalyst. Although H_2 chemisorbed on supported MoC_{1-x} surface, it appeared to be inferior to CO adsorption with higher uptake and heat of desorption. CO chemisorption was also enhanced with doped catalysts in the order; K>Na>Ce>undoped parallel to the trend for CO consumption rate suggesting that CO adsorption site is active site for FTS over MoC_{1-x} catalysts. CO reaction rate over MoC_{1-x}/Al_2O_3 catalysts was stable with time-on-stream and K-promoted catalyst exhibited an optimum for FT activity and olefin formation rate while unpromoted catalyst performed highest olefin selectivity. CO consumption rate increased with H_2 mole fraction and reached a maximum at $y_{H_2} = 0.67$. Chain growth probability increased with time followed by a gradual drop beyond 72 h and α value improved by up to 37% for promoted catalysts. BET surface area of catalyst after reaction reduced exponentially with reaction temperature probably due to pore blockage with carbon deposition. Time-on-stream rate data revealed that the Mo carbide catalysts were generally stable after about 10 hours online. A reaction-deactivation model was developed to capture the TOS data revealed that while K-promoted catalyst exhibited the highest level of hydrocarbon synthesis activity, the Ce-containing catalyst showed the greatest resistance to long-term deactivation.

Acknowledgments

The authors appreciate financial support from the Australian Research Council (ARC).

Appendix: Deactivation Model Derivation

Activity decay may be given as;

$$-\frac{da}{dt} = k_d a^m \tag{14}$$

From equation (14), if m=1, the catalyst activity, *a*, may be derived as;

$$a = e^{-k_d t} \text{ (Exponential law)} \tag{15}$$

In case, m≠1, integration of equation (14) may give;

$$a = [1 + (m-1)k_d t]^{\frac{1}{1-m}} \tag{16}$$

CO reaction rate may be expressed as;

$$-r_{CO} = k' a(t) C_{A_0}^n \tag{17}$$

For a differential fixed-bed reactor;

$$\frac{W}{F_{A_0}} = \frac{X}{-r_{CO}} \tag{18}$$

Substituting equations (16) and (17) into equation (18) provides;

$$\frac{W}{F_{A_o}} = \frac{X}{k'[1 + (m-1)k_d t]^{\frac{1}{1-m}} C_{A_0}^n (1-X)^n} \tag{19}$$

In Synthetic Liquids Production and Refining; de Klerk, A., et al.;
ACS Symposium Series; American Chemical Society: Washington, DC, 2011.

Downloaded by STANFORD UNIV GREEN LIBR on June 6, 2012 | http://pubs.acs.org
Publication Date (Web): November 29, 2011 | doi: 10.1021/bk-2011-1084.ch007

Since space time, τ' is defined as $\tau' = \dfrac{WC_{A_0}}{F_{A_0}}$, equation (19) may be rearranged as;

$$\frac{X}{(1-X)^n} = k'\boldsymbol{\tau}'C_{A_0}^{n-1}[1+(m-1)k_d t]^{\frac{1}{1-m}} \tag{20}$$

References

1. Eliason, S. A.; Bartholomew, C. H. *Appl. Catal., A* **1999**, *186*, 229–243.
2. Saib, A. M.; Moodley, D. J.; Ciobica, I. M.; Hauman, M. M.; Sigwebela, B. H.; Weststrate, C. J.; Niemantsverdriet, J. W.; Van de Loosdrecht, J. *Catal. Today* **2010**, *154*, 271–282.
3. Tsakoumis, N. E.; Rønning, M.; Borg, Ø.; Rytter, E.; Holmen, A. *Catal. Today* **2010**, *154*, 162–182.
4. Anderson, R. B. *The Fischer-Tropsch Synthesis*; Academic Press: New York, 1984.
5. Levy, R. L.; Boudart, M. *Science* **1973**, *181*, 547–549.
6. Sinfelt, J. H.; Yates, D. J. C. *Nature (London), Phys. Sci.* **1971**, *229*, 27–28.
7. Kojima, R.; Aika, K.-i. *Appl. Catal., A* **2001**, *219*, 141–147.
8. Furimsky, E. *Appl. Catal., A* **2003**, *240*, 1–28.
9. Xiang, M.; Li, D.; Li, W.; Zhong, B.; Sun, Y. *Catal. Commun.* **2007**, *8*, 513–518.
10. LaMont, D. C.; Gilligan, A. J.; Darujati, A. R. S.; Chellappa, A. S.; Thomson, W. J. *Appl. Catal., A* **2003**, *255*, 239–253.
11. Ranhotra, G. S.; Bell, A. T.; Reimer, J. A. *J. Catal.* **1987**, *108*, 40–49.
12. Saito, M.; Anderson, R. B. *J. Catal.* **1980**, *63*, 438–446.
13. Griboval-Constant, A.; Giraudon, J.-M.; Leclercq, G.; Leclercq, L. *Appl. Catal., A* **2004**, *260*, 35–45.
14. Chen, H.; Adesina, A. A. *Appl. Catal., A* **1994**, *112*, 87–103.
15. Patel, M.; Subrahmanyam, J. *Mater. Res. Bull.* **2008**, *43*, 2036–2041.
16. Preiss, H.; Meyer, B.; Olschewski, C. *J. Mater. Sci.* **1998**, *33*, 713–722.
17. Hyeon, T.; Fang, M.; Suslick, K. S. *J. Am. Chem. Soc.* **1996**, *118*, 5492–5493.
18. Oyama, S. T. *Introduction to the Chemistry of Transition Metal Carbides and Nitrides*; Blackie Academic & Professional Publisher: New York, 1996.
19. Lee, J. S.; Oyama, S. T.; Boudart, M. *J. Catal.* **1987**, *106*, 125–133.
20. Lee, J. S.; Volpe, L.; Ribeiro, F. H.; Boudart, M. *J. Catal.* **1988**, *112*, 44–53.
21. Li, S.; Kim, W. B.; Lee, J. S. *Chem. Mater.* **1998**, *10*, 1853–1862.
22. Claridge, J. B.; York, A. P. E.; Brungs, A. J.; Green, M. L. H. *Chem. Mater.* **2000**, *12*, 132–142.
23. Oyama, S. T. *Catal. Today* **1992**, *15*, 179–200.
24. Kim, H. -G.; Lee, K. H.; Lee, J. S. *Res. Chem. Intermed.* **2000**, *26*, 427–443.
25. Xiao, T.; Wang, H.; Da, J.; Coleman, K. S.; Green, M. L. H. *J. Catal.* **2002**, *211*, 183–191.

Downloaded by STANFORD UNIV GREEN LIBR on June 6, 2012 | http://pubs.acs.org
Publication Date (Web): November 29, 2011 | doi: 10.1021/bk-2011-1084.ch007

26. Hanif, A.; Xiao, T.; York, A. P. E.; Sloan, J.; Green, M. L. H. *Chem. Mater.* **2002**, *14*, 1009–1015.
27. Xiao, T.; York, A. P. E.; Coleman, K. S.; Claridge, J. B.; Sloan, J.; Charnock, J.; Green, M. L. H. *J. Mater. Chem.* **2001**, *11*, 3094–3098.
28. Nguyen, T. H.; Nguyen, T. V.; Lee, Y. J.; Safinski, T.; Adesina, A. A. *Mater. Res. Bull.* **2005**, *40*, 149–157.
29. Vo, D. -V. N.; Adesina, A. A. *Fuel Process. Technol.* **2011**, *92*, 1249–1260.
30. Bartholomew, C. H.; Guczi, L. *Stud. Surf. Sci. Catal.* **1991**, *64*, 158–224.
31. Dry, M. E. *Catal. Today* **2002**, *71*, 227–241.
32. Shi, H. B.; Li, Q.; Dai, X. P.; Yu, C. C.; Shen, S. K.; Xinhe, B.; Yide, X. *Stud. Surf. Sci. Catal.* **2004**, *147*, 313–318.
33. Kissinger, H. E. *Anal. Chem.* **1957**, *29*, 1702–1706.
34. Brown, M. E. *Introduction to Thermal Analysis: Techniques and Application*; Kluwer Academic Publishers: The Netherlands, 2001; p 214.
35. JCPDS Powder Diffraction File, International Centre for Diffraction Date, Swarthmore, PA, 2000.
36. Patterson, A. L. *Phys. Rev.* **1939**, *56*, 978.
37. Bej, S. K.; Bennett, C. A.; Thompson, L. T. *Appl. Catal., A* **2003**, *250*, 197–208.
38. Pierson, H. O. *Handbook of Refractory Carbides and Nitrides: Properties, Characteristics, Processing and Applications*; Noyes Publications: Westwood, NJ, 1996.
39. Bukur, D. B.; Mukesh, D.; Patel, S. A. *Ind. Eng. Chem. Res.* **1990**, *29*, 194–204.
40. Solymosi, F.; Bugyi, L. *Catal. Lett.* **2000**, *66*, 227–230.
41. Adesina, A. A.; Hudgins, R. R.; Silveston, P. L. *Can. J. Chem. Eng.* **1986**, *64*, 447–454.
42. Pham-Huu, C.; Ledoux, M. J.; Goille, J. *J. Catal.* **1993**, *143*, 249–261.
43. Claridge, J. B.; York, A. P. E.; Brungs, A. J.; Marquez-Alvarez, C.; Sloan, J.; Tsang, S. C.; Green, M. L. H. *J. Catal.* **1998**, *180*, 85–100.
44. Dictor, R. A.; Bell, A. T. *J. Catal.* **1986**, *97*, 121–136.
45. Donnelly, T. J.; Satterfield, C. N. *Appl. Catal.* **1989**, *52*, 93–114.
46. Park, K. Y.; Seo, W. K.; Lee, J. S. *Catal. Lett.* **1991**, *11*, 349–356.
47. Woo, H. C.; Park, K. Y.; Kim, Y. G.; Nam, I.-S.; Chung, J. S.; Lee, J. S. *Appl. Catal.* **1991**, *75*, 267–280.
48. Adesina, A. A. *J. Catal.* **1990**, *124*, 297–300.
49. Moodley, D. J.; van de Loosdrecht, J.; Saib, A. M.; Overett, M. J.; Datye, A. K.; Niemantsverdriet, J. W. *Appl. Catal., A* **2009**, *354*, 102–110.
50. Dalai, A. K.; Davis, B. H. *Appl. Catal., A* **2008**, *348*, 1–15.
51. Hardiman, K. M.; Trujillo, F. J.; Adesina, A. A. *Chem. Eng. Process.* **2005**, *44*, 987–992.
52. Vo, D. -V. N.; Adesina, A. A. *Prepr. Pap. - Am. Chem. Soc., Div. Fuel Chem.* **2010**, *55*, 445–447.
53. Gritschneder, S.; Iwasawa, Y.; Reichling, M. *Nanotechnology* **2007**, *18*, 1–6.

Downloaded by STANFORD UNIV GREEN LIBR on June 6, 2012 | http://pubs.acs.org
Publication Date (Web): November 29, 2011 | doi: 10.1021/bk-2011-1084.ch007

Downloaded by STANFORD UNIV GREEN LIBR on June 6, 2012 | http://pubs.acs.org
Publication Date (Web): November 29, 2011 | doi: 10.1021/bk-2011-1084.ch008

Chapter 8

Fischer-Tropsch Synthesis Investigation in a Gas-Inducing Agitated Reactor Using Electrical Capacitance Tomography

**Bawadi Abdullah, Chirag Dave, Cyrus G. Cooper,
Tuan Huy Nguyen, and Adesoji A. Adesina***

**Reactor Engineering & Technology Group,
School of Chemical Engineering,
The University of New South Wales,
Sydney, New South Wales, Australia 2052
*E-mail: a.adesina@unsw.edu.au**

Non-intrusive electrical capacitance tomography (ECT) has been used to analyse the dynamic feedback between the fluid phase characteristics (such as dispersed phase hold-up, mixing time constants, etc) and reaction metrics in gas-liquid-solid reactor using the Fischer-Trospch synthesis (FTS) as a case study. The coupling between these two processes (transport and reaction) is due to the changing physicochemical properties of the liquid phase medium as product accumulates with reaction progression. Gas recirculation within the reactor was improved by using a gas-inducing impeller at speeds above the minimum required for gas entrainment (293 rpm) thus ensuring better gas conversion per pass. The steady-state gas phase hold-up, ε_G, dependency on temperature was due to contributions from both thermal expansion and reaction-induced changes in the liquid phase. The behaviour was adequately captured by the 3-parameter Chapman-Richards model, which combined with the Arrhenius representation of the rate behaviour to yield a new relation that coupled the dispersed phase hold-up and reaction rate. The advantages of using this model for inferential control or optimization purposes is immediately evident. Several runs conducted in the range 473-533 K at different operating pressures (1, 11 and 21 atm) and wide spectrum of feed H_2:CO

In Synthetic Liquids Production and Refining; de Klerk, A., et al.;
ACS Symposium Series; American Chemical Society: Washington, DC, 2011.

ratio (1:5 to 5:1) over a 36-hour period permitted further development of ECT-based models for chain growth factor, olefin-to-paraffin ratio and the thermotemporal relationship for dispersed phase hold-up in an FT slurry reactor. The effect of total operating pressure was relatively modest compared to temperature on both FT reaction metrics and dispersed phase hold-up.

Introduction

Downloaded by STANFORD UNIV GREEN LIBR on June 6, 2012 | http://pubs.acs.org
Publication Date (Web): November 29, 2011 | doi: 10.1021/bk-2011-1084.ch008

The slurry reactor is particularly suitable for hydrocarbon synthesis from CO hydrogenation over Fe and Co catalysts because of its ability to achieve better control of the exothermic reaction and better catalyst usage (*1*, *2*). However, the complex hydrodynamics involved and the impact of changing liquid physicochemical properties as a result of products dissolution in the liquid phase have led to compounded reactor analysis and scale-up challenges (*3*). Possible variation in dispersed phase hold-up and spatial distribution may give rise to unexpected results even in the absence of mass transport resistances. Within the last two decades, several investigators, including Joshi and co-workers (*4*–*6*), have reported the advantages of the gas-inducing stirred tank (GIST) in the provision of improved mixing and single gas conversion per pass over conventional agitators. The associated hydrodynamics, mixing and mass transfer characteristics have been examined using residence-time distribution (RTD) and computational fluid dynamics methods to secure correlations for design and scale-up purposes. The increased gas recirculation also promotes solid mixing and hence better catalyst utilization when applied in a slurry reactor. However, the agitation rate msut exceed the critical impeller speed, N_{sc}, given by the Sawant-Joshi criterion (*7*) for the gas-inducing stirrer before the benefits of enhanced gas recirculation may be realized. For a slurry reactor, N_{sc}, is well below the rotational speed necessary to ensure absence of gas absorption and external liquid-solid transport resistances.

In view of the product-induced changes in the fluid phase properties in a multiphase reactor – e.g. viscosity, density and surface tension - and hence, phase holdup variation with time-on-stream during reaction, a non-invasive evaluation of the reactor would provide useful insight into the coupling effect of transport processes and reaction metrics. Indeed, non-intrusive flow visualization of the reactor contents with time-on-stream may provide additional information to complement standard chromatographic exit gas phase composition analysis leading to better understanding and ability to carry out superior scale-up and modeling, for example, using computational fluid dynamics approach (*8*). This is especially germane to FT operation in a mechanically-agitated slurry reactor fitted with a gas-entrainment impeller to improve gas recirculation and hence, CO conversion per pass. In this paper, we report the first investigation of in-situ electrical capacitance tomography diagnosis of the Fischer-Tropsch reaction. The objective was to determine the relationship between reaction metrics and dispersed phase hold-up characteristics with time-on-stream.

Downloaded by STANFORD UNIV GREEN LIBR on June 6, 2012 | http://pubs.acs.org
Publication Date (Web): November 29, 2011 | doi: 10.1021/bk-2011-1084.ch008

Materials and Method

Catalyst Preparation and Characterisation

The catalyst (10wt%Co/Al_2O_3) was synthesised by impregnating requisite amount of cobalt nitrate solution onto spray-dried gamma-alumina particles (60-90 μm obtained from Saint-Gobain Nopro Corporation, USA) at 298 K for 3 h under constant stirring and pH of 3.6 (5M HNO_3 solution as pH control) using a Metler-Toledo T90 Titration Excellence system. The resulting slurry was dried in the oven at 303 K for 20 h. The dried catalyst was then calcined in an oven at 673 K for 5 h at rate of 5 K min^{-1}. The calcined catalyst was further crushed and sieved to 45-90 μm using Retsch AS 200 Analytical Sieve Shaker and loaded into stainless steel fixed bed reactor (OD = 12.5 mm) where it was activated at 623 K for 8 h in 5% CO/H_2 mixture at a heating rate of 5 K min^{-1}. High purity research grade H_2 (99.99%), CO(99.99%) and N_2(99.99%) supplied by Linde (Sydney) were used in all runs. Gas flowrates were controlled and metered via calibrated mass flow controllers (Brooks 5850E).

BET surface area and pore volume were obtained from N_2 physisorption measurements at 77 K on a Quantachrome Autosorb-1 unit while acid-base properties were determined via NH_3 and CO_2-TPD respectively on Micromeritics Autochem 2910 using 5 heating rates (5-30 K min^{-1}) for up to 973 K. H_2 chemisorption on the same unit provided the metal dispersion and crystallite size. X-ray diffractograms from Philips X'pert MPD (at 45 kV, 40 mA and 0.2°min^{-1}(2θ)) were used to identify the solid oxide phases present in the catalyst.

Reactor Characterisation and ECT Set-Up

The experimental system depicted in Figure 1 consists of a gas manifold-station, an electrical capaictiance tomography (ECT) module connected to the 2-litre Parr stainless steel reactor (ID = 105 mm) via a 12-electrode cylindrical basket sensor snuggly fitted around the perimeter of the vessel. The stainless steel electrode has a temperature-resistant coating to permit operation up to 553 K and pressure to 30 atm.

The reactor was mounted in a temperature-controlled electrical furnace and equipped with a gas-inducing stirrer as illustrated in Figure 2. The gas-inducing mixer comprises of hollow shaft with gas inlet port at the top (125 mm above the liquid surface) and a 4-blade flat impeller - each blade has 3 gas outlet ports -with a clearance of 60 mm from the reactor base. The final section is a product collection and analysis station consisting of two condensers placed downstream of the reactor (for C_{7+} hydrocarbons and water removal) and a Shimadzu gas chromatograph (model GC17A) for product composition determination. The activated catalyst is transferred under a N_2 blanket pneumatically into the reactor containing paraffin oil (boiling point 633 K) maintained at the reaction temperature prior to the FT runs.

In Synthetic Liquids Production and Refining; de Klerk, A., et al.;
ACS Symposium Series; American Chemical Society: Washington, DC, 2011.

Downloaded by STANFORD UNIV GREEN LIBR on June 6, 2012 | http://pubs.acs.org
Publication Date (Web): November 29, 2011 | doi: 10.1021/bk-2011-1084.ch008

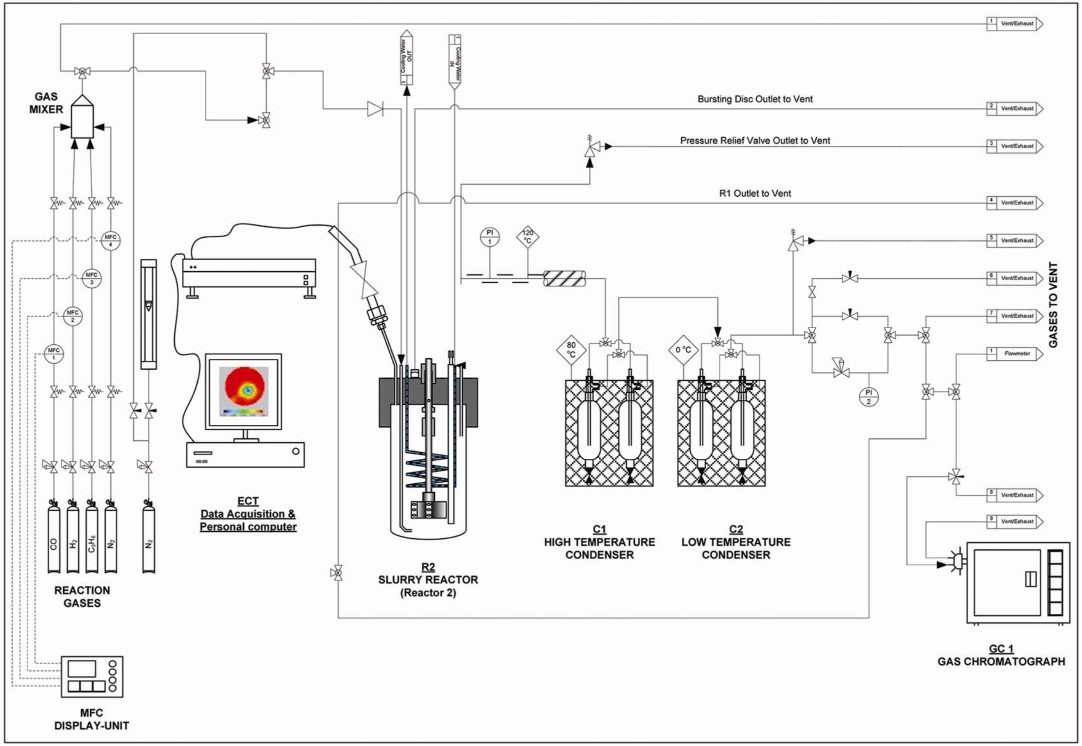
GAS MIXER
Cooling Water OUT
Cooling Water IN
Bursting Disc Outlet to Vent
Pressure Relief Valve Outlet to Vent
R1 Outlet to Vent
1 Vent/Exhaust
2 Vent/Exhaust
3 Vent/Exhaust
4 Vent/Exhaust
5 Vent/Exhaust
6 Vent/Exhaust
7 Vent/Exhaust
1 Flowmeter
8 Vent/Exhaust
9 Vent/Exhaust
GASES TO VENT
MFC 1
MFC 2
MFC 3
MFC 4
PI 1
120 °C
80 °C
0 °C
PI 2
CO
H₂
C₃H₈
N₂
N₂
REACTION GASES
ECT
Data Acquisition &
Personal computer
R2
SLURRY REACTOR
(Reactor 2)
C1
HIGH TEMPERATURE CONDENSER
C2
LOW TEMPERATURE CONDENSER
GC 1
GAS CHROMATOGRAPH
MFC
DISPLAY-UNIT

Figure 1. Experimental apparatus for the Fischer-Tropsch synthesis study.

Downloaded by STANFORD UNIV GREEN LIBR on June 6, 2012 | http://pubs.acs.org
Publication Date (Web): November 29, 2011 | doi: 10.1021/bk-2011-1084.ch008

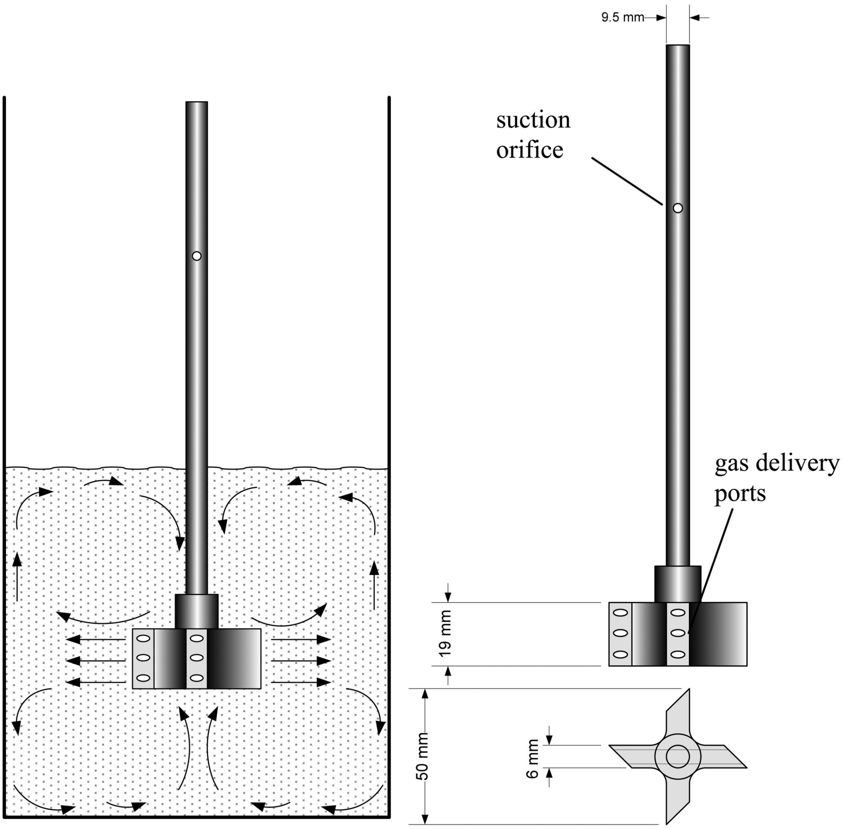

Figure 2. Schematic of the gas-inducing impeller.

The minimum stirring speed required for gas induction through the gas inlet port on the shaft was estimated from the Sawant-Joshi equation (7) given by:

$$\frac{N_{sc}^2 D_I^2}{gh}\left(\frac{\mu}{\mu_{water}}\right) = 0.21 \qquad (1)$$

may be used to estimate the critical agitation speed, N_{sc}, where h is the impeller submersion depth, D_I = impeller diameter, μ is the liquid phase viscosity, μ_{water} is the water viscosity while g is the acceleration due to gravity. For the present stirred tank arrangement, h = 56 mm, D_I = 50 mm and the liquid phase was water, μ/μ_{water} =1.93 which gives N_{sc} = 4.9 rps (293 rpm). As a result preliminary investigation of the effect of stirring speed on reaction rate was done with agitation rate greater than 300 rpm. Indeed, to avoid both external mass transport and pore diffusional limitations, a stirring speed of 1200 rpm with catalyst average particle in the range 45-90 μm was used for all experiments.

The response of the experimental system to a step change in gas phase composition (from pure nitrogen to argon) under typical FTS temperature and pressure (cf. Figure 3) provided the transport lag and characteristic time constant for the fluid phase mixing. The ECT sensor was connected to a central processing module (M3000) – both supplied by Industrial Tomography Systems (ITS), Manchester, UK. Data analysis was carried out using the ITS M3000 Tool Suite. The software utilises a non-iterative algorithm based on linear back-projection for fast image reconstruction for real-time imaging of moving processes to provide relevant tomograms of the vessel radial cross-section at the sensor plane. Tomograms were recorded at 500 kHz over a 100-second interval at one frame per second to ensure excellent spatiotemporal resolution for each run. The reconstructed image during an experiment contained information about the cross-sectional distribution of electrical permittivity of the vessel contents within the measurement plane. Tomograms collected were analysed to obtain the cross-sectional average phase hold-up.

FT runs were carried out at total operating pressures between 1 to 21 atm and temperature, 473 to 533 K as well as H_2 feed composition, y_{H2} (0.0-1.0) The catalyst loading was kept constant at 10 gL^{-1} for all runs. The liquid products were collected in the hot and cold traps located downstream of the Parr reactor. The uncondensed gases passed through the back-pressure regulator for analysis on the Shimadzu GC (model 17A) using 30m GS-Q capillary column. A bubble flowmeter was used to measure the non-condensable gas flow rate prior to analysis. Although hydrocarbon formation rates were obtained from the transient gas phase composition analysis from the GC, the liquid products from the hot and cold traps contained cumulative composition over the run period and so could not be used for instantaneous formation rate estimation. Even so, GC analysis of the liquid aliquots revealed only modest hydrocarbon quantities (ca.14 mol% C_8-C_{10} in the cold trap and 30.6 mol% C_{10}-C_{16}) with non-detectable alcohols or acids. Heptane was.used as the solvent carrier for dissolving the liquid products in each condenser.

Results and Discussion

Physicochemical Attributes

Table 1 summarises the physicochemical properties of the catalyst. The BET surface area and pore volume of 170.8 m^2 g^{-1} and 0.474 ml g^{-1} respectively are lower than the corresponding values for the calcined alumina support probably due to pore blockage by the Co oxide crystallites (*9*).

The formation of cobalt oxides during cobalt nitrate decomposition in the calcination phase proceeded according to the reactions given by Eqs. (2) to (4) below.

$$Co(NO_3)_2 \rightarrow CoO + NO + NO_2 + O_2 \tag{2}$$

$$3CoO + \frac{1}{2}O_2 \rightarrow Co_3O_4 \tag{3}$$

Downloaded by STANFORD UNIV GREEN LIBR on June 6, 2012 | http://pubs.acs.org
Publication Date (Web): November 29, 2011 | doi: 10.1021/bk-2011-1084.ch008

$$CoO + Al_2O_3 \rightarrow CoAl_2O_4 \qquad (4)$$

Qualitative examination of the crystalline phases present in the calcined cobalt catalyst was performed by X-ray diffractogram (XRD) analysis and the result is illustrated in Figure 4. The presence of multiple Co_3O_4 peaks (2θ = 31.2° and 18.5°) and a cobalt aluminate phase ($CoAl_2O_4$) at the major peak of 2θ = 32° is evident. The peaks at 44° and 64° represent the CoO phase. This XRD analysis reconfirmed the postulated phases during calcination process (*10*, *11*)

Table 1. Physicochemical properties of alumina support and cobalt catalyst

Parameters	*γ-alumina support (calcined in air at 673 K)*	*Co/Al₂O₃*
BET area ($m^2.g^{-1}$)	205.1	170.8
Pore volume (cm^3 g^{-1})	0.62	0.47
Average pore size, (nm)	12.0	11.1
Metal dispersion (%)	-	0.72
Metal surface area (m^2g^{-1})	-	0.48
Active particle size (nm)	-	139.0
$\Delta H_{d,NH3}$ (kJ mol^{-1})	61.75	47.52 (Peak I)
Acid site concentration	-	73.80 (Peak II)
(μmol m^{-2})	1.20	0.79 (Peak I)
	-	2.47 (Peak II)
$\Delta H_{d,CO2}$ (kJ mol^{-1})	32.57 (Peak I)	54.23 (Peak 1)
Basic site concentration	42.61 (Peak II)	45.69 (Peak II)
(μmol m^{-2})	0.41	0.03
	0.59	0.04

Based on Figure 3, the slurry reactor system seems to follow first order with time delay, t_d=6 minutes and mixing time constant, τ=26 minutes estimated from a fit of the data to Eq. (5) for both Ar and N_2.

$$y_p = y_p^{ss}\left(1 - \exp\left(-\frac{(t - t_d)}{\tau}\right)\right) \text{ for Ar}$$

and **(5)**

$$y = y_0\left(1 - \exp\left(-\frac{(t - t_d)}{\tau}\right)\right) \text{for } N_2$$

Downloaded by STANFORD UNIV GREEN LIBR on June 6, 2012 | http://pubs.acs.org
Publication Date (Web): November 29, 2011 | doi: 10.1021/bk-2011-1084.ch008

Downloaded by STANFORD UNIV GREEN LIBR on June 6, 2012 | http://pubs.acs.org
Publication Date (Web): November 29, 2011 | doi: 10.1021/bk-2011-1084.ch008

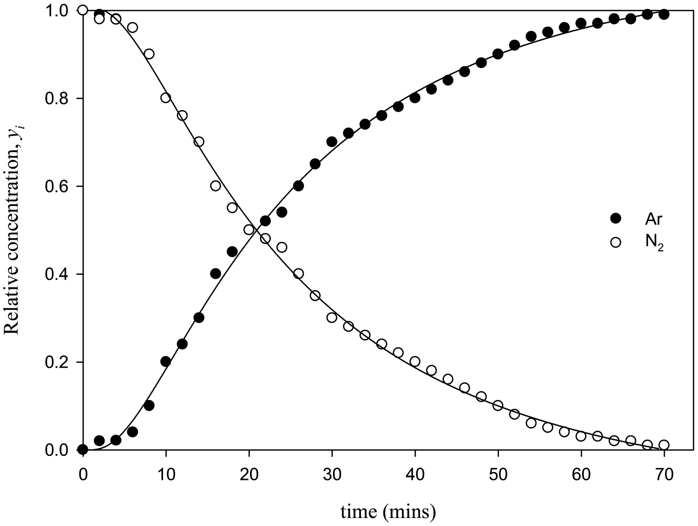

Figure 3. Experimental system response to a step change in feed gas composition (pure nitrogen to argon).

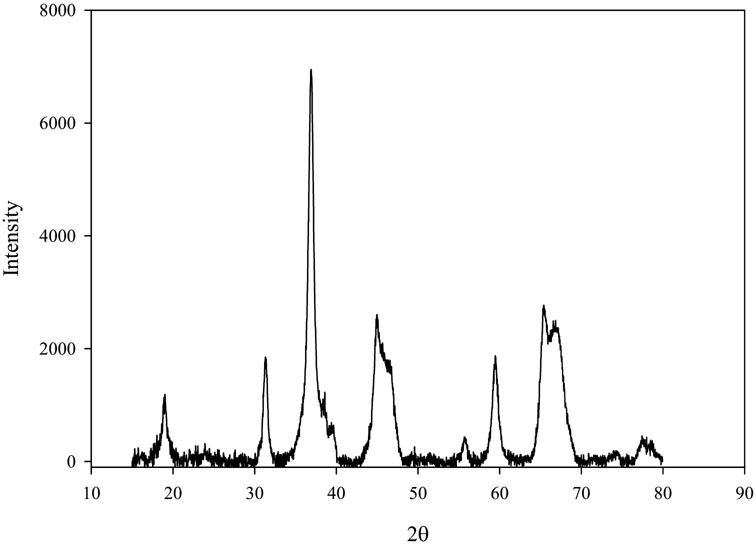

Figure 4. XRD of a freshly calcined catalyst at 673 K.

The active sites for FTS were produced during the activation (reduction) stage (*12*, *13*), namely;

$$Co_3O_4 + H_2 \rightarrow 3CoO + H_2O \uparrow \tag{6}$$

$$CoO + H_2 \rightarrow Co + H_2O \uparrow \tag{7}$$

$$CoAl_2O_4 + H_2 \rightarrow Co + Al_2O_3 + H_2O \uparrow \tag{8}$$

or

$$Co_3O_4 + \mathrm{CO} \rightarrow 3CoO + CO_2 \uparrow \tag{9}$$

$$CoO + CO \rightarrow Co + CO_2 \uparrow \tag{10}$$

$$CoAl_2O_4 + CO \rightarrow Co + Al_2O_3 + CO_2 \uparrow \tag{11}$$

NH_3 temperature-desorption curves implicated the existence of two acid sites on the catalyst surface, namely; peak P1 located between 515-580 K and the second peak, P2 straddling 680-740 K. A fit of the data to,

$$\ln\left(\frac{\beta}{T_p^2}\right) = -\frac{\Delta H_d}{RT_p} + \frac{\Delta H_d A_{acid}}{RC} \tag{12}$$

gave straight lines in all cases having R-squared values of between 0.93 to 0.99 with slope and intercept used to evaluate the surface acidity parameters. Acid site strength and concentration on the solid sample are represented by the NH_3 heat of desorption, ($-\Delta H_d$), and the acid site concentration, A_{acid}, respectively. The low temperature peak (P1) is a weak Lewis acid centre (*14*) while P2 appears to be a strong Lewis acid site since the corresponding NH_3 heat of desorption has a value of 73.8 kJ mol^{-1} (*15*, *16*). Similar analysis performed on the pure alumina support calcined at 673 K revealed the presence of only the weak acid site (desorption peak at 529 to 568 K) although both weak and strong basic sites were present in the reduced catalyst. The strong Lewis acid centres may be due to the interaction between NH_3 and water formed during Co oxide reduction (which may be chemisorbed either on the Co site or metal-support interface) since the introduction of Co significantly increased this type of acid site concentration (from 1.2 μmol m^{-2} in calcined support and 3.17 μmol m^{-2} in the Co catalyst). However,, the weak basic sites seemed to decrease with addition of Ço species probably because they were supplanted by the strong acid sites during impregnation and and subsequent calcination.

Downloaded by STANFORD UNIV GREEN LIBR on June 6, 2012 | http://pubs.acs.org
Publication Date (Web): November 29, 2011 | doi: 10.1021/bk-2011-1084.ch008

Downloaded by STANFORD UNIV GREEN LIBR on June 6, 2012 | http://pubs.acs.org
Publication Date (Web): November 29, 2011 | doi: 10.1021/bk-2011-1084.ch008

Fischer-Trospch Reaction Metrics

ECT-Assisted Reactor Analysis

The dispersed phase hold-up, ε_D, was determined from the instantanenous tomograms (permittivity data) taken over the vessel cross-sectional area using the Maxwell equation (*17*) given as:

$$\varepsilon_D = \frac{2\chi_C + \chi_D - 2\chi_M - \chi_M\left(\dfrac{\chi_D}{\chi_C}\right)}{\chi_M - \left(\dfrac{\chi_D}{\chi_C}\right) + 2\left(\chi_C - \chi_D\right)} \tag{13}$$

where χ_C is the permittivity of the continuous phase (liquid), χ_D is the permittivity of dispersed phase (gas and catalyst particle) , and χ_M is the measured permittivity of the mixture obtained from pixel-averaged cross-sectional ECT data.

Figure 5 shows typical tomograms obtained from the reactor during a run. Since the ECT sensor cannot discriminate between a solid particle and the gas bubble, the dispersed phase hold-up, ε_D is a combination of the gas phase hold-up (ε_G) and the solid phase hold-up (ε_S).

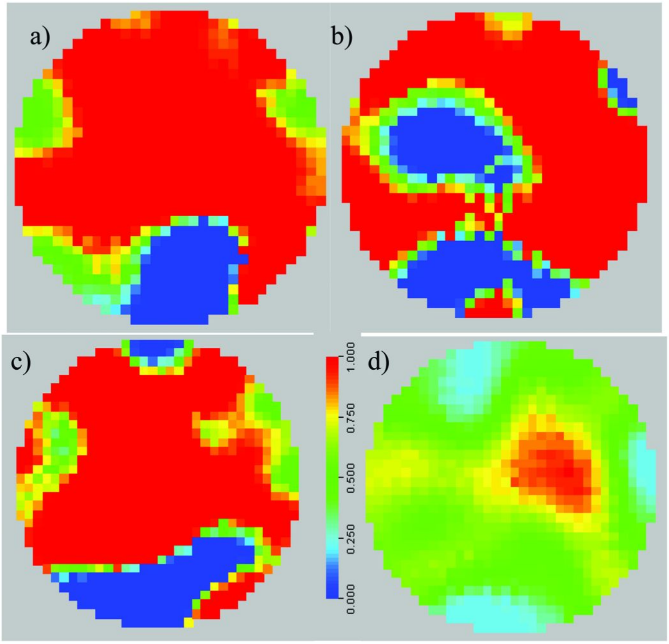

Figure 5. Tomography images at different temperature a)473 K b) 493 K c) 513 K and d) 533 K. The operating condition: Pressure: 21 atm, catalyst loading: 10g L^{-1} stirring speed: 1200 rpm. (see color insert)

Preliminary experiments were carried using a conventional stirrer (with no gas inlet port on the shaft and exit ports on the impeller blades) with identical geometry and dimensions to the gas-inducing agitator (cf. Figure 2). Figure 6 reveals that the dispersed phase hold-up initially increased with solid loading for both impellers and seemed to level off at higher values.

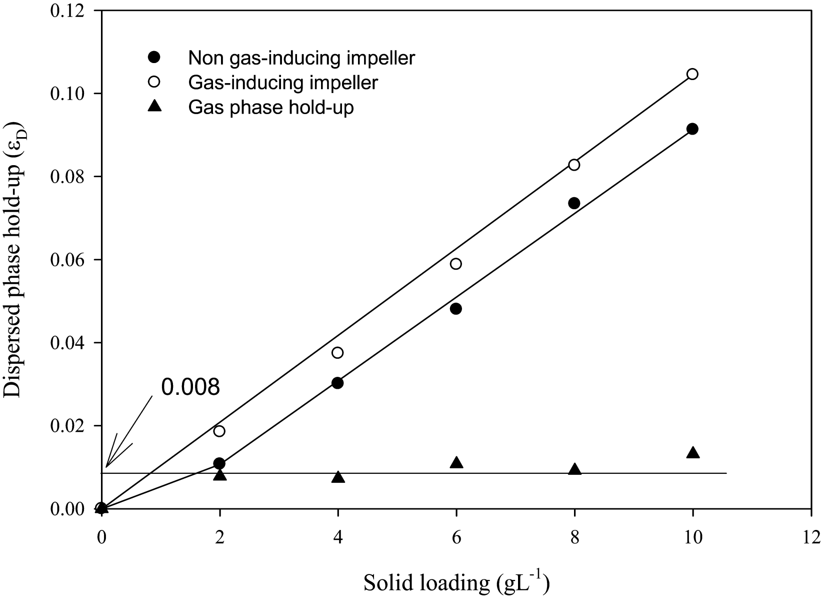

Figure 6. Dispersed holdup as function of solid loading for the two impellers used.

Both runs were conducted under non-reactive conditions with N_2 as the inert gas and alumina particles as the solid entities. Comparing the results for the conventional stirrer and gas-inducing stirrer shows that at the speed used (1200 rpm), there was a constant difference between the two stirrer types which represents the gas phase hold-up (since gas was not introduced into the reactor during the run with the conventional stirrer). Consequently, it may be assumed that the dispersed phase hold-up is simply the sum of the solid and gas phase hold-ups over the range of solid loading employed. Thus,

$$\varepsilon_D = \varepsilon_S + \varepsilon_G \qquad (14)$$

Additionally, the effect of temperature on fluid phase permittivity (and hence, hold-up) was investigated.

As may be seen from Figure 7, the dispersed phase hold-up for the conventional stirrer was essentially invariant with temperature between 293-530 K (which covers the range for subsequent FTS runs).

Downloaded by STANFORD UNIV GREEN LIBR on June 6, 2012 | http://pubs.acs.org
Publication Date (Web): November 29, 2011 | doi: 10.1021/bk-2011-1084.ch008

Downloaded by STANFORD UNIV GREEN LIBR on June 6, 2012 | http://pubs.acs.org
Publication Date (Web): November 29, 2011 | doi: 10.1021/bk-2011-1084.ch008

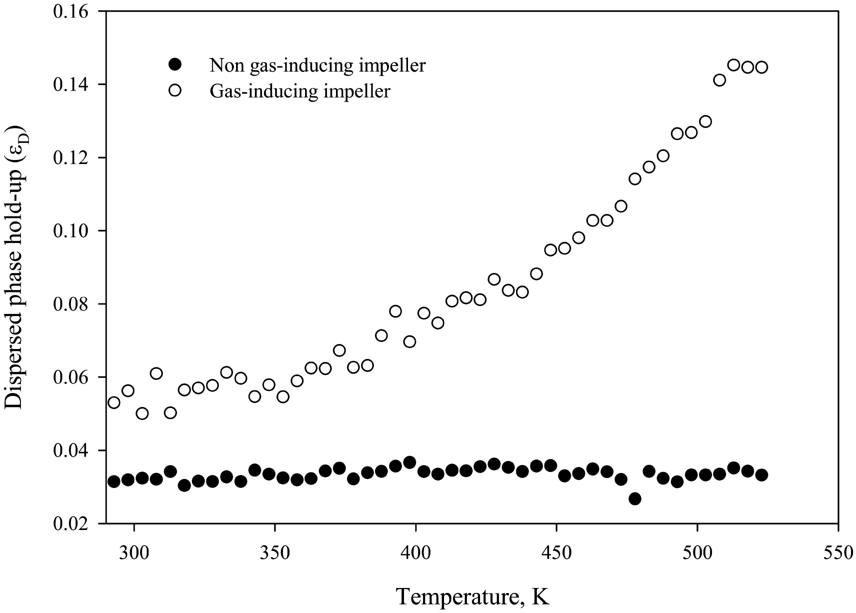

Figure 7. Effect of dispersed hold-up as function of temperature for different impeller geometry.

It would therefore seem that there was no significant change in the electrical permittivity of the alumina particles and the paraffin oil (used as the reaction medium) with temperature since the dispersed phase hold-up was constant. However, the data for the gas-inducing impeller demonstrated that the dispersed phase hold-up increased monotonically with temperature. The increased dispersed phase hold-up for the gas-inducing stirrer may be attributed to change only in the gas phase hold-up (consistent with the earlier results from Figure 6) which may be associated with volume increase due to gas expansion with increasing temperature. Given that the coefficient of expansion at constant pressure for a gas is, $\frac{1}{V}\left(\frac{\partial V}{\partial T}\right)_P$, which is simply the reciprocal of the absolute temperature for an ideal gas, then the change witnessed in gas phase hold-up over the temperature range used, may be given as, $\frac{V_2}{V_1}=\frac{T_2}{T_1}=\frac{\varepsilon_{G_2}}{\varepsilon_{G_1}}$) which is about 1.8 with T_1 and T_2 as 293 and 530 K respectively, in agreement with a doubling of the dispersed phase hold-up within the same temperature window in Figure 7. Indeed, a fit of the dispersed (gas) phase hold-up data for the gas-inducing impeller in Figure 7 to an Arrhenius expression yielded a low activation energy of 5.81 kJ mol^{-1} indicative of a purely physical process such as gas diffusion or solubility in liquids. As a result of these initial considerations, changes in dispersed phase hold-up during isothermal FTS reaction may be readily decoupled from thermal expansion effects.

The influence of total operating pressure on the dispersed phase hold-up was also examined. Figure 8 evinces a linear, albeit gentle, increase in dispersed phase hold-up with increased operating pressure. The behaviour is readily captured by;

$$\varepsilon_D = \varepsilon_{D_0,P} + \lambda P \qquad (15)$$

where, $\varepsilon_{D0,P}$ is the dispersed phase hold-up at atmospheric conditions, P is the total operating gauge pressure and λ an empirical constant for the syngas in paraffin oil. Linear regression gave ε_{G0} and λ as 0.112 and 5×10^{-4} atm^{-1} respectively.

Downloaded by STANFORD UNIV GREEN LIBR on June 6, 2012 | http://pubs.acs.org
Publication Date (Web): November 29, 2011 | doi: 10.1021/bk-2011-1084.ch008

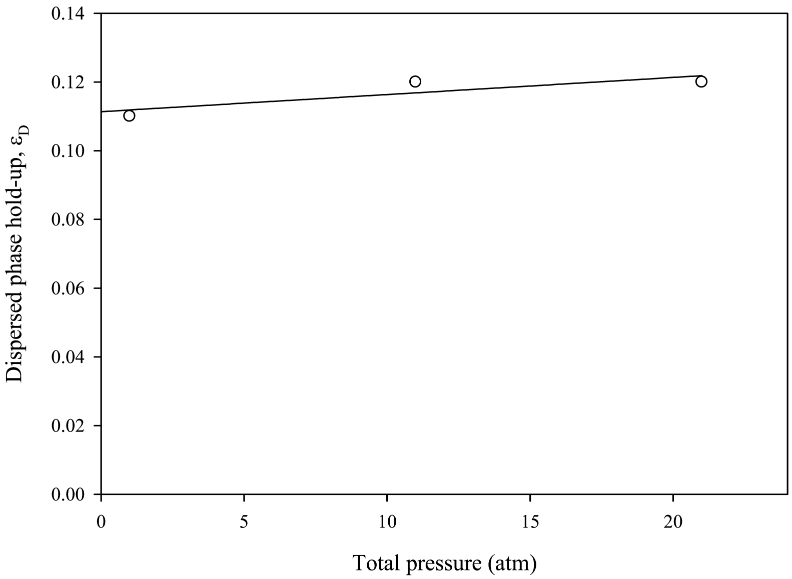

Figure 8. Dispersed phase hold-up as function of total pressure for reaction conditions:T = 498 K, and syngas with H_2:CO ratio = 2:1.

Cooper *et al.* (*13*) had previously shown that external transport and pore diffusional limitations may be avoided in the same FT reactor using impeller speed in excess of 600 rpm and average particle size smaller than 425 μm.

ECT-Based Reaction Runs

FTS runs were performed at different temperatures and at the constant pressure of 21 atm using syngas with H_2:CO ratio of 2:1. The rise in dispersed (gas) phase hold-up (since the contribution due to the alumina supported catalyst particles has been previously determined to be temperature-insensitive) with temperature seemed to level off at higher temperature as may be seen in Figure 9 hence, the behaviour was described by;

$$\varepsilon_D = \varepsilon_{D_0} + b_0\left[1 - \exp(-b_1\theta)\right] \tag{16}$$

where θ is the dimensionless temperature ($\theta = T-T_0/T_0$), with T_0 as the room temperature (=295 K). Nonlinear regression of the data provided, $\varepsilon_{D0} = 0.04\pm0.0013$, $b_0 = 19.54\pm0.047$ and $b_1 = 0.0048\pm0.0002$. The change in gas phase hold-up over the reaction temperature range employed is more than what was expected due to mere gas volume expansion (6% from 493 to 523 K) since ε_G increased by more than 19% over the same temperature range suggesting that extant liquid phase properties as product accumulation continued was probably responsible for the large variation in gas hold-up with temperature. This finding is in line with the original proposition of reaction-induced change in hydrodynamic attributes. Clearly, the sensible change in gas phase hold-up due to product accumulation would also affect mixing characterisitics and thus, reaction rate. Indeed, this increase in gas holdup with temperature was also reported by others (*18*, *19*) due to decreased the liquid viscosity and surface tension. On the other hand, it is evident from Figure 9 that the reaction rate followed the expected Arrhenius behaviour with b_2 estimated as the Arrhenius number, $E/RT_0 = 26.58$, for the FT reaction at T_0 and hence, an activation energy, E, of 65.2 kJ mol^{-1} (cf. Eq. (17)).

$$\left(-r_{rxn}\right) = r_0 \exp\left(-\frac{b_2}{\left(\theta+1\right)}\right) \tag{17}$$

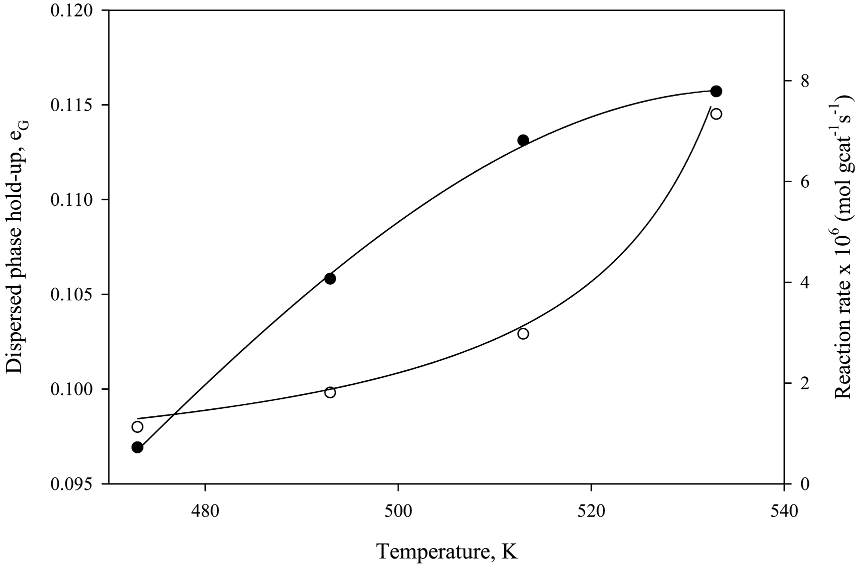

Figure 9. Dispersed phase hold-up (●) and reaction rate (○) as function of temperature.

Downloaded by STANFORD UNIV GREEN LIBR on June 6, 2012 | http://pubs.acs.org
Publication Date (Web): November 29, 2011 | doi: 10.1021/bk-2011-1084.ch008

Thus, combining Eqs. (16) and (17), the coupling between reaction rate and dispersed phase hold-up may be expressed by;

$$\left(-r_{rxn}\right) = r_0 \exp\left[\frac{-b_1 b_2}{b_1 - \ln\left\{\frac{b_0 - \left(\varepsilon_D - \varepsilon_{D_0}\right)}{b_0}\right\}}\right] \tag{18}$$

The effect of syngas composition on FTS rate is shown in Figure 10. The profile is strongly skewed towards the high H2 mole fraction, yH2, due to relatively weak adsorption of H2 on the catalyst surface in the presence of CO.

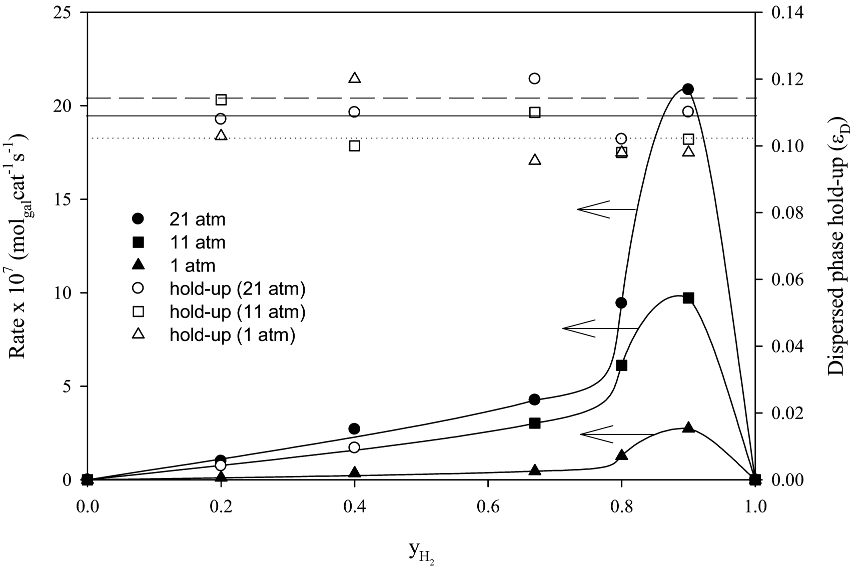

Figure 10. Effect of reaction rate and dispersed hold-up on syngas feed composition at T = 523 K.

The latter is reportedly more strongly chemisorbed on the same site as H2 (*20*). Interestingly, the associated gas phase hold-up is practically constant over the feed composition, yH2, values used as seen on the same plot regardless of the total pressure. This indicates that the change in liquid phase properties as result of product accumulation was probably similar for different syngas concentrations.

Downloaded by STANFORD UNIV GREEN LIBR on June 6, 2012 | http://pubs.acs.org
Publication Date (Web): November 29, 2011 | doi: 10.1021/bk-2011-1084.ch008

Figure 10 further shows that the reaction rate–composition profiles are similarly shaped at all three total operating pressures investigated. The optimum composition is a feed gas with H_2:CO ratio of 9:1 in all cases. These qualitative features suggest that the FT reaction mechanism was probably unchanged at the different operating pressures used. Indeed, as evident from Figure 11, the hydrocarbon synthesis rate has a linear dependency on the total operating pressure with a proportionality constant of $9.73 \pm 0.13 \times 10^{-7}$ mol $gcat^{-1}$ s^{-1} atm^{-1}.

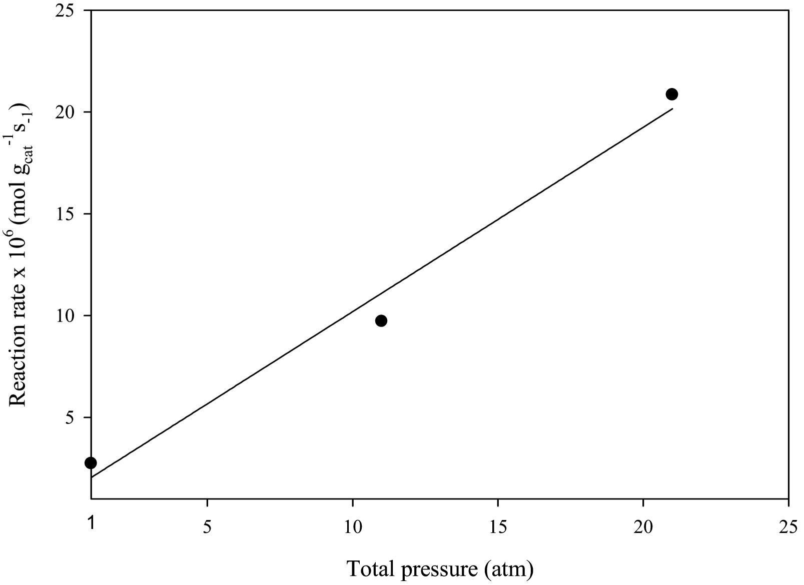

Figure 11. Reaction rate as function of total pressure.

The chain growth probability, *α*, was obtained from a fit of the individual hydrocarbon formation rate to the Anderson-Schulz-Flory model given by:

$$r_{C_n} = k(1-\alpha)^2 \alpha^{n-1} \qquad (19)$$

Figure 12a displays the variation of *α* with feed compostion at the three operating total pressures used. However, Figure 12b illustrates the trend in olefin-to-paraffin ratio, ROP, for each carbon number with respect to feed composition. The decreasing ROP with increased feed H_2 mole fraction is a reflection of the fact that nearly identical surface H:C ratio is required for the formation of olefins and paraffins as the chain carbon number increased.

Downloaded by STANFORD UNIV GREEN LIBR on June 6, 2012 | http://pubs.acs.org
Publication Date (Web): November 29, 2011 | doi: 10.1021/bk-2011-1084.ch008

Downloaded by STANFORD UNIV GREEN LIBR on June 6, 2012 | http://pubs.acs.org
Publication Date (Web): November 29, 2011 | doi: 10.1021/bk-2011-1084.ch008

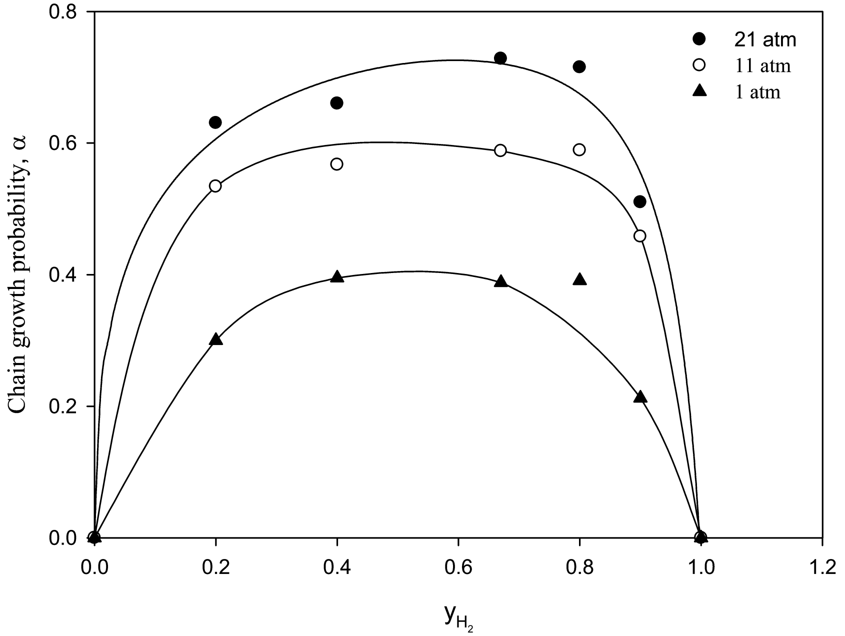

Figure 12a

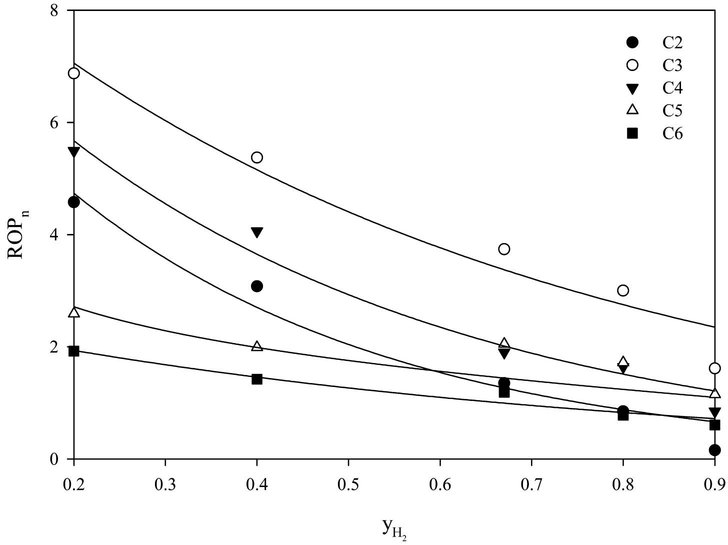

Figure 12b

Figure 12. (a) Effect of syngas feed composition on chain growth probability, α. (b) ROP_n as function of feed composition, y_{H2}.

As was observed in the case of rate envelopes, the shape similarity of the curves in Figure 12a is indicative of a common reaction mechanism regardless of the pressure employed. In particular, the “plateau” in chain growth probability values for syngas composition with $0.4 \leq y_{H2} \leq 0.8$ implicates the existence of a common surface monomeric species in the propagation step – most likely a CH_2 species - for higher hydrocarbon formation. However, the average carbon chain length, $\bar{n} = \frac{1}{1-\alpha}$, clearly increased with total pressure as may be expected for a surface polymerization reaction. In fact, the linear expression (cf. Figure 13);

$$\bar{n} = \bar{n}_0 + \psi P_T \qquad (20)$$

governs the relationship between $\bar{n}$ and P_T. where, $\bar{n}_0$ is the average carbon number for FTS at subatmospheric pressure and estimated as 1.48 and ψ is the pressure coefficient for chain growth obtained as 0.087 atm^{-1} for the present catalyst.

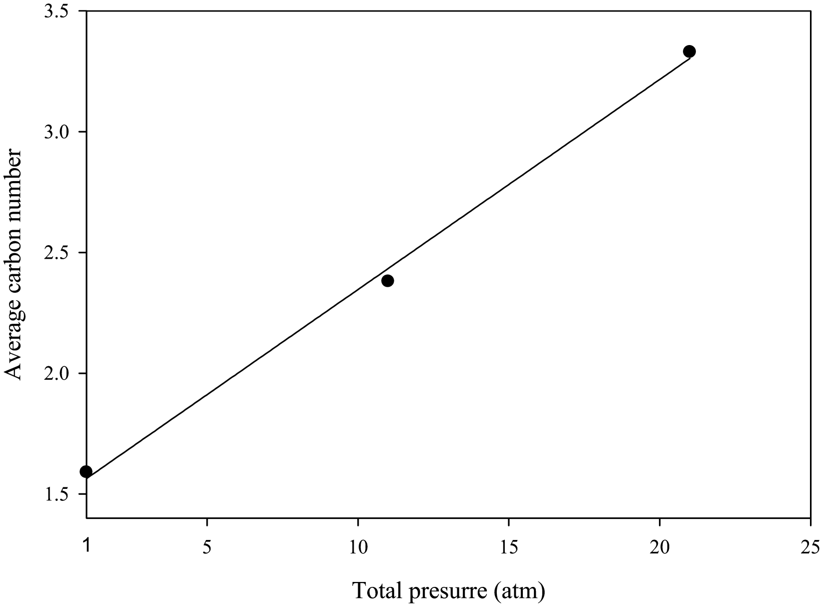

Figure 13. Average carbon number as function of total pressure.

This finding is in agreement with the reports of other investigators (*21*, *22*) on the beneficial effects of high pressure operation for FTS although other FT catalysts will be characterized by different values of $\bar{n}_0$ and ψ. Eq. (20) may be used to estimate the required total pressure for a desired value of $\bar{n}$ or α.

Downloaded by STANFORD UNIV GREEN LIBR on June 6, 2012 | http://pubs.acs.org
Publication Date (Web): November 29, 2011 | doi: 10.1021/bk-2011-1084.ch008

The behaviour of the olefin-to-paraffin ratio, ROP as a function of hydrogen mole fraction in the feed, y_{H2}, plotted in Figure 14 reveals that propene and butene are the most favoured olefins on the catalyst since the maximum ROP may be located between carbon number 3 to 4 across the range of syngas compositions studied. The ROP values for C_{7+} species would appear to be well below 2 suggesting that the rate with which the olefins or paraffins for the higher hydrocarbons are produced was probably the same due to the nearly identical H:C ratio in these species at n ≥7. Additionally, the gas phase composition of the species may be less reliable because of their higher solubilities in the liquid phase and the relatively smaller amounts produced under FTS conditions.

Downloaded by STANFORD UNIV GREEN LIBR on June 6, 2012 | http://pubs.acs.org
Publication Date (Web): November 29, 2011 | doi: 10.1021/bk-2011-1084.ch008

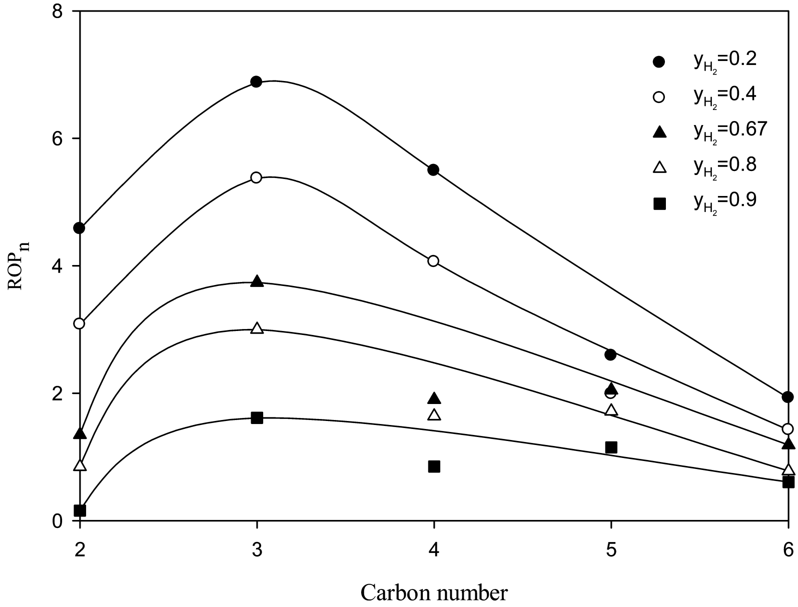

Figure 14. The behaviour of olefin-to-paraffin ratio, ROP as function of syngas feed composition at different carbon number.

The relationship between ROP and the carbon number, n, irrespective of the syngas composition may be adequately described by:

$$ROP = \frac{\Lambda}{\left[1+\omega(n-\eta)^2\right]} \tag{21}$$

where Λ represents the maximum ROP value with and η as the carbon number at which it may be produced while ω is an olefin attenuation index .

Table 2 contains the estimates of these parameters obtained from nonlinear regression of the data.

Downloaded by STANFORD UNIV GREEN LIBR on June 6, 2012 | http://pubs.acs.org
Publication Date (Web): November 29, 2011 | doi: 10.1021/bk-2011-1084.ch008

Table 2. The estimate of parameter of Eq. (21)

Feed composition, yH2	*Model parameters*		
	Λ	η	ω
0.2	6.97±0.04	3.14±0.02	0.40±0.01
0.4	5.42±0.03	3.21±0.02	0.50±0.01
0.67	3.26±0.08	3.28±0.08	0.44±0.01
0.8	3.18±0.16	3.30±0.17	0.58±0.03
0.9	1.25±0.10	3.89±0.30	0.27±0.02

It is manifest from this table that while olefin selectivity (Λ) decreased with increasing feed H_2 content, the carbon chain length corresponding to maximum ROP (η) exhibited an opposing trend. It would therefore seem that it is infeasible to simultaneously optimize both olefin selectivity and carbon chain length by manipulating only feed composition.

Effect of Temperature and Time-on-Stream

The role of temperature and time-on-stream on dispersed phase hold-up is shown in Figure 15. The transient profile has a characteristic sigmoid shape at all temperatures and thus, the thermotemporal behaviour may be expressed as:

$$\varepsilon_D = \varepsilon_{D_0} + \varepsilon_{D_1}\left[1-\exp\left(-\zeta t\right)\right]^{\upsilon} \tag{22}$$

where $\varepsilon_{D,0}$ is the initial dispersed hold-up, $\varepsilon_{,D1}$ is the deviation between the ultimate dispersed phase hold-up (at infinite time) and the initial value, ζ is the time constant for the dispersed phase and υ is an empirical exponent.

Table 3 displays the estimates from nonlinear regression of the data. It is apparent that all the model parameters (with the exception of υ estimated as 2.0) are temperature-sensitive. In particular, while ε_{D0} reflects essentially the contribution due to thermal expansion of the gas phase, ε_{D1} is indicative of a reaction-induced involvement. Interestingly, an Arrehnius treatment of the data provided an activation energy, E_{D0} of 5.6 kJ mol^{-1} (symptomatic of a physical process and in agreement with the activation energy, i.e 5.8 kJ mol^{-1}, found for the data in Figure 7 under non-reactive conditions) for the initial dispersed phase hold-up, ε_{D0} and a corresponding, but larger, value, E_{D1} of 23 kJ mol^{-1} for ε_{D1} confirming its association with a reaction-controlled step. The empirical exponent represents the number of dispersed phase entities involved in any interaction occasioning a change in the hold-up with time-on-stream. A value of 2.0 for υ suggests that at least 2 gas bubbles are implicated in the bubble-bubble interaction.

Downloaded by STANFORD UNIV GREEN LIBR on June 6, 2012 | http://pubs.acs.org
Publication Date (Web): November 29, 2011 | doi: 10.1021/bk-2011-1084.ch008

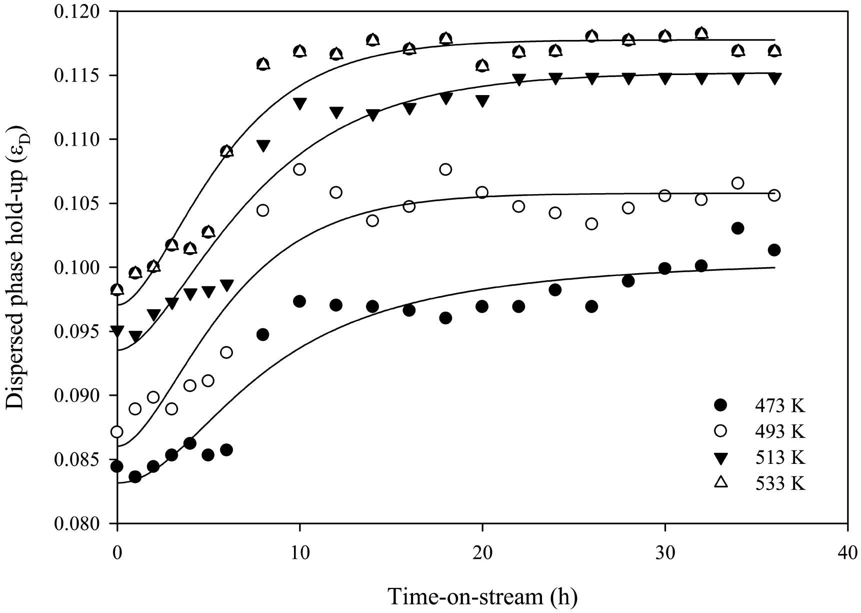

Figure 15. Dispersed phase hold-up as function of TOS at different temperature. Reaction conditions: H2:CO =2:1 at total pressure of 21 atm.

Table 3. Estimates of parameter of Eq. (22)

Temperature	ε_{D0}	ε_{D1}	ζ	υ
473 K	0.0830±0.0021	0.0168±0.0004	0.1566±0.0040	2.0
493 K	0.0860±0.0017	0.0199±0.0004	0.2276±0.0046	2.0
513 K	0.0922±0.0023	0.0222±0.0006	0.2300±0.0058	2.0
533 K	0.0970±0.0030	0.0339±0.0010	0.2333±0.0071	2.0

As may be seen in Figure 16, the effect of total operating pressure on the dispersed phase hold-up with time-on-stream also followed a first-order exponential rise to an ultimate value. Consequently, a model structurally similar to Eq. (16) may be used to represent the behaviour, namely;

$$\varepsilon_{D,P} = \varepsilon_{D_0,P} + \varepsilon_{D_1,P}\left[1 - \exp(-\varsigma_P t)\right] \tag{23}$$

The resulting parameter estimates are provided in Table 4.

Table 4. Values of the model parameter in Eq. (23)

Pressure (atm)	$\varepsilon_{D0,P}$	$\varepsilon_{D1,P}$	ζ_P
1	0.0533±0.0008	0.0682±0.0010	0.1712±0.0026
11	0.0641±0.0013	0.0567±0.0011	0.2129±0.0043
21	0.0673±0.0035	0.0510±0.0026	0.4068±0.0209

Consistent with earlier finding (cf. Figure 8) on the relatively mild influence of pressure (compared to temperature) on gas phase hold-up, the results here reinforce the modest role of operating pressure on gas hold-up during reaction, Even so, there is a discernible trend in the values of the model parameters with increased pressure.

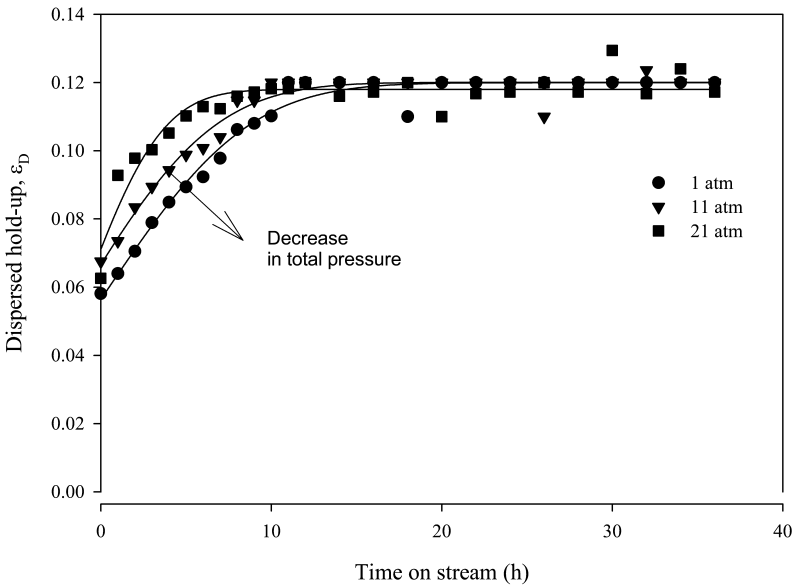

Figure 16. Transient profile of the dispersed phase hold-up at different total pressures, reaction condition: H_2:CO=9:1, Temperature = 498 K.

Figure 17 shows that the total hydrocarbon synthesis rate followed a 1st order exponential rise to a final steady-state value with time-on-stream. Although this behaviour is similar to the stirred reactor dynamics under non-reactive conditions (cf. Figure 3), the difference in time-constants is evident when data in Figure 3 and 17 were individually fitted to the expression:

$$y_P = y_P^{SS}\left[1-\exp(-t/\tau_P)\right] \qquad (24)$$

Downloaded by STANFORD UNIV GREEN LIBR on June 6, 2012 | http://pubs.acs.org
Publication Date (Web): November 29, 2011 | doi: 10.1021/bk-2011-1084.ch008

where y_P is the time-dependent response of the operation P to a step-change in y and y_P^{SS} is the final or ultimate value of y at steady-state while τ_P is the time-constant for the particular operation. The data in Figure 3 were collected when the reactor was operated under identical conditions (temperature and pressure to FT reaction) but using pure Ar as the feed before an abrupt switch to pure N_2 stream. Nonlinear regression of the data in both plots to Eq. (24) provided τ_P for the non-reactive conditions as 26 mins while the reaction rate has a corresponding value of 1.28 hours. This clearly suggests that the net reaction relaxation time constant (a hybrid of the surface relaxation time constants for all elementary steps) during FTS is larger than the resistance due to mixing. The data in Figure 3, also showed an initial transport lag of about 6 mins. A mixing time constant of 26 mins confirms that the reaction dynamics (monitored for about 48 hours) was not disguised by fluid phase hydrodynamics or mixing.

Downloaded by STANFORD UNIV GREEN LIBR on June 6, 2012 | http://pubs.acs.org
Publication Date (Web): November 29, 2011 | doi: 10.1021/bk-2011-1084.ch008

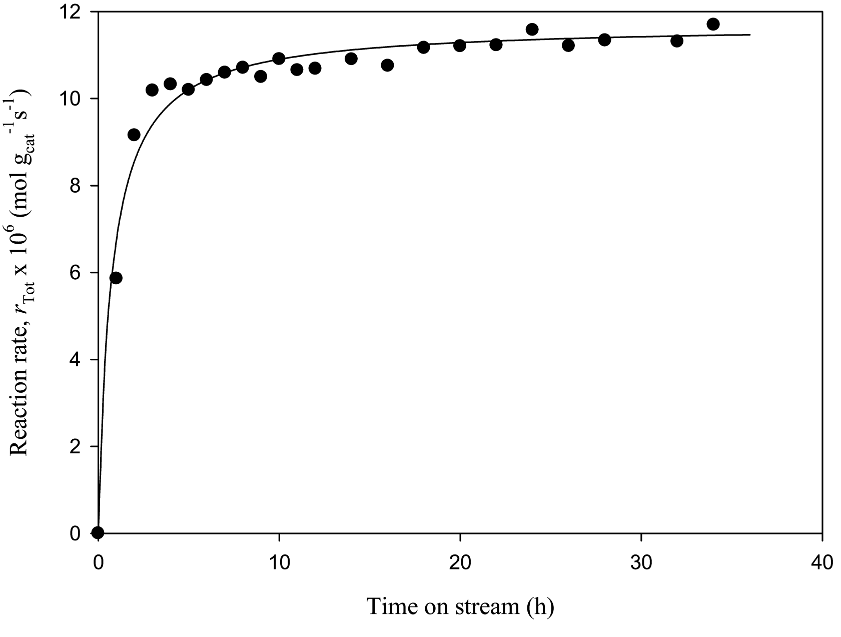

Figure 17. Reaction rate profile with time-on-stream at 498 K, 21 atm using feed with H_2:CO=9:1.

Interestingly, the plots in Figure 18(a, b) reveals that the individual hydrocarbon species also experienced similar reaction dynamics albeit characterized by different formation time-constants (reciprocal of the surface rate velocity) when the production rate data were fitted to Eq. (24). These estimates are summarized in Table 5.

Downloaded by STANFORD UNIV GREEN LIBR on June 6, 2012 | http://pubs.acs.org
Publication Date (Web): November 29, 2011 | doi: 10.1021/bk-2011-1084.ch008

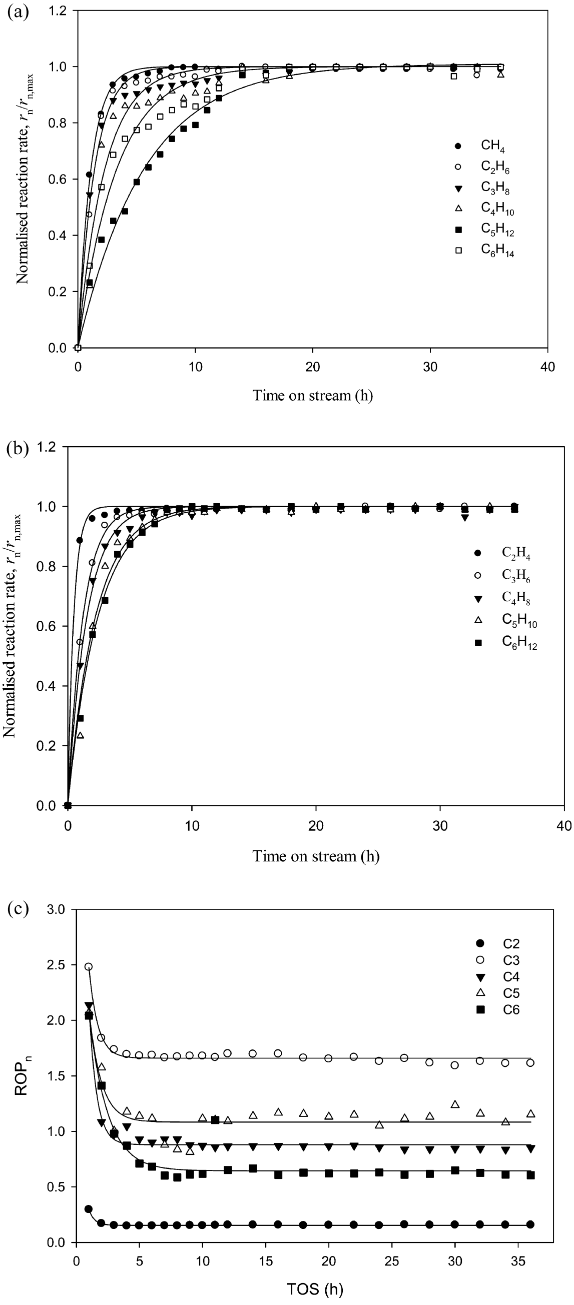

Figure 18. (a) Normalised reaction rate history of individual paraffinic species at T = 498 K, and 21 atm with a feed H_2:CO ratio= 9:1. (b) Normalised reaction rate history of individual olefinic species at T = 498 K, and 21 atm with a feed H_2:CO ratio= 9:1. (c) ROP as a function of time-on-stream, T = 498 K, y_{H2}=0.9.

Table 5. Estimation of time-constant, τP, (hours) for individual hydrocarbons from Eq. (24)

	C_1	C_2	C_3	C_4	C_5	C_6
Paraffins	1.09	1.40	2.27	3.27	4.42	5.64
Olefins	-	0.48	1.22	1.54	2.23	2.43

These estimates revealed that for any carbon number, olefin has a shorter relaxation surface time constant than paraffin indicating that it is more reactive and serves as the precursor to paraffin. Additionally, the relationship between τ_P and carbon number, n, for both homologous series seemed to be adequately captured by;

$$\tau_P = \phi n^{\xi} \tag{25}$$

with the pair φ and ξ as 0.91 and 0.95 for paraffins and 0.20 and 1.47 for olefins. The power-law dependency of the relaxation time constant on carbon chain length is consistent with the polymerization nature of the FT reaction. Figure 18c suggestes that the ROP value initiallydropped with time-on-stream but reached an essentially constant value after about 10 hours for all hydrocarbon species. Even so, it is apparent that the time to complete this initial drop increased with carbon number.

The associated chain growth probability with time-on-stream is also shown in Figure 19, The data suggests an initial regime (within the first 5 hours –Region I) where the chain growth factor increased linearly with TOS followed by a longer period of about 25 hours (Region II) during which α was essentially constant and a final stage (Region III) where another linear increase with TOS was experienced. However, the chain growth factor was somewhat insensitive to temperature.This behaviour has also been observed in previous studies (*2*, *13*, *20*), In particular, the relation between α and temperature, T may be written as;

$$\alpha = \frac{r_p}{r_p + r_t} = \frac{A_p f_p \exp(-E_p / RT)}{A_p f_p \exp(-E_p / RT) + A_t f_t \exp(-E_t / RT)} = \frac{1}{\left[1 + \frac{A_t f_t}{A_p f_p} \exp\{-(E_t - E_p)/RT\}\right]} \tag{26}$$

where both A_p and A_t are the propagation and termination rate frequency factors respectively with f_p and f_t as associated functions of feed composition i.e. H_2 and CO partial pressures for the propagation and termination steps respectively. It is apparent that for a given composition, the variation of α with increasing temperature may either show a decreasing ($E_t > E_p$) or increasing ($E_t < E_p$) trend or be somewhat insensitive or even diffused depending on the relative magnitude of

Downloaded by STANFORD UNIV GREEN LIBR on June 6, 2012 | http://pubs.acs.org
Publication Date (Web): November 29, 2011 | doi: 10.1021/bk-2011-1084.ch008

E_p and E_t and the ratio A_tf_t/A_pf_p This explains why different effects of temperature has been reported in the literature (*22*).

The changes observed in the present work implicate an ongoing interaction between the physicochemical properties of the reaction medium and reaction metrics and hence, the transient behaviour observed in the dispersed phase hold-up as reaction progressed. While the initial rise in α value in Region I is a reflection of the intrinsic propagation step in hydrocarbon synthesis on the catalyst surface, the plateau in Region II suggests an equilibration between the liquid phase and the gas phase individual hydrocarbon composition. These two regimes parallel the behaviour seen in the dispersed phase hold-up with time-on-stream. The trend seen in Region III may, however, be due to the production of hydrocarbons from the break-down of waxy deposit (which had accumulated in the previous two regions). Although gas phase CO conversion would remain constant in this regime, hydrocarbon production would be a combination of the intrinsic FT propagation step as well as the cracking of waxy deposit on the catalyst surface and hence, a rejuvenative increase in α-value. Intuitively, Region III itself would attain a new climax and then level off, although the 2-day run period was probably insufficient to realize this proposed stage. The dispersed phase hold-up would not be affected in Region III since the same hydrocarbon species were produced but only in greater amounts and hence, no discernible variation in the physicochemical properties of the liquid phase composition.

Downloaded by STANFORD UNIV GREEN LIBR on June 6, 2012 | http://pubs.acs.org
Publication Date (Web): November 29, 2011 | doi: 10.1021/bk-2011-1084.ch008

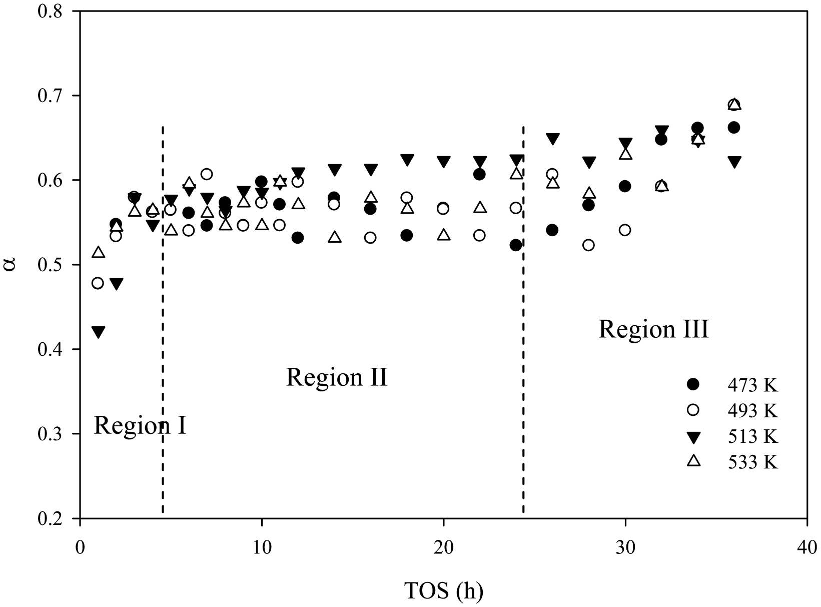

Figure 19. ASF chain growth factor as function of time-on-stream (TOS), P = 21 atm.

Figure 20 indeed confirms that CO conversion also rose to a final steady-state value consistent with the individual hydrocarbon production history.

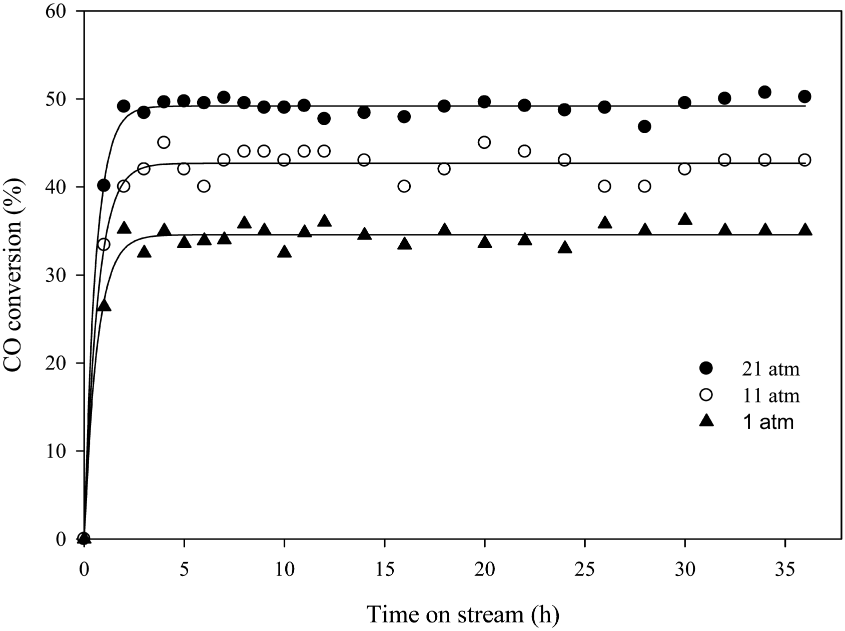

Figure 20. CO conversion history for FTS at T =: 498 K, and syngas ratio H_2:CO=9:1.

Conclusions

The non-invasive monitoring of an FTS slurry reactor using electrical capacitance tomography has shown that the multiphase hydrodynamic attributes such as dispersed phase hold-up (and by inference solid recirculation rate and distribution) are intimately intertwined with the reaction metrics (rate, product selectivity, etc). This coupling is due to the changing physicochemical properties of the liquid phase medium as product accumulation continues in the course of the reaction. This phenomenon is especially important in FTS operation since it can help to unlock some of the peculiar reaction performance (evolution of chain growth factor, α) observed over a long run time and we have attermpted to understand this association using ECT probing in the present work. This dynamic feedback between transport and reaction processes has not been previously unabmiguously identified. However, the present analysis has provided, for the first time, a quantitative relation between reaction rate and dispersed phase hold-up. Furthermore, the data demonstrated that under non-isothermal conditions, changes in gas phase hold-up could not be accounted for by simple thermal expansion. Indeed, the sigmoid-shaped thermotemporal relationship for the disepred phase hold-up in the slurry FT reactor was also derived and shown

Downloaded by STANFORD UNIV GREEN LIBR on June 6, 2012 | http://pubs.acs.org
Publication Date (Web): November 29, 2011 | doi: 10.1021/bk-2011-1084.ch008

Downloaded by STANFORD UNIV GREEN LIBR on June 6, 2012 | http://pubs.acs.org
Publication Date (Web): November 29, 2011 | doi: 10.1021/bk-2011-1084.ch008

to be a combination of volumetric expansion and a reaction-controlled increment. Although the gas phase hold-up increased linearly with operating total pressure, the accompanying improvement was relatively small compared to thermal or reaction-induced effects. Analysis of the FT reaction rate data showed that the olefin-to-paraffin ratio, ROP, is has a maximum at carbon number between 3 and 4. Moreover, ROP is also a strong function of the hydrogen composition in the feed mixture and this was confirmed by the dependency of the parameters of the proposed ROP model on feed H_2:CO ratio.

The approach taken in this study (tomographical analysis and empirical modeling) represents a new paradigm in the treatment of reaction rate data from a gas-solid-liquid reactor and over time, would help elucidate some of the apparent anomalous or pathoglogical behaviour observed in slurry reactor systems. The ECT-based models developed may also be reliably employed for process simulation and optimization as well as providing additional insights into the fundamental nature of the reaction chemistry (since the tomographical inquiry is non-obtrusive)

Acknowledgments

The authors acknowledge the financial support of the Australian Research Council. BA is grateful to PETRONAS, Malaysia and UTP for scholarship and study leave.

References

1. Bai, L.; Xiang, H.-W.; Li, Y.-W.; Han, Y.-Z.; Zhong, B. *Fuel* **2002**, *81*, 1577–1581.
2. Bukur, D. B.; Sivaraj, C. *Appl.Catal., A* **2002**, *231*, 201–214.
3. Adesina, A. A. *Appl.Catal., A* **1996**, *138*, 345–367.
4. Joshi, J. B. *Chem. Eng. Commun.* **1980**, *5*, 109.
5. Joshi, J. B.; Sharma, M. M. *Can. J. Chem. Eng.* **1977**, *65*, 683.
6. Forrester, S. F.; Reilly, C. D.; Carpenter, K. J. *Chem. Eng. Sci.* **1998**, *53*, 603–615.
7. Sawant, S. B.; Joshi, J. B. *Chem. Eng. J.* **1979**, *18*, 87–91.
8. Murthy, B. N.; Kasundra, R. B.; Joshi, J. B. *Chem. Eng. J.* **2008**, *141*, 332–345.
9. Hardiman, K. M.; Cooper, C. G.; Adesina, A. A. *Ind. Eng. Chem. Res.* **2004**, *43*, 6006–6013.
10. Cheng, C. K.; Foo, S. Y.; Adesina, A. A. *Catal. Today*, *164* (1), 268–274.
11. Chu, W.; Chernavskii, P. A.; Gengembre, L.; Pankina, G. A.; Fongarland, P.; Khodakov, A. Y. *J. Catal.* **2007**, *252* (2), 215–230.
12. Jacobs, G.; Chaney, J. A.; Patterson, P. M.; Das, T. K.; Davis, B. H. *Appl. Catal., A* **2004**, *264* (2), 203–212.
13. Cooper, C. G.; Nguyen, T.-H.; Lee, Y.-J.; Hardiman, K. M.; Safinski, T.; Lucien, F. P.; Adesina, A. A. *Catal. Today* **2008**, *131* (1-4), 255–261.

14. Yaluris, G.; Larson, R. B.; Kobe, J. M.; González, M. R.; Fogash, K. B.; Dumesic, J. A. *J. Catal.* **1996**, *158*, 336–342.
15. Mekhemer, G. A. H.; Abd-Allah, H. M. M.; Mansour, S. A. A. *Colloids Surf., A* **1999**, *160* (3), 251–259.
16. Morterram, C.; Colluccia, S.; Chionino, A.; Bocuzzi, F. *J. Catal.* **1978**, *54*, 348.
17. Vilar, G.; Williams, R. A.; Wang, M.; Tweedie, R. J. *Chem. Eng. J.* **2008**, *141*, 58–66.
18. Bell, A. T. *Catal. Rev. − Sci. Eng.* **1981**, *23*, 203–232.
19. Ma, W.; Ding, Y.; Carreto-Vaquez, V. H.; Bukur, D. B. *Appl. Catal., A* **2004**, *268*, 99–106.
20. Satterfield, C. N.; Huff, G. A. *Chem. Eng. Sci.* **1980**, *35*, 195–202.
21. Neathery, J. K.; Davis, B. H. *Catal. Today* **2003**, *84*, 3–8.
22. Vo, D. V. N.; Adesina, A. A. *Appl. Catal., A* **2011**, in press.

Downloaded by STANFORD UNIV GREEN LIBR on June 6, 2012 | http://pubs.acs.org
Publication Date (Web): November 29, 2011 | doi: 10.1021/bk-2011-1084.ch008

Downloaded by PENNSYLVANIA STATE UNIV on June 6, 2012 | http://pubs.acs.org
Publication Date (Web): November 29, 2011 | doi: 10.1021/bk-2011-1084.ch009

Chapter 9

Indirect Liquefaction Carbon Efficiency

Arno de Klerk*

**Department of Chemical and Materials Engineering,
University of Alberta, Edmonton, Alberta, Canada T6G 2V4
*Tel: +1 780-248-1903. E-mail: deklerk@ualberta.ca.**

The carbon efficiency of indirect liquefaction is studied to determine factors affecting carbon loss. Carbon loss takes place during all conversion steps: feed pretreatment, feed-to-syngas conversion, syngas conditioning, syngas-to-syncrude conversion and refining. Carbon loss is associated with both energy and chemistry demands. Indirect liquefaction has a carbon efficiency around 34 % (coal) depending on the feed.

Introduction

Biomass, coal, natural gas and waste can be employed as raw materials for the production of useful carbon-based commodities. The first step is to convert the aforementioned raw materials into a synthetic crude oil. The synthetic crude oil, like conventional crude oil, can then be refined to produce the carbon-based transportation fuels, lubricants and petrochemicals.

The conversion of alternative carbon sources into a synthetic crude oil requires some work. Whenever work is performed, according to the Second Law of thermodynamics some energy must be irreversibly expended. Since the carbon sources are also energy carriers, some of the carbon can be sacrificed in order to perform the work that is required to transform the raw material into a synthetic crude oil. The energy is extracted through the combustion of the carbon and the carbon is sacrificed as carbon dioxide (CO_2). Considering the current political sensitivity surrounding CO_2 emissions, this is an unpalatable but unavoidable consequence of transforming a carbon based raw material into a different form. For example, the transformation of a carbon-based energy carrier into electricity has an efficiency of 45 % (*1*). That is, only 45 % of the carbon-based energy is converted into electric energy; 55 % of the carbon is rejected in order to perform the work.

Depending on the ultimate application, an efficiency calculation based on the energy content of the product may be a good metric. However, in the case of lubricants and petrochemicals, the product is not an energy carrier, but a carbon-based product. In these cases the conservation of carbon during the transformation is a better metric.

Carbon efficiency can also be employed for energy applications, but the chemical nature of the carbon determines its energy content and there is not a direct correlation between the carbon efficiency and the thermal efficiency. Furthermore, transportation fuels must meet specific requirements and it is not just the energy content that is important. The usefulness of the carbon-based energy carrier as a transportation fuel is measured against these requirements that include performance characteristics for the specific engine type. Carbon efficiency is a useful metric to quantify this transformation, because it speaks to the ultimate objective of indirect liquefaction, namely to produce a useful liquid fuel with specific performance characteristics.

Downloaded by PENNSYLVANIA STATE UNIV on June 6, 2012 | http://pubs.acs.org
Publication Date (Web): November 29, 2011 | doi: 10.1021/bk-2011-1084.ch009

Table I. Yield of main transportation fuels that could be obtained from conventional crude oil refining in United States oil refineries over time

Transportation fuel	*Yield of product (%)* [a]				
	1964	*1974*	*1984*	*1994*	*2003*
Motor-gasoline	44.1	45.9	46.7	45.7	46.9
Jet fuel	5.6	6.8	9.1	10.1	9.5
Diesel fuel	22.8	21.8	21.5	22.3	23.7
Total for transportation fuels	72.5	74.5	77.3	78.1	80.1
Overall yield [b]	90.1	92.3	92.9	95.4	96.8

[a] Units of yield are ambiguous in source, but it is likely based on volume, not mass. [b] Includes other potentially useful products, such as liquefied petroleum gas, fuel oil, coke and asphalt.

Conventional crude oil is an efficient carbon-based raw material for the production of transportation fuels, as can been seen from Table I (*2*). Over time improvements in refining enabled increasingly higher yields of motor-gasoline, jet fuel and diesel fuel. These yields roughly correspond to carbon efficiency.

When the decision is made to employ an alternative carbon source to conventional crude oil for the production of transportation fuels or chemicals, it is anticipated that the carbon efficiency will be lower. Of specific interest in this study is the carbon efficiency during indirect liquefaction and what the prognosis is for improving it over time. Thereby this work also addresses the CO_2 footprint of indirect liquefaction technology.

Downloaded by PENNSYLVANIA STATE UNIV on June 6, 2012 | http://pubs.acs.org
Publication Date (Web): November 29, 2011 | doi: 10.1021/bk-2011-1084.ch009

Indirect Liquefaction

Indirect liquefaction is a collective term for the group of technologies that convert carbon based raw materials into synthetic crude oil through synthesis gas as intermediate product. Synthesis gas is a mixture of hydrogen (H_2) and carbon monoxide (CO). It is a convenient intermediate that allows the removal of heteroatoms and metals from the feed, with a significant benefit for subsequent refining of the synthetic crude oil. It also decouples the production and composition of the synthetic crude oil from the nature of the raw material that is employed as feed.

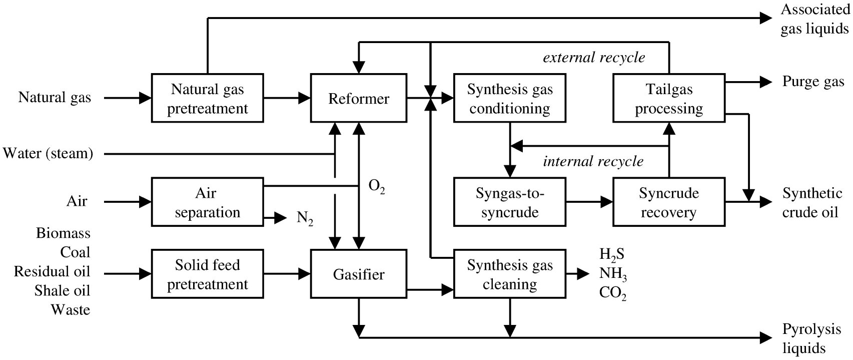
Associated gas liquids
Natural gas
Natural gas pretreatment
Reformer
external recycle
Synthesis gas conditioning
Tailgas processing
Purge gas
Water (steam)
internal recycle
Air
Air separation
O_2
N_2
Syngas-to-syncrude
Syncrude recovery
Synthetic crude oil
Biomass
Coal
Residual oil
Shale oil
Waste
Solid feed pretreatment
Gasifier
Synthesis gas cleaning
H_2S
NH_3
CO_2
Pyrolysis liquids

Figure 1. Generic indirect liquefaction process flow diagram indicating the most common recycle loops and product streams.

A generic indirect liquefaction process is shown in Figure 1. It indicates the pathways from gaseous, liquid and solid raw materials. Distinct steps can be identified, each of which requires work to be performed and potentially carbon to be sacrificed. It highlights the complexity associated with indirect liquefaction and the effort that is required to transform a carbon-based raw material into a synthetic crude oil. It should be noted that not all steps are required and that the design can be simplified. The extent of simplification depends on the raw material employed as feed and the technologies selected.

Feed Pretreatment

Natural gas may contain associated natural gas liquids, which are heavier hydrocarbons that be recovered by condensation. These associated liquid products allow some carbon to bypass the indirect liquefaction process and this stream increases the overall carbon efficiency. There is of course work performed during the recovery of the associated liquid products, which requires energy to be expended. The recovered associated liquid products can be refined with the synthetic crude oil, as is industrially practiced at the PetroSA gas-to-liquids facility in Mossel Bay, South Africa (*3*).

The feed pretreatment required for solid feed materials depends on the nature of the raw material and the requirements of the gasifier. Frequently it involves one or more of the following: mechanical size reduction, classifying (based on particle size), drying and slurrying. All of these feed pretreatment operations require work.

For clarification, it is necessary to point out that some carbon may be "lost" during pretreating because it does not conform to the physical requirements of the gasification technology. This carbon is not rejected as CO_2. The energy value of this carbon is still available and the chemical nature of carbon-carrier has not changed. For example, of the run of mine (ROM) coal prepared for moving bed gasification, approximately 25 % is rejected as fines (*4*). The fine coal can be employed in a different type of gasifier or it can be employed as an energy source. Carbon rejected based on particle size before entering the indirect liquefaction process is not considered a loss in carbon efficiency related to indirect liquefaction.

Downloaded by PENNSYLVANIA STATE UNIV on June 6, 2012 | http://pubs.acs.org
Publication Date (Web): November 29, 2011 | doi: 10.1021/bk-2011-1084.ch009

Air Separation

The use of air or pure oxygen (O_2) as oxidant in reforming or gasification is a design decision. Air separation requires work. Dry air contains roughly 78 % nitrogen (N_2), 21 % oxygen (O_2) and 1 % argon (Ar) in addition to various minor compounds. The minimum 'ideal' work (W_{ideal}) that is required to separate these three major compounds present in air, can be calculated as a function of the ideal gas constant ($R = 8.314\ J \cdot mol^{-1} \cdot K^{-1}$), temperature ($T$) and mol fractions of the respective compounds (x_j):

$$W_{ideal} = RT\sum_{j=1}^{3} x_j \ln x_j \tag{1}$$

The thermodynamic efficiency of an air separation unit is around 33 % (*5*), and at standard conditions the energy requirement is around 0.6-0.7 $MJ \cdot kg^{-1}$ O_2.

There is a complex trade-off between air separation and the direct use of air for synthesis gas production. An air separation unit adds to the capital and operating cost, but inefficiencies caused by inert material are limited. When air is employed as oxidant the N_2 and Ar must also be heated to reforming or gasification conditions. Even with proper waste heat recovery, the inert gases place a significant burden on the energy requirements of all downstream processes. One exception is steam reforming, where energy is indirectly provided and the oxidant is not mixed with the carbon-based feed.

Large-scale industrial applications of indirect liquefaction that involves partial combustion by direct contact of the oxidant with the feed employ O_2 as oxidant. Incurring the penalty up front in the process is preferable and the pure N_2 that is produced as by-product from air separation also has value.

Gas Reforming

The term 'gas reforming' will be restricted to refer only to catalytic gas reforming. Thermal (non-catalytic) gas reforming technologies will be referred to as gasification. The chemistries in gas reforming and gasification are similar, but the use of a catalyst lowers the operating severity that is required.

Downloaded by PENNSYLVANIA STATE UNIV on June 6, 2012 | http://pubs.acs.org
Publication Date (Web): November 29, 2011 | doi: 10.1021/bk-2011-1084.ch009

Gas reforming technologies can be divided into two main categories: steam reforming and adiabatic oxidative reforming. The main difference between these to categories is the way in which heat is supplied.

In steam reforming the process feed that is converted into synthesis gas is kept separate from the heat source. The fuel and oxidant that supplies the energy to drive steam reforming can therefore be selected independently from the carbon source for indirect liquefaction. A further advantage is that the oxygen to carbon ratio in the feed can be manipulated independently of the energy requirements and it is only subject to catalytic requirements, thereby enabling some control over the synthesis gas composition:

$$CH_4 + H_2O \rightleftharpoons CO + 3\ H_2\ ,\ \Delta H_{298K} = +206\ kJ{\cdot}mol^{-1} \qquad \textbf{(2)}$$

$$CH_4 + CO_2 \rightleftharpoons 2\ CO + 2\ H_2\ ,\ \Delta H_{298K} = +247\ kJ{\cdot}mol^{-1} \qquad \textbf{(3)}$$

In adiabatic oxidative reforming the oxidant is mixed with the process feed and energy is supplied directly to the process by partial combustion of the feed. This simplifies the process and results in a more compact and efficient gasifier design, but the fuel and oxidant are now part of the process feed and cannot be selected independently. Control over the synthesis gas composition is limited and for the most part determined by the energy requirements and the catalytic requirements of the process. In addition to the endothermic steam reforming (Eq. 2) and dry reforming (Eq. 3) reactions, energy is supplied by partial or complete combustion of the natural gas feed:

$$CH_4 + 1\tfrac{1}{2}\ O_2 \rightarrow CO + 2\ H_2O\ ,\ \Delta H_{298K} = -519\ kJ{\cdot}mol^{-1} \qquad \textbf{(4)}$$

$$CH_4 + 2\ O_2 \rightarrow CO_2 + 2\ H_2O\ ,\ \Delta H_{298K} = -802\ kJ{\cdot}mol^{-1} \qquad \textbf{(5)}$$

It is theoretically possible to convert all of the carbon in natural gas into synthesis gas. By combining Eq. 2 and 4 it can be shown that all of the carbon in the feed ends up in synthesis gas:

$$3\ CH_4 + 1\tfrac{1}{2}\ O_2 \rightarrow 3\ CO + 6\ H_2\ ,\ \Delta H_{298K} = -107\ kJ{\cdot}mol^{-1} \qquad \textbf{(6)}$$

In practice some of the carbon is lost due to CO_2 production and unconverted CH_4 effectively bypassing the gas reformer (*6*). It is possible to recover this lost carbon by appropriate gas loop design. In practise this recovery and recycling costs work. This outcome may seem counterintuitive. How is it possible to retain all of the carbon if work is being performed to enable these high temperature transformations?

Part of the answer lies in the loss of thermal efficiency due to partial carbon oxidation. The energy value of the carbon containing reforming product, carbon monoxide (CO), is considerably lower than that of the methane (CH_4) feed. Even though the carbon was retained, energy was rejected as lost heat. In Eq.6 the entropy change is is positive (ΔS_{298K} = +296 $J{\cdot}K^{-1}{\cdot}mol^{-1}$), indicating that some energy had to be expended to satisfy the Second Law of thermodynamics.

Although the carbon efficiency from natural gas reforming can theoretically be 100 %, the thermal efficiency is less. The second part of the answer is related to the H:C balance of the feed. Methane is sufficiently hydrogen-rich so that it is not necessary to sacrifice CO to produce H_2 from water.

Gasification

The term ‘gasification’ is employed for the thermal conversion of natural gas, as well as other solid and liquid carbon sources, such as coal, biomass, waste and petroleum waste products (e.g. petroleum coke and ashphaltenes). Gasification takes places at very high temperature, usually in the range 800-1800 °C. All carbon containing compounds in the feed material is broken down to C_1 fragments at gasification temperatures.

There are many different types of gasifiers (Table II). Many of the gasifier technologies were originally developed for coal gasification and the literature on coal gasification is consequently more extensive than that for other feed types. The selection and operation of gasifier technology is very dependent on the feed material (*7*). The gasifier type and raw material employed as feed, both affect the composition of the syngas, but ultimately most of the carbon is converted to C_1 fragments, mainly CO, CO_2 and CH_4. There are two important exceptions: (a) Some gasifiers co-produce pyrolysis products ($>C_1$ fragments), and (b) not all carbon is necessarily converted and some solid carbon may remain as an unconverted solid carbonaceous product.

Table II. Main gasifier types and their associated carbon conversion characteristics

Description	*Moving bed*	*Fluidized bed*	*Entrained flow*
Carbon conversion	>98 %	<97 %	>99 %
Pyrolysis products in gas	Yes	Possibly	No
H_2:CO in raw syngas	>2:1 to <1:1	<1:1	~1:2

The conversion chemistry is very similar to that of gas reforming. The gas reforming reactions (Eq. 2–6) take place in parallel with carbon conversion that can be viewed as hydrogen-deficient analogues of gas reforming. Steam gasification (Eq. 7), the Boudouard reaction (Eq. 8), methanation (Eq. 9) and water gas shift (WGS) reaction (Eq. 10) all contribute to the production of syngas during gasification:

$$C + H_2O \rightleftharpoons CO + H_2\ ,\ \Delta H_{298K} = +131\ kJ{\cdot}mol^{-1} \qquad \textbf{(7)}$$

$$C + CO_2 \rightleftharpoons 2\ CO\ ,\ \Delta H_{298K} = +172\ kJ{\cdot}mol^{-1} \qquad \textbf{(8)}$$

Downloaded by PENNSYLVANIA STATE UNIV on June 6, 2012 | http://pubs.acs.org
Publication Date (Web): November 29, 2011 | doi: 10.1021/bk-2011-1084.ch009

$$C + 2\ H_2 \rightarrow CH_4\ ,\ \Delta H_{298K} = -75\ kJ{\cdot}mol^{-1} \quad \textbf{(9)}$$

$$CO + H_2O \rightleftharpoons CO_2 + H_2\ ,\ \Delta H_{298K} = -41\ kJ{\cdot}mol^{-1} \quad \textbf{(10)}$$

Steam gasification, like steam reforming, is endothermic. Partial and complete oxidation of the carbon provides the energy for gasification:

$$C + \tfrac{1}{2}\ O_2 \rightarrow CO\ ,\ \Delta H_{298K} = -110\ kJ{\cdot}mol^{-1} \quad \textbf{(11)}$$

$$C + O_2 \rightarrow CO_2\ ,\ \Delta H_{298K} = -393\ kJ{\cdot}mol^{-1} \quad \textbf{(12)}$$

Downloaded by PENNSYLVANIA STATE UNIV on June 6, 2012 | http://pubs.acs.org
Publication Date (Web): November 29, 2011 | doi: 10.1021/bk-2011-1084.ch009

What should be immediately apparent is that the conversion of hydrogen-poor feed material (Eq. 11–12) is 409 $kJ{\cdot}mol^{-1}$ less exothermic than the conversion of hydrogen-rich feed material (Eq. 4–5). The heat of hydrogen combustion to water markedly affects the energy balance. The H:C ratio of the feed is critical to both the thermal and the carbon efficiency of syngas production and is a topic that will be revisited later on. For a pure carbon source, gasification with steam and oxygen can be approximated by a combination of the endothermic and exothermic reactions, for example:

$$2\ C + 2\ H_2O + \tfrac{1}{2}\ O_2 \rightarrow CO + CO_2 + 2\ H_2\ ,\ \Delta H_{298K} = -20\ kJ{\cdot}mol^{-1} \quad \textbf{(13)}$$

$$4\ C + 3\ H_2O + O_2 \rightarrow 3\ CO + CO_2 + 3\ H_2\ ,\ \Delta H_{298K} = 0\ kJ{\cdot}mol^{-1} \quad \textbf{(14)}$$

The syngas composition is affected by both the lack of hydrogen in the carbon source, as well as the steam to oxygen ratio. The examples (Eq. 13–14) of combined reactions are just two possible linear combinations of Eq. 7–12. It nevertheless illustrates how operating conditions during gasification affect the H_2:CO ratio in syngas, which varies from more than 2:1 to around 1:2 (Table II). It also determines the amount of carbon that is rejected as CO_2.

When a H_2:CO ratio of 2:1 is required, 50 % of the carbon from the feed is sacrificed (Eq. 13) to produce the syngas.

Water Gas Shift Conditioning

The H_2:CO ratio that is required by the syngas-to-syncrude conversion technology may be different from the H_2:CO ratio produced during syngas production by refomring or gasification. It is possible to adjust the H_2:CO ratio by making use of the water gas shift reaction (Eq. 10).

The carbon efficiency of WGS conditioning must not be considered in isolation. It is a conditioning step. Carbon in the form of CO can be sacrificed to produce H_2 from water. Likewise, with some additional energy input, surplus H_2 can be sacrificed to recover carbon that was rejected as CO_2. The need for WGS conditioning is apparent only in the context of the overall XTL process.

Downloaded by PENNSYLVANIA STATE UNIV on June 6, 2012 | http://pubs.acs.org
Publication Date (Web): November 29, 2011 | doi: 10.1021/bk-2011-1084.ch009

Syngas Cleaning

The purpose of syngas cleaning is to remove contaminants from the syngas and notably all the sulfur compounds. Syngas cleaning technologies make use of either chemical or physical absorption of the contaminant gases. The impact on carbon efficiency is mainly that of the energy footprint of the technology.

Syngas-to-Syncrude Conversion

All of the conversion steps thus far discussed were needed to prepare the syngas for indirect liquefaction. The actual conversion of the syngas into liquid products takes place during syngas-to-syncrude conversion. At present there are two main classes of syngas-to-syncrude conversion technologies that are industrially applied: syngas-to-methanol conversion (Eq. 15) and Fischer–Tropsch hydrocarbon synthesis (Eq. 16).

$$CO + 2\,H_2 \rightarrow CH_3OH\ ,\ \Delta H_{298K} \approx -130\ kJ{\cdot}mol^{-1} \qquad \textbf{(15)}$$

$$CO + 2\,H_2 \rightarrow -(CH_2)- + H_2O\ ,\ \Delta H_{298K} \approx -180\ kJ{\cdot}mol^{-1} \qquad \textbf{(16)}$$

Fischer–Tropsch hydrocarbon synthesis, as expressed by Eq. 16, is an oversimplification of the reaction network found during Fischer–Tropsch synthesis. In addition to hydrocarbons, Fischer–Tropsch conversion produces different classes of oxygenates. The co-production of oxygenates (alcohols, carbonyls and carboxylic acids) have implications for downstream refining. The production of oxygenates instead of hydrocarbons do not directly affect the carbon efficiency. Indirectly, oxygenates result in higher carbon efficiency, because less H_2 is rejected as water. Water gas shift conditioning can use the H_2 that is thus retained to convert some CO_2 into CO for synthesis.

No carbon is lost during the actual syngas-to-syncrude conversion process, but there are important differences between the different industrial processes (Table III) (*8–13*) that indirectly affects carbon efficiency.

The temperature at which conversion is conducted determines the quality of the energy recovered from the exothermic reaction. Steam generated to remove reaction heat is available at a higher pressure when the operating temperature is higher and more work can be recovered.

The per pass CO conversion affects the potential for carbon loss during syncrude recovery and recycling of the unconverted syngas. A higher per pass CO conversion is likely to lead to higher overall carbon efficiency and the degree of recycle is determined by the gas loop design (*6*). In fact, the design of the gas loop affects more than just carbon loss from unconverted syngas.

Downloaded by PENNSYLVANIA STATE UNIV on June 6, 2012 | http://pubs.acs.org
Publication Date (Web): November 29, 2011 | doi: 10.1021/bk-2011-1084.ch009

Table III. Typical operating conditions and per pass CO conversion of the main industrial syngas-to-syncrude conversion processes

Syngas-to-syncrude technology	*Temperature (°C)*	*Pressure (MPa)*	*Per pass CO conversion (%)*
High temperature Fischer–Tropsch (Fe)	320-340	1-3	>80
Low temperature Fischer–Tropsch (Fe)	200-250	1-5	40-60
Low temperature Fischer–Tropsch (Co)	170-220	<3	40-60
Methanol synthesis ($CuO/ZnO/Al_2O_3$)	200-300	3.5-5.5	10-35

Table IV. Syncrude composition and product phases at ambient conditions, excluding unconverted syngas ($CO + H_2$), CO_2 and inert gases (N_2 + Ar)

Fischer-Tropsch products	*Syncrude (mass %)*		
	Fe-HTFT	*Fe-LTFT*	*Co-LTFT*
Gaseous products			
methane	6.5	2	2.5
ethene	2.9	0.5	< 0.1
ethane	2.3	0.5	0.5
propene	5.9	1.6	0.9
propane	0.8	0.4	0.4
butenes	5	1.2	0.6
butanes	0.7	0.4	0.4
Organic liquid products			
naphtha (C_5-C_{10})	17.2	5.8	8.9
distillate (C_{11}-C_{22})	3.7	9.1 [a]	9.7 [a]
residue (>360 °C)	1.5 [a]	-	-
Organic solid products			
waxes	-	23.4	19.8
Aqueous phase products			
oxygenates	5	2	0.7
water	48.5	53.1	55.6

[a] Part of this fraction may precipitate as a waxy solid at ambient conditions.

Unlike methanol, Fischer–Tropsch syncrude consists of a multi-phase mixture of many different compounds (Table IV). Syncrude recovery after Fischer–Tropsch synthesis is more complicated and the design of this aspect of the gas loop also affects carbon loss due to unrecovered syncrude (*13*).

Unless the gas loop design includes recovery of the gaseous hydrocarbons, the carbon efficiency is decreased when the tail gas is used as fuel gas. Even when the tail gas is recycled to produce synthesis gas, some carbon is indirectly lost. Every carbon atom in the syncrude was produced by CO hydrogenation and is accompanied by an effective decrease in the H:C ratio relative to the feed (Table V). Although Fischer–Tropsch synthesis itself conserves carbon, it does so at the expense of hydrogen, which affects the carbon efficiency of syngas production.

Downloaded by PENNSYLVANIA STATE UNIV on June 6, 2012 | http://pubs.acs.org
Publication Date (Web): November 29, 2011 | doi: 10.1021/bk-2011-1084.ch009

Table V. Effective decrease in feed H:C ratio when recycling Fischer–Tropsch tail gas for syngas production instead of recovering the hydrocarbons in the tail gas as final products

Syncrude product	*Syngas requirement*			*Product H:C ratio*	*Decrease in H:C ratio (%)*
	H_2	*CO*	*H:C*		
Methane (CH_4)	3	1	6	4	33
Ethene (C_2H_4)	4	2	4	2	50
Ethane (C_2H_6)	5	2	5	3	40
Propene (C_3H_6)	6	3	4	2	50
Propane (C_3H_8)	7	3	4.7	2.7	43
Butene (C_4H_8)	8	4	4	2	50
Butane (C_4H_{10})	9	4	4.5	2.5	44

Syncrude Refining

It was shown (Table I) that modern crude oil refineries are quite efficient at the conversion of crude oil into final products, with a transportation fuel yield of around 80 %. It was reported that a properly designed Fischer–Tropsch refinery could be more efficient than a crude oil refinery (*14*). A transportation fuel yield of around 85 % on a mass basis is possible in a Fischer–Tropsch fuels refinery and the volumetric yield is even higher, at around 1.1 $m^3 \cdot t^{-1}$ (*13*, *15*). When the production of liquid petroleum gas is included in the marketable liquid yield, the carbon efficiency of a Fischer–Tropsch fuels refinery without petrochemical co-production is around 90 %.

In order to achieve such a high carbon efficiency in the refinery, it is necessary to refine all of the carbon containing material in the syncrude that is sent to the refinery. This includes refining of the aqueous product and light hydrocarbons recovered from the tail gas:

(a) Methane does not have any refining pathway. It can be sold as a final product though, namely as substitute natural gas (SNG). This is nonsensical if natural gas is the raw material feed to the XTL process. When a solid raw material feed is employed for XTL, methane may indeed be a useful final product. For example, the Great Plains synfuels plant in North Dakota was designed specifically to turn coal into SNG (*16*). Methane is a useful carbon carrier when the necessary pipeline infrastructure for distribution exists.

(b) Ethene is a typical petrochemical product. It can be purified and sold as final commodity chemical. In XTL facilities that are far from petrochemical markets, this may present a problem. Alternative refining pathways include aromatic alkylation, oligomerization and hydration.

(c) Ethane does not have a clear fuel refining pathway, but it is a preferred feed for thermal cracking (steam cracking) to produce ethene. It can to a limited extent also be included in SNG. As precursor to ethene it suffers from the same drawbacks when the XTL facility is far from petrochemical markets.

(d) The aqueous product from Fischer–Tropsch synthesis has no equivalent counterpart in a conventional crude oil refinery. Refining pathways have been suggested (*17*), but there is no clear pathway for the efficient recovery of the carboxylic acids. The carboxylic acids have higher boiling points than water and after recovery of most of the other oxygenates from the aqueous product, the carboxylic acids remain as a dilute (~1 %) aqueous solution. Recovery by distillation is too energy intensive. A solvent extraction process was piloted with methyl tertiary butyl ether (MTBE), but it was not economical either (*18*).

Downloaded by PENNSYLVANIA STATE UNIV on June 6, 2012 | http://pubs.acs.org
Publication Date (Web): November 29, 2011 | doi: 10.1021/bk-2011-1084.ch009

The advantage of methanol synthesis over Fischer–Tropsch synthesis with respect to carbon efficiency is clear. Methanol is a liquid, a commodity chemical and a final product that can easily be transported from the XTL facility without further refining. Fischer–Tropsch syncrude may be easier to refine than crude oil, but the carbon efficiency in the refinery can easily be degraded by the abundance of material in the light hydrocarbon and aqueous product fractions. On a carbon basis, methane, ethene, ethane and the aqueous product oxygenates constitute 32-33% of Fe-HTFT syncrude, 10-11 % of Fe-LTFT syncrude and 8-9 % of Co-LTFT syncrude (Table IV).

The Fischer–Tropsch gas loop design will determine whether the light hydrocarbons are recovered from the tail gas for refining (*13*), and strictly speaking, carbon loss must be divided between the gas loop and refinery.

Effective H:C Ratio

In the previous section it was shown that the carbon efficiency during syngas generation depends directly on the H:C ratio of the feed. Tracking the fate of carbon only, can be misleading.

Methane has a H:C ratio of 4:1, which is the highest of any of the carbon sources (Table VI). It is therefore not surprising to find that natural gas reforming is the most efficient way to produce synthesis gas. This is partly due to the high H:C ratio of the feed material and partly to the simplicity of the feed. No C-C bond scission is required. There is also “spare” hydrogen to reject as water in order to provide reaction heat for the endothermic reforming reactions, instead of rejecting carbon as carbon dioxide to provide reaction heat.

Table VI. Hydrogen to carbon ratio and heteroatom content of alternative carbon sources based on mineral moisture free matter

Carbon source	*H:C ratio*	*Heteroatom content (mass %)*
Coal, anthracite	0.25 - 0.5	1 - 5
Coal, bituminous	0.6 - 0.8	5 - 15
Coal, subbituminous	~ 0.8	15 - 25
Coal, lignite	~ 0.8	25 - 35
Peat	1.1 - 1.2	30 - 40
Biomass, lignin-rich	~ 1.2	25 - 30
Biomass, cellulosic	1.6 - 1.7	~ 50
Biomass, oils and fats	~ 1.9	10 - 15
Waste, plastic [a]	~ 2.0	< 1
Natural gas	~ 4.0	< 1

[a] Polyethylene and polypropylene

Most alternative carbon sources do not consist of just hydrocarbons, but include heteroatoms (Table VI). The main heteroatoms are oxygen, nitrogen and sulfur.

The rejection of oxygen, nitrogen and sulfur provides some energy benefit during gasification, but at the cost of lowering the effective H:C ratio (Table VII) and having a lower energy release. Under gasification conditions nitrogen and sulfur in heteroatom compounds will be mainly converted into H_2S, COS, N_2, HCN and NH_3 (1).

Furthermore, in coal, peat and biomass the dominant heteroatom is oxygen. In terms of energy content, one can consider these carbon sources as “partially combusted”, with a lower amount of energy that is released when producing either CO and CO_2 (Eq. 11–12) or H_2O during conversion into syngas. In fact, oxygen loss by dehydration is endothermic (Eq. 17).

$$CH_3CH_2OH \rightleftharpoons H_2C{=}CH_2 + H_2O\ ,\ \Delta H_{298K} = +46\ kJ{\cdot}mol^{-1} \qquad \textbf{(17)}$$

Downloaded by PENNSYLVANIA STATE UNIV on June 6, 2012 | http://pubs.acs.org
Publication Date (Web): November 29, 2011 | doi: 10.1021/bk-2011-1084.ch009

Downloaded by PENNSYLVANIA STATE UNIV on June 6, 2012 | http://pubs.acs.org
Publication Date (Web): November 29, 2011 | doi: 10.1021/bk-2011-1084.ch009

Table VII. Effective hydrogen to carbon ratio before and after reductive elimination of oxygen, nitrogen and sulfur (ONS)

Carbon source	*Heteroatom content (mass %)*	*H:C ratio*	
		feed	*after ONS elimination*
Biomass, cellulosic (Bermuda grass)	47.4	1.6	0.06
Biomass, lignin-rich (Pine wood)	40.4	1.4	0.29
Coal, lignite (Beulah-Zap)	22.2	0.79	0.32
Coal, subbituminous (Wyodak)	19.6	0.85	0.45
Coal, bituminous (Pocahontas #3)	4.3	0.58	0.50
Biomass, plant oil (Rapeseed oil)	10.8	1.9	1.7

There is consequently a meaningful energy difference between a high H:C feed, where partial oxidation can pay for much the energy requirements of the carbon transformation and the more modest contribution of a feed where hydrogen is lost due to heteroatom removal. The effective H:C ratio of carbon based feed materials after heteroatom removal (Table VII) is therefore a better indication of the carbon efficiency that can be expected than actual H:C ratio of the feed itself (Table VI).

It is interesting to note from Table VII that in a number of instances coals have higher effective H:C ratios than biomass and by implication, coal will have a higher carbon efficiency than biomass as feed for indirect liquefaction.

Carbon Efficiency

Carbon efficiency is a measure of how much carbon is retained in products compared that in the feed. In this respect it is a good indication of how successful indirect liquefaction is in converting one carbon-carrier into another. Although the subsequent discussion will focus on carbon efficiency, tracking the carbon alone is an insufficient measure of the overall efficiency of indirect liquefaction and there are other important aspects that must be borne in mind:

(a) Effective H:C ratio. The carbon efficiency of syngas generation is to a large extent determined by the chemistry. Hydrogen-rich carbon sources are inherently more carbon efficient, because energy can be derived from hydrogen rejection as H_2O, the oxide of hydrogen. Without excess hydrogen, energy must be derived from carbon rejection as CO_2, the oxide of carbon, thereby reducing the carbon efficiency.

(b) Energy consumption. The energy requirement of each conversion step has an associated carbon footprint. The energy use can be expressed on a carbon basis through the heat of combustion (Eq. 12). Depending on the application, more or less of the combustion heat can be gainfully employed by the process. An appropriate efficiency factor must therefore be included in the calculation to describe how much of the combustion heat is actually useful to the process. This is determined by the method of heat transfer, post-combustion heat recovery and the nature of the energy requirement, i.e. work or heat.

(c) Phase change. The conversion of a gaseous feed material into a liquid product gains some energy of condensation. Conversely, the conversion of a solid feed material into a liquid product must supply the energy associated with the phase change from solid to liquid.

(d) Thermal efficiency. Carbon efficiency and thermal efficiency are not independent of each other, but the relationship is complex. The thermal efficiency indicates how much of the energy content of the feed ends up in the products. This is a meaningful measure only if the product will be used as an energy carrier. In petrochemical applications the thermal efficiency becomes a mute point.

Downloaded by PENNSYLVANIA STATE UNIV on June 6, 2012 | http://pubs.acs.org
Publication Date (Web): November 29, 2011 | doi: 10.1021/bk-2011-1084.ch009

Effect of Carbon Source

In order to assess the carbon efficiency of indirect liquefaction, it is necessary to decouple the impact of the carbon source as feed, from the impact of the process itself. The carbon efficiency is improved as the effective H:C ratio of the carbon source increases. The carbon efficiency is also improved as the physical state of the carbon source changes from solid to liquid to gas phase, since less energy is required to enable the phase change to the gaseous state. Qualitatively it implies that the carbon efficiency of an indirect liquefaction process will improve purely due to the impact of the feed in the following order: biomass < coal < waste (plastic) < natural gas.

A comparison of the carbon efficiency of indirect liquefaction using coal and a coal-biomass mixture as feed material, indicated that the biomass cause the carbon efficiency to decrease (*19*). It was calculated that a 30 % increase in biomass (switch grass) content of a coal (Illinois #6 bituminous) feed resulted in a 1 % (absolute) decrease in carbon efficiency.

The impact of the carbon source can also be seen from the thermal efficiency, which should be in the same direction as carbon efficiency when the same liquefaction process is employed for the comparison. It has been reported that Fischer–Tropsch based gas-to-liquids (GTL) conversion has a thermal efficiency of around 60 %, with a theoretical maximum around 80 %, whereas Fischer–Tropsch based coal-to-liquids (CTL) conversion has a thermal efficiency of around 50 %, with a theoretical maximum around 60 % (*20*). A recent overview of CTL and biomass-to-liquids (BTL) configurations for energy applications indicated that the thermal efficiencies ranged from 43 to 53 % based on the higher heating value of the products (*21*).

Downloaded by PENNSYLVANIA STATE UNIV on June 6, 2012 | http://pubs.acs.org
Publication Date (Web): November 29, 2011 | doi: 10.1021/bk-2011-1084.ch009

Coal-to-Liquids Carbon Efficiency

In order to reduce the effect that different carbon sources have on the calculation of carbon efficiency, the following discussion will be restricted to coal-to-liquids conversion. Some feed based variation remains, since different coal types have different effective H:C ratios. Coal was selected despite this shortcoming, since coal formed the basis for more studies that allowed the calculation of indirect liquefaction carbon efficiency (Table VIII).

Table VIII. Carbon efficiencies of similar sized coal-to-liquids facilities based on Fischer–Tropsch synthesis

Carbon efficiency	*Gasifier type*	*Fischer–Tropsch technology*	*Refinery*	*Ref.*
28 %	[a]	HTFT	[a]	(*22*)
32 %	[a]	HTFT	excluded	(*23*)
32 %	Entrained flow	HTFT	excluded	(*20*)
33 %	Moving bed, dry ash	HTFT	included	(*4*)
34 %	Entrained flow	LTFT	excluded	(*20*)
34 %	Entrained flow	LTFT	included	(*19*)

[a] Information not provided in the source reference.

As mentioned before, the design of the facility and especially the design of the Fischer–Tropsch gas loop, has a tremendous impact on the ultimate carbon efficiency. There is a trade-off between capital cost and carbon efficiency. An open loop design (power generation from unconverted syngas) is only 75 % of the cost of a closed loop design (unconverted syngas recycled), but the carbon efficiency decreases from 34 to 25 % (*19*).

Carbon Loss

Carbon is lost in each step of the indirect liquefaction process. The main sources of carbon loss are indicated in Figure 2.

Downloaded by PENNSYLVANIA STATE UNIV on June 6, 2012 | http://pubs.acs.org
Publication Date (Web): November 29, 2011 | doi: 10.1021/bk-2011-1084.ch009

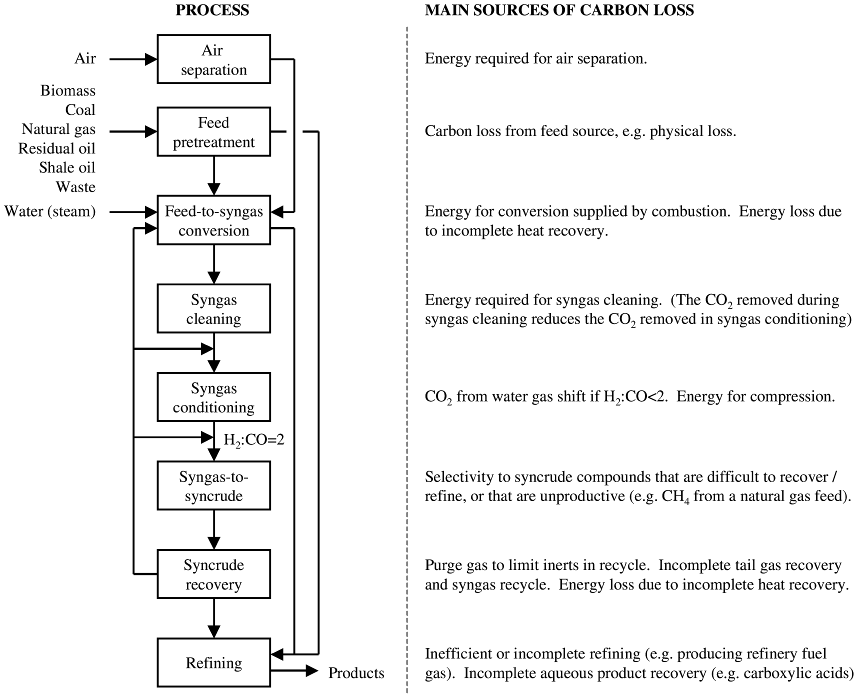
PROCESS
MAIN SOURCES OF CARBON LOSS
Air
Air separation
Biomass
Coal
Natural gas
Residual oil
Shale oil
Waste
Feed pretreatment
Water (steam)
Feed-to-syngas conversion
Syngas cleaning
Syngas conditioning
H_2:CO=2
Syngas-to-syncrude
Syncrude recovery
Refining
Products
Energy required for air separation.
Carbon loss from feed source, e.g. physical loss.
Energy for conversion supplied by combustion. Energy loss due to incomplete heat recovery.
Energy required for syngas cleaning. (The CO_2 removed during syngas cleaning reduces the CO_2 removed in syngas conditioning)
CO_2 from water gas shift if H_2:CO<2. Energy for compression.
Selectivity to syncrude compounds that are difficult to recover / refine, or that are unproductive (e.g. CH_4 from a natural gas feed).
Purge gas to limit inerts in recycle. Incomplete tail gas recovery and syngas recycle. Energy loss due to incomplete heat recovery.
Inefficient or incomplete refining (e.g. producing refinery fuel gas). Incomplete aqueous product recovery (e.g. carboxylic acids)

Figure 2. Simplified indirect liquefaction process flow diagram with the main associated sources of carbon loss.

Despite the seemingly diffuse nature of carbon loss, the carbon losses can be grouped into different categories. These are:

(a) Carbon lost due to energy requirements. Many of the steps in indirect liquefaction are nett consumers of energy. Incomplete heat recovery is also a source of energy loss and can occur in units that are nett energy consumers and nett energy producers, such as syngas-to-syncrude conversion. It is possible to reduce this type of carbon loss through improvement in energy efficiency.

(b) Carbon lost as CO_2 due to syngas conditioning. When the different conversion units are considered in isolation, a false impression may be created of the main CO_2 source/s. Some gasification technologies and water gas shift active syngas-to-syncrude technologies produce CO_2. This does not imply that these technologies have poor carbon efficiency. One must look at the overall indirect liquefaction process. In the syngas-to-syncrude conversion step, H_2 and CO are consumed in a specific ratio, called the usage ratio. Any deviation from this ratio must be corrected by water gas shift conversion (Eq. 10) somewhere in

Downloaded by PENNSYLVANIA STATE UNIV on June 6, 2012 | http://pubs.acs.org
Publication Date (Web): November 29, 2011 | doi: 10.1021/bk-2011-1084.ch009

the process. If the syngas is H_2-rich, some CO_2 can be sequestered. If the syngas is CO-rich, some CO_2 must be produced. There is very little that can be done to this type of carbon loss, because it is dictated by the stoichiometry of the indirect liquefaction process.

(c) Carbon lost due to incomplete conversion. Feed related carbon loss take place in two ways. The first is physical feed loss during feed preparation, which takes place even before it enters the first conversion unit. Arguably this is not a real carbon loss attributable to indirect liquefaction. The second is due to incomplete conversion, which only becomes a real carbon loss if it is not possible to recycle the unconverted carbon.

(d) Carbon lost due to incomplete recovery. Some carbon may be lost due to deliberate design decisions, such as incomplete tail gas recovery or an open gas loop design. These are discretionary carbon losses and the technology exists to prevent such losses. There are also carbon losses due to the difficulty of separation, as in the case of carboxylic acid recovery from the Fischer–Tropsch aqueous product. With appropriate technology it is in principle possible to limit such losses, but such technology may not have been devised yet.

(e) Carbon lost due to unselective conversion. During syngas-to-syncrude conversion some products may be produced, which within the specific facility, are unproductive, cannot be recovered, or cannot be converted into useful carbon-carriers. For example, the production of methane during syngas-to-syncrude conversion is unproductive when the carbon source is natural gas. Likewise, if the gas loop has not been designed to recover light hydrocarbons, production of such compounds will lead to carbon loss. Carbon may be lost during refining for similar reasons. Carbon losses due to unselective conversion can be reduced by improving the selectivity of the conversion processes, as well as by improving the design of the facility to enable the recovery, recycle or re-conversion of undesirable compounds.

Considering the carbon loss already incurred to produce the syncrude, failure to recover and convert syncrude into final products carries a significant penalty in terms of carbon loss. Each mole of carbon in the syncrude comes at a cost of 2 mol of carbon that were rejected (Table VIII) in order to produce the syncrude. Unfortunately carbon efficiency is not a sensitive measure to reflect the impact of syncrude wastage on top of the carbon that was sacrificed to produce the syncrude. The carbon E-factor (*24*), which is calculated in terms of the kg carbon waste per kg carbon in the product/s, is a better metric for this purpose.

E-factors and carbon E-factors were calculated (Table IX) for methanol synthesis and Fischer–Tropsch synthesis that employ different syngas sources and different gas loop product recovery configurations (*4*, *6*, *13*, *25*).

Downloaded by PENNSYLVANIA STATE UNIV on June 6, 2012 | http://pubs.acs.org
Publication Date (Web): November 29, 2011 | doi: 10.1021/bk-2011-1084.ch009

Table IX. Calculated E-factors and carbon E-factors for different syngas conversion technologies and product recovery configurations

Process description	*E-factor*	*carbon E-factor*
Methanol synthesis		
gasloop for Mobil methanol-to-gasoline [a]	0.76	0.76
syngas from moving bed gasifier	0.40	0.46
syngas from entrained flow bed gasifier	0.15	0.08
Fe-HTFT synthesis [b]		
gasloop with no light gas recovery	0.77	0.58
gasloop with C_3+ pressure recovery	0.67	0.31
gasloop with cryogenic recovery	0.62	0.20
Co-LTFT synthesis [c]		
gasloop with no light gas recovery	0.74	0.38
gasloop with C_3+ pressure recovery	0.72	0.34
gasloop with C_3+ and aqueous recovery	0.72	0.33
gasloop with cryogenic and aqueous recovery	0.71	0.32

[a] Inferred to be a moving bed gasifier based on tar, but not stated in source. [b] PetroSA HTFT gas loop used as basis for different scenarios; base case includes C_3 and heavier oil phase products and non-acid aqueous chemical recovery. [c] Oryx GTL LTFT gas loop used as basis for different scenarios; base case uses light gas as a fuel gas and does not beneficially recovery aqueous chemicals.

The E-factor calculations are intrinsically sensitive to the definition of "waste". For the present calculations fuel gas was taken as waste, since it is not a desired product from indirect liquefaction, even though fuel gas has value. The rationale is that one does not need an indirect liquefaction facility to convert natural gas into fuel gas. For the same reason all water gas shift products that are not consumed during gas recycle are also considered waste, i.e. such products do not require methanol or Fischer–Tropsch synthesis to be produced, even though unconverted CO and H_2 are useful. The calculations exclude subsequent refining efficiencies.

Some conclusions that can be drawn from the E-factor and carbon E-factor calculations (Table IX) are:

(a) The syngas generation technology must be properly paired with the syngas conversion technology and gas loop design. If the gas loop does not include a way to reform light hydrocarbons and methane specifically, the methane in the feed, or produced during synthesis, causes an increase in the E-factors. This can be clearly seen from the pairing of methanol synthesis with different synthesis gas generation and gas loop design strategies.

(b) Among the sources of preventable carbon loss during indirect liquefaction, the most prominent source is the gas loop design and the associate syncrude recovery strategy within the gas loop. It is clear that a closed gas loop design with complete tail gas recovery is the preferred design approach from a carbon efficiency perspective. This can be clearly seen from the different levels of syncrude recovery that is achieved after Fischer–Tropsch synthesis.

Is Indirect Liquefaction Worth the Carbon Cost?

The aim of indirect liquefaction is to transform carbon from a less useful to a more useful carbon-carrier. The value of the process lies in the usefulness of the carbon-carrier being produced, irrespective of whether the final application of the carbon-carrier is as a transportation fuel, portable heating fuel, or as a petrochemical. Energy is the price that must be paid for this transformation.

The energy required for the transformation can be expressed as a carbon cost, by calculating the amount of feed that must be combusted to supply this energy. In fact, two thirds of the carbon in the feed is sacrificed during indirect liquefaction to supply the energy needed to drive the conversion process. Employing conventional crude oil with an carbon efficiency of around 90 % (Table I) is clearly a better way to produce carbon-based fuels and chemicals than indirect liquefaction with a carbon efficiency of around 30 % (Table VIII). However, crude oil supplies are finite. Indirect liquefaction should not be seen as technology that competes with crude oil, but rather as a potential supplementary source of carbon-carriers when crude oil production and supply can no longer meet the total global demand.

Conclusions

The different steps involved in indirect liquefaction were evaluated to determine the carbon efficiency of the process. Carbon efficiency is defined as the fraction of carbon in the feed to the process that is transformed to carbon in useful products.

Irrespective of the specific technology choices made, there are energy demands (thermodynamic laws) and chemistry demands (stoichiometry) that must be satisfied by all indirect liquefaction processes. These chemistry and energy demands, and the factors affecting carbon loss are the following:

(a) In order to supply the energy for indirect liquefaction, either carbon or hydrogen must be oxidized. Energy derived from partial oxidation of carbon to produce CO does not affect the carbon efficiency (only the thermal efficiency is affected). Oxidation of carbon to produce CO_2 decreases the carbon efficiency directly. Oxidation of hydrogen to produce H_2O decreases the carbon efficiency indirectly by lowering the effective H:C ratio of the feed.

Downloaded by PENNSYLVANIA STATE UNIV on June 6, 2012 | http://pubs.acs.org
Publication Date (Web): November 29, 2011 | doi: 10.1021/bk-2011-1084.ch009

In Synthetic Liquids Production and Refining; de Klerk, A., et al.;
ACS Symposium Series; American Chemical Society: Washington, DC, 2011.

Downloaded by PENNSYLVANIA STATE UNIV on June 6, 2012 | http://pubs.acs.org
Publication Date (Web): November 29, 2011 | doi: 10.1021/bk-2011-1084.ch009

(b) In order to meet the stoichiometric chemistry demands of indirect liquefaction, the feed must be converted into syngas with H_2:CO ~ 2 (H:C ~ 4). This is the stoichiometric usage ratio for syngas-to-syncrude conversion, irrespective of whether the conversion takes place by syngas-to-methanol or Fischer–Tropsch hydrocarbon synthesis. (Aromatic and non-alcohol oxygenate containing products require a somewhat lower usage ratio, whereas light alkanes require a somewhat higher usage ratio).

(c) Depending on the feed material employed, the H:C ratio of the feed ranges from H:C ~ 4 for natural gas to H:C < 0.5 for antracite. In order to meet the stoichiometric syngas requirement of H:C ~ 4, carbon must be rejected or hydrogen must be added. Carbon rejection (as CO_2) supplies energy, but hydrogen addition (from H_2O) requires energy and indirectly requires carbon rejection to supply the energy.

(d) Decreasing the H:C ratio of the feed decreases the carbon efficiency that can be obtained by indirect liquefaction.

(e) The carbon efficiency of indirect liquefaction is dependent on both the carbon and the hydrogen balance, since the syngas composition must ultimately be adjusted to H:C ~ 4 (i.e. H_2:CO ~ 2). Any hydrogen that is rejected in order to provide energy, must later be compensated for by rejecting carbon to satisfy the H:C ratio requirement of the syngas. It does not matter where in the process the carbon is rejected, the rejection of carbon is dictated by stoichiometry.

(f) The interconversion between useful carbon (CO) and useful hydrogen (H_2) in the syngas can be performed by water gas shift. Roughly speaking, one mol of C can be exchanged for two mol of H and *vice versa*.

(g) Heteroatoms (oxygen, nitrogen and sulfur) in the feed indirectly reduces the carbon efficiency by lowering the effective H:C ratio of the feed.

(h) The carbon efficiencies of indirect liquefaction processes based on coal that were reported in literature are in the range 28-34 %. The carbon efficiency that can be obtained from waste plastic and natural gas will be higher, whereas the carbon efficiency from biomass will be lower.

(i) The impact of carbon loss increases with each successive conversion step, much like yield loss during multi-step synthesis. Carbon lost during the syncrude recovery and refining represents not only the actual carbon lost, but also the carbon that was lost in the previous steps to produce the syncrude (about 2 mol C for every 1 mol C in syncrude).

(j) Carbon loss that decreases the carbon efficiency of indirect liquefaction can be divided into different categories. There are inevitable losses due to the energy requirements (thermodynamic laws) and the syngas conditioning requirements (stoichiometry for H:C ~ 4). There are also losses that can be reduced by design. Two categories can be singled out as having the most scope for improvement: carbon lost due to incomplete recovery and carbon lost due to unselective conversion. The first is mainly related to the gas loop design and the second is related to the syngas-to-syncrude conversion and refinery design.

References

1. Higman, C.; Van der Burgt, M. *Gasification*, 2ed; Elsevier: Amsterdam, 2008.
2. Gary, J. H.; Handwerk, G. E.; Kaiser, M. J. *Petroleum Refining: Technology and Economics*, 5ed; Taylor & Francis: Boca Raton, FL, 2007.
3. Terblanche, K. *Oil Gas J.* **1999**, *97* (49), 48–52.
4. Mangold, E. C.; Muradaz, M. A.; Ouellette, R. P.; Rarah, O. G.; Cheremisinoff, P. N. *Coal Liquefaction and Gasification Technologies*; Ann Arbor Science Publishers: Ann Arbor, MI, 1982.
5. Miller, J.; Luyben, W. L.; Blouin, S. *Ind. Eng. Chem. Res.* **2008**, *47*, 1132–1139.
6. Dry, M. E.; Steynberg, A. P. *Stud. Surf. Sci. Catal.* **2004**, *152*, 406–481.
7. Collot, A.-G. *Int. J. Coal Geol.* **2006**, *65*, 191–212.
8. Dry, M. E. In *Catalysis Science and Technology*, Volume 1; Anderson, J. R., Boudart, M., Eds.; Springer-Verlag: Berlin, 1981, pp 159−255.
9. Tijm, P. J. A.; Waller, F. J.; Brown, D. M. *Appl. Catal., A* **2001**, *221*, 275–282.
10. Larson, E. D.; Tingjin, R. *Energy Sustainable Dev.* **2003**, *7* (4), 79–102.
11. Steynberg, A. P.; Dry, M. E.; Davis, B. H.; Breman, B. B. *Stud. Surf. Sci. Catal.* **2004**, *152*, 64–195.
12. De Klerk, A.; Furimsky, E. *Catalysis in the Refining of Fischer–Tropsch Syncrude*; Royal Society of Chemistry: Cambridge, U.K., 2010.
13. De Klerk, A. *Fischer–Tropsch Refining*; Wiley-VCH: Weinheim, Germany, 2011.
14. De Klerk, A. *Green Chem.* **2007**, *9*, 560–565.
15. De Klerk, A. *Energy Environ. Sci.* **2011**, *4*, 1177–1205.
16. Stelter, S. *The New Synfuels Energy Pioneers. A History of Dakota Gasification Company and the Great Plains Synfuels Plant*; Dakota Gasification Company: Bismarck, ND, 2001.
17. Nel, R. J. J.; De Klerk, A. *Prepr. Pap. - Am. Chem. Soc., Div. Fuel Chem.* **2009**, *54* (1), 118–119.
18. Collings, J. *Mind over Matter. The Sasol Story: A Half-Century of Technological Innovation*; Sasol: Johannesburg, 2002.
19. Williams, R. H.; Larson, E. D.; Liu, G.; Kreutz, T. G. *Energy Procedia* **2009**, *1*, 4379–4386.
20. Steynberg, A. P.; Nel, H. G. *Fuel* **2004**, *83*, 765–770.
21. Liu, G.; Larson, E. D.; Williams, R. H.; Kreutz, T. G.; Guo, X. *Energy Fuels* **2011**, *25*, 415–437.
22. De Malherbe, R.; Doswell, S. J.; Mamalis, A. G.; De Malherbe, M. C. *Synthetic Fuels from Coal*; VDI-Verlag: Düsseldorf, 1983.
23. Nowacki, P. *Coal Liquefaction Processes*; Noyes Data Corp.: Park Ridge, NJ, 1979.
24. Sheldon, R. A. *Green Chem.* **2007**, *9*, 1273–1283.
25. Probstein, R. F.; Hicks, R. E. *Synthetic Fuels*; McGraw-Hill: New York, 1982.

Downloaded by PENNSYLVANIA STATE UNIV on June 6, 2012 | http://pubs.acs.org
Publication Date (Web): November 29, 2011 | doi: 10.1021/bk-2011-1084.ch009

Downloaded by CORNELL UNIV on June 6, 2012 | http://pubs.acs.org
Publication Date (Web): November 29, 2011 | doi: 10.1021/bk-2011-1084.ch010

Chapter 10

Effect of Feed Distribution on Hydrocracking of Fischer-Tropsch Wax

Vincenzo Calemma* **and Chiara Gambaro**

Eni SpA, R&M Division, Via Maritano 26, 20097 San Donato Mil.se, Italy
***E-mail: vincenzo.calemma@eni.com**

Two Fischer–Tropsch waxes having a different chain length distribution (i.e. heavy wax with C22+: 73%; light wax with C22+: 36%) have been subjected to hydrocracking. The tests were carried out in the range of temperature and pressure of 616-648 K and 3.5-6.0 MPa respectively. The catalyst used was platinum (0.6%) on amorphous silica-alumina. Hydrocracking reaction led in both cases to an increase of middle distillate yields and maximum values achieved was 80-85%. The results obtained show a strong effect of feed carbon distribution on isomer content of hydrocracking products. Particularly, it was found that C5-9 and middle distillate (C10-22) fractions from the heavy feed have a higher isomerization degree than the products from the light feed. The higher isomer content of products from heavier Fischer-Tropsch wax was explained in terms of currently known hydrocracking reaction pathways of n-paraffins and vapour-liquid equilibrium in the reacting system.

Introduction

Low temperature Fischer-Tropsch synthesis on cobalt based catalysts leads to a mixture made up essentially of normal paraffins, ranging literally from methane up to C100 and even more, whose distribution can be described by the Anderson-Schulz-Flory model (*1*). Depending on operating conditions and type of catalyst, the distribution of products can be more or less shifted towards heavy molecular weights; however, since the chain grow mechanism is not selective for a specific

In Synthetic Liquids Production and Refining; de Klerk, A., et al.;
ACS Symposium Series; American Chemical Society: Washington, DC, 2011.

Downloaded by CORNELL UNIV on June 6, 2012 | http://pubs.acs.org
Publication Date (Web): November 29, 2011 | doi: 10.1021/bk-2011-1084.ch010

range, maximum yields achievable in the middle distillate range C_{10-22} are rather low (~ 40%) while a significant fraction is present as lighter and heavier products.

The need, for economic reasons, to lower the gas selectivity (C_{1-4}) leads to run the process with the highest possible α values (≈ 0.95) and the products so obtained are characterized by a high fraction of heavy paraffins with a boiling point higher than 360 °C. In these circumstances an effective route to maximize the overall yields in the middle distillate cut is to subject the FT wax to a hydrocracking step which besides the increase of the middle distillate yields improves also their cold flow properties by the concomitant isomerization reaction. Lately, following the renewed interest shown by most oil companies in Fischer-Tropsch synthesis, as a mean to convert natural gas to distillate fuels, (*2*–*6*), hydrocracking of FT wax has been the subject of several papers where the effect of operating conditions, type feed and catalyst on activity, selectivity for middle distillates and their quality have been investigated. Leckel (*7*) studied the performance of a commercial NiMo on SiO_2/Al_2O_3 catalyst for the hydrocracking of iron catalyzed FT waxes. Middle distillate (C_{10-22}) yields up to 65-70% were achieved with a wax containing ca 90% of C_{23+} fraction. Selectivity for C_{10-22} fraction was found to be significantly affected by the operating conditions and decreased with the increase of C_{23+} conversion. In two subsequent studies by the same author (*8*, *9*) low temperature FT waxes were hydrocracked using silica-alumina supported sulfided metal and platinum catalysts. Both sulfided and noble metal based catalysts were able to produce diesel fuel with high cetane number (>70) and good cold flow properties (cloud point < -15 °C). Hydrocracking of a LTF wax (61% C_{10-22}, 39% C_{22+}) using a platinum /amorphous silica-alumina catalyst was reported by Calemma et al. (*10*). The middle distillate yields increased with C_{22+} conversion up to 85-90% and thereafter decreased owing to the consecutive reaction of first formed products. Maximum yield achieved was 82-87%. A strong increase of isomer content of C_{10-14} and C_{15-22} fractions at higher conversion degree of C_{22+} fraction was observed and as a consequence the Freezing Point and Pour Point decreased reaching values of – 50 °C and -30 °C respectively. In a subsequent work (*11*) a light cobalt catalyzed FT wax (C_{22+}: 36%) was subjected to hydrocracking in the range of temperature 319-351 °C and pressure between 3.5 and 6.0 MPa. A maximum yield achieved of C_{10-22} fraction was 85% while the changes of cold flow properties of kerosene and gasoil cuts were similar to the previous study. A detailed GC analysis of C_{22-} fraction evidenced that isoparaffins are mainly made of mono-branched paraffins while in agreement with the accepted hydroconversion scheme of paraffins, multi-branched paraffins are more abundant at the highest conversion levels. Blending Cetane Number of gasoil fraction ranged between 75 and 80. The present study describes the hydrocracking of two FT waxes characterized by a different chain length distribution. Overall middle distillate yields, changes in product distribution and modification and selectivity at increasing hydrocracking severity have been investigated.

Downloaded by CORNELL UNIV on June 6, 2012 | http://pubs.acs.org
Publication Date (Web): November 29, 2011 | doi: 10.1021/bk-2011-1084.ch010

Experimental

Hydrocracking Experiments

Two FT waxes presenting a different chain length distribution named light (LW) and heavy (HW) wax and from which olefins and oxygenated compounds had been previously removed, were used as feedstock. As will be shown later -figure 1- the HW wax shows a bimodal distribution which derives from the fact that it was obtained by mixing two different cuts of FT wax centred at C_{16} and C_{32}. The mass chain length distribution corresponding to the usual refinery cuts is reported in Table I.

Table I. FT waxes mass chain length distribution

	Light wax (%w)	*Heavy wax (%w)*
Naphtha; (C5-9)	5	0.00
Kerosene; (C10-14)	25	7
Gas oil; (C15-22)	34	20
Atmospheric residue (C22+)	36	73

The hydrocracking tests were carried out with a lab-scale unit equipped with a down-flow trickle bed reactor (ID = 16 mm), loaded with 9 g of powdered fresh catalyst. The catalyst is a typical bifunctional system made up of Platinum (0.6%) loaded on amorphous silica-alumina. The extruded particles are crushed and sieved in the range of 20-40 mesh (average particle size (Dp) = 0.625 mm, catalytic bed height (Hb) = 86 mm) in order to approximate the ideal plug flow behaviour (*12*). In our case ID/Dp is higher than 25 to minimize by-pass and Hb/Dp is higher than 100 to minimize back mixing. Before the testing campaign, the catalyst was activated in-situ by reduction with pure H_2 at 50 atm and 400 °C. HDK tests were planned according to a Central Composite Design, CCD (*13*, *14*). The range of operating conditions in the LW series was: temperature 327-351°C, pressure 41-67 bar, H_2/wax 0.06-0.150 g/g, WHSV 1-3 h^{-1}. The range of operating conditions in the HW series was: temperature 338-360°C, pressure 35-56 bar, H_2/wax 0.06-0.127, WHSV 1-3 h^{-1}.

Product Analysis

The gaseous fraction of products was analyzed by a GC HP 5890 II equipped with an FID detector. The column used was an HP PONA crosslinked methyl siloxane, 50 m (L) x 0.2 mm (ID) x 0.5 μm (film thickness). Temperature programming of the oven was 7.5 min at 35 °C then up to 70 °C with a linear ramp rate of 3 °C min^{-1}, subsequently up to 220 °C at 7.5 °C min^{-1} and maintaining the final temperature for 45 min. Analysis of liquid fraction of converted feed was accomplished by GC HP-5890 II equipped with on column injection system, Electronic Pressure Control, and FID detector. The column used was a SPB-1 (Supelco) 15 m (l) x 0.53 (i.d.)x 0.1 μm (film thickness). Temperature programming of the oven was 1 min at 0 °C the up to 315 °C, with a linear ramp rate of 5 °C min^{-1} and a holding time at the final temperature of 37 min.

Temperature programming of injector was 1 min. at 50 °C then up to 330 °C with a linear ramp rate of 5 °C min^{-1} and a holding time at the final temperature of 37 min.

Merging the results of both gas and liquid analysis, according to their weight fraction the overall distribution of converted products in terms of normal and isoparaffin lump for each chain length is obtained.

Downloaded by CORNELL UNIV on June 6, 2012 | http://pubs.acs.org
Publication Date (Web): November 29, 2011 | doi: 10.1021/bk-2011-1084.ch010

Terminologies

Definition of different cuts was done according to the usual refinery cuts based on boiling point. Accordingly we defined: C_{1-2} fraction, fuel gas; C_{3-4} fraction, LPG; C_{5-9} fraction, naphtha; C_{10-14} fraction, kerosene; C_{15-22}, gas oil; C_{10-22} fraction, middle distillate; C_{22+} fraction, residue. Hydrocracking conversion is defined according to equation 1

$$\%C_{22+}conv. = \left(\frac{\%wtC_{22+}in - \%wtC_{22+}out}{\%wtC_{22+}in}\right)*100 \qquad \text{eq. 1}$$

while the selectivities of various cuts were calculated according to equation 2

$$Selectivity\ cut_i = \left(\frac{\%wt\ cut_i\ out - \%wt\ cut_i\ in}{\%wtC_{22+}in - \%wtC_{22+}out}\right)*100 \qquad \text{eq. 2}$$

Results and Discussion

The comparison of carbon distribution in feed and in the products obtained at different conversion degrees, shown in Figures 1 and 2, point out that during hydrocracking there is the progressive decrease of the longer aliphatic chains accompanied by the contemporary increase of compounds in the middle distillate (MD) region and to a lower degree of lighter compounds belonging to naphtha, LPG and Fuel Gas fractions. The observed behaviour is consistent, as widely reported in literature, with a progressive higher reactivity of aliphatic chains as a function of molecular weight.

Literature data show that the reactivity of n-alkanes increases with the molecular weight (*15*). This can be accounted for by the fact that the reactivity is expected to be proportional to the number of secondary carbon atoms per molecule or, as proposed by Sie, to C_{n-6} and C_{n-4} for hydrocracking and hydroisomerization, respectively (*16*). However, as reported in several works (*17*, *18*), the higher reactivity of heavier n-paraffins can be also ascribed to their stronger physisorption, which cause an enrichment of the heavier components on the catalyst surface respect to the bulk composition and consequently to higher reaction rates. Denayer et al. (*19*) reported the hydroconversion of a quaternary mixture of normal paraffins C_6, C_7, C_8 and C_9 in vapour phase conditions. It was observed that longer alkanes were preferentially converted due to the competitive adsorption favouring the heavy compounds. However, the apparent overall reactivity of normal paraffin could be the result of different factors such as intrinsic reactivity, physisorption and vapour–liquid equilibrium (VLE) in the reaction environment. In this regard, it has been shown that, in hydroconversion of a binary mixture of n-heptane and n-nonane, the physisorption behaviour in liquid phase is very different from that observed in vapour phase (*20*, *21*). More specifically, both in liquid and vapour phase, the n-nonane is more reactive than n-heptane but the difference in reactivity is much more pronounced in vapour phase than in liquid phase. On the basis of the results obtained the authors concluded that the observed rates in liquid phase conditions mainly reflects the intrinsic reactivity of normal paraffins rather than differences of the physisorption behaviour. A recent study (*22*) concerning the adsorption behaviour of long chain paraffins $C_{28\text{-}36}$, over an amorphous microporous silica-alumina, has shown that in liquid phase conditions there are not significant differences of adsorption as a function of chain length. This last result strongly support the view that physisorption and intrinsic reactivity plays a minor role in determining the apparent higher reactivity of long chain paraffins observed during hydrocracking of FT wax, and a significant role is played by the VLE as previously suggested (*10*). Actually, it is known that VLE in the range of operating condition used in this work leads to a liquid phase enriched in the heavier components (*23*).

Downloaded by CORNELL UNIV on June 6, 2012 | http://pubs.acs.org
Publication Date (Web): November 29, 2011 | doi: 10.1021/bk-2011-1084.ch010

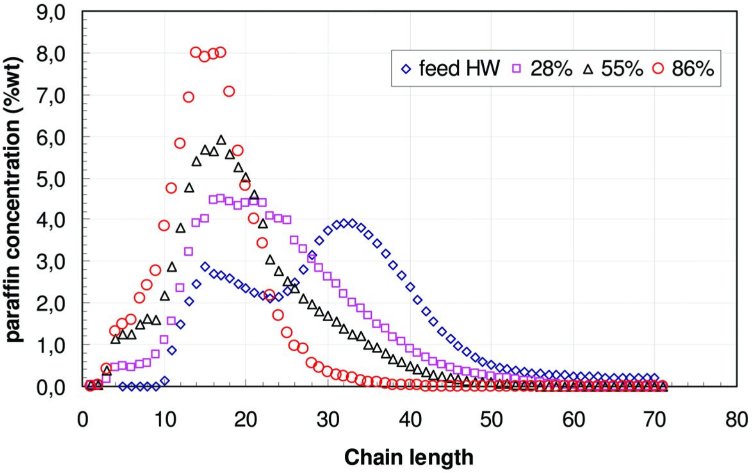

Figure 1. Chain length distribution of normal and iso-paraffin at different conversion degree of C_{22+} fraction. Heavy feed.

Downloaded by CORNELL UNIV on June 6, 2012 | http://pubs.acs.org
Publication Date (Web): November 29, 2011 | doi: 10.1021/bk-2011-1084.ch010

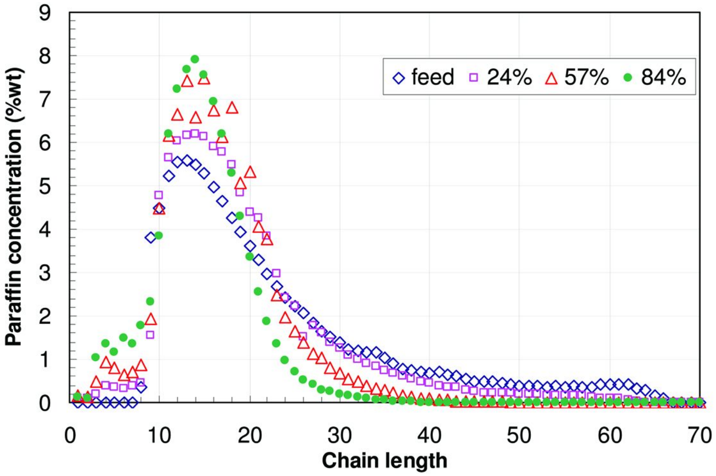

Figure 2. Chain length distribution of normal and iso-paraffin at different conversion degree of C_{22+} fraction. Light feed.

The data reported in Figure 3 show that both for LW and HW middle distillate (C_{10-22}), yields increase linearly up to 85-90% of C_{22+} conversion and thereafter a decrease is observed owing to the consecutive hydrocracking reactions of first formed products leading to lower molecular weight compounds falling outside the middle distillate range. Although the HW presents a lower initial content of MD the maximum MD yields achieved are similar being close to 80% in both cases.

Within the MD cut an important aspect concerns the evolution of the ratio kerosene/gasoil during hydroconversion. The data presented in Figure 4 show that in the case of LW the kerosene/gasoil ratio remains basically constant up to high conversion values while in the case of HW the ratio shows a constant increase up to 60-70% of conversion followed by a exponential like trend for higher. Both trends derive from the initial kerosene/gasoil ratio in the feed, the carbon distribution of cracking products of longer paraffins and consecutive reaction of the products formed. The latter is responsible for the strong increase at high conversion values.

Besides the formation of MD, hydrocracking leads to the formation in lower amount of lighter products namely naphtha (C_{5-9}), LPG (C_{3-4}) and fuel gas (C_{1-2}).

The results reported in Figure 5 and 6 indicate that the yields of naphtha remain rather low up to 70-80 % of C_{22+} conversion while for higher conversion values an exponential like increase is observed. A similar trend as a function of the C_{22+} conversion is shown by the fraction C_{1-4} but in a lower range of values. Roughly 80% of C_{1-4} fraction is made up of propane, butane and isobutane which are formed by carbenium route while the formation of methane and ethane are formed by hydrogenolysis reactions on the metal site (*24*) which to some extent are always present on platinum based catalyst.

Downloaded by CORNELL UNIV on June 6, 2012 | http://pubs.acs.org
Publication Date (Web): November 29, 2011 | doi: 10.1021/bk-2011-1084.ch010

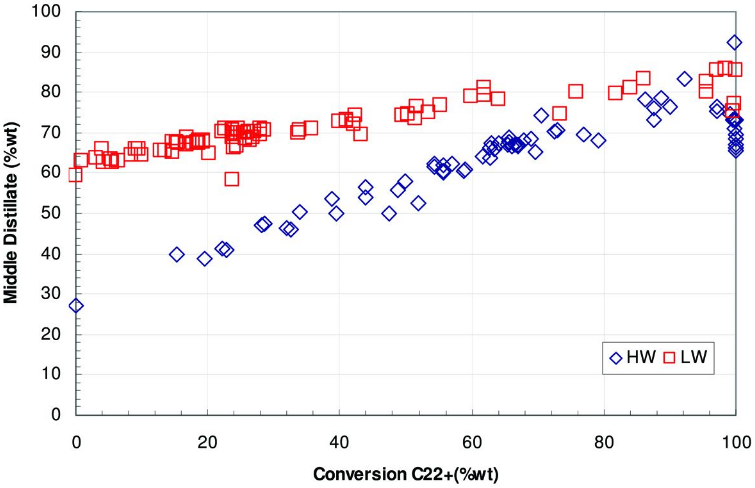

Figure 3. Middle distillate yields as a function of C_{22+} conversion.

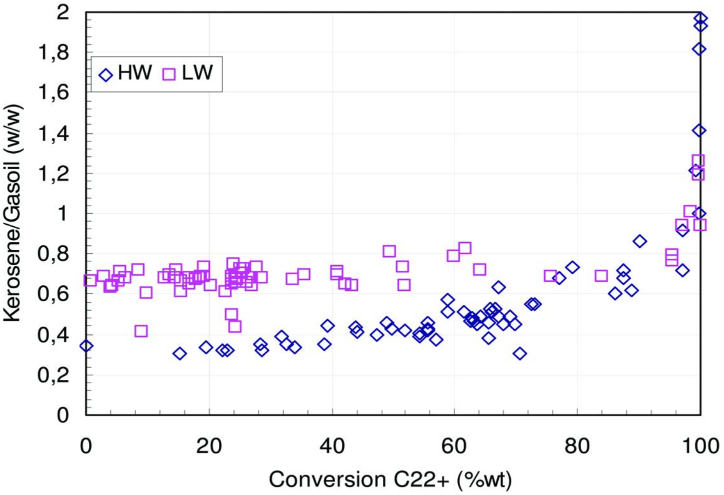

Figure 4. Kerosene ($C_{10\text{-}14}$)/gasoil ($C_{15\text{-}22}$) ratio vs. C_{22+} fraction conversion.

Downloaded by CORNELL UNIV on June 6, 2012 | http://pubs.acs.org
Publication Date (Web): November 29, 2011 | doi: 10.1021/bk-2011-1084.ch010

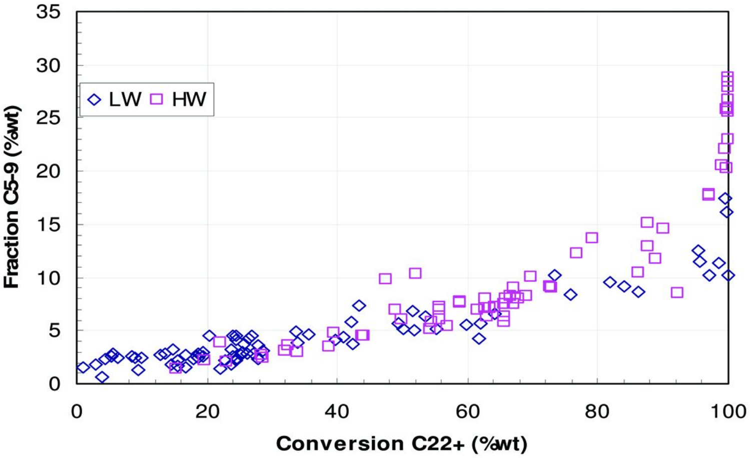

Figure 5. Yields of $C_{5\text{-}9}$ fraction as function of C_{22+} conversion.

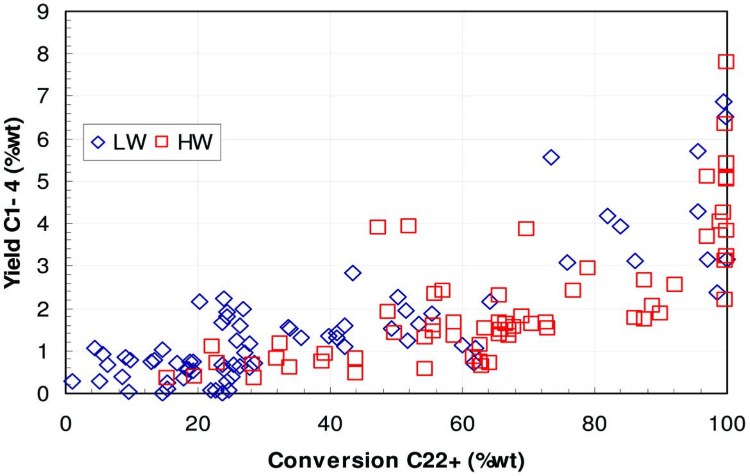

Figure 6. Yields of $C_{1\text{-}4}$ fraction as function of C_{22+} conversion.

The results shown so far are consistent with a picture where the heaviest aliphatic chains belonging to the fraction C_{22+} are hydrocracked preferentially respect with the shorter one, leading mainly to middle distillate and in lower amount to $C_{5\text{-}9}$ and $C_{1\text{-}4}$ fractions. The slight decrease of selectivity of MD, reported in Figure 7, up to 70-80% C_{22+} conversion indicate that the consecutive cracking of first formed products by reaction of heavier aliphatic chains is present but still at low levels whereas at higher conversion value the phenomenon became progressively more significant.

Studies on hydrocracking of normal paraffins over noble metal based bifunctional catalysts (*15*, *25*) show that in "ideal hydrocracking" conditions and medium low conversion degree where consecutive reaction of first formed products is negligible the cracking products exhibit a distribution where the fragments corresponding to the breakage of the C-C bonds inner than 3rd are produced in almost equimolar amount; methane, ethane and the correspondent fragment C_{n-1} and C_{n-2} are virtually absent while propane and C_{n-3} are formed into somewhat higher amount. Such a distribution is explained in terms of stability of carbenium intermediate involved in the formation of the products (*26*). Assuming an equal probability of breakage between the 4th and Cn-4th C-C bond of n-paraffins longer than C_{22} carbon atoms and no formation of products resulting from rupture of α, β and γ C-C terminal bonds, the selectivity in the C_{10-22} range is 83%. Similar results have been previously calculated for the C_{10-20} range (*4*, *27*). Dispersion of selectivity values reported in Figure 7 results from standard deviation associated with the measures and operating conditions which may foster or not the consecutive cracking of first formed products. The high selectivity values observed at low conversion, to some extent higher than expected on the basis of the reasoning above reported, could derive from the fact that the real distribution of cracking products from long aliphatic chains is bell shaped centred on chain length with carbon number half of the converted molecule (*28*) which leads to higher selectivity to MD. At any rate the data indicate that the catalyst used is characterized by excellent selectivity to MD.

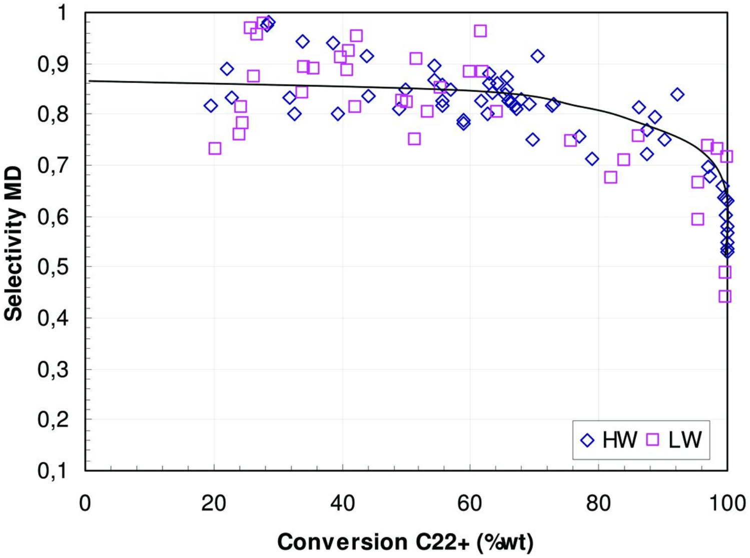

Figure 7. Selectivity to middle distillate as a function of conversion of C_{22+} fraction.

Downloaded by CORNELL UNIV on June 6, 2012 | http://pubs.acs.org
Publication Date (Web): November 29, 2011 | doi: 10.1021/bk-2011-1084.ch010

Besides the selectivity to MD another important facet is the isomerization degree of the products which are related to some important characteristics: cetane number and cold flow properties for gasoil and octane number for the naphtha fraction.

The data presented in Figure 8 point out a strong effect of the feed composition on the isomer content of $C_{5\text{-}9}$ fraction. Conversion of HW leads to isomer content in the $C_{5\text{-}9}$ fraction remarkably higher than in the case of LW. The difference is particularly strong at low conversion degrees. We suggest that the differences of the isomerization degree of $C_{5\text{-}9}$ fractions from LW and HW is the consequence of three factors, namely vapour liquid equilibrium (VLE) established in the reacting system, the feed composition and isomerization degree of cracking products from the C_{22+} fraction.

Downloaded by CORNELL UNIV on June 6, 2012 | http://pubs.acs.org
Publication Date (Web): November 29, 2011 | doi: 10.1021/bk-2011-1084.ch010

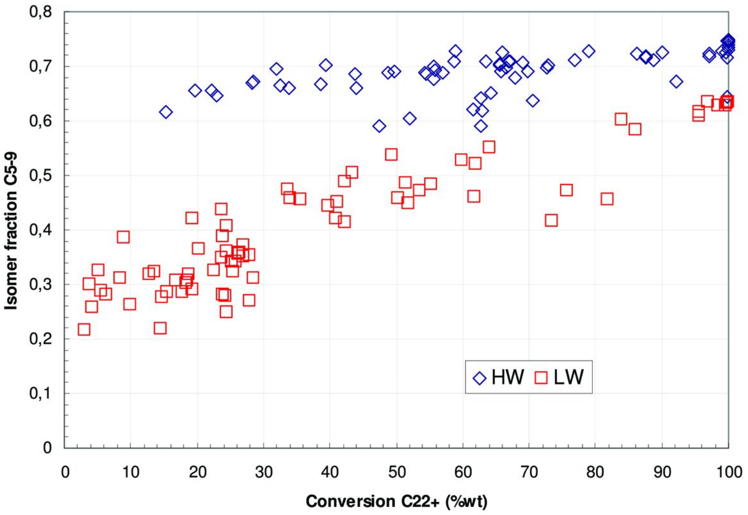

Figure 8. Isomer concentration of C $_{5\text{-}9}$ fraction.

It is largely agreed (*29*) that the hydroconversion process of normal paraffins proceeds through consecutive isomerization reactions and concomitant hydrocracking reactions as depicted in Figure 9.

In this scheme the hydrocracking rate increases with the branching degree of the isomers and the fastest hydrocracking reactions are those of dibranched and tribranched isomers by β-scission of type B1, B2 and A (*30*). In the case of C-C bond scission of type A two fragments both isomerized are formed. Differently, in the case of type B1, B2 only one fragment of the two is isomerized. Consequently, the cracking products from the conversion of C_{22+} fraction will be characterized by a high degree of isomerization.

VLE calculations show that in the range of operating conditions used the feed or reacting mixture is present as gas and liquid phase and their ratio is affected by the operating conditions and composition of the mixture (*23*).

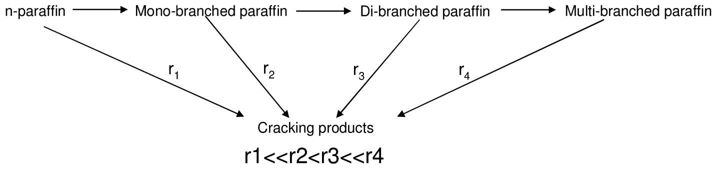

Figure 9. Reaction scheme for the formation of isomers and cracking products.

Downloaded by CORNELL UNIV on June 6, 2012 | http://pubs.acs.org
Publication Date (Web): November 29, 2011 | doi: 10.1021/bk-2011-1084.ch010

Therefore, we can assume that the hydroconversion of FT wax occurs in an ideal trickle flow regime, where the catalyst particles are completely covered with flowing liquid and the reaction occurs only at the interface between the surface of the catalyst and the liquid phase which in turn is in equilibrium with the gas phase. In these conditions the reactivity of each compound can be assumed to be proportional to its concentration in the liquid phase rather than the overall one.

As previously shown (*23*) the gas phase is enriched in the lighter components while the opposite happens for the liquid phase. Particulaly, VLE calculations carried out using the Redlich-Kwong-Soave equation show that in the range of operating conditions used the fraction in the gas phase of naphtha fraction ranges from 92-94% to 97-99% for nonane and pentane respectively and therefore their tendency to react will be very low. The compositional data presented in table I show that HW does not contain $C_{5\text{-}9}$ paraffins whereas their content in LW is 5 %. In the case of HW $C_{5\text{-}9}$ compounds are formed totally from the hydrocracking of heavier paraffins which as we have previously shown are characterized by a high degree of isomerization.

In the case of LW the cracking products belonging to the $C_{5\text{-}9}$ are diluted with the n-paraffins already present in feed so leading to a lower overall isomer concentration.

If in the case of LW we consider that the normal paraffins of $C_{5\text{-}9}$ fraction present in the feed do not react and subtract their contribution to the overall composition we obtain, as shown in Figure 10, that the isomer content of $C_{5\text{-}9}$ from HW and LW overlap completely, confirming in this way the hypothesis of a very low reactivity of compounds present in gas phase.

A further proof that compounds present in the gas phase do not react significantly comes from, considering the isomerization equilibrium constants of $C_{5\text{-}9}$ paraffins (*31*). Combing the data of equilibrium constants for the isomerization reaction of normal paraffins $C_{5\text{-}9}$ and their concentration in the hydrocracking products, we obtain that in the range of operating conditions used the isomer content of $C_{5\text{-}9}$ fraction at the equilibrium is between 0,59 and 0,62.

Such range of values is significantly lower than the values determined for the HW, see Figure 10, suggesting that the isomers content is in this case controlled kinetically rather than by thermodynamic factors. In other words once the isomers are formed by β-scission of heavier alkanes they do not show, in our experimental conditions, a significant tendency to shift towards equilibrium values. In this light the measured isomerization degree of $C_{5\text{-}9}$ fraction reflect the formation ratio of normal and iso-paraffin fragments by hydrocracking of

Downloaded by CORNELL UNIV on June 6, 2012 | http://pubs.acs.org
Publication Date (Web): November 29, 2011 | doi: 10.1021/bk-2011-1084.ch010

long chain paraffins. Particularly, the fastest hydrocracking route of alkanes is β-scission of type A occurring on tribranched isomers with branching groups in ααγ position. Remarkably lower is the cracking via β-scission of type B1 and B2 occurring on dibranched isomers with branching groups in αα and αγ positions. β-scission of type A gives two isomerized fragments while β-scission of type B forms two fragments of which only one is isomerized. Values of relative β-scission rates reported in literature for type A, B1, and B2 are 1050/170, 2.8 and 1 respectively (*30*).

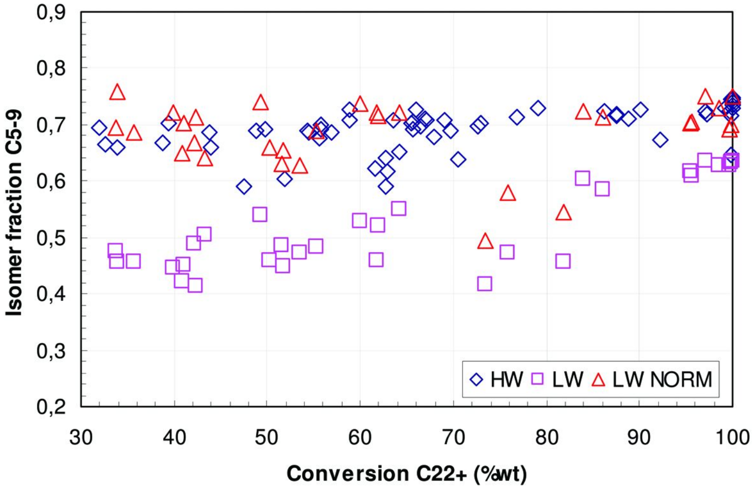

Figure 10. Isomers concentration in C_{5-9} fractions from hydrocracking of HW, LW and from LW after subtracting the contribution of normal paraffin initially present in the feedstock.

In our case the average isomerization degree of 0.7 measured for the fraction C_{5-9} suggests that a significant part, larger than expected on the basis of literature data, of cracking fragments should be formed by β-scission of type B.

A similar situation occurs also for the kerosene fraction C_{10-14} (see Figure 11), which in the case of HW presents higher isomer content. The underlying reasons for this result are similar to those presented above for the naphtha fraction. However, the isomerization of normal paraffins already present in the feed should be in this case more relevant in the light of VLE calculations showing that the fraction in vapour phase of kerosene fraction is between 0.70 and 0.85.

Hydroconversion of HW leads to more isomerized kerosene fraction and consequently better cold flow properties (*11*).

Depending on operating conditions fraction in vapour phase of C_{15-22} fraction ranges between 35% and 62%. In agreement with VLE calculations showing that a larger fraction is present in liquid phase, as reported in Figure 12, differences between HW and LW are less pronounced owing to the larger contribution of isomerization reaction of normal paraffins present in the feed.

Downloaded by CORNELL UNIV on June 6, 2012 | http://pubs.acs.org
Publication Date (Web): November 29, 2011 | doi: 10.1021/bk-2011-1084.ch010

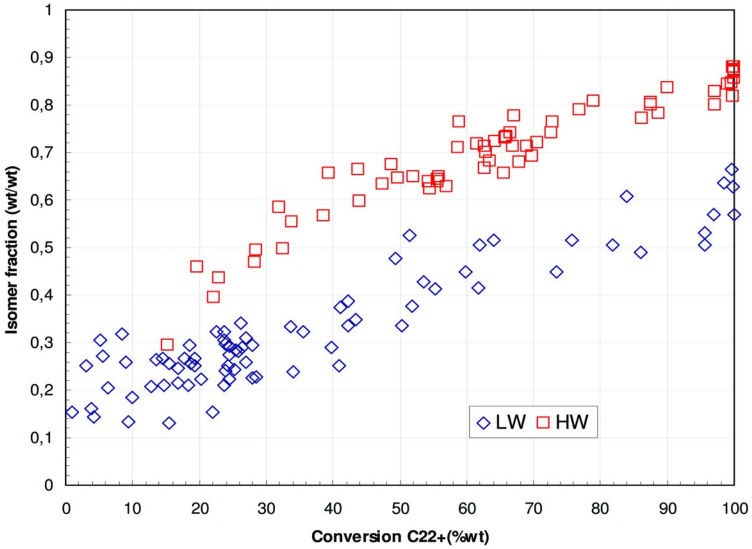

Figure 11. Isomer concentration of C10-14 cut as a function of conversion of C_{22+} fraction.

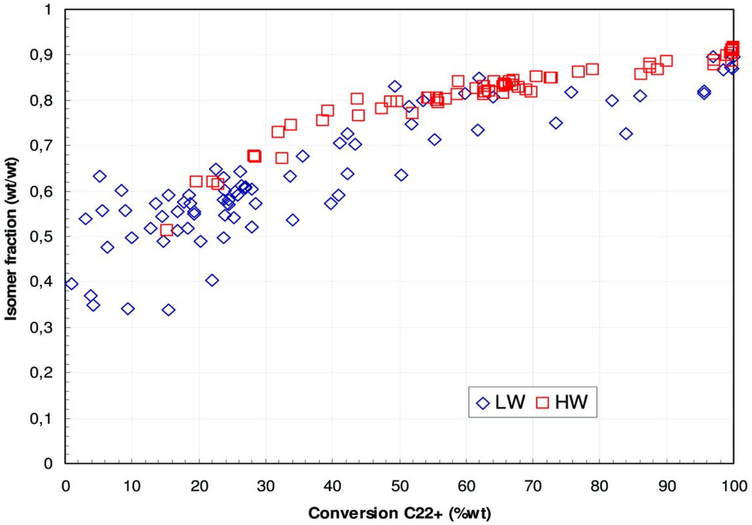

Figure 12. Isomer concentration of $C_{15\text{-}22}$ cut as a function of conversion of C_{22+} fraction.

Conclusions

The results of this study show that products distribution and their isomerization degree heavily depend on the feed composition.

Differences in isomer content of products from HW and LW have been explained in terms of the VLE established in the reacting system and differences in carbon distribution of the feed. The isomer content of light fraction $C_{5\text{-}9}$ formed by hydrocracking of HW is higher than the value of thermodynamic equilibrium and is consistent with the view that isomers of naphtha fraction are almost exclusively formed by cracking of heavier alkanes while components present in gas phase do not react significantly. The wax with the highest content of C_{22+} fraction leads to more isomerized products, which consequently have better cold flow properties. We notice that all the findings presented in the paper are consistent with a system characterized by the presence of a reacting liquid phase enriched in heavier components in contact with the catalyst and a gas phase enriched in lighter components basically in equilibrium with the liquid phase.

References

1. Anderson, R. B. *The Fischer-Tropsch Synthesis*; Academic Press: New York, 1984.
2. Perego, C.; Bortolo, R.; Zennaro, R. *Catal. Today* **2009**, *142*, 9–16.
3. Eisemberg, B.; Fiato, R. A.; Mauldin, C. H.; Say, G. R.; Soled, S. L. Natural gas conversion V. *Stud. Surf. Sci. Catal.* **1998**, *119*, 943−948.
4. Sie, S. T.; Senden, M. M. G.; Van Wechem, H. M. H. *Catal. Today* **1991**, *8* (3), 371–394.
5. Dancuart, L. P.; de Haan, R.; de Klerk, A. Fischer-Tropsch technology. *Stud. Surf. Sci. Catal.* **2004**, *152*, 482−582.
6. Collins, J. P.; Font Freide, J. J. H. M.; Nay, B. *J. Nat. Gas Chem.* **2006**, *15* (1), 1–10.
7. Leckel, D. *Energy Fuels* **2005**, *19* (5), 1795–1803.
8. Leckel, D. *Ind. Eng. Chem. Res.* **2007**, *46* (11), 3505–3512.
9. Leckel, D. *Energy Fuels* **2007**, *21* (3), 1425–1431.
10. Calemma, V.; Peratello, S.; Pavoni, S.; Clerici, G.; Perego, C. Natural conversion VI. *Stud. Surf. Sci. Catal.* **2001**, *136*, 307−312.
11. Calemma, V.; Gambaro, C.; Parker, W. O.; Carbone, R.; Giardino, R.; Scorletti, P. *Catal. Today* **2010**, *149*, 40–46.
12. Perego, C.; Peratello, S. *Catal. Today* **1999**, *52*, 133–145.
13. Calemma, V.; Correra, S.; Perego, C.; Pollesel, P.; Pellegrini, L. *Catal. Today* **2005**, *106*, 282–287.
14. Khuri, A. I.; Cornell, J. A. *Response Surface: Design and Analyses*, 2nd ed.; Marcel Dekker, Inc.: New York, 1966; p 120.
15. Weitkamp, J. In *Hydrocracking and Hydrotreating*; Ward, J. W., Quader, S. A., Eds.; ACS Symposium Series 20; American Chemical Society: Washington, DC, 1975; pp 1−27.
16. Sie, S. T. *Ind. Eng. Chem. Res.* **1993**, *32*, 403–408.

Downloaded by CORNELL UNIV on June 6, 2012 | http://pubs.acs.org
Publication Date (Web): November 29, 2011 | doi: 10.1021/bk-2011-1084.ch010

17. Denayer, J. F.; Baron, G. V.; Jacobs, P. A.; Martens, J. A. *Phys. Chem. Chem. Phys.* **2000**, *2*, 1007–1014.
18. Denayer, J. F.; Baron, G. V.; Martens, J. A.; Jacobs, P. A. *Phys. Chem. B* **1998**, *102*, 3077–3081.
19. Denayer, J. F.; Baron, G. V; Souverijns, V.; Martens, J. A.; Jacobs, P. A. *Ind. Eng. Chem.* **1997**, *36*, 3242–3247.
20. Denayer, J. F. M.; De Jonckheere, B.; Hloch, M.; Marin, G. B.; Vanbutsele, G.; Martens, J. A.; Baron, G. V. *J. Catal.* **2002**, *210*, 445–452.
21. Denayer, J. F. M.; Ocakoglu, R. A.; Huybrechts, W.; De Jonckheere, B.; Jacobs, P.; Calero, S.; Krishna, R.; Smit, B.; Baron, G. V.; Martens, J. A. *J. Catal.* **2003**, *220*, 66–73.
22. Li, B.; Calemma, V.; Gambaro, C.; Baron, G. V.; Denayer, J. F. M. *Ind. Eng. Chem. Res.* **2010**, *49*, 7541–7549.
23. Correra, S.; Calemma, V.; Pellegrini, L.; Bonomi, S. *Chem. Eng. Trans.* **2005**, *6*, 849.
24. Weitkamp, J.; Ernst, S. Guidelines for mastering the properties of molecular sieves. *NATO ASI Ser., Ser. B* **1990**, *221*, 343.
25. Weitkamp, J. *Erdoel Kohle, Erdgas, Petrochem.* **1978**, *31*, 13–22.
26. Martens, J. A.; Jacobs, P. A.; Weitkamp, J. *Appl. Catal.* **1986**, *20*, 283–303.
27. Bouchy, C.; Hastoy, G.; Guillon, E.; Martens, J. A. *Oil Gas Sci. Technol.* **2009**, *64* (1), 91–112.
28. Rossetti, I.; Gambaro, C.; Calemma, V. *Chem. Eng. J.* **2009**, *154* (1−3), 295–301.
29. Marcilly, C. *Catalyse acido-basique. Application au raffinage et à la pétrochimie*; 2003, Volume 1, Chapter 4; pp 217−222, Edition Technip.
30. Marcilly, C. *Catalyse acido-basique. Application au raffinage et à la pétrochimie*; 2003, Volume 1, Chapter 4; pp 212−217, Edition Technip.
31. Pellegrini, L. A.; Gamba, S.; Bonomi, S.; Calemma, V. *Ind. Eng. Chem, Res.* **2007**, *46*, 5446–5452.

Downloaded by CORNELL UNIV on June 6, 2012 | http://pubs.acs.org
Publication Date (Web): November 29, 2011 | doi: 10.1021/bk-2011-1084.ch010

Downloaded by CORNELL UNIV on June 6, 2012 | http://pubs.acs.org
Publication Date (Web): November 29, 2011 | doi: 10.1021/bk-2011-1084.ch011

Chapter 11

Hydrocracking Different Fischer-Tropsch Waxes: Model Simulations

Chiara Gambaro* **and Vincenzo Calemma**

Eni s.p.a., R&M Division, via F. Maritano 26,
20097 San Donato Milanese, Italy
***E-mail: chiara.gambaro@eni.com**

This work assesses the applicability of a lumped kinetic model, developed by Eni, to Fischer-Tropsch synthesis derived waxes with different composition. In particular, products distribution and the effect of operating conditions on conversion will be investigated, along with the evolution of kinetic and thermodynamic constants. Results are quite satisfactory: the model demonstrated to suit different feedstocks, providing a good agreement with experimental paraffins distributions, mainly at medium-low conversion levels. Furthermore, the effects of temperature, WHSV and pressure on conversion are well simulated by the model. On the other hand, strong differences are detected in model parameters, which account for the differences in feedstocks compositions.

Introduction

The hydrocracking process (HDK) is fundamental in the oil refining industry to obtain high quality fuels. For this reason, in literature there are plenty of experimental works on this topic: earlier papers describe HDK of short-chain linear paraffins, such as n-hexane (*1*), n-decane and n-dodecane (*2*, *3*), up to n-C16 (*4*, *5*). More recently, lab works with heavier paraffins, like n-C28 (*6*, *7*), n-C36 and n-C44 (*7*), and complex mixtures, as Fischer-Tropsch waxes (*8–14*), have been published. For a proper scale-up of the HDK process, the development of a kinetic model is of basic importance. Many efforts have been carried out also in

In Synthetic Liquids Production and Refining; de Klerk, A., et al.;
ACS Symposium Series; American Chemical Society: Washington, DC, 2011.

this direction. The former and easier approach is based on lumped models, where the reaction scheme is simplified by the introduction of pseudo-components (or lumps):

$$\text{n-paraffin} \leftrightarrows \text{iso-paraffin} \rightarrow \text{cracked products} \tag{1}$$

The prediction ability of such models could be enhanced for example by increasing the number of lumps and thus of reactions: the "iso-paraffin" lump could be split into "mono-branched" (MB) and "multi-branched" (MTB) isomers (*15*, *16*):

$$\text{n-paraffin} \leftrightarrows \text{MB-paraffin} \leftrightarrows \text{MTB-paraffin} \rightarrow \text{cracked products} \tag{2}$$

Another way to improve these models could be the introduction of a mechanistic approach, such as the Langmuir-Hinshelwood-Hougen-Watson (LHHW). In practice, the lumps involved in the main reaction are supposed to undergo elementary steps, which describe the reaction pathway. In the case of bifunctional HDK catalysts, the generally accepted reaction scheme foresees the following steps: the normal paraffin is first adsorbed on the catalyst surface, dehydrogenated at the metal sites to form the olefin, which migrates to the acid site where the secondary carbenium is formed by protonation of the double bond. The carbenium ion so formed undergoes rearrangement to tertiary carbenium, which in turn can either deprotonate to the corresponding iso-olefin or produce lower molecular weight compounds via β-scission. The desorbed olefin formed by deprotonation of tertiary carbenium migrates to the metal particle to form the saturated compound, which can eventually further react according to the scheme presented above (*16*, *17*).

When complex paraffins mixtures are considered, the physical behaviour of the reacting system is crucial and vapour-liquid equilibrium (VLE) has to be accounted for in the model (*18*).

It seems clear that the more detailed the model is, the more complicated it results: the number of equations is raised and thus the computational time increases. Nevertheless, there are some particular cases which suit well to the application of detailed lumped models, like the hydrocracking of Fischer-Tropsch waxes. This is quite an easy system to model, if compared to e.g. VGO, because continuous series of molecules of the same nature (i.e., linear and branched paraffins) are involved in the process. As a consequence, some tricks can be introduced to simplify the model by decreasing the number of equations. This strategy was followed during the development of the Eni - PoliMi model (*17*): the kinetic and thermodynamic constants of the model have been expressed as functions of the chain length (NC). The fitting and simulation ability of the model can be implemented by choosing proper forms for each correlation (*19*).

A step forward is represented by the so called "single event" kinetic models (*20*), which account for the complete reaction network that describes the

Downloaded by CORNELL UNIV on June 6, 2012 | http://pubs.acs.org
Publication Date (Web): November 29, 2011 | doi: 10.1021/bk-2011-1084.ch011

formation of each single component of the product mixture. The single events coefficients of elementary steps considered should be independent of the structure of reactant and products and therefore of feedstock composition. However, this approach, if applied without any simplifying assumption, originates a huge number of elementary steps even for relatively simple molecules, which makes its use problematic for more complex mixtures such as Fischer-Tropsch waxes. Even though in the last decade different authors have proposed some strategies to develop detailed mechanistic kinetic models that can be extended to the HDK of mixtures of paraffins (*21–23*), lumped models are still preferred for the scaling-up of processes involving complex mixtures.

In this scenario, Eni recently presented an evolution of the lumped kinetic model for the HDK of Fischer-Tropsch waxes (*19*). In this work, the application of that model to waxes with different composition is presented. The goal is to optimize model parameters with FT waxes of different composition. This means testing the tool under different conditions and, most of all, checking the model sensitivity to feed composition.

Downloaded by CORNELL UNIV on June 6, 2012 | http://pubs.acs.org
Publication Date (Web): November 29, 2011 | doi: 10.1021/bk-2011-1084.ch011

Experimental

Hydrocracking Experiments

Hydrocracking experiments have been carried out on a lab plant, equipped with a down flow fixed bed reactor (inner diameter = 16 mm), loaded with 9 g of powder catalyst, sieved in the range 20-40 mesh to approximate plug-flow behaviour. The catalyst is a bi-functional system, made of Pt particles dispersed on a silica-alumina amorphous matrix (*19*). Fresh catalyst was activated *in situ* with pure hydrogen, at high temperature and pressure. Liquid and gas products samples were collected daily and analyzed with dedicated gaschromatographic methods (*12*) to calculate material balances, residue conversion and product selectivity.

In this work, the HDK behaviour of two different FT waxes is compared: a light wax (LW), with 36%w of residue (i.e., C22+ fraction), and a heavy wax (HW), with 73%w of residue. Feed waxes distributions are shown in Figure 1, while the concentration of the main fractions (C10-: gas and gasoline, C10-C14: kerosene, C15-C22: gasoil, C22+: residue) are listed in Table I.

HDK tests were planned according to a Central Composite Design, CCD (*17*). The range of operating conditions in the LW series was: temperature 327-351°C, pressure 41-67 bar, H_2/wax 0.06-0.150 g/g, WHSV 1-3 h^{-1}. The range of operating conditions in the HW series was: temperature 338-360°C, pressure 35-56 bar, H_2/wax 0.06-0.127, WHSV 1-3 h^{-1}.

Model regression for parameter estimation was carried out on 51 runs in the case of LW and 53 runs in the case of HW.

Downloaded by CORNELL UNIV on June 6, 2012 | http://pubs.acs.org
Publication Date (Web): November 29, 2011 | doi: 10.1021/bk-2011-1084.ch011

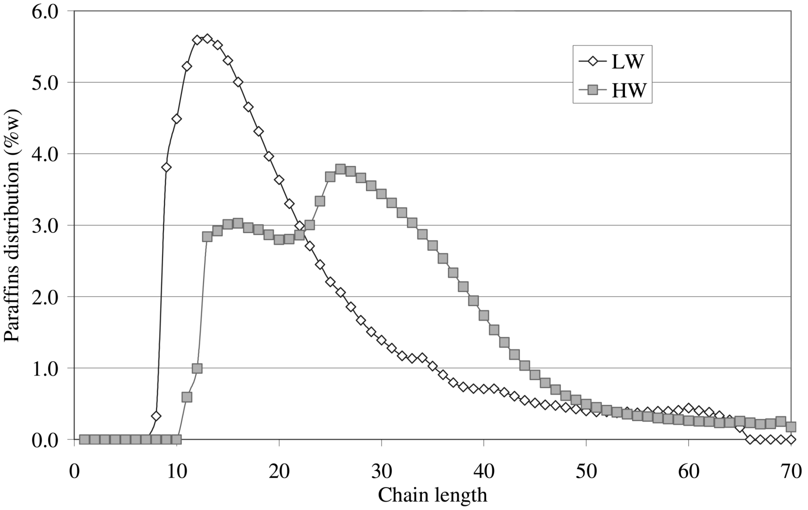

Figure 1. Light (LW) and heavy (HW) waxes distribution.

Table I. Concentration of the main fractions for LW and HW

	LW	*HW*
C10- (%w)	5	0
C10-C14 (%w)	25	7
C15-C22 (%w)	34	20
C22+ (%w)	36	73

Kinetic Model

The kinetic model developed in Eni labs has been widely described elsewhere (*19*). The model base hypotheses will be briefly summarized below.

•The simplified reaction scheme adopted is based on the lumped reaction

$$\text{n-C}_{NC}\text{H}_{2NC+2} \leftrightarrows \text{iso-C}_{NC}\text{H}_{2NC+2} \rightarrow a\ \text{iso-C}_{m}\text{H}_{2m+2} + (1\text{-}a)\ \text{n-C}_{(NC\text{-}m)}\text{H}_{2(NC\text{-}m)+2}$$

where NC represents the paraffin chain length and a is a model parameter. All the iso-paraffins with the same carbon number are considered as a unique lump, regardless of the number and length of branching.

•Only iso-paraffins in the range C_6-C_{70} can undergo cracking reaction.

•Cracking occurs according to statistical breakage of the C-C bonds. The probability function, which resembles the bell-like cracking products distribution observed experimentally and widely reported in literature for model compounds

In Synthetic Liquids Production and Refining; de Klerk, A., et al.;
ACS Symposium Series; American Chemical Society: Washington, DC, 2011.

(*4*), is defined as follows: the C-C bonds between C_4 and C_{NC-4} are cracked with the same probability, let's call it p; the cracking probability of the third and (NC-3)th bonds is p/2; the cracking probability of the four terminal bonds (i.e.,1st, 2nd, (NC-1)th and NCth) is 0. These assumptions are based on the rules of carbenium ion chemistry.

•The model is developed according to a classic Langmuir-Hinshelwood approach, which takes into account the bi-functional nature of the catalyst. The "ideal hydrocracking" mechanism, described in the Introduction, is considered (*16*): the adsorption–desorption and the hydrogenation–dehydrogenation steps are assumed to be in quasi-equilibrium, while each step involving the carbenium ion could be a rate-determining step (RDS). In literature different approaches have been compared, but this one seems to be the most suitable to describe the hydrocracking process.

•Physisorption of the linear paraffin on the catalyst surface is described by the complete form of the Langmuir model (*20*): this form includes the adsorption term called *ADS*2 that contains the constant K_{PD}, defined as the product of the equilibrium constants for dehydrogenation and protonation elementary steps. The rate expressions are defined as follows:

$$r_{isom}(i)=\frac{k_{isom}(i)\cdot\left(f_n(i)-\dfrac{f_{iso}(i)}{K_{eq}(i)}\right)}{ADS1+ADS2} \tag{3}$$

$$r_{ck}(i)=\frac{k_{ck}(i)\cdot f_{iso}(i)}{ADS1+ADS2} \tag{4}$$

$$ADS1=f_{H_2}\cdot\left[1+\sum_{i=1}^{nC}f_n(i)\cdot K_{L,n}(i)+\sum_{i=4}^{nC}f_{iso}(i)\cdot K_{L,iso}(i)\right] \tag{5}$$

$$ADS2=K_{PD}(i)\cdot\left(K_{L,n}(i)\cdot f_n(i)+K_{L,iso}(i)\cdot f_{iso}(i)\right) \tag{6}$$

•The net production rate expression for each component is the sum of three terms: isomerization (r_{isom}), cracking (r_{ck}) and "formation by cracking" rate. The latter is different for iso-paraffins ($r_{prod,iso}$) and linear paraffins ($r_{prod,n}$), and depends on the cracking reaction rate and the cracking probability function defined above:

Downloaded by CORNELL UNIV on June 6, 2012 | http://pubs.acs.org
Publication Date (Web): November 29, 2011 | doi: 10.1021/bk-2011-1084.ch011

$$r_{prod,iso}(i) = Par15 \cdot \sum_{j=i+4}^{70} \left(\frac{2}{j-6} \cdot r_{ck}(j) \right) + \left(\frac{2}{2 \cdot (i+3) - 12} \cdot r_{ck}(i+3) \right) \tag{7}$$

$$r_{prod,n}(i) = (1 - Par15) \cdot \sum_{j=i+4}^{70} \left(\frac{2}{j-6} \cdot r_{ck}(j) \right) \tag{8}$$

$$r_{prod,n}(i=3) = \sum_{j=7}^{70} \left(\frac{2}{2 \cdot j - 12} \cdot r_{ck}(j) \right) \tag{9}$$

Model parameter *Par*15 represents the iso-paraffins fraction, i.e. iso/(n + iso), that can be obtained from cracking of a generic iso-paraffin.

•Vapour–liquid equilibrium is accounted for by introducing the fugacity for each component. Fugacity of each molecule in the reaction mixture (paraffins and H_2) is estimated by means of vapour–liquid equilibrium calculations, using the Redlich-Kwong-Soave cubic equation of state. Flash calculations are performed at the reactor inlet and at nine points along the length of the catalytic bed.

•Kinetic (i.e., preexponential factors and activation energies) and thermodynamic constants (i.e., Langmuir constants, isomerization equilibrium constant and K_{PD}) are expressed by proper functions of chain length (NC). This allows to reduce significantly the number of model parameters. As demonstrated in a previous paper (*19*), the goodness of the fit strongly depends on the kind of functions chosen: proper expressions, respectful of the physical meaning of the constant, provide a better model prediction ability. The expressions of the model constants are listed below:

$$K_{L,n}(i) = Par1 \cdot (th_n(i) + 1) \tag{10}$$

with

$$th_n(i) = \frac{\exp(i \cdot Par2 - 2) - \exp(-(i \cdot Par2 - 2))}{\exp(i \cdot Par2 - 2) + \exp(-(i \cdot Par2 - 2))} \tag{11}$$

$$K_{L,iso}(i) = Par3 \cdot (th_{iso}(i) + 1) \tag{12}$$

with

$$th_{iso}(i) = \frac{\exp(i \cdot Par4 - 2) - \exp(-(i \cdot Par4 - 2))}{\exp(i \cdot Par4 - 2) + \exp(-(i \cdot Par4 - 2))} \tag{13}$$

Downloaded by CORNELL UNIV on June 6, 2012 | http://pubs.acs.org
Publication Date (Web): November 29, 2011 | doi: 10.1021/bk-2011-1084.ch011

$$E_{isom}(i) = Par5 \cdot i^{Par6} \tag{14}$$

$$E_{ck}(i) = Par7 \cdot i^{Par8} \tag{15}$$

$$k°_{isom}(i) = Par9 \cdot i^{Par10} \tag{16}$$

$$k°_{ck}(i) = Par11 \cdot i^{Par12} \tag{17}$$

$$K_{eq}(i) = Par13 \cdot \left(i^2 - 9\right) + Par14 \cdot \left(i - 3\right) \tag{18}$$

$$K_{PD}(i) = Par16 \cdot i^{Par17} \tag{19}$$

The kinetic constants are expressed by a reparametrization of the Arrhenius equation, suitable to break the correlation between the preexponential factor and activation energy (*24*):

$$k(i) = k°(i) \cdot \exp\left[-\frac{E(i)}{R} \cdot \left(\frac{1}{T} - \frac{1}{T_{ref}}\right)\right] \tag{20}$$

Product distributions are calculated coupling the kinetic model with the ideal plug-flow reactor model and 138 mass balance equations are solved (*26*).

Model discrimination has been performed by means of two statistical parameters: when comparing rival models, the one characterized by the lowest values of these parameters is the best.

•AAR, Average Absolute Residual:

$$AAR = \frac{\sum_{i=1}^{NR} \sum_{j=1}^{NL} \left|r_{ij}\right|}{NR \cdot NL} \tag{21}$$

where r_{ij} is the residual of the jth lump (the overall number of lumps, NL, is 9) in the ith run (the overall number of runs is NR, 51 for the LW series and 53 for the HW series).

•AIC, Akaike Information Criterion, which is a more accurate parameter for model discrimination, since it also accounts for the number of estimated parameters (NP):

$$AIC = NP \cdot \frac{2}{NR \cdot NL} + \ln\left(\frac{RSS}{NR \cdot NL}\right) + NP \cdot \frac{2}{NR \cdot NL} \cdot \frac{NP + 1}{NR \cdot NL - NP - 1} \tag{22}$$

RSS is the Residuals Sum of Squares.

Downloaded by CORNELL UNIV on June 6, 2012 | http://pubs.acs.org
Publication Date (Web): November 29, 2011 | doi: 10.1021/bk-2011-1084.ch011

Results and Discussion

Results of model regressions, expressed as estimated parameters and statistical analysis, are presented in Table II (for LW) and Table III (for HW). The model constant where a parameter is used is indicated in parentheses by the name of the parameter itself.

The statistical analysis suggests that regressions are quite good, since high values of R^2 are obtained and the adjusted-R^2 are close to the R^2 in both the cases (i.e., no redundant parameters are present in the model). The values of AAR and AIC are very similar in the two regressions, indicating that the quality of the two fittings is comparable.

A good achievement is that the two regressions estimated a high number of parameters: 13 out of 17 in both the cases. Notably, only Par10 in the HW regression was not optimized, since the "optimal estimate" and the "first guess" values are identical. The others were optimized, but the code was not able to provide statistics. An interesting feature is that Par13 and Par14, used in the expression for the isomerization equilibrium constant (K_{eq}), were not estimated in both regressions. The result suggests that a different equation should be used to correlate K_{eq} and the chain length. Here the hint was not followed, since the aim of the work is to check the existing model with various feedstocks.

The quality of regression could also be appreciated by the analysis of the parity plots. The most significant are those of residue conversion (Figure 2), middle distillate (linear and iso-paraffins C_{10-22}, Figure 3) and gasoline (linear and iso-paraffins C_{5-9}, Figure 4) fractions.

The fitting is good for conversion and MD fraction, slightly better in the case of HW. The quality decreases for lighter components: it is still satisfactory for the gas oil (C_{15-22}) and kero (C_{10-14}) fractions; it slightly worsen for the gasoline (C_{5-9}) fraction, as shown in Figure 4, and is really poor for the gas cut. This is a weakness of the present model, as clearly explained elsewhere (*19*), but no corrective actions have been adopted because the goal was to check the model as such.

The most important model assumption is represented by the set of equations used to correlate model constants with chain length (eqs. 5-14). If the expressions chosen are correct, values and trends of the kinetic and thermodynamic constants should reflect their true physical behaviour. As an example, the evolution with NC of the apparent activation energies and kinetic constants for isomerization and cracking reactions is shown in Figure 5 and Figure 6; the evolution of the Langmuir constants for linear and branched paraffins is plotted in Figure 7. Results obtained for LW and HW are directly compared in the plots.

Downloaded by CORNELL UNIV on June 6, 2012 | http://pubs.acs.org
Publication Date (Web): November 29, 2011 | doi: 10.1021/bk-2011-1084.ch011

Table II. Results of model regression for LW

Asymptotic Statistical Analysis	
R-Square	0.933
Adjusted R-Square	0.931
RSS	3.04×10^3
AAR	1.94
AIC	1.95

Parameter	*First guess*	*Optimal estimate*	*Asymptotic 95% Confidence Intervals*	*t-value*	*Standard deviation*
*Par*1 (K_{Ln})	1.25×10^1	1.34×10^1			
*Par*2 ($K_{L,n}$)	1.15×10^{-1}	1.15×10^{-1}	$\pm 4.77 \times 10^{-4}$	4.77×10^2	2.42×10^{-4}
*Par*3 ($K_{L,iso}$)	8.52×10^0	6.11×10^0	$\pm 8.22 \times 10^{-1}$	1.47×10^1	4.17×10^{-1}
*Par*4 ($K_{L,iso}$)	1.53×10^{-1}	1.79×10^{-1}	$\pm 3.88 \times 10^{-3}$	9.11×10^1	1.97×10^{-3}
*Par*5 (E_{isom})	4.54×10^4	4.44×10^4	$\pm 3.41 \times 10^2$	2.56×10^2	1.73×10^2
*Par*6 (Eisom)	4.96×10^{-1}	5.06×10^{-1}	$\pm 3.26 \times 10^{-3}$	3.06×10^2	1.65×10^{-3}
*Par*7 (E_{ck})	4.47×10^4	4.90×10^4	$\pm 2.54 \times 10^3$	3.81×10^1	1.29×10^3
*Par*8 (E_{ck})	5.35×10^{-1}	5.35×10^{-1}	$\pm 2.07 \times 10^{-4}$	5.11×10^3	1.05×10^{-4}
*Par*9 ($k°_{isom}$)	1.81×10^{-3}	1.93×10^{-3}	$\pm 4.66 \times 10^{-6}$	8.17×10^2	2.37×10^{-6}
*Par*10 ($k°_{isom}$)	4.91×10^0	4.90×10^0	$\pm 1.02 \times 10^{-2}$	9.48×10^2	5.17×10^{-3}
*Par*11 ($k°_{ck}$)	2.49×10^{-4}	2.26×10^{-4}	$\pm 3.11 \times 10^{-6}$	1.43×10^2	1.58×10^{-6}
*Par*12 ($k°_{ck}$)	4.78×10^0	4.88×10^0	$\pm 4.97 \times 10^{-2}$	1.93×10^2	2.52×10^{-2}
*Par*13 (K_{eq})	2.45×10^0	4.51×10^0			
*Par*14 (K_{eq})	9.96×10^{-1}	4.39×10^{-1}			
*Par*15 (iso/ n+iso)	6.52×10^{-1}	5.90×10^{-1}	$\pm 1.25 \times 10^{-1}$	9.33×10^0	6.32×10^{-2}
*Par*16 (K_{PD})	4.27×10^1	3.51×10^1			
*Par*17 (K_{PD})	1.76×10^0	1.85×10^0	$\pm 2.71 \times 10^{-2}$	1.35×10^2	1.37×10^{-2}

Downloaded by CORNELL UNIV on June 6, 2012 | http://pubs.acs.org
Publication Date (Web): November 29, 2011 | doi: 10.1021/bk-2011-1084.ch011

Table III. Results of model regression for HW

Asymptotic Statistical Analysis	
R-Square	0.937
Adjusted R-Square	0.935
RSS	4.48 × 10^3
AAR	2.05
AIC	2.30

Parameter	*First guess*	*Optimal estimate*	*Asymptotic 95% Confidence Intervals*	*t-value*	*Standard deviation*
*Par*1 (K_{Ln})	8.02 × 10^1	7.92 × 10^1	± 2.89 × 10^0	5.40 × 10^1	1.47 × 10^0
*Par*2 ($K_{L,n}$)	2.08 × 10^{-1}	2.13 × 10^{-1}	± 4.13 × 10^{-5}	1.02 × 10^4	2.10 × 10^{-5}
*Par*3 ($K_{L,iso}$)	3.48 × 10^1	3.85 × 10^1	± 1.81 × 10^0	4.21 × 10^1	9.15 × 10^{-1}
*Par*4 ($K_{L,iso}$)	1.00 × 10^{-1}	3.49 × 10^{-2}	± 1.08 × 10^{-2}	6.35 × 10^0	5.49 × 10^{-3}
*Par*5 (E_{isom})	4.53 × 10^4	3.57 × 10^4	± 9.78 × 10^2	7.19 × 10^1	4.96 × 10^2
*Par*6 (E_{isom})	3.22 × 10^{-1}	2.53 × 10^{-1}	± 1.94 × 10^{-4}	2.58 × 10^3	9.82 × 10^{-5}
*Par*7 (E_{ck})	4.31 × 10^4	4.25 ·10^4	± 1.20 ·10^2	6.98 ·10^2	6.09 × 10^1
*Par*8 (E_{ck})	5.14 ·10^{-1}	5.18 × 10^{-1}	± 6.03 × 10^{-4}	1.69 × 10^3	3.06 × 10^{-4}
*Par*9 (k°_{isom})	2.86 × 10^{-4}	2.49 × 10^{-4}	± 1.54 × 10^{-7}	3.19 × 10^3	7.79 × 10^{-8}
*Par*10 (k°_{isom})	5.02 × 10^0	5.02 × 10^0			
*Par*11 (k°_{ck})	2.45 × 10^{-4}	3.01 × 10^{-4}	± 4.34 × 10^{-7}	1.37 × 10^3	2.20 × 10^{-7}
*Par*12 (k°_{ck})	4.66 × 10^0	4.67 × 10^0	± 9.69 × 10^{-4}	9.51 × 10^3	4.91 × 10^{-4}
*Par*13 (Keq)	6.62 × 10^1	1.33 × ·10^2			
*Par*14 (K_{eq})	5.55 × 10^2	9.65 × 10^2			
*Par*15 (iso/ n+iso)	9.03 × 10^{-1}	8.95 × 10^{-1}	± 1.68 × 10^{-3}	1.05 × 10^3	8.50 × 10^{-4}
*Par*16 (K_{PD})	1.82 × 10^1	4.09 × 10^1	± 2.18 × 10^1	3.70 × 10^0	1.11 × 10^1
*Par*17 (K_{PD})	9.59 × 10^{-1}	3.44 × 10^{-2}			

Downloaded by CORNELL UNIV on June 6, 2012 | http://pubs.acs.org
Publication Date (Web): November 29, 2011 | doi: 10.1021/bk-2011-1084.ch011

Downloaded by CORNELL UNIV on June 6, 2012 | http://pubs.acs.org
Publication Date (Web): November 29, 2011 | doi: 10.1021/bk-2011-1084.ch011

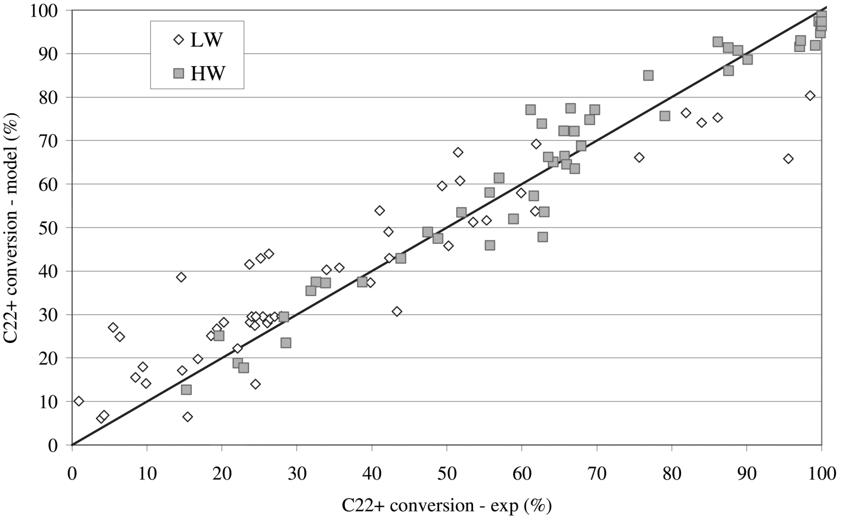

Figure 2. Parity plots for residue (C_{22+}) conversion of LW and HW.

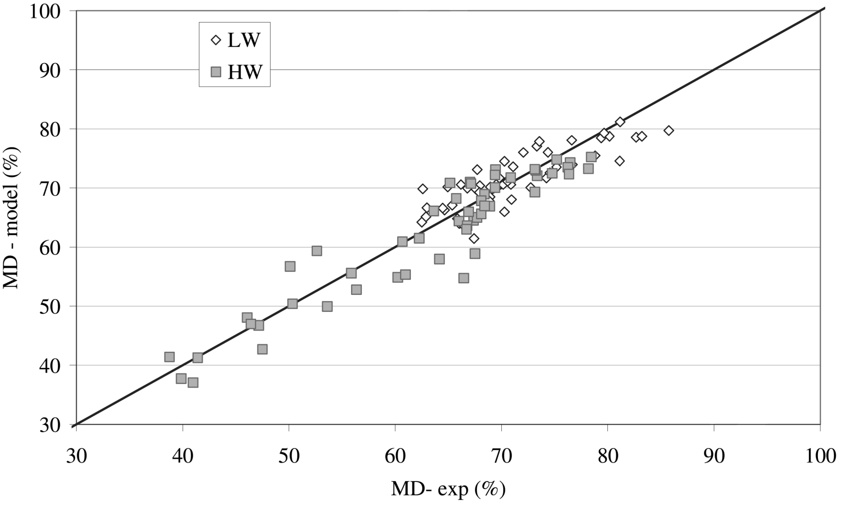

Figure 3. Parity plots for Middle Distillates fraction ($C_{10\text{-}22}$) of LW and HW.

Downloaded by CORNELL UNIV on June 6, 2012 | http://pubs.acs.org
Publication Date (Web): November 29, 2011 | doi: 10.1021/bk-2011-1084.ch011

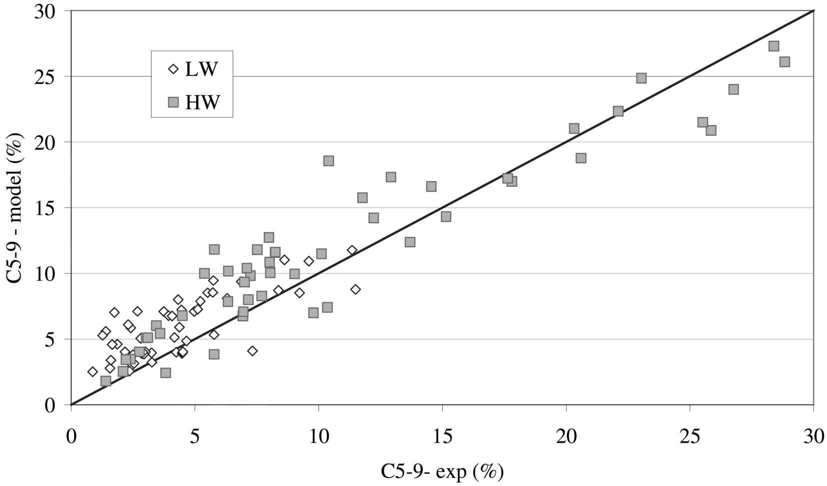

Figure 4. Parity plots for the gasoline fraction (C_{5-9}) of LW and HW.

Literature evidences (*7*, *16*, *20*) indicate that the energy of activation for isomerization and cracking are similar, do not show significant variation with chain length and range between 30 and 37 kcal/mol. Model results show that the isomerization energy for LW significantly depends on chain length and the values exceed the range indicated. On the contrary, in the case of HW the trend and values are closer to data published. Furthermore, activation energies strongly depends on the feedstocks, since values estimated for LW are 2-3 times higher than those relative to HW. The estimated cracking activation energy increases significantly with carbon number for both LW and HW, going beyond the experimental ranges. Summarizing, the model estimates similar values for cracking and isomerization energies in the case of LW, in line with literature data, but the dependence on chain length is very strong. Otherwise, the model foresees a strong difference between isomerization and cracking activation energies in the case of HW, since the former are almost independent on carbon number. A possible explanation of the dependence to chain length and the differences with literature data lies in the fact that the model estimates apparent activation energies, defined as the sum of the activation energy for the reaction and the adsorption enthalpy, as the nominator of eqs. 1 and 2 contains both the kinetic and the Langmuir constants (*16*).

The kinetic constants for isomerization and cracking (Figure 6) increase exponentially with chain length, as already shown by Froment (*16*). For both LW and HW, the isomerization constant is higher than the cracking constant, suggesting that paraffins are more reactive in the former reaction. Comparing different feedstocks at the same temperature, kinetic constants for LW are always higher than for HW, suggesting that light paraffins are more reactive than the heavier ones. This peculiar behaviour will be explained below.

Downloaded by CORNELL UNIV on June 6, 2012 | http://pubs.acs.org
Publication Date (Web): November 29, 2011 | doi: 10.1021/bk-2011-1084.ch011

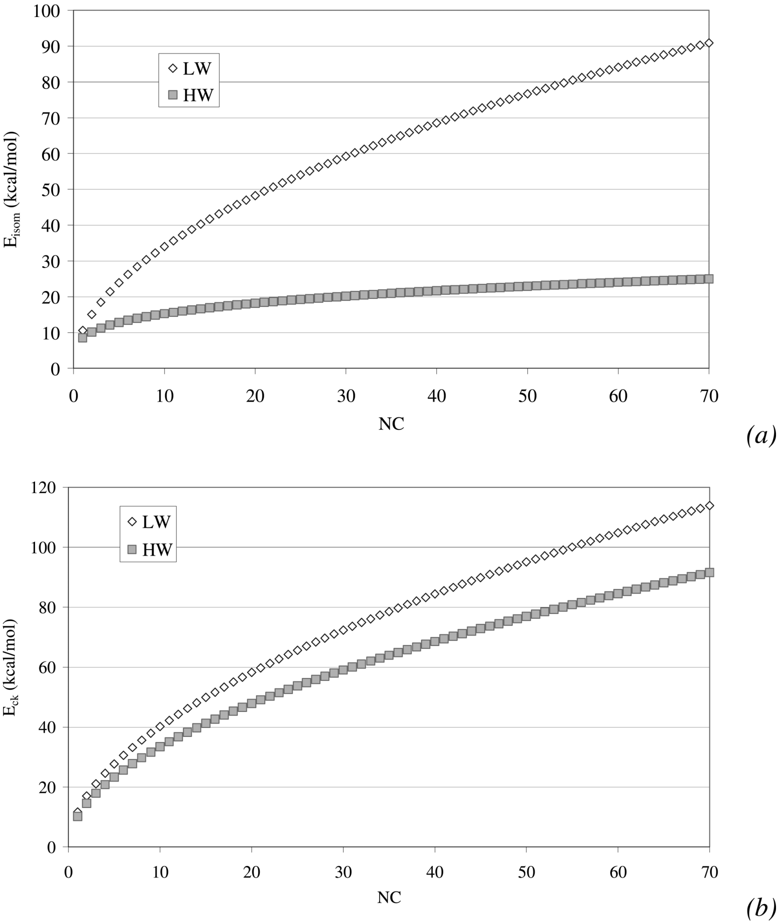

Figure 5. Evolution with chain length of the (a) isomerization and (b) cracking activation energy for LW and HW.

The Langmuir constant (K_L), which accounts for hydrocarbons physisorption, is correlated to chain length through a flexible function, the hyperbolic tangent, since it can change its shape according to the parameters values (*19*). As shown in Figure 7, model optimization foresees a sigmoidal trend for the Langmuir constant relative to n-paraffins (Figure 7 a) for both LW and HW, but the values are significantly different, being higher (even 5 times) for HW. In the case of isomers (Figure 7 b), the trends displayed by the two series of feedstocks are different, since the sigmoid-like shape is still evident for LW, while an exponential increase with NC can be observed for HW. Finally, the values of K_L for linear and branched paraffins are comparable only in the case of LW, since for HW $K_{L,iso}$ are less than a half of $K_{L,n}$.

Downloaded by CORNELL UNIV on June 6, 2012 | http://pubs.acs.org
Publication Date (Web): November 29, 2011 | doi: 10.1021/bk-2011-1084.ch011

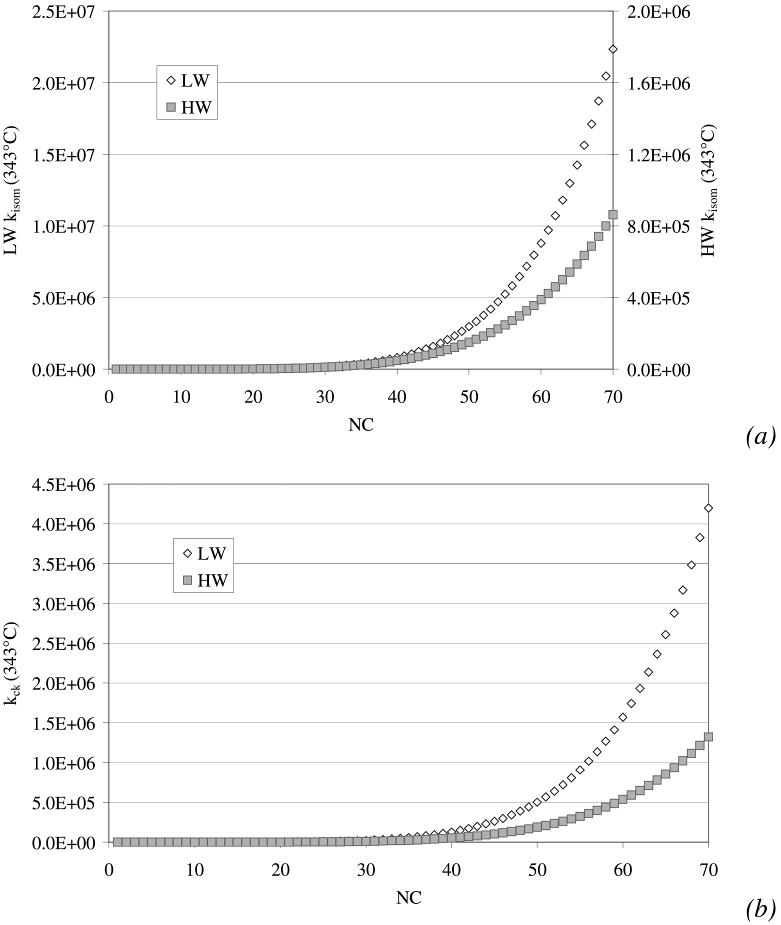

Figure 6. Evolution with chain length of the (a) isomerization and (b) cracking constants, calculated at T=343°C, for LW and HW.

The sigmoid shape of the Langmuir constant for paraffins up to C_{70} was already observed and explained in the light of adsorption mechanism (*19*). VLE plays a major role, since lighter paraffins are mainly concentrated in the gas phase and thus are selectively adsorbed on the catalyst surface (K_L increases with NC). On the contrary, heavier hydrocarbons are more abundant in the liquid phase, where adsorption is independent on chain length (K_L remains almost constant with NC).

Interesting information about the model prediction ability can be inferred by comparing the experimental and calculated product distribution plots. Data collected at different conversion levels (low, medium and high) are presented in Figure 8 for LW and in Figure 9 for HW. Products are split into linear (n-par) and branched (iso-par) paraffins. Furthermore, the plots show the feed (experimental) distribution, to better appreciate the role of hydrocracking on conversion of FT waxes.

Downloaded by CORNELL UNIV on June 6, 2012 | http://pubs.acs.org
Publication Date (Web): November 29, 2011 | doi: 10.1021/bk-2011-1084.ch011

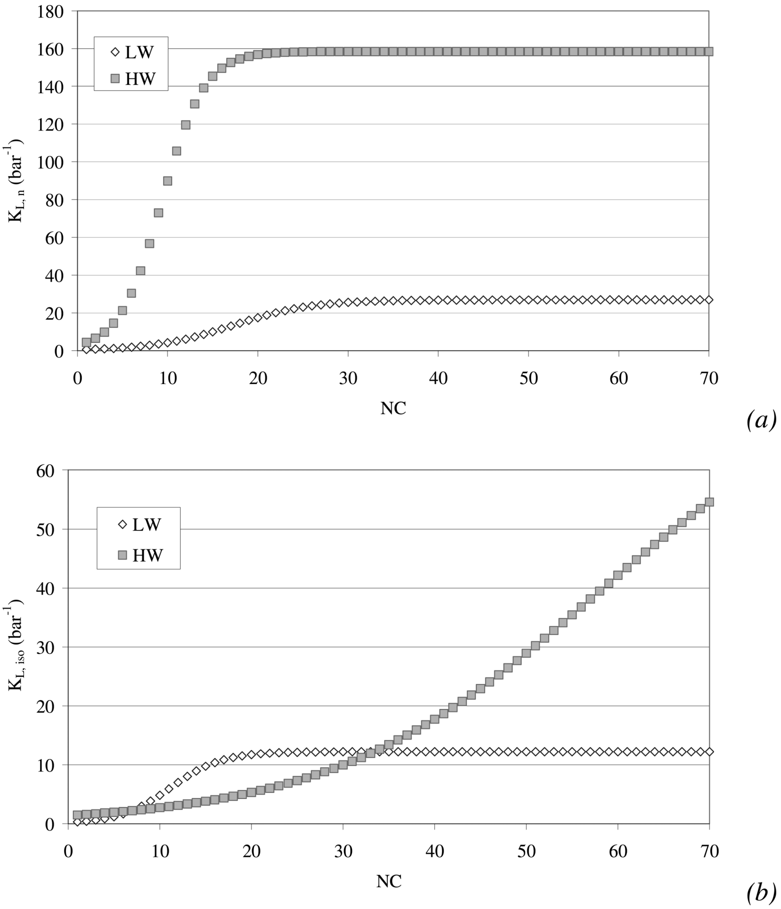

Figure 7. Evolution with chain length of the Langmuir constants for LW and HW: (a) linear paraffins, (b) iso-paraffins.

The model provides a good description of the role of HDK on conversion of FT waxes: in the two cases, at low conversion product distribution resembles the feed distribution, meaning that cracking reaction plays a minor role in the process mechanism, compared to isomerization. Isomers concentration increases with conversion and the distribution peak shifts towards lower carbon numbers, suggesting that cracking importance is higher. Concerning the quality of the simulation, good agreement between experimental and model results is always achieved at medium-low conversion levels; at high conversion (> 80%) the model hardly foresees the behaviour of LW, in particular in the case of isomers distribution, which is underestimated. Finally, the graphics show that the agreement between model and experimental results is better for heavier paraffins (NC>10), as already pointed out by the parity plots.

Downloaded by CORNELL UNIV on June 6, 2012 | http://pubs.acs.org
Publication Date (Web): November 29, 2011 | doi: 10.1021/bk-2011-1084.ch011

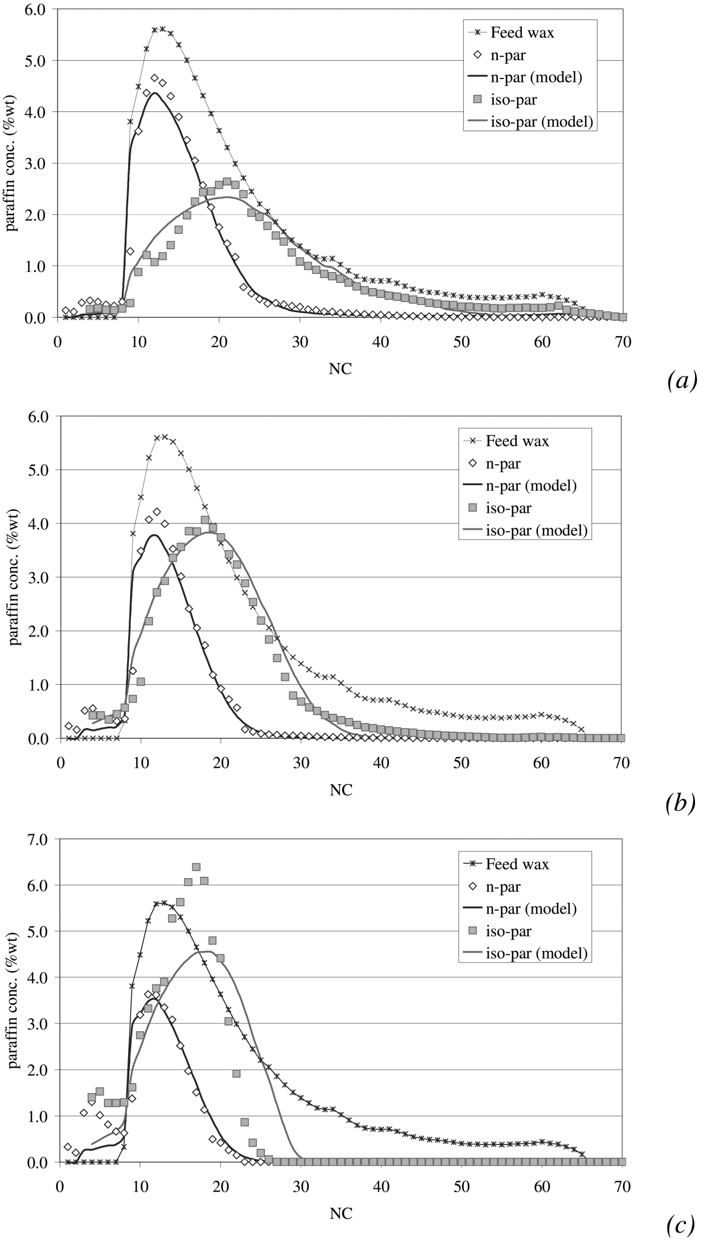

Figure 8. Feed and products distribution plots for LW at different conversion levels: (a) 10%, (b) 55%, (c) 95%.

Downloaded by CORNELL UNIV on June 6, 2012 | http://pubs.acs.org
Publication Date (Web): November 29, 2011 | doi: 10.1021/bk-2011-1084.ch011

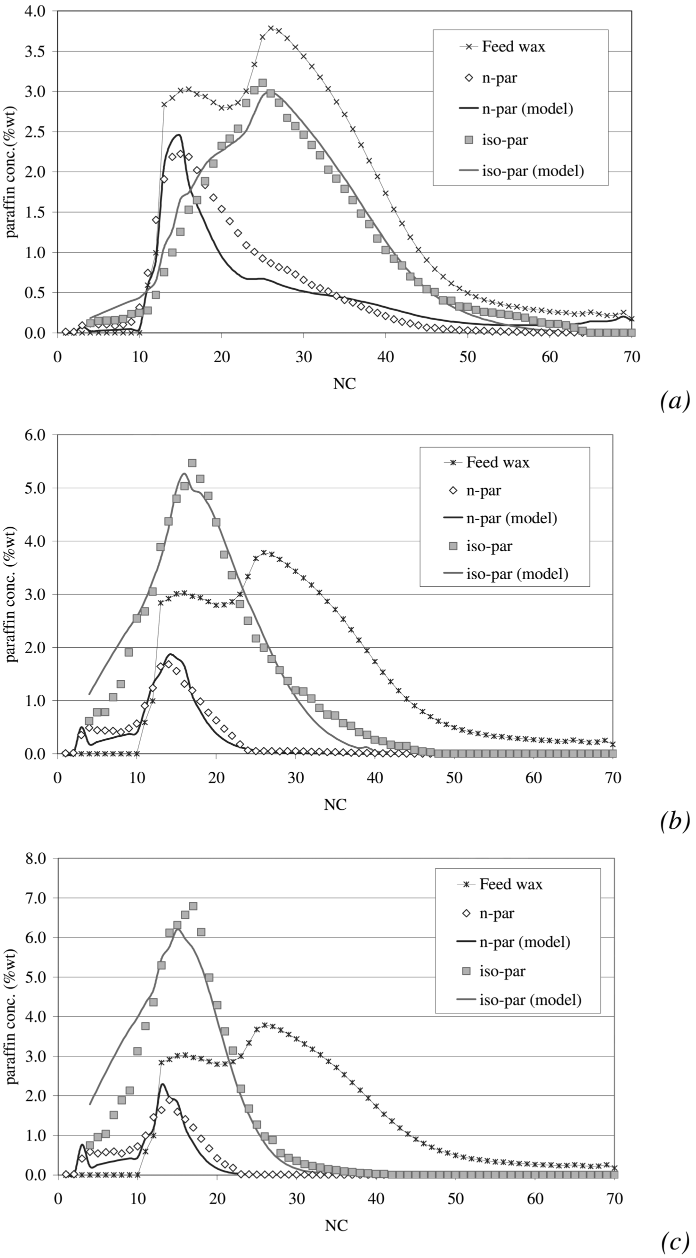

Figure 9. Feed and products distribution plots for HW at different conversion levels: (a) 15%, (b) 66%, (c) 86%.

The model can be considered a suitable tool for the description of hydrocracking of FT waxes if it is able to predict the effect of operating conditions on residue conversion. Results are reported in Figure 10 to Figure 13. Due to the different reactivity of the two feedstocks, the LW and HW series have been carried out at different temperature ranges. In particular, the reference temperature is 335°C for LW and 353°C for HW. On the contrary, the other conditions were changed in the same ranges. This means that the two series could be directly compared only when the effect of temperature is analyzed, since pressure, WHSV and H_2/feed ratio are the same for the two datasets, as indicated in caption of Figure 10.

It is well known that temperature has a positive effect on wax conversion (*8*). The model simulates well the experimental effect of temperature (Figure 10). Furthermore, the tool puts in evidence the different reactivity of the two feedstocks: LW are more reactive than HW, since the same conversion degree is reached at lower temperature.

Results in Figure 11 show that the model is able to predict the negative effect of WHSV on conversion (*8*). Simulation of HW is better, while the model underestimates conversion of LW at the highest space velocity. As said above, the data of the two series cannot be directly compared, since the experiments were carried out at different temperatures, as explained in the figure caption.

Concerning the role of pressure (Figure 12), the model provides a good simulation of the experimental results, even if some deviations are evident at the endpoints. Notably, a positive result is obtained despite of the different experimental trends of the two series: while conversion decreases with pressure for HW, in line with literature data (*8*), an almost flat profile is shown (at P>45 bar) for the LW series.

Downloaded by CORNELL UNIV on June 6, 2012 | http://pubs.acs.org
Publication Date (Web): November 29, 2011 | doi: 10.1021/bk-2011-1084.ch011

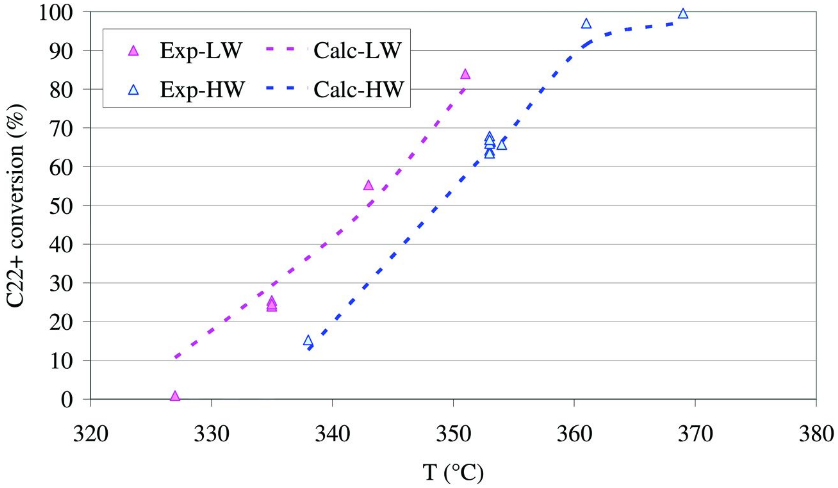

Figure 10. Comparison of experimental and calculated effect of temperature on residue conversion for LW and HW. Other conditions are: P=50 bar, WHSV=2h^{-1}*, H*$_2$*/feed=0.105 g/g.*

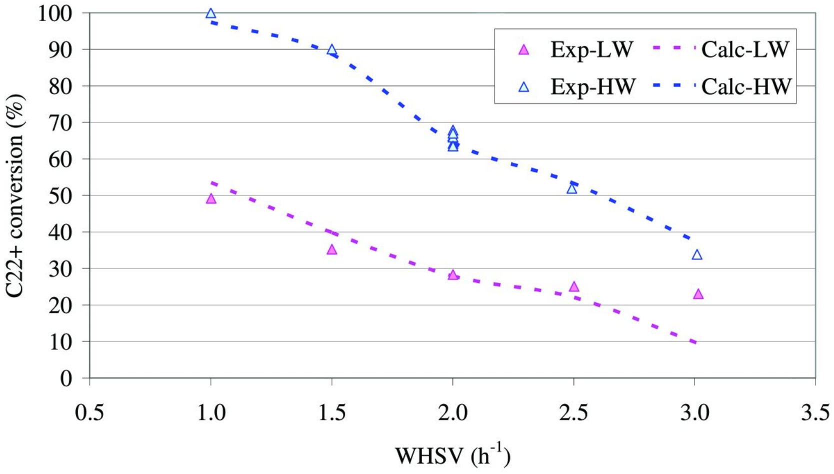

Figure 11. Comparison of experimental and calculated effect of WHSV on residue conversion for LW and HW. Other conditions are: T=335°C for LW and T=353°C for HW, P=50 bar, H_2/feed=0.105 g/g.

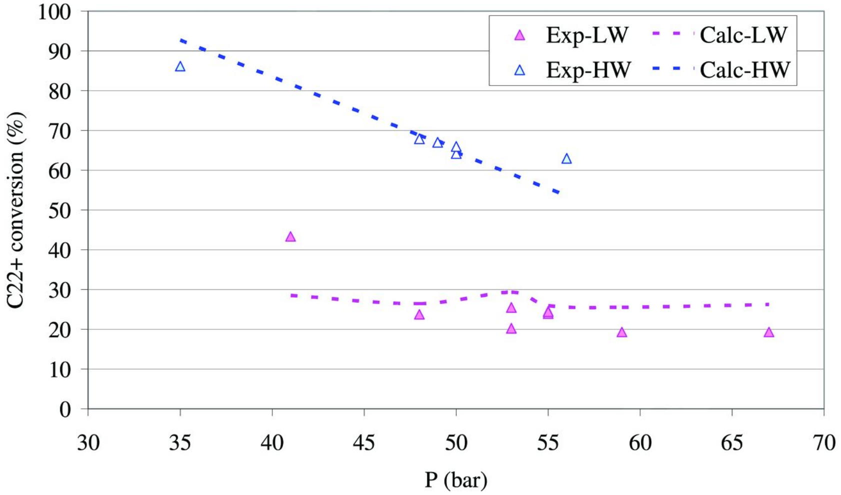

Figure 12. Comparison of experimental and calculated effect of pressure on residue conversion for LW and HW. Other conditions are: T=335°C for LW and T=353°C for HW, WHSV=2h^{-1}, H_2/feed=0.105 g/g.

Downloaded by CORNELL UNIV on June 6, 2012 | http://pubs.acs.org
Publication Date (Web): November 29, 2011 | doi: 10.1021/bk-2011-1084.ch011

The last effect analyzed is that of the H_2/feed ratio at the reactor inlet (Figure 13). The data relative to LW are generally overestimated and a flat profile of conversion is foreseen at increasing H_2/wax, in contrast with experimental evidences (*8*). The same behaviour was already observed in previous works (*19*, *25*). On the contrary, the model is in good agreement with experimental results in the case of HW. Clearly the different response of the model in fitting the experimental data results from the different feed composition but more work is still necessary to identify the underlying reasons. This is an important achievement, since confirms the goodness of the model hypotheses.

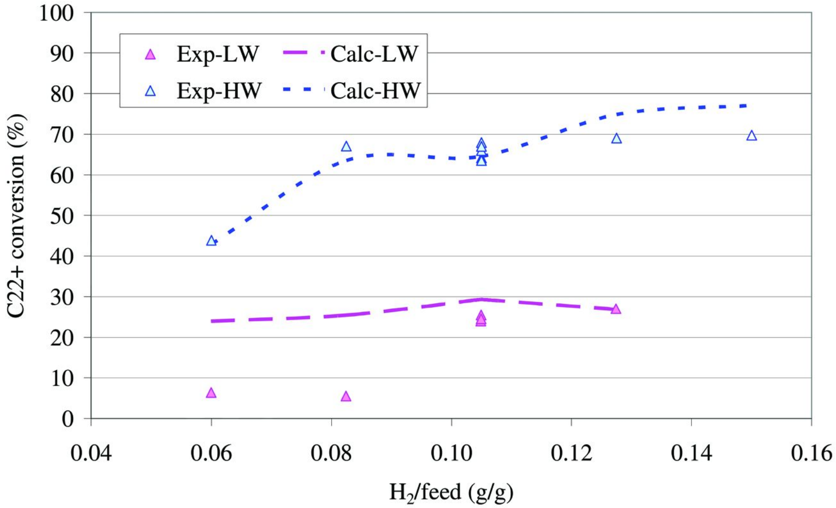

Figure 13. Comparison of experimental and calculated effect of the H_2/feed ratio on residue conversion for LW and HW. Other conditions are: T=335°C for LW and T=353°C for HW, P=50 bar, WHSV=2h^{-1}.

Downloaded by CORNELL UNIV on June 6, 2012 | http://pubs.acs.org
Publication Date (Web): November 29, 2011 | doi: 10.1021/bk-2011-1084.ch011

Data relative to the effect of temperature on conversion (Figure 10) and the kinetic constants (Figure 6) clearly show that LW are more reactive than HW. This tendency can be explained in the light of the different VLE behaviour of the two feedstocks. For this purpose, vapour-liquid equilibrium calculation results for LW and HW are shown in Figure 14. When the LW is fed to the HDK reactor at 343°C and 47.5 bar, in presence of hydrogen (Figure 14a), the mixture is flashed between a vapour phase, rich in light paraffins (essentially in the range C_{10-30}), that represents about 57% of the feed and a liquid phase, rich in heavier paraffins (C_{30+}). On the contrary, when the HW is flashed at the same conditions, vaporization is only 31% (Figure 14b). On the light of these data, although the overall WHSV is the same for both LW and HW the liquid phase flow rate (or equivalently, the liquid phase space velocity) of HW and LW is different. In ideal trickle flow regime, the reactive phase is the liquid contacting the catalyst while the gas phase can be considered in equilibrium with the reacting liquid phase: as a consequence, the apparent conversion rate of the feedstock, measured in our case as conversion of

C22+ fraction, will depend on liquid phase flow rate. In these circumstance at the same WHSV value the corresponds in the case of HW a residence time of liquid phase lower than the LW. This situation leads to a lower apparent conversion rate in comparison with the LW, as experimentally observed.

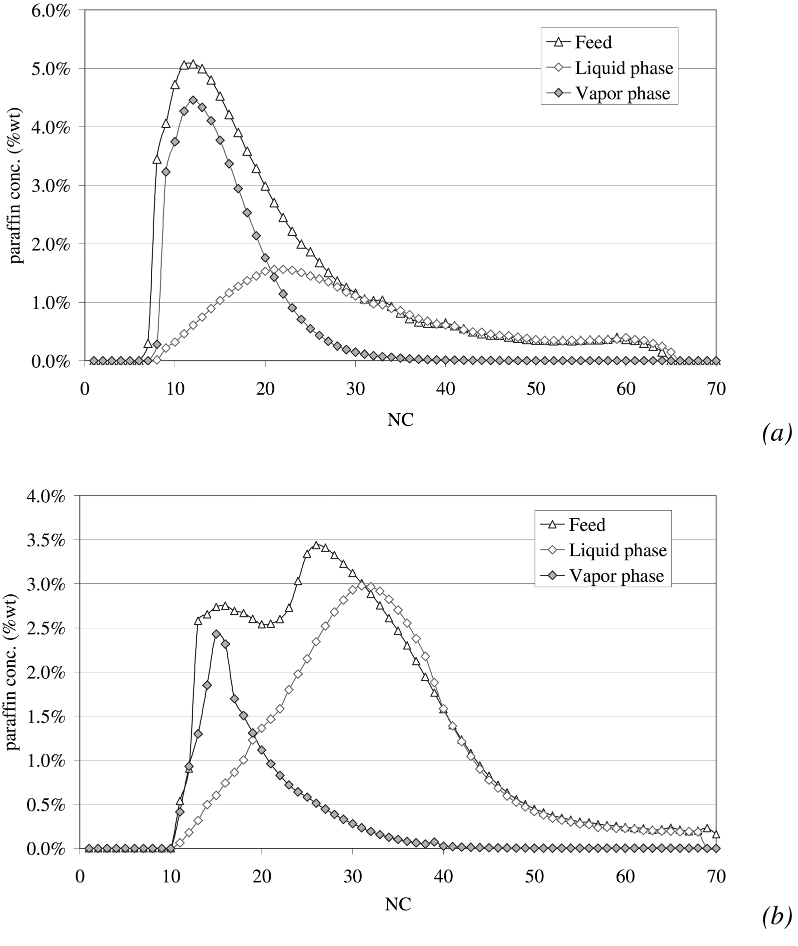

Figure 14. VLE calculation for (a) LW (V/F=0.57) and (b) HW (V/F=0.31). Operating conditions: T=343°C, P=47.5 bar, H_2/feed=0.105 g/g.

Conclusions

The kinetic model was developed to describe hydrocracking of complex paraffins mixtures in trickle bed reactors. The tool demonstrated to suit different feedstocks, being able to describe quite well product distributions and operating conditions effects. Furthermore, the model is able to foresee differences in reactivity with waxes composition, thanks to the introduction of VLE calculations. The physical behaviour of kinetic and thermodynamic constants is also accounted

Downloaded by CORNELL UNIV on June 6, 2012 | http://pubs.acs.org
Publication Date (Web): November 29, 2011 | doi: 10.1021/bk-2011-1084.ch011

for by proper functions of chain length. Their values and trends strongly depend upon the feedstock composition. The use of the complete form of the rate expression provides better results compared to the previous versions, suggesting that non-ideal behaviour is more likely when complex mixtures of heavy paraffins are considered. In this light, the model was useful to better understand the reaction mechanism.

Despite of the very promising results reached, the model can be further improved to fit better the lightest hydrocarbons concentration and the effect of H_2/feed ratio, for example by considering gas and liquid phases separately.

Downloaded by CORNELL UNIV on June 6, 2012 | http://pubs.acs.org
Publication Date (Web): November 29, 2011 | doi: 10.1021/bk-2011-1084.ch011

References

1. Ribeiro, F.; Marcilly, C.; Guisnet, M. *J. Catal.* **1982**, *78*, 267–274.
2. Schulz, H. F.; Weitkamp, J. H. *Ind. Eng. Chem. Prod. Res. Dev.* **1972**, *11*, 46–53.
3. Steijns, M.; Froment, G.; Jacobs, P.; Uytterhoeven, J.; Weitkamp, J. *Ind. Eng. Chem. Prod. Res. Dev.* **1981**, *20*, 654–660.
4. Weitkamp, J.; Jacobs, P. A.; Martens, J. A. *Appl. Catal.* **1983**, *8*, 123–141.
5. Martens, J. A.; Jacobs, P. A.; Weitkamp, J. *Appl. Catal.* **1986**, *20*, 239–281.
6. Rossetti, I.; Gambaro, C.; Calemma, V. *Chem. Eng. J.* **2009**, *154*, 295–301.
7. Calemma, V.; Peratello, S.; Perego, C. *Appl. Catal., A.* **2000**, *190*, 207–218.
8. Leckel, D. *Energy Fuels* **2005**, *19*, 1795–1803.
9. Leckel, D.; Liwanga-Ehumbu, M. *Energy Fuels* **2006**, *20*, 2330–2336.
10. Leckel, D. *Energy Fuels* **2007**, *21*, 1425–1431.
11. Calemma, V.; Correra, S.; Perego, C.; Pollesel, P.; Pellegrini, L. *Catal. Today* **2005**, *106*, 282–287.
12. Calemma, V.; Gambaro, C.; Parker, W. O., Jr.; Carbone, R.; Giardino, R.; Scorletti, P. *Catal. Today* **2010**, *149*, 40–46.
13. Zhou, Z.; Zhang, Y.; Tierney, J. W.; Wender, I. *Fuel Process. Technol.* **2003**, *83*, 67–80.
14. Bouchy, C.; Hastoy, G.; Guillon, E.; Martens, J. A. *Oil Gas Sci. Technol.* **2009**, *64*, 91–112.
15. Martens, J. A.; Jacobs, P. A.; Weitkamp, J. *Appl. Catal.* **1986**, *20*, 283–303.
16. Debrabandere, B.; Froment, G. F. *Stud. Surf. Sci. Catal.* **1997**, *106*, 379–389.
17. Pellegrini, L.; Locatelli, S.; Rasella, S.; Bonomi, S.; Calemma, V. *Chem. Eng. Sci.* **2004**, *59*, 4781–4787.
18. Pellegrini, L.; Gamba, S.; Calemma, V.; Bonomi, S. *Chem. Eng. Sci.* **2008**, *63*, 4285–4291.
19. Gambaro, C.; Calemma, V.; Molinari, D.; Denayer, J. *AIChE J.* **2011**, *57*, 711–723.
20. Baltanas, M. A.; Vansina, H.; Froment, G. F. *Ind. Eng. Chem. Prod. Res. Dev.* **1983**, *22*, 531–539.
21. Froment, G. F. *Catal. Today* **1987**, *1*, 455–47.
22. Martens, G. G.; Marin, G. B. *AIChE J.* **2001**, *47*, 1607–1622.
23. Kumar, H.; Froment, G. F. *Ind. Eng. Chem. Res.* **2007**, *46*, 4075–4090.

24. Steijns, M.; Froment, G. F. *Ind. Eng. Chem. Prod. Res. Dev.* **1981**, *20*, 660–668.
25. Gamba, S.; Pellegrini, L.; Calemma, V.; Gambaro, C. *Ind. Eng. Chem. Res.* **2009**, *48*, 5656–5665.
26. Pellegrini, L.; Bonomi, S.; Gamba, S.; Calemma, V.; Molinari, D. *Chem. Eng. Sci.* **2007**, *62*, 5013–5020.

Downloaded by CORNELL UNIV on June 6, 2012 | http://pubs.acs.org
Publication Date (Web): November 29, 2011 | doi: 10.1021/bk-2011-1084.ch011

Downloaded by UNIV OF GUELPH LIBRARY on June 6, 2012 | http://pubs.acs.org
Publication Date (Web): November 29, 2011 | doi: 10.1021/bk-2011-1084.ch012

Chapter 12

Hexadecane Hydrotreating as a Surrogate for Fischer-Tropsch Wax Upgrading to Aviation Fuel Using a Co/MoO_3/Silica-Alumina Catalyst

Heinz J. Robota,* Jeremy Jones, Mingsheng Luo, and Amanda Stewart

**University of Dayton Research Institute, 300 College Park,
Dayton, Ohio 45469-0145
*E-mail: heinz.robota@udri.udayton.edu**

The U.S. Air Force has flight-certified 50/50 blends of synthetic/petroleum-derived fuels and will soon be followed by the commercial aviation fleet. To move to synthetic-rich fuels, the Air Force is constructing a facility for producing its own samples of synthetic research fuels. In support of that effort, we have investigated the activity and selectivity of a commercial Co/MoO_3/Silica-Alumina catalyst using n-hexadecane as a model feed. This unsulfided catalyst exhibits predominantly hydrogenolysis rather than bifunctional hydrocracking. Two distinct types of hydrogenolysis can be discerened: 1) interior C-C bond cleaveage with near equal likelihood at all interior bonds; and 2) sequential terminal methane cleavage.

Introduction

The United States Air Force has set the goal of fueling 50% of its domestic flight operations with a fuel blend composed of 50% petroleum-derived fuel plus 50% domestically sourced synthetic fuel (*1*). To date, the Air Force has certified nearly all of its aircraft to use a blend where the synthetic component is either a Fischer-Tropsch derived synthetic paraffinic kerosene (SPK) or a chemically very similar composition prepared by hydrotreating either plant or animal oils and fats (*2*). In these blends, many of the critical properties are supplied by the petroleum-derived fraction. Thus, in order to advance beyond a 50/50 blend, synthetic fuels and fuel components must be engineered to fulfill a wider range of requirements.

In Synthetic Liquids Production and Refining; de Klerk, A., et al.;
ACS Symposium Series; American Chemical Society: Washington, DC, 2011.

Current fuel specifications derive largely from the properties of and experience with petroleum-derived fuels. As a consequence, many potential synthetic fuel compositions would fail these specifications. In order to better understand which specifications can be modified to explicitly allow a broader range of synthetic fuels, working quantities of these types of fuels and fuel components are required.

As part of a wide-ranging effort, the Air Force has established the Assured Aerospance Fuels Research Facility (AAFRF). The AAFRF is comprised of both a laboratory-scale research facility and a larger scale sample production unit capable of producing 10-15 gallons of fuel or fuel components per day. The sample production unit will be commissioned by simulating the production of a Fischer-Tropsch SPK using a commercially produced $Co/MoO_3/SiO_2$-Al_2O_3 catalyst in an unsulfided state. In order to better understand the properties and behavior of this catalyst, we have undertaken a laboratory investigation using neat n-hexadecane as a surrogate for the wax alkanes of a Fischer-Tropsch feed.

Experimental

A tubular fixed-bed reactor system, illustrated schematically in Figure 1, was employed in this work. The reactor comprises a ½ in. diameter, 24 in. long, 316 stainless steel tube with 18 in. of heated zone, oriented vertically inside a 3-zone Applied Testing Systems Inc. furnace. Each 6 in. heating zone in the furnace can be controlled independently. A zone of constant temperature at the center of the reactor was maintained within ±1°C, and could be monitored by a traveling thermocouple located within a thermowell extending through the center of the ½ in. tube. n-Hexadecane (>99% from Sigma-Aldrich) was charged to an ISCO-500D syringe pump from a feed reservoir. Reservoir, syringe pump, and associated tubing were all heated to 30° C. Hydrogen was supplied at a constant rate using a Brooks mass flow controller and combined with the n-C_{16} at the top of the fixed-bed column. While passing through roughly 8 in. of 54 mesh silicon carbide in the heated zone above the catalyst bed, the n-C_{16} vaporizes and the reaction mixture is heated to reaction temperature before contacting the catalyst-containing portion of the bed. The catalyst, purchased from Albemarle, is a commercially produced $Co/MoO_3/SiO_2$-Al_2O_3. 1 gram of catalyst, sized 40-60 mesh (about 1.6 mL), was mixed with SiC at a SiC:catalyst volumetric ratio of 4:1 and charged to the central heated zone.

Liquid reaction products are collected in two 500 mL vessels maintained at 30° C and 3.5° C. No liquids were recovered from the cooled trap, presumably because the concentration of vaporized hydrocarbons in the H_2 stream from the first collector was sufficiently low to preclude condensation. Incondensable vapors were analyzed on-line with an Agilent 3000A refinery gas analyzer. Quantitative analysis of collected liquid samples was by gas chromatography-flame ionization detection using an Agilent Model 7890 GC on a 30-m DB-5MS column with a 0.25 mm inside diameter and a 0.25-μm film. The liquid hydrocarbons were quantified in three groupings: 1) the normal paraffin for each carbon number; 2) the

Downloaded by UNIV OF GUELPH LIBRARY on June 6, 2012 | http://pubs.acs.org
Publication Date (Web): November 29, 2011 | doi: 10.1021/bk-2011-1084.ch012

mono-methyl isomers of each carbon number; and 3) the multi-branched isomers of each carbon number. Mass balances were monitored by summing the calculated total moles of carbon recovered in the liquid and compared with the total moles of carbon delivered to the reactor system. Typical carbon mass balances were >95%.

The catalyst was activated and stabilized in accordance with the manufacturer's recommendations. Once completed, liquid feed LHSV was dropped to 1/hr (0.05 ml/min) while maintaining the H_2-to-feed ratio of 600 vol/vol (30 ml/min). The reactor temperature was then increased at a rate of 10° C/hr to 330° C. Once stable, the product traps were emptied and experimentation began.

Downloaded by UNIV OF GUELPH LIBRARY on June 6, 2012 | http://pubs.acs.org
Publication Date (Web): November 29, 2011 | doi: 10.1021/bk-2011-1084.ch012

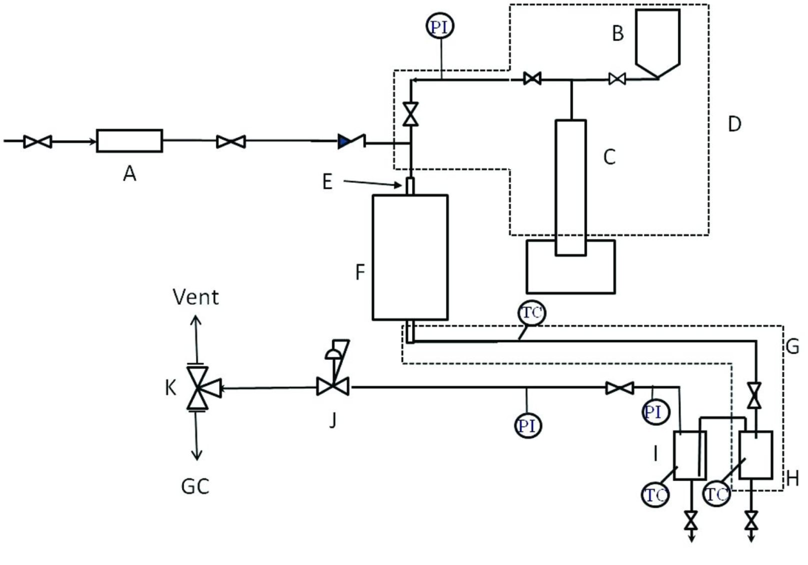

Figure 1. Schematic of the experimental system. A: H_2 mass flow controller; B: Hydrocarbon feed reservoir; C: ISCO high pressure syringe pump with 500 ml capacity; D: The dashed outline shows the heated feed section; E: ½ Stainless steel reactor tube; F: Three zone furnace; G: Heated product collection section; H: Higher temperature liquid receiver; I: Chilled liquid receiver; J: Back-pressure regulator: K: Two-position effluent gas valve for flow to either vent or the on-ling GC. TC denotes a thermocouple and PI denotes a pressure indicator.

Downloaded by UNIV OF GUELPH LIBRARY on June 6, 2012 | http://pubs.acs.org
Publication Date (Web): November 29, 2011 | doi: 10.1021/bk-2011-1084.ch012

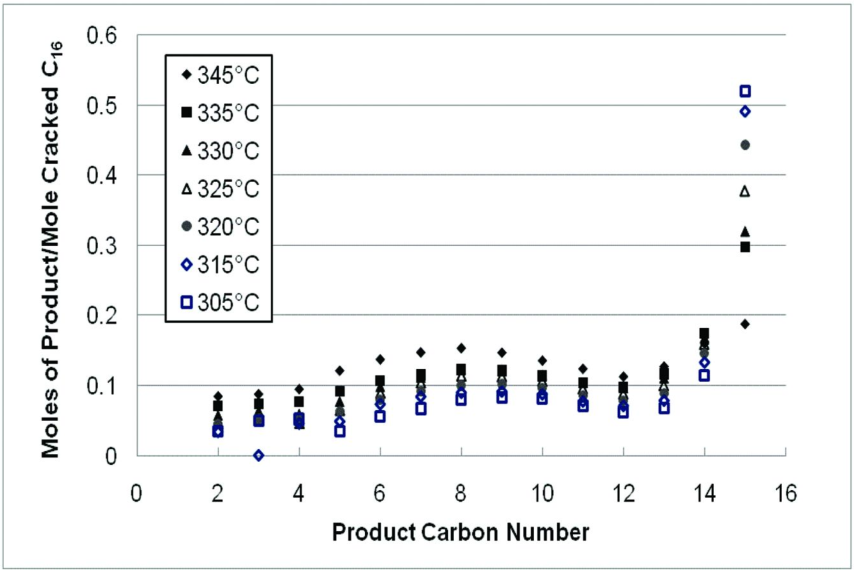

Figure 2. Molar distribution of cracked products with P=400 psig, LHSV=1/hr, H_2/feed=600vol/vol and different temperatures. Between 0.81 and 1.60 moles of methane per mole of cracked C_{16} were produced over this range of temperatures (see Table I).

Results and Discussion

Figure 2 depicts the molar selectivity of cracked products (moles of product ofa given carbon number/moles cracked C_{16}) with varying temperature. Details regarding conversion, isomerization, and methane selectivity are presented in Table I. Three features of the molar product distribution are immediately apparent. First, molar methane selectivity is extremely high. Second, the most abundant single component group after methane, C_{15}, as well as contributions by C_2, C_3, and C_{14} are unexpectedly high for bifunctional hydrocracking. Third, while the remainder of the product distribution appears typical of bifunctional cracking reactions, isomer content of the cracked product is extremely low. These findings are similar to those of Böhringer *et al.* who investigated the conversion of n-C_{14} over a similar unsulfided $Co/MoO_3/SiO_2$-Al_2O_3 catalyst (*3*).

If the temperature is held constant and conversion is varied by changing the feed rate at constant H_2/feed ratio, similar results are obtained, as seen in Figure 3. (Data at 345° C, LHSV=1/hr are from a return to this condition after collecting the temperature sequence data and differ slightly from those in Figure 2.) As when conversion was altered by varying temperature, at low cracking conversion, the single most abundant component group after methane is C_{15}, which diminishes in relative abundance as conversion increases.

Downloaded by UNIV OF GUELPH LIBRARY on June 6, 2012 | http://pubs.acs.org
Publication Date (Web): November 29, 2011 | doi: 10.1021/bk-2011-1084.ch012

Table I. Summary of operating conditions, conversions, methane selectivity, and extent of isomerization in the cracked product fraction (at constant H_2/feed ratio = 600vol/vol)

Temp.	*Pressure*	*LHSV*	*Total n-C_{16} Conversion*	*C_{16} Cracking Conversion*	*Moles of Methane/ Mole Cracked C_{16}*	*Isomerization in total C_4-C_{13} Fraction*
°C	psig	1/hr	Fractional	Fractional	Fractional	Fractional
345	400	1	0.99	0.89	1.53	0.29
335	400	1	0.88	0.69	1.60	0.15
330	400	1	0.74	0.56	1.32	0.15
325	400	1	0.55	0.38	1.06	0.11
320	400	1	0.38	0.23	1.00	0.10
315	400	1	0.24	0.12	0.81	0.07
305	400	1	0.11	0.05	0.81	0.08
345	800	1	0.90	0.78	0.86	0.16
345	400	1	0.98	0.89	1.52	0.29
345	400	2	0.89	0.74	1.21	0.16
345	400	3	0.79	0.62	1.53	0.12
345	400	5	0.60	0.46	1.41	0.08
345	400	10	0.34	0.24	1.23	0.06

A closer examination of the composition of the cracked products finds very low levels of isomerization. In bifunctional hydrocracking, a normal alkane first undergoes a sequence of isomerizations before the energetics of the transition state become sufficiently favorable to permit cracking at a rate comparable to further isomerization (*4*). Generally, two methyl rearrangements are required before the cracking rate of such a carbenium ion becomes competitive with the rate at which a third methyl rearrangement occurs. The low energy pathways to cracking such dimethyl carbenium ions always yield at least one isomerized product. For the fraction which undergoes a third methyl isomerization before cracking, the low energy pathway results in both fragments being isomerized. Therefore, finding cracked fractions with such low abundance of isomers is further indication that bifunctional hydrocracking is not responsible for the cracked products. This is in accordance with the conclusions of Böhringer *et al.* (*3*) regarding the degree of isomerization found in the cracked products from the conversion of n-C_{14} over a similar unsulfided $Co/MoO_3/SiO_2$-Al_2O_3 catalyst.

Downloaded by UNIV OF GUELPH LIBRARY on June 6, 2012 | http://pubs.acs.org
Publication Date (Web): November 29, 2011 | doi: 10.1021/bk-2011-1084.ch012

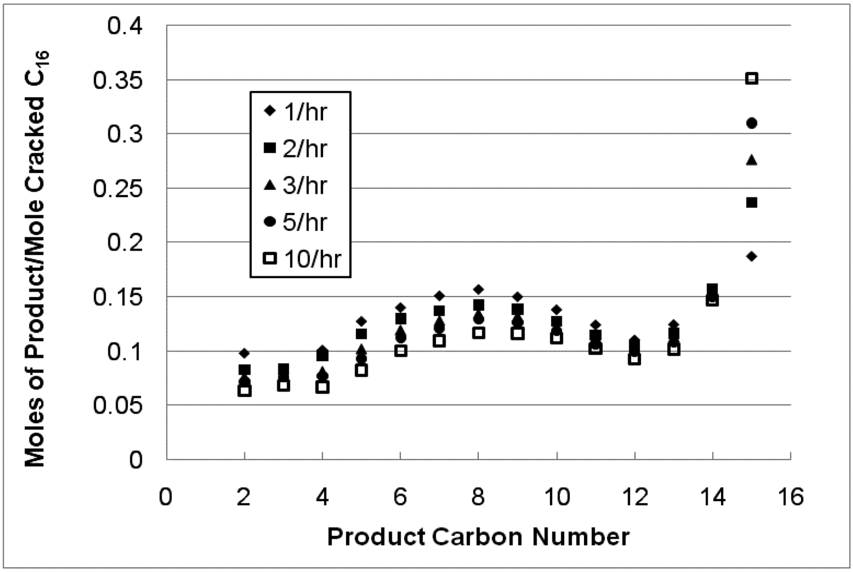

Figure 3. Molar distribution of cracked products with T=345° C, P=400 psig, H_2/feed=600 vol/vol, and different LHSV. Between 1.2 and 1.5 moles of methane per mole of cracked C_{16} were produced over this range of LHSV (see Table I).

A final way to clarify the relative contribution of bifunctional hydrocracking in the reactions of n-C_{16} over this catalyst is to examine the relative selectivities of the products as a function of total n-C_{16} conversion. Even in cases of imbalance between the hydrogenation/dehydrogenation and acid functions of bifunctional hydrocracking catalysts, considerable isomerization of the fed normal alkane preceeds the onset of cracking (*5*). Figure 4 shows the results under conditions applicable to Figure 3 in the form of a selectivity *versus* conversion plot. The selectivity trends with total conversion are not at all consistent with bifunctional hydrocracking (*4*, *5*). Rather than cracking being delayed until after higher isomers of the parent molecule appear in appreciable abundance, the cracked fraction dominates the distribution of products from even the lowest conversions. When the trends in selectivity are extrapolated back to zero conversion, only di-methylated feed isomers tends toward zero, indicating that all other products appear as apparently primary products.

Downloaded by UNIV OF GUELPH LIBRARY on June 6, 2012 | http://pubs.acs.org
Publication Date (Web): November 29, 2011 | doi: 10.1021/bk-2011-1084.ch012

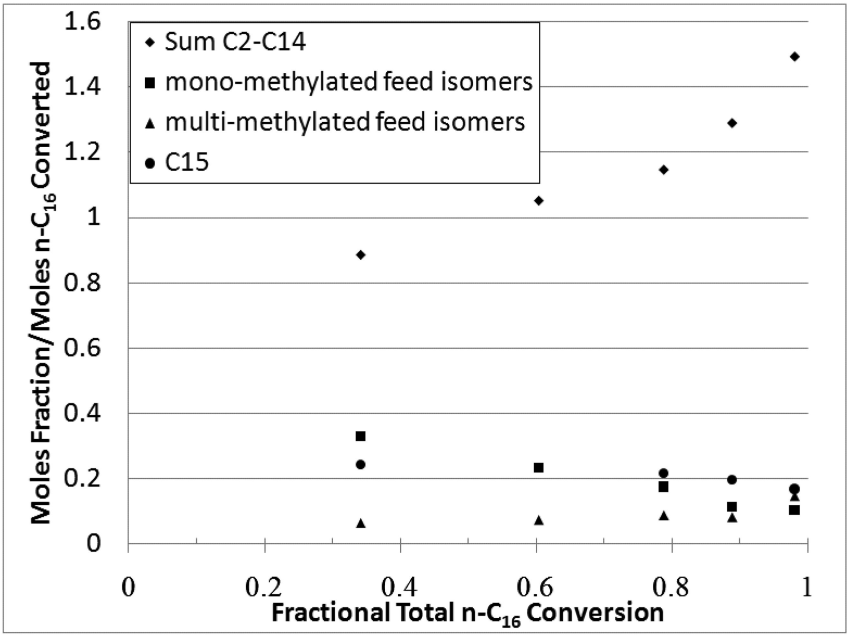

Figure 4. Selectivity to isomerized feed, C_{15}, and summed cracking product fractions with T=345° C, P=400 psig,H_2/feed=600vol/vol, and different LHSV.

When extrapolated to zero conversion, the selectivity for isomerization of the n-C_{16} feed molecules to produce a single methyl branch trends toward 0.5 In cases of bifunctional hydrocracking, this primary monomethyl isomerization selectivity is often well in excess of 0.8 (*4*, *5*) In bifunctional hydrocracking, the mono-methylated feed isomers next progress to di-methylated feed isomers, resulting in a growing selectivity of di-branched feed isomers at increasing conversions. At still higher conversions, further isomerization occurs, cracking increases and eventually becomes prevalent (*4*). However, over this catalyst, cracking dominates selectivity at all conversions. The selectivity to mono-methylated feed isomers decreases with increasing conversion, but without producing a substantial di-methylated C_{16} isomer fraction in the product stream. Rather than progressing to di-methylated and higher feed isomers prior to cracking at increasing conversion, both the n-C_{16} feed molecules and the monomethylated feed isomers formed undergo interior bond cleavage and contribute to the increasing selectivity of overall cracking, indicated by the sum of C_2-C_{14} products. The small isomer content in the cracked product fraction likely results from the cleavage of molecules in the monomethylated feed fraction. These observations are consistent with a catalyst exhibiting primarily hydrogenolysis which, through interior C-C bond cleavage, gives rise to the high abundance of cracked products from C_2 to C_{14}.

Downloaded by UNIV OF GUELPH LIBRARY on June 6, 2012 | http://pubs.acs.org
Publication Date (Web): November 29, 2011 | doi: 10.1021/bk-2011-1084.ch012

A second C-C bond cleavage reaction is the scission of methane from the terminus of an available alkane. The C_{15} fraction is uniquely produced by methane scission from either normal or isomerized feed C_{16}. The selectivity of the methyl scission reactions to produce C_{15} is nearly constant at about 0.25-0.20 until the total fractional conversion exceeds about 0.80, see Figure 4. At higher conversions, the C_{15} fraction declines while the remainder of the cracked product distribution increases more rapidly. This suggests that as the relative amount of C_{15} approaches the abundance of residual C_{16}, the C_{15} fraction undergoes secondary reaction through interior bond cleavage. Once a terminal alkyl group is formed on the catalyst's surface, the C_{n-1} fragment remaining after the first methyl scission has a significant likelihood to cleave yet another methane in progressive fashion. Similarly, the terminally bound alkyl fragments formed during general hydrogenolysis when an interior C-C bond is cleaved also must undergo secondary methane cleavage in order to account for the overall high abundance of methane at all conversions. Osterloh *et al.* observed both interior bond cleavage through general hydrogenolysis and progressive methyl scission on monometallic Co catalysts (*6*). The progressive methyl scission dominated the reactive behavior when feeding an α-alkene at low temperature while interior bond hydrogenolysis was observed when feeding an α-alkene or an alkane at high temperature. While the feed in our measurements was the n-C_{16} alkane, the isomerization of the hexadecane to methylpentadecanes suggests some bifunctional hydroisomerization through limited alkene formation. Thus, both alkenes and alkanes are available to undergo the different types of hydrogenolysis over Co observed by Osterloh. An attempt to account for all of the methane as the outcome of progressive methane scission of only C_{16} was made by comparing methane abundance with the sum: $C_{15} + 2(C_{14}-C_2) + 3(C_{13}-C_3)$. Since C_{14} and C_{13} can arise through either the direct cracking of C_{16} into two fragments (C_{14} plus C_2 and C_{13} plus C_3) or progressive methane cleavage from a longer chain to the next shorter chain, account must be taken of the interior bond cleavage fraction by the differences between the observed larger fragment abundance and its corresponding smaller fragment abundance. The remaining excess is then assigned to progressive methane cleavage of feed C_{16} and the residual is weighted by y, the number of methanes produced in creating the final chain of length $16-y$. At fractional cracking conversions less than 0.15, this approach accounts for the observed methane abundance within about 20%. However, at cracking conversions in excess of 0.25, the loss of C_{15} to secondary cracking reactions nullifies the applicability of this approach. Consequently, it is not possible to ascertain how much of the methane derives from progressive methane scission of C_{16} and how much might arise from methane scission from alkyl fragments produced by interior bond cleavage.

Since this catalyst was selected for the upgrading of the longer normal alkanes found in FT waxes to jet fuel, the absence of significant isomerization is grounds for concern. The JP-8 specification requires a fuel with a freezing point below -47° C (*7*). SPK is generally considered to be a mixture of alkanes distributed from C_8 to C_{16}. Within this range, only normal octane and nonane have freezing points below the specified value. Without significant isomerization, the $C_{10}+$ fraction will not meet this low temperature specification. Consequently, in agreement with the assessment of Böhringer *et al.*, the dominance of hydrogenolysis exhibited by this type of catalyst would suggest it to be a less than ideal choice for the production of jet fuel samples.

Conclusions

Under typical bifunctional hydrocracking conditions, the unsulfided $Co/MoO_3/SiO_2\text{-}Al_2O_3$ catalyst cracks n-hexadecane predominantly through Co-catalyzed hydrogenolysis. Two distinct types of hydrogenolysis can be discerened. In the first, interior C-C bonds are cleaved with near equal likelihood at all interior bonds. In the second, methane is sequentially cleaved from the end of an alkane precursor. The volume of methane produced and overall product distribution indicate that the original n-C_{16} undergoes multiple successive methane cleavages in addition to secondary methane cleavage from alkyl fragments formed during interior C-C bond cleavage. At low conversions, isomerization of n-C_{16} to the monomethylpentadecanes is also a significant reaction. However, as conversion increases, isomerization declines in importance relative to the C-C cleavage reactions. In the absence of bifunctional hydrocracking, the cracked products exhibit very low degrees of isomerization.

Downloaded by UNIV OF GUELPH LIBRARY on June 6, 2012 | http://pubs.acs.org
Publication Date (Web): November 29, 2011 | doi: 10.1021/bk-2011-1084.ch012

References

1. Dersch, D. M., Jr. *Meeting the Air Force's 2016 JP-8 Purchasing Goal*; Maxwell Air Force Base, Alabama, December 2009
2. Edwards, T.; Moses, C.; Dryer, F. Evaluation of Combustion Performance of Alternative; 46th AIAA/ASME/SAE/ASEE Joint Propulsion Conference & Exhibit, Nashville, TN, July 25–28, 2010, Paper AIAA 2010-7155.
3. Böhringer, W.; Kotsiopoulos, A.; de Boer, M.; Knottenbelt, C.; Fletcher, J. C. Q. In *Fischer-Tropsch Synthesis, Catalysts and Catalysis*; Davis, B. H., Occelli, M. L., , Eds.; Elsevier B.V.: Amsterdam, The Netherlands, 2007; pp 345−36.
4. Bouchy, C.; Hastoy, G.; Guillon, E.; Martens, J. A. *Oil Gas Sci. Technol. – Rev. IFP* **2009**, *64*, 91–112.
5. Girgis, M. J.; Tsao, P. Y. *Ind. Eng. Chem. Res.* **1996**, 386–396.
6. Osterloh, W. T.; Cornell, M. E.; Pettit, R. *J. Am. Chem. Soc.* **1982**, *104*, 3759–3761.
7. Detail Specification: Turbine Fuel, Aviation, Kerosene Type, JP-8 (NATO F-34), NATO F-35, and JP-8+100 (NATO F-37); MIL-DTL-83133G; U.S. Department of Defense, Washington, DC, 2010.

Downloaded by DUKE UNIV on June 6, 2012 | http://pubs.acs.org
Publication Date (Web): November 29, 2011 | doi: 10.1021/bk-2011-1084.ch013

Chapter 13

Experimental Investigation of the Oxidation of Methyl Oleate: One of the Major Biodiesel Fuel Components

Mingming Lu* **and Ming Chai**

Department of Civil and Environmental Engineering,
University of Cincinnati, P.O. Box 210071,
Cincinnati, Ohio 45221
***Tel.: +1 513 5560996. Fax: +1 513 5562599.**
E-mail: LUMG@ucmail.uc.edu.

As a new oxygenated fuel, the mechanistic connection between the emission of carbonyl compounds and biodiesel remains unknown, which warrants further study. Although currently unregulated, some of these carbonyl compounds are known to have adverse health and environmental impacts. This chapter provides an overview of the benefits of the biodiesel fuel, the air pollutants emitted from the use of various biodiesel blends, both regulated and unregulated. With increased biodiesel use, the evolvement of mechanistic studies from short chain and saturated to the long chain and unsaturated methyl esters also have been observed in recent years. This chapter summarized existing mechanistic studies, followed by a temperature series of the thermal decomposition of methyl oleate (C18:1), one of the major components in biodiesel. The temperature series range from 200 to 900 °C, and the main byproducts include carbon dioxide, light (C1-C4) hydrocarbons, carbonyl compounds, methyl esters, organic acids, and alcohols, etc.

In Synthetic Liquids Production and Refining; de Klerk, A., et al.;
ACS Symposium Series; American Chemical Society: Washington, DC, 2011.

Introduction

Biodiesel as an Alternative Fuel

It has been recognized that energy and environment are among the most challenging issues the society will be facing in the near future (*1*, *2*). Our dependence on fossil fuels has resulted in fuel shortage, global warming and environmental pollution (*3*, *4*). The imminent energy crisis has catalyzed the rapid development of renewable fuels, especially in the transportation sector, *i.e.* ethanol for gasoline engines and biodiesel for diesel engines.

Renewable and produced domestically, biodiesel is also claimed as a "drop in solution" as it can be mixed with petro-diesel at any percentage, and therefore requires almost no change to the diesel engines (*3*). Biodiesel is considered nearly carbon neutral (*5*): the CO_2 released in biodiesel combustion can be used again by the oil producing plants, and results in 78% less CO_2 emissions than fossil fuels. The commercially available biodiesel are usually methyl esters made from a variety of oils producing plants, animal fats and recycled oils (both yellow and brown grease) with the transesterification process using methanol and a alkali catalyst (*6*, *7*). The feedstock varies by region, such as soybean methyl ester (SME) produced in the U.S., rapeseed methyl ester (RME) used in Europe, and palm or coconut oil esters in tropical and subtropical regions, which results in variation of fuel composition (*8*).

Biodiesel production has significantly grown in the recent years and all over the world. European Union (EU) is still the leading biodiesel production region (*9*). Twenty-six European countries have reported biodiesel production in 2009 which totaled 9,046,000 tons (approximately 2.72 billion gallons). Germany and France are the largest producing countries, whose production account for 28% and 22% of the EU capacity respectively. In the U.S., biodiesel production reached 691 millions gallons in 2008, almost five times more than that of 2005 (*10*).

Though the production of biodiesel has increased, it is still a small portion compared to the petro-diesel consumption. For example, the U.S. has consumed approximately 43.4 billion gallons of diesel in 2009. The biodiesel production is only 1.6% to total diesel consumption, which is much less than the 20% market share predicted by many (*11*). Biodiesel production tends to be affected by government incentives, the cost of petroleum, and the economy. As an example, the production of biodiesel in the US decreased 315 million gallons in 2010 than that of 2008 due to tax incentive expiration and slow economy (*10*) .

Compositions of the Biodiesel Fuel

The first generation biodiesel fuel is a mixture of saturate and unsaturated alkyl esters, usually in the form of methyl esters. The compositions of some typical biodiesel fuels are listed in Table 1 (*12*, *13*). Methyl esters in natural products only have even numbers of carbons on the chain. The common esters include: methyl palmitate (C16:0), methyl palmitoleate (C16:1), methyl stearate

Downloaded by DUKE UNIV on June 6, 2012 | http://pubs.acs.org
Publication Date (Web): November 29, 2011 | doi: 10.1021/bk-2011-1084.ch013

Downloaded by DUKE UNIV on June 6, 2012 | http://pubs.acs.org
Publication Date (Web): November 29, 2011 | doi: 10.1021/bk-2011-1084.ch013

(C18:0), methyl oleate (C18:1), methyl linoleate (C18:2), and methyl linolenate (C18:3). Other possible minor constituents are methyl caprylate (C8:0), methyl caprate (C10:0), methyl laurate (C12:0), methyl myristate (C14:0), methyl arachidate (C20:0), methyl behenate (C22:0), methyl erucate (C22:1), and methyl lignocerate (C24:0). The compositions and their relative distribution depend on the feedstock of biodiesel fuels. They are typically in the C16-C18 range and are dominated by unsaturated fractions, such as C18:1 and C18:2.

The composition of algal biodiesel is more complex, due to the vast number of species and different strains within a species. C14-C22 methyl esters have been reported for algal biodiesel (*14*). However, the major fractions reported vary even for the different strains of the same species, e.g. for chlorella vulgaris, the major fractions reported include C18 (*15*, *16*), C22 (*17*), C20 (*18*), C16:0 (*19*) and C15:0 and C17:1 (*20*).

The blends of biodiesel and petro-diesel are usually referred to as Bxx, with xx being the percentage of biodiesel in the mixture. Various blends of biodiesel have been sold at the gas pumps throughout the US. Reports of biodiesel use have been numerous and all around the world, just to list a few examples local to the authors. In 2006, the Cincinnati Metro bus system has used approximately 1.8 million gallons of biodiesel and claimed to have saved $450,000 in doing so. B75 was used in summer and B20 in winter (*21*). Various blends of biodiesel are also been used by school buses in Kentucky (*22*). Minnesota has mandated the use of B5 diesel fuel in 2009 and will gradually increase to B20 by 2015 (*23*) . Under the Energy Policy Act, both neat biodiesel (B100) and B20 (20% biodiesel and 80% petro-diesel) are considered alternative fuels (*11*). B20 currently has the largest market potential and is the most often used percentage for blending.

Pollutant Emissions from Neat Biodiesel and Biodiesel Blends

As an oxygenated fuel, it is expected that biodiesel combustion can be more complete and result in less incomplete combustion byproducts, such as CO, particulate matter (PM) and hydrocarbons. Pure biodiesel does not contain sulfur and therefore SO_2 emission is almost negligible. Currently most of the biodiesel studies focus on emission measurements from the use of various biodiesel blends, from B5 to B100, especially the air pollutants regulated under the National Ambient Air Quality Standards, such as CO, PM and NO_x. Only a few of the Bxx emission measurements are listed here as examples (*24–32*). Varies feedstock types and blends of biodiesel have been studied, and most of the results have indicated that biodiesel usage can result in less CO, less hydrocarbons, less particulate matter (PM) but with a slight increase in NO_x (*33*) as illustrated in Figure 1. However, there are also studies that observed higher PM emissions from biodiesel blends (*34*), which may be related to the engine type, engine age, and the method of collection. A more acceptable notion with regard to the PM emissions is that using biodiesel blends tend to decrease the elemental carbon fraction with the increase of the soluble organic fractions of the PM.

Downloaded by DUKE UNIV on June 6, 2012 | http://pubs.acs.org
Publication Date (Web): November 29, 2011 | doi: 10.1021/bk-2011-1084.ch013

Table 1. Compositions of various types of biodiesel (relative %)

Methyl ester	*Soybean oil*	*Recycled cooking oil*	*Rapeseed oil*	*Palm oil*	*Animal fat*
C10:0	0.02	0	0	0	0
C12:0	0.03	0.02	0	0.3	0
C14:0	0.46	0.03	0	1.1	3-6
C15:0	0.03	0	0	0	0
C16:0	11.34	3.31	4.3	41.9	24-32
C16:1	1.41	0.13	0	0.2	0
C17:0	0.60	0.76	0	0	0
C17:1	0.16	0.04	0	0	0
C18:0	11.71	2.07	1.3	4.6	20-25
C18:1	46.26	79.10	59.9	41.2	37-43
C18:2	25.26	12.29	21.1	10.3	2-3
C18:3	2.46	2.02	13.2	0.1	0
C20:0	0.23	0.22	0	0	0
C22:0	0	0	0	0	0
Saturated	24.42	6.41	5.6	47.9	47-63

The rapid development of various NO_x control technologies specific for diesel engines has benefited from the fundamental studies on NO_x increase in biodiesel combustion. It is found that the increased NO_x formation in biodiesel combustion is caused by the advance timing of injection and also corresponds to the ignition delay, which can be intrinsic to the engine design (*35*, *36*). The higher temperature and highly fuel lean combustion conditions of diesel engines also have resulted in difficulties in directly using the control technologies for gasoline engines (such as the catalytic converter). However, the zero sulfur content of biodiesel makes it feasible to effectively reduce NO_x emissions by catalysts without the concern of catalyst poisoning by SO_2 (*37*). As a result, various NO_x control technologies have been suggested, such as delaying fuel injection, fuel reformulation, and the use of fuel additives to reduce NO_x, etc. (*38*) Another study indicated that the NO_x formed in biodiesel combustion is mainly thermal NO_x, which can be controlled by technologies that lower the combustion temperature (*39*).

In addition to the regulated air pollutants, currently unregulated carbonyl compounds have also been reported using various biodiesel blends. Compounds such as formaldehyde, acetylaldehyde and acrolein are labeled as motor vehicle air toxics (*40*) and are known human carcinogens or irritants. Some aldehydes, such as formaldehyde, acetylaldehyde, acrolein and some di-aldehydes, have high incremental reactivity for ozone formation (*41*), which may result in increased ground level ozone (a regulated air pollutant) and affect the attainment status of the areas. Many urban areas in the US are already facing ozone non-attainment when the ozone standard has been tightened from 120 ppb (1-hour average) to the current 75 ppb (8-hour average). More areas will fall to non-attainment if the ozone standard will be further reduced (*42*).

Out of the twenty-two studies the authors have found that reported carbonyl compounds emission from neat or biodiesel blends, fourteen reported higher carbonyl emissions than petro-diesel, five reported less carbonyl emissions and three from the same group reported different trends between different testing protocols and biodiesel fuels.

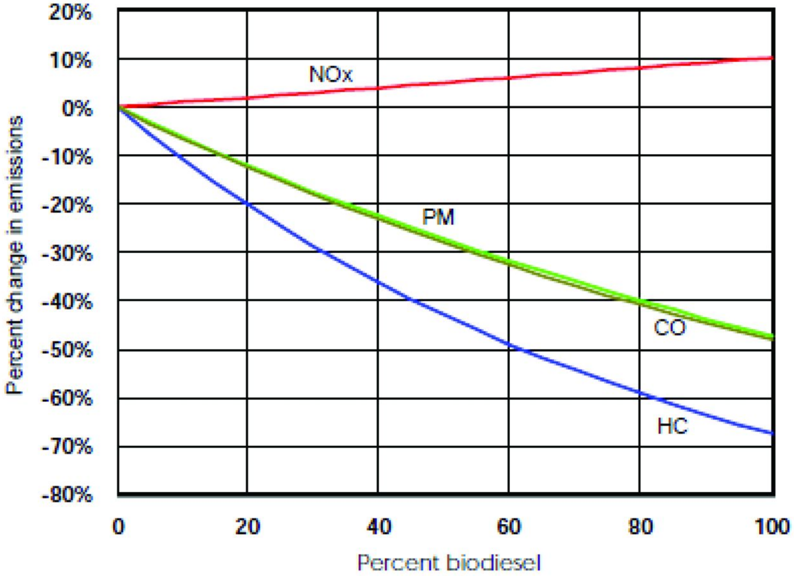

Figure 1. Pollutant emission of biodiesel for heavy-duty highway engines. (33)

The studies in Europe (*43–45*) were the first ones to report higher carbonyl emissions from biodiesel (rapeseed methyl ester) than petro-diesel, and now many other studies have been published on carbonyl emissions with SME and other types of biodiesel (*46–55*). He *et al.* have observed much higher (about three times more) carbonyl compounds concentrations in the exhaust gas from the pure biodiesel combustion. Lin *et al.* used palm biodiesel and found pure biodiesel has a 5.88% higher carbonyl emission only, and the B20 did not have an obvious difference from petroleum diesel. Liu *et al.* have found that B50 has the highest carbonyl emission comparing with other blends, B10, B30, B75, and B100. Di *et al.* have noticed that formaldehyde and acetaldehyde have different emission trends with increasing biodiesel percentages. Correa *et al.* have reported the carbonyl compounds emissions from biodiesel blend up to 20% are higher than those from diesel with the exception of benzaldehyde. The decrease of aromatic aldehydes has also been observed by several other researchers, and is due to the less aromatic presence in biodiesel fuel. Cardone *et al.* have found higher total carbonyl emission from pure biodiesel fuel over diesel fuel under all test conditions. Fontaras *et al.* have observed significant carbonyl emission increases

Downloaded by DUKE UNIV on June 6, 2012 | http://pubs.acs.org
Publication Date (Web): November 29, 2011 | doi: 10.1021/bk-2011-1084.ch013

Downloaded by DUKE UNIV on June 6, 2012 | http://pubs.acs.org
Publication Date (Web): November 29, 2011 | doi: 10.1021/bk-2011-1084.ch013

under all four testing protocols. Several other studies have reported the same trend: biodiesel or biodiesel blend have higher carbonyl emissions.

On the other hand, Guarieiro *et al.* have reported a lower carbonyl emission for test blends from B10 to B100, though slight increases were observed for B2 and B5. Peng *et al.* also observed that B20 emitted less carbonyl compounds compared to petroleum diesel. Karavalakis *et al.* have performed engine test by using palm biodiesel up to B40. They found the carbonyl compounds emissions from biodiesel blends are lower than those from diesel under all test conditions (*56*). In another study, Karavalakis *et al.* also reported lower carbonyl emissions from palm biodiesel and higher carbonyl from rapeseed biodiesel (*57*). The same group also found the different carbonyl compounds emission trends when using two different testing protocols, Athens Driving Cycle (ADC) and New European Driving Cycle (NEDC) (*58*). A 1998 Toyota Corolla 2.0 TD was used for two studies and the third one used a 2003 Toyota Hilux 2.5 TD. The inconclusiveness indicated that the carbonyl compounds emission from biodiesel blends can be a complex issue, which might not be adequately understood by engine measurements alone.

So far, more studies indicated higher carbonyl emissions from biodiesel blends. Earlier studies indicated that in cylinder formation is the major source of the carbonyl compounds as opposed to the exhaust pipe (*59*, *60*). The issue of carbonyl emissions from diesel engines is aggravated even more since the combustion condition is highly fuel lean (*61*) and most of the engines have no catalytic converters to reduce these compounds.

The studies on carbonyl compounds from biodiesel emissions are mainly from engine tests with biodiesel blends, with limited mechanistic studies on the formation of carbonyls, partially due to that lack of regulation on these compounds. While carbonyl emission from engines can be affected by many factors, such as composition of the biodiesel, impurities in biodiesel fuel, engine status (year, type, maintenance), and testing conditions (test protocols, engine load) etc., the correlation of carbonyl compounds with biodiesel fuel use warrants further mechanistic investigation.

Existing Mechanistic Studies on Methyl Esters

The commercially available biodiesel is a mixture of methyl esters with various carbon chains and different degrees of unsaturation like the hydrocarbons found in the fossil fuels. The combustion studies of fatty acid esters have evolved overtime, from short chain to long chain esters especially in recent years, largely due to the wide use of biodiesel.

The early studies were motivated to produce value added hydrocarbon fuels from vegetable and animal oils (*62–75*). Schwab *et al.* have measured the products of soybean oil thermal decomposition under both air and nitrogen. The products observed include alkanes, alkenes, aromatics and carboxylic acids in C4 to C20 range. They reported that the products under nitrogen or air are similar, which indicates that oxygen may not play an important roll in the thermal decomposition. Hurd *et al.* have found that in a moisture-free environment, the pyrolysis of triglycerides can produce acid and ethene via six-atom-ring-closure.

Downloaded by DUKE UNIV on June 6, 2012 | http://pubs.acs.org
Publication Date (Web): November 29, 2011 | doi: 10.1021/bk-2011-1084.ch013

Crossley *et al.* have found acrolein and di-n-nonyl ketone in products of tricaprin (C10:0 glycerides) pyrolysis. However, some of those proposed reactions can not occur in biodiesel-range methyl esters due to the structural differences between the oil and the esters.

Recently, the combustion kinetics of biodiesel have attracted more studies due to the more widely usage of biodiesel. Two approaches were found: one investigated a long carbon chain alkane, such as hexadecane (C16) (*76*) and the other used a methyl ester as biodiesel surrogate, such as methyl formate (C1:0), methyl acetate (C2:0), methyl butanoate (C4:0), methyl hexanoate (C6:0), methyl heptanoate (C7:0), methyl nonanoate (C9:0), methyl 3-nonenoate (3-C9:1), methyl 2-nonenoate (2-C9:1) and methyl decanoate (C10:0) (*77–87*).

Fisher *et al.* modeled the combustion of methyl butanoate (C4:0) and methyl formate (C1:0). The experimental data indicated a 10 to 50 times lower reactivities than the model. Osswald *et al.* have studied the combustion of two isomeric esters, methyl acetate (C2:0) and ethyl formate, in premixed flames. The methyl acetate led to the formation of formaldehyde, while the ethyl formate tended to form acetaldehyde, which indicates the different carbonyl formation mechanisms between methyl ester and ethyl esters. The authors also observed formation of hydrocarbons and aromatics during the combustion. Westbrook *et al.* have proposed detailed kinetics of four small esters based on the experiments in fuel-rich, low-pressure, premixed laminar flames. The four esters have been selected include methyl formate (C1:0), methyl acetate (C2:0), ethyl formate, and ethyl acetate. The proposed computed results have a good agreement with experimental results. Huynh *et al.* have modeled the detailed pyrolysis of methyl butanoate (C4:0) and concluded that the formation of methyl butanoate radical is through hydrogen abstraction reaction. The reaction forms small radicals and compounds, such as CH_3, C_2H_3, CO, CO_2, and formaldehyde. Gail *et al.* have studied methyl butanoate (C4:0) in both a jet stirred reactor and various pressure flow reactors. CO, CO_2, small hydrocarbons (up to C4), formaldehyde, acetaldehyde, acrolein, alcohols and small esters were identified, and the initial reaction suggested is hydrogen abstraction.

Some research, such as (*88*) has indicated that the small methyl esters may not be good surrogates to model biodiesel combustion because the negative temperature coefficient behavior were not observed in the combustion of small methyl esters. Dayma *et al.* (*84*, *85*) have conducted both experimental research and modeling on methyl hexanoate and methyl heptanoate (C6:0 and C7:0). Both experiments were performed in a jet-stirred reactor under 10 atm. Besides CO, CO_2, short chain hydrocarbons, and methyl esters, various carbonyls were detected, including formaldehyde, acetaldehyde, propanal, and propenal. Reasonable agreements have been reached between model predications and experimental observation, though some disagreements of certain combustion products were still existed. Zhang and Boehman have studied the low temperature heat release of methyl heptanoate (C7:0) and its isomer, ethyl hexanoate in a motored engine (*87*). Both esters showed typical paraffin-like oxidation reactions on their alkyl chain. However, ethyl hexanoate has a six-centered unimolecular elimination reaction on its ester side. Zhang *et al.* have investigated the ignition behaviors of four C9 esters (methyl nonanoate, C9:0; methyl 3-nonenoate,

Downloaded by DUKE UNIV on June 6, 2012 | http://pubs.acs.org
Publication Date (Web): November 29, 2011 | doi: 10.1021/bk-2011-1084.ch013

3-C9:1; methyl 2-nonenoate, 2-C9:1; and ethyl nonanoate) in a motored engine (*86*). Various carbonyl compounds have been detected, including acetaldehyde, butanal, pentanal, pentenal, hexanal, heptanal, butanone, and pentanone. Szybist *et al.* have compared the ignition behaviors of heptane and methyl decanoate in a motored engine (*89*). They have observed a series of acid products from methyl decanoate combustion. They have concluded that under low temperature heat release, the methyl ester acts very similar to n-paraffins. Herbinet *et al.* have modeled the oxidation of a longer methyl ester, methyl decanoate (C10:0). They concluded that the methyl decanoate is a better surrogate of biodiesel. Its reaction may be closer to the actual biodiesel fuel since it has both ester group and a relative long carbon chain. The small methyl esters cannot predict the early CO_2 formation and the reactivity.

Two researchers have studied the pyrolysis of biodiesel-range methyl esters. Billaud *et al.* have measured the products from the pyrolysis of a mixture of methyl esters from rapeseed oil in a tubular reactor. The operating conditions include residence time of 320 ms, dilution rate of 13:1 in moles of nitrogen to mole of feedstock, and the temperature range is between 550 and 850 ºC. The constituent of the mixture is similar to those of biodiesel, which is high in C18:1 and C18:2. They have observed 1-olefins, n-paraffins, esters, CO, CO_2, aromatics, and coke in products without acids and saturated methyl esters higher than C3:0. They have found linear 1-olefins (C10-C14 cut) and methyl esters (C6:1-C12:1), the high added value products, abundant at 700 ºC (*90*). Archambault *et al.* have conducted both experimental and modeling studies of methyl oleate pyrolysis between 500 and 650 ºC in a tubular flow reactor. The residence time was set between 230 and 600 ms and the purity of the reactant is 82%. The products observed in this study are similar to Billaud *et al* (*91*).

Dagaut *et al.* have conducted experiments on rapeseed methyl ester (RME) oxidation in a jet-stirred reactor (*92*). The reactant was a complex mixture, containing C14-C22 esters with different degrees of unsaturation. The products identification focused on hydrocarbons and the only carbonyl compound observed was formaldehyde. Hakka *et al.* have performed oxidation experiments of two surrogates for diesel and biodiesel fuels in a jet-stirred reactor (*93*). A blend of n-decane and n-hexadecane was used to simulate the diesel fuel and a blend of n-decane and methyl palmitate was chosen as the model biodiesel fuel. Thirteen C17 5-membered ring cyclic ethers were detected, while no other cyclic ethers, ketones, and aldehydes were observed. The authors concluded that the reason of low oxygenated species is low fraction of methyl palmitate in the blend fuel (26% methyl palmitate vs. 74% n-decane in mole). Bax *et al.* have investigated the oxidation of a blend of n-decane and methyl oleate in a jet-stirred reactor (*94*). Various hydrocarbons and shorter unsaturated methyl esters were observed as the products of carbon bond cleavage of methyl oleate and oxidized methyl ester were detected, which are intermediate products of methyl oleate oxidation. The authors proposed the initial reaction of methyl oleate oxidation is hydrogen abstraction at the 9- or 10- carbon (the double bond) position. However, none of the three researchers used a pure biodiesel-range methyl ester; as a result, the contribution to products formation of the individual reactant is unclear.

In Synthetic Liquids Production and Refining; de Klerk, A., et al.;
ACS Symposium Series; American Chemical Society: Washington, DC, 2011.

Downloaded by DUKE UNIV on June 6, 2012 | http://pubs.acs.org
Publication Date (Web): November 29, 2011 | doi: 10.1021/bk-2011-1084.ch013

The common reactor to investigate fuel combustion includes the shock tube, jet-stirred reactor (JSR) and tubular flow reactor. Numerous studies have been conducted to achieve the combustion data in those reactors. Shock tube is advantageous in simulating the combustion under high temperature and high pressure. While the disadvantage of the shock tube is the reaction could be too complete to lose information on early stage products. Jet-stirred reactor can also simulate combustion at a high pressure. Tubular flow reactor, which was utilized in this research, has been extensively used in studying combustion chemistry. And the most common tubular flow reactors are operated in the laminar flow regime. Plug flow reactor (PFR) is the simplest mathematic model for tabular flow reactors. The PFR model assumes the flow of reactants is one-dimensional with no radial variations in concentration and velocity.

Ranzi *et al.* has built a model to descript the thermal decomposition of heavy n-alkanes. He has validated the model with experimental data of various compounds under various reaction conditions. The pressures ranges from 0.08 atm to 50 atm, the temperature ranges are from 550 to 2000 K and all common reactors, shock tube, jet-stirred reactor and tubular reactor are included. This indicates that the reaction pathways obtained can be used for different types of reactors (*95*).

Experimental Setup

In terms of determining carbonyl formation, olefins are more important than paraffins, or aromatics. Studies indicated that aldehyde formation is in increasing order as follows: aromatics < naphthene < paraffins < olefins (*96*, *97*). The RO_2 (alkyl-peroxide) radical plays a significant role in the partial oxidation of fuels and subsequent product formation pathways including the carbonyls. Both the chemical reactivity and the abundance in biodiesel warrant the selection of methyl oleate (C18:1) as a model compound. It is a liquid under room temperature, has a molecular weight of 296 grams per mole, and the double bond is at the 9th position from the methyl ester end ($CH_3(CH_2)_7CH{=}CH(CH_2)_7COOCH_3$).

The experimental setup for mechanistic studies of methyl esters' thermal decomposition is shown in Figure 2. The experimental system includes a semi-isothermal tubular reactor at atmospheric pressure in a tube furnace (Thermolyne, model 79400), a reactant input system and a product collection system. The quartz tube has an inner diameter of 1.7 centimeters and is 0.965 meters long. The middle part of the quartz tube, approximate 0.61 m long was heated in the furnace. The temperature profile along the tube under each reaction temperature was measured by a thermo couple (Omega molded quick-connect probe KQSUP-14G-12). The temperature distribution is even in the middle part, approximately 0.58 m long, and is within ±5 ºC of the setting value. The reaction temperatures used in the mechanism studies range from 200 to 900 ºC.

The quartz tube flow reactor system has been used to investigate pollutant formation mechanisms by various researchers including the authors (*98–100*). The gas flow rate was adjusted by the flow meter to set the residence time at two seconds for each reaction temperature. The reactant, methyl oleate, liquid under room temperature, was continuously injected into the preheated glass vaporizer by a syringe injection pump (Sage Instruments, model 355). The vaporizer was heated by heating tape and maintained at approximate 200 ºC to ensure methyl ester vaporization without decomposition. The experiment was conducted under oxidative conditions with equivalence ratios between 8 and 20. The residence time was set at 2 seconds, which is comparable to other researchers (*93*, *94*).

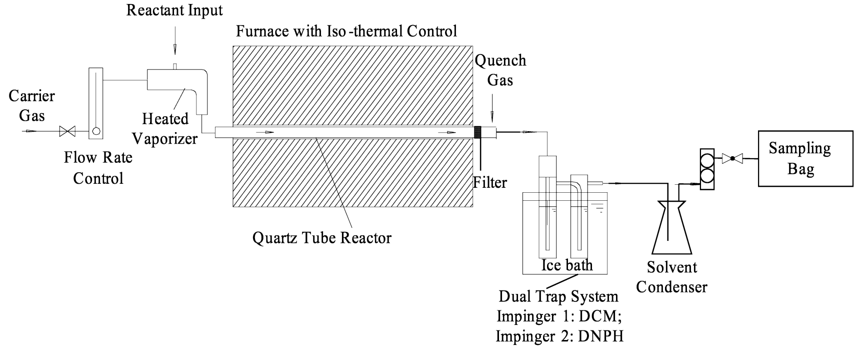

Figure 2. Experimental set-up for methyl oleate oxidation.

A quartz filter (SKC Inc., 225-1826) was placed at the end of the tube to collect soot particles. The dual trap system was placed in the ice bath to minimize solvent evaporation. The first impinger was filled with dichloromethane (DCM, Fisher Scientific, HPLC grade) to collect liquid products and residual reactants. The second impinger contained acidified 2,4-dinitrophenylhydrazine (DNPH, Alfa Aeser, 97%) to collect carbonyl compounds. Particles collected by the quartz filter and deposited on the inside walls of tube are added together as soot. The weight differences before and after experiment were considered as soot produced during reaction, though the experimental results showed the soot formation under the test conditions were insignificant. At the end of the dual trap system, a solvent condenser was used to remove DCM and/or DNPH solutions, so that the light hydrocarbons collected in Teflon bags can be less subjected to solvent interference in the subsequent analysis.

Different types of byproducts were analyzed with different instruments. The carbonyl compounds collected on the DNPH cartridge was extracted with acetone, and analyzed with the HPLC UV-vis system equipped with a C18 reverse phase column as described in EPA method TO-11A (*101*). After each experiment, the inlet, the quartz tube and sample collection system downstream was solvent rinsed with DCM and combined with the liquid in impinger 1. Products collected on the filter was also extracted and analyzed. The byproducts were analyzed by a Gas Chromatography – Mass Spectrometry system (GC/MS, Varian Inc., CP-3800 GC, Saturn 2200 MS) equipped with an autosampler (Varian Inc., model CP-8400). A series of alkanes, alkenes, alcohols, acids, methyl esters and other organics were detected by a DB5-ms nonpolar capillary column (30m × 0.25mm × 0.2μm). The gas collected in a sampling bag was injected into a GC-FID system to analyze light alkanes, alkenes, and aromatics. A MultiGas 2030 Analyzer FTIR

Downloaded by DUKE UNIV on June 6, 2012 | http://pubs.acs.org
Publication Date (Web): November 29, 2011 | doi: 10.1021/bk-2011-1084.ch013

(MKS Instrument 2000) was used to quantify the inorganic gases, including CO and CO_2.Commercial standards of alkanes, alkenes, DNPH-carbonyls and methyl esters were used to identify unknown or unsure peaks in spectra. The NIST MS-Spectra library and other references, such as the 8-peak index, were used when the chemical standard is not available.

Results and Discussion

The temperature series of reactant conversion and product recovery (on carbon basis) of methyl oleate oxidation are shown in Figure 3. Each experimental point is an average of two to five runs. Fifty microliters of the reactant (C18:1) has been used for each run. The error bar represents the actual min/max value. In the presence of oxygen, the methyl oleate has a much higher conversion compared to pyrolysis. The conversion rate is 58% at 200 ºC and reaches 98% at 700 ºC, an indication that the selected temperature range captured most of the C18:1 reactivity. The carbon recovery of methyl oleate oxidation is between 70% and 99%, an indication that the sample collection-detection system is capable of resolving most of the products. The major oxidation products include inorganic gases, alkanes, alkenes, methyl esters, alcohols, aldehydes, and acids. Soot (insoluble fraction) is negligible over the temperature range studied. Details of product analysis are presented in subsequent Figures 4-8. Error bars are not shown as they are consistent with those in Figure 3 and also for clarity reasons.

The yields of inorganic gases from methyl oleate oxidation are shown in Figure 4. The yields of CO_2 increased with temperature, while on the other hand, the yields of CO increase until up to 500 ºC, and then decrease with temperature increase. The different trends of these two gases suggest that they are likely formed from different pathways. The CO_2 (6-18%) observed is higher than that of C18:1 pyrolysis (3-6%), an indication that it is from both decarboxylation from the ester as reported by other ester studies, and the oxidation of other carbon components.

The light hydrocarbons (C1-C4) are the main products in methyl oleate oxidation (Figure 5), the top three most abundant compounds are methane, ethane and propane. The yield increased with temperature up to 600 ºC and then decreased. The yields of C9-C17 hydrocarbons and >C18 hydrocarbons have the similar trends with temperature change, though the highest yields were reached at 500 ºC and 700 ºC respectively, and their yields are much lower than those of light hydrocarbons. The formation of shorter HCs is likely due to the oxidation of the alkyl chain of C18:1, which is analogous to those of hydrocarbon oxidation.

Numerous oxygenated products were detected in the liquid portion of the methyl oleate oxidation. The yields of carbonyls, alcohols, and acids are grouped and shown in Figure 6. The yields of carbonyls increase with temperature, while the yields of alcohols and acids first increased and then decreased with temperatures. The alcohols reached the highest yield at 700 ºC and the acids at 600 ºC.

Downloaded by DUKE UNIV on June 6, 2012 | http://pubs.acs.org
Publication Date (Web): November 29, 2011 | doi: 10.1021/bk-2011-1084.ch013

Downloaded by DUKE UNIV on June 6, 2012 | http://pubs.acs.org
Publication Date (Web): November 29, 2011 | doi: 10.1021/bk-2011-1084.ch013

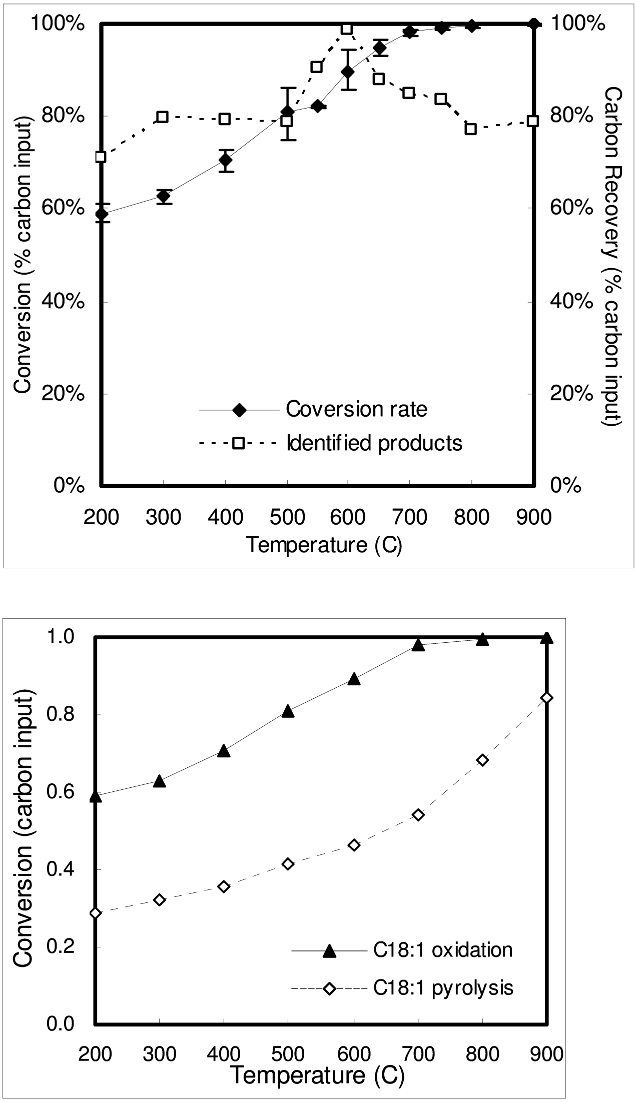

Figure 3. Upper: reactant conversion and carbon recovery of methyl oleate oxidation; lower: reactant conversion of methyl oleate pyrolysis and oxidation.

Up to twenty-eight types of carbonyls were detected by either HPLC or GC-MS, including formaldehyde (C1 aldehyde), acetaldehyde (C2 aldehyde), propaldehyde (C3 aldehyde), hexanal (C6 aldehyde), 2-heptanone (C7 ketone), 2-heptenal (C7 unsaturated aldehyde), octanal (C8 aldehyde), 5-ethylcyclopent-1-enecarboxaldehyde (C8 unsaturated aldehyde), 2-octenal and its isomer (C8 unsaturated aldehyde), nonanal (C9 aldehyde), 2-isononenal (C9 unsaturated aldehyde), 3-nonen-2-one (C9 unsaturated ketone), 2-nonenal (C9 unsaturated aldehyde), 2,4-nonadienal (C9 double unsaturated aldehyde), 2-(1-methyl)ethyl cyclohexanone (C9 ketone), 4-dodecanone (C10 ketone), cyclodecanone (C10 ketone), decanal (C10 aldehyde), 2-decenal (C10 unsaturated aldehyde), 2,4-decadienal (C10 double unsaturated aldehyde), undecanal (C11 aldehyde), 3,7-dimethyl-6-nonenal (C11 unsaturated aldehyde), 2-undecenal (C11 unsaturated aldehyde), 2,4-undecadienal (C11 double unsaturated aldehyde), 2-dodecenal (C12 unsaturated aldehyde), 6,8,10-trimethyl-3,7-undecanedione (C14 di-ketone), and 11-pentadecenal (C15 aldehyde). Among the carbonyls detected, the C1, C2 and C3 aldehydes have the highest yield and followed by nonanal. Nonanal might be formed by the oxidation at the double bond side (C-9), and the yield of nonanal increased with temperature. Nonanal was also found by Bax *et al.*

The alcohols detected include cyclohexanol (C6 alcohol), 3,5-dimethyl cyclohexanol (C8 alcohol), 1-octanol (C8 alcohol), 2-methyl-oct-2-enedial (C8 di-alcohol), 1,3-nonadien-3-ol (C9 unsaturated alcohol), 1-nonen-4-ol (C9 unsaturated alcohol), 3-decen-1-ol (C10 alcohol), 1-vinyl-1-cyclohexanol (C11 alcohol), C12 alcohol, C14 alcohol, C16 alcohol, 3,13-octadecadienol (C18 alcohol). Acids found in the products include hexanoic acid (C6 acid), octanoic acid (C8 acid), undecenoic acid (C11 unsaturated acid), 2-dodecenoic acid (C12 unsaturated acid), and 9-hexadecenoic acid (C16 unsaturated acid). Other two acid derivates were detected and plotted as total acids: 2-oxo-cyclooctaneacetic acid, and hexanoic acid, anhydride. The identification of organic acids has also been reported by Szybist *et al.*, which has not been reported in the combustion of hydrocarbon fuels. The major alcohols and acids products are with C6, C8, and C9 in chain length. The presence of C9 carbonyls and alcohols (C8 and C9) are indications of reactivity at the double bond side (C9 position).

The major shorter (than C18) methyl esters detected in methyl oleate oxidation include C6:0 to C16:0 and C7:1 to C16:1 methyl esters (Figure 7). Those shorter chain methyl esters are mainly from carbon-carbon bond cleavage. C18:0 and C18:2 methyl esters were observed, especially at low temperatures. Under some certain reaction temperatures, longer methyl esters (C20:1 and C22:1) were detected, which are products of radical addition reactions. The methyl esters with chain length of 18 or higher carbon atoms are low in quantities.

Other types of esters were identified in the products are shown in Figure 8. Oxidized methyl esters are the oxidation products of short methyl esters: oxo-C8:0, 4-oxo-C9:0, 9-oxo-C9:0, 9-oxo-C10:0, 10-oxo-C10:0, methyl 6, 8-dioxononanoate, 8-hydroxy-octanoic acid methyl ester, 8-hydroxy-decenoic acid methyl ester, and nonanedioic acid monomethyl ester. The highest yield of oxidized methyl esters occur at 600 °C. Cyclopropyl methyl esters are likely formed from carbon radial addition to carbon-carbon double bond.

Downloaded by DUKE UNIV on June 6, 2012 | http://pubs.acs.org
Publication Date (Web): November 29, 2011 | doi: 10.1021/bk-2011-1084.ch013

The detected cyclopropyl methyl esters are undecanoic acid, 10,11 -epoxy-, methyl ester, 4-(4-methoxycarbonylbutyl)-4-butanolide, dodecanoic acid, 10,11-epoxy-, methyl ester, cyclopropaneoctanoic acid, 2-hexyl-, methyl ester, and cyclopropaneoctanoic acid, 2-octyl-, methyl ester. The other esters are mainly long chain ethyl esters. Oxiraneoctanoic acid, 3-octyl-, methyl ester, cis-, oxiraneoctanoic acid, 4-octyl-, methyl ester, cis-, are formed from oxygen atom addition to carbon-carbon double bond. These compounds can be the unique intermediates of methyl ester oxidation. Similar types of compounds have been reported by Hakka *et al* and Bax *et al* (*93*, *94*).

The product formation mechanisms in the oxidation of methyl oleate included decarboxylation and the reactivity at the double bond side, in addition to those known to hydrocarbons. This suggests that the biodiesel surrogate should include the representative functional groups, such as the double bond, and C18:1 might be more suitable than other methyl esters. No PAH compounds have been identified. Organic acids of lower molecular weight have been identified, which has not been much reported. Combustion studies of C18:0 and C18:2 are proposed to further understand the combustion characteristics of biodiesel fuel.

Downloaded by DUKE UNIV on June 6, 2012 | http://pubs.acs.org
Publication Date (Web): November 29, 2011 | doi: 10.1021/bk-2011-1084.ch013

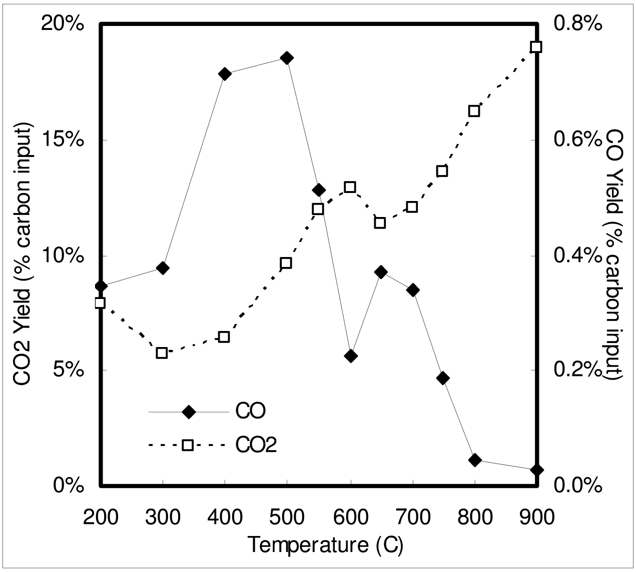

Figure 4. Yields of CO and CO_2 of methyl oleate oxidation.

Downloaded by DUKE UNIV on June 6, 2012 | http://pubs.acs.org
Publication Date (Web): November 29, 2011 | doi: 10.1021/bk-2011-1084.ch013

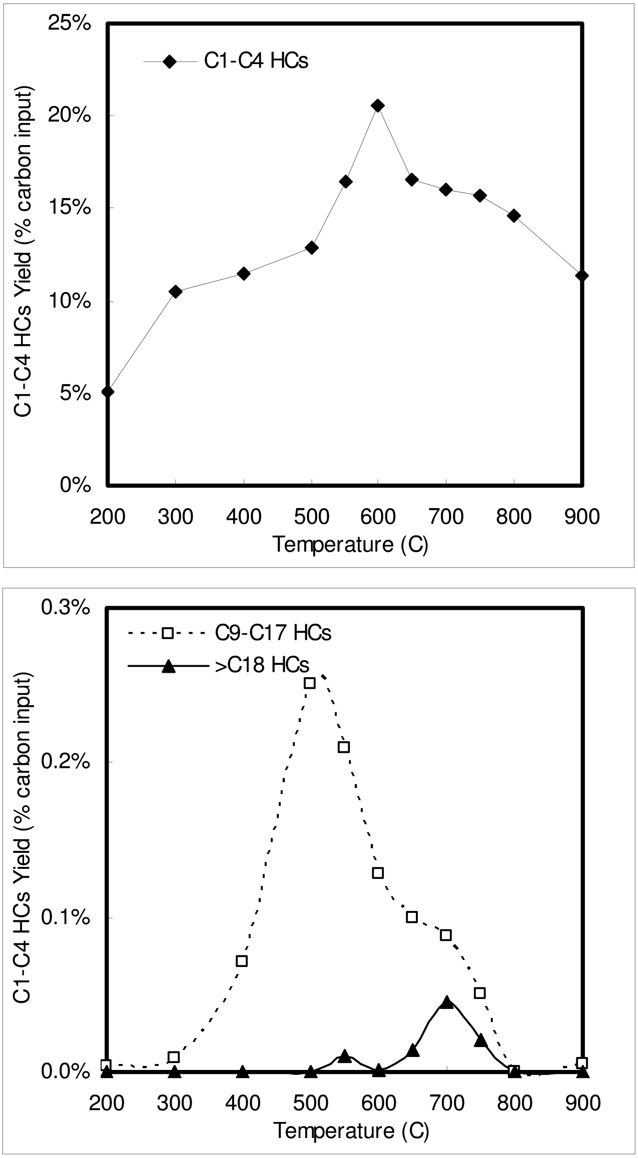

Figure 5. Yields of hydrocarbons of methyl oleate oxidation.

Downloaded by DUKE UNIV on June 6, 2012 | http://pubs.acs.org
Publication Date (Web): November 29, 2011 | doi: 10.1021/bk-2011-1084.ch013

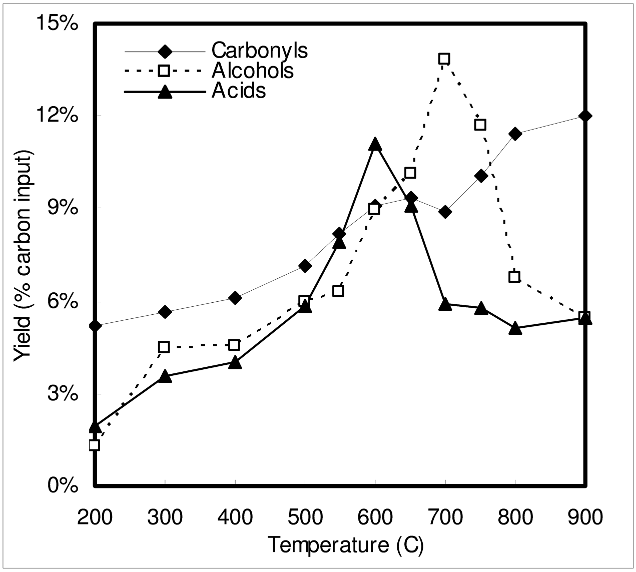

Figure 6. Yields of oxygenated products of methyl oleate oxidation.

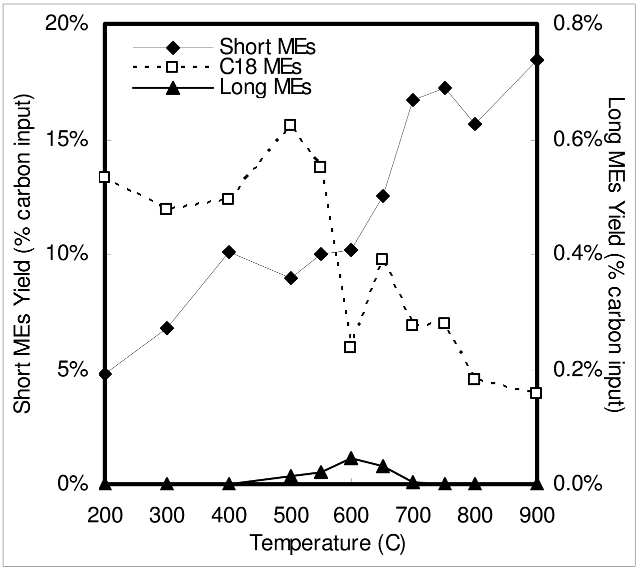

Figure 7. Yields of methyl esters in methyl oleate oxidation.

Downloaded by DUKE UNIV on June 6, 2012 | http://pubs.acs.org
Publication Date (Web): November 29, 2011 | doi: 10.1021/bk-2011-1084.ch013

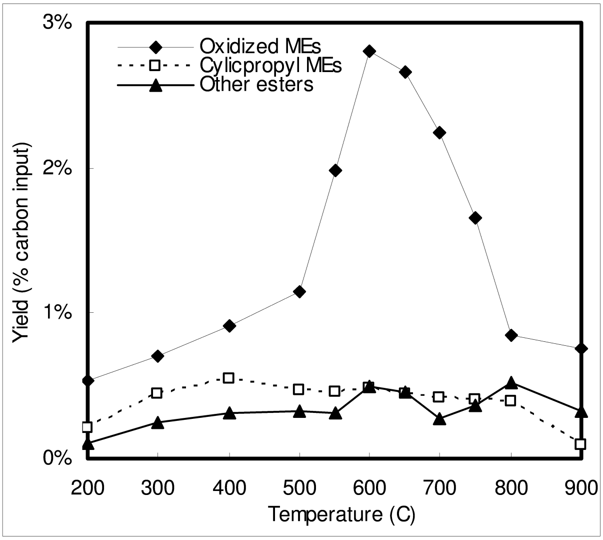

Figure 8. Yields of other esters in methyl oleate oxidation.

Acknowledgments

The authors wish to thank Dr. M. Eileen Birch at the National Institute of Occupational Safety and Health for the access of GC-FID, and Dr. San-Mou Jeng for the use of FTIR in this work. Partial support from the NSF RET (research experience for teachers) project is gratefully acknowledged. The authors thank Mr. Qingshi Tu and Ms. Qi Zhao for their help in this work.

References

1. Smalley, R. Richard Smalley on Energy, University lecture, 2003. http://cnst.rice.edu/content.aspx?id=246(accessed February 2011).
2. Szuromi, P.; Jasny, B.; Clery, D.; Austin, J.; Hanson, B. Energy for the long haul. *Science* **2007**, *315* (5813), 781.
3. Tickell, J. *From the Fryer to the Fuel Tank: The Complete Guide to Using Vegetable Oil as an Alternative Fuel* , 3rd ed.; Joshua Tickell Media Productions: New Orleans, LA, 2003; pp 12, 29−45.
4. Campbell, C. J.; Laherrère, J. H. The end of cheap oil: Global production of conventional oil will begin to decline sooner than most people think, probably within 10 years. *Sci. Am.* **1998**March, 78–83.
5. Sheehan, J.; Camobreco, V.; Duffield, J.; Graboski, M.; Shapouri, H. An Overview of Biodiesel and Petroleum Diesel Life Cycles; NREL/TP-580-24772; U.S. Department of Agriculture and U.S. Department of Energy, 1998.

6. Agnew, R.; Chai, M.; Lu, M.; Dendramis, N. Research and solutions: Making biodiesel from recycled cooking oil generated in campus dining facilities. *Sustainability: J. Record* **2009**, *2* (5), 303–307.
7. Srivastave, A.; Prasad, R. Triglycerides-based diesel fuels. *Renewable Sustainable Energy Rev.* **2000**, *4*, 111–133.
8. Worldwide Review on Biodiesel Production. National Renewable Energy Laboratory (NREL), U.S. Department of Energy. http://www.senternovem.nl/mmfiles/135528_tcm24-124334.pdf (accessed February 2010), pp 7−14.
9. Statistics, The EU Biodiesel Industry. European Biodiesel Board. http://www.ebb-eu.org/stats.php (accessed March 2011).
10. National Biodiesel Board. http://ww.biodiesel.org/resources/faqs/ (accessed March 2011.
11. Pahl, G. Biodiesel: Growing a New Energy Economy; Chelsea Green Publishing Company: White River Junction, VT, pp 237−238, 2005.
12. Moser, B. R. Influence of blending canola, palm, soybean, and sunflower oil methyl esters on fuel properties of biodiesel. *Energy Fuel* **2008**, *22* (6), 4301–4306.
13. Klouda, G. A.; Filliben, J. J.; Parish, H. J.; Chow, J. C.; Watson, J. G.; Cary, R. A. Reference material 8785: Air particulate matter on filter media. *Aerosol Sci. Technol.* **2005**, *39*, 173–183.
14. Rezanka, T.; Podojil, M. The very long chain fatty acids of the green alga, *Chlorella kessleri*. *Lipids* **1984**, *19* (6), 472–473.
15. Otles, S.; Pire, R. Fatty acid composition of Chlorella and Spirulina microalgae species. *J. AOAC Int.* **2001**, *84* (6), 1708–1714.
16. Lee, J.-Y.; Yoo, C.; Jun, S.-Y.; Ahn, C.-Y.; Oh, H.-M. Comparison of several methods for effective lipid extraction from microalgae. *Bioresour. Technol.* **2010**, *101*, 575–577.
17. Marchese, A. J. Algae Derived Biofuels for the Transportation Sector. Greenhouse Gas Emissions from Advanced Diesel Technologies: What To Expect Now and in the Future. 2009 Transportation Planning, Land Use and Air Quality Conference, Denver, CO, July 28−29, 2009.
18. Podojil, M.; Livansky, K.; Prokes, B.; Wurst, M. Fatty acids in green algae cultivated on a pilot-plant scale. *Folia Microbiol.* **1978**, *23*, 444–447.
19. Cojocarut, M.; Shlosberg, M.; Dubinsky, Z.; Finkel, A. Gas chromatographic/mass spectrometric analysis of fatty acids found in aquatic algae. *Biomed. Environ. Mass Spectrom.* **1988**, *16*, 477–480.
20. Francisco, E. C.; Neves, D. B.; Lopes, E. J.; Francoa, T. T. Microalgae as feedstock for biodiesel production: Carbon dioxide sequestration, lipid production and biofuel quality. *J. Chem. Technol. Biotechnol.* **2010**, *85*, 395–403.
21. Biodiesel Saved Metro $450,000. *The Enquirer*, January 9, 2007.
22. Kenning, C. Schools Drive Home Lesson of Biodiesel. *Courier-Journal*, January 22, 2007.
23. Minnesota Passes B20 Mandate!, 2008. General Biodiesel. http://www.biodieselnow.com/general_biodiesel_21/f/5/p/21204/149024.aspx (accessed February 2011).

Downloaded by DUKE UNIV on June 6, 2012 | http://pubs.acs.org
Publication Date (Web): November 29, 2011 | doi: 10.1021/bk-2011-1084.ch013

Downloaded by DUKE UNIV on June 6, 2012 | http://pubs.acs.org
Publication Date (Web): November 29, 2011 | doi: 10.1021/bk-2011-1084.ch013

24. Graboski, M.; McCormick, R. L. Combustion of fat and vegetable oil derived fuels in diesel engines. *Prog. Energy Combust. Sci.* **1998**, *24*, 125–164.
25. Choi, C.; Bower, G.; Retiz, R. *Mechanisms of Emissions Reduction Using Biodiesel Fuels*; Final Report for the National Biodiesel Board; Engine Research Center, University of Wisconsin: Madison, WI, 1997.
26. Dorado, M.; Ballesteros, E.; Arnal, J.; Gómez, J.; López, F. Exhaust emissions from a diesel engine fueled with transesterified waste olive oil. *Fuel* **2003**, *82*, 1311–1315.
27. Durbin, T.; Collins, J.; Norbeck, J.; Smith, M. Effects of biodiesel, biodiesel blends, and a synthetic diesel on emissions from light heavy-duty diesel vehicles. *Environ. Sci. Technol.* **2000**, *34* (3), 349–355.
28. Gomez, M.; Howard-Hildige, R.; Leahy, J.; O'Reilly, T.; Supple, B.; Malone, M. Emission and performance characteristics of a 2-litre Toyota diesel van operating on esterified waste cooking oil and mineral diesel fuel. *Environ. Monit. Assess.* **2000**, *65*, 13–20.
29. Ramadhas, A.; Muraleedharan, C.; Jayaraj, S. Performance and emission evaluation of a diesel engine fueled with methyl esters of rubber seed oil. *Renewable Energy* **2005**, *30*, 1789–1800.
30. Serdari, A.; Fragioudakis, K.; Teas, C.; Zannikos, F.; Stournas, S.; Lois, E. Effect of biodiesel addition to diesel fuel on engine performance and emissions. *J. Propul. Power* **1999**, *15* (2), 224–231.
31. Turrio-Baldassarri, L.; Battistelli, C.; Conti, L.; Crebelli, R.; De Berardis, B.; Iamiceli, A.; Gambino, M.; Iannaccone, S. Emission comparison of urban bus engine fueled with diesel oil and 'biodiesel' blend. *Sci. Total Environ.* **2003**, *327*, 147–162.
32. Wang, W.; Lyons, D.; Clark, N.; Gautam, M. Emissions from nine heavy trucks fueled by diesel and biodiesel blends without engine modification. *Environ. Sci. Technol.* **2000**, *34* (6), 933–939.
33. A Comprehensive Analysis of Biodiesel Impacts on Exhaust Emissions; EPA420-P-02-001; U.S. Environmental Protection Agency (USEPA), 2002. http://www.epa.gov/OMS/models/analysis/biodsl/p02001.pdf (accessed February 2011).
34. Tzillah, A. The Emissions of Criteria Air Pollutants from Biodiesel Fuel Usage. MS Thesis, University of Cincinnati, 2009.
35. Szybist, J. P.; Boehman, A. L.; Taylor, J. D.; McCormick, R. L. Evaluation of formulation strategies to eliminate the biodiesel NOx effect. *Fuel Process. Technol.* **2005**, *86*, 1109–1126.
36. Glassman, I. *Combustion*; Academic Press: San Diego, CA, 1996; pp 359−385.
37. Corro, G. Sulfur impact on diesel emission control: A review. *React. Kinet. Catal. Lett.* **2002**, *75* (1), 89–106.
38. McCormick, R. L.; Graboski, M. S.; Alleman, T. L.; Herring, A. M.; Tyson, K. S. Impact of biodiesel source material and chemical structure on emissions of criteria pollutants from a heavy-duty engine. *Environ. Sci. Technol.* **2001**, *35* (9), 1742–1747.
39. Fernando, S.; Hall, C.; Jha, S. NOx reduction from biodiesel fuels. *Energy Fuels* **2006**, *20*, 376–382.

40. Tang, T.; Claggett, M.; Byun, J.; Roberts, M.; Granell, J.; Aspy, D. Mobile6.2 Air Toxic. U.S. Department of Transportation, 2003.
41. Seinfeld, J. H.; Pandis, S. N. *Atmospheric Chemistry and Physics: From Air Pollution to Climate Change*; John Wiley & Sons, Inc.: New York, 1998; pp 309−313.
42. National Ambient Air Quality Standards for Ozone. *Fed. Regist.* **2010**, *75* (11), 2938−3052. http://www.epa.gov/air/ozonepollution/fr/20100119.pdf.
43. Wagner, T.; Wyszynski, M. L. Aldehydes and ketones in engine exhaust emissions: A review. *Proc. Inst. Mech. Eng., Part D* **1996**, *210*, 109–122.
44. Krahl, J.; Munack, A.; Bahadir, M.; Schumacher, L.; Elser, N. Review: Utilization of Rapeseed Oil, Rapeseed Oil Methyl Ester or Diesel Fuel: Exhaust Gas Emissions and Estimation of Environmental Effects. Society of Automotive Engineers, Inc., International Fall Fuels and Lubricant Meeting, San Antonio, TX, Paper No. 962096, 1996.
45. Staat, F.; Gateau, P. The Effects of Rapeseed Oil Methyl Ester on Diesel Engine Performance, Exhaust Emissions and Long-Term Behavior: A Summary of Three Years of Experimentation. Society of Automotive Engineers, Inc., International Congress & Exposition, February 1995, Detroit, MI, Paper No. 950053, 1995.
46. He, C.; Ge, Y.; Tan, J.; You, K.; Han, X.; Wang, J.; You, Q.; Shah, A. N. Comparison of carbonyl compounds emissions from diesel engine fueled with biodiesel and diesel. *Atmos. Environ.* **2009**, *43* (24), 3657–3661.
47. Lin, Y. C.; Wu, T. Y.; Ou-Yang, W. C.; Chen, C. B. Reducing emissions of carbonyl compounds and regulated harmful matters from a heavy-duty diesel engine fueled with paraffinic/biodiesel blends at one low load steady-state condition. *Atmos. Environ.* **2009**, *43* (16), 2642–2647.
48. Liu, Y. Y.; Lin, T. C.; Wang, Y. J.; Ho, W. L. Carbonyl compounds and toxicity assessments of emissions from a diesel engine running on biodiesels. *J. Air Waste Manage. Assoc.* **2009**, *59* (2), 163–171.
49. Di, Y.; Cheung, C. S.; Huang, Z. Experimental investigation on regulated and unregulated emissions of a diesel engine fueled with ultra-low sulfur diesel fuel blended with biodiesel from waste cooking oil. *Sci. Total Environ.* **2009**, *407* (2), 835–846.
50. Guarieiro, L. L. N.; Pereira, P. A. P.; Torres, E. A.; Rocha, G. O.; Andrade, J. B. Carbonyl compounds emitted by a diesel engine fuelled with diesel and biodiesel–diesel blends: Sampling optimization and emissions profile. *Atmos. Environ.* **2008**, *42* (35), 8211–8218.
51. Peng, C. Y.; Yang, H. H.; Lan, C. H.; Chien, C. M. Effects of the biodiesel blend fuel on aldehyde emissions from diesel engine exhaust. *Atmos. Environ.* **2008**, *42* (5), 906–915.
52. Correa, S. M.; Arbilla, G Carbonyl emissions in diesel and biodiesel exhaust. *Atmos. Environ.* **2008**, *42* (4), 769–775.
53. Baldassarri, L. T.; Battistelli, C. L.; Conti, L.; Crebelli, R.; Berardis, B. D.; Iamiceli, A. L.; Gambino, M.; Iannaccone, S Emission comparison of urban bus engine fueled with diesel oil and 'biodiesel' blend. *Sci. Total Environ.* **2004**, *327* (1-3), 147–162.

Downloaded by DUKE UNIV on June 6, 2012 | http://pubs.acs.org
Publication Date (Web): November 29, 2011 | doi: 10.1021/bk-2011-1084.ch013

54. Cardone, M.; Prati, M. V.; Rocco, V.; Seggiani, M.; Senatore, A.; Vitolo, S *Brassica carinata* as an alternative oil crop for the production of biodiesel in Italy: Engine performance and regulated and unregulated exhaust emissions. *Environ. Sci. Technol.* **2002**, *36* (21), 4656–4662.
55. Fontaras, G.; Karavalakis, G.; Kousoulidou, M.; Tzamkiozis, T.; Ntziachristos, L.; Bakeas, E.; Stournas, S.; Samaras, Z. Effects of biodiesel on passenger car fuel consumption, regulated and non-regulated pollutant emissions over legislated and real-world driving cycles. *Fuel* **2009**, *88* (9), 1608–1617.
56. Karavalakis, G.; Alvanou, F.; Stournas, S.; Bakeas, E. Regulated and unregulated emissions of a light duty vehicle operated on diesel/palm-based methyl ester blends over NEDC and a non-legislated driving cycle. *Fuel* **2009**, *88* (6), 1078–1085.
57. Karavalakis, G.; Stournas, S.; Bakeas, E. Light vehicle regulated and unregulated emissions from different biodiesels. *Sci. Total Environ.* **2009**, *407* (10), 3338–3346.
58. Karavalakis, G.; Stournas, S.; Bakeas, E. Effects of diesel/biodiesel blends on regulated and unregulated pollutants from a passenger vehicle operated over the European and the Athens driving cycles. *Atmos. Environ.* **2009**, *43* (10), 1745–1752.
59. Scull, N.; Kim, C.; Foster, D. E. Comparison of Unburned Fuel and Aldehyde Emissions from a Methanol-Fueled Stratified Charge and Homogeneous Charge Engine. Society of Automotive Engineers, Inc., Paper No. 861543, 1986.
60. Kim, C.; Foster, D. E. Aldehyde and Unburned Fuel Emission Measurement from a Methanol-Fueled Texaco Stratified Charge Engine. Society of Automotive Engineers, Inc., Paper No. 852120, 1985.
61. Challen, B.; Baranescu, R., Eds.; *Diesel Engine Reference Book*, 2nd ed.; Butterworth Heinemann: Oxford, 1999; p 91.
62. Maher, K. D.; Bressler, D. C. Pyrolysis of triglyceride materials for the production of renewable fuels and chemicals. *Bioresour. Technol.* **2007**, *98*, 2351–2368.
63. Hurd, C. D.; Blunck, F. H. The pyrolysis of esters. *J. Am. Chem. Soc.* **1938**, *60*, 2419.
64. Higman, E. B.; Schmeltz, I.; Schlotzhauer, W. S. Products from the thermal degradation of some naturally occurring materials. *J. Agric. Food Chem.* **1970**, *18* (4), 636–639.
65. Higman, E. B.; Schmeltz, I.; Higman, H. C.; Chortyk, O. T. Products from the thermal degradation of some naturally occurring materials. II. Products from the pyrolysis of triglycerides at 400º. *J. Agric. Food Chem.* **1973**, *21* (2), 202–204.
66. Nawar, W. W.; Dubravcic, M. D. *J. Am. Oil Chem. Soc.* **1968**, *45*, 100.
67. Nawar, W. W. Thermal degradation of lipids: A review. *J. Agric. Food Chem.* **1969**, *17* (1), 18–21.
68. Lipinsky, E. S.; Anson, D.; Longanbach, J. R.; Murphy, M. Thermochemical applications for fats and oils. *J. Am. Oil Chem. Soc.* **1985**, *62* (5), 940–942.

Downloaded by DUKE UNIV on June 6, 2012 | http://pubs.acs.org
Publication Date (Web): November 29, 2011 | doi: 10.1021/bk-2011-1084.ch013

Downloaded by DUKE UNIV on June 6, 2012 | http://pubs.acs.org
Publication Date (Web): November 29, 2011 | doi: 10.1021/bk-2011-1084.ch013

69. Crossley, A.; Heyes, T. D.; Hudson, B. J. F. The effect of heat on pure triglycerides. *J. Am. Oil Chem. Soc.* **1962**, *39* (1), 9–14.
70. Schwab, A. W.; Dykstra, G. J.; Selke, E.; Sorenson, S. C.; Pryde, E. H. Diesel fuel from thermal decomposition of soybean oil. *J. Am. Oil Chem. Soc.* **1988**, *65* (11), 1781–1786.
71. Ramanathan, V.; Sakuragi, T.; Kummerow, F. A. Thermal oxidation of methyl esters of fatty acids. *J. Am. Oil Chem. Soc.* **1959**, *36*, 244–248.
72. Lima, D. G.; Soares, V. C. D.; Ribeiro, E. B.; Carvalho, D. A.; Cardoso, E. C. V.; Rassi, F. C.; Mundim, K. C.; Rubim, J. C.; Suarez, P. A. Z. Diesel-like fuel obtained by pyrolysis of vegetable oils. *J. Anal. Appl. Pyrolysis* **2004**, *71*, 987–996.
73. Uzun, B. B.; Putun, A. E.; Putun, E. Composition of products obtained via fast pyrolysis of olive-oil residue: Effect of pyrolysis temperature. *J. Anal. Appl. Pyrolysis* **2007**, *79*, 147–153.
74. Sadrameli, S. M.; Green, A. E. S. Systematics of renewable olefins from thermal cracking of canola oil. *J. Anal. Appl. Pyrolysis* **2007**, *78*, 445–451.
75. Canakci, M.; Van Gerpen, J Biodiesel production from oils and fats with high free fatty acids. *Trans. ASAE* **2001**, *44* (6), 1429–1436.
76. Ristori, A.; Dagaut, P.; Cathonnet, M. The oxidation of n-Hexadecane: experimental and detailed kinetic modeling. *Combust. Flame* **2001**, *125* (3), 1128–1137.
77. Westbrook, C. K.; Pitz, W. J.; Westmoreland, P. R.; Dryer, F. L.; Chaos, M.; Osswald, P.; Kohse-Hoinghaus, K.; Cool, T. A.; Wang, J.; Yang, B.; Hansen, N.; Kasper, T. A detailed chemical kinetic reaction mechanism for oxidation of four small alkyl esters in laminar premixed flames. *Proc. Combust. Inst.* **2009**, *32*, 221–228.
78. Hurley, M. D.; Ball, J. C.; Wallington, T. J.; Toft, A.; Nielsen, O. J.; Bertman, S.; Perkovie, M. Atmospheric chemistry of a model biodiesel fuel, $CH_3C(O)O(CH_2)_2OC(O)CH_3$: Kinetics, mechanisms, and products of Cl atom and OH radical initiated oxidation in the presence and absence of NOx. *J. Phys. Chem. A* **2007**, *111*, 2547–2554.
79. Osswald, P.; Struckmeler, U.; Kasper, T.; Kohse-Hoinghaus, K.; Wang, J.; Cool, T. A.; Hansen, N.; Westmoreland, P. R. Isomer-specific fuel destruction pathways in rich flames of methyl acetate and ethyl formate and consequences for the combustion chemistry of esters. *J. Phys. Chem. A* **2007**, *111*, 4093–4101.
80. Fisher, E. M.; Pitz, W. J.; Curran, H. J.; Westbrook, C. K. Detailed chemical kinetic mechanisms for combustion of oxygenated fuels. *Proc. Combust. Inst.* **2000**, *28*, 1579–1586.
81. Gail, S.; Thomson, M. J.; Sarathy, S. M.; Syed, S. A.; Dagaut, P.; Dievart, P.; Marchese, A. J.; Dryer, F. L. A wide-ranging kinetic modeling study of methyl butanoate combustion. *Proc. Combust. Inst.* **2007**, *31*, 305–311.
82. Huynh, L. K.; Violi, A. Thermal decomposition of methyl butanoate: Abinitio study of a biodiesel fuel surrogate. *J. Org. Chem.* **2008**, *73*, 94–101.

In Synthetic Liquids Production and Refining; de Klerk, A., et al.;
ACS Symposium Series; American Chemical Society: Washington, DC, 2011.

83. Herbinet, O.; Pitz, W. J.; Westbrook, C. K. Detailed chemical kinetic oxidation mechanism for a biodiesel surrogate. *Combust. Flame* **2008**, *154*, 507–528.
84. Dayma, G.; Gail, S.; Dagaut, P Experimental and kinetic modeling study of the oxidation of methyl hexanoate. *Energy Fuels* **2008**, *22*, 1469–1479.
85. Dayma, G.; Togbe, C.; Dagaut, P Detailed kinetic mechanism for the oxidation of vegetable oil methyl esters: New evidence from methyl heptanoate. *Energy Fuels* **2009**, *23*, 4254–4268.
86. Zhang, Y.; Yang, Y.; Boehman, A. L. Premixed ignition behavior of C9 fatty acid esters: A motored engine study. *Combust. Flame* **2009**, *156*, 1202–1213.
87. Zhang, Y.; Boehman, A. L. Experimental study of the autoignition of $C_8H_{16}O_2$ ethyl and methyl esters in a motored engine. *Combust. Flame* **2010**, *157*, 546–555.
88. Lai, J. Y. W.; Lin, K. C.; Violi, A. Biodiesel combustion: Advances in chemical kinetic modeling. *Prog. Energy Combust. Sci.* **2011**, *37*, 1–14.
89. Szybist, J. P.; Boehman, A. L.; Haworth, D. C.; Koga, H. Premixed ignition behavior of alternative diesel fuel-relevant compounds in a motored engine experiment. *Combust. Flame* **2007**, *149*, 112–128.
90. Billaud, F.; Dominguez, V.; Broutin, P.; Busson, C Production of hydrocarbons by pyrolysis of methyl esters from rapeseed oil. *J. Am. Oil Chem. Soc.* **1995**, *72* (2), 1149–1154.
91. Archambault, D.; Billaud, F Experimental and modeling study of methyl oleate pyrolysis between 500 and 650 ºC. *J. Chim. Phys.* **1999**, *96*, 778–796.
92. Dagaut, P.; Gail, S.; Sahasrabudhe, M. Rapeseed oil methyl ester oxidation over extended ranges of pressure, temperature, and equivalence ratio: Experimental and modeling kinetic study. *Proc. Combust. Inst.* **2007**, *31*, 2955–2961.
93. Hakka, M. H.; Glaude, P.-A.; Herbinet, O.; Battin-Leclerc, F Experimental study of the oxidation of large surrogates for diesel and biodiesel fuels. *Combust. Flame* **2009**, *156*, 2129–2144.
94. Bax, S.; Hakka, M. H.; Glaude, P.-A.; Herbinet, O Experimental study of the oxidation of methyl oleate in a jet-stirred reactor. *Combust. Flame* **2010**, *157*, 1220–1229.
95. Ranzi, E.; Frassoldati, A.; Granata, S.; Faravelli, T. Wide-range kinetic modeling study of the pyrolysis, partial oxidation, and combustion of heavy n-alkanes. *Ind. Eng. Chem. Res.* **2005**, *44* (14), 5170–5183.
96. Oberdorfer, P. E. The Determination of Aldehydes in Automobile Exhaust Gas. Society of Automotive Engineers, Inc., Paper No. 670123, 1967.
97. Shore, P. R.; Humphries, D. T.; Hsdded, O. Speciated Hydrocarbon Emissions from Aromatic, Olefinic, and Paraffinic Model Fuel. Society of Automotive Engineers, Inc., Paper No. 930373, 1993.
98. Wornat, M. J.; Ledesma, E. B.; Marsh, N. D. Polycyclic aromatic hydrocarbons from the pyrolysis of catechol (ortho-dihydroxybenzene): A model fuel representative of entities in tobacco, coal, and lignin. *Fuel* **2001**, *80*, 1711–1726.

Downloaded by DUKE UNIV on June 6, 2012 | http://pubs.acs.org
Publication Date (Web): November 29, 2011 | doi: 10.1021/bk-2011-1084.ch013

99. Yang, J.; Lu, M. Thermal decomposition of methylnaphthalenes. *Environ. Sci. Technol.* **2005**, *39*, 3077–3082.

100. Mulholland, J. A.; Sarofim, A. F.; Sosothikul, P.; Lafleur, A. Effects of organic chlorine on the chemical-composition and carbon number-distribution of pyrolysis tars. *Combust. Flame* **1993**, *92* (1-2), 161–177.

101. Compendium of Methods for the Determination of Toxic Organic Compounds in Ambient Air, 2nd ed.; Compendium Method TO-11A; EPA/625/R-96/010b; U.S. Environmental Protection Agency (USEPA): Washington, DC, 1999.

Downloaded by DUKE UNIV on June 6, 2012 | http://pubs.acs.org
Publication Date (Web): November 29, 2011 | doi: 10.1021/bk-2011-1084.ch013

Editors' Biographies

Arno de Klerk

Arno de Klerk holds a Ph.D. in Chemical Engineering and MSc in Analytical Chemistry, both from the University of Pretoria. He is a registered professional engineer in South Africa and in Alberta, Canada. After completion of his engineering degree, he spent approximately 3 years in Forensic Science, before moving to industry as a process engineer. The next 14 years were spent in the energy sector where he was involved with industrial coal-to-liquids and gas-to-liquids facilities, mainly in the field of design, catalysis and refining. He was research manager of the Fischer–Tropsch Refinery Catalysis group in Sasol Technology from 2001–2008. In 2009, he took up a position in the Department of Chemical and Materials Engineering at the University of Alberta, where he is presently the Nexen Professor in Catalytic Reaction Engineering. His research is still in the energy sector and is presently focused on coal and oil sands conversion. He has published approximately 50 papers, many of which have appeared in ACS journals, as well as authored books on "Catalysis in the Refining of Fischer–Tropsch Syncrude" (2010) and "Fischer–Tropsch Refining" (2011).

David L. King

David L. King has a Ph.D. from Harvard University in Physical Chemistry. He is a Laboratory Fellow and Team Lead of the Catalysis Science and Application Group at the Pacific Northwest National Laboratory (PNNL). He is co-lead for the Energy Conversion Initiative, a laboratory level initiative that has a goal to develop PNNL as a Center of Excellence for Air- and Water-Neutral Hydrocarbon Conversions, focusing on clean coal and CO_2 capture technologies. Dr. King has served as principal investigator and project manager for several programs at PNNL, including solid oxide on-anode natural gas reforming, liquid and gaseous hydrocarbon fuel desulfurization, hydrogen production from bio-derived liquids, and SOx removal from diesel engine emissions. He has a long-standing interest in production of hydrocarbon liquids from coal and biomass. Prior to Dr. King's arrival at PNNL in 2000, he spent over 20 years with Catalytica, where he was the Principal Investigator for projects in solid acid isobutane (gasoline) alkylation, fuel reforming and desulfurization, synthesis and application of novel molecular sieves, and synthesis of nano-structured metal oxides and zeolites. He also wrote and edited several Catalytica Multiclient Studies. Prior to his years at Catalytica, Dr. King spent 3 years in R&D at Amoco (now BP-Amoco) where his primary efforts focused on Fischer Tropsch catalysis and methanol-to-gasoline conversions. Dr. King holds 16 patents and over 45 peer reviewed publications.

Downloaded by DUKE UNIV on June 6, 2012 | http://pubs.acs.org
Publication Date (Web): November 29, 2011 | doi: 10.1021/bk-2011-1084.ot001

In Synthetic Liquids Production and Refining; de Klerk, A., et al.;
ACS Symposium Series; American Chemical Society: Washington, DC, 2011.

Subject Index

A

AAFRF. *See* Assured Aerospance Fuels Research Facility (AAFRF)
Absorbance spectra
  $Ca(OAc)_2$, 80*f*
  profile for 100 ppb As, 91*f*
  profile for 100 ppb Sb, 80*f*, 92*f*
  profile for 100 ppb Se, 92*f*
  third-derivative of absorbance spectra for organic sulfur model compounds, 106*f*
  third-derivative of absorbance spectra for pyrite and pyrrhotite model compounds, 105*f*
  vs. GFAAS software, 80
Activation energies calculations, 79
  application and comparison of various methods, 82
  slope and pre-exponentials, 81
ADC. *See* Athens Driving Cycle (ADC)
Agilent Model 7890 GC, 280
AIC. *See* Akaike Information Criterion (AIC)
Akaike Information Criterion (AIC), 261
Anderson-Schulz-Flory model, 200, 239
Argonne Premium Coals, 104
Arrhenius equation, 261
Arrhenius plot, 80
ASF chain growth factor, 210*f*
Assured Aerospance Fuels Research Facility (AAFRF), 280
Athens Driving Cycle (ADC), 294
Atomization, 77
  activation energies for As, Sb, and Se, 91*t*
Avicel cellulose, 30
  first order reaction kinetic model, 31
  study, 47

B

Badische Analin und Soda Fabrik (BASF), 17
BASF. *See* Badische Analin und Soda Fabrik (BASF)
BET measurements
  catalysts, 130
  surface area, porosity, and hydrogen chemisorption with pulse reoxidation, 132*t*
Biodiesel
  alternative fuel, 290
  blends, 291
  compositions of fuel, 290
  compositions of various types, 292*t*
  experimental setup, 33
  pollutant emission for heavy-duty highway engines, 293*f*
  pollutant emissions, 291
Biomass
  feedstocks, 9
  flash pyrolysis, 38
  hydro-pyrolysis, 30
  kinetic parameters current studies, 55*t*
  kinetic parameters previous studies, 57*t*
  thermochemical degradation, 40
Biomass to Ethanol (BTE), 112
Biomass to Liquids (BTL), 2, 11, 111, 112
Blending Cetane Number, gasoil fraction, 240
Boudouard reaction, 39, 44
β-Scission, 248
BTE. *See* Biomass to Ethanol (BTE)
BTL. *See* Biomass to Liquids (BTL)

C

CAER kinetic model, 127
Calcined catalyst
  surface area, pore volume, phase- and elemental composition, 115*t*
  X-ray diffractograms, 116*f*
  XRD, 192*f*
Carbon dioxide (CO_2), 215
Carbon E-factors, 231, 232*t*
Carbon efficiency, 227
  coal-to-liquids, 229
    facilities based on Fischer–Tropsch synthesis, 229*t*
  energy consumption, 227
  H:C ratio, 227
  phase change, 228
  thermal efficiency, 228
Carbon loss, 229
  CO_2, 230
  energy requirements, 230
  incomplete conversion, 231

Downloaded by 89.163.35.42 on June 6, 2012 | http://pubs.acs.org
Publication Date (Web): November 29, 2011 | doi: 10.1021/bk-2011-1084.ix002

Downloaded by 89.163.35.42 on June 6, 2012 | http://pubs.acs.org
Publication Date (Web): November 29, 2011 | doi: 10.1021/bk-2011-1084.ix002

  incomplete recovery, 231
  unselective conversion, 231
Carbon monoxide (CO), 217
Carbon source
  effect, 217
  impact, 228
Carburization, 157
  temperature-programmed, 158
Catalyst characterization, 132
Catalyst pretreatment, 131
Catalytic direct liquefaction, 9
CCD. *See* Central Composite Design (CCD)
C_{22+} conversion
  kerosene/gasoil, 245*f*
  middle distillate, 247*f*
  middle distillate yields, 245*f*
  yields of C_{1-4} fraction, 246*f*
  yields of C_{5-9} fraction, 246*f*
Cellulosic biomass, principle, 112
Central Composite Design (CCD), 241, 257
C_{5-9} fraction, isomer concentration, 248*f*
Chapman-Richards model, 185
Chung's method, 81
  application and comparison of various methods, 83
  full derivation, 96
  lnk1 vs. 104/T for 100 ppb Sb constructed using, 84
Cincinnati Metro bus system, 291
CO. *See* Carbon monoxide (CO)
CO_2. *See* Carbon dioxide (CO_2)
Coal, trace elements, 77*f*
Co/Al_2O_3 catalysts, 132
  CO conversion on olefin and paraffin selectivities, 139
  effect of H_2/CO ratio, 136, 136*t*
  HC selectivities, 136, 136*t*
  Pt on hydrocarbon selectivities, 139*t*
  Pt promoter on HC selectivities, 142
Coal pyrolysis, 4
Coal-to-liquids (CTL), 2, 12
  process comparison based 25 000 t/day dry coal, 3*t*
Cobalt catalyst, physicochemical properties of alumina support, 191*t*
CO conversion, 129
CO_2 gasification, 35
  cellulose derivative mass loss, 41*f*
  cellulose mass loss, 41*f*
  CH_4 gas evolution, 67*f*
  CO gas evolution, 66*f*
  gasification kinetic parameters, 53*t*
  grasses and residues derivative mass loss, 44*f*
  grasses and residues mass loss, 43*f*
  H_2 gas evolution, 66*f*
  lignin derivative mass, 36*f*
  lignin mass loss fraction, 36*f*
  pyrolysis kinetic parameters, 52*t*
  thermal decomposition products, 64
  woods derivative mass loss, 43*f*
  woods mass loss fraction, 42*f*
Co/MoO_3/silica-alumina catalyst, 279
  molar distribution, 282*f*
Continuously Stirred Tank Reactor (CSTR), 114, 127, 131
Crude oil refining in United States, transportation, 216*t*
Crystal growth, 121
CSTR. *See* Continuously Stirred Tank Reactor (CSTR)
CTL. *See* Coal-to-liquids (CTL)

D

DCL. *See* Direct coal liquefaction (DCL)
DCM. *See* Dichloromethane (DCM)
Dichloromethane (DCM), 298
Direct coal liquefaction (DCL), 9
  development during 1968-1980, 10*t*
  hydrogen transfer, 13*f*
  Shenhua facility, 15*f*
Direct liquefaction, 9
  conventional crude oil conversion, 8*t*
  historical overview, 9
Drop in solution, 290

E

ECT. *See* Electrical capacitance tomography (ECT)
E-factors, 231, 232*t*
Electrical capacitance tomography (ECT), 185
  average carbon number as function of total pressure, 202*f*
  catalyst preparation and characterisation, 187
  dispersed phase hold-up, 198*f*
  images at different temperature, 194*f*
  physicochemical attributes, 190
  reaction rate and dispersed hold-up on syngas feed composition, 199*f*
  reaction rate as function of total pressure, 200*f*
  reaction runs, 197
  reactor analysis, 194

Downloaded by 89.163.35.42 on June 6, 2012 | http://pubs.acs.org
Publication Date (Web): November 29, 2011 | doi: 10.1021/bk-2011-1084.ix002

- reactor characterisation, 187
- results and discussion, 190
- values of the model parameter, 206*t*

Electronic Pressure Control, 241
Energy Policy Act, 291
Eni - PoliMi model, 256
- kinetic model developed, 258

Escravos GTL project, 20
EU. *See* European Union (EU)
European Union (EU), 290

F

Face-centered cubic (FCC), 162
FAME. *See* Fatty acid methyl esters (FAME)
Fatty acid methyl esters (FAME), 14
FCC. *See* Face-centered cubic (FCC)
Feed gas composition, experimental system response to step change, 192*f*
Feed-to-liquid (XTL), 1
- CO_2 footprint, 5, 7*f*
- future perspective, 3
- history, 2
- non-carbon based carriers, 4
- overview, 1
- sustainability, 3
- technologies, 2
- technology classification, 7

FeFT. *See* Fisher-Tropsch (FeFT) catalysts
Ferric iron, hydrolysis behavior, 122
Ferrihydrite, 119
Fibre glass insulation, 158
FID detector, 241
Final mass, 44
Fischer-Tropsch evaluation, 171
Fischer–Tropsch hydrocarbon synthesis, 222
- effective decrease in feed H:C ratio, 224*t*

Fischer-Tropsch plants, 112
Fischer-Trospch reaction metrics, 194
Fischer-Trospch synthesis (FTS), 9, 17, 18, 114, 128, 156, 185
- BET measurements, 130
- catalyst characterization, 132
- catalyst preparation, 129
- catalyst pretreatment, 131
- catalytic activity, 157
- CO conversion history, 211*f*
- commercial facilities, 20*t*
- experiment, 129
- experimental apparatus, 188*f*
- hydrogen chemisorption with pulse reoxidation, 130
- kinetic experiment, 131
- polymerization pathway, 143
- product analysis, 131
- promoters, 129
- Pt promotional effects, 129

Fisher-Tropsch (FeFT) catalysts, 111
- activities investigated, 117*f*
- calcined precursor pore volume, 118*f*
- calcined precursor iron (hydr)oxide phase, 118*f*
- calcined precursor surface area, 117*f*, 118*f*
- experiment, 113
- performance, 115

Flash pyrolysis, biomass, 14
Freeport coal sample, 104
FTS. *See* Fischer-Trospch synthesis (FTS)
Fuel Gas fractions, 242
Fugacity, molecule, 260

G

Gas Chromatography – Mass Spectrometry system (GC/MS), 298
Gas evolution data, 33
Gas hourly space velocity (GHSV), 158
Gasification, 16, 220
- carbon conversion characteristics, 220*t*

Gasification system, 33
- experimental apparatus, 34*f*
- slow heating rate, 38
- testing methodologies, 33
- volatile evolution products, 64

Gas-inducing impeller, 189*f*
- dispersed holdup as function of solid loading, 195*f*
- effect of dispersed hold-up as function of temperature, 196*f*

Gas-inducing stirred tank (GIST), 186
Gasoil fraction, blending cetane number, 240
Gas reforming, 218
Gas-to-liquid (GTL), 2, 13, 156
GC/MS. *See* Gas Chromatography – Mass Spectrometry system (GC/MS)
GFAAS. *See* Graphite furnace atomic absorption spectrometer (GFAAS)
GHSV. *See* Gas hourly space velocity (GHSV)
GIST. *See* Gas-inducing stirred tank (GIST)
Global emissions standards, 28
Global energy consumption, 2007, 5*t*
Global warming, 290

Downloaded by 89.163.35.42 on June 6, 2012 | http://pubs.acs.org
Publication Date (Web): November 29, 2011 | doi: 10.1021/bk-2011-1084.ix002

Goethite method, 113
Graphite furnace atomic absorption spectrometer (GFAAS), 75
  reducing environment, 86
  software vs. absorbance, 80, 80*f*
GTL. *See* Gas-to-liquid (GTL)

H

H_2. *See* Hydrogen (H_2)
HCP. *See* Hexagonal closed packed (HCP)
H:C ratio, 225
  heteroatom content of alternative carbon sources, 226*t*
  oxygen, nitrogen and sulfur, 227*t*
HDK. *See* Hydrocracking process (HDK)
Heavy wax (HW), 241
  activation energy, 267*f*
  comparison of experimental and calculated effect of pressure, 273*f*
  comparison of experimental and calculated effect of temperature, 272*f*
  comparison of experimental and calculated effect of WHSV, 273*f*
  evolution with chain length of the Langmuir constants, 269*f*
  feed and products distribution plots, 271*f*
  H_2/feed ratio on residue conversion, 274*f*
  parity plots for gasoline fraction, 266*f*
  parity plots for middle distillates fraction, 265*f*
  parity plots for residue, 265*f*
  results of model regression, 264*t*
  VLE calculation, 275*f*
Hematite, 119
Hemi-cellulose, structural component, 39
Hexagonal closed packed (HCP), 162
High temperature Fischer–Tropsch (HTFT), 19
H_2O gasification
  gasification kinetic parameters, 54*t*
  lignin derivative mass loss, 37*f*
  lignin mass loss fraction, 37*f*
  pyrolysis kinetic parameters, 53*t*
HP5890 GC, 131
HTFT. *See* High temperature Fischer–Tropsch (HTFT)
Hubbert-model, 1
HW. *See* Heavy wax (HW)
Hydrocarbon
  estimation of time-constant, 209*t*
  synthesis on catalyst surface, 210
Hydrocarbon feed reservoir, 281*f*
Hydrocarbon synthesis, 156
Hydrocracking of Fischer-Tropsch wax
  experiments, 241
  mass chain length distribution, 241*t*
  product analysis, 241
  terminologies, 242
Hydrocracking process (HDK), 255
  experiments, 257
  tests, 257
Hydrocracking tests, 241
Hydrogen, feed ratio, 283*t*
Hydrogen chemisorption with pulse reoxidation, 130
Hydrogen (H_2), 217
Hydro-pyrolysis, biomass, 30

I

Ideal hydrocracking, 247
Indirect liquefaction, 8, 217
  carbon cost, 233
  carbon efficiency
    air separation, 218
    employed for energy applications, 216
    feed pretreatment, 217
    gas reforming, 218
  conventional crude oil conversion, 8*t*
  generic process flow diagram, 16*f*
  historical overview, 16
  process flow diagram, 217*f*
  sources of carbon loss, 230*f*
IR. *See* Modline 5 infrared (IR) thermometer
Isomer
  C10-14 cut as a function of conversion of C_{22+} fraction, 251*f*
  C_{15-22} cut as a function of conversion of C_{22+} fraction, 251*f*
  C_{5-9} fractions from hydrocracking of HW, LW and from LW, 250*f*
  reaction scheme for the formation of cracking product, 249*f*
Iso-paraffin, chain length distribution, 243*f*, 244*f*

J

JCPDS. *See* Joint Committee on Powder Diffraction Standards (JCPDS)
Jet-stirred reactor (JSR), 297
Joint Committee on Powder Diffraction Standards (JCPDS), 162
JSR. *See* Jet-stirred reactor (JSR)

Downloaded by 89.163.35.42 on June 6, 2012 | http://pubs.acs.org
Publication Date (Web): November 29, 2011 | doi: 10.1021/bk-2011-1084.ix002

K

K-doped catalyst, 163
Kissinger equation, 159

L

Langmuir constant, 267
Langmuir-Hinshelwood-Hougen-Watson (LHHW), 256, 259
Langmuir model, 259
Lewis acid centres, 193
LHHW. *See* Langmuir-Hinshelwood-Hougen-Watson (LHHW)
Light wax (LW), 241
  activation energy, 267*f*
  comparison of experimental and calculated effect of pressure, 273*f*
  comparison of experimental and calculated effect of temperature, 272*f*
  comparison of experimental and calculated effect of WHSV, 273*f*
  evolution with chain length of the Langmuir constants, 269*f*
  feed and products distribution plots, 270*f*
  H_2/feed ratio on residue conversion, 274*f*
  parity plots for middle distillates fraction, 265*f*
  parity plots for residue, 265*f*
  parity plots for the gasoline fraction, 266*f*
  results of model regression, 263*t*
  VLE calculation, 275*f*
Lignin
  pyrolysis, 39
  thermal degradation, 39
  vs. cellulose reaction, 63
Ligno-cellulosics material, 28
  thermal degradation, 29
Liquefied natural gas (LNG), 13
LNG. *See* Liquefied natural gas (LNG)
Low temperature FeFT (LTFeFT), 112
Low temperature Fischer–Tropsch (LTFT), 19
LTFeFT. *See* Low temperature FeFT (LTFeFT)
LTFT. *See* Low temperature Fischer–Tropsch (LTFT)
LW. *See* Light wax (LW)

M

Maghemite, 119
Magnetite, 119
MB. *See* Mono-branched isomer (MB)
MD. *See* Middle distillate (MD)
Methanol, 225
Methanol synthesis, 18
Methyl esters, 290
  existing mechanistic studies, 294
  experimental setup, 297
Methyl oleate oxidation
  experimental set-up, 298*f*
  reactant conversion and carbon recovery, 300*f*
  yields of CO and CO_2, 302*f*
  yields of hydrocarbons, 303*f*
  yields of methyl esters, 304*f*
  yields of other esters, 305*f*
  yields of oxygenated products, 304*f*
Methyl tertiary butyl ether (MTBE), 225
Middle distillate (MD), 242
Mineral inclusions, effect of inorganic matrices, 90
Mo carbide catalysts, 155
  associated arrhenius parameters for FTS, 174*t*
  catalyst characterisation, 158
  catalyst preparation, 157
  CO consumption rate, 172*f*, 173*f*
  effect of H_2 mole fraction on CO consumption rate, 172*f*
  effect of promoter on H_2 and CO heat of desorption, 171*f*
  estimated activation energy difference, 176*t*
  Fischer-Tropsch activity evaluation, 158
  influence of H_2 mole fraction on total olefin-to-paraffin ratio, 177*f*
  influence of promoter on H_2 and CO chemisorption, 170*f*
  influence of reaction temperature on BET surface area, 181*f*
  influence of time-on-stream on chain growth probability, 178*f*
  olefin formation rate, 173, 174*f*
  physical properties, 164*t*
  physicochemical properties, 162, 168*t*
  post-reaction characterisation, 180
  temperature-programmed calcination, 165*f*
  temperature-programmed carburization, 160*f*
  thermogravimetric analysis, 158
  thermogravimetric studies, 159

Downloaded by 89.163.35.42 on June 6, 2012 | http://pubs.acs.org
Publication Date (Web): November 29, 2011 | doi: 10.1021/bk-2011-1084.ix002

  time-on-stream behaviour of total olefin-to-paraffin ratio, 175*f*
  XRD patterns for both promoted and unpromoted, 163*f*
MoC_{1-x} catalysts
  CO-TPD spectrum, 170*f*
  effect of time-on-stream on chain growth factor, 178*f*
  H_2 mole fraction on chain growth factor, 179*f*
  H_2-TPD spectrum, 169*f*
  NH_3-TPD spectra, 166*f*
  physicochemical properties of alumina-supported, 165
Modline 5 infrared (IR) thermometer, 79
  lnk1 vs. 104/T obtained using the temperatures recorded, 86*f*
  temperature vs. time plots recorded, 86*f*
Mono-branched isomer (MB), 256
MTB. *See* Multi-branched (MTB) isomers
MTBE. *See* Methyl tertiary butyl ether (MTBE)
Multi-branched (MTB) isomers, 256

N

NEDC. *See* New European Driving Cycle (NEDC)
New European Driving Cycle (NEDC), 294
n-Hexadecane, 279, 280
NH_3-TPD spectra
  calcined pure Al_2O_3 support, 166*f*
  MoC_{1-x} catalysts, 166*f*
Non-catalytic direct liquefaction, 10
n-Paraffins, 267

O

Oil crisis, 14
Olefin/paraffin ratio, 134*f*, 135*f*
  CO conversion and carbon number on selectivities, 140*f*, 141*f*
  H_2/CO ratio and carbon number on selectivities, 137*f*, 138*f*
  Pt promoter and carbon number on selectivities, 144*f*, 145*f*, 146*f*
Organic acid method, 121
Organic acid preparation, 113
  iron (hydr)oxides as monitored by solution pH, 123*f*
Organosolv lignin, 36
Oxycarbide, 159
  activation energy, 162*f*
  estimation of activation energy, 162*f*
Oxygenate selectivities
  H_2/CO ratios and CO conversions, 148*t*
  Pt promoter, 147

P

P1. *See* Temperature peak (P1)
Paraffinic species, normalised reaction rate history, 208*f*
Paraffins
  Langmuir constant, 268
  oil, 196
  physisorption, 259
Parameter estimates of equation, 180*t*
Particulate matter (PM), 291
Peak oil, 1
Pennsylvania Upper Freeport third-derivative spectrum, 105*f*
Petro-diesel consumption, 290
PetroSA gas-to-liquids, 217
PFR. *See* Plug flow reactor (PFR)
Plateau, 202
Plug flow reactor (PFR), 297
PM. *See* Particulate matter (PM)
Potassium waterglass, 113
Pott-Broche process, 10
Precipitation, fundamentals, 119
Pre-exponential factors, calculated for As, Sb, Se, 91*t*
Process engineering, 6
Pt promoter, 127
  CO conversion, 133*f*
  kinetic behavior of 15%Co/Al_2O_3, 150, 150*t*
  oxygenate selectivities, 147
Pyrite, 104
  sample, 104
Pyrolysis, 9
  almond shells, 29
  kinetic parameters, 44

Q

Quantachrome Autosorb-1 unit, 187
Quartz filter, 298

R

Rapeseed methyl ester (RME), 290
  experiment, 296

Downloaded by 89.163.35.42 on June 6, 2012 | http://pubs.acs.org
Publication Date (Web): November 29, 2011 | doi: 10.1021/bk-2011-1084.ix002

Rate-determining step (RDS), 259
RDS. *See* Rate-determining step (RDS)
Redlich-Kwong-Soave equation, 249
Residence-time distribution (RTD), 186
Reverse water gas shift reaction (rWGS), 64
RME. *See* Rapeseed methyl ester (RME)
ROM. *See* Run of mine (ROM)
RTD. *See* Residence-time distribution (RTD)
Ruhrchemie preparation, 113
  modified, 113
Run of mine (ROM), 218
rWGS. *See* Reverse water gas shift reaction (rWGS)

S

Shenhua DCL facility, 15, 15*f*
Shimadzu gas chromatograph, 187
Sigma Aldrich Organosolv lignin, 34
Site time yield (STY), 127
SME. *See* Soybean methyl ester (SME)
Smets' method, 79
  application and comparison of various methods, 82
  full derivation, 94
  lnk1 vs. 104/T function for 100 ppb Sb constructed, 81*f*
SNG. *See* Substitute natural gas (SNG)
Soybean methyl ester (SME), 290
Spectrum Manufacturing Chemical Corporation, 104
SPK. *See* Synthetic paraffinic kerosene (SPK)
SSITKA method, 128
Stoichiometry, 6
STY. *See* Site time yield (STY)
Substitute natural gas (SNG), 225
Sulfur X-ray Near-Edge Absorption Spectroscopy (S-XANES), 103
  experiment, 104
  Illinois #6 third-derivative fit, 107*t*
  result, 106
  third-derivative fit results, 107*t*
Sustainability, 3
S-XANES. *See* Sulfur X-ray Near-Edge Absorption Spectroscopy (S-XANES)
Synchronization, 85
Syncrude refining, 224
Syngas cleaning, 222
Syngas feed composition, 201*f*
  behaviour of olefin-to-paraffin ratio, 203*f*
Syngas-to-syncrude conversion, 222
  product phases at ambient conditions, 223*t*
  typical operating conditions and per pass CO conversion, 223*t*
Synthesis gas, 217
Synthesis gas generation, 17
Synthetic paraffinic kerosene (SPK), 279
  Fischer-Tropsch, 280

T

Ta-lined furnaces, 78
  absorbance profiles for 100 ppb As, 88*f*
  absorbance profiles for 100 ppb Se, 88*f*
  activation energies for As and Se, 89*t*
  lnk1 vs. 104/T for 100 ppb As, 88*f*
  lnk1 vs. 104/T for 100 ppb Se, 89*f*
  neutral environment representing excluded mineral, 87
TCD. *See* Thermal conductivity detector (TCD)
TE. *See* Trace elements (TE)
Temperature peak (P1), 159
Temperature Programmed Reduction (TPR), 130
Temperature Programmer Interface/ Thermal Analyzer, 33
Thermal conductivity detector (TCD), 130
Thermal decomposition, 30
Thermodynamics, second law, 6
Time-on-stream, effect of temperature, 204
TOPR. *See* Total olefin-to-paraffin ratio (TOPR)
Total olefin-to-paraffin ratio (TOPR), 177
TPR. *See* Temperature Programmed Reduction (TPR)
Trace elements (TE), 75
  absorbance measurements, 78
  activation energies, 87*t*
  atomization activation energies, 77
  behavior, 76
  coal, 77*f*
  instrument operation, 78
  materials and reagents, 78
  organically associated, 77
  original biomass, 76
  partitioning in coal, 76
  solutions, 78
  temperature measurements and instrument modifications, 79
Tubular fixed-bed reactor system, 280

U

U.S. Air Force, 279, 280

V

Vaporization, 77
Vapour–liquid equilibrium (VLE), 242
  calculation, 248
  paraffin, 256
VLE. *See* Vapour–liquid equilibrium (VLE)

W

Waste-to-liquids (WTL), 2, 14
Water gas shift conditioning, 221
Waxes distribution, LW and HW, 258*f*
WTL. *See* Waste-to-liquids (WTL)

X

X-ray diffraction, 162
X-ray diffractograms, 114
  calcined catalyst, 116*f*
XTL. *See* Feed-to-liquid (XTL)

Y

Yan's method, 81
  application and comparison of various methods, 81
  full derivation, 96
  ln Y vs. 104/T for 100 ppb Sb constructed, 85*f*

Downloaded by 89.163.35.42 on June 6, 2012 | http://pubs.acs.org
Publication Date (Web): November 29, 2011 | doi: 10.1021/bk-2011-1084.ix002